CYGNSS Handbook

Cyclone Global Navigation Satellite System

Measuring Surface Wind Speed In Tropical Cyclones
Deriving Heat Flux at the Ocean Surface
Imaging Wetlands, Rivers and Floodwater Extent
Retrieving Near Surface Soil Moisture

Contents

Revision History

Date	Version
1 April 2016	Original copy
1 December 2022	2nd edition

Key Authors

Chris Ruf (Principal Investigator)
Department of Climate and Space Sciences and
  Engineering
University of Michigan
Ann Arbor, MI 48109
Email: cruf@umich.edu

Darren McKague (Science Team Member, University of
Michigan Project Manager)
Department of Climate and Space Sciences and
  Engineering
University of Michigan
Ann Arbor, MI 48109
Email: dmckague@umich.edu

Derek Posselt (Science Team Member)
Jet Propulsion Laboratory
California Institute of Technology
Pasadena, CA 91109
Email: Derek.Posselt@jpl.nasa.gov

Scott Gleason (Science Team Member, Instrument
Scientist)
Daaxa LLC
Boulder, CO 80305
Email: gleason@ucar.edu

Maria-Paola Clarizia (Science Team Member)
DEIMOS
Harwell Oxford, Didcot OX11 0RL, United Kingdom
Email: maria-paola.clarizia@deimos-space.com

Valery Zavorotny (Science Team Member)
National Oceanic and Atmospheric Administration
Earth System Research Laboratory, Physical Sciences
  Division
Boulder, CO 80305
Email: vzavorotny@gmail.com

Tim Butler (Science Operations Center Engineering
Lead)
Space Physics Research Laboratory
University of Michigan
Ann Arbor, MI 48109
Email: butlerti@umich.edu

Jillian Redfern (Mission Operations Center Engineering
Lead)
Southwest Research Institute
Boulder, CO 80302
Email: jillian.redfern@swri.org

William Wells (Systems Engineer)
Southwest Research Institute
San Antonio, TX 78238-5166
Email: wwells@swri.edu

Mary Morris (Science Team Member)
Jet Propulsion Laboratory
California Institute of Technology
Pasadena, CA 91109
Email: mary.g.morris@jpl.nasa.gov

Juan Crespo (Science Team Member)
Jet Propulsion Laboratory
California Institute of Technology
Pasadena, CA 91109
Email: juan.a.crespo@jpl.nasa.gov

Clara Chew (Science Team Member)
University Corporation for Atmospheric Research
Boulder, CO 80307
Email: clarac@ucar.edu

Eric Small (Science Team Member)
University of Colorado at Boulder
Boulder, CO 80309
Email: eric.small@colorado.edu

Daniel Pasqual (Science Team Member)
DEIMOS, UK
Harwell Oxford, Didcot OX11 0RL, United Kingdom
Email: daniel.pasqual@deimos-space.com

Tianlin Wang (Science Team Member)
Ohio State University
Columbus, OH 43210
Email: wang.15085@osu.edu

April Warnock (Science Team Member)
SRI International
Ann Arbor, MI 48105
Email: april.warnock@sri.com

David Mayers (Science Team Member)
SRI International
Ann Arbor, MI 48105
Email: david.mayers@sri.com

Mohammad Al-Khaldi (Science Team Member)
Ohio State University
Columbus, OH 43210
Email: al-khaldi.2@osu.edu

Andrew J. O'Brien (Research Scientist)
Ohio State University
Columbus, OH 43212
Email: obrien.200@osu.edu

Preface

The *CYGNSS Handbook* was compiled in 2015 to serve as a source of information about the mission and its data products for potential data users. The handbook was updated to describe multiple changes to data processing and products in 2022. The collaborative effort of many individuals has enabled its production. The organization of the handbook is as follows:

Chapter 1 describes the motivation for the project and includes a discussion about tropical cyclones and current technologies for observing and forecasting them, as well as the unique impact the CYGNSS mission will have on the advancement of our scientific understanding in this field.

Chapter 2 outlines the science objectives as well as the baseline mission requirements. Additionally, a mission synopsis explains the different phases of the mission and provides an overview of the flow of information, the ground data processing, and the flight segment hardware required to support the mission.

Chapter 3 explains the mission design in detail, including the orbital elements, the observatory, and the science payload.

Chapter 4 gives the reader an overview of the data products at each level of processing, including descriptions of their temporal and spatial resolutions.

Chapters 5 through 10 provide relevant excerpts from the project Algorithm Theoretical Basis Documents (ATBDs). The ATBDs give the reader a more comprehensive explanation of each level of data product, including the physical and mathematical descriptions of the algorithms used in the generation of the Science Data Products, an explanation of uncertainty estimates, and considerations of calibration, validation, exception control, and diagnostics.

Chapter 11 presents both a top-down and a bottom-up assessment of Level 1 (basic observable) and Level 2 (wind speed estimate) uncertainties.

The handbook concludes with a list of project publications in Chapter 12 and a list of acronyms in Chapter 13. The document concludes with an appendix describing the ocean surface bistatic scattering forward model. The forward model relates the state of the ocean to the measurements made by CYGNSS and is a fundamental mathematical framework for the science behind the CYGNSS data products.

The unique role of CYGNSS in our understanding of tropical cyclones derives from its ability to use the reflected signal from the GPS constellation in order to determine sea surface wind speed with unprecedented spatial and temporal coverage. CYGNSS is a constellation of eight low-Earth-orbiting microsatellites, each capable of measuring four simultaneous reflections for a total of 32 spatially separated wind measurements every second. Its use of L-band GPS signals allows CYGNSS to make measurements within the eyewall of hurricanes with no significant degradation in performance arising from the intense precipitation (a significant concern with higher frequency scatterometers). As such, the CYGNSS mission will enable a more comprehensive understanding of air-sea exchange processes and thus an enhanced capability to forecast tropical storm formation and intensification.

Acknowledgments

Some of the information in this handbook has been drawn from material that has been previously published or material that was in press or under review at the time this handbook was being compiled. To provide proper recognition conveniently in one location for the reader, the sections of this handbook that come from other material and their appropriate citations will be listed below. Each section that contains reused material is listed individually.

Chapter 4

The text in the first paragraph of Chapter 4, Part I A and the text in Chapter 4, Part I B, Level 2 Wind Speed, are taken from the following article, which was under review at the time this handbook was compiled:

Clarizia, M. P., & Ruf, C. S. (2016). Wind speed retrieval algorithm for the Cyclone Global Navigation Satellite System (CYGNSS) mission. *IEEE Transactions on Geoscience and Remote Sensing, 54*(8), 4419–4432. https://doi.org/10.1109/TGRS.2016.2541343.

In addition, the error quantification described in the last paragraph of Chapter 4, Part I A, is taken from the text and from Tables II and V of the following article, which was in press at the time this handbook was compiled:

Gleason, S., Ruf, C., Clarizia, M. P., & O'Brien, A. (2016). Calibration and unwrapping of the normalized scattering cross section for the Cyclone Global Navigation Satellite System (CYGNSS). *IEEE Transactions on Geoscience and Remote Sensing, 54*(5), 2495–2509. https://doi.org/10.1109/TGRS.2015.2502245.

Chapter 5

Much of the material in Chapter 5 is taken from the following document, which was in press at the time this handbook was compiled:

Gleason, S., Ruf, C. S., Clarizia, M. P., & O'Brien, A. J. (2016). Calibration and unwrapping of the normalized scattering cross section for the Cyclone Global Navigation Satellite System (CYGNSS). *IEEE Transactions on Geoscience and Remote Sensing, 54*(5), 2495–2509. https://doi.org/10.1109/TGRS.2015.2502245.

Additionally, much of the material on updates to the Level 1 calibration comes from the following publications:

Gleason, S., Al-Khaldi, M. M., Ruf, C. S., McKague, D. S., Wang, T., & Russel, A. (2022). Characterizing and mitigating digital sampling effects on the CYGNSS Level 1 calibration. *IEEE Transactions on Geoscience and Remote Sensing, 60*, 1–12. https://doi.org/10.1109/TGRS.2021.3120026.

Gleason, S., Ruf, C. S., O'Brien, A. J., & McKague, D. S. (2019). The CYGNSS Level 1 calibration algorithm and error analysis based on on-orbit measurements. *IEEE Journal of Selected Topics in Applied Earth Observations and Remote Sensing, 12*(1), 37–49. https://doi.org/10.1109/JSTARS.2018.2832981.

Wang, T., Ruf, C. S., Block, B., McKague, D. S., & Gleason, S. (2019). Design and performance of a GPS constellation power monitor system for improved CYGNSS L1B calibration. *IEEE Journal of Selected Topics in Applied Earth Observations and Remote Sensing, 12*(1), 26–36. https://doi.org/10.1109/JSTARS.2018.2867773.

Specifically, much of the text and many equations in Chapter 5 are taken verbatim from the above articles. In addition, the following figures and tables are taken from the above article:

- Figure 5.1 appears as Figure 2 in Gleason et al., 2016
- Figure 5.2 appears as Figure 7 in Gleason et al., 2019
- Figure 5.3 appears as Figure 3 in Gleason et al., 2019
- Figure 5.4 appears as Figure 4 in Gleason et al., 2019
- Figure 5.5 appears as Figure 2 in Gleason et al., 2019
- Figure 5.6 appears as Figure 5 in Gleason et al., 2022
- Figure 5.7 appears as Figure 7 in Gleason et al., 2022
- Figure 5.8 appears as Figure 11 in Gleason et al., 2022

Chapter 10

Much of the material from Chapter 10 on the Level 3 Soil Moisture product comes from the following document:

Chew, C. C., & Small, E. E. (2018). Soil moisture sensing using spaceborne GNSS reflections: Comparison of CYGNSS reflectivity to SMAP soil moisture. *Geophysical Research Letters, 45*(9), 4049–4057. https://doi .org/10.1029/2018GL077905.

Specifically, much of the text and many equations from Chapter 10 are taken verbatim from the above article. In addition, the following figure is taken from the above article:

- Figure 10.3 is from Figure 2 in Chew and Small, 2018

Chapter 11

Some of the material in Chapter 9 is taken from the following documents:

Clarizia, M. P., & Ruf, C. S. (2016). Wind Speed Retrieval Algorithm for the Cyclone Global Navigation Satellite System (CYGNSS) Mission. *IEEE Transactions on Geoscience and Remote Sensing, 54*(8), 4419–4432. https://doi.org/10.1109/TGRS.2016.2541343.

Ruf, C. S., & Balasubramaniam, R. (2019). Development of the CYGNSS geophysical model function for wind speed. IEEE *Journal of Selected Topics in Applied Earth Observations and Remote Sensing, 12*(1), 66–77. https://doi.org/10.1109/JSTARS.2018.2833075.

Specifically, certain portions of the text and some equations in Chapter 11 are taken verbatim from the above articles. In addition, the following figures are taken from the above articles:

- Figure 11.3 appears in Figures 5 and 17 of Ruf and Balasubramaniam, 2019
- Figure 11.7 appears in Figure 10 of Ruf and Balasubramaniam, 2019
- Figure 11.8a appears in Figure 10 of Ruf and Balasubramaniam, 2019

Appendix

In the appendix to the *CYGNSS Handbook*, some of the figures have been taken, with the author's permission, from the following book:

Gleason, S., & Gebre-Egziabher, D., eds. (2009). *GNSS applications and methods*. Artech House.

- Figure A.2 appears as Figure 16.4 in Gleason and Gebre-Egziabher, 2009
- Figure A.6 appears in Figure 16.8 in Gleason and Gebre-Egziabher, 2009

Also, one figure has been taken, with the author's permission, from the following:

Voronovich, A. G., & Zavorotny, V. U. (2014). Full-polarization modeling of monostatic and bistatic radar scattering from a rough sea surface. *IEEE Transactions on Antennas and Propagation, 62*(3), 1362–1371. https://doi.org/10.1109/TAP.2013.2295235.

- Figure A.10 appears as Figure 1 in Voronovich and Zavorotny, 2014

Also, three figures have been taken, with the author's permission, from the following:

Zavorotny, V. U., & Voronovich, A. G. (2014, July). Recent progress on forward scattering modeling for GNSS reflectometry. In *Geoscience and Remote Sensing Symposium (IGARSS), 2014 IEEE International* (pp. 3814–3817). IEEE.

- Figure A.11a appears as Figure 1 in Zavorotny and Voronovich, 2014
- Figure A.11b appears as Figure 2 in Zavorotny and Voronovich, 2014
- Figure A.12 appears as Figure 3 in Zavorotny and Voronovich, 2014

Also, one figure has been taken from the following:

Clarizia, M. P., & Ruf, C. S. (2016). Wind speed retrieval algorithm for the Cyclone Global Navigation Satellite System (CYGNSS) mission. *IEEE Transactions on Geoscience and Remote Sensing, 54*(8), 4419–4432. https://doi.org/10.1109/TGRS.2016.2541343.

- Figure A.3 appears as Figure 1a in Clarizia and Ruf, 2016

1. Introduction and Background

1.1. Motivation for CYGNSS

1.1.1. Tropical Cyclones

Tropical cyclones (TCs) pose a threat to life and property in coastal locations around the globe and to vessels and structures (e.g., wind farms, oil drilling platforms) on the ocean. Impacts include damaging winds, storm surges, and heavy rains. A TC is defined by the National Oceanic and Atmospheric Administration (NOAA) National Hurricane Center (NHC) as "a warm-core, non-frontal synoptic-scale cyclone, originating over tropical or subtropical waters, with organized deep convection and a closed surface wind circulation about a well-defined center" (National Hurricane Center and Central Pacific Hurricane Center, 2020). The vast majority of TCs form and reach their maximum intensity between 35°S and 35°N latitude, and those that make landfall commonly do so within this latitude band (with a few notable exceptions; e.g., Hurricane Sandy in 2012).

TCs form over the ocean through the organization of convective thunderstorms, and air-sea exchange processes are critical to their formation and intensification. Accurate measurements of ocean surface winds, together with temperature and moisture fluxes, are crucial to the understanding and prediction of TCs. In contrast to midlatitude cyclones, TCs possess a warm core due to latent heat released by condensation, while mature TCs tend to have a more axisymmetric structure. TCs play an important role in the global atmospheric energy budget via their transport of heat and moisture from the tropics to higher latitudes.

1.1.2. Predicting TC Track and Intensity

Numerical weather prediction (NWP) models are the primary tools used to predict the track (position and movement) and intensity of TCs. These models have traditionally been global in extent and comprise solutions of the atmospheric momentum, mass, and energy and water vapor conservation equations. They are commonly run on horizontal grids with scales of 10–20 km—sufficient to simulate large-scale and mesoscale circulations but too coarse to resolve the convective systems that are crucial for TC formation and evolution. As a result, convection, cloud microphysical processes, and turbulence must be approximated (or "parameterized"). In order to more accurately predict the evolution of TCs, NWP centers use data assimilation to combine short-term predictions with a large volume of satellite and in situ data to form initial conditions for NWP models. The main purpose of data assimilation is to provide an improved estimate of atmospheric conditions over what is provided by observations or a previous forecast alone. Improved initial conditions lead to more accurate forecasts of TC track, intensity, and structure. Over the past 20 years, estimates of the range of possible TC forecasts due to uncertainties in both physical parameterization schemes and model initial conditions have been generated using ensembles of global model forecasts. More recently, ensembles have been used as part of the data assimilation system as well.

The leading global models used to provide guidance to US weather prediction are as follows:

- NOAA Global Forecast System (GFS)
- European Centre for Medium-Range Weather Forecasts (ECMWF)
- UK Meteorological Office (UKMET)
- Navy Global Environmental Model (NAVGEM)

In addition to global models, limited-area regional models are used to predict TC structure, track, and intensity. Regional model simulations encompass a smaller geographic area and therefore can be run with higher horizontal resolution than global models. In most TC-specific limited-area simulations, the innermost nested domains with the highest resolution are centered on the TC. As of 2015, the three US operational regional models currently used for TC prediction, along with their finest horizontal grid spacings, are as follows:

- NOAA Hurricane Weather Research and Forecasting (HWRF): 2 km
- Coupled Ocean Atmosphere Mesoscale Prediction System (COAMPS-TC): 5 km
- NOAA Geophysical Fluid Dynamics Laboratory (GFDL): 9 km

In addition to the above-listed dynamical models, statistical models, such as the statistical hurricane intensity prediction scheme (SHIPS) and the logistic growth equation model (LGEM) are used to predict intensity. Several regions around the world use their own global and regional models to predict TC track and intensity.

After decades of focused research into TC dynamics and evolution, operational centers are now able to predict TC track out to a lead time of 5 days with a high degree of accuracy. But during this time, forecast skill for TC intensity has not kept the same pace. There are likely many reasons for slowing improvement in TC intensity forecasts, but the one that is cited often in the community is a *lack of frequent and accurate observations of winds in the inner core of TCs.* Specifically, current satellite observing systems are unable to penetrate heavy rainfall, and in situ measurements by aircraft and dropsondes are limited in space and time. Paucity of observations of surface wind speeds in the most dynamically active portion of a TC leads to (1) inaccuracies in the initial conditions used in subsequent model forecasts and (2) insufficient information for evaluating parameterizations of convection and surface fluxes. The CYGNSS mission is designed to address these shortcomings by providing more accurate and timely observations of surface winds in all precipitation conditions.

1.1.3. Existing Observing Capabilities

Over 90% of the observational data that are routinely assimilated into global forecast models come from geostationary (e.g., the Geostationary Operational Environmental Satellites [GOES]), and polar-orbiting (e.g., the Polar-Orbiting Environmental Satellites [POES]) satellites. The data include radiances, atmospheric motion vectors, infrared and microwave soundings, and GPS radio occultations. Another satellite of particular relevance to TCs is the Global Precipitation Measurement (GPM) platform (the follow-up to the successful Tropical Rainfall Measuring Mission [TRMM] from 1997 to 2014), which provides a three-dimensional view of TC structure using spaceborne scanning radar at two wavelengths. In addition, there are scatterometers that measure wind speed and direction at the ocean surface. However, these scatterometers are unable to provide accurate measurements in regions of heavy precipitation (e.g., convective regions), and therefore sea surface wind data in the inner core of TCs are lacking. Even those satellites that can penetrate heavy rain and view the inner core of hurricanes have revisit times that are too infrequent to capture the fast-evolving processes that lead to rapid TC development.

If a TC poses a potential threat to the United States, NOAA and the US Air Force deploy the "hurricane hunter" aircraft inside and around the TC to better measure its central pressure as well as thermodynamic and dynamic characteristics of the TC and its immediate environment. Ocean surface wind speeds are measured via the stepped frequency microwave radiometer (SFMR). However, the quantity, sampling duration, and range of aircraft missions are limited, and therefore only a small fraction of the total TC activity in the Atlantic basin is sampled by aircraft. No other nations measure ocean surface winds from aircraft.

1.1.4. Unique Role of CYGNSS

The goal of the CYGNSS mission is to understand the relationship among ocean surface properties, moist atmospheric thermodynamics, radiation, and convective dynamics in the inner core of TCs. Near surface winds are major contributors to, and indicators of, momentum and energy fluxes at the air-sea interface. An understanding of the coupling between the surface winds and the moist atmosphere within the TC inner core is required to properly model and forecast its genesis and intensification. The CYGNSS team hypothesizes that the limited degree of improvement in intensity forecasting in recent decades is largely due to a lack of observations and proper modeling of the TC inner core. The inadequacy in observations results from two causes:

1. Much of the TC inner core ocean surface is obscured from conventional remote sensing instruments by intense precipitation in the eyewall and inner rain bands.
2. Conventional polar-orbiting, wide-swath imagers provide poor temporal sampling of the rapidly evolving processes associated with TC genesis and intensification.

CYGNSS addresses these two limitations by combining the all-weather performance of GPS bistatic radar with the spatial and temporal sampling properties of a constellation of eight low Earth orbit observatories at an inclination of 35°.

Each observatory contains a delay-Doppler mapping instrument (DDMI), which receives direct signals from GPS satellites as well as signals reflected off the ocean surface. The direct signals pinpoint the location of the observatory, while the reflected signals respond to ocean surface roughness, from which wind speed is derived. Signals are measured at 1 Hz, and each of the eight observatories is capable of measuring four simultaneous reflections, resulting in 32 wind measurements per second around the globe. This provides the ability to measure ocean surface winds with unprecedented temporal resolution and spatial coverage under all precipitating conditions, up to and including those experienced in the hurricane eyewall.
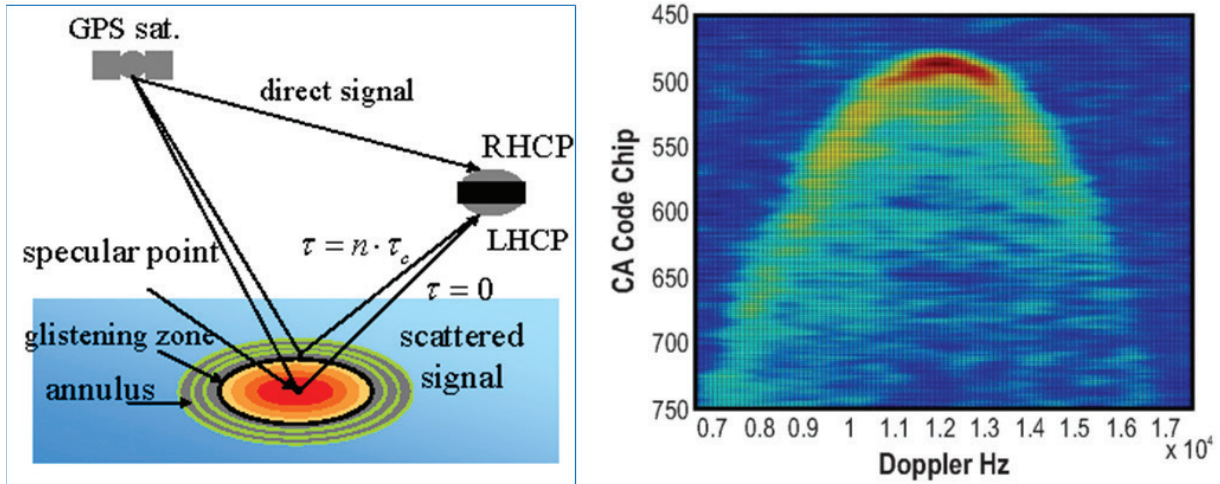
Figure 1.1. *Left:* GPS signal propagation and scattering geometries for ocean surface bistatic quasi-specular scatterometry. *Right:* Spatial distribution of the ocean surface scattering measured by the UK-DMC-1 demonstration spaceborne mission, referred to as the DDM (Gleason, 2007).

Figure 1.1 illustrates the propagation and scattering geometries associated with the GPS bistatic radar approach to ocean surface scatterometry. The direct GPS signal provides a coherent reference for the coded GPS transmitted signal. It is received by a right-hand circularly polarized (RHCP) receive antenna on the zenith side of the space-craft. The quasi-specular, forward-scattered signal from the ocean surface is received by a downward-looking, left-hand circularly polarized (LHCP) antenna on the nadir side of the spacecraft. The properties of the scattered signal are sensitive to the sea surface roughness, from which local wind speed can be derived (Zavorotny & Voronovich, 2000). The scattering cross-section image produced by the Disaster Monitoring Constellation (UK-DMC-1) demonstration spaceborne mission is shown in Figure 1.1. Variable lag correlation and Doppler shift, the two coordinates of the image, enable the spatial distribution of the scattering cross section to be resolved (Gleason et al., 2005). This type of scattering image is referred to as a delay-Doppler map (DDM). Estimation of the ocean surface roughness and wind speed is possible from two properties of the DDM. The maximum scattering cross section (the dark-red region in Figure 1.1) is related to roughness and therefore wind speed. This requires power calibration of the DDM. Wind speed can also be estimated from the shape of the scattering cross-section pattern in the DDM (the red and yellow regions in Figure 1.1). The pattern is produced by scattering from an area surrounding the nominal specular point (SP) on the surface. For a smooth, mirrorlike surface, the pattern would be defined by the GPS bistatic radar ambiguity function. But as the surface becomes

rougher, the GPS signal is scattered by a larger area of the surface in many directions. This causes a reduction in the maximum cross section near the SP and the "spreading" of power into wider delay-Doppler bins. The shape of the DDM pattern also contains information about the sea surface winds. In particular, the shape of its dependence on delay is sensitive to the significant wave height of the surface, which is correlated with wind speed.

CYGNSS measures the power in the GPS signal scattered by the ocean surface after the signals are selectively filtered by time delay and Doppler shift to create a DDM. The time delay is the difference in the time of arrival between the direct signal (propagating directly from the GPS satellite to the CYGNSS satellite) and the signal scattered by the ocean surface. The Doppler shift is the difference in frequency between the received direct signal and the received ocean-scattered signal. Both delay and Doppler are varied in the DDM across a range that includes the nominal specular reflection point on the surface. Shorter delays correspond to locations above the surface, from which there is no significant scattered signal. Longer delays can be mapped to iso-delay contours on the surface surrounding the SP. Varying Doppler of the scattered signals can also be mapped to iso-Doppler contours on the surface that intersect the delay contours to create the DDM. The DDM is thus a map of the diffuse surface scattering in the vicinity of the nominal SP. The transformation between spatial location on the sea surface and location in the DDM is one to one at the DDM specular location but can have ambiguities (i.e., multiple spatial locations mapped to the same DDM location) outside the specular region.
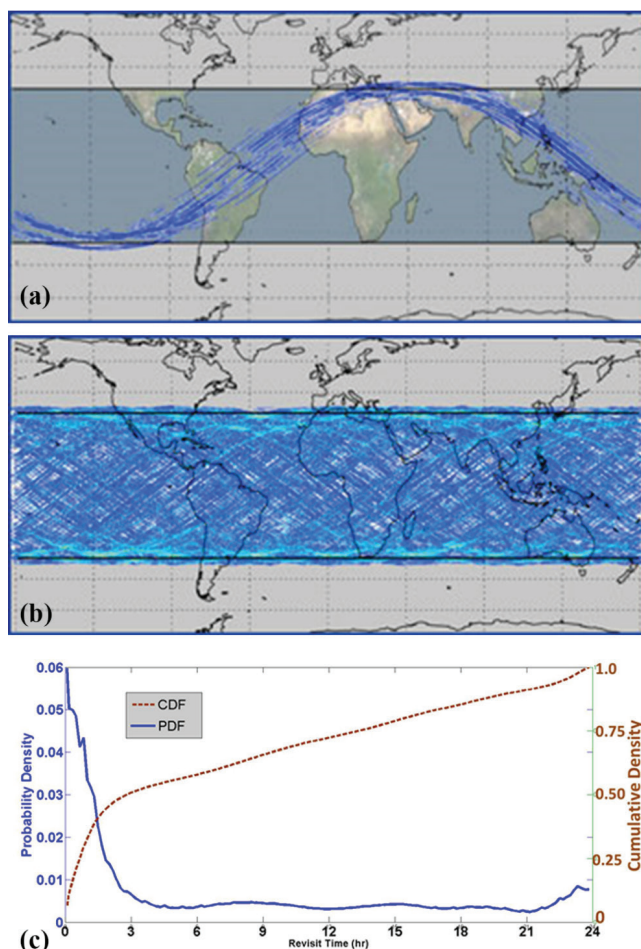
Figure 1.2. Each low-Earth-orbiting CYGNSS observatory will orbit at an inclination of 35° and is capable of measuring four simultaneous reflections, resulting in 32 wind measurements per second across the Earth. The configuration is optimized for high temporal resolution wind field imagery of TC genesis, intensification, and decay. Shown here are the CYGNSS spatial coverage tracks after (a) 90 minutes and (b) 24 hours. Temporal sampling is characterized by the probability and cumulative density functions of revisit time, shown in (c). Sampling occurs randomly due to the asynchronous nature of the CYGNSS and GPS satellite orbits, and revisit time is best characterized via statistics of these distributions. The median and mean revisit times are, respectively, 2.8 and 7.2 hours.

CYGNSS spatial sampling produces Level 2 wind speed data products that consist of 32 simultaneous single-pixel "swaths" that are 25 km wide and typically hundreds of kilometers long, as the SPs move across the surface due to orbital motion by CYGNSS and the GPS satellites. Examples of the spatial coverage obtained after 90 minutes (one orbit) and 24 hours are shown in Figure 1.2a–b. Temporal and spatial sampling occur randomly due to the asynchronous nature of the CYGNSS and GPS satellite orbits. As a result, the CYGNSS revisit time is best described by its probability distribution. The distribution, shown in Figure 1.2c, is derived empirically by using a mission simulator to determine the time and location of each sample within the ±38° latitude coverage zone and then examining the time difference between samples at the same location. The empirical distribution features a high probability of very short revisit times (resulting from sequential samples by trailing satellites spaced 10 minutes apart) and a long, tapering "tail" at higher revisit times. Its median value is 2.8 hours, and the mean revisit time is 7.2 hours.

1.1.5. Description of Previous Airborne and Spaceborne Missions

The first global navigation satellite system reflectometry (GNSS-R) sensor was field tested in 1997 over the Chesapeake Bay, collecting GPS signals scattered from the water surface (Garrison et al., 1998). The first reported wind speed retrieval using GPS ocean-reflected signals occurred in 1999 (Lin et al., 1999) with data taken in 1998. Additional data were

acquired in underflights of the Ocean TOPography Experiment (TOPEX)/Poseidon in 1998 and during the US Navy Electro-Optical Propagation Assessment in Coastal Environments (EOPACE) experiment off the Outer Banks of North Carolina (Garrison et al., 2002). A theoretical framework was then developed that describes the received global navigation satellite system (GNSS) signal as a function of the sea state, the measurement geometry, and the signal processing performed by the receiver (Zavorotny & Voronovich, 2000).

The first effort to study the high wind regimes found in TCs was accomplished in 1998 with flights into the outer bands of Hurricane Bonnie as it made landfall near Topsail Beach, North Carolina. With the cooperation of NOAA, a GPS delay mapping receiver was installed on one of the hurricane hunters in 2000 and acquired the first GPS-reflected data from inside a TC (Katzberg et al., 2001). Since that time, penetration data from TCs have been acquired nearly annually, with only one missing year. Wind speed retrievals have been compared with a large set of dropsonde data and show the GPS method capable of responding well to TC-level wind speeds (Katzberg & Dunion, 2009).

The first successful detection of a GPS surface-reflected signal in space was reported by Lowe et al. (2002). Subsequently, data from the GPS experiment on the UK-DMC satellite demonstrated that signal retrievals of sufficient signal-to-noise ratio (SNR) could be used to perform successful ocean wave and wind estimation (Gleason et al., 2005, 2010; Clarizia et al., 2009, 2014). These results show that it is possible to detect reflected GPS signals from space across a range of surface wind and wave conditions using a relatively modest instrument configuration. Notably, the UK-DMC sensor had a lower receiver antenna gain (11.8 dBi) and is in a higher orbit (686 km) than the CYGNSS design (14 dBi and 510 km, respectively). Therefore, CYGNSS measurements have better sensitivity to surface roughness.

Results from the UK-DMC experiment demonstrate a connection between the near surface wind speed and the measured DDMs. The UK-DMC measurements were made when the specular reflection point passed within 50 km of an active National Data Buoy Center (NDBC) ocean buoy, which provides near surface (at 10 m height referenced) wind information (Gleason, 2013). One example of wind-retrieval performance using UK-DMC data is described by Clarizia et al. (2014), in which a minimum variance (MV) wind speed estimator was developed and tested. The estimator is a composite of winds retrieved using five different observables that are derived from the DDMs. Regression-based wind retrievals are developed for each individual observable using empirical geophysical model functions (GMFs) that are derived from NDBC buoy winds. The root mean square (RMS) error in the MV estimator, for wind speeds over the range $2-12$ m/s^{-1}, is 1.65 m/s^{-1}.

A second GPS bistatic radar satellite experiment, flown on TechDemoSat-1 (TDS-1), was launched in July 2014 and orbits at an altitude of 635 km with an inclination of 98° and a 9:00 p.m. local time of ascending node (Jales & Unwin, 2015). The spaceborne payload consists of a zenith-pointing antenna for direct GPS signal acquisition and the determination of SP locations on the ground, a nadir-pointing antenna with a peak gain of 13.3 dBi for capturing the GPS reflection, and a remote sensing receiver called the SGR-ReSI. The SGR-ReSI operates for 2 days out of an 8-day cycle, generating DDMs. Early analysis of TDS-1 measurements of ocean surface wind speed indicates an RMS error of 2.2 m/s^{-1} over a dynamic range of $3-18$ m/s^{-1} (Foti et al., 2015).

1.2. Project Status Overview

CYGNSS was selected by NASA as its first Earth Venture mission under NASA's Earth System Science Pathfinder (ESSP) program. CYGNSS is classified as Category 3, Class D per NASA Procedural Requirements (NPR) 8704.5. Phase A efforts on the CYGNSS mission began in December 2012. CYGNSS launched on December 15, 2016, and has a 2-year design lifetime. The mission is now in the extended mission phase. Principal investigator (PI) Dr. Chris Ruf of the University of Michigan (UM) Climate and Space Sciences and Engineering Department leads the team of institutions. UM is responsible for the science team, communications and public engagement, science operations and data analysis, payload stimulator, and overall successful execution of the mission and implementation of the proposed science investigations. The Southwest Research Institute (SwRI) is a subcontractor to UM and serves as the "implementing organization." SwRI is responsible for overall mission project management, systems engineering, safety and mission assurance, procurement and management of the payload, spacecraft development, oversight of the deployment module (DM), integration and testing, launch vehicle interfaces, commissioning, and mission operations. Surrey Satellite Technologies provided the DDMI and Sierra Nevada Corporation (SNC) provided the DM. The eight observatories were affixed to the DM and then attached to the Orbital Alliant Techsystems (ATK) Pegasus launch vehicle. An overview of the mission's motivation, goals, objectives, requirements, and design is given in Ruf et al. (2015).

1.3. References

Clarizia, M. P., Gommenginger, C. P., Gleason, S. T., Srokosz, M. A., Galdi, C., & Di Bisceglie, M. (2009). Analysis of GNSS-R delay-Doppler maps from the UK-DMC satellite over the ocean. *Geophysical Research Letters, 36*(2). https://doi.org/10.1029/2008GL036292.

Clarizia, M. P., Ruf, C. S., Jales, P., & Gommenginger, C. (2014). Spaceborne GNSS-R minimum variance wind speed estimator. *IEEE Transactions on Geoscience and Remote Sensing, 52*(11), 6829–6843.

Foti, G., Gommenginger, C., Jales, P., Unwin, M., Shaw, A., Robertson, C., & Roselló, J. (2015). Spaceborne GNSS reflectometry for ocean winds: First results from the UK TechDemoSat-1 mission. *Geophysical Research Letters, 42*(13), 5435–5441.

Garrison, J. L., Katzberg, S. J., & Hill, M. I. (1998). Effect of sea roughness on bistatically scattered range coded signals from the global positioning system. *Geophysical Research Letters, 25*(13), 2257–2260.

Garrison, J. L., Komjathy, A., Zavorotny, V. U., & Katzberg, S. J. (2002). Wind speed measurement using forward scattered GPS signals. *IEEE Transactions on Geoscience and Remote Sensing, 40*(1), 50–65.

Gleason, S. (2013). Space-based GNSS scatterometry: Ocean wind sensing using an empirically calibrated model. *IEEE Transactions on Geoscience and Remote Sensing, 51*(9), 4853–4863.

Gleason, S., Gommenginger, C., & Cromwell, D. (2010). Fading statistics and sensing accuracy of ocean scattered GNSS and altimetry signals. *Advances in Space Research, 46*(2), 208–220. https://doi.org/10.1016/j.asr.2010.03.023.

Gleason, S., Hodgart, S., Sun, Y., Gommenginger, C., Mackin, S., Adjrad, M., & Unwin, M. (2005). Detection and processing of bistatically reflected GPS signals from low Earth orbit for the purpose of ocean remote sensing. *IEEE Transactions on Geoscience and Remote Sensing, 43*(6), 1229–1241.

Jales, P., & Unwin, M. (2015). *Mission description-GNSS reflectometry on TDS-1 with the SGR-ReSI* (Surrey Satellite Technology Report No. 0248367, Revision 001). Retrieved from http://www.merrbys.co.uk.

Katzberg, S. J., & Dunion, J. (2009). Comparison of reflected GPS wind speed retrievals with dropsondes in tropical cyclones. *Geophysical Research Letters, 36*(17). https://doi.org/10.1029/2009GL039512.

Katzberg, S. J., Walker, R. A., Roles, J. H., Lynch, T., & Black, P. G. (2001). First GPS signals reflected from the interior of a tropical storm: preliminary results from Hurricane Michael. *Geophysical Research Letters, 28*(10), 1981–1984.

Lin, B., Katzberg, S. J., Garrison, J. L., & Wielicki, B. A. (1999). Relationship between GPS signals reflected from sea surfaces and surface winds: Modeling results and comparisons with aircraft measurements. *Journal of Geophysical Research: Oceans (1978–2012), 104*(C9), 20713–20727.

Lowe, S. T., Zuffada, C., Chao, Y., Kroger, P., Young, L. E., & LaBrecque, J. L. (2002). 5-cm-precision aircraft ocean altimetry using GPS reflections. *Geophysical Research Letters, 29*(10), 13-1–13-4.

National Hurricane Center and Central Pacific Hurricane Center (NOAA). (2020). Main web page. http://www.nhc.noaa.gov.

Ruf, C. S., Atlas, R., Chang, P. S., Clarizia, M. P., Garrison, J. L., Gleason, S., . . . O'Brien, A. (2015). New ocean winds satellite mission to probe hurricanes and tropical convection. *Bulletin of the American Meteorological Society, 97*(3), 385–395. https://doi.org/10.1175/BAMS-D-14-00218.1.

Zavorotny, V. U., & Voronovich, A. G. (2000). Scattering of GPS signals from the ocean with wind remote sensing application. *IEEE Transactions on Geoscience and Remote Sensing, 38*(2), 951–964.

2. Mission Overview

2.1. Science Objectives

2.1.1. Baseline Science Objectives

The CYGNSS science goals are enabled by meeting the following mission objectives:

- Measure ocean surface wind speed in most naturally occurring precipitating conditions, including those experienced in the tropical cyclone eyewall.
- Measure ocean surface wind speed in the tropical cyclone inner core with sufficient frequency to resolve genesis and rapid intensification.

2.1.2. CYGNSS Application Areas

A variety of applications for CYGNSS exist outside of the required baseline science objectives. These include, but are not necessarily limited to, soil moisture, hydrology, coastal flooding, ocean wave modeling, and numerical weather prediction.

The CYGNSS mission, which will obtain denser surface wind field observations to improve tropical cyclone intensity forecasts, is also expected to provide new insights into air-sea interactions related to tropical convection and measurements of soil moisture and surface water extent, as well as observations of ocean surface dynamics in insufficiently sampled regions from 38ºN to 38ºS latitude.

In the areas of modeling, forecasting, and tropical convection applications, forecast model representation of the Madden-Julian oscillation (MJO) could be improved. The ability to provide fast-repeat wind sampling unbiased by the presence of precipitation could enable improved observations of convectively induced phenomena such as westerly wind bursts and gust fronts. The CYGNSS fast-repeat wind sampling, especially in precipitating regions, will complement existing polar satellite ocean surface winds and should improve the prediction of atmospheric phenomena with connections to the tropics, such as monsoons, atmospheric rivers, and the extratropical transitions of tropical cyclones.

For monitoring of tropical cyclones, CYGNSS surface wind data could be used to assess the intensity and intensity change rate that are critical for coastal preparations to protect life and property in land-falling storms. In the areas of coastal, terrestrial, and hydrological applications, soil moisture and wetlands extent mapping with CYGNSS is

possible. These two applications are the most mature and aligned with the existing capabilities of the L-band sensor and mission design. The fast-repeat sampling characteristics of CYGNSS measurements of soil moisture would add value to existing sensors and possibly allow studies of subdiurnal soil moisture, crop evolution, and flood forecasting.

In the areas of physical oceanography and surface wave applications, more accurate estimations of surface fluxes along with improved surface wind analysis products generated using CYGNSS observations will be highly valuable for evaluating and improving the performance of ocean and wave models within coupled systems. Another application is the use of Level 3 CYGNSS products in conjunction with other atmosphere-ocean observations to study climate modes such as the MJO and El Niño Southern Oscillation (ENSO) cycles that have signatures over the tropics and subtropics.

2.2. Baseline Science Mission Requirements

The CYGNSS baseline science requirements, defined to meet the mission objectives, are listed as follows:

1. Provide estimates of ocean surface wind speed over a dynamic range of 3 to 70 m/s^{-1} as determined by a spatially averaged wind field with a resolution of 5 × 5 km.
2. Provide estimates of ocean surface wind speed during precipitation rates up through 100 mm hr^{-1} as determined by a spatially averaged rain field with a resolution of 5 × 5 km.
3. Retrieve ocean surface wind speed with a retrieval uncertainty of 2 m/s^{-1} or 10%, whichever is greater, with a spatial resolution of 25 × 25 km.
4. Collect space-based measurements of ocean surface wind speed at all times during the science mission with the following temporal and spatial sampling: (1) temporal sampling better than a 12-hour mean revisit time and (2) spatial sampling of 70% of all storm tracks between 35°N and 35°S latitude to be sampled within 24 hours.
5. Conduct a calibration and validation program to verify that the data delivered meet the requirements within individual wind speed bins above and below 20 m/s^{-1}.

6. Support the operational hurricane forecast community for assessment of CYGNSS data impacts on numerical prediction of tropical cyclones in retrospective studies.

2.3. Mission Synopsis

The CYGNSS mission schedule is composed of distinct, sequential phases. Phase A defines high-level mission requirements and culminates in the System Requirements Review (SRR). Phase B defines the preliminary design of the mission and the relationship between the mission's requirements and its design. It culminates in the Preliminary Design Review (PDR). Phase C defines the detailed design of the mission—in particular, of the flight segment (consisting of the eight observatories and the deployment module) and of the ground segment (consisting of the data telemetry ground stations, the Mission Operations Center [MOC], the Science Operations Center [SOC], and the NASA Distributed Active Archive Center [DAAC]). Phase C culminates in the Critical Design Review

(CDR) and the System Integration Review (SIR). Phase D consists of the flight segment build and test phase, followed by the launch vehicle integration. It culminates in the launch and early on-orbit engineering commissioning. Phase E consists of the on-orbit science mission execution, including science payload calibration, Science Data Product calibration and validation, and engagement with the wider science community of data users. Phase F occurs after the end of on-orbit operations and typically consists of final science algorithm revisions, a last cycle of reprocessing of the mission science data, and final archiving of data products and associated documentation. Figure 2.1 shows the summary mission timeline. Table 2.1 gives a list and brief description of significant mission milestones along with their associated dates.

2.3.1. Launch

The eight CYGNSS satellites were affixed to a deployment module and shipped to Vandenberg Air Force Base for integration with the Orbital Alliant Techsystems (ATK)
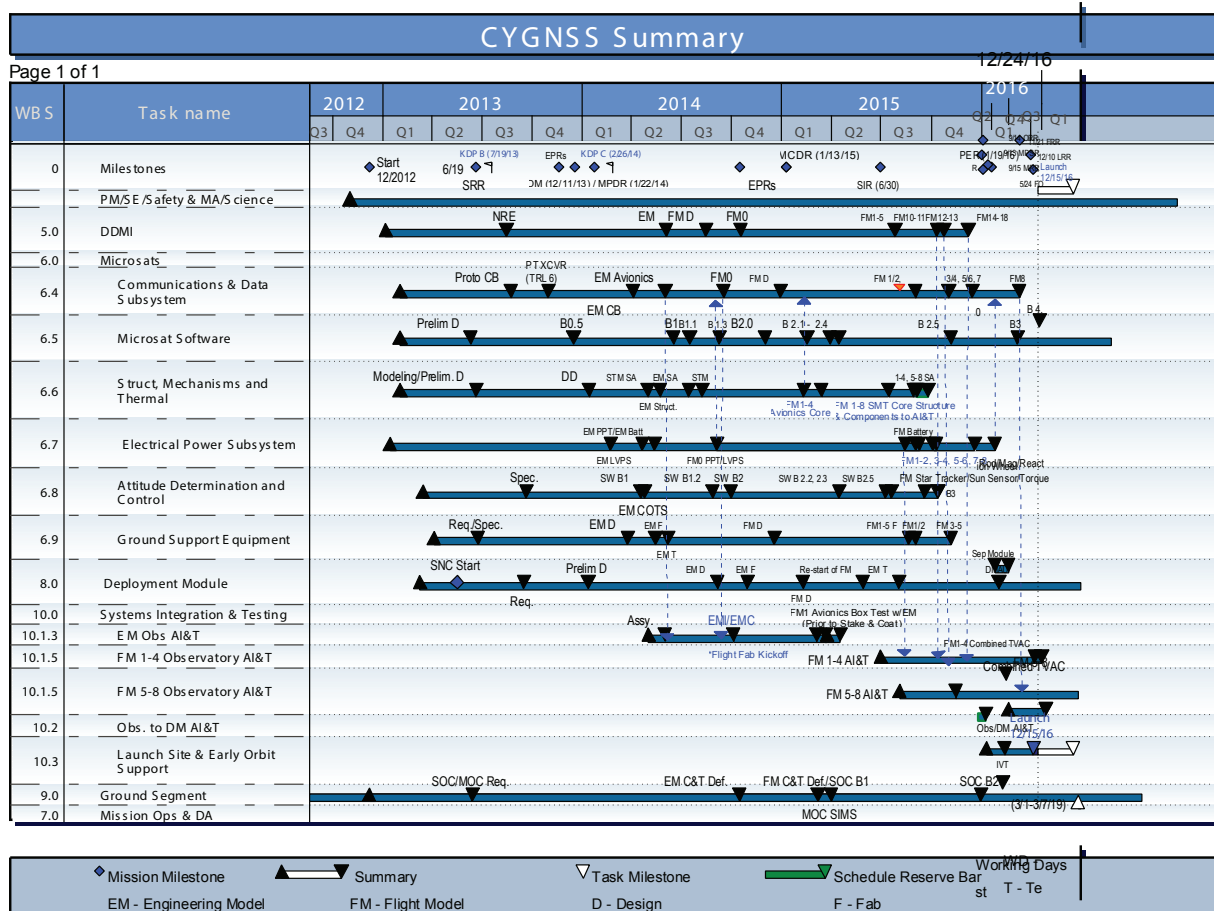
Figure 2.1. Summary mission timeline.

Table 2.1. Significant Mission Milestones

Completed date	Description/status
Dec. 2012	Project kickoff
Jul. 19, 2013	KDP B, SRR completed
Feb. 26, 2014	KDP C
Jan. 13, 2015	Mission Critical Design Review
Sep. 2015	Mission Readiness Review
Dec. 15, 2017	Launch
Jan. 4, 2017	First light!
Jan. 16, 2017	First S/C to nadir
Jan. 16, 2017	First S/C to 10-degree roll-off of nadir
Feb. 25, 2017	First raw data collection
Mar. 23, 2017	Postlaunch Acceptance Review
May 22, 2017	First PO.DAAC delivery
June 16, 2017	FSW v4.4 deployment complete
Aug. 21–27 2017	Science data taken over Hurricane Harvey
Sep. 5–8, Sep. 18–21, 2017	Science data taken over Hurricanes Irma and Maria, respectively
Oct. 6–8, 2017	Science data taken over Hurricane Nate
Dec. 5, 2017	FSW v4.5 deployment complete
Sep. 21, 2018	V2.1 released to public via PO.DAAC
Feb. 2019	End of Prime Mission Review
Mar. 2019	Begin Extended Mission Phase E
Spring 2020	Climate Data Record Science Data Product release
Spring 2020	V3.0 Science Data Product release with real-time GPS EIRP tracking
Summer 2020	Level 1 calibration over land with digital elevation map and coherence detection

Key: EIRP, effective isotropic radiated power; FSW, Flight Software; KDP, Key Decision Point; PO.DAAC, Physical Oceanography Distributed Active Archive Center.

Pegasus three-stage launch vehicle in November 2016. Once integrated, the Pegasus was attached to the underside of Orbital ATK's L-1011 airplane and performed a ferry flight to Cape Canaveral Air Force Station in Florida. After completing final inspections and checkouts, the L-1011 flew to the specified drop location off the coast of Florida at an altitude of 39,000 ft. for launch on December 15, 2016. After approximately 8 minutes of total flight time from drop to stage three burnout, the eight observatories were deployed in opposite pairs off the deployment module. Initial orbital altitudes for the eight spacecraft varied from approximately 514 to 536 km.

2.3.2. Commissioning

The commissioning phase included deployment of solar arrays, checkout of the spacecraft subsystems and payload, and initial drag maneuvers to spread the constellation into the desired spacing. The initial baseline constellation configuration was an even spacing of ~45º between observatories. The science coverage requirement for the mission can be met when the observatories ≥ 20° apart from each other. Once on orbit, multiple drag maneuvers were performed to adjust constellation spacing, with the execution of drag maneuvers traded off against the continuation of science mode operations to achieve a balance of continued science data flow and ideal constellation spacing, with the former weighted more heavily than the later during the Atlantic basin hurricane season (approximately June through November). The orbital position of the constellation as of May 4, 2022, is shown in Figure 2.2. The commissioning phase extended from launch until both the ground elements and the spacecraft and instrument subsystems were fully functional and had demonstrated the required on-orbit performance to begin routine science data collection. The Level 1 requirements call for these activities to be completed within 60 days after launch.

2.3.3. Operations

The science operations phase is the period of near-continuous data collection extending from the end of commissioning for 2 years. Each observatory is maintained in a nadir-pointing attitude, except for brief periods when drag maneuvers are required to maintain the constellation spacing or for potential collision avoidance maneuvers. Nominally, each observatory is contacted once every 48 hours for commanding and data downlinking, an average of four contacts per day for the ground segment. If a sufficient number of observatories are still functioning adequately at the end of the 2-year baseline mission duration, the science operations phase may be extended, subject to review and approval by NASA.

Science data products are made available to the public via NASA's Physical Oceanography Distributed Active Archive Center (PO.DAAC). CYGNSS delivered the initial Level 1 and 2 data products 2 months after initial operational capability (IOC) and Level 3 data products four months after IOC. After the initial delivery, all data products have been made publically available within 6 days of the data being downlinked.

2.3.4. Decommissioning

CYGNSS postmission disposal will be accomplished via uncontrolled atmospheric reentry within 25 years of the end
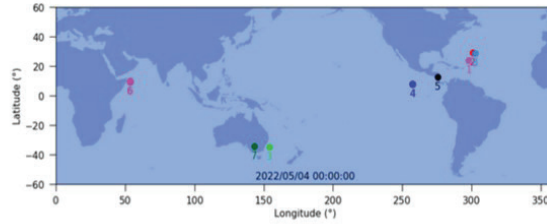
Figure 1: Snapshot of CYGNSS positions.

2022/05/04 00:00:00						
Observatory	Perigee (km)	Apogee (km)	Trailing/Leading Time (min)	Distance (km)	Trailing/Leading Separation (°)	Phase rate difference (°/day)
FM01	503.0	540.6	59.0/36.0	16433.8	224/136	1.29
FM02	501.0	534.9	65.5/39.5	18033.4	210/150	0.145
FM03	506.5	526.2	0.0/96.0	0.0	0/360	0
FM04	504.6	539.9	67.2/27.8	12684.9	255/105	0.073
FM05	503.8	542.7	64.8/30.2	13789.8	246/114	1.84
FM06	507.4	536.5	27.5/67.5	12563.3	104/256	0.195
FM07	506.5	526.6	2.3/92.7	1031.0	9/351	0.023
FM08	501.6	536.5	55.9/39.1	17836.0	212/148	0.96

Table 1: Current orbit parameters.
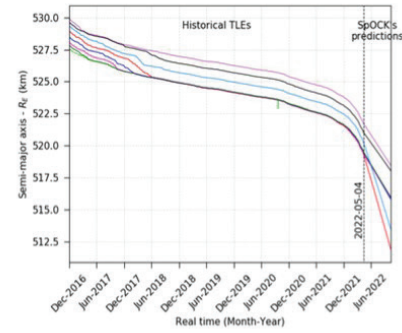
Figure 2: CYGNSS orbit decay - historical and predictions assuming the satellites are nadir pointing.

Figure 2.2. CYGNSS constellation orbital configuration as of May 4, 2022. The relative space, perigee, apogee, orbital separation, and phase rate of each spacecraft are shown, as is the evolution of the semimajor axis of the orbit for each spacecraft. Multiple high drag maneuvers were employed to achieve spacing between the eight CYGNSS spacecraft adequate to meet mission-level requirements while maximizing constellation time in science mode.

of the mission. As such, no systems are required to be operational, and there are no plans for any special maneuvers to support the disposal. The micro reaction wheels onboard each observatory will be commanded off at the end of the mission.

2.4. Mission System Description

In developing the design concepts for the CYGNSS observatories, the Systems Engineering team kept in mind the safety of the observatories without ground intervention. Providing onboard systems that minimize the need to develop time-tagged command sequences for each observatory for routine operations also supports a simplified operational cadence for maintaining the constellation.

2.4.1. Launch Through Commissioning

Each observatory is deployed with solar arrays stowed. After deployment from the launch vehicle, each observatory transitioned automatically through the initial three states to reach standby mode. Deployment of the solar arrays occurred next. Additional commissioning activities for the observatories began once the solar arrays were deployed and continued for a period of 4 weeks while the health of each spacecraft was confirmed.

Commissioning activities for a CYGNSS delay-Doppler mapping instrument (DDMI) commenced once its microsat completed its commissioning sequence. DDMI commissioning lasted an additional 4 weeks. During this time, the DDMI was operated in two engineering modes, which were used to verify on-orbit performance and tune the onboard delay-Doppler map (DDM) generation and subsampling algorithms. At the end of the DDMI commissioning activities, the instrument was transitioned into its science mode, where it collects data continuously, save when interrupted by scheduled high drag maneuvers and unscheduled safing events.

2.4.2. Nominal Operations

Upon completion of commissioning activities, the observatories were transitioned into the science mode of operation. At this point, the DDMI is set to science mode for the duration of the mission, except as noted above for high drag maneuvers and safing events. In science mode, subsampled DDMs are generated onboard and downlinked with a 100% duty cycle.

The observatories are designed to implement nominal observatory operations and science data collection without onboard time-tagged command sequences. With the DDMI in its continuous science mode and the observatory set to maintain all nominal operations without additional commands, the primary "routine" activity performed on a

regular basis is communication with the ground network to downlink the accumulated science and engineering data.

Science and engineering data files are generated, stored onboard, and automatically added to an onboard downlink file list. Retrieval of the science data occurs during communications passes, which occur at the rate of one pass per observatory every 1.5–2 days. Onboard microsat data storage provides storage for greater than 10 days of science data, allowing flexibility in pass scheduling and supporting recovery from loss of communications during a pass.

Downlink pass acquisition operations are automated using an onboard automated event recognition (AER) capability. The mission operations team schedules passes for each observatory, and when the observatory is within range of the scheduled ground antenna asset, the antenna illuminates the microsat with a clear channel communication. On board, the AER switches the microsat transmitter on when the receiver detects the ground network signal. Once the transmitter is enabled, housekeeping telemetry is transmitted, allowing the ground antenna to synchronize with the microsat. Once a lock has been established, a notification of the acquisition status is relayed to the CYGNSS MOC.

After establishing contact, the following steps are performed:

- Real-time housekeeping data are continuously transmitted by the microsat, received on the ground, and flowed to the MOC.
- Based on the transmitter configuration (low or high speed) and idle pattern received, the microsat automatically plays back the housekeeping and science data collected since the last pass was transmitted to the ground and collected at the antenna site. If a nonunique idle pattern is seen, the microsat waits for playback commands from the MOC or from the onboard Absolute Time Sequence (ATS; time-tagged command sequences).
- If needed, the MOC can send the command to thaw the CCSDS File Delivery Protocol (CFDP) engine on board the microsat. In a nominal pass, this is done autonomously by the microsat.
- Any incomplete transmissions from the previous pass, based on the commands from the MOC, will be downlinked by the microsat CFDP engine.
- The AER system on board the microsat has a backup transmitter off command, which will be triggered by a timer that is set when the transmitter is turned on to ensure the transmitter is not inadvertently left on for a long period of time.

- Postpass, the collected files are transferred from the antenna site to the Swedish Space Corporation (SSC) Network Management Center (NMC), where they are then transferred to the CYGNSS MOC for processing and distribution.

The raw CCSDS data files from the remote SSC antenna sites are sent to the SSC NMC after the completion of the pass. This flow decouples the file processing from the real-time flow of the pass, which simplifies the operations and does not levy any bandwidth requirements on the links from the remote antenna sites to the NMC.

Postpass, the files collected during the pass are flowed to the CYGNSS MOC, where they are processed through the data processing system and any replay commands are generated for the next contact with the observatory if data gaps large enough for mission-level data coverage requirements to be exceeded are found. All data are then transferred to the SOC via automated scripts at the SOC that monitor data downloads at the MOC.

2.4.3. Routine Maintenance and Calibration

The majority of postcommissioning operations for CYGNSS occur using the automated features available in the microsat and in the MOC. However, there are also routine microsat maintenance (e.g., upload of flight software updates, commanding of high drag and high solar beta angle power preservation roll maneuvers) and DDMI special science activities (raw intermediate frequency [IF] and high-resolution DDM modes) that occur throughout the operational period of the constellation.

Maintenance activities for the microsat do not need to be scheduled on a specific cadence. Reviews of microsat systems and positioning information are used to assess the status of each subsystem as well as the location of each observatory to determine when maintenance activities are needed. Based on the type of activity, either real-time commanding or time-tagged command sequences are developed to perform the required activities.

2.4.4. Ground System Overview

The CYGNSS ground system, as shown in Figure 2.3, consists primarily of the MOC; existing SSC PrioraNet ground stations in Australia, Hawaii, and Santiago, Chile; and the SOC facility. Additional interfaces between the MOC and the microsat engineering team and the DDMI instrument engineering teams are supported. The MOC coordinates operational requests from all facilities and develops long-term operations plans.
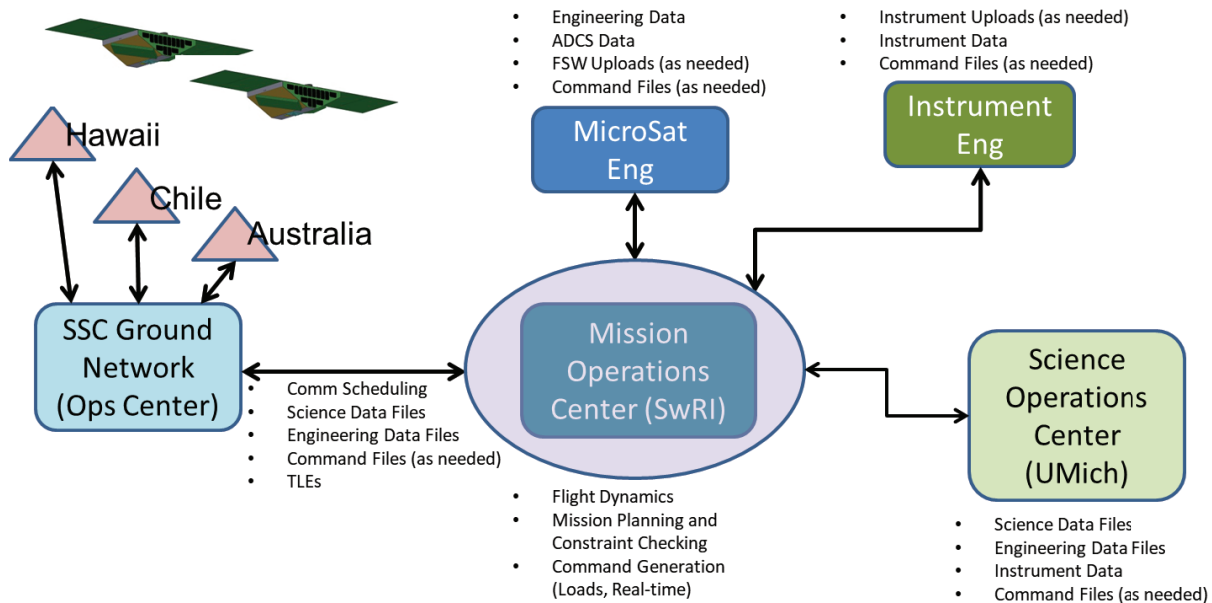
Figure 2.3. Diagram of the CYGNSS mission system.

2.4.4.1. Ground Data Network—SSC

CYGNSS selected SSC for the ground data network due to their experience in autonomously acquiring spacecraft (S/C) per our baselined approach. Colocation of a backup CYGNSS MOC server at the SSC NMC is also supported.

The observatories within the CYGNSS constellation are visible to three ground stations within the SSC—located in Hawaii, Australia, and Santiago, Chile—for periods that average 470–500 seconds of visibility per pass. Each observatory passes over each of the three ground stations six to seven times each day, thus providing a large pool of scheduling opportunities for communications passes.

MOC personnel schedule passes as necessary to support commissioning and operational activities. High-priority passes were scheduled to support the observatory solar array deployment for each of the constellation microsats and are scheduled to support anomaly resolution as issues arise during nominal operations. Each observatory can accommodate gaps in contacts with storage capacity for >10 days of data with no interruption of science.

2.4.4.2. Mission Operations Center (MOC)

During the mission, the CYGNSS MOC, located at the Southwest Research Institute (SwRI) Boulder location, is responsible for the mission planning, flight dynamics, and command and control tasks for each of the observatories in the constellation. A summary of the primary MOC tasks includes the following:

- coordinating activity requests,
- scheduling ground network passes,
- maintaining the CFDP ground processing engine,
- collecting and distributing engineering and science data,
- tracking and adjusting the orbit location of each observatory in the constellation,
- trending microsat data,
- creating real-time command procedures or command loads required to perform maintenance and science activities, and
- maintaining configuration of onboard and ground parameters for each observatory.

2.4.4.3. Science Operations Center (SOC)

The CYGNSS SOC, located at the University of Michigan, is responsible for the following items:

- support DDMI testing and validation both pre-launch and on orbit,
- provide science operations planning tools,
- generate instrument command requests for the MOC,
- ingest Level 0 telemetry data from the MOC,
- produce science data Levels 1–3,
- ingest science data Level 4 from CYGNSS science team collaborators,

- perform reprocessing of science data Levels 1–3 during the course of the mission as algorithm improvements are made, and
- archive Levels 0–4 data products, DDMI commands, code, algorithms, and ancillary data at a NASA DAAC. NASA's Physical Oceanography Distributed Active Archive Center (PO.DAAC) at the Jet Propulsion Laboratory has been chosen as the archive site for the mission.

2.4.4.4. Command and Control System

The requirements for the MOC are to implement a command and control system that can handle all unique aspects of the CYGNSS mission. For uplink, it must support real-time commanding at 2,000 bps, including memory load-dump-compare operations. On downlink, it must support ingesting of CFDP data, Reed-Solomon decoding, and derandomization and include real-time telemetry display and long-term archival and analysis tools. For the ground segment, the tools need to be able to interface, configure, and monitor the ground network. It is also important that the system is easily deployed and low cost and facilitates use by a team distributed across the country.

The CYGNSS mission chose the Integrated Test and Operations System (ITOS) for its command and control system. ITOS is a suite of software developed by the Real-Time Software Engineering Branch at the Goddard Space Flight Center and is supported by the Hammers Company. This government off-the-shelf (GOTS) solution also has no license costs for NASA missions and runs on inexpensive Linux hardware.

ITOS itself is not uniquely customized from mission to mission. Instead, mission customization is accomplished through database-driven command and telemetry specifications and a small set of configuration files. This obviates the need for additional software development and training. The database includes limit checking and engineering unit configurations as well as highly customizable display pages for monitoring spacecraft data. The ITOS telemetry server can interface across a firewall to a public server, which can display telemetry and events remotely via a web browser, which facilitates simple, real-time monitoring of the spacecraft from a geographically diverse mission team.

For the success of the CYGNSS mission, it is critical for the command and control system to be able to define eight unique and concurrent spacecraft and be able to manage and display data unique to each. Though the spacecraft are identical by design, they have unique aspects that the ground system must take into account, including unique command constraints, telemetry conversions, and limit checking. The ITOS tools provide the database elements necessary to support and maintain a constellation configuration.

The CYGNSS team used ITOS throughout the spacecraft development, including as the main control system during system integration and environmental testing. This bench-to-flight approach allows for heavy reuse of existing spacecraft test and operations language (STOL) procedures that were baselined into the Mission Operations configuration management system as the standard scripts and processes the team uses to fly the mission.

The CYGNSS mission planning system takes inputs from flight dynamics and science activities from the SOC as well as event files, such as eclipse periods and ground tracks. In addition, it must resolve resource conflicts, such as power load, recorder usage, or oversubscription of ground antenna resources. The system must also check that planned events do not result in violation of flight constraints—either for a single observatory or for the constellation. Resolving the conflicts, the system then generates a command load, when required, that is handed off to the command and control system for uplink to the spacecraft.

3. Constellation Design

3.1. Orbital Elements

The baseline CYGNSS constellation design comprised eight observatories dispersed over a common 510 km circular orbit at a 35° inclination angle. Orbit insertion on December 15, 2016, was close to 2 σ high such that the constellation now operates at an average altitude of ~527 km with an orbit eccentricity of ~ 0.0015 and an inclination of ~34.95°. The temporal and spatial coverage of the constellation depends on each of these parameters. A useful measure of sampling performance is the number of 3-hour intervals during the lifetime of a tropical cyclone (TC) in which at least one sample is made. A sample is considered made if it is located within 75 nm of the eye. This coverage statistic is estimated using a software simulator in which CYGNSS (or other spaceborne mission) is flown over all TCs recorded during the 2003–7 Atlantic hurricane seasons. As points of comparison, the 3-hour coverage statistics for three heritage ocean wind scatterometer missions are QuikScat on NASA SeaWinds (27.1%), Ocean Scatterometer (OSCAT) on Indian Space Research Organization (ISRO) OceanSat-2 (23.5%), and ASCAT Advanced Scatterometer (ASCAT) on European Organisation for the Exploitation of Meteorological Satellites (EUMETSAT) Metop (16.7%). Applying the same analysis to the CYGNSS baseline design produces a 3-hour coverage statistic of 33.6%. Deviations in the achieved orbit compared to the baseline orbit design, as described above, have had minimal impact on these coverage statistics.

The 3-hour coverage statistic reduces to 32.9%–32.6% when one of the eight observatories is removed, depending on which one it is. Coverage reduces further, to 32.2%–32.8%, when two observatories are removed, illustrating the graceful degradation in performance provided by the CYGNSS constellation should one or more observatories fail.

A second statistical measure of sampling performance is the percentage of CYGNSS samples made in a 24-hour interval that are coincident with the complete historical storm track record for the 10-year period 2000–2009. This 24-hour storm coverage statistic is shown in Figure 3.1 as a function of the number of observatories lost from the initial constellation of eight. A coverage statistic of 70%, which is consistent with the coverage that would have been provided by both the OSCAT and ASCAT missions operating as a constellation, meets the mission requirement.

Orbit altitude can affect coverage in competing ways. As altitude increases, the projected antenna footprint on the ground grows, increasing the potential number of observable GPS reflections. Increasing altitude also lengthens the propagation path and lowers received signal strength, thus narrowing the usable solid angle of the antenna pattern. The increase in footprint size would dominate if the number of observable reflections was allowed to grow. However, because the delay-Doppler mapping instrument (DDMI) can simultaneously observe a maximum of only four reflections, coverage does not improve much above an altitude of ~350 km. Coverage begins to decrease due to the longer propagation path above ~550 km. This behavior is illustrated in Figure 3.2. The baseline altitude of 510 km was chosen to satisfy the mission lifetime requirement while staying within the broad range indicated by this coverage analysis. The achieved orbit at ~527 km similarly meets these criteria.
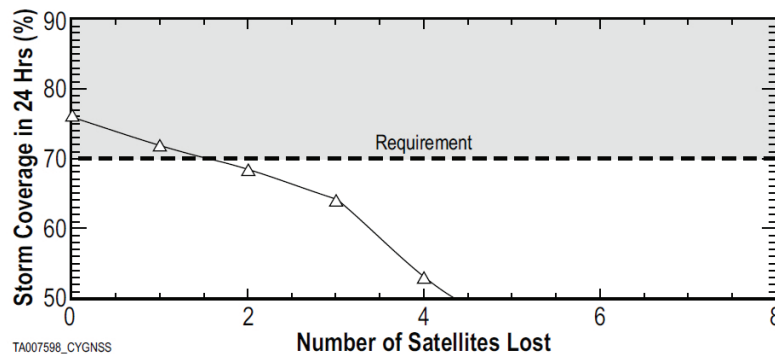
Figure 3.1. Dependence of 24-hour coverage on the number of observatories lost. The 70% storm coverage requirement is met by seven or more observatories.

Orbit inclination affects storm coverage in two ways. Very low inclination angles reduce coverage because the prevailing latitudinal "corridors" favored by tropical storms become undersampled or missed altogether. Inclination angles too far above these preferred latitudes also tend to decrease coverage because more time is spent over midlatitude regions with a low probability of TC occurrence. These competing dependencies are shown in Figure 3.3. The baseline mission design of 35° is located at the center of a broad maximum in coverage.

3.2. Observatory

The CYGNSS observatory is based on a single-string hardware architecture with functional and selective redundancy included for critical areas. It consists of the DDMI and a highly integrated microsatellite. The simple operational nature of the DDMI and science profile allows the microsatellite to be designed for autonomous control during all normal science and communication operations without the need for daily onboard command sequences.

The microsatellite is a three-axis stabilized, nadir-pointed vehicle using a star tracker for primary attitude knowledge and a reaction wheel triad for control. Fixed solar arrays, stowed for launch and then deployed soon thereafter, provide power to the onboard peak power tracking electronics for battery charging. Communication is provided by an S-band transceiver and low-gain patch antennas to provide near 4π steradian communications without interrupting science operations. The vehicle's structure and thermal design are driven by the physical accommodation of the DDMI antennas, the solar arrays, and launch configuration constraints.

Microsatellite performance is enabled by key nanosatellite technology, specifically the star tracker and reaction wheels, both provided by Blue Canyon Technologies of Boulder, Colorado. The form factor, mass, and power requirements of these components are well suited for the highly integrated nature of the CYGNSS observatory. The Southwest Research Institute (SwRI) avionics, including the flight computer, S-band transceiver, peak power tracker (PPT), and low-voltage power supply (LVPS), are based on heritage solutions that have been used on more than 20 previous missions. The avionics leverage recent developments in high-density microelectronics to achieve a packaging volume of a 3U CubeSat—a 4:1 volume reduction.

TA007599_CYGNSS
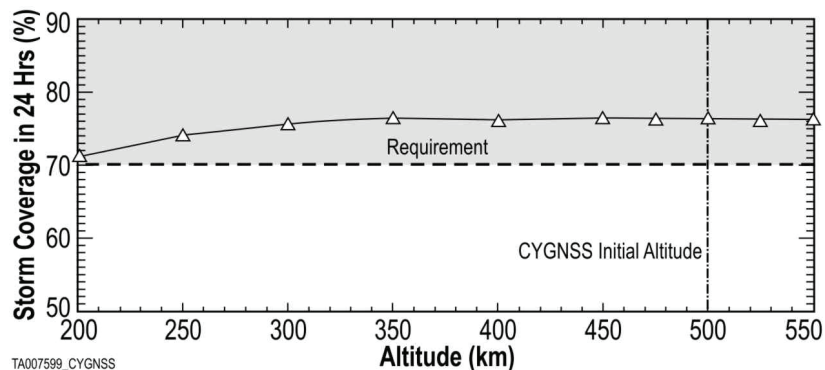
Figure 3.2. Dependence of 24-hour coverage on orbit altitude. The 70% storm coverage requirement is met by a wide range of altitudes. The 510 km baseline altitude meets the mission lifetime requirement.

TA007600_CYGNSS
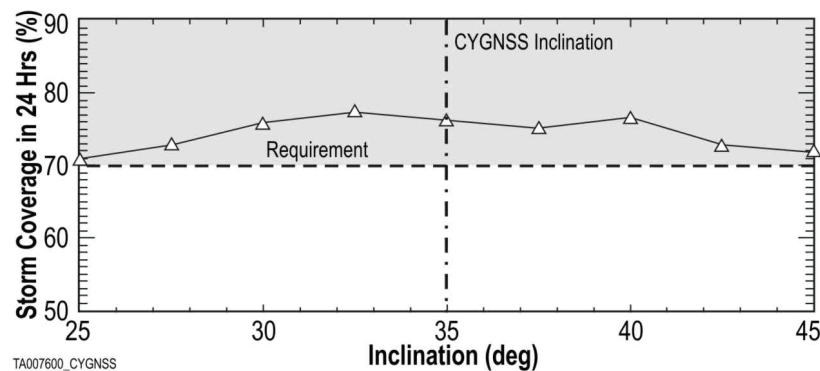
Figure 3.3. Dependence of 24-hour coverage on orbit inclination angle. The 35° baseline inclination is centered in a broad maximum of storm coverage dependence.

The mass of each observatory at launch was 29.00 +0.00/−0.25 kg, which reflects an early decision to ballast observatories up to a fixed target of 29 kg to ensure a favorable center of gravity (CG) location and limit uncertainty in various analyses. Observatory power dissipation is ~37 watts. Exploded graphic views of the observatory from three perspectives and the overall observatory dimensions with solar arrays deployed are shown in Figure 3.4a–d. Photographs of the fully assembled observatories are shown in Figure 3.5a–c.

3.3. Science Payload

A functional schematic of the CYGNSS science payload, the DDMI is shown in Figure 3.6. The DDMI performs the following primary tasks:

a. It performs all the core functions of a space GPS receiver, with the front end supporting three single-frequency antenna ports.

b. It stores a quantity of raw sampled data from multiple front ends or processed data in its 1 GB solid-state data recorder.

c. It has a dedicated field-programmable gate array (FPGA) coprocessor (Virtex 4).

The coprocessor is included for the real-time processing of the raw reflected GPS data into delay-Doppler maps (DDMs). For the coprocessor to generate DDMs of the sampled reflected data, it needs to be primed with the pseudorandom noise (PRN) code of the transmitting GPS satellite and the estimated time delay and Doppler of the reflection as seen from the satellite. These are calculated
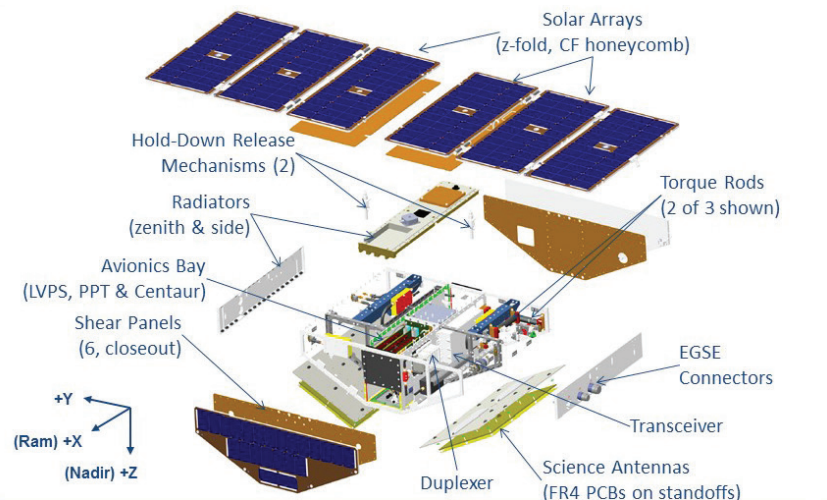
Figure 3.4a. Ram view of a CYGNSS observatory (courtesy of Keith Smith, Southwest Research Institute).
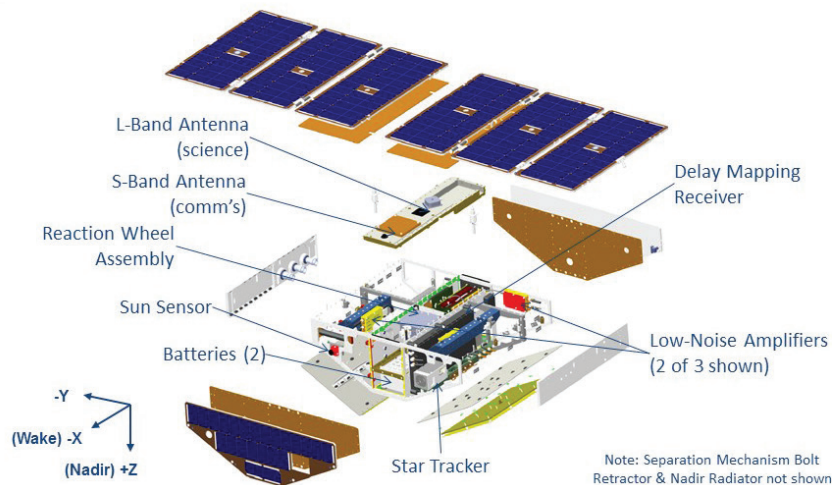
Figure 3.4b. Wake view of a CYGNSS observatory (courtesy of Keith Smith, Southwest Research Institute).
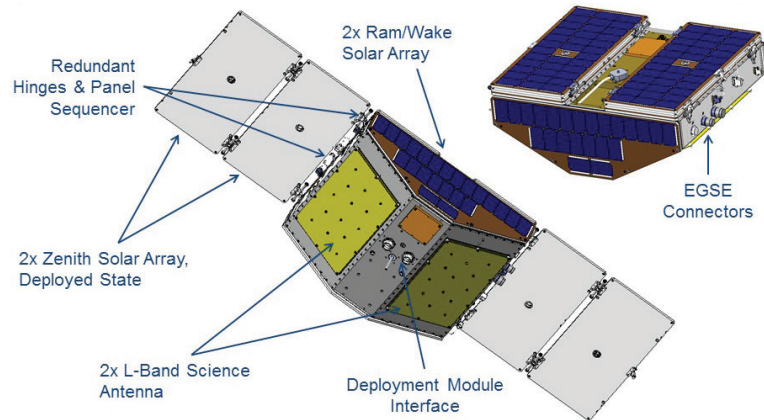
Figure 3.4c. Underside view of a CYGNSS observatory (courtesy of Keith Smith, Southwest Research Institute).
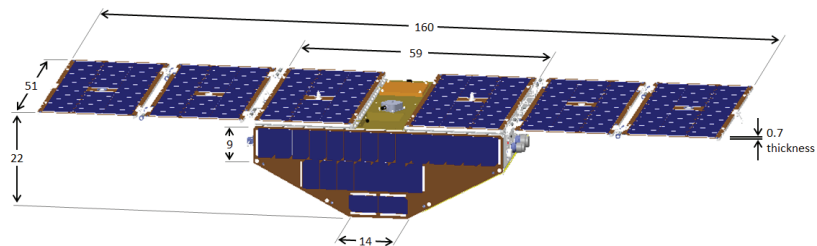
Figure 3.4d. Observatory overall dimensions (cm; courtesy of William Wells, Southwest Research Institute).

Figure 3.5a. One of the eight CYGNSS observatories prior to integration with the deployment module.

by the processor in conjunction with the main navigation solution—the data flow for this is shown in Figure 3.7. Direct signals (received by the zenith antenna) are used to acquire and track GPS signals. From the broadcast ephemerides, the GPS satellite positions are known. Then from the geometry of the position of the transmit and receive satellites, the bistatic radar geometry can be calculated.

The processing of the DDM is performed on the coprocessor using data directly sampled from the nadir antenna. In common with a standard GPS receiver, the local PRN is generated onboard the coprocessor. As an alternative to synchronizing and decoding the reflected signal in a stand-alone manner, the direct signals can be used to feed the navigation data sense and assist the synchronization. The sampled data are multiplied by a replica carrier
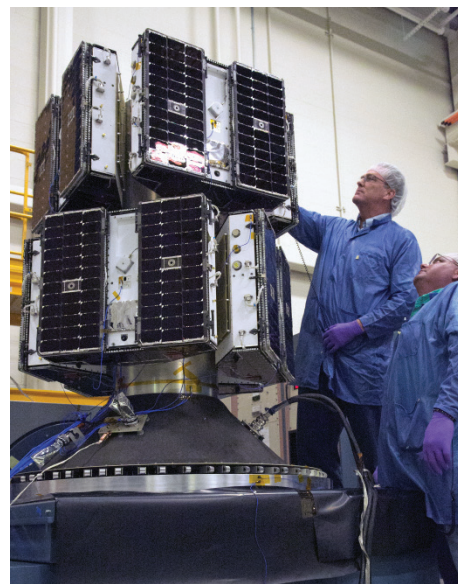
Figure 3.5b. All eight CYGNSS observatories integrated into the deployment module prior to flight segment vibration testing.

and fed into a matrix that performs a Fast Fourier Transform (FFT) on a row-by-row basis to form the DDM, to achieve in effect a 7,000-channel correlator, integrating over 1 ms. Each point is then accumulated incoherently over 1,000 ms to bring the weak signals out of the noise.
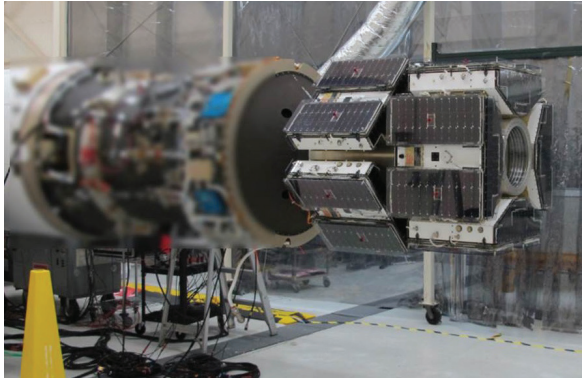
Figure 3.5c. CYGNSS flight segment integrated into Pegasus launch vehicle.

This processing is performed in real time onboard the satellite, which greatly reduces the quantity of data required to be stored and for the satellite's downlink. CYGNSS uses the DDMI in an autonomous manner, generating DDMs at a low data rate continuously, which provides gap-free measurements of the surface roughness.

3.4. Reference

Unwin, M., Van Steenwijk, R., Gommenginger, C., Mitchell, C., & Gao, S. (2010, September). The SGR-ReSI—a new generation of space GNSS receiver for remote sensing. In *Proceedings of the 23rd International Technical Meeting of the Satellite Division of the Institute of Navigation (ION GNSS 2010)* (pp. 1061–1067). Manassas, VA: Institute of Navigation.
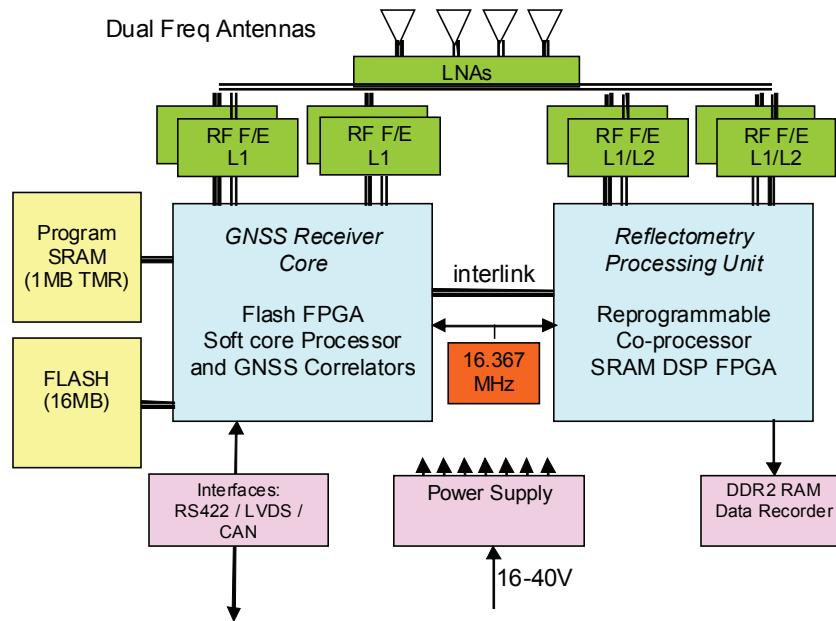
Figure 3.6. DDMI configuration (Unwin et al., 2010).
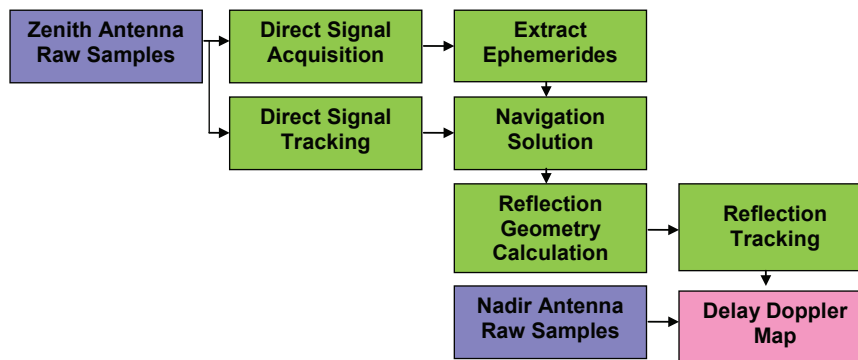
Figure 3.7. GPS reflectometry data flow.

4. Data Product Overview

4.1. Data Levels

The CYGNSS mission makes three levels of data products available to the public. A brief description of each data product level is given below. A table of the products is also provided in Part II of this section. More detailed information about the processing and the products for each data level are provided in the Algorithm Theoretical Basis Documents (ATBDs) in Chapters 5 through 10.

Level 1, 2, and 3 data products are produced in the form of netCDF files and are made available to the public through the NASA Physical Oceanography Distributed Active Archive Center (PO.DAAC). The maximum data latency from spacecraft downlink to PO.DAAC availability is 6 days.

4.1.1. Level 1 Data

The goal of the Level 1 calibration is to attain delay-Doppler maps (DDMs) of bistatic radar cross sections (BRCSs), which will be used to determine the ocean surface wind speeds in proceeding algorithms. The Level 1 calibration consists of two parts. First, the Level 1A calibration converts the individual bins of raw Level 0 DDMs from processed counts into DDMs of received power (P_g) in units of watts. These Level 1A DDMs are provided at a spatial resolution of 17 delay × 11 Doppler bins, corresponding to a surface area of about 50 km^2. Second, the Level 1A DDMs are converted to Level 1B DDMs of BRCS values by unwrapping the forward scattering model and generating two additional data products: one 17 delay × 11 Doppler DDM of unnormalized BRCS values (σ) in units of m^2 and a second 17 delay × 11 Doppler DDM of effective scattering areas (also in units of m^2). Dividing the unnormalized BRCS by the effective scattering area results in σ_0, the normalized bistatic radar cross section (NBRCS). All Level 1 data products are provided at a time resolution of 1 Hz. These data products are generated in such a way as to allow for flexible processing of variable areas of the DDM, which correspond to different regions on the surface (Clarizia & Ruf, 2014).

The process of quantifying the error in the Level 1 data products is described in detail in Chapters 5 and 7. For Level 1A, errors in the received power in watts, P_g, depend on wind speed. For ocean surface winds below 20 m/s^{-1} (corresponding to σ_0 = 20 dB), P_g has a total root sum square (RSS) error of 0.50 dB. For winds above 20 m/s^{-1} (corresponding to σ_0 = 12 dB), P_g has an RSS error of 0.23 dB. For the Level 1B

product, the total RSS errors for σ (including errors from the Level 1A calibration) are 0.82 dB (for winds below 20 m/s^{-1}) and 0.70 dB (for winds above 20 m/s^{-1}; Gleason et al., 2016).

Chapter 5 includes a detailed derivation of the Level 1A calibration and a term-by-term error analysis as well as the derivation of the Level 1B data products and error analysis. This includes analysis related to using only near specular DDM bins to calculate the NBRCS over a subset of DDM pixels, or DDM area (DDMA) used in the baseline Level 2 wind retrieval algorithm.

4.1.2. Level 2 Data

The Level 2 mean square slope (MSS) product is the spatially averaged MSS, plus uncertainty, over a 25 × 25 km^2 region centered at the specular point. The Level 2 wind speed product is the spatially averaged wind speed, plus uncertainty, over a 25 × 25 km^2 region centered at the specular point. Each Level 2 netCDF file contains the wind speeds and the MSS generated by the entire CYGNSS constellation during a single Coordinated Universal Time (UTC) day.

4.1.2.1. Level 2 MSS

The primary mission of the CYGNSS Project is to measure ocean surface winds by fitting the calibrated delay-Doppler map peak power data to the empirical or modeled geophysical functions. Those functions relate the measured signal parameters directly to surface wind. At the same time, the forward scattering model based on the bistatic radar equation directly relates the DDM to the BRCS, which in turn can be characterized by the MSS of the ocean surface. Therefore, this Level 2 data product is available during the CYGNSS mission.

The MSS of the ocean surface is a very important quantity. It is crucial for understanding the physical processes at the air-sea interface and for interpreting altimeter and scatterometer radar backscatter measurements. The practical need for global MSS datasets in air-sea interaction research is increasingly apparent—for example, for estimating the dynamics of gas transfer rates across a water boundary layer. Another important issue related to the availability of MSS measurements in hurricanes is an opportunity to verify new advanced models of hurricane development.

The purpose of Chapter 6 is to describe the CYGNSS Level 2 MSS algorithms and provide all necessary equations

for implementing the algorithm during the mission. It describes the physics of the problem and explains the connection between the BRCS and the MSS and between the MSS and the ocean surface spectrum. It provides a theoretical description of the MSS baseline retrieval algorithm. Since the MSS algorithm relies on the BRCS retrieval, all temporal and spatial resolution criteria developed in the documents for Level 1 are valid here as well.

The issue of the MSS retrieval accuracy is addressed in Chapter 6, "Performance Characterization." The creation of the Level 2 MSS product is contingent on the availability of input observational data (from CYGNSS and ancillary data sources) and accurate estimates of their errors. The accuracy of the Level 2 MSS product is dependent on the accuracy of the BRCS retrieval, the accuracy of the scattering geometry determination (incidence angle), and the accuracy of the Fresnel reflection coefficient estimates. This error analysis of the Level 2 MSS retrieval algorithm is presented at the end of Chapter 6.

4.1.2.2. Level 2 Wind Speeds

The Level 2 wind speeds are obtained from two observables known as the delay-Doppler map average (DDMA) and the leading edge slope (LES; see Chapter 7, Part I). The observables are calculated from DDMs that derive from the specular point selection algorithm (illustrated in Chapter 7) over a limited delay and Doppler range to comply with the 25 km spatial resolution requirements for the CYGNSS retrieved winds. In cases where the true resolution is finer than 25 km, time averaging between consecutive observables is applied to further reduce the noise in the observables. An empirical geophysical model function (GMF) is developed separately for DDMA and LES, relating the observable value to the ground truth matchup winds and the incidence angle using a training subset of high-quality data. The empirical GMF is then used to estimate the winds from a generic dataset of observables independent of the training one. In addition, the degree of decorrelation between winds retrieved from DDMA and from LES is exploited to derive a minimum variance (MV) estimator, which provides improved wind estimates compared to DDMA or LES alone. A simple quality control flag is applied to the final wind speed product to remove nonfeasible wind values.

The retrieval algorithm is applied and tested using matchups with model analysis wind fields and remotely sensed winds (Chapter 10). The performance and error analysis of the retrieval algorithm highlights that for those specular points acquired with high enough gain of the receiver antenna, the root mean square error meets the CYGNSS requirements on

wind speed uncertainty of 2 m/s^{-1} for winds below 20 m/s^{-1} and approaches the requirement of 10% of the measured wind for winds above 20 m/s^{-1}. In particular, the uncertainty is 1.8 m/s^{-1} for wind speeds lower than 20 m/s^{-1}, and it is 10.3% of the measured wind speed for winds higher than 20 m/s^{-1}.

The wind speeds retrieved using this algorithm have a spatial resolution of 25 km, and the estimation refers to a time interval between 1 and 5 seconds of data, depending on the amount of time averaging applied.

Two general classes of Level 2 winds are retrieved: (1) the Sensor Data Record (SDR) winds, which are the CYGNSS real-time product, and (2) the Climate Data Record (CDR) winds, which use model input to improve upon the Level 1 calibration to provide a postprocessed wind speed estimate with lower uncertainty and higher stability. The general algorithms for both are given in Chapter 7, and the details of the Level 1 postprocessing used by the CDR winds are given in Chapter 5.

4.1.3. Level 3 Data

The Level 3 gridded wind product is surface wind speed averaged in space and time on a 0.2° latitude, longitude grid (Chapter 8). Each Level 3 gridded wind file covers one 24-hour time period for the entire CYGNSS constellation. This product is produced for both the Level 2 SDR and CDR wind speed products. In addition, there is also a storm-centric gridded wind product. This product reports averaged wind speeds from the Level 2 SDR winds in a regular 7.2° × 7.2° grid centered on the tropical cyclone. Gridded wind speeds are reported every 6 hours for each tropical cyclone, though some grids may be empty. Each wind speed measurement is made by a particular combination of CYGNSS spacecraft and GPS spacecraft. Because there are 8 CYGNSS spacecraft and 32 GPS spacecraft, there are 256 different combinations of spacecraft that combine to make measurements. Details for both Level 3 gridded wind products are given in Chapter 8.

In addition to winds, CYGNSS provides gridded soil moisture estimates. The University Corporation for Atmospheric Research, University of Colorado (UCAR/CU) Cyclone Global Navigation Satellite System (CYGNSS) Soil Moisture Product is an L-band bistatic radar dataset that provides estimates of 0–5 cm soil moisture at a 6-hour discretization for the majority of the extratropics on an Equal-Area Scalable Earth (EASE)-2 36 km grid. Details are provided in Chapter 9.

4.1.4. Level 4 Data

Currently there are no Level 4 data products, but several are under development by CYGNSS science team members. As these products are released, this section will be updated in future versions of this handbook.

4.2. Table of Data Products

4.2.1. Level 1 Data and Metadata Products

The data and metadata contained in the Level 1 netCDF file are shown in Table 4.1 and are current as of the writing of this document. The most recent Level 1 data dictionary can be downloaded from JPL's PO.DAAC Drive at https://podaac -tools.jpl.nasa.gov/drive/files/allData/cygnss/L1. Each Level 1 netCDF file contains the DDMs produced by one

CYGNSS observatory during one UTC day and the metadata used to convert from Level 0 (raw telemetry) to Level 1 data products. Note that the timestamp of all values is DDM time unless otherwise indicated. LNA stands for low noise amplifier, Tx is the transmitting spacecraft, and Rx is the receiving spacecraft.

Table 4.1. CYGNSS Level 1 Data and Metadata

netCDF name	Comment
Global Values	
time_coverage_start	ddm_timestamp_utc of the first sample in the file in ISO-8601 form
time_coverage_end	ddm_timestamp_utc of the last sample in the file in ISO-8601 form
time_coverage_duration	The time interval between time_coverage_start and time_coverage_end in ISO-1806 form
time_coverage_resolution	The nominal time interval between samples in ISO-1806 form
spacecraft_id	The CCSDS spacecraft identifier: 0xF7 (247): CYGNSS 1 0xF9 (249): CYGNSS 2 0x2B (43): CYGNSS 3 0x2C (44): CYGNSS 4 0x2F (47): CYGNSS 5 0x36 (54): CYGNSS 6 0x37 (55): CYGNSS 7 0x49 (73): CYGNSS 8 0x00 (0): E2ES 0x0E (14): Engineering model 0x0D (15): Default 0xFF (255): Unknown
spacecraft_num	The CYGNSS spacecraft number: Ranges from 1 through 8 and 99; 1 through 8 are on-orbit spacecraft; 99 is the CYGNSS end-to-end simulator.
ddm_source	The source of the Level 0 DDM raw counts and metadata. 0 = End-to-end simulator (E2ES) 1 = GPS signal simulator 2 = CYGNSS spacecraft 3 = Source unknown
ddm_time_type_selector	Determines the position of ddm_timestamp_utc relative to the DDM sampling period. Set to "Middle of DDM sampling period" for nominal science operations. Other settings are used for prelaunch testing only. 0 = Start of DDM sampling period (used for prelaunch testing only) 1 = Middle of DDM sampling period 2 = End of DDM sampling period (used for prelaunch testing only) 3 = pvt_timestamp_utc (used for prelaunch testing only)
delay_resolution	DDM delay bin resolution in chips. One chip is equal to 1/1,023,000 seconds.

(continued)

netCDF name	Comment
dopp_resolution	DDM Doppler bin resolution in Hz
l1_algorithm_version	The version number of the L1 processing algorithm.
lna_data_version	The version number of the LNA data lookup table.
eff_scatter_version	The version number of the effective scattering area lookup table.
ant_data_version	The version number of the antenna data lookup table.
ant_temp_version	The version number of the radiometric antenna temperature lookup table.
prn_sv_maps_version	The version number of the pseudorandom number (PRN) code to space vehicle number (SVN) lookup table.
gps_eirp_param_version	The version number of the GPS effective isotropic radiated power parameter lookup table.
land_mask_version	The version number of the Earth land mask lookup table.
near_land_mask_version	The version number of the Earth near-land mask lookup table.
very_near_land_mask_version	The version number of the Earth very-near-land mask lookup table.
open_ocean_mask_version	The version number of the open ocean mask lookup table.
ddm_a2d_version	The version number of the DDM digital to analog power conversion lookup table.
milky_way_version	The version number of the Milky Way mask lookup table.
fresnel_coeff_version	The version number of the Fresnel coefficient lookup table.
brcs_uncert_lut_version	The version number of the BRCS uncertainty lookup table.
ddma_les_sel_luts_version	The version number of the NBRCS (formerly known as DDMA) and LES bin selection table.
mean_sea_surface_version	The version of the mean sea surface lookup table.
per_bin_ant_version	The version of the per-bin antenna gain lookup table.
Per-Sample Values	
ddm_timestamp_utc	DDM sample time. The number of seconds since time_coverage_start with nanosecond resolution. Its position relative to the DDM sampling period is determined by ddm_time_type_selector. Some metadata required for DDM calibration are generated relative to pvt_timestamp_utc or att_timestamp_utc. These metadata are interpolated to ddm_timestamp_utc before being used for DDM calibration. Note that the DDM sampling period is not synchronized with the UTC change of second and can occur at any time relative to the UTC change of second.
ddm_timestamp_gps_week	The GPS week number of ddm_timestamp_utc.
ddm_timestamp_gps_sec	The GPS second of week of ddm_timestamp_utc with nanosecond resolution.
pvt_timestamp_utc	The spacecraft position and velocity epoch. The number of seconds since time_coverage_start with nanosecond resolution. This is the timestamp of the position and velocity reported by the delay-Doppler mapping instrument (DDMI). This is also the timestamp of the most recent GPS pulse per second.
pvt_timestamp_gps_week	The GPS week number of pvt_timestamp_utc.
pvt_timestamp_gps_sec	The GPS second of week of pvt_timestamp_utc with nanosecond resolution.
att_timestamp_utc	The spacecraft attitude epoch. The number of seconds since time_coverage_start with nanosecond resolution. This is the timestamp of the spacecraft attitude reported by the spacecraft attitude determination system.
att_timestamp_gps_week	The GPS week number of att_timestamp_utc.
att_timestamp_gps_sec	The GPS second of week of att_timestamp_utc with nanosecond resolution.
sc_pos_x	The X component of the spacecraft WGS-84 reference frame Earth-centered, Earth-fixed (ECEF) position, in meters, at ddm_timestamp_utc. Fill value is –99999999.
sc_pos_y	The Y component of the spacecraft WGS-84 reference frame ECEF position, in meters, at ddm_timestamp_utc. Fill value is –99999999.

(continued)

netCDF name	Comment
sc_pos_z	The Z component of the spacecraft WGS-84 reference frame ECEF position, in meters, at ddm_timestamp_utc. Fill value is –99999999.
sc_vel_x	The X component of the spacecraft WGS-84 reference frame ECEF velocity, in m/s, at ddm_timestamp_utc
sc_vel_y	The Y component of the spacecraft WGS-84 reference frame ECEF velocity, in m/s, at ddm_timestamp_utc
sc_vel_z	The Z component of the spacecraft WGS-84 reference frame ECEF velocity, in m/s, at ddm_timestamp_utc.
sc_pos_x_pvt	The X component of the spacecraft WGS-84 reference frame ECEF position, in meters, at pvt_timestamp_utc. Fill value is –99999999.
sc_pos_y_pvt	The Y component of the spacecraft WGS-84 reference frame ECEF position, in meters, at pvt_timestamp_utc. Fill value is –99999999.
sc_pos_z_pvt	The Z component of the spacecraft WGS-84 reference frame ECEF position, in meters, at pvt_timestamp_utc. Fill value is –99999999.
sc_vel_x_pvt	The X component of the spacecraft WGS-84 reference frame ECEF velocity, in m/s, at pvt_timestamp_utc.
sc_vel_y_pvt	The Y component of the spacecraft WGS-84 reference frame ECEF velocity, in m/s, at pvt_timestamp_utc.
sc_vel_z_pvt	The Z component of the spacecraft WGS-84 reference frame ECEF velocity, in m/s, at pvt_timestamp_utc.
nst_att_status	The nano star tracker attitude status. 0 = OK 1 = NOT_USED2 2 = BAD 3 = TOO_FEW_STARS 4 = QUEST_FAILED 5 = RESIDUALS_TOO_HIGH 6 = TOO_CLOSE_TO_EDGE 7 = PIX_AMP_TOO_LOW 8 = PIX_AMP_TOO_HIGH 9 = BACKGND_TOO_HIGH 10 = TRACK_FAILURE 11 = PIX_SUM_TOO_LOW 12 = UNUSED 13 = TOO_DIM_FOR_STARID 14 = TOO_MANY_GROUPS 15 = TOO_FEW_GROUPS 16 = CHANNEL_DISABLED 17 = TRACK_BLK_OVERLAP 18 = OK_FOR_STARID 19 = TOO_CLOSE_TO_OTHER 20 = TOO_MANY_PIXELS 21 = TOO_MANY_COLUMNS 22 = TOO_MANY_ROWS
sc_roll	Spacecraft roll angle relative to the orbit frame, in radians, at ddm_timestamp_utc.
sc_pitch	Spacecraft pitch angle relative to the orbit frame, in radians, at ddm_timestamp_utc.
sc_yaw	Spacecraft yaw angle relative to the orbit frame, in radians, at ddm_timestamp_utc.
sc_roll_att	Spacecraft roll angle relative to the orbit frame, in radians, at att_timestamp_utc.

(continued)

netCDF name	Comment
sc_pitch_att	Spacecraft pitch angle relative to the orbit frame, in radians, at att_timestamp_utc.
sc_yaw_att	Spacecraft yaw angle relative to the orbit frame, in radians, at att_timestamp_utc.
sc_lat	Subsatellite point latitude, in degrees north, at ddm_timestamp_utc.
sc_lon	Subsatellite point longitude, in degrees east, at ddm_timestamp_utc.
sc_alt	Spacecraft altitude above World Geodetic System (WGS)84 ellipsoid, in meters, at ddm_timestamp_utc.
zenith_sun_angle_az	The azimuth angle of the Sun in the zenith antenna spherical frame, at ddm_timestamp_utc, 0 <= angle < 360°. See University of Michigan (UM) document 148-0336, CYGNSS Science Data Processing Coordinate Systems Definitions.
zenith_sun_angle_decl	The declination angle of the Sun in the zenith antenna spherical frame, at ddm_timestamp_utc, 0 <= angle < 180°. See UM document 148-0336, CYGNSS Science Data Processing Coordinate Systems Definitions.
zenith_ant_bore_dir_x	The X component of the Earth-centered inertial (ECI) direction unit vector of the zenith antenna boresight at ddm_timestamp_utc.
zenith_ant_bore_dir_y	The Y component of the ECI direction unit vector of the zenith antenna boresight at ddm_timestamp_utc.
zenith_ant_bore_dir_z	The Z component of the ECI direction unit vector of the zenith antenna boresight at ddm_timestamp_utc.
rx_clk_bias	The receiver clock bias (in seconds) multiplied by the speed of light as reported by the DDMI, interpolated to ddm_timestamp_utc, in meters.
rx_clk_bias_rate	The receiver clock bias rate (in seconds/second) multiplied by the speed of light as reported by the DDMI, interpolated to ddm_timestamp_utc, in m/s.
rx_clk_bias_pvt	The receiver clock bias (in seconds) multiplied by the speed of light as reported by the DDMI, at pvt_timestamp_utc, in meters.
rx_clk_bias_rate_pvt	The receiver clock bias rate (in seconds/second) multiplied by the speed of light, as reported by the DDMI, at pvt_timestamp_utc, in m/s.
lna_temp_nadir_starboard	The temperature of the starboard antenna LNA at ddm_timestamp_utc, in °C.
lna_temp_nadir_port	The temperature of the port antenna LNA at ddm_timestamp_utc, in °C.
lna_temp_zenith	The temperature of the zenith antenna LNA at ddm_timestamp_utc, in °C.
ddm_end_time_offset	For diagnostic use only. See UM document 148-0372 CYGNSS L1 netCDF Diagnostic Variables for more information.
bit_ratio_hi_lo_starboard	For diagnostic use only. See UM document 148-0372 CYGNSS L1 netCDF Diagnostic Variables for more information.
bit_ratio_hi_lo_port	For diagnostic use only. See UM document 148-0372 CYGNSS L1 netCDF Diagnostic Variables for more information.
bit_null_offset_starboard	For diagnostic use only. See UM document 148-0372 CYGNSS L1 netCDF Diagnostic Variables for more information.
bit_null_offset_port	For diagnostic use only. See UM document 148-0372 CYGNSS L1 netCDF Diagnostic Variables for more information.
status_flags_one_hz	One Hz status flags. These flags apply to all four DDMs; 1 indicates presence of condition. Flag masks: 1 = Milky way in zenith antenna field of view 2 = Sun in zenith antenna field of view 4 = Subsatellite point over open ocean 8 = Subsatellite point latitude ascending (i.e., sc_lat is increasing)

netCDF name	Comment
Per-DDM Values	
prn_code	The PRN code of the GPS signal associated with the DDM. Ranges from 0 to 32; 0 = reflectometry channel idle; 1 to 32 = GPS PRN codes.
sv_num	The GPS unique space vehicle number that transmitted prn_code.
track_id	A track is a temporally contiguous series of DDMs that have the same prn_code. Each track in the file is assigned a unique track_id starting with 1; track_id ranges from 1 to N, where N is the total number of tracks in the file.
ddm_ant	The antenna that received the reflected GPS signal associated with the DDM. 0 = none 1 = zenith (never used) 2 = nadir_starboard 3 = nadir_port
zenith_code_phase	The DDMI-measured code phase of the direct GPS signal for prn_code interpolated to ddm_timestamp_utc. 0 <= zenith_code_phase < 1023.0.
sp_precise_delay	The specular point delay at ddm_timestamp_utc, in chips. One chip is equal to 1/1,023,000 seconds. Calculated on the ground from zenith_code_phase, tx_pos, sp_pos, and rx_pos.
sp_precise_dopp	The specular point Doppler at ddm_timestamp_utc, in Hz. Calculated on the ground from tx_pos, tx_vel, rx_pos, rx_vel, sp_pos, and rx_clk_bias_rate.
sp_ddmi_delay_correction	For diagnostic use only. See UM document 148-0372 CYGNSS L1 netCDF Diagnostic Variables for more information.
sp_ddmi_dopp_correction	For diagnostic use only. See UM document 148-0372 CYGNSS L1 netCDF Diagnostic Variables for more information.
add_range_to_sp	For diagnostic use only. See UM document 148-0372 CYGNSS L1 netCDF Diagnostic Variables for more information.
add_range_to_sp_pvt	For diagnostic use only. See UM document 148-0372 CYGNSS L1 netCDF Diagnostic Variables for more information.
sp_ddmi_dopp	For diagnostic use only. See UM document 148-0372 CYGNSS L1 netCDF Diagnostic Variables for more information.
sp_fsw_delay	For diagnostic use only. See UM document 148-0372 CYGNSS L1 netCDF Diagnostic Variables for more information.
sp_fsw_dopp	For diagnostic use only. See UM document 148-0372 CYGNSS L1 netCDF Diagnostic Variables for more information.
sp_delay_error	For diagnostic use only. See UM document 148-0372 CYGNSS L1 netCDF Diagnostic Variables for more information.
sp_dopp_error	For diagnostic use only. See UM document 148-0372 CYGNSS L1 netCDF Diagnostic Variables for more information.
fsw_comp_delay_shift	For diagnostic use only. See UM document 148-0372 CYGNSS L1 netCDF Diagnostic Variables for more information.
fsw_comp_dopp_shift	For diagnostic use only. See UM document 148-0372 CYGNSS L1 netCDF Diagnostic Variables for more information.
prn_fig_of_merit	The range corrected gain (RCG) figure of merit (FOM) for the DDM. Ranges from 0 to 15. The DDMI selects the four strongest specular points (SP) for DDM production. It ranks the strength of SPs using an antenna RCG map. The map converts the position of the SP in antenna azimuth and declination angles to an RCG FOM; 0 represents the least FOM value, and 15 represents the greatest FOM value.
tx_clk_bias	The GPS spacecraft (sv_num) clock time minus GPS constellation time in seconds times the speed of light, in meters.

(continued)

netCDF name	Comment
sp_lat	Specular point latitude, in degrees north, at ddm_timestamp_utc
sp_lon	Specular point longitude, in degrees east, at ddm_timestamp_utc
sp_alt	Altitude of the specular point relative to the WGS-84 datum in meters, at ddm_timestamp_utc, as calculated on the ground. Note that an approximated DTU 10 mean sea surface height model is used to calculate the specular point altitude.
sp_pos_x	The X component of the specular point position in the ECEF coordinate system, in meters, at ddm_timestamp_utc, as calculated on the ground. Fill value is –99999999.
sp_pos_y	The Y component of the specular point position in the ECEF coordinate system, in meters, at ddm_timestamp_utc, as calculated on the ground. Fill value is –99999999.
sp_pos_z	The Z component of the specular point position in the ECEF coordinate system, in meters, at ddm_timestamp_utc, as calculated on the ground. Fill value is –99999999.
sp_vel_x	The X component of the specular point velocity in the ECEF coordinate system, in m/s, at ddm_timestamp_utc, as calculated on the ground.
sp_vel_y	The Y component of the specular point velocity in the ECEF coordinate system, in m/s, at ddm_timestamp_utc, as calculated on the ground.
sp_vel_z	The Z component of the specular point velocity in the ECEF coordinate system, in m/s, at ddm_timestamp_utc, as calculated on the ground.
sp_inc_angle	The specular point incidence angle, in degrees, at ddm_timestamp_utc. This is the angle between the line normal to the Earth's surface at the specular point and the line extending from the specular point to the spacecraft. See UM document 148-0336, CYGNSS Science Data Processing Coordinate Systems Definitions.
sp_theta_orbit	The angle between the orbit frame +Z axis and the line extending from the spacecraft to the specular point, in degrees, at ddm_timestamp_utc. See UM document 148-0336, CYGNSS Science Data Processing Coordinate Systems Definitions.
sp_az_orbit	Let line A be the line that extends from the spacecraft to the specular point at ddm_timestamp_utc. Let line B be the projection of line A onto the orbit frame XY plane. sp_az_orbit is the angle between the orbit frame +X axis (the velocity vector) and line B, in degrees, at ddm_timestamp_utc. See UM document 148–0336, CYGNSS Science Data Processing Coordinate Systems Definitions.
sp_theta_body	The angle between the spacecraft body frame +Z axis and the line extending from the spacecraft to the specular point, in degrees, at ddm_timestamp_utc. See UM document 148-0336, CYGNSS Science Data Processing Coordinate Systems Definitions.
sp_az_body	Let line A be the line that extends from the spacecraft to the specular point, at ddm_timestamp_utc. Let line B be the projection of line A onto the spacecraft body frame XY plane. sp_az_body is the angle between the spacecraft body frame +X axis and line B, in degrees, at ddm_timestamp_utc. See UM document 148-0336, CYGNSS Science Data Processing Coordinate Systems Definitions.
sp_rx_gain	The receive antenna gain in the direction of the specular point, in dBi, at ddm_timestamp_utc.
gps_eirp	The estimated effective isotropic radiated power (EIRP) of the L1 course acquisition (C/A) code signal within ± 1 MHz of the L1 carrier radiated by space vehicle, sv_num, in the direction of the CYGNSS spacecraft, in watts, at ddm_timestamp_utc.
gps_tx_power_db_w	Power input to SV Tx antenna.
gps_ant_gain_db_i	SV antenna gain in the direction of the specular point.
gps_off_boresight_angle_deg	SV antenna off boresight angle in the direction of the specular point.
direct_signal_snr	10log(zenith signal power/zenith signal noise) at ddm_timestamp_utc.
ddm_snr	10log(Smax/Navg), where Smax is the maximum value (in raw counts) in a single DDM bin and Navg is the average per-bin raw noise counts. ddm_snr is in dB, at ddm_timestamp_utc.

(continued)

netCDF name	Comment
ddm_noise_floor	For non–black body DDMs: Is equal to the average bin raw counts in the first 45 delay rows of the uncompressed 20 × 128 DDM, in counts, at ddm_timestamp_utc. For black body DDMs: Is equal to the average bin raw counts in all 128 delay rows of the uncompressed 20 × 128 DDM, in counts, at ddm_timestamp_utc.
inst_gain	The black body noise counts divided by the sum of the black body power and the instrument noise power, in count/W, at ddm_timestamp_utc.
lna_noise_figure	The LNA noise figure, in dB, at ddm_timestamp_utc. Estimated from prelaunch characterization of LNA performance as a function of LNA temperature.
rx_to_sp_range	The distance between the CYGNSS spacecraft and the specular point, in meters, at ddm_timestamp_utc.
tx_to_sp_range	The distance between the GPS spacecraft and the specular point, in meters, at ddm_timestamp_utc.
tx_pos_x	The X component of the GPS spacecraft WGS-84 reference frame ECEF position, in meters, at ddm_timestamp_utc. Fill value is −99999999.
tx_pos_y	The Y component of the GPS spacecraft WGS-84 reference frame ECEF position, in meters, at ddm_timestamp_utc. Fill value is −99999999.
tx_pos_z	The Z component of the GPS spacecraft WGS-84 reference frame ECEF position, in meters, at ddm_timestamp_utc. Fill value is −99999999.
tx_vel_x	The X component of the GPS spacecraft WGS-84 reference frame ECEF velocity, in meters, at ddm_timestamp_utc.
tx_vel_y	The Y component of the GPS spacecraft WGS-84 reference frame ECEF velocity, in meters, at ddm_timestamp_utc.
tx_vel_z	The Z component of the GPS spacecraft WGS-84 reference frame ECEF velocity, in meters, at ddm_timestamp_utc.
bb_nearest	The time between ddm_timestamp_utc and the ddm_timestamp_utc of the closest (in time) black body reading, in signed seconds. A positive value indicates that the black body reading occurred after ddm_timestamp_utc. A negative value indicates that the block body reading occurred before ddm_timestamp_utc.
radiometric_antenna_temp	The top-of-atmosphere radiometric brightness temperature of the Earth at 1575 MHz and left-hand circular polarization, averaged over the nadir antenna pattern in which the specular point lies, in Kelvins.
fresnel_coeff	The square of the left-hand circularly polarized Fresnel electromagnetic voltage reflection coefficient at 1575 MHz for a smooth ocean surface at the specular point location and incidence angle. See UM document 148-0361 Fresnel coefficient calculation for more information.
ddm_nbrcs	Normalized BRCS of a 3 delay × 5 Doppler bin box that includes the specular point bin. The specular point bin is in the top (least delay) row and the center Doppler column of the 3 × 5 box.
ddm_les	Leading edge slope of a 3 delay × 5 Doppler bin box that includes the specular point bin. The specular point bin is in the top (least delay) row and the center Doppler column of the 3 × 5 box.
nbrcs_scatter_area	The scattering area of the 3 × 5 region of the DDM used to calculate ddm_nbrcs.
les_scatter_area	The scattering area of the 3 × 5 region of the DDM used to calculate ddm_les.
brcs_ddm_peak_bin_delay_row	The zero-based delay row of the peak value in the bistatic radar cross section DDM (BRCS). Ranges from 0 to 16.
brcs_ddm_peak_bin_dopp_col	The zero-based Doppler column of the peak value in the bistatic radar cross section DDM (BRCS). Ranges from 0 to 10.
brcs_ddm_sp_bin_delay_row	The zero-based delay row of the specular point delay in the bistatic radar cross section DDM (BRCS). Note that this is a floating point value.

netCDF name	Comment
brcs_ddm_sp_bin_dopp_col	The zero-based Doppler column of the specular point Doppler in the bistatic radar cross section DDM (BRCS). Note that this is a floating point value.
ddm_brcs_uncert	Uncertainty of the BRCS.
quality_flags	Per-DDM quality flags; 1 indicates presence of condition. Flag bit masks:
	1/0x00000001 = poor_overall_quality: the logical OR of large_sc_attitude_err, black_body_ddm, ddmi_reconfigured, spacewire_crc_invalid, ddm_is_test_pattern, channel_idle, low_confidence_ddm_noise_floor, sp_over_land, sp_very_near_land, large_step_noise_floor, large_step_lna_temp, direct_signal_in_ddm, low_confidence_gps_eirp_estimate, rfi_detected, brcs_ddm_sp_bin_delay_error, brcs_sp_bin_dopp_error, gps_pvt_sp3_error, brcs_lut_range_error, ant_data_lut_range_error, bb_framing_error, fsw_comp_shift_error.
	2/0x00000002 = s_band_powered_up: Set if S-band transmitter is powered up.
	4/0x00000004 = small_sc_attitude_err: Set if the absolute value of the spacecraft roll is between 1° and 30°, the pitch is between 1° and 10°, or the yaw is between 1° and 5°.
	8/0x00000008 = large_sc_attitude_err: Set if the absolute value of the spacecraft roll is greater than or equal to 30°, the pitch is greater than or equal to 10°, or the yaw is greater than or equal to 5°.
	16/0x00000010 = black_body_ddm: Set if the black body load was selected during the DDM sampling period.
	32/0x00000020 = ddmi_reconfigured: Set if the DDMI was reconfigured during the DDM sampling period.
	64/0x00000040 = spacewire_crc_invalid: Set if the DDM Cyclic Redundancy Check (CRC) transmitted from the DDMI to the spacecraft computer was not valid.
	128/0x00000080 = ddm_is_test_pattern: Set if the DDM is a test pattern generated by the DDMI.
	256/0x00000100 = channel_idle: Set if this reflectometry channel was not tracking a PRN.
	512/0x00000200 = low_confidence_ddm_noise_floor: Set if the difference between this DDM noise floor and the previous DDM noise floor is greater than 10%.
	1024/0x00000400 = sp_over_land: Set if the specular point is over land.
	2048/0x00000800 = sp_very_near_land: Set if the specular point is within 25 km of land.
	4096/0x00001000 = sp_near_land: Set if the specular point is within 50 km of land.
	16384/0x00004000 = large_step_lna_temp: Set if the LNA temperature rate of change is greater than 1°C per minute.
	32768/0x00008000 = direct_signal_in_ddm: Set if the absolute value of the difference between the direct signal code phase and the DDM signal code phase is less than or equal to 4.
	65536/0x00010000 = low_confidence_gps_eirp_estimate: Set when there is low confidence in the GPS effective isotropic radiated power estimate.
	131072/0x00020000 = rfi_detected: Set when the kurtosis of the DDM noise floor deviates from pure Gaussian (3.0) by more than 1.0.
	262144/0x00040000 = brcs_ddm_sp_bin_delay_error: Set if the calculated specular point bin zero-based delay row is less than 6 or greater than 10.
	524288/0x00080000 = brcs_ddm_sp_bin_dopp_error: Set if the calculated specular point bin zero-based Doppler column is less than 4 or greater than 6.
	1048576/0x00100000 = neg_brcs_value_used_for_nbrcs: Set if any bin in the 3 × 5 BRCS area used to calculate ddm_nbrcs has a negative value.
	2097152/0x00200000 = gps_pvt_sp3_error: Cannot calculate GPS SV position/velocity/time from SP3 file.
	4194304/0x00400000 = sp_non_existent_error: Specular point does not exist.

netCDF name	Comment
	8388608/0x00800000 = brcs_lut_range_error: Unable to index into BRCS uncertainty lookup table.
	16777216/0x01000000 = ant_data_lut_range_error: Unable to index into antenna data lookup table.
	33554432/0x02000000 = bb_framing_error: Insufficient black body data for calibration.
	67108864/0x04000000 = fsw_comp_shift_error: Flight software telemetry encoding error of the fsw_comp_delay_shift and fsw_comp_dopp_shift variables. Corrected in Flight Software (FSW) version 4.5.
	134217728/0x08000000 = low_quality_gps_ant_knowledge: The directional gain pattern of the GPS transmit antenna, and hence the value of its gain in the direction of the specular point, is less well known for block IIF GPS satellites. This flag indicates that Level 1 calibration was based on a GPS antenna gain value with a higher than normal uncertainty. The impact on retrieved wind speed values is typically less than 1 m/s at low to moderate wind speeds, so this is considered a nonfatal flag.
	268435456/0x10000000 = sc_altitude_out_of_nominal_range: The spacecraft's altitude is out of nominal altitude range. Nominal altitude is defined as between 490 km and 550 km.
Per-Bin Values	
raw_counts	17 × 11 array of DDM bin raw counts. These are the uncalibrated power values produced by the DDMI.
power_digital	17 × 11 array of DDM bin digital power, watts. See power_analog for more information.
power_analog	17 × 11 array of DDM bin analog power, watts. analog_power is the true power that would have been measured by an ideal (analog) power sensor. power_digital is the power measured by the actual 2-bit sensor, which includes quantization effects. power_analog has been corrected for quantization effects.
brcs	17 × 11 array of DDM bin bistatic radar cross section, m^2. The specular point is located in DDM bin round(brcs_ddm_sp_bin_delay_row), round(brcs_ddm_sp_bin_dopp_col).
eff_scatter	17 × 11 array of DDM bin effective scattering area, m^2. This is an estimate of the true surface scattering area that contributes power to each DDM bin after accounting for the GPS signal spreading function. It is calculated by convolving the GPS ambiguity function with the surface area that contributes power to a given DDM bin as determined by its delay and Doppler values and the measurement geometry. The specular point bin location matches the specular point bin location in BRCS.

4.2.2. Level 2 Data and Metadata Products

The Level 2 data and metadata in effect at the writing of this handbook are listed in Table 4.2. The most recent Level 2 data dictionary can be downloaded from JPL's PO.DAAC Drive at https://podaac-tools.jpl.nasa.gov/drive/files/allData/cygnss/L2.

Table 4.2. CYGNSS Level 2 Data and Metadata

Name	Comment
Global values	
time_coverage_start	sample_time of the first sample in the file in ISO-8601 form.
time_coverage_end	sample_time of the last sample in the file in ISO-8601 form.
time_coverage_duration	The time interval between test_coverage_start and test_coverage_end in ISO-8601 form.
time_coverage_resolution	The nominal time interval between samples in ISO-8601 form.
ddm_source	The source of the Level 0 DDM raw counts and metadata utilized to derive wind_speed. 0 = E2ES (CYGNSS end-to-end simulator) 1 = GPS signal simulator 2 = CYGNSS spacecraft 3 = Source unknown
nbrcs_les_sel_lookup_ tables_version	The GMF NBRCS and LES selection lookup table version number.
time_averaging_lookup_ tables_version	The GMF time-averaging lookup table version number.
nbrcs_wind_lookup_tables_ version	The GMF NBRCS to wind speed lookup table version number.
les_wind_lookup_tables_ version	The GMF LES to wind speed lookup table version number.
covariance_lookup_tables_ version	The GMF minimum covariance lookup table version number.
standard_deviation_lookup_ table_version	The GMF standard deviation lookup table version number.
l2_algorithm_version	Level 2 processing algorithm version number.
source	Level 1 netCDF source file names.
Per-sample values	
spacecraft_id	The CCSDS spacecraft identifier: 0xF7 (247): CYGNSS 1 0xF9 (249): CYGNSS 2 0x2B (43): CYGNSS 3 0x2C (44): CYGNSS 4 0x2F (47): CYGNSS 5 0x36 (54): CYGNSS 6 0x37 (55): CYGNSS 7 0x49 (73): CYGNSS 8 0x00 (0): E2ES 0x0E (14): engineering model 0x0D (15): default 0xFF (255): unknown
spacecraft_num	The CYGNSS spacecraft number: Ranges from 1 to 8 and 99; 1 to 8 are on-orbit spacecraft; 99 is the CYGNSS end-to-end simulator.
prn_code	The PRN code of the GPS signal associated with the DDMs utilized to derive wind_speed. Ranges from 0 to 32; 0 = reflectometry channel idle; 1 to 32 represents PRN code.

Name	Comment
sv_num	The GPS unique space vehicle number that transmitted prn_code.
antenna	The CYGNSS nadir antenna that received the reflected GPS signal associated with the DDMs utilized to derive wind_speed. 0 = none 1 = zenith (never used) 2 = nadir_starboard 3 = nadir_port
sample_time	The mean of ddm_timestamp_utc of the DDMs that were utilized to derive wind_speed. Note that the DDM sampling period is not synchronized with the UTC change of second, so sample_time can occur at any time relative to the UTC change of second.
lat	The mean of the specular point latitudes of the DDMs that were utilized to derive wind_speed, degrees north.
lon	The mean of the specular point longitudes of the DDMs that were utilized to derive wind_speed, degrees east.
sc_lat	The mean of the subsatellite point latitudes of the DDMs that were utilized to derive wind_speed, degrees north.
sc_lon	The mean of the subsatellite point longitudes of the DDMs that were utilized to derive wind_speed, degrees east.
sc_alt	The mean of the satellite altitudes above the WGS-84 ellipsoid of the DDMs that were utilized to derive wind_speed, meters.
wind_speed	The average surface wind speed of the 25 × 25 km cell centered on latitude and longitude derived from both the NBRCS and the LES observables using the fully developed seas geophysical model function, m/s. Multiple DDMs are utilized to derive wind_speed. The number of utilized DDMs ranges from 1 to 5.
fds_nbrcs_wind_speed	The average surface wind speed of the 25 × 25 km cell centered on latitude and longitude derived only from the NBRCS observable using the fully developed seas geophysical model function, m/s. Multiple DDMs are utilized to derive fds_nbrcs_wind_speed. The number of DDMs ranges from 1 to 5.
fds_les_wind_speed	The average surface wind speed of the 25 × 25 km cell centered on latitude and longitude derived only from the LES observable using the fully developed seas geophysical model function, m/s. Multiple DDMs are utilized to derive fds_les_wind_speed. The number of DDMs ranges from 1 to 5.
wind_speed_uncertainty	Standard deviation of the additive wind speed error in the minimum variance fully developed seas wind speed retrieval (dependent on the RCG of the specular point location, the block type of the GPS satellite, and the wind speed), in m/s.
yslf_nbrcs_wind_speed	The surface wind speed centered on latitude and longitude derived only from the NBRCS observable using the young seas / limited fetch geophysical model function, m/s. Multiple DDMs are utilized to derive wind_speed. The number of utilized DDMs ranges from 1 to 5.
yslf_les_wind_speed	The surface wind speed centered on latitude and longitude derived only from the LES observable using the young seas / limited fetch geophysical model function, m/s. Multiple DDMs are utilized to derive wind_speed. The number of utilized DDMs ranges from 1 to 5.
yslf_nbrcs_wind_speed_ uncertainty	Standard deviation of the additive wind speed error in yslf_nbrcs_wind_speed (dependent on the RCG of the specular point location, the block type of the GPS satellite, and the wind speed), in m/s.
yslf_les_wind_speed_ uncertainty	Standard deviation of the additive wind speed error in yslf_les_wind_speed (dependent on the RCG of the specular point location, the block type of the GPS satellite, and the wind speed), in m/s.
mean_square_slope	The average MSS of the 25 × 25 km cell centered on latitude and longitude, unitless.
mean_square_slope_ uncertainty	The uncertainty of mean_square_slope, unitless.

Name	Comment
incidence_angle	The mean of the incidence angles of the specular points of the DDMs that were utilized to derive wind_speed, degrees.
azimuth_angle	The mean of the orbit frame azimuth angles of the specular points of the DDMs that were utilized to derive wind_speed, degrees.
nbrcs_mean	The mean of the DDM NBRCS values that were utilized to derive wind_speed, unitless.
les_mean	The mean of the DDM LES values that were utilized to derive wind_speed, unitless.
range_corr_gain	The mean of the RCGs of the DDMs that were utilized to produce wind_speed. Individual RCGs are equal to the receive antenna gain in the direction of the specular point multiplied by 1e27 divided by the square of the receiver to the specular point range and the square of the transmitter to specular point range. Units: 1e27 *dBi * m^-4
fresnel_coeff	The square of the left-hand circularly polarized Fresnel electromagnetic voltage reflection coefficient at 1575 MHz for a smooth ocean surface at latitude, longitude. See UM document 148-0361 for a description of the calculation of the Fresnel coefficient, unitless.
num_ddms_utilized	The number of DDMs averaged together to produce wind_speed. The number of DDMs utilized depends on the incidence angle. Ranges from 1 to 5.
sample_flags	Set of flags indicating general conditions for the sample, set to 1 if condition is true. Flag bit masks: 1 = low_quality_gps_ant_knowledge. The directional gain pattern of the GPS transmit antenna, and hence the value of its gain in the direction of the specular point, is less well known for block type IIF GPS satellites. This flag indicates that Level 1 calibration was based on a GPS antenna gain value with a higher than normal uncertainty. The increase in uncertainty at higher wind speeds is reflected in the uncertainty data fields.
fds_sample_flags	Set of fully developed seas (FDS) status flags, set to 1 if condition is true. Flag bit masks: 1 = fatal_composite_wind_speed_flag, logical OR of fatal FDS flags (fatal_neg_wind_speed OR fatal_high_wind_speed OR fatal_retrieval_ambiguity OR fatal_low_range_corr_gain OR fatal_single_observable OR fatal_low_quality_gps_ant_knowledge) 2 = non_fatal_neg_wind_speed_flag, $-5 <$ wind_speed < 0 m/s 4 = non_fatal_neg_fds_nbrcs_wind_speed, $-5 <$ fds_nbrcs_wind_speed < 0 m/s 8 = non_fatal_neg_fds_les_wind_speed, $-5 <$ fds_les_wind_speed < 0 m/s 16 = fatal_neg_wind_speed, wind_speed $<= -5$ m/s 32 = fatal_neg_fds_nbrcs_wind_speed, fds_nbrcs_wind_speed $<= -5$ m/s 64 = fatal_neg_fds_les_wind_speed, fds_les_wind_speed $<= -5$ m/s 128 = fatal_high_wind_speed, fatal_high_fds_nbrcs_wind_speed and fatal_high_fds_les_wind_speed are both 1 256 = fatal_high_fds_nbrcs_wind_speed, nbrcs_mean corresponds to a wind speed > maximum FDS NBRCS lookup table wind speed at incidence_angle 512 = fatal_high_fds_les_wind_speed, les_mean corresponds to a wind speed > maximum FDS LES lookup table wind speed at incidence_angle 1024 = non_fatal_ascending, satellite is on the ascending node of the orbit (subsatellite point latitude is increasing) 2048 = fatal_retrieval_ambiguity, wind_speed was derived from both fds_nbrcs_wind_speed and fds_les_wind_speed AND the absolute value of the difference between fds_nbrcs_wind_speed and fds_les_wind_speed is > 10.0 m/s 4096 = fatal_single_observable, wind_speed was derived from a single observable, either fds_nbrcs_wind_speed or fds_les_wind_speed but not both 8192 = fatal_low_range_corr_gain, range_corr_gain < 1 16384 = fatal_low_quality_gps_ant_knowledge. The directional gain pattern of the GPS transmit antenna, and hence the value of its gain in the direction of the specular point, is less well known for block type IIF GPS satellites. This flag indicates that Level 1 calibration was based on a GPS antenna gain value with a higher than normal uncertainty. The increase in uncertainty at higher wind speeds is reflected in the wind_speed_uncertainty data field.

Name	Comment
yslf_sample_flags	Set of young seas limited fetch (YSLF) status flags, set to 1 if condition is true. Flag bit masks: 1 = fatal_composite_yslf_wind_speed, logical OR of fatal YSLF flags (fatal_neg_yslf_wind_speed OR fatal_high_yslf_wind_speed OR fatal_low_range_corr_gain OR fatal_low_quality_gps_ant_knowledge) 2 = spare_3, always zero 4 = spare_4, always zero 8 = fatal_neg_yslf_wind_speed, non_fatal_neg_yslf_nbrcs_wind_speed and non_fatal_neg_yslf_les_wind_speed are both 1 16 = non_fatal_neg_yslf_nbrcs_wind_speed, yslf_nbrcs_wind_speed <= –5 m/s 32 = non_fatal_neg_yslf_les_wind_speed, yslf_les_wind_speed <= –5 m/s 64 = spare_5, always zero 128 = fatal_high_yslf_wind_speed, either fatal_high_yslf_nbrcs_wind_speed or fatal_high_yslf_les_wind_speed is 1 (or both are one) 256 = fatal_high_yslf_nbrcs_wind_speed, nbrcs_mean corresponds to a YSLF wind speed ≥ 99.9 m/s 512 = fatal_high_yslf_les_wind_speed, les_mean corresponds to a YSLF wind speed ≥ 99.9 m/s 1024 = non_fatal_ascending, satellite is on the ascending node of the orbit (subsatellite point latitude is increasing) 2048 = spare_6, always zero 4096 = spare_7, always zero 8192 = fatal_low_yslf_range_corr_gain, range corrected gain of the DDM used for YSLF winds is < 1 16384 = fatal_low_quality_gps_ant_knowledge. The directional gain pattern of the GPS transmit antenna, and hence the value of its gain in the direction of the specular point, is less well known for block IIF GPS satellites. This flag indicates that Level 1 calibration was based on a GPS antenna gain value with a higher than normal uncertainty. The increase in uncertainty at higher wind speeds is reflected in the yslf_nbrcs_wind_speed_uncertainty and yslf_les_wind_speed_uncertainty data fields.
sum_neg_brcs_values_used_for_nbrcs_flags	The number of DDMs utilized to produce wind_speed that used at least one negative BRCS value to calculate NBRCS. Ranges from 1 to 5.

Per-DDM values

Wind retrievals are produced utilizing from one to five DDMs. The values below are five element arrays, which contain per-DDM values. The DDMs that were utilized for wind retrieval are indicated by the ddm_obs_utilized_flag array. Unutilized DDMs are assigned fill values.

Name	Comment
ddm_obs_utilized_flag	A five-element array, one element per DDM. Each element is a flag set to 1 if the corresponding DDM was utilized to produce wind_speed.
ddm_sample_index	A five-element array, one per DDM. Contains the Level 1 netCDF sample index of the corresponding DDM. Can be utilized together with ddm_channel, spacecraft_num and "source" to look up the corresponding Level 1 DDM data and metadata.
ddm_channel	A five-element array, one per DDM. Contains the Level 1 netCDF reflectometry channel of the corresponding DDM. Can be utilized together with the ddm_sample_index, spacecraft_num and "source" to look up the corresponding Level 1 DDM data and metadata.
ddm_les	A five-element array, one element per DDM. Contains the corresponding DDM leading edge slope value, unitless.
ddm_nbrcs	A five-element array, one element per DDM. Contains the corresponding DDM normalized bistatic radar cross section value, unitless.

4.2.3. Level 3 Data and Metadata Products

The Level 3 data and metadata in effect at the writing of this handbook are listed in Table 4.3. The most recent Level 3 data dictionary can be downloaded from JPL's PO.DAAC Drive at https://podaac-tools.jpl.nasa.gov/drive/files/allData/cygnss/L3.

Table 4.3. CYGNSS Level 3 Data and Metadata

Global values	
Time (time)	Timestamp coordinate at the center of the 1 hr bin, at 1 hr resolution. Range is one UTC day.
Latitude (lat)	Latitude coordinate at the center of the 0.2° bin, degrees_north, at 0.2° resolution. Range is −39.9 to 39.9.
Longitude (lon)	Longitude coordinate at the center of the 0.2° bin, degrees_east, at 0.2 °resolution. Range is 0.1 to 359.9.
Wind speed (wind_speed)	Minimum variance estimate of the mean wind speed in the bin over the spatial and temporal intervals specified by the bin's boundaries. This is done using an inverse-variance weighted average of all Level 2 samples of the wind speed that were made within the bin.
Wind speed uncertainty (wind_speed_uncertainty)	Standard deviation of the error in the mean of all Level 2 samples of the wind speed within the bin.
Young sea limited fetch wind speed (yslf_wind_speed)	Minimum variance estimate of the young sea limited fetch mean wind speed in the bin over the spatial and temporal intervals specified by the bin's boundaries. This is done using an inverse-variance weighted average of all Level 2 samples of the wind speed that were made within the bin.
Young sea limited fetch wind speed uncertainty (yslf_wind_speed_uncertainty)	Standard deviation of the error in the mean of all Level 2 samples of the young sea limited fetch wind speed within the bin.
Number of wind speed samples (num_wind_speed_samples)	The number of Level 2 wind speed samples used to calculate wind_speed.
Mean square slope (mean_square_slope)	Minimum variance estimate of the mean MSS in the bin over the spatial and temporal intervals specified by the bin's boundaries. This is done using an inverse-variance weighted average of all Level 2 samples of the MSS that were made within the bin.
Mean square slope uncertainty (mean_square_slope_uncertainty)	Standard deviation of the error in the mean of all Level 2 samples of the MSS within the bin.
Number of mean square slope samples (num_mss_samples)	The number of Level 2 MSS samples used to calculate mean_square_slope.

Next, Chapters 5–10 provide the reader with relevant excerpts from the ATBDs, which describe the physical and mathematical descriptions of the algorithms used in the generation of Science Data Products in more detail. The ATBDs include a description of variance and uncertainty estimates and considerations of calibration and validation, exception control, and diagnostics. Internal and external data flows are also described. Users requiring more information than what is found in this section should consult Chapters 5–10 as well as the appendix (Ocean Surface Bistatic Scattering Forward Model) found at the end of this handbook.

4.3. References

Clarizia, M. P., & Ruf, C. (2014). Wind speed retrieval algorithm for the Cyclone Global Navigation Satellite System (CYGNSS) mission. *IEEE Transactions on Geoscience and Remote Sensing, 54*(8), 4419–4432. https://doi.org/10.1109/TGRS.2016.2541343.

Gleason, S., Ruf, C. S., Clarizia, M. P., & O'Brien, A. (2016). Calibration and unwrapping of the normalized scattering cross section for the Cyclone Global Navigation Satellite System (CYGNSS). *IEEE Transactions on Geoscience and Remote Sensing, 54*(5), 2495–2509. https://doi.org/10.1109/TGRS.2015.2502245.

5. Instrument Calibration and Error Analysis

5.1. Instrument Level 0 Measurements

This is a portion of the overall Level 1 (L1) Calibration Algorithm Theoretical Basis Document (ATBD) describing the Level 1A (L1A) calibration and error analysis (Gleason et al., 2019).

Individual bins of the delay-Doppler map (DDM) generated by the delay-Doppler mapping instrument (DDMI) are measured in raw, uncalibrated units referred to as "counts." These counts are linearly related to the total signal power processed by the DDMI. In addition to the ocean surface scattered GPS signal, the total signal includes contributions from the thermal emission by the Earth and by the DDMI itself. The power in the total signal is the product of all the input signals multiplied by the gain of the DDMI receiver. L1A calibration converts each bin in the DDM from raw counts to units of watts. A flowchart of the L1A calibration procedure is shown in Figure 5.1.

5.1.1. Calibration Intervals

The black body calibration will be performed every 60 seconds on orbit for each nadir science antenna. The routine
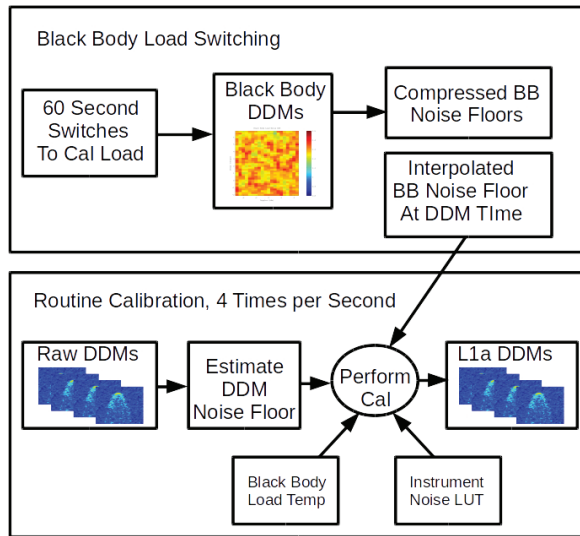
Figure 5.1. Overview of CYGNSS L1A calibration. The switches to the calibration load on each of the nadir antennas are performed every 60 seconds to obtain an estimate of the instrument-only noise counts C_B. This in combination with the estimated DDM noise floor C_N, black body load physical temperature T_l and prelaunch characterized instrument noise power P_r are used to generate the calibrated L1A DDMs.

calibration will be performed at 1 Hz on all DDM output by the DDMI (4 per second).

5.1.2. Level 0 Delay-Doppler Map

The DDM values output from the CYGNSS science instrument will be sent to the CYGNSS spacecraft as arbitrary counts. The count values will be a result of the signal traveling through the various stages of the instrument, which will add a gain to the received power levels. The value of the pixels in the DDM in arbitrary counts can be linked to the arriving signal power in watts such that

$$C = G(P_a + P_r + P_g), \qquad (5.1)$$

where

    C are the DDM values in counts output from the instrument at each delay-Doppler bin.

    P_a is the thermal noise power received by the antenna in watts.

    P_r is the thermal noise power generated by the instrument in watts.

    P_g is the scattered signal power received by the instrument in watts.

    G is the total instrument gain applied to the incoming signal and noise in counts per watt.

The terms C and P_g are functions of delay and Doppler, while P_a and P_r are assumed to be independent of the delay-Doppler bin in the DDM. Every DDM includes a number of delay bins where signal power is not present and an individual DDM noise floor level can be estimated. These bins physically represent delays above the ocean surface. These delay and Doppler bins provide an estimate of the DDM noise power, expressed in counts as

$$C_N = G(P_a + P_r). \qquad (5.2)$$

Assuming P_a and P_r are independent of delay and Doppler, the DDM samples above the ocean surface can be used to estimate the noise-only contribution to the raw counts expressed in Equation 5.1.

5.1.3. Noise Power Expressions

The input antenna noise can be generically expressed as

$$P_a = kT_aB_W, \tag{5.3}$$

where T_a is the top of the atmosphere brightness temperature integrated over the receive antenna pattern, k is Boltzmann's constant, and $B_W = \dfrac{1}{T_i} = 1000Hz$ is the signal bandwidth (Ruf et al., 2016). The bandwidth of the GPS signal at the antenna is determined by the coherent integration processing interval, which is $T_i = 1$ ms. When the instrument input is switched to the calibration load, the input antenna noise becomes

$$P_B = kT_lB_W, \tag{5.4}$$

where P_B and T_l are the noise power and effective temperature of the instrument black body load source. The black body load resistor lies on the thermal continuous LNA main board, where the temperature sensor is located, thus the black body (BB) load temperature and LNA portion of the instrument are assumed to be nearly equivalent (Jansen et al., 1995). T_l refers to the physical temperature of the instrument LNA and black body load resistor in this analysis. The instrument thermal noise power can be expressed as a function of the instrument noise figure

$$P_r = kT_rB_W = k[(NF - 1)290]B_W, \tag{5.5}$$

where P_r and T_r are the instrument noise power and temperature. The receiver noise figure NF is directly related to the instrument noise temperature. The noise figure versus temperature profile was characterized prelaunch for all instrument LNAs, providing an accurate estimate of the instrument noise figure as a function of temperature, from which the instrument noise power can be calculated using Equation 5.5.

5.1.4. Instrument Calibration Measurements

The instrument noise power will be initially calculated using gain and noise figure temperature profiles generated prelaunch for both instrument LNAs on each satellite. Using these tables, the instrument noise power can be estimated directly from the LNA temperature T_r and Equation 5.5. Subsequently, the expression for the DDM noise counts when the instrument is switched to the black body calibration load can be calculated as

$$C_B = G(P_B + P_r), \tag{5.6}$$

where P_B is the black body noise power and P_r is the instrument power. P_B can be calculated using Equation 5.4, and P_r is calculated using prelaunch lookup tables and Equation 5.5.

5.1.5. Instrument Noise Power Estimation Using a Lookup Table

It will be necessary to estimate the instrument noise power at every measurement due to LNA temperature fluctuations. This will be done using a lookup table derived from measured characteristics of the LNA gain and noise figure as a function of temperature. Thermal testing of the LNA noise figure performance as a function of temperature for all 27 CYGNSS LNAs (1 zenith and 2 nadir per spacecraft) was performed over several thermal cycles to generate a best linear fit function, which is used to estimate the noise figure as a function of temperature on orbit.

The mean standard deviation of the noise figure across the range of temperatures is 0.027 dB. The maximum slope is 0.0088 dB/°C, which when multiplied by the temperature uncertainty results in an estimated error in the instrument noise figure of 0.018 dB due to temperature uncertainty. The total noise figure error is taken as the RSS of the standard deviation of the measurements and the temperature error, which is 0.032 dB.

The temperature of the LNA is read at 1 Hz, and the value of the instrument noise figure is retrieved from a lookup table (LUT) generated from prelaunch testing. The LUT is then updated on orbit using instrument noise floor estimates performed at sufficient intervals to track slow changes in the LNA performance. The instrument noise figure from the LUT is related to the instrument noise power using Equation 5.5.

5.1.6. Updating Instrument LUTs On-Orbit

The strategy for updating the prelaunch NF versus temperature LUTs has changed from the initial L1A ATBD. During its first year on orbit, it was not possible to identify Earth surface areas that produced consistent and predictable noise levels from which a stable open ocean noise value could be reliably obtained. This is believed to be due largely to the fact that the CYGNSS science antennas are both canted toward the spacecraft along track and have a relatively large main lobe with significant gain. This large field of view to both the port and starboard sides of the spacecraft enabled surface noise from very large areas over the Earth's surface to enter the main antenna beams. This made it very difficult to isolate even the most remote regions of open ocean and obtain a reliable open ocean noise reference.

Therefore, an alternative method is being designed for the monitoring and updating of the NF calibration tables

on orbit. Fortunately, the CYGNSS LNAs are proving to be remarkably stable, even after more than 1 year on orbit. A number of techniques using the full set of existing on-orbit data are being used to quantify the changing instrument noise figure as the instrument ages on orbit.

5.2. Routine Calibration of Signal Power

The generic instrument DDM in counts is expressed in Equation 5.1, which includes the received signal power, P_g. These DDMs will be generated by the instrument every second and will be corrected by the estimated noise floor expressed in Equation 5.2 and calculated using noise-only bins in the DDM such that we are left with a signal-only DDM:

$$C_g = C - C_N = GP_g. \tag{5.7}$$

Subsequently, the instrument gain at the collection time of the DDM can be calculated using the current estimate of the LNA physical temperature, T_I, from which we estimate the instrument noise power, P_r. This is achieved by rearranging Equation 5.7 into an expression of the instrument gain and setting this equal to the instrument gain expression obtained from the black body load calibration DDM from Equation 5.6,

$$G = \frac{C - C_N}{P_g} = \frac{C_B}{P_B + P_r}, \tag{5.8}$$

where

- C_B is the best estimate mean counts of the black body load DDM at the time of the measurement being calibrated. The black body load counts are linearly interpolated to the second of the measurement using black body DDMs before and after the DDM being calibrated.
- P_B is the estimated black body load noise power estimated using the last LNA instrument thermistor temperature reading T_I near the load itself in the LNA and Equation 5.4, taken within a second of the DDM being calibrated.
- P_r is the estimate of the instrument noise power, estimated from the noise figure versus physical temperature (T_I) lookup table generated prelaunch for this specific LNA.

5.2.1. Generating the L1A Data Product

The routine calibration assumes that the gain G, antenna noise temperature T_a, and instrument noise power P_r

remain constant over the combined collection interval for Equation 5.1 (DDM to be calibrated) and Equation 5.2 (noise floor estimate for the DDM being calibrated). The black body noise counts used in Equation 5.6 are linearly interpolated from black body DDMs before and after the calibration DDM to the measurement time. By substituting Equation 5.8 into Equation 5.7 and solving for the signal power term, P_g, we arrive at the final L1A calibration:

$$P_g = \frac{(C - C_N)(P_B + P_r)}{C_B} \tag{5.9}$$

Equation 5.9 is applied to all pixels of the compressed Level 0 (L0) DDMs (11 Doppler bins × 17 delay bins) four times per second for each instrument measurement channel.

5.2.2. Digital to Analog DDM Scaling Issue

In the original CYGNSS L1A calibration algorithm, the entire L1A DDM was scaled from digitally sampled DDM values to the equivalent analog sampled power based on the 2-bit analog to digital sample distribution. This correction was based on well-known methods in radio astronomy for dealing with finite digital sampling of analog signals. However, examination of closely geolocated tracks between different observatories at very close time intervals revealed an observed bias between measurements over nearly identical conditions. Figure 5.2 (top) shows one such case, where Flight Model (FM) 6 and FM 8 pass over nearly the same surface within 5 minutes of each other, yet a clear difference in the normalized bistatic radar cross section (NBRCS) values can be observed over the length of the track. Upon subsequent investigation, an issue in the analog to digital scaling being applied was found in which the calculated correction between digital and analog measurements was incorrect and introduced significant statistical biases between observatories.

Upon removal of the existing digital to analog scaling, the overall intersatellite bias statistics improved significantly. Figure 5.2 (bottom) shows the same two tracks after the scaling has been removed, with good agreement across the entire track.

The exact problem with the digital to analog scaling is being investigated and has not yet been identified. However, as a significant reduction in intersatellite measurement bias was demonstrated with the removal of the digital to analog scaling factor, it was incorporated into v2.1 of the publically released data.
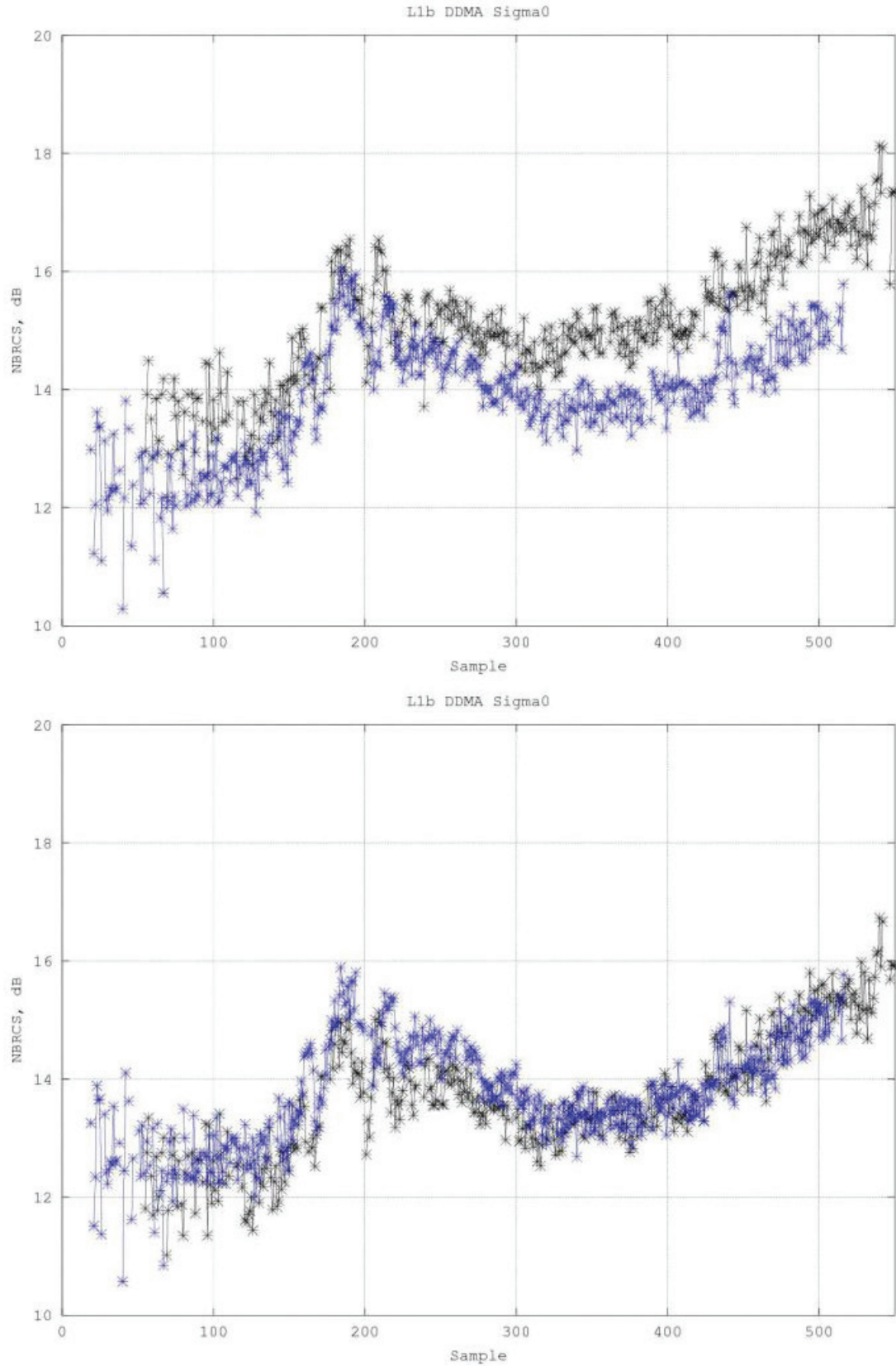
Figure 5.2. *Top:* Intersatellite bias between tracks of FM 6 and FM 8 on August 23, 2018, less than 5 minutes apart. *Bottom:* After digital to analog scaling is removed, NBRCS values agree much better across the same ocean track.

5.2.3. Consideration of Time and Temperature Dependencies

All the terms in Equation 5.9 are collected at slightly different times than the actual science measurements themselves, and during these time intervals, it is possible that the noise temperatures can vary slightly from the measurement time. Each of the terms in the L1A calibration equation is addressed below with regard to this time difference:

1. C = The science measurement is made once per second per channel and provides the reference time for all the other parameters.
2. C_N = The noise measurements for each science DDM are made at delays above the ocean surface, which are only on the order of a handful of microseconds from the time of the science measurement.
3. P_B = The blackbody target power is determined from a physical temperature sensor measured at 1 Hz and near enough in time to the 1 Hz science measurements that the physical temperature will not have changed significantly between the thermistor reading and the science measurement.
4. P_r = The receiver noise power is derived from a prelaunch-generated LUT and will be subject to change over the mission lifetime due to instrument aging effects. This will be corrected by periodically updating the calibration LUTs over the duration of the mission as described above. It is expected that the aging effects will occur on a very slow time scale, on the order of several months.
5. C_B = The black body target measurement is made within 30 seconds of the science measurement and linearly interpolated to the measurement time using black body measurements before and after the DDM being calibrated. Any changes in the instrument temperature over up to 30 seconds should be adequately mitigated by this interpolation.

The LUTs used to estimate P_r will be periodically updated on orbit. The dependence of P_r on temperature has been initially characterized in prelaunch environmental testing, and the baseline flight lookup table was derived from those test data. As monthly data are analyzed, the lookup tables for each LNA on each satellite will be updated on orbit as required.

5.3. Level 1B Calibration Approach

This document is the second part of the overall L1 Calibration Algorithm Theoretical Basis Document (ATBD) describing the Level 1B (L1B) calibration. Portions of this ATBD have been republished in Gleason et al. (2019).

The L1B calibration is performed after the L1A calibration and uses external metadata to convert the L1A mapped power in watts to a delay-Doppler map (DDM) of NBRCS values. This conversion is done for every pixel in every DDM and requires the following information at the time the science DDM is collected:

1. The CYGNSS satellite GPS time, position, and velocity in the WGS-84 Earth-centered, Earth-fixed (ECEF) reference frame
2. The GPS satellite position and velocity in the WGS-84 ECEF reference frame
3. Detailed knowledge of the CYGNSS nadir antenna gain patterns
4. Best estimated attitude knowledge of the CYGNSS spacecraft at the time of the measurement
5. An estimate of the GPS effective isotropically radiated power (EIRP) in the direction of the specular reflection point in the GPS satellite reference frame

Additional information calculated using the per-DDM science metadata and used in the L1B calibration of each DDM includes the following:

1. An accurate surface geolocation of the reflection specular point (SP) in the WGS-84 ECEF reference frame
2. A precise estimate of the specular reflection point location in the measurement DDM pixel delay and Doppler bins
3. The path length between the GPS satellite and specular reflection point and between the specular reflection point and the CYGNSS spacecraft making the measurement
4. The effective scattering area per DDM bin surrounding the specular point over all delay and Doppler bins

The above parameters are then used to estimate values of the bistatic radar cross section for each DDM pixel using the forward model described below.

5.4. Forward Model of Scattered Signal Power

A full expression for the GPS scattered signal power has been previously derived and published in 2000 by Zavorotny and Voronovich, shown in Equation 5.17. The original representation has been slightly modified in form and variable names:

$$P_{\hat{\tau},\hat{f}}^{g} = \frac{P^T \lambda^2}{(4\pi)^3} \iint_A \frac{G_{x,y}^T \sigma_{x,y}^0 G_{x,y}^R}{(R_{x,y}^R)^2 (R_{x,y}^T)^2} \Lambda_{\hat{\tau};x,y}^2 S_{\hat{f};x,y}^2 \, dxdy,$$ **(5.17)**

where $P_{\hat{\tau},\hat{f}}^{g}$ is the coherently processed scattered signal power in watts. P^T is the GPS satellite transmit power and $G_{x,y}^T$ is the GPS satellite antenna gain. $G_{x,y}^R$ is the CYGNSS satellite receiver antenna gain. $R_{x,y}^T$ and $R_{x,y}^R$ are the transmitter to surface and surface to receiver ranges, respectively. $\sigma_{x,y}^0$ is the NBRCS. Λ is the GPS signal carrier wavelength (approx. 19 cm). $\Lambda_{\hat{\tau};x,y}$ is the GPS signal spreading function in delay, and $S_{\hat{f};x,y}$ is the frequency response of the GPS signal. A is the surface integration area covering the effective region of diffuse scattering for each delay-Doppler bin. The scattered signal power is processed using 1 ms coherent integration intervals over a range of relative delays τ and Doppler frequencies f, followed by 1 second of noncoherent averaging. These delay and frequency bins map nonuniquely and spatially to physical coordinates on the surface.

The above expression can be simplified using the effective values of several variables across delay and Doppler bins under the integrand of Equation 5.1. The effective values include the effects of delay and Doppler spreading functions, Λ and S, which have been eliminated from the equation and are indicated by the overbar in the following equations. The surface mapping from physical (x,y) coordinates to delay and Doppler coordinates reflects the actual processing as performed in the CYGNSS delay-Doppler mapping instrument (DDMI),

$$P_{\hat{\tau},\hat{f}}^{g} = \frac{P^T \lambda^2 G_{\hat{\tau},\hat{f}}^T < \sigma_{\hat{\tau},\hat{f}}^0 > \overline{G}_{\hat{\tau},\hat{f}}^R \overline{A}_{\hat{\tau},\hat{f}}}{(4\pi)^3 (\overline{R}_{\hat{\tau},\hat{f}}^R)^2 (\overline{R}_{\hat{\tau},\hat{f}}^T)^2},$$ **(5.18)**

where $\overline{G}_{\hat{\tau},\hat{f}}^R$ = the effective receiver antenna gain at each delay-Doppler bin. $\overline{R}_{\hat{\tau},\hat{f}}^T$ and $\overline{R}_{\hat{\tau},\hat{f}}^R$ are the effective range losses at each delay-Doppler bin, and $\overline{A}_{\hat{\tau},\hat{f}}$ is the effective surface scattering area at each delay-Doppler bin. All variables in Equation 5.18 vary with respect to delay and Doppler (which map to the x,y surface grid over the glistening zone); however, for the sake of simplification and with negligible loss in accuracy, several parameters can be estimated and applied as constants across the DDM measurement as expressed below.

5.5. Geolocation of Measurement: Solving for the Surface Specular Reflection Point

The estimated location of the center of the surface glistening zone of the reflected signal provides the main point of reference for the geolocation of the global navigation satellite system reflectometry (GNSS-R) measurement. This point on the surface is referred to as the specular point and can be estimated mathematically using the physical geometry of the transmitting and receiving satellites and a model of the Earth's ocean surface. It should be noted that the surface specular point estimation algorithm described below is designed for ocean surfaces. Land specular points over varying topography present unique challenges and will contain additional geolocation errors not yet accounted for in the current CYGNSS L1 calibration.

In the original L1 calibration approach, the specular point was solved using (a) the position of the receiving satellite as estimated by the 1 Hz single frequency position estimate, (b) the estimate of the transmitting satellite using ground-based precise ephemeris, and (c) the WGS-84 ellipsoid model of the Earth. This Earth model, although generally accurate enough for most applications, relied on approximations that resulted in residual specular point position estimation errors that were large enough to significantly impact the pixels in the DDM used to calculate the bistatic radar cross section. Subsequently, an improved specular point solver was implemented that used a more accurate DTU10 mean sea surface model (Andersen, 2010) combined with a brute force, computationally efficient specular point solver algorithm.

The specular point on the Earth maps to a single point in the delay-Doppler coordinates in the CYGNSS DDM. The exact specular point location in the DDM will be at a fractional pixel within a single DDM bin. The pixels in the DDM at and surrounding the specular point bin determine the region used to make the surface bistatic radar cross section measurement, the DDM area (DDMA). The estimation of the DDMA within the L1A DDM is described in more detail below using the precise location of the specular point described here. This region of the DDM represents the bins of highest reflected power and smallest spatial footprint on the surface, and accurate knowledge of these regions is critical for calibration and wind speed retrievals.

The specular point location on the surface cannot be reliably estimated using the peak power bin of the DDM. The peak power pixel results from a combination of effects in addition to the specular point location, including thermal

noise, speckle noise, or asymmetries in the reflected signal waveform (as a result of geometry and antenna pattern nonuniformity). For this reason, the specular point surface location and location of the specular point in the instrument-generated DDM are calculated to a subpixel level from first principles (i.e., geometry and timing metadata).

5.5.1. Mean Sea Surface Height Model

In order to more precisely predict the specular location, it is necessary to account for deviations in the Earth's mean sea surface height as compared to the WGS-84 model. For this purpose, we have utilized the DTU 10 mean sea surface model (Andersen, 2010). The mean sea surface is the displacement of the sea surface relative to a mathematical model of the Earth, and it closely follows the Earth's geoid. The amplitude of the deviation from the WGS-84 ellipsoid is generally within approximately ± 100 m over the Earth's ocean surfaces. The original DTU 10 data were reduced to a 1° by 1° resolution to improve the efficiency of the calculation, which is reasonable due to the fact that height variations are relatively small. The DTU 10 map of sea surface height variations relative to the WGS-84 ellipsoid used in the specular point solver is shown in Figure 5.3.

The path delay error manifests itself as an error in the predicted reflection path delay, which, in turn, becomes an error in the predicted location of the specular bin in the DDM. The error in predicted path delay can be expressed as

$$\rho = 2\cos(\theta)\delta h, \tag{5.19}$$

where ρ is the path delay error, θ is the reflection incidence angle, and Δ is the relative surface height error with respect to the WGS-84 ellipsoid. The height difference manifests as a path delay error, which becomes an error in the predicted location of the specular bin in the DDM. For a typical incidence angle of 30°, a surface height error of 100 m could result in 170 m of path delay error. In the CYGNSS DDM, the delay pixel resolution is approximately 0.25 GPS L1 coarse acquistion (C/A) code chips, and one chip corresponds to approximately 293 m of delay. Therefore, a 170 m path delay error results in the predicted specular bin in the DDM being offset by 2.25 pixels from where we would expect it on the WGS-84 ellipsoid.

Figure 5.4 shows a plot of specular bin delay difference when using DTU 10 as opposed to using WGS-84. Specular delay differences are shown for 1 day of measurements for four satellites (each shown in four separate colors). We can observe that the delay difference (or correction) due to the improved specular point solver varies between −2 and 2.5 pixels in delay space in the DDM. Figure 5.4 also shows an example measured CYGNSS DDM. In the DDM, the original specular bin solved using WGS-84 model is shown as
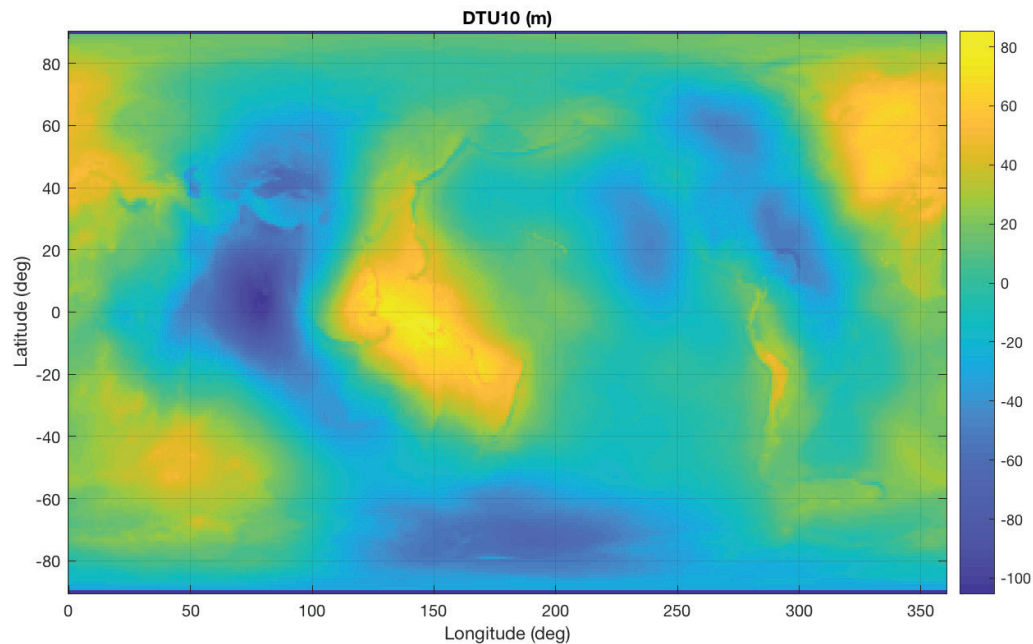
Figure 5.3. DTU 10 mean sea surface data used for specular point calculation.
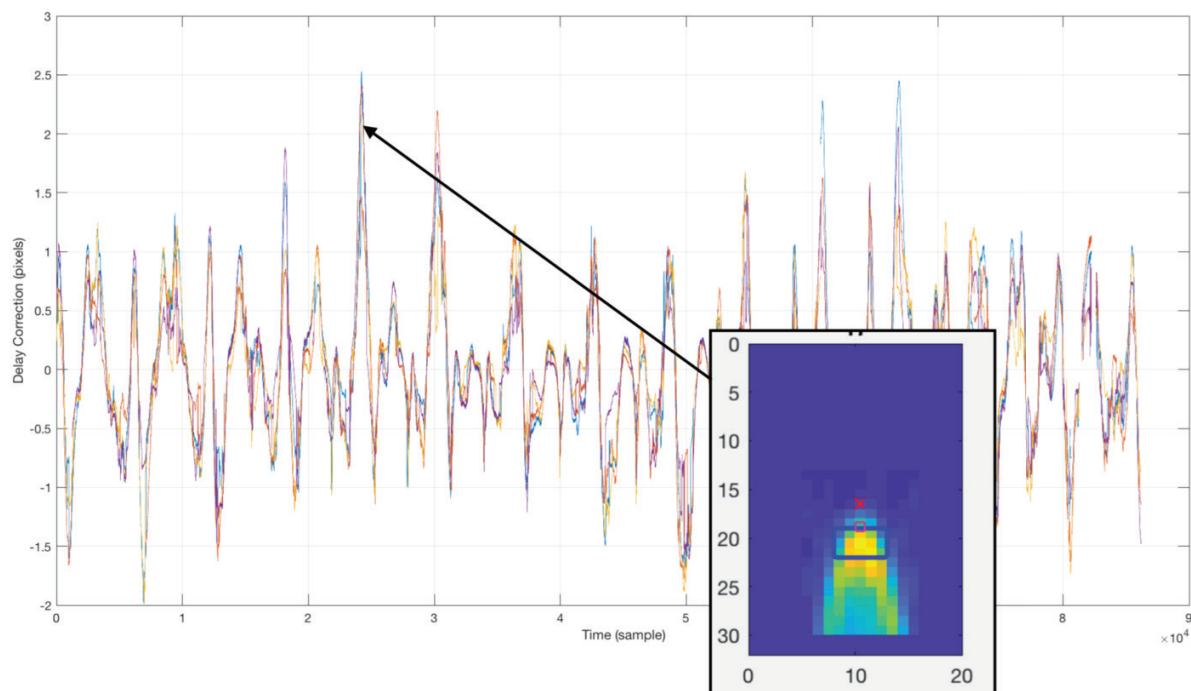
Figure 5.4. One day of specular point corrections using the DTU 10 model as compared to the WGS-84 model. The correction due to the improved specular point solver varies between −2 and 2.5 pixels in delay space in the DDM.

a red X, while the new specular bin solved using DTU 10 is shown with a red square. Visually, it is clear the specular bin location calculated with DTU 10 is at the correct location in the reflected waveform. Range errors introduced by incorrect specular point prediction primarily impact the L1 calibration due to misidentifying the correct specular point bins (and specular region reflected power) in the DDM measurements. These errors will also degrade the surface vertical ranging accuracy and horizontal geolocation if not corrected.

5.5.2. Specular Point Solver Implementation

The new specular point solution is reported in the CYGNSS L1 data in the form of the specular point position and velocity variables. It takes approximately 20 seconds to calculate one day of precise specular points within CYGNSS DDMs from one satellite (approximately 320,000 DDMs). The new algorithm used to solve for the specular point is as follows:

1. The original specular point solution based on the WGS-84 ellipsoid model is used as our initial estimate of the specular point.
2. A large 3D grid of points is constructed around the estimated specular point. This grid has uniform latitude and longitude spacing and is conformal to the WGS-84 ellipsoid at each point.

3. At each grid point, the DTU 10 mean sea surface height is used to shift the altitude. The 1° resolution DTU 10 data is bilinearly interpolated to find the altitude value at each grid point. The resulting grid is then conformal to the DTU 10 surface.
4. Next, the point in the grid with the minimum reflection path length (from transmitter to the grid point to the receiver) is found. This minimum-path-delay grid point becomes the new specular point location estimate.
5. An additional higher resolution grid is constructed around this estimated specular point location, and Steps 2–4 are repeated several times. In this way, a series of search grids sequentially zooms in on the estimated specular point. The initial grid size and resolution are carefully chosen to prevent erroneous convergence.

The specular point we solve for here is defined as the point on the Earth with the minimum reflection path delay. As the surface we use is conformal to an arbitrary geoid topology at each grid point, no mathematical constraint is placed on transmitter and receiver incidence angles in this solution. In a strict sense, it is no longer a "specular" point, since (if the ocean surface were smooth) a specular reflection would occur at surface locations with equal transmitter and receiver incidence angles, not minimum delay. Nonetheless,

the minimum delay point is sufficiently relevant for our purposes, since the corresponding specular bin defines the leading edge of the reflected waveform and the specular point represents the center of our iso-delay surface contours within the reflection glistening zone.

The DTU 10 mean surface height model contains data over both ocean and land. The updated specular point estimates are valid and accurate over ocean only, as the DTU 10 elevation model does not consider variations in land topography. An additional surface height map will be implemented in future versions of the L1 calibration, which includes land surface height variations.

The updated specular point solution is differenced with the instrument estimated specular point solution to produce a correction term in the DDM's delay and Doppler space. This correction is applied to the original prediction of the specular bin location in the DDM during the estimation of the DDMA measurement area.

5.6. L1B Calibration Algorithm: Watts to σ_0

The L1A calibrated DDM represents the received surface signal power in watts binned over a range of time delays and Doppler frequencies. Before any geophysical parameters can be estimated, these power values must be corrected for non–surface related terms by inverting the forward model shown in Equation 5.18. The CYGNSS L1B calibration generates three data products associated with each L1A DDM: (1) a bin-by-bin calculation of the surface bistatic scattering cross section, σ (not normalized by scattering area); (2) bin-by-bin values of the effective scattering areas; and (3) an NBRCS value for a DDMA in a 3 delay × 5 Doppler bin region around the estimated specular point location in the DDM. The first two products will allow users to normalize values of σ to values of σ_0 (scattering cross section per meter squared) over configurable surface extents using summations of the effective scattering areas for individual DDM bins. The values of σ are corrected for the effects of the transmit and receive antennas, range losses, and other non–surface related parameters. The effective scattering areas are calculated based on the measurement-specific reflection geometry and include the GPS-specific delay and Doppler spreading functions. However, care should be taken when using DDM bins away from the specular point, as some of the corrections applied (such as the receive antenna gain and path losses) will degrade at pixels outside the DDMA area. An overview of the CYGNSS L1B calibration is shown in Figure 5.5.

5.6.1. Expression for Bistatic Radar Cross Section

The final expression for the L1B DDM can be derived from the expression of the signal forward model, expressed in Equation 5.18, by solving for the scattering cross section term, σ_0. As the DDM L1B σ product will not be normalized, we have removed $\overline{A}$ from Equation 5.18 and replaced the normalized radar cross section σ_0 with the nonnormalized σ. Additionally, receive antenna gain G_{SP}^R, the GPS antenna gain G_{SP}^T, and total path loss (simplified into a single value) R_{SP}^{Total} terms are approximated with their values at the specular point and applied across the whole DDM. The resulting expression for the bin-by-bin scattering cross section, σ, is

$$P_{\hat{\tau},\hat{f}}^{L1b} = <\sigma_{\hat{\tau},\hat{f}}> = \frac{P_{\hat{\tau},\hat{f}}^g (4\pi)^3}{P^T \lambda^2 G_{SP}^T G_{SP}^R R_{SP}^{Total}},\qquad (\mathbf{5.20})$$

where the individual terms in Equation 5.20 are as follows:

1. $P_{\hat{\tau},\hat{f}}^{L1b}$ is the L1A calibrated signal power at a specific delay and Doppler bin.
2. R_{SP}^{Total} is the total range loss from the transmitter to the surface and the surface to the receiver at the specular point. When using a relatively small area of the DDM near the specular reflection point, this value can be approximated as the total range from the

Level 1B Calibration Summary: Power to Sigma0
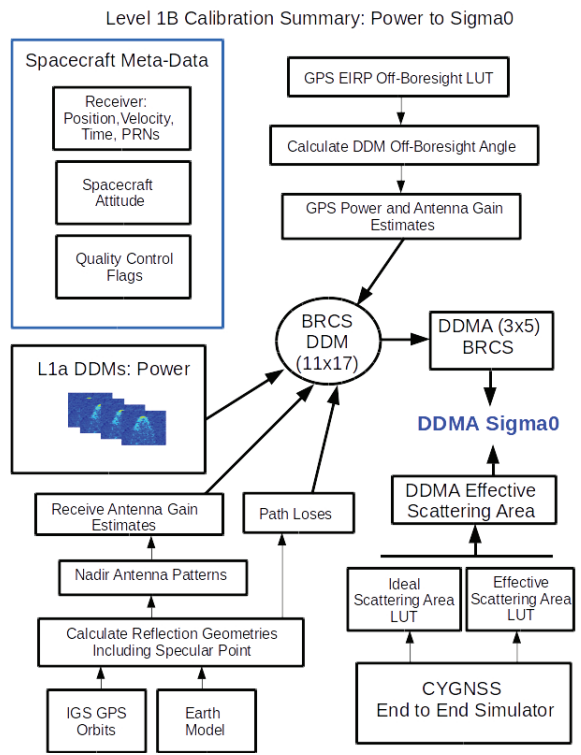
Figure 5.5. Overview of CYGNSS L1B calibration.

transmitter to the specular point to the receiver. This term is included in the denominator, as it is calculated as a loss $R^{Total} = \dfrac{1}{(R^R)^2} \dfrac{1}{(R^T)^2}$.

3. P^T and G^T_{SP} are the GPS satellite transmit power and antenna gain at the specular point. These values are estimated using a ground-based GPS power monitor and measurements from the CYGNSS navigation antenna to map the transmit power of individual GPS satellites. Details can be found in Wang et al. (2018b).

4. G^R_{SP} is the receiver antenna gain at the specular point applied across all DDM bins. The *SP* antenna gain outside the DDMA region will introduce errors that should be accounted for when using pixels outside the DDMA region (3 delay and 5 Doppler around *SP*).

5.6.2. CYGNSS Bin Ratio Correction

5.6.2.1. CYGNSS Analog to Digital Convertor (ADC) Design

A full explanation of the CYGNSS analog to digital sampling configuration and calibration corrections can be found in Gleason et al. (2021).

The CYGNSS instrument input signal processing chain includes the following steps: After capturing the off-air signal by the receive antenna, the signal enters the low noise amplifier (LNA) and is processed through a cavity filter and initial fixed voltage gain stage. Following this initial amplification stage, the received signal travels to the instrument front end, where additional down-conversion and filtering are applied. This includes added amplification by a commandable voltage gain, which permits adjustment of the analog signal level into the ADC. It is noted that numerous GPS receivers configure the front end into an automatic gain control (AGC) mode in order to autonomously adjust this variable gain stage, thereby securing an ideal normal sampling distribution. However, the need for knowledge of the precise input power level for a science observation prohibits this convenience on the CYGNSS instruments and necessitates that the commandable gain stage remain at a constant commanded value for the CYGNSS receivers.

The need to manually command the front-end gain settings adds the requirement that the input signal levels be compatible with the 2-bit ADC digital sampling thresholds (which are fixed within the front end). When the gain is set too high (increased magnitude of real analog voltage samples), the sampled input signal falls disproportionally into the outer sampled bins, which results in a nonideal inverted sampling. Alternatively, if the commanded gain is too low, the sampling shifts to the (lower voltage) inner two bins of the 2-bit

sampling and results in a peaked sampling distribution. The optimal configuration is when the gain is commanded to a level that results in a near-ideal normal (Gaussian) sampling distribution over the four digital sampled bins.

As the sampling distribution deviates from the Normal (Gaussian) shape, a small and gradual degradation in the downstream processed retrieved signal power levels arises (Ulaby & Long, 2014). It is important to note that GNSS signals, when sampled off-air, are typically at levels well below the input noise floor and are subsequently detected using a coherent (spread spectrum) processing technique in the digital signal processor such that the sampling distribution in a GNSS receiver is driven mostly by the input noise level (Misra & Enge, 2001).

It is convenient to define a single metric to quantify the digital sampling distribution. We have chosen to do this in a parameter called the bin ratio (BR), which is defined as

$$BR = \frac{b2 + b3}{b1 + b4}, \tag{5.21}$$

where $b1$, $b2$, $b3$, and $b4$ are the number of counts accumulated into each of the four digital sampling bins, -3, -1, $+1$, and $+3$, respectively, over a short time interval that in the case of the CYGNSS receivers is 1 second.

5.6.2.2. Impact of On-Orbit Bin Ratio Fluctuations on L1B Calibration

To demonstrate the impact of a fluctuating bin ratio on the primary CYGNSS L1 (NBRCS) and Level 2 (L2; wind speed) products, a 1-year-long CYGNSS data record was analyzed across all observatories for both port and starboard science channels.

Figure 5.5 illustrates the positive correlation of NBRCS and bin ratio (BR) over a full year of CYGNSS data (2019). Bin ratio estimates over this yearlong data record are computed using Equation 5.21, and the NBRCS is the mean value across all CYGNSS observatories within narrow (0.05 width) bins. The surface mean square slope (MSS) and wind speed reference data are based on temporal and spatial match-ups from ECMWF ocean surface wind speed (in 0.25 m/s bins). The estimated uncertainty in the European Centre for Medium-Range Weather Forecasts (ECMWF) winds has been estimated to be on the order of 0.5 m/s root mean squared error (RMSE; Bechtold et al., 2012/13). Additionally, the WAVEWATCH III (WW3) wave mean square slope model (WW3DG, 2016) has been used as a surface reference. To account for the CYGNSS observation frequency, an L-band adjusted spectral tail (Wang et al., 2019) has been applied to the WW3 outputs and the surface isolated over

narrow MSS conditions (in 0.0005 width bins). The accuracy of this L-band spectral tail corrected model MSS is unknown and the subject of ongoing research. Yet these data provide a more direct surface link to the CYGNSS L-band observations than the near surface wind speeds and are included as a secondary comparison source.

In the idealized scenario of no calibration errors or uncertainties, NBRCS estimates should be independent of all instrument quantities with no correlation to bin ratios. Figure 5.6 shows the relationship between NBRCS and

bin ratio for a wide range of ocean MSS (left) and wind speeds (right). Ideally, there would be no correlation between NBRCS and bin ratio, and the colored curves in Figure 5.6 would be flat. As they are not, a correction is required to avoid sampling errors in the retrieved MSS and wind speeds.

5.6.2.3. *Nadir Bin Ratio Correction*

The input noise power is the dominant component of the precorrelated GPS signal received at the instrument analog
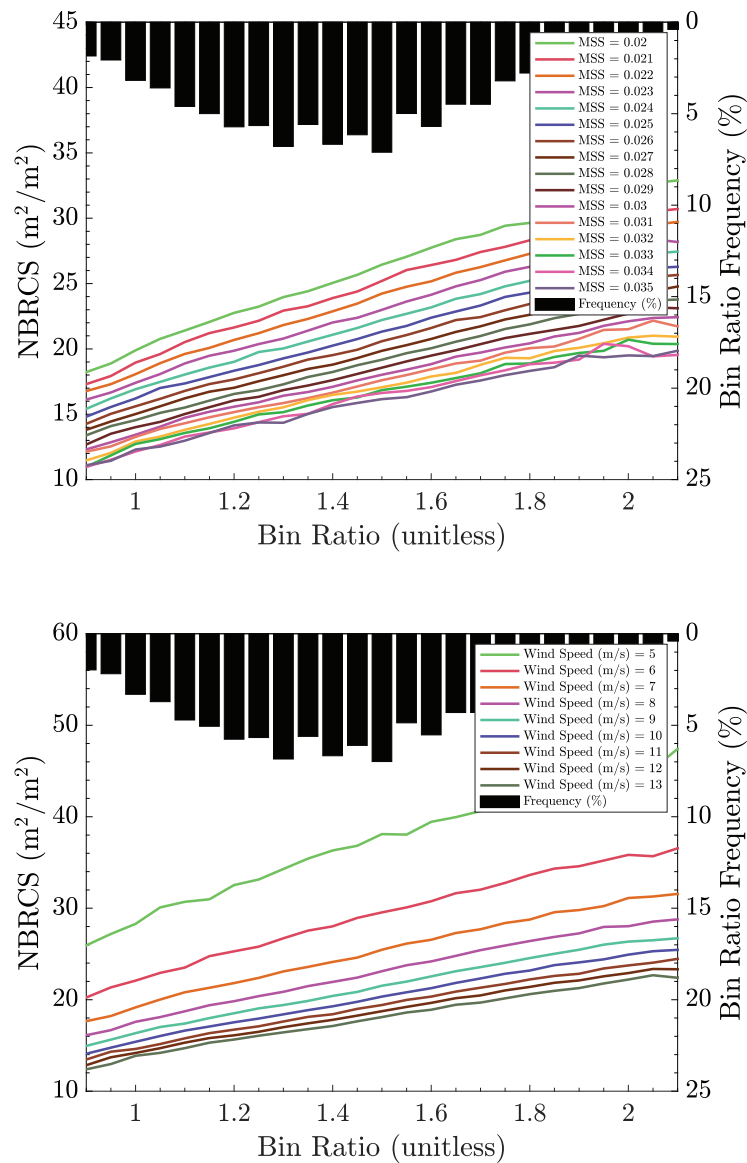
Figure 5.6. Mean NBRCS estimates versus science channel bin ratio for a wide range of ocean conditions without digital sampling correction: *left*, over a range of surface MSS conditions (ref. WW3); *right*, over a range of wind conditions (ref. ECMWF).

to digital converter (ADC). Thus, a correction to the observed noise floor can be performed to mitigate received power uncertainty due to BR fluctuations driven largely by external noise variations. The correction is designed as an adjustment to the per-observation estimated CYGNSS L0 noise counts. The received signal power counts in the CYGNSS L1 calibration are estimated after subtraction of the estimated noise floor; that is the difference of the total counts and noise counts. As a result, by correcting the noise counts, we are directly adjusting the downstream estimated L1 power levels, including the NBRCS estimate.

The noise floor correction was derived using a theoretical simulation of the CYGNSS hardware configuration as detailed in Gleason et al. (2021). Upon application of the theoretical correction, it was observed that the results could be improved slightly by adding a modest multiplicative scaling factor to the theoretical correction. The final nadir channel noise floor corrections applied to the CYGNSS L1 data are the empirical correction curve shown in Figure 5.7. The noise floor correction versus BR is stored in a LUT and applied to every CYGNSS L1 observation based on the BR calculated in Equation 5.1 and the empirical correction LUT as shown in Figure 5.7.

The postcorrection NBRCS versus BR performance is shown in Figure 5.8 across ranges of MSS and wind speed bins. A summary of the results of this analysis is included in Table 5.1. These statistics are generated using all CYGNSS data from 2019 with temporal and spatial colocations data from ECMWF (U10 wind speed) and WAVEWATCH III (L-band corrected MSS) used as the validation reference dataset.
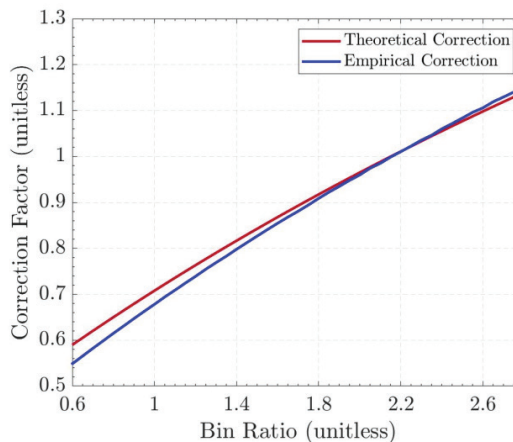
Figure 5.7. Theoretical and empirically adjusted digital sampling noise floor corrections applied to CYGNSS v3.1 L0 noise levels.

5.6.2.4. Zenith Bin Ratio Correction

The CYGNSS zenith observations consist of integrated signal plus noise counts only, without a reference noise floor. This prohibits the application of the nadir noise floor correction to the zenith channel observations. Therefore, the observed zenith signal plus noise counts need to be corrected directly before a real-time EIRP estimate is formed (Wang et al., 2021). Note that a decrease in the noise floor in the nadir calibration is equivalent to an opposite adjustment to the total signal plus noise counts.

Like the nadir digital sampling correction, the zenith correction can also be optimized using empirical tuning factor(s) to ensure consistency of the EIRP estimation as a function of natural bin ratio fluctuations. Due largely to the spread of zenith bin ratio probability density functions (PDFs) with

Table 5.1. Summary of CYGNSS Precorrection and Postcorrection NBRCS Root Mean Square Deviations Across Wind Speed (Ref. ECMWF) and MSS (Ref. WW3) Surface Conditions

Surface conditions	NBRCS RMSD (linear)	NBRCS slope ($|\Delta NBRCS/\Delta BR|$)	NBRCS RMSD (linear)	NBRCS slope ($|\Delta NBRCS/\Delta BR|$)
	Uncorrected		*Corrected*	
Wind total (5–20 m/s)	12.90	9.34	2.79	1.48
Low winds (5–7 m/s)	19.50	13.91	4.19	2.24
Medium winds (7–12 m/s)	13.75	9.90	1.60	0.38
High winds (12–20 m/s)	10.64	7.80	3.11	1.93
MSS total (0.020–0.025)	12.86	9.30	1.89	0.84
Low MSS (0.020–0.025)	15.04	10.80	2.06	0.99
Medium MSS (0.025–0.030)	12.59	9.09	1.35	0.26
High MSS (0.030–0.035)	10.93	7.99	2.19	1.19

RMSD, root mean squared difference
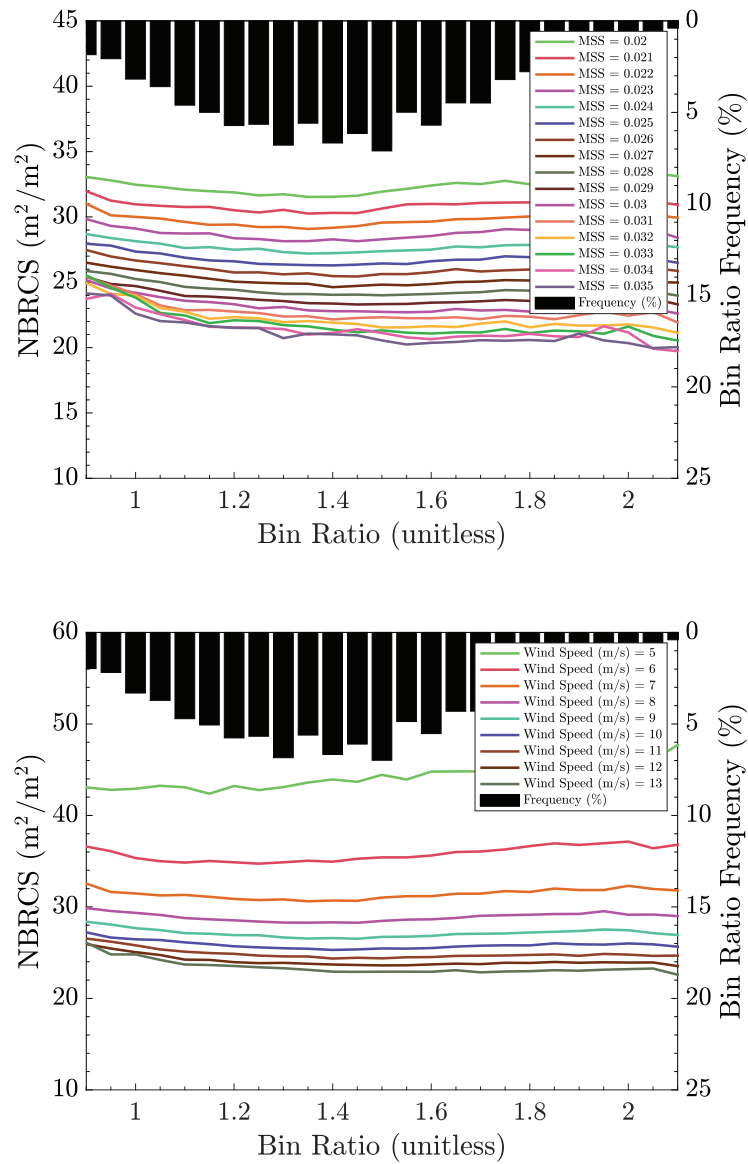
Figure 5.8. NBRCS estimates versus science channel bin ratio over a range of ocean conditions with noise floor correction: *left*, with respect to surface MSS conditions (ref. WW3); *right*, over a range of near surface wind conditions (ref. ECMWF).

means under that associated with an ideal Gaussian distribution, applying a single correction across all zenith observations was not possible, and individual per-observatory corrections are required.

The per-FM zenith digital correction functions are shown in Figure 5.8. To better illustrate the need for an increased empirical correction factor as the mean BR of the distributions decreases, the per-FM corrections are shown only between their 5% and 95% bin ratio limits to better illustrate the correction values where the on-orbit observations occur for each CYGNSS FM. As a given zenith bin ratio distribution approaches that of an ideal Gaussian distribution, only modest empirical adjustments are needed. For example, see the CYG05 correction in Figure 5.9. In contrast, as the bin ratio distribution diverges from this ideal reference PDF, a need for significantly increasing

the correction "weights" at a given bin ratio is evident. An example of this is CYG04, which requires a much larger empirical scale factor.

The zenith signal digital corrections are evaluated with respect to the consistency of EIRP estimation across BR by each CYGNSS FM. An example of the before and after correction EIRP estimation across BR for CYGNSS FM 3 is shown in Figure 5.10. Before the digital sampling correction is applied, there is a clear positive linear trend in the EIRP over a large range of BR (the bin ratio limits over which 95% of data occurs for a given FM). After the correction is applied, the EIRP estimation is significantly more consistent (i.e., flatter) over the same BR range, reducing the maximum EIRP slopes by ~92%. The precorrection and postcorrection estimated EIRP root mean square difference (RMSD) presented on a per-FM basis are listed in Table 5.2.
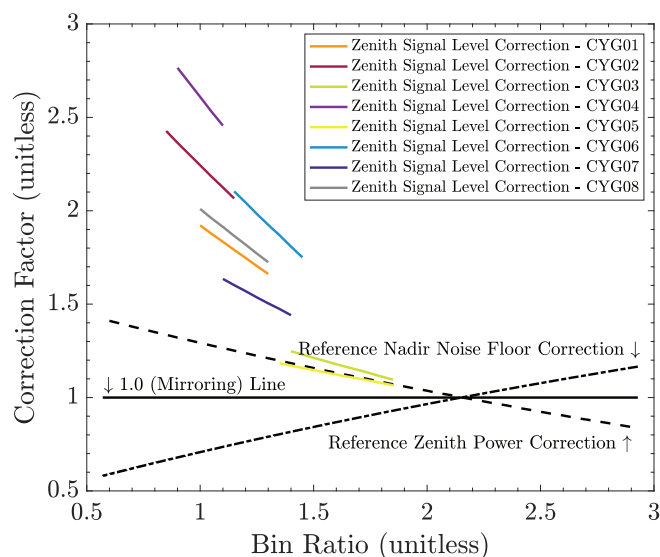
Figure 5.9. CYGNSS FM specific zenith digital correction functions. Reference nadir correction is flipped around the 1.0 axis to accommodate the opposite signal plus noise counts correction. Scale factors are derived and applied to each FM individually. Corrections are shown for each FM over the 5%–95% range of observations where they are applied. This clearly demonstrates the deviation from the reference correction as the BR distribution shifts downward.

Table 5.2. Summary of CYGNSS Zenith Channel Bin Ratio Distributions and EIRP Precorrection and Postcorrection Performance

Parameter	FM 1	FM 2	FM 3	FM 4	FM 5	FM 6	FM 7	FM 8
Empirical scale factor, Y(FM)	3.15	4.25	1.35	5.50	0.93	4.40	2.40	3.45
Zenith BR mean	1.17	0.99	1.64	1.01	1.64	1.35	1.25	1.16
EIRP RMSD, uncorrected	113.97	123.88	96.76	101.19	72.69	130.30	101.17	102.85
EIRP RMSD, corrected	23.91	28.99	20.91	16.18	22.83	23.40	24.21	19.57
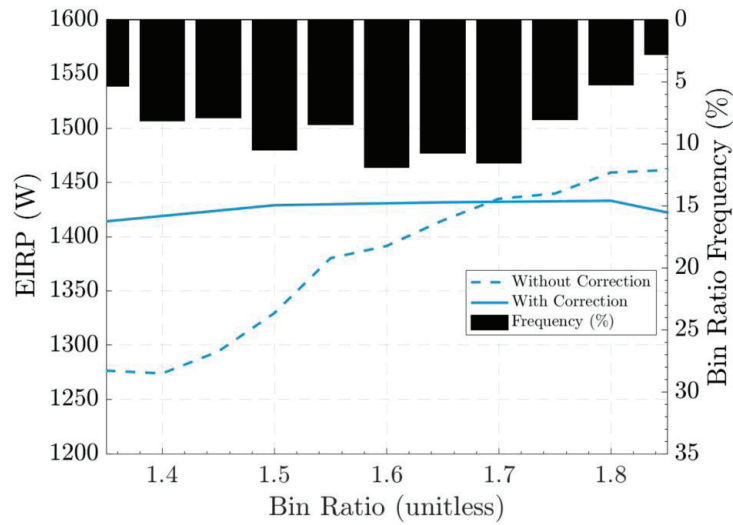
Figure 5.10. Example zenith mean EIRP estimation over the BR range containing 95% of zenith observations for CYGNSS FM 5. The precorrection estimates (dotted line) clearly show a positive trend with BR that is largely mitigated with the digital sampling correction (solid line).
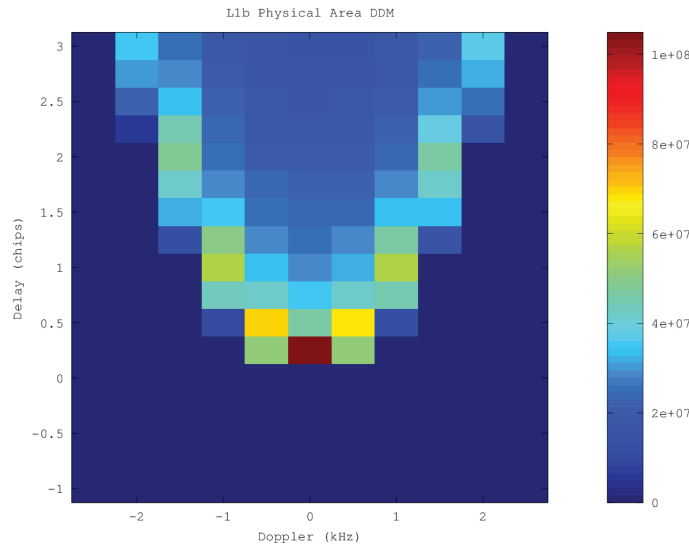
Figure 5.11 Physical scattering area for a typical DDM reflection geometry. The delays before the specular reflection point do not correspond to any physical region on the surface.

5.6.3. Calculating Effective and Physical Scattering Areas

A single delay-Doppler bin will contain the captured scattered power across one or more physical regions on the ocean surface. For each delay-Doppler bin in the DDM, this region will vary in both actual physical size (on the ground surface area) and effective area (combined with the GPS spreading functions). The GPS ambiguity functions (in both delay and Doppler) increase the effective area of each delay-Doppler bin, causing power to be "spread" into adjacent delay and Doppler bins from outside the geometry-determined physical scattering area. These functions change the levels of overall processed power observed. The physical area of each DDM bin can be calculated as follows:

$$A_{\hat{\tau},\hat{f}} = \iint_A dxdy. \tag{5.22}$$

An example of the physical scattering area for a typical DDM is shown in Figure 5.11. Note that points up to and before the specular point bin (i.e., at delays shorter than

the specular reflection point delay) have no physical surface scattering area. The power received in the bins before the specular point is due to power being spread into these bins by the GPS ambiguity functions from physical areas near the specular point. The effective surface scattering area for each delay-Doppler bin is expressed as the ambiguity function weighted surface integration,

$$A_{\hat{\tau},\hat{f}} = \iint_A \Lambda^2_{\hat{\tau};x,y} S^2_{\hat{f};x,y} dxdy, \tag{5.23}$$

where the delay spreading function, $\Lambda_{\hat{\tau};x,y'}$ and the Doppler spreading function, $S_{\hat{f};x,y'}$ are integrated over the physical surface corresponding to each individual delay-Doppler bin. Figure 5.12 shows the effective scattering area DDM corresponding to the physical scattering areas illustrated in Figure 5.11.

Initial analysis has shown that when only using a relatively small area of the DDM (corresponding to approximately a 25 km^2 area on the surface), it is sufficient to approximate the receive antenna gain, range loss terms, and the GPS transmit antenna power and gain using constant values calculated at the specular reflection point.

5.6.3.1. Rescaling from End-to-End Simulator
Using the CYGNSS End-to-End simulator, estimates of the physical scattering areas and, subsequently, the effective scattering areas under varying observation geometries are derived and used to generate a reference A_{tot} LUT for use in the normalization of DDMA radar cross section

estimates. An example of this is shown in Figure 5.13, where surface delay-Doppler solutions are developed on a high-resolution (50 m) grid and subsequently used to identify surface grid pixels corresponding to a given delay τ – Doppler f pair.

It is noted that the determination of the relevant areas is limited to resolutions of ~0.25 chips and ~500 Hz to match the delay Δ_τ Doppler Δ_f resolutions of the L1 DDM. The original scattering area estimates were based on a forward binning scheme where the physical scattering area at delay τ and Doppler f composes the footprint spanning $\in [\tau + \Delta_\tau, f + \Delta_f]$. It follows that the maximum delay-Doppler binning errors associated with the estimation of the physical area are comparable to Δ_τ and Δ_f, respectively.

An example of how this may compromise normalized radar cross section estimates σ_0 is shown in Figure 5.14, where the forward binning scheme appears to lead to an overestimation of scattering areas, which in turn reduces CYGNSS NBRCS estimates relative to reference model NBRCS estimates.

The revised DDMA normalization area estimates used as part of CYGNSS's v3.1 data release are derived using the same procedures while substituting the forward binning scheme with a central binning scheme such that the physical scattering area at delay τ and Doppler f composes the footprint spanning $\in [\tau - \Delta_\tau / 2 \leq \tau < \tau + \Delta_\tau / 2, f - \Delta_f / 2 \leq f \leq f + \Delta_f / 2]$, thereby limiting maximum delay-Doppler sampling errors to $\Delta_\tau / 2$ and $\delta \Delta_f / 2$, respectively.
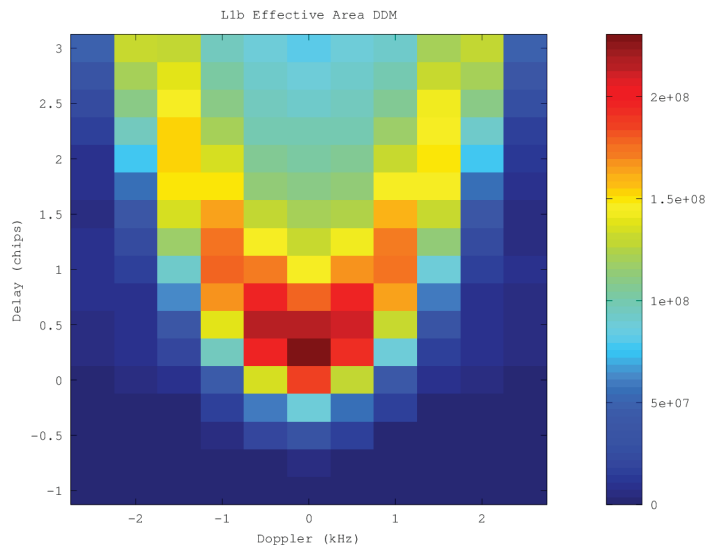
Figure 5.12. Effective scattering area corresponding to the physical scattering area shown in Figure 5.11. This DDM of the effective scattering area is a key output product of the L1B calibration, which allows users to calculate normalized values of σ_0.
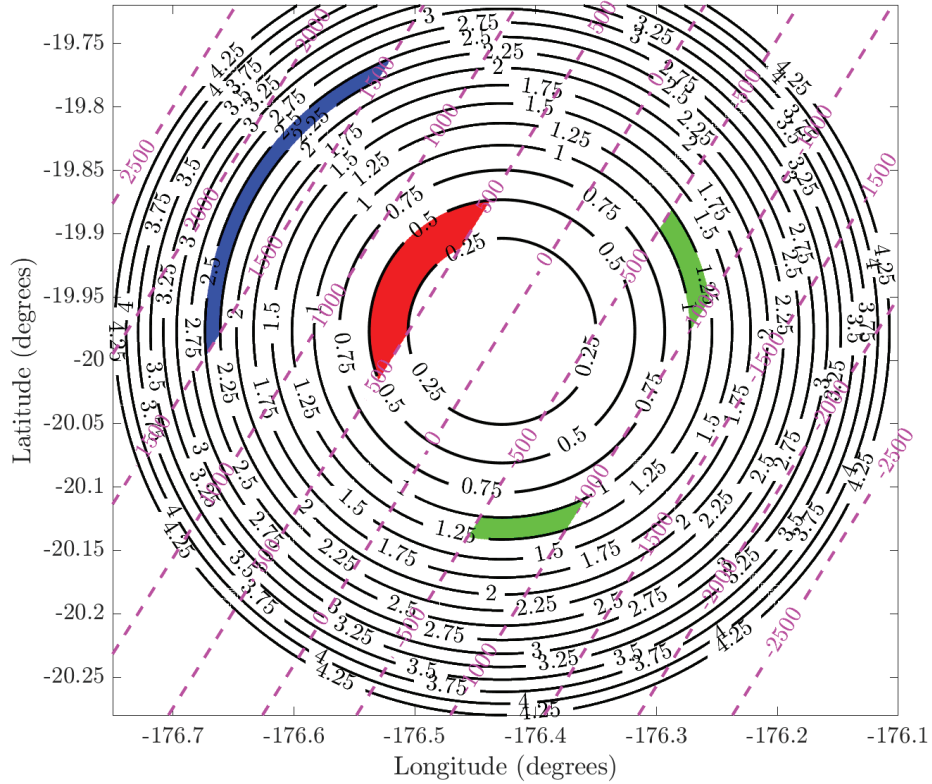
Figure 5.13. Example of surface grid used to develop physical scattering area DDMs. Iso-delay (chips) lines are in black; iso-Doppler (Hz) lines are in magenta. For illustrative purposes, the physical area using a forward binning scheme corresponding to $A(\tau = 0.25$ chips, $f = 500$ Hz) is in red, $A(\tau = 1$ chips, $f = 1000$ Hz) is in green, and $A(\tau = 2.25$ chips, $f = 1500$ Hz) is in blue.
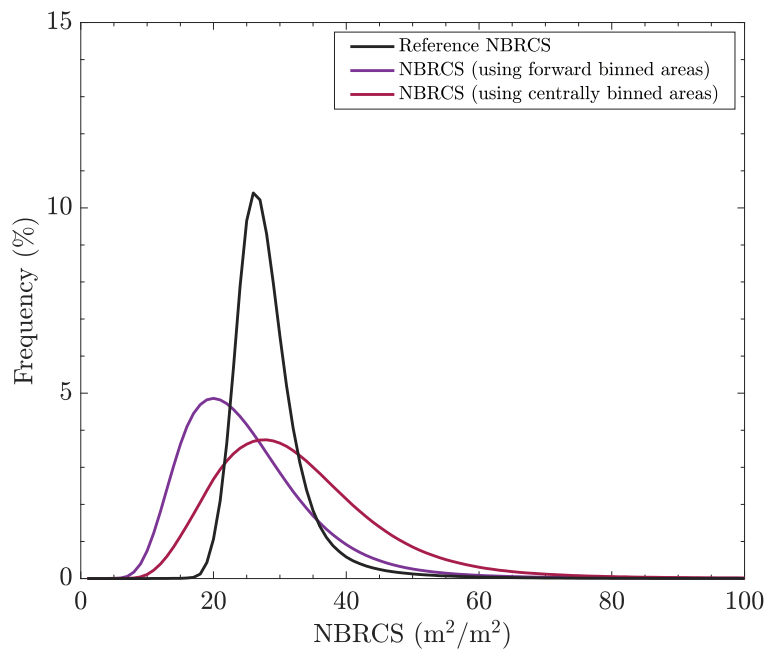
Figure 5.14. NBRCS PDFs summarizing the effects of revised DDMA normalization area estimates.

An example of the physical area solutions using the revised binning scheme is shown in Figure 5.15.

It is estimated that the forward binning scheme was associated with a ~22% average overestimation of DDMA normalization areas such that a reduction of A_{tot} significantly improved the correspondence of CYGNSS's NBRCS estimates to reference NBRCS estimates (see Figure 5.14).

As a result of the switch from forward binning to central binning, the effective area normalization of the DDMA was reduced by 22.36% using a constant scale factor applied to all v3.1 DDMA effective area lookup-table entries.

5.6.4. On-Orbit Estimation and Correction of Receive Antenna Pattern Errors

As a standard L1 data product, CYGNSS data include DDMs over 11 Doppler bins and 17 delay bin pixels around the specular point. The NBRCS $\sigma_{\hat{\tau},\hat{f}}$ is calculated as per Equation 5.4 for each delay-Doppler bin.

Prior to launch, antenna pattern measurements were made for all the port and starboard antennas. In addition, the predicted effects of the spacecraft body were extensively modeled using pattern simulation tools to attempt to accurately predict the final antenna patterns when attached to the spacecraft. These simulations included mechanical computer-aided design (CAD) models of the physical spacecraft with electromagnetic field simulations using the Altair Feko FEKO and Savant software packages. Additionally, full pattern measurements of the port and starboard antennas were made while mounted to a CYGNSS engineering model (EM) in an anechoic chamber. From the modeling effort, which was confirmed by the EM chamber measurements, we know that the solar panels have a significant impact on the observatory antenna gain patterns.

The individual modeled pattern measurements were adjusted using a constant gain factor based on measured differences between the flight antennas to create the at-launch gain patterns for each CYGNSS Flight Model (FM) antenna calibration table.

However, we know that there is potentially significant variability in the exact deployed positions of the solar panels from repeated prelaunch panel deployment tests. It therefore stands to reason that applying a simple constant offset for each of the FM antennas from the modeling and EM
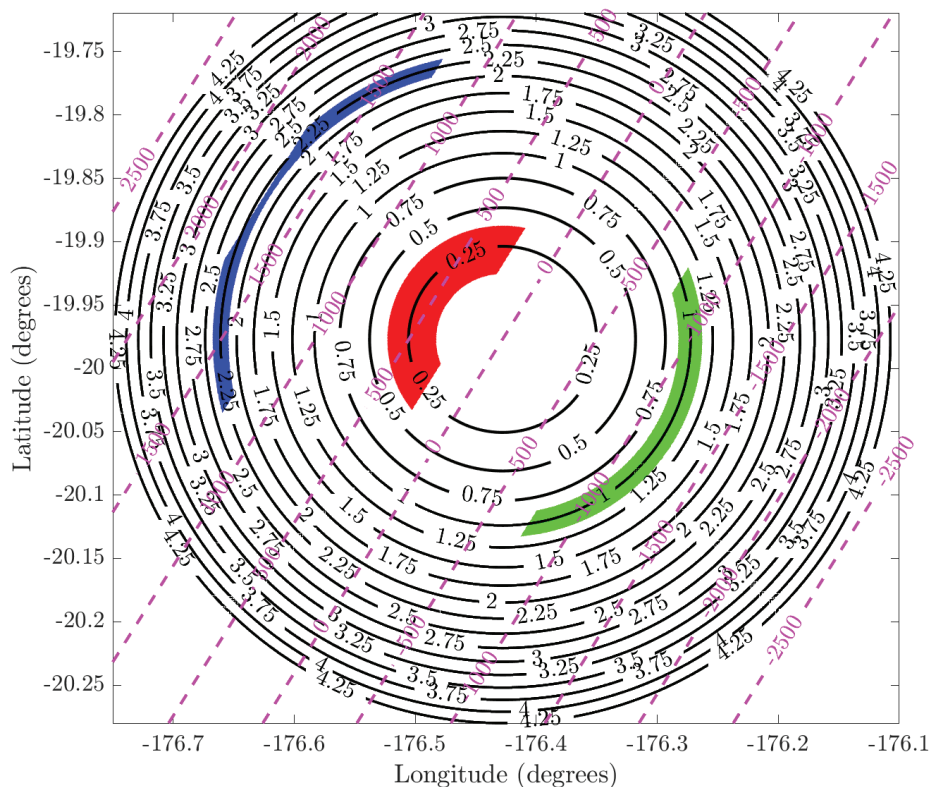
Figure 5.15. Example of surface grid used to develop physical scattering area DDMs. Iso-delay (chips) lines are in black; iso-Doppler (Hz) lines are in magenta. For illustrative purposes, the physical area using a central binning scheme corresponding to $A(\tau = 0.25$ chips, $f = 500$ Hz) is in red, $A(\tau = 1$ chips, $f = 1000$ Hz) is in green, and $A(\tau = 2.25$ chips, $f = 1500$ Hz) is in blue.

measurements is overly simplistic. It was evident from the initial analysis of the CYGNSS on-orbit data that an improved estimate of the CYGNSS antenna patterns was needed for each antenna in the constellation.

5.6.4.1. *Estimation of Receive Antenna Gain Error*

Analysis of the initial CYGNSS data, released in May 2017, shows a significant dependence of observed σ_0 on the azimuthal observation angle of the specular point with respect to the CYGNSS spacecraft. While the NBRCS values are expected to depend on wind and incidence angle, the dependence on azimuthal angle was expected to be negligible. These anomalies were quantified in terms of a normalized NBRCS anomaly $\sigma_{0,anom}$, expressed as

$$\sigma_{0,anom} = \frac{(\sigma_0 - <\sigma_0>)}{<\sigma_0>}. \tag{5.24}$$

σ_0 is expected to vary as a function of wind speed and geometry, so σ_0 anomalies are computed as the difference between each calibrated σ_0 from the mean value for all σ_0 within 2 m per second wind speed and 2° incidence angle bins. Reference wind speeds are from colocated ECMWF reanalysis fields to within 90 minutes and 25 km of the corresponding CYGNSS observations. To determine the dependence of these anomalies on azimuth angle, average anomalies were computed in 1° azimuth bins. The results using the original calibration algorithm between day of year 77 and 121 are shown in Figure 5.16. Results are averaged across all eight CYGNSS satellites for the starboard and port antennas. For this and future analysis shown, the average of the σ_0 in the DDM is computed using the estimates σ_0 over the DDMA region near specular point DDM bins. It is important to note that due to the cross track ground projection of the receive antenna patterns and onboard track selection algorithm, most of the measurements are distributed within 30° in azimuth angle around 90° (for the starboard) and 270° (for the port) measurement orientations.

The key variables in the L1B calibration are the transmit power P^T, the transmit antenna gain G^T, the receiver antenna gain G^R, and geometric factors, including the range correction. Additionally, the effective scattering area used to normalize σ also contributes to the overall level of σ_0. Of these, only the antenna gain patterns G^T and G^R depend directly on azimuthal angle. The transmit antenna gain G^T will vary from observation to observation, but not in a manner highly correlated with specular point azimuth with respect to the CYGNSS spacecraft. Therefore, it was hypothesized

that the likely candidate for the observed azimuthal variation was the receiver antenna gain G^R.

5.6.4.2. *Improved CYGNSS Antenna Patterns*

To develop updated antenna patterns, an independent estimate of expected σ_0 was computed from a model-based MSS from the Wave Watch III model (WW3DG, 2016) with an L-band wave spectrum extension model (Wang et al., 2019). This was then used with a relationship between MSS and σ_0 described in Chapter 6 and given in Equation 6.1. The ratio of this model-based σ_0 to the observed σ_0, matched in 1° latitude/longitude and 30 minutes time, is then used to compute an update to the receive antenna gain in antenna azimuth and elevation coordinates. For each flight antenna in the constellation (1 port and 1 starboard antenna for each of 8 spacecraft = 16 total antennas), σ_0 updates were computed in 1° increments of spacecraft off-nadir and azimuth
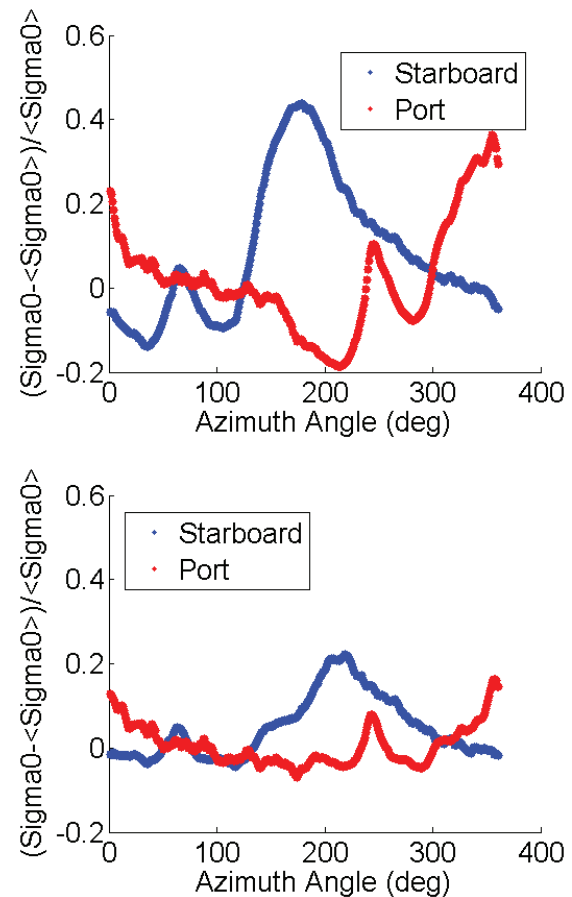
Figure 5.16. *Left:* σ_0 anomalies computed for L1 data between day of year 77 and 121 of 2017 on the Version 1 using prelaunch estimated receive antenna patterns. *Right:* σ_0 anomalies computed for L1 corrected data for Version 2 of the L1 calibration. The anomalies reduce the worst-case error of 40% to less than 10%.

angle. These antenna correction maps were then smoothed over 5° windows in azimuth and off-nadir angle in order to reduce measurement noise.

These results were then interpolated using nearest neighbor interpolation to a resolution of 0.1°. This map of σ_0 obs/model ratios as a function of antenna coordinates was used to scale the original patterns to produce a new estimate of the receive pattern gain, which greatly reduced the observed azimuthal anomalies (anomaly subtracted from original antenna pattern in logarithmic space from estimates of gain in dB). This was done for all 16 operational flight antennas on all 8 observatories.

An example of the resulting σ_0 ratio and the resulting updated gain maps is shown in Figure 5.17 for the FM 1 starboard antenna. Results for the other 15 antennas are similar. The anomalies, which were initially greater than 40%, are reduced to less than 20% residual anomalies across all azimuth angles. The regions near the azimuth angles where most measurements are taken (90° and 270° for starboard and port, respectively) have errors reduced to 10% or less. The remaining errors are most likely due to variability within the data not related to wind speed, incidence angle, or receiver antenna pattern effect accounted for in this analysis.
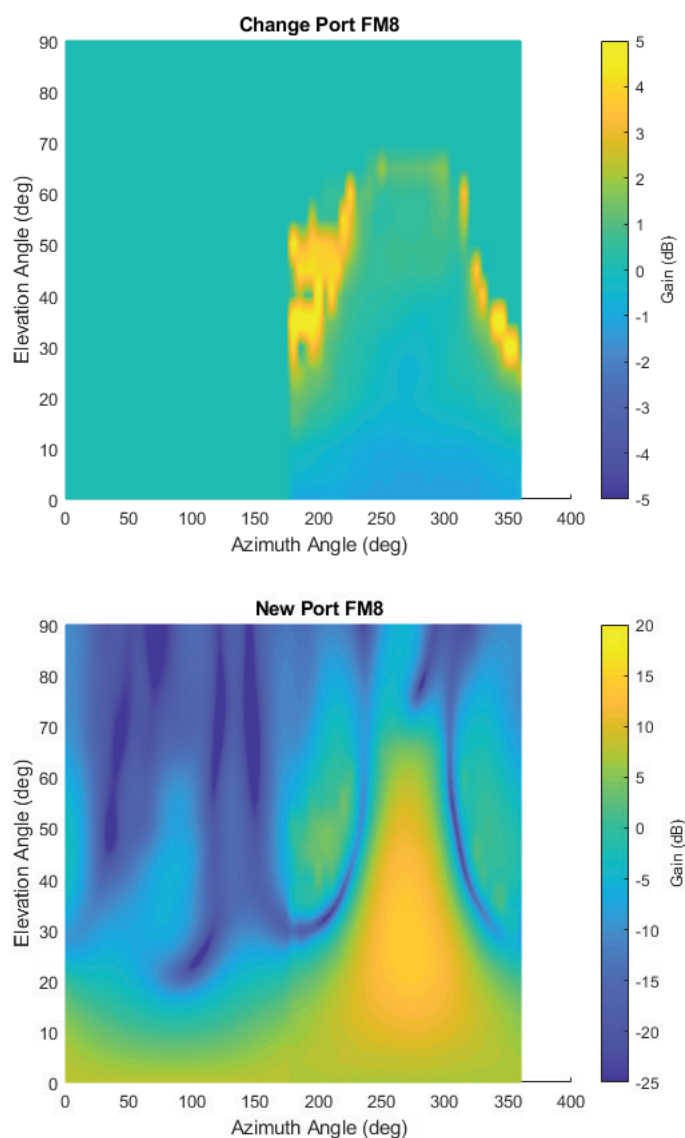
Figure 5.17. *Left:* Antenna pattern change (obs/model σ_0) for FM 1 starboard antenna pattern. *Right:* FM 1 starboard antenna pattern with corrections applied to produce the improved pattern.

It should also be noted that off-nadir angle is highly correlated to incidence angle for a given spacecraft orientation, with the relationship directly tied to the spacecraft roll, which changes periodically as the spacecraft are adjusted to maintain a power positive orientation for high solar beta angles.

5.6.5. Calculating a Normalized Bistatic Radar Cross Section

The L1B bin-by-bin DDM of σ_0 and the bin-by-bin DDM of effective scattering areas can be combined to calculate a normalized radar cross section value, σ_0, over selected regions of the measurement DDM called the DDMA. The CYGNSS L2 wind retrieval products use the DDMA to

generate geophysical model functions (GMFs) to estimate near surface winds. The DDMA consists of three delay bins and five Doppler bins, with the specular point located in the first row (shortest delay) of this region. Figure 5.18 shows this DDMA region in red, overlapped with the normal instrument processed DDM delay and Doppler pixels in black. The true (best) estimate of the DDMA region (as calculated by the precise specular point estimation method described above) is marked as a red dot in this figure, while the white dot is the L1B DDM that the "true" specular point falls into.

These precise DDMA bins will not normally align exactly with the L1B DDM bins generated by the instrument (due

Single DDMA Bin
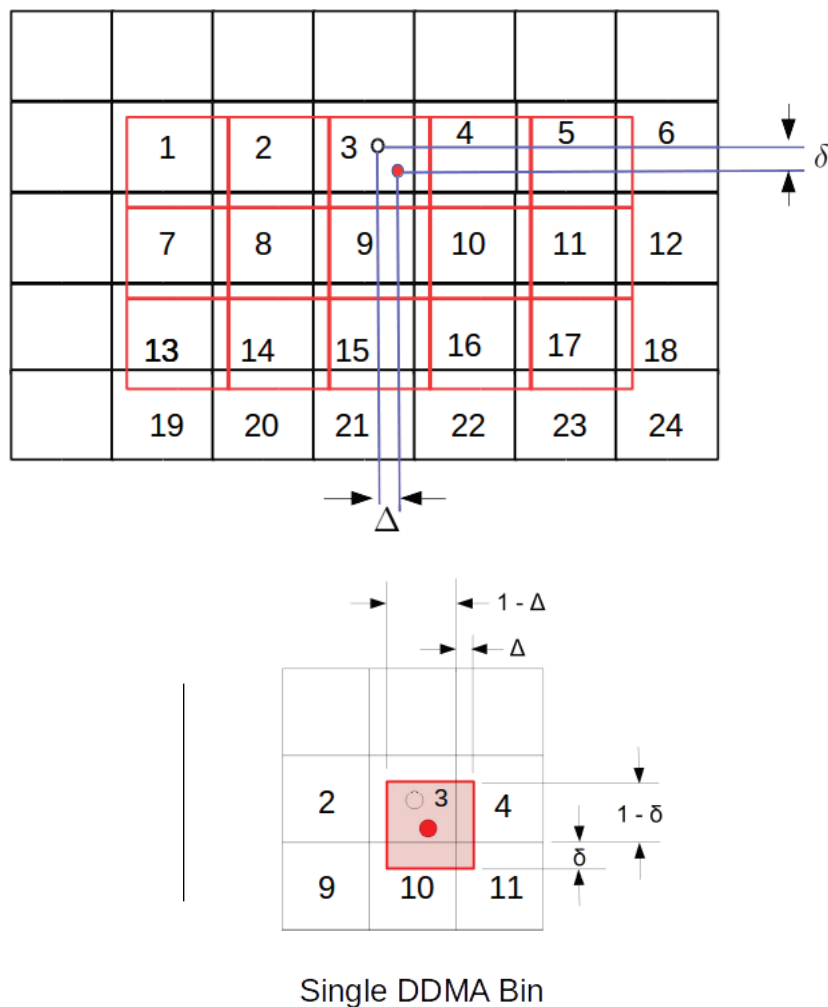
Figure 5.18. Bins used in computing DDMA quantities. *Left:* L1B DDM of σ values, numbered to correspond to the same pixels with DDMA overlaid and bin numbers referenced to Equation 5.9. The red group of DDMA bins is the overlay of the 3 by 5 DDMA measurement area with the processed L0 DDM pixels, containing a typical misalignment. The best estimate DDMA is based on a refined specular point estimate and represents the true measurement error. *Right:* Detail of the overlap areas of a single DDMA bin (the specular point bin) and adjacent L1B bins.

to errors in the instrument's open loop signal tracker), making a simple summation over 15 total bins in the L1B DDM problematic. The "true" DDMA radar cross section is the weighted combination of L1B DDM bins around the best estimate surface specular point and fractional contributions from bins around the edge of the DDMA region. This set of overlapping DDM bins is, when weighted and summed, the best estimate of the "true" multibin DDMA total radar scattering cross section σ_0. The misalignment between the measured L1B DDM bins and the "true" DDMA bins is illustrated in Figure 5.10. The DDMA specular point is offset by fractional bin amounts in delay and Doppler from the L1B measurement DDM shown in the figure.

In order to calculate the total radar cross section in the red DDMA area, the actual measurement L1B values (one per white box/pixel) need to be combined using a weighting scheme that includes only a fractional amount of power from bins around the edges of the DDMA bins. The fractional weighting scheme used is approximated to be linear in both the delay and Doppler dimensions. Figure 5.18 shows the regions of overlap for a single red DDMA bin with respect to the surrounding measurement bin values. The total DDMA radar cross section can be calculated as per Equation 5.25, resulting in a combined expression for the DDMA σ_0,

$$\sigma^0 = \frac{\sigma_{weighted}}{A_{total}} = \frac{W_{i,j} \sum_{i=1}^{N} \sum_{j=1}^{M} \sigma_{\tau_i, f_j}}{\sum_{i=1}^{N} \sum_{j=1}^{M} A_{\tau_i, f_j}}, \qquad \textbf{(5.25)}$$

where N and M represent the delay and Doppler bin in the L1B DDM, respectively (with $N = 4$ and $M = 6$, a single bin more than the DDMA size in both dimensions):

$$\begin{aligned} \sigma_{weighted} &= (1-\delta)(1-\Delta)\sigma_1 + (1-\delta)(\sigma_2 + \sigma_3 + \sigma_4 + \sigma_5) \\ &+ (1-\delta)\Delta\sigma_6 + (1-\Delta)(\sigma_7 + \sigma_{13}) + \Delta(\sigma_{12} + \sigma_{18}) \\ &+ \delta(1-\Delta)\sigma_{19} + \delta(\sigma_{20} + \sigma_{21} + \sigma_{22} + \sigma_{23}) + \delta\Delta\sigma_{24} \\ &+ (\sigma_8 + \sigma_9 + \sigma_{10} + \sigma_{11}) + (\sigma_{14} + \sigma_{15} + \sigma_{16} + \sigma_{17}). \end{aligned}$$

$$\textbf{(5.26)}$$

Each bin in the L1B DDM contributing to the weighted $\sigma_{weighted}$ is scaled by a weighting factor $W_{i,j}$ based on the overlap with the respective "true" DDMA bin. $\sigma_{weighted}$ is then normalized by the sum of the effective area DDMA bins (which are centered at the ideal specular reflection point and require no weighting correction) to arrive at the final σ_0 measurement over the "true" DDMA region. The summations and weighting involved in calculating $\sigma_{weighted}$ for the example above are expressed in Equation 5.25, where the delay and

Doppler index values are simplified to single bin numbers as illustrated in Figure 5.9, and terms with the same weighting factor are combined.

5.6.6. Altitude-Dependent DDMA Area Normalization

The CYGNSS satellites were launched into slightly elliptical orbits, causing altitude fluctuations between perigee and apogee of up to approximately 35 km. This was not taken into account in the V2.0 calibration algorithm, where a circular orbit at a constant altitude was assumed during the generation of the initial LUTs used to perform the scattering area normalization of the DDMA to arrive at NBRCS estimates of σ_0. This has been corrected in Version 2.1 with an updated normalization area LUT, which accounts for the changing altitude of the CYGNSS spacecraft.

After the calculation of the weighted DDMA σ total as described above, $\sigma_{weighted}$, the bistatic scattering cross section is normalized as shown in Equation 5.24. In Version 2.0 of the calibration, this was performed with a lookup table, which was a function of incidence angle and elevation angle only at a constant altitude. This ignored the effects of the changing satellite altitudes and introduced (relatively) small errors (up to 0.1 dB) into the σ_0 estimation used in subsequent wind speed and MSS retrievals. In Version 2.1, a new LUT has been generated with an additional altitude dimension. This will allow the area normalization to correct for changes in the scattering area due to their slight eccentricity as well as longer time scale orbit changes. An example subset of the new DDMA normalization areas (reduced to better reveal the changing LUT area magnitudes) is shown in Figure 5.19 as a function of incidence and altitude (at a constant azimuth angle). Testing of the new altitude-dependent LUT has been validated to significantly reduce correlation of σ_0 with the satellite altitude.

5.6.7. Correction for Dependence of Calibration Error on Receiver Noise Floor

The v2.0 L1B calibration algorithm produces two measurement observables, DDMA and leading edge slope (LES), which are subsequently used by the L2 algorithm to retrieve wind speed. The correction described here is added to the v2.1 L1B calibration algorithm. It applies a small additive offset to each observable. The correction minimizes mean differences between the measured observable and simulated values of the observable obtained by applying the geophysical model function to coincident wind speeds modeled by ECMWF. The correction is a linear function
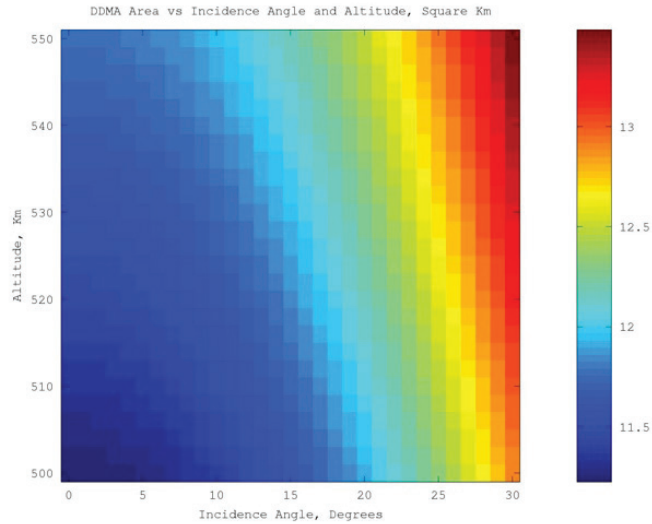
Figure 5.19. Version 2.1 DDMA LUT values for altitudes between 500 and 550 km (covering the full range of the CYGNSS orbits, with margin on the low side) and incidence angles between 0° and 30°. The increases in DDMA area with incidence angle and altitude are both clearly observable in the new LUTs. These data were generated at a constant 90° azimuth angle. Color scale is in km² for the entire DDMA region.

of the noise floor of the DDM from which the observable is computed. The slope and y-intercept of the linear function are themselves functions of the FM number, the range corrected gain (RCG), and the angle of incidence (θ_{inc}) associated with each DDM. The correction applied to each L1 observable has the form

$$Obs_{corr} = Obs + m(FM, RCG, \theta_{inc})NF + b(FM, RCG, \theta inc)_,$$

$$(\mathbf{5.27})$$

where

1. Obs_{corr} is the corrected L1 observable
2. Obs is the v2.0 L1 observable, either the DDMA (σ_0) or the LES
3. $m(FM, RCG, \theta_{inc})$ is the slope of the linear regression, which is a tabulated function of FM, RCG, and θ_{inc}
4. NF is the noise floor of the DDM (designated as ddm noise floor in the L1 data files)
5. $b(FM, RCG, \theta_{inc})$ is the y-intercept of the linear regression, which is a tabulated function of FM, RCG, and θ_{inc}

5.6.8. Characterization of GPS EIRP

The GPS transmit power, P_T, and transmit antenna gain, G_T, or the EIRP can be estimated using a combination of ground-based measurements and a parametrized model as a function of the transmitter space vehicle number (SVN) for all GPS satellites.

5.6.8.1. Transmit Power Estimation

A ground-based GPS constellation power monitor (GCPM) system has been designed, built, calibrated, and operated to measure the direct GPS L1 C/A signal (Wang et al., 2018b). The calibration subsystem and low noise amplifier (LNA) are implemented on a proportional–integral–derivative (PID)-controlled thermal plate with extremely stable temperature control.

The measured GPS received power has been found to be highly repeatable as tested for different satellites of three different block types. The measured EIRPs are verified by Deutsches Zentrum für Luft- und Raumfahrt (DLR) German Operations Center (GSOC) independent measurements using a calibrated 30 m dish antenna with 50 dB L-band gain.

An optimization algorithm is used to estimate the transmit power of GPS L1 C/A code by minimizing a cost function based on the difference between an engineering forward model prediction and the measurement of received power. We determine our best estimate of the GPS transmit power for the L1 C/A signal by averaging 32 days of estimates of P_T as given in Table 5.3. More technical details of the GCPM system and the optimization algorithm can be found in Wang et al. (2018b). The following should be noted:

1. The estimated power values are indeed an "effective transmit power" as the product of the exact transmit power and the transmit system gain correction factor (GCF).

Table 5.3. Estimates of GPS Transmit Power (L1 C/A)

Pseudorandom noise code (PRN)	P_T (dBW)	Block	PRN	P_T (dBW)	Block
1	15.09	IIF	17	16.39	IIR-M
2	13.79	IIR	18	14.04	IIR
3	14.77	IIF	19	13.66	IIR
4	—	—	20	13.48	IIR
5	16.28	IIR	21	14.43	IIR
6	15.38	IIF	22	14.39	IIR
7	16.86	IIR	23	15.41	IIR
8	15.42	IIF	24	15.03	IIF
9	15.49	IIF	25	15.32	IIF
10	16.28	IIF	26	15.22	IIF
11	13.67	IIR	27	15.34	IIF
12	16.88	IIR	28	14.27	IIR
13	13.89	IIR	29	16.84	IIR-M
14	13.20	IIR	30	15.47	IIF
15	16.08	IIR	31	16.35	IIR-M
16	13.93	IIR	32	15.87	IIF

2. The accuracy of the estimated power values is dependent on the accuracy of the baseline pattern (5th-order power series of transmit antenna gain in Marquis & Reigh, 2015) used in the forward model simulation.

5.6.8.2. Transmit Antenna Gain Estimation

The transmit antenna directivity of IIR and IIR-M block type SVs has been published in Marquis and Reigh (2015), while that of IIF block type SVs is unavailable to the public. The baseline antenna pattern (Wang et al., 2017) used in the L1 calibration is a 5th-order power series (polynomial fitting) of the azimuthally averaged published antenna pattern for IIR and IIR block types and that of the averaged pattern of all 12 SVs using improved antenna panel (4 IIR and 8 IIR-M) for IIF block.

5.6.8.3. Discussion of GPS Transmitter EIRP Characterization

1. *Transmit power and antenna pattern:* The high-resolution full transmit antenna pattern will be retrieved using the direct GPS signal measured by the CYGNSS zenith antenna, as discussed in Wang et al. (2018a). Then the transmit power table will be further updated when the full patterns are applied to the optimization algorithm.

2. *IIF block type power switching issue:* 10 of the 12 IIF SVs switch the power sharing between the components in L1 over the US East Coast and back over the West Pacific in every orbit. It has been a stable behavior since the first quarter of 2017. Currently, the data measured by the IIF block are flagged. This issue will be resolved by incorporating the CYGNSS zenith antenna measurement in L1 calibration.

3. *SV retirement for PRN 18:* On March 5, 2018, space vehicle number (SVN) 54 (operating as PRN 18) retired. SVN 34 (Block IIA) has been used for PRN 18 since March 20, 2018. CYGNSS data using PRN 18 since then are flagged.

4. *Power redistribution for block IIR-M:* A commanded redistribution of transmit power from M code to C/A code was performed for the 7 active IIR-M satellites on February 7 and February 8, 2017 (Steigenberger et al., 2017). The measured carrier-to-noise (C/N0) density ratio from different geodetic receivers experienced an approximately 1.5 dB-Hz increase on average. This phenomenon indicates an increase in the L1 C/A code power for all 7 satellites after the maintenance was performed (Thoelert et al., 2017). This event happened before the CYGNSS satellites were transitioned to science mode. No additional power redistribution for IIR-M satellites has been reported since then.

5.7. L1 Trackwise Correction for Climate Data Records

Determination of the NBRCS of a scattering surface from CYGNSS measurements of received power requires that the EIRP of the L1 signal transmitted by the GPS satellite in the direction of the specular reflection point be known (Gleason et al., 2016). EIRP is the product of the GPS transmit power and transmit antenna gain in the direction of the specular reflection point. Since NBRCS is used to estimate ocean surface wind speed (Clarizia & Ruf, 2016), retrieval of wind speed also requires knowledge of the EIRP. The L1 calibration algorithm converts raw received power into calibrated NBRCS. The L1 algorithm uses GPS transmit antenna gain patterns provided by the GPS manufacturers. The power transmitted by each GPS satellite was initially determined from measurements made by an accurately calibrated ground-based GPS power monitor (Wang et al., 2018b). A single value for transmit power was determined for each GPS satellite from measurements made over many days. This implicitly assumes that the power transmitted by each GPS satellite does not vary over time. This approach is used for L1 Science Data Products Sensor Data Record (SDR) versions 1.0, 1.1, 2.0, and 2.1 and for the corresponding L2 and L3 products derived from them. Analysis of GPS power monitor measurements since CYGNSS's launch has shown that GPS transmit power variations have in fact occurred, sometimes suddenly for short periods of time and sometimes more gradually over long time periods. The L1 trackwise correction algorithm is intended to correct for those variations.

The leading edge slope (LES) L1 data product is derived from calibrated measurements of the scattering cross section as the slope of the leading edge of the delay waveform at the specular point (Clarizia & Ruf, 2016). LES calibration similarly requires knowledge of the GPS EIRP, and the trackwise correction algorithm is also applied to it.

CYGNSS data acquired prior to August 1, 2018, were measured with the flight GPS navigation receiver commanded to operate in automatic gain control (AGC) mode, which automatically adjusts receiver gain so the strength of direct (not scattered) signals received from the constellation of GPS satellites is restricted to a narrow dynamic range prior to signal processing. AGC mode is intended primarily to compensate for expected variations in received signal strength due to changes in the distance between transmitter and receiver and in a number of other characteristics of the signal propagation. It also inadvertently compensates for changes in the GPS transmit power. The AGC mode was disabled on all eight observatories in August 2018 in order to enable the use of the received direct signal strength to monitor the GPS transmit power level, determine the GPS EIRP, and use that information to better calibrate the L1 NBRCS and LES. L1 and higher data products beginning with SDR version 3.0 use the new real-time GPS EIRP monitoring capability to correct for its variations in the L1 calibration algorithm. The trackwise correction algorithm is intended to mitigate the effect of variations in GPS transmit power on the NBRCS and LES calibration for measurements made prior to August 2018. It is also applied to data taken after August 2018 and serves to correct for other secondary inaccuracies in the calibration. The data products produced with it are considered Climate Data Records (CDRs) in the sense that they are reprocessed products that rely on the use of ancillary reanalysis wind speed products to improve the calibration and produce data products with reliable long-term calibration stability.

5.7.1. Trackwise Correction Methodology

CYGNSS surface scattering measurements are made by first identifying a GPS satellite for which the specular reflection point on the surface between it and the CYGNSS satellite lies in the CYGNSS receive antenna pattern and then processing the scattered signal received using matched filter correlation with the unique pseudorandom noise (PRN) code used to modulate the transmissions from each GPS satellite (Gleason & Gebre-Egziabher, 2009). The matched filter correlation includes a final incoherent integration time of 1 second, and an output measurement is produced once every second that is proportional to the strength of the scattered signal. This is the L0 CYGNSS data that are converted to NBRCS and LES. A CYGNSS "track" is defined as the continuous once-per-second measurements made while a single CYGNSS observatory processes scattered signals from a single GPS PRN. The length of the track is determined by the time over which its specular reflection point stays within the CYGNSS receive antenna mainbeam. In practice, tracks last between 10s of seconds and > 1000 seconds, with an average length of ~650 seconds. Given the orbit velocities involved, this corresponds to an average track length of ~3000 km.

The trackwise correction algorithm acts, as its name implies, on individual tracks. All ocean samples in a track are used. Each sample is matched to an independent reanalysis model estimate of the ocean surface wind speed. The model wind speed is applied in reverse to the geophysical model functions that are normally used by CYGNSS to infer wind speed from measurements of NBRCS and LES (Ruf

& Balasubramaniam, 2019). In this case, NBRCS and LES are estimated from wind speed. For each track, this produces a population of observed and modeled values. A scale difference between them can be explained by a change in the transmit power of the GPS PRN that is responsible for the specular reflection. An offset difference between them can be explained by a change in the noise floor of the received signal, which is sensitive to the sum of transmit powers of all visible GPS satellites. The trackwise correction algorithm consists of applying a linear regression to the two populations and applying its regression coefficients to the CYGNSS observations. Deviations of the slope of the regression from unity can be related to deviations of the true GPS PRN transmit power from the mean value used in the L1 calibration algorithm. In practice, this correction can also mitigate other scale errors in the L1 algorithm. Likewise, the y-intercept (offset) correction will mitigate multiple sources of change in the noise floor, in addition to changes in the transmit power of the overall GPS constellation.

CDR L2 and 3 products (ocean surface wind speed, mean square slope, and latent and sensible heat flux) are generated from the CDR L1 data using the same L2 and L3 data processing algorithms as are used for the standard SDR data products without the trackwise correction. The L2 and L3 CDR products also exhibit improved calibration accuracy and stability over the SDR versions.

5.7.2. Input Data Description

A complete track of observations ($NBRCS_{obs}$) is used for each trackwise correction. (A track is defined as a continuous time series of samples using the same GPS PRN and CYGNSS observatory.) All samples in the track that are over ocean are matched up with the closest (in time and space) wind speed value provided by ERA5. Model values for the NBRCS ($NBRCS_{mod}$) and LES (LES_{mod}) are derived from the ERA5 wind speed using the L2 wind speed retrieval algorithm GMFs that tabulate wind speed as a function of NBRCS, LES, and incidence angle. The samples are then filtered, and the subset satisfying the following conditions is selected:

1. 1.5 m/s < ERA5 wind speed
2. $0 < NBRCS_{obs} < GMF(1.5 \text{ m/s})$ or $0 < LES_{obs} < GMF(1.5 \text{ m/s})$

Filter 1 is intended to remove samples with wind speeds below 1.5 m/s, for which the GMF is considered less reliable because the NBRCS and LES become more sensitive

to long wave swell that is not as well correlated with local wind speed. Filter 2 is intended to remove samples that are either nonphysical (negative values) or above the GMF value that corresponds to a wind speed of 1.5 m/s. If less than 50 samples are available after these filters are applied, then the track is fatally flagged, and CDR wind speeds are not produced.

5.7.3. Trackwise Correction Processing

The filtered track of observed and modeled samples is ordered by the modeled values from minimum to maximum. The range of values is subdivided evenly into 10 bins, and for every bin with more than 1/20th of the total number of samples, the samples within the bin are averaged. A linear regression is performed of the average values in each bin, with observations as the independent variable. This version of linear regression is used to better balance the contributions of samples across the full dynamic range of values, since with most tracks, the distribution of wind speed samples is highly nonuniform and concentrated near 5–9 m/s.

The linear regression coefficients are then applied to the observation samples, resulting in preliminary trackwise corrected values given by

$$NBRCS_{obs2} = m * NBRCS_{obs} + b \tag{5.28a}$$

$$LES_{obs2} = m * LES_{obs} + b, \tag{5.28b}$$

where m and b are the regression coefficients.

Outlier samples are identified by examining the difference between model and corrected values. Specifically, a sample is considered an outlier if it satisfies

$$|NBRCS_{obs2} - NBRCS_{mod}| > 40 \tag{5.29a}$$

$$|LES_{obs2} - LES_{mod}| > 20. \tag{5.29b}$$

All outliers are removed from the population of filtered samples, and the linear regression is repeated with the original filtered samples less the outliers. This is done to reduce the influence of outlier samples on the final trackwise correction. After the second iteration of the linear regression, Equation 5.28 is then applied to all samples in the track, resulting in the final trackwise correction version of the observations given by

$$NBRCS_{obs\_cor} = m * NBRCS_{obs} + b \tag{5.30a}$$

$$LES_{obs\_cor} = m * LES_{obs} + b, \tag{5.30b}$$

where *m* and *b* are now the regression coefficients from the second iteration of the linear regression.

5.7.4. Quality Control Considerations

The trackwise correction is assessed for reliability and confidence using several quality control metrics at L1. The outlier test described by Equation 5.32 is applied to all samples over ocean, for which modeled values of the L1 observables are available, and all outliers are flagged. Samples over land cannot be tested in this way. The slope of the linear regression from which the trackwise correction is derived (*m* in Equation 5.30) is required to be above 0 and below 3. Negative slopes indicate a nonphysical dependence of the L1 observable on wind speed. Slopes larger than 3 are an indication that the scale error in the observations cannot readily be explained by an error in the assumed GPS EIRP given its expected range of variability. The y-intercept of the linear regression (*b* in Equation 5.30) is required to be between −20 and +50 for the LES and between −40 and +100 for the NBRCS observable. These ranges are consistent with expected levels of bias correction. The explained variance (i.e., the r^2) of the linear regression is required to be greater than 0.02. This is an indication of nonnegative correlation between the measured and modeled observable. Violations of any of these conditions are flagged with low confidence in the linear regression–based correction, since the behavior of the correction is not consistent with expected behavior. In practice, all of these quality control tests combined together typically flag ~22% of the samples.

L2 CDR wind speed estimates are derived from the L1 CDR data using the same retrieval algorithm as is used for regular data production. Hence the same quality control filters are used.

5.7.5. Output Data Product Description

The trackwise corrected L1 observables, $NBRCS_{obs\_cor}$ and LES_{obs_cor}, are included in the CDR data files as these data fields:

> *ddm_nbrcs*—the trackwise corrected variable $NBRCS_{obs\_cor}$ given by Equation 5.30a
> *ddm_les*—the trackwise corrected variable LES_{obs_cor} given by Equation 5.30b

In addition, a number of ancillary data fields are also output that are related to the trackwise correction. These include the following:

> **l1*_tw_outlier* (**l1** = *nbrcs or les*)—a quality control bit signifying that a sample was identified as an outlier according to the criteria given in Section 5.7.2 above
> **l1*_tw_r2* (**l1** = *nbrcs or les*)—the correlation coefficient of the linear regression used to determine the trackwise correction given by Equation 5.30
> **l1*_tw_slope* (**l1** = *nbrcs or les*)—the slope of the linear regression used to determine the trackwise correction, *m* in Equation 5.30
> **l1*_tw_yint* (**l1** = *nbrcs or les*)—the y-intercept of the linear regression used to determine the trackwise correction, *b* in Equation 5.30
> *ddm_*l1*_orig* (**l1** = *nbrcs or les*)—the value of the L1 observable prior to trackwise correction
> **l1*_mod* (**l1** = *nbrcs or les*)—the model value of the L1 observable derived from the matchup ERA5 wind speed and the GMF
> *tw_num*—the number of samples within a track that are included in the linear regression used to determine the trackwise correction given by Equation 5.30
> *era5_wind_speed*—the matchup ERA5 wind speed that corresponds to a particular sample

5.8. CYGNSS End-to-End Simulator

The CYGNSS end-to-end simulator (E2ES) is a software simulator of the CYGNSS mission. In support of prelaunch CYGNSS Science Team activities, the E2ES played an important role in demonstrating the ability of the baseline CYGNSS instrument to satisfy mission requirements—in particular, the accuracy of the retrieved winds for both typical ocean wind speeds and the extreme winds of tropical cyclones. Prelaunch simulations incorporating high-fidelity tropical cyclone input wind and rain fields were performed to provide a realistic, high-resolution, time-varying truth wind field capturing all phases of the tropical cyclone life cycle and the associated highly nonuniform wind and rain fields with intensities that exceed those typically used by other simulators. Internally, the simulator models all critical steps of the DDM production process: dynamic orbit propagators for the GPS and CYGNSS constellations; signal propagation (including rain attenuation) to and from the specular reflection point on the Earth's surface; bistatic forward scattering from the wind-driven, roughened ocean surface; transmit and receive antenna gain patterns projected onto the Earth's surface; and fading and thermal noise statistics of the received signal. These steps culminate in the generation of DDM measurements that simulate observations to be obtained on orbit.

5.8.1. CYGNSS E2ES Implementation

The CYGNSS E2ES is organized into a set of fundamental blocks that are executed sequentially as depicted in Figure 5.20. The E2ES process starts with an initialization phase. A configuration file is provided by the user and used to allocate memory for data structures, load input files, and set a number of user-definable parameters.

First, the transmitter and receiver orbit information is input by the user. Currently, the full CYGNSS and GPS constellations are input in the form of time-varying positions and velocities in ECEF coordinates based on the predicted distribution of CYGNSS satellites and International GNSS Service (IGS) orbit files for the GPS satellites. Using the WGS-84 Earth ellipsoid model, the E2ES solves for the point on the Earth where the reflection of the transmitted signal takes place (i.e., the specular point) using an efficient iterative approach until precise convergence is reached. The specular point is found for each receiver/transmitter combination for which a line of sight exists. Later in the process, a down-selection is applied to select the four specular points from each CYGNSS satellite with the highest receive antenna gain.

Next, if the specular point is over the ocean, the surface around the specular location is discretized into a grid. The main contribution to the scattered signal power at the receiver comes from the specular point and a "glistening zone" around it. For typical CYGNSS measurements, it is sufficient to limit the grid around the specular point to a $200 \times 200 \text{ km}^2$ region that is gridded into roughly 1×1 km patches. The curvature of the Earth is accounted for using a conformal grid around the specular location. The discretized surface is then composed of a dense grid of patches, each having its own geometry with respect to the transmitter and receiver. A depiction of the grid is shown in Figure 5.21. Once the grid is constructed, the geometric parameters of each patch are evaluated. These parameters include the range, delay, Doppler shift, and scattering angle. The relative angle of each patch to the transmitter and receiver antennas is calculated,
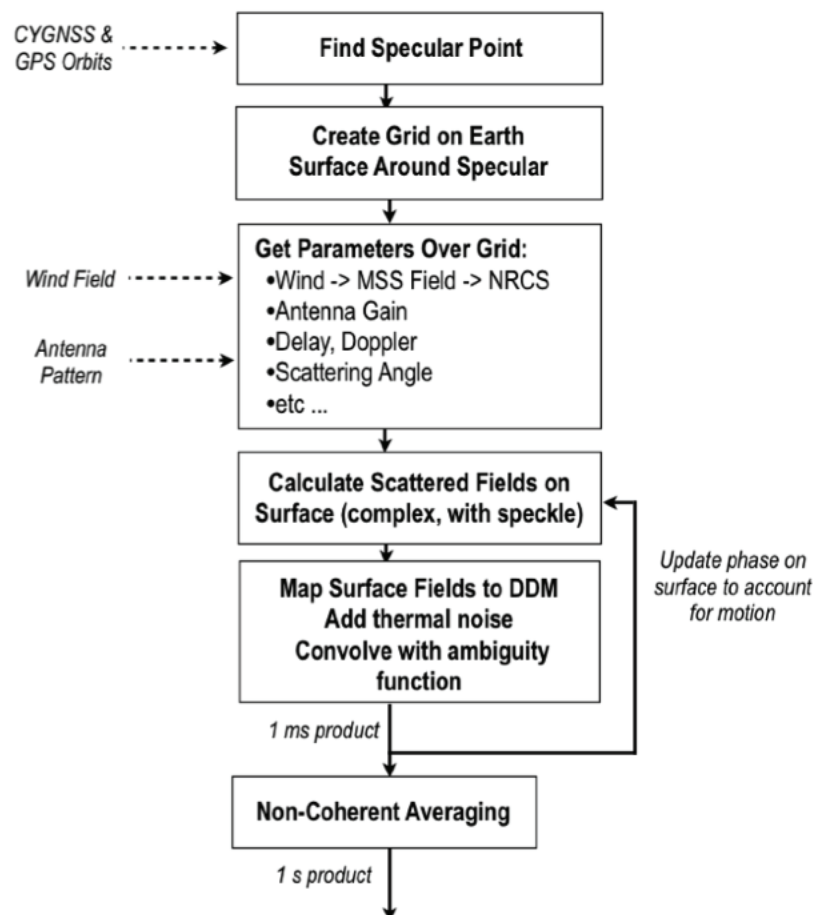
Figure 5.20. High-level flow diagram of the CYGNSS end-to-end simulator.
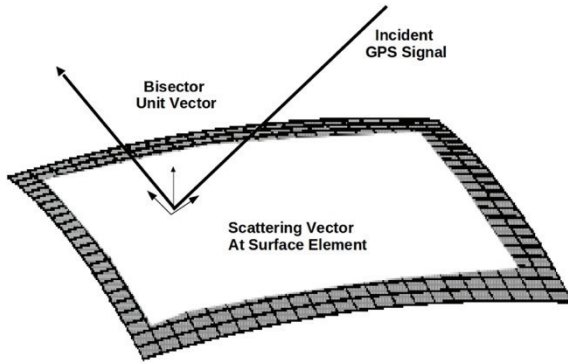
Figure 5.21. Depiction of the E2ES internal discretized surface grid around the specular point showing how each surface patch possesses a distinct geometry with respect to the receiver and transmitter satellites.

and the transmit and receive antenna gains are found for each location on the surface. The surface grid resolution has been chosen so that these parameters can be considered uniform over each patch.

At this point, the geophysical parameters of the surface are incorporated. These include the wind speed and direction, rain rate, and freezing level in the atmosphere (the last two are required to evaluate the rain attenuation). The original geophysical data are in the form of a time series at a native resolution that is then interpolated in both space and time to match the surface grid. For our tropical cyclone simulations, the input wind and rain field data were high-resolution datasets sampled at 1 km. The wind fields are used to calculate the expected MSS of the ocean surface based on a modified Katzberg semiempirical model. This, in turn, is used to calculate the radar cross section of the surface patch and ultimately the total scattered power.

The bistatic radar cross section (BRCS) of the surface patch is calculated using the Zavorotny-Voronovich model. The expected value of GPS scattered power as a function of delay and Doppler is a product of the receive (CYGNSS) antenna gain pattern on the surface, the transmit (GPS) antenna gain, the range from the specular point to the transmitter, the range from the specular point to the receiver, the GPS transmit power, the coherent integration time, and the GPS L1 wavelength. Within the E2ES, the equations are implemented in discrete form—that is, the discretized surface data are mapped into a discretized delay-Doppler space and then convolved with the ambiguity function in order to produce the DDM. The grid sizes on the surface and DDM are chosen to be at a high enough resolution such that discretization errors are small. This produces the statistically

expected value of the received DDM; however, the E2ES must also accurately incorporate the effects of fading and thermal noise in order to capture the correct error statistics for the wind speed retrieval.

Note that the CYGNSS E2ES also models the effects of rain attenuation. The GPS L1 band has inherently low attenuation due to rain, snow, and hail (as was the original intent when it was selected for satellite navigation). This is a key advantage of CYGNSS over other wind speed measurement instruments, especially when measuring within extreme rain conditions, such as hurricanes. Within the eyewall of tropical cyclones, small, short-lived cells can experience extreme rain rates that have a small but nonnegligible attenuation on reflected GPS signals, and the CYGNSS E2ES has been designed to incorporate the two-way path-specific attenuation using the model in International Telecommunication Union (ITU) R838-3 given the rain rate and freezing level at the specular point.

5.8.2. CYGNSS E2ES DDM Generation

In the CYGNSS DDMI, each DDM pixel is obtained through a cross correlation of the received scattered GPS signal with a locally generated replica of the C/A code of the transmitted signal for the delay-Doppler (DD) coordinate corresponding to that pixel. In preparation for downlink to the ground, the onboard CYGNSS DDMs consist of 17×11 pixels, extending from -1 chip to 3 chips in delay and from -2.5 kHz to 2.5 kHz in Doppler, with a resolution of 0.25 chip and 500 Hz. This DDM is very compact in delay-Doppler space, and the E2ES was designed to efficiently simulate this size DDM (as opposed to other potential implementations that would more efficiently capture waveforms, which are much longer in delay).

Given the expected scattered power of each surface patch as described in the previous section, the E2ES can produce simulated CYGNSS observations containing both speckle and thermal noise effects. The direct DDM synthesis mode in the E2ES produces complex DDMs that represent the output of a 1 ms coherent integration. The process is repeated 1,000 times as the geometry (and associated phase to individual surface patches) evolves, and after adding thermal noise, the resulting powers incoherently average to produce a single 1-second DDM product. The reflected GPS signal is formed by contributions from a large number of independent surface scatterers. This random scattering generates multiplicative self-noise (i.e., fading or speckle noise), which is proportional to the signal. In the E2ES, the scattered field of each discretized surface patch is initialized as a complex random

variable with a fixed magnitude and uniformly distributed random initial phase. The evolution of this phase depends on the changes in geometry as the receiver and transmitter satellites move in time relative to each patch. This results in random fading noise in the reflected signal and realistically represents the correct statistical properties to be observed in space-based GNSS-R measurements. The scattered field from the patches is then mapped into delay-Doppler space to form a DDM. Note that time evolution of the sea surface itself is not considered, as it has been shown that the fading statistics of spaceborne GNSS-R measurements are dominated by changes in geometry due to the high velocities associated with satellite platforms. The internal "finely resolved" DDM is then down sampled to match the delay and Doppler resolution of the actual CYGNSS measurements.

5.8.3. Use of E2ES in CYGNSS L1B Calibration

Prior to launch, the CYGNSS E2ES was used to generate test sets of DDMs with which to evaluate the L1A and 1B calibration algorithms. The calibration algorithms themselves utilize the CYGNSS E2ES in two ways. First, the CYGNSS L1B calibration utilizes precise specular point solutions based on algorithms first developed for the E2ES. The specular point solver utilizes a gridded surface conformal to the DTU10 mean sea surface topology at each grid point. The specular point we solve for here is defined as the point on the Earth with the minimum reflection path delay and is solved for using an iterative approach accurate to centimeters. No mathematical assumptions are used.

Second, the CYGNSS E2ES is used as part of the conversion of DDM BRCS values into an NBRCS. The E2ES is used to calculate the effective scattering area of different DDM pixels for different geometries. The effective scattering areas per pixel are tabulated, and these values are retrieved during the calibration process based on the measurement-specific reflection geometry and include the GPS-specific delay and Doppler spreading functions. Normalization of the BRCS for the scattering area is a key step in the inversion of the forward model so that geophysical parameters can be estimated from the NBRCS values.

5.9. Quality Control Flags

The L1 data product will include a set of quality control flags. Each of the quality control flags is briefly described below.

1. *Overall Quality Flag.* Logical OR of a subset of the flags listed below. Flags OR'd together include 4, 5,
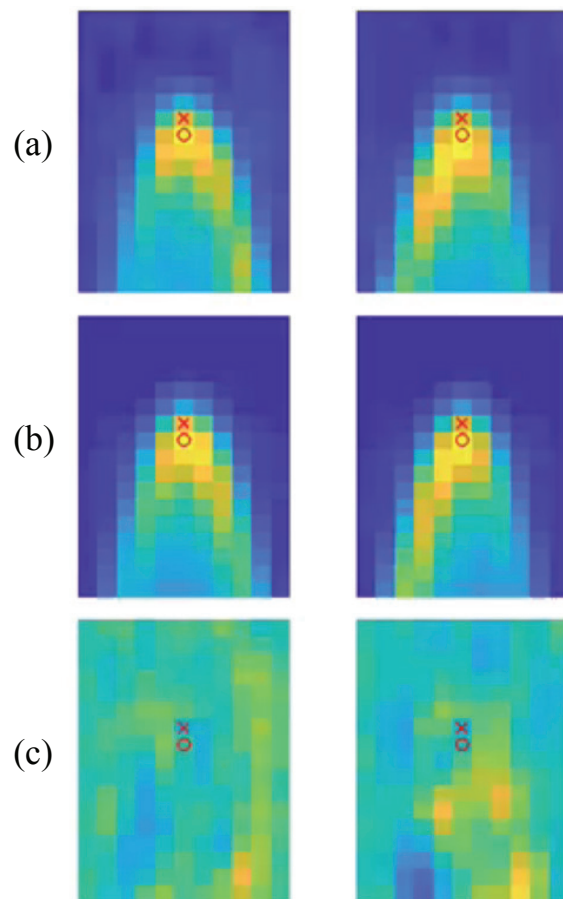
Figure 5.22. Comparison of (a) CYGNSS L1 DDM measurements, (b) CYGNSS E2ES simulated DDM measurements, and (c) the respective residual for two different cases (left and right columns).

6, 7, 8, 9, 10, 11, 12, 14, 15, 16, 17, 18, 19, 20, 22, 25, 26, 27, and 28.

2. *S-Band Transmitter Power On.* Set when the spacecraft S-band transmitter is powered on, which increases the possibility of radio frequency interference (RFI) in the measurements.

3. *Small Spacecraft Attitude Error.* Set when spacecraft attitude is between 1° and up to 30° off nominal pointing in any axis.

4. *Large Spacecraft Attitude Error.* Set when spacecraft attitude is equal to or greater than 30° off nominal pointing in any axis.

5. *Black Body Load Switched.* Set if black body calibration load was switched in during this measurement.

6. *DDMI Reconfiguration.* Set before and after black body calibration load switched to indicate the given DDM is a mixture of antenna and calibration load

signals and should not be used. Also set when processed PRN changes during integration interval.

7. *Communications Error Between Instrument and Spacecraft.* Set when Cyclic Redundancy Check (CRC) error detected in packet communications between instrument and spacecraft for this DDM.

8. *DDM Is a Test Pattern.* Set when DDMI is in a test mode, producing test patterns.

9. *DDMI Channel Idle.* Set if the DDMI was not actively tracking a satellite PRN when this measurement was taken.

10. *Low Confidence in DDM Noise Floor.* Set if more than a 10% change in noise floor levels is observed between consecutive DDMs.

11. *Specular Point Over Land.* Set when specular point is over land.

12. *Specular Point Very Near Land.* Set when specular point is within 25 km of land.

13. *Specular Point Near Land.* Set when specular point is within 50 km of land.

14. *Large Step in Noise Floor.* Set if more than a 0.24 dB jump in noise floor levels is observed between consecutive DDMs.

15. *Large Step in LNA Temperature.* Set if more than a 1 °C change in temperature over 1 minute is observed in the LNA temperature.

16. *Direct Signal in DDM.* Set if the direct signal code phase from the same PRN as the reflection is within 4 chips of the estimated specular point code phase.

17. *Low Confidence in GPS EIRP Estimate.* Set when the ground estimate of the transmitting GPS satellite power and antenna gain is believed to be significantly in error.

18. *RFI Detected.* Set when the kurtosis of the DDM noise floor varies more than the ideal Gaussian (3.0) by more than 1.0.

19. *Specular Point Bin Delay Error.* Set if specular point, zero-based delay bin is less than 6 or more than 10.

20. *Specular Point Bin Doppler.* Set if specular point, zero-based Doppler bin is less than 4 or more than 6.

21. *Negative Value in BRCS Area.* Set if any bin in the 3 × 5 DDMA measurement area in the DDM is negative.

22. *GPS PVT Error.* Set if the position, velocity, and time information for the GPS satellite was not successfully calculated on the ground.

23. *Specular Point Calculation Error.* Set if specular point was not able to be calculated on the ground.

24. *Specular Point Bin Delay Error.* Set if specular point, zero-based delay bin is less than 6 or more than 10.

25. *BRCS LUT Error.* Set if index into BRCS error LUT is out of range.

26. *Antenna Gain LUT Error.* Set if index into antenna LUT is out of range.

27. *Black Body Framing Error.* Set if unable to calculate black body calibration load counts.

28. *Flight Software Compression Shift Error.* This flag is triggered by a known (and fixed) bug in the flight software. This primarily occurs in low signal-to-noise ratio (SNR) conditions or in cases of high asymmetry in the DDM (also typical in low-SNR DDMs). For DDMs where SNR ≥ 3, receive antenna gain ≥ 3, measurement > 25 km from land and star tracker status is valid, this flag is set for approximately 0.35% of data.

5.10. CYGNSS L1 Error Estimation Method

This analysis assumes that the uncertainties in the CYGNSS L1 calibration algorithm are generally independent, uncorrelated error sources, which can be characterized with a zero mean Gaussian distribution. This may not be strictly the case for some terms (most notably the GPS transmit power levels), yet to a first order, this analysis serves to bound the expected error and, as shown in the top-down analysis in Ruf et al. (2018), is consistent with the best estimate of the overall on-orbit observed CYGNSS wind retrieval performance. The method for this error analysis is based on the partial derivative method presented in Jansen et al. (1995). Additionally, the rolled-up error was simulated using a Monte Carlo simulation and was in agreement with the partial derivative estimated error levels presented below. For more details on the partial derivatives for individual error terms in the L1A and L1B calibration equations, refer to Gleason et al. (2016).

5.10.1. Error Analysis Methodology

The total error in the L1A or L1B calibrated DDM is the root sum square (RSS) of the individual error sources in the independent terms of their respective expressions, which can be expressed generically as

$$\Delta L_1^{a,b} = \left[\sum_{i=1}^{x} [E(q_i)]^2 \right]^{1/2}, \tag{5.28}$$

where $L_1^{a,b}$ are the L1A and L1B estimated error values, x is the number of independent error terms, and q_i are the respective input error parameters. The individual error terms can be estimated by taking the partial derivatives of the calibration

equation such that each error term in the process can be quantized as

$$E(q_i) = \left| \frac{\partial L_1^{a,b}}{\partial q_i} \right| \Delta q_i. \tag{5.29}$$

5.10.2. Rolled-Up On-Orbit L1 Calibration Errors

The wrapped-up errors of the L1B calibration can be expressed in a similar manner, with the total L1A error rolled in and estimated over the DDMA region of the DDM (3 delays × 5 Dopplers):

$$\overline{\sigma}_{DDMA}^0 = \frac{P_{g,DDMA}(4\pi)^3 L_{atm}}{P^T \lambda^2 G_{SP}^T G_{SP}^R R_{SP}^{Total} A_{DDMA}}. \tag{5.30}$$

Substituting this equation into Equation 5.28 results in

$$E(q_i) = \left| \frac{\partial \overline{\sigma}_{DDMA}^0}{\partial q_i} \right| \Delta q_i, \tag{5.31}$$

where

$$q_1 = P_g, q_2 = DDMA_{crop}, q_3 = L_{atm}, q_3 = R_{SP}^{Total},$$
$$q_4 = P_T, q_5 = G^T, q_6 = G^R, q_7 = A.$$

The on-orbit estimated L1 calibration errors 1-σ estimates are shown below for each input parameter as well as explanations for each term.

1. $E(Pg)$ is the rolled-up L1A error from Gleason et al. (2016).
2. $E(DDMAcrop)$ is an estimate of the error in the DDMA weighting algorithm detailed in Table 5.4. The weighting algorithm uses a linear interpolation over nonlinear DDM bins, and this will introduce some error in the cropping of the final value. The value of 0.1 dB is an approximation based on ideal simulations of the DDMA weighting algorithm.
3. $E(R\ Total)$ is the total error due to misestimation of the path loss from the GPS transmitter to the specular point to the receiver. Given the relatively high accuracies of all three of these parameters, this error is expected to be negligible. More details on the contribution due to the single-frequency GPS receiver position estimation performed on CYGNSS can be found in Wang et al. (2021).
4. $E(EIRP) = E(PT) + E(GT)$ is the error in the GPS transmit power and antenna gain correction. The best estimate for this error is based on the top-down analysis reported in Wang et al. (2021).

Table 5.4. L1B Input Parameter Error Estimates

Error term	Error magnitude (at 10 m/s reference wind)	Comment
$E(Pg)$	0.23 dB	Rolled-up L1A error (Gleason et al., 2016)
$E(DDMA)$	0.1 dB	Error in DDMA weighting algorithm
$E(R\_total)$	0.01 dB	Based on total range error estimates of 2000 m (very conservative)
$E(EIRP)$	0.32 dB	GPS transmitter EIRP error
$E(GR)$	0.43 dB	Estimated receiver antenna gain error from Monte Carlo (MC) simulation
$E(A)$	0.05 dB	Effective scattering area error from E2ES

5. $E(GR)$ is the error in the receive antenna gain and is based on the analysis of σ_0 anomalies described in Section 5.6.4.2 after the described corrections to the receive antenna patterns were applied. The antenna gain error was estimated using Monte Carlo simulations based on the predicted statistical spacecraft attitude performance and best estimate of the receive antenna gain pattern described in more detail in Gleason et al. (2016).
6. $E(A)$ is the estimated error in the effective scattering normalization area used to convert σ to σ_0. The CYGNSS end-to-end simulator was used to generate these values. Given the extensive validation of the E2ES, this error was at a relatively low value, driven by errors introduced due to the integration step size used in the table generation, plus a small amount of margin.

The rolled-up L1 error budget is a function of multiple terms, all of which are impractical to include in a per-observation lookup table. For this reason, the L1 uncertainty included with each L1 σ_0 estimate in the CYGNSS official products is considered only for the two most influential variables: the magnitude of the σ_0 itself and the range corrected gain at each observation (which wraps up both the receive antenna gain and range losses). As can be seen from Equations 5.13 and 5.14 (and derived in greater detail in Gleason et al., 2016), the partial derivative contributions weight the error magnitudes differently based on the observation parameter inputs. The largest scaling factor is the overall received power,
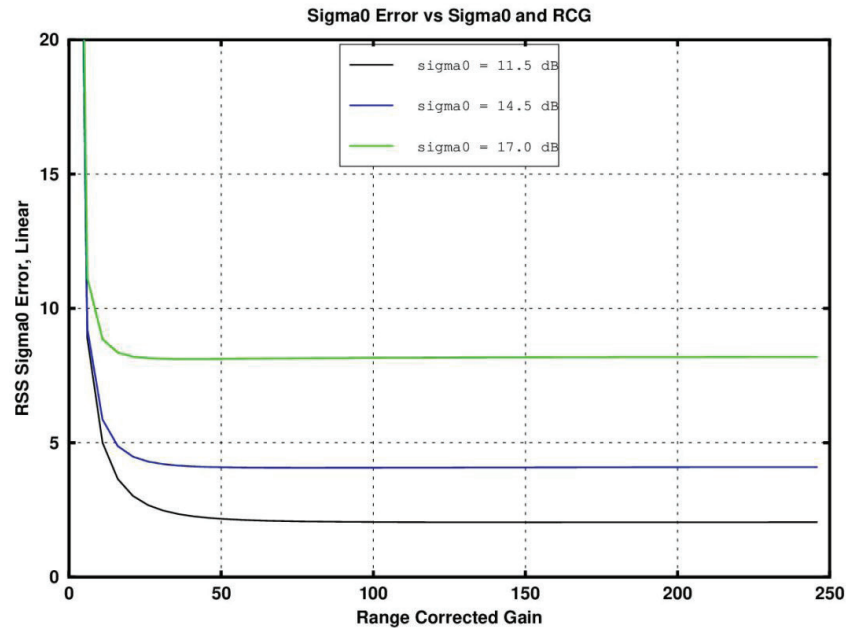
Figure 5.23. L1 σ_0 uncertainty at three reference σ_0 levels and over a full range of received RCG. These corrections correspond to roughly 13% of the reference σ_0 at the typical (greater than 50) values of RCG.

which scales directly with the surface σ_0 and the receive antenna gain and path losses. Other variables that impact the received power or otherwise weight the error terms are not considered for simplicity and because they are generally of a lower order than the changes induced by the surface conditions and receive antenna gain. The resulting rolled-up L1 errors for three example σ_0 reference values and over a full range of RCG are shown in Figure 5.23.

5.11. References

Algorithm Theoretical Basis Document (ATBD): CYGNSS Level 1A DDM Calibration and Error Analysis, April 2018.

Andersen, O. B. (2010). The DTU10 Gravity field and Mean sea surface. Second international symposium of the gravity field of the Earth (IGFS2), Fairbanks, Alaska.

Bechtold, P., Bauer, P., Bidlot, J. R., Cardinali, C., Magnusson, L., Prates, F., & Rodwell, M. (Winter 2012/13). Uncertainty in tropical winds. *ECMWF Newsletter, 134,* 33–37. https://www.ecmwf.int/en/elibrary/14577-newsletter-no-134-winter-2012-13.

Clarizia, M. P., & Ruf, C. S. (2016). Wind speed retrieval algorithm for the Cyclone Global Navigation Satellite System (CYGNSS) mission. *IEEE Transactions on Geoscience and Remote Sensing, 54*(8), 4419–4432. https://doi.org/10.1109/TGRS.2016.2541343.

Gleason, S., Al-Khaldi, M., Ruf, C., McKague, D., Wang, T., & Russel, A. (2021). Characterizing and mitigating digital sampling effects on the CYGNSS Level 1 calibration. *IEEE Transactions on Geoscience and Remote Sensing, 60,* 1–12. https://doi.org/10.1109/TGRS.2021.3120026.

Gleason, S., & Gebre-Egziabher, D., eds. (2009). *GNSS applications and methods.* Artech House, 530 pp., ISBN-13: 978-1596933293.

Gleason, S., Ruf, C., Clarizia, M. P., & O'Brien, A. J. (2016). Calibration and unwrapping of the normalized scattering cross section for the Cyclone Global Navigation Satellite System (CYGNSS). *IEEE Transactions on Geoscience and Remote Sensing, 54*(5), 2495–2509. https://doi.org/10.1109/TGRS.2015.2502245.

Gleason, S., Ruf, C. S., O'Brien, A. J., & McKague, D. S. (2019). The CYGNSS Level 1 calibration algorithm and error analysis based on on-orbit measurements. *IEEE Journal of Selected Topics in Applied Earth Observations and Remote Sensing, 12*(1), 37–49. https://doi.org/10.1109/JSTARS.2018.2832981.

Jansen, M. A., Ruf, C. S., & Keihm, S. J. (1995). TOPEX/Poseidon Microwave Radiometer (TMR): II. Antenna pattern correction and brightness temperature algorithm. *IEEE Transactions on Geoscience and Remote Sensing, 33*(1) 138–146.

Marquis, W. A., & Reigh, D. L. (2015). The GPS block IIR and IIR-M broadcast L-band antenna panel: Its pattern and performance. *Navigation, 62*(4), 329–347.

Misra, P., & Enge, P. (2001). *Global positioning system: Signals, measurements, and performance.* Ganga Jamuna Press. ISBN 0-9709544-0-9.

Ruf, C., et al. (20 Oct. 2020). *Algorithm Theoretical Basis Document Level 1B DDM calibration.* Revision 3 Change 0, University of Michigan Doc. 148-0137. http://cygnss.engin.umich.edu/wp-content/uploads/sites/534/2021/07/148-0137_ATBD-L1B-DDM-Calibration_R3_release.pdf.

Ruf, C., & Balasubramaniam, R. (2019). Development of the CYGNSS geophysical model function for wind speed. *IEEE Journal of Selected Topics in Applied Earth Observations and Remote Sensing, 12*(1), 66–77. https://doi.org/10.1109/JSTARS.2018.2833075.

Ruf, C. S., Gleason, S., & McKague, D. S. (2018). Assessment of CYGNSS wind speed retrieval uncertainty. *IEEE Journal of Selected Topics in Applied Earth Observations and Remote Sensing, 12*(1), 87–97. https://doi.org/10.1109/JSTARS.2018.2825948.

Steigenberger, P., Hauschild, A., Thoelert, S., & Langley, R. (2017). US Air Force puts more power into GPS block IIR-M C/A-code. *GPS World, 28*(4), 8–9.

Thoelert, S., Hauschild, A., Steigenberger, P., & Langley, R. (Sept. 2017). GPS IIR-M L1 transmit power redistribution: Analysis of GNSS receiver and high-gain antenna data. *Proceedings of the 30th International Technical Meeting of the Satellite Division of the Institute of Navigation* (pp. 1589–1602). https://doi.org/10.1002/navi.250.

Ulaby, F. T., & Long, D. G. (2014). *Microwave radar and radiometric remote sensing.* Ann Arbor, MI: Univ. Michigan Press.

Wang, T., Ruf, C., Gleason, S., O'Brien, A., McKague, D., Block, B., & Russel, A. (2021). Dynamic calibration of GPS effective isotropic radiated power for GNSS-reflectometry Earth remote sensing. *IEEE Transactions on Geoscience and Remote Sensing, 60.* https://doi.org/10.1109/TGRS.2021.3070238.

Wang, T., Ruf, C., Block, B., & McKague, D. (2018a). *Characterization of the transmit power and antenna pattern of the GPS constellation for the CYGNSS mission.* Paper presented at the July 2018 IEEE International Geoscience and Remote Sensing Symposium (IGARSS), Valencia, Spain.

Wang, T., Ruf, C. S., Block, B., McKague, D. S., & Gleason, S. (2018b). Design and performance of a GPS constellation power monitor system for improved CYGNSS L1B calibration. *IEEE Journal of Selected Topics in Applied Earth Observations and Remote Sensing, 12*(1), 26–36. https://doi.org/10.1109/JSTARS.2018.2867773.

Wang, T., Ruf, C., Gleason, S., Block, B., McKague, D., & Provost, D. (2017, July). Development of GPS constellation power monitor system for high accuracy calibration/validation of the CYGNSS L1B data. *2017 IEEE International Geoscience and Remote Sensing Symposium (IGARSS).* (pp. 1008–1011). https://doi.org/10.1109/IGARSS.2017.8127125.

Wang, T., Zavorotny, V. U., Johnson, J., Yi, Y., & Ruf, C. (2019). Integration of CYGNSS wind and wave observations with the WAVEWATCH III numerical model. *IGARSS 2019—2019 IEEE International Geoscience and Remote Sensing Symposium* (pp. 8350–8353). https://doi.org/10.1109/IGARSS.2019.8900481.

WAVEWATCH III Development Group (WW3DG). (2016). *User manual and system documentation of WAVEWATCH III version 5.16 MMAB* (Technical Note 329, NOAA/NWS/NCEP/MMAB, College Park, MD, USA, 326 pp.+ Appendices). https://polar.ncep.noaa.gov/mmab/papers/tn276/MMAB_276.pdf.

Zavorotny, V., & Voronovich, A. (2000). Scattering of GPS signals from the ocean with wind remote sensing application. *IEEE Transactions on Geoscience and Remote Sensing, 38,* 951–964. https://doi.org/10.1109/36.841977.

6. Level 2 Mean Square Slope Retrieval

6.1. Introduction

The primary mission of the CYGNSS Project is to collect measurements of ocean surface winds through variations in the direct versus reflected GPS signals. It will be achieved through fitting the calibrated data obtained by the eight CYGNSS microsatellite observatories to the empirical or modeled functions, which relate the measured signal parameters to surface wind. At the same time, such an ocean surface characteristic as the mean square slope (MSS) will be available also.

Within the framework of the scattering model adopted here, the MSS can be related directly to the normalized bistatic radar cross section (NBRCS) σ_0. On the other hand, the bistatic radar equation allows the connection of σ_0 to the calibrated estimates of power for each delay-Doppler bin through the instrument calibration algorithm. The algorithm theory is based on the details of the instrument processing chain hardware and firmware, a model of the received signal power (Zavorotny & Voronovich, 2000), and estimates of the external and internally generated noise power. The purpose of this document is to describe the CYGNSS Level 2 (L2) MSS algorithms and provide all necessary equations for implementing the algorithm during the mission. Section 6.1.1 provides science background and objectives. It explains the need for ocean MSS. Section 6.2 describes the physics of the problem and explains the connection between the NBRCS and the MSS and between the MSS and the ocean surface spectrum. Section 6.3 provides an overview of the MSS retrieval algorithm. Section 6.4 discusses the performance characterization and the error analysis of the retrieval algorithm. Section 6.5 presents a short overview of new approaches that use measured and modeled MSS for improvement of CYGNSS L2 wind speed retrievals.

The MSS of the ocean surface is a very important quantity. It is crucial for understanding the physical processes at the air-sea interface and for interpreting altimeter and scatterometer radar backscatter measurements (Jähne et al., 1987; Wu, 1990; Liu et al., 1997; Walsh et al., 1998; Chapron et al., 2000; Liu et al., 2000). The need for global MSS datasets in air-sea interaction research is increasingly apparent. Indeed, the presence of waves significantly enhances gas transfer rates across a water boundary layer. The transfer rates correlate well with the MSS of the waves. It has been observed in laboratory conditions that gas transfer velocities significantly increase at the onset of surface wave generation (Jähne et al., 1987).

The need for ocean MSS is also evident in satellite radiometry, specifically for salinity measurements (Font et al., 2004; Guimbard et al., 2012). At L-band, the brightness temperature of the ocean surface depends equally on three surface parameters: the sea surface salinity, the sea surface temperature, and the sea state, which is responsible for the deviations of the brightness temperature with respect to the flat sea model. To estimate the sea roughness effect on brightness temperature, various models driven either directly by 10 m height wind speed, U_{10}, or by the significant wave height (SWH) have been tried without significant success. With the advent of the GPS bistatic radar technique, which uses L-band signals, the idea has been proposed to measure L-band limited MSS to provide sea surface roughness estimates for L-band radiometric measurements of ocean salinity (Font et al., 2004; Guimbard et al., 2012).

6.2. Physics of the Problem

6.2.1. Connection Between the Bistatic Radar Cross Section and the MSS

According to the forward model based on the bistatic radar equation adopted for the case of GPS scattered signals, the DDM emerges as a result of the integration of the product of several factors over a certain ocean surface area. One of those factors is the bistatic radar cross section (BRCS) σ_0, which describes the effect of ocean surface roughness. In the geometric optics (GO) limit of the Kirchhoff approximation (KA) this term is represented by the following expression (Barrick, 1968; Bass & Fuks, 1979):

$$\sigma_0 = \pi \left| \Re \right|^2 \left(q / q_z \right)^4 P\left(-q_\perp / q_z \right), \tag{6.1}$$

where $\vec{q}$ is the scattering vector, which can be regarded as a function of the coordinate $\vec{\rho}$ in the mean surface plane, and $\Re$ is the complex Fresnel coefficient, which depends on signal polarization state; a complex dielectric constant of the reflecting medium, ε; and the local incidence angle. In the case of GPS bistatic radar, the reflected signal is left-hand circularly polarized (LHCP). The factor $P\left(\vec{s} \right)$ in Equation 8.1 is the probability density function (PDF) of large-scale "smoothed" surface slopes. The adjective "smoothed" implies that very small-scale components of the surface spectrum (of the order of several tens of centimeters) are filtered out.

This is a consequence of using in this technique 0.2 m long L-band waves, which obey the GO limit of the KA. In order to sense all surface scales in this scattering regime, one would need to use 1 mm (or shorter) electromagnetic (EM) waves.

It should be noted here that the GO limit of the KA is valid when the surface waves are high enough—namely, when the Rayleigh parameter for the rough ocean surface, $R_a = kh\cos\theta$ >> 1, where $k = 2\pi/\lambda$ and h is the root mean square (RMS) of surface elevations. This regime holds for wind speeds greater than 4–5 m/s. For the case of a small Rayleigh parameter, $R_a < 1$ (and respectively small MSS), which corresponds to low winds $U < 4$–5 m/s^{-1}, the scattering mechanism changes toward a weak diffuse scattering. Instead of quasi-specular scattering, driven by surface slopes, higher-order Bragg scattering governed by parameter R_a comes into play. Since R_a is proportional to h, which in turn results from integrating the entire surface elevation spectrum, it, in contrast to the GO-KA approximation, also includes very small-scale components of the surface spectrum. Recently, a bistatic scattering model was proposed that describes such a weak diffuse scattering providing a smooth transition to the regime of strong diffuse scattering (Voronovich & Zavorotny, 2017).

It is believed that for linear surface gravity waves, the slope PDF $P(\vec{s})$ can be approximated by the anisotropic bivariate Gaussian distribution (Zavorotny & Voronovich, 2000; Elfouhaily et al., 2002; Soulat, 2004), which for the case of wind directed along the x- or y-axis is

$$P(\vec{s}) = \frac{1}{2\pi\sqrt{mss_x mss_y (1 - b_{x,y}^2)}}$$
$$\exp\left[-\frac{1}{2(1-b_{x,y}^2)}\left(\frac{s_x^2}{mss_x} - 2b_{x,y}\frac{s_x s_y}{\sqrt{mss_x mss_y}} + \frac{s_y^2}{mss_y}\right)\right], \quad \textbf{(6.2)}$$

where mss_x and mss_y are MSSs of the sea surface for two orthogonal components, one along the wind direction and another across it; $b_{x,y}$ is the correlation coefficient between two slope components. Upon substitution of Equation 6.2 into Equation 6.1, we obtain an algebraic expression that connects the MSS components with the NBRCS, σ_0:

$$\sigma_0(\vec{q}) = \frac{|\mathfrak{R}|^2 (q/q_z)^4}{2\sqrt{mss_x mss_y (1 - b_{x,y}^2)}}$$
$$\exp\left[-\frac{1}{2q_z^2(1-b_{x,y}^2)}\left(\frac{q_x^2}{mss_x} - \frac{2b_{x,y}q_x q_y}{\sqrt{mss_x mss_y}} + \frac{q_y^2}{mss_y}\right)\right]. \quad \textbf{(6.3)}$$

6.2.2. Connection Between the MSS and the Surface Elevation Spectrum

By definition, the MSS components are introduced as

$$mss_{x,y} = \left\langle s_{x,y}^2 \right\rangle = \iint\limits_{\kappa < \kappa_*} \kappa_{x,y}^2 \Psi(\vec{\kappa})d^2\kappa; \quad \textbf{(6.4)}$$

$$b_{x,y} = \left\langle s_x s_y \right\rangle / \sqrt{mss_x mss_y}; \quad \textbf{(6.5)}$$

$$\left\langle s_x s_y \right\rangle = \iint\limits_{\kappa < \kappa_*} \kappa_x \kappa_y \Psi(\vec{\kappa})d^2\kappa. \quad \textbf{(6.6)}$$

Therefore, two MSS components, mss_x and mss_y, are determined solely by the wave-number integral from the ocean elevation spectrum $\Psi(\vec{\kappa})$ times $\kappa_{x,y}^2$. This product is called a slope spectral density. The limit of integration at high wavenumbers is $\kappa_* = k\cos\theta / 3$, which plays the role of a low-pass filter, which is related to the EM wavelength $\lambda = 2\pi/k$ and the angle of incidence θ. There are some indications that the actual PDF of slopes does not exactly follow a Gaussian shape at their tails (Cardellach & Ruis, 2008). In terms of the glistening zone, it implies that this departure affects the periphery of the zone. However, for the conditions of the CYGNSS mission, most of the contribution to the signal comes from the peak area of the PDF of slopes. Frequently, when it is not possible to measure each of two orthogonal components, the total MSS is used:

$$mss = \left\langle s^2 \right\rangle = \left\langle s_x^2 \right\rangle + \left\langle s_y^2 \right\rangle = mss_x + mss_y = \iint\limits_{\kappa < \kappa_*} \kappa^2 \Psi(\vec{\kappa})d^2\kappa. \quad \textbf{(6.7a)}$$

An alternative definition of the total MSS (Soulat, 2004), which better fits the expression in Equation 8.3 for σ_0, can be used here:

$$mss = 2\sqrt{mss_x mss_y}. \quad \textbf{(6.7b)}$$

When the wave spectrum is directionally isotropic, the definitions in Equations 6.7a and 6.7b are equivalent.

In the case of global winds, the model spectrum $\Psi(\vec{\kappa})$ proposed by Elfouhaily et al. (1997) is widely used. An example of the Elfouhaily et al. (1997) slope spectrum taken along the wind direction is shown in Figure 6.1.

This empirical model describes deep-water waves driven by winds of constant direction under diverse wave-age (often called "fetch") conditions. This model has two input parameters, the local wind speed at 10 m height, U_{10}, and the wave age, or fetch. It was designed to agree with in situ observations of the first sun-glint-derived wave slope measurements of Cox and Munk (1954), performed several decades ago.
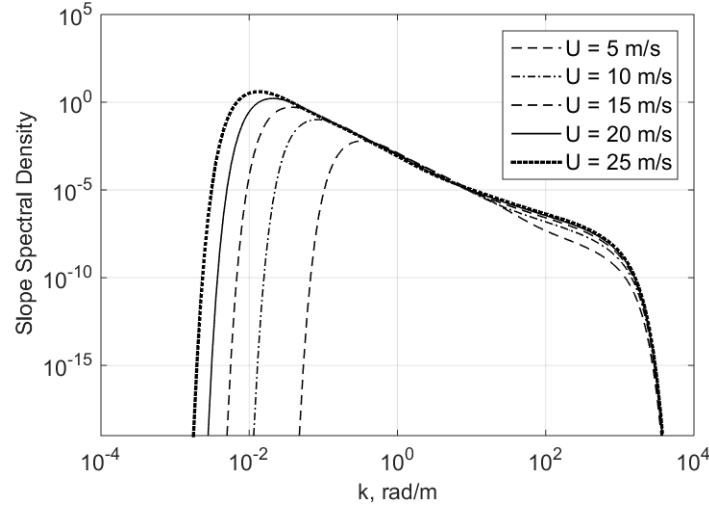
Figure 6.1. Ocean surface slope spectrum from Elfouhaily et al. (1997) taken along the wind direction.

For conditions when the surface can be described by the Elfouhaily et al. (1997) spectrum (assuming that the fetch is known), it is possible to retrieve the wind U_{10} from the CYGNSS measurement. At the same time, the retrieval of the total MSS is available as a by-product of the wind retrieval. In some cases, the total MSS retrieval may be the only product that has a high level of validity. This may occur when sea roughness cannot be described solely by the local wind (e.g., in the presence of unknown swell, currents, surfactants), so the surface cannot be described by the Elfouhaily et al. (1997) spectrum or its proxy. For example, if swell is present that does not interact with the waves driven by the local wind, then the total spectrum of the wave will be

$$\Psi_{tot}\left(\vec{\kappa}\right) = \Psi_{wind}\left(\vec{\kappa}\right) + \Psi_{swell}\left(\vec{\kappa}\right). \tag{6.8}$$

And the total MSS component will obey the equation

$$mss_{x,y,tot} = mss_{x,y,wind} + mss_{x,y,swell}. \tag{6.9}$$

As was pointed out above, the MSS that determines the BRCS through the PDF of slopes is not a full-wave slope. Even though the sea surface contains wave harmonic components both longer and shorter than the L-band electromagnetic waves, the short waves can be disregarded in a process of forward quasi-specular reflection under the strongly diffuse GO approximation. Therefore, the full surface spectrum should be cut off at the high end of wave numbers. There are various choices of cutoff wave number κ_* that are discussed in the appendix: Ocean Surface Bistatic Scattering Forward Model.

6.3. Retrieval Algorithm Overview

6.3.1. Theoretical Description

Since the regime of CYGNSS measurements does not allow one to distinguish between the along- and cross-wind directions, one can assume that $mss_y = mss_x = mss\,/\,2$ and $b_{x,y}^2 = 0$. Then the expression for the bistatic radar cross section from Equation 6.3 simplifies to

$$\sigma_0\left(\vec{q}\right) = \frac{\left|\Re\right|^2}{mss}\left(\frac{q}{q_z}\right)^4 \exp\left(-\frac{q_\perp^2}{q_z^2 mss}\right). \tag{6.10}$$

Factors containing components of the scattering vector $\vec{q}$ can be expressed through local (at the point of reflection) incidence and scattering angles, θ_1 and θ_2 (see Figure 6.2).

$$\left(\frac{q}{q_z}\right)^2 = \frac{2\left(1 - \sin\theta_1 \sin\theta_2 \cos\varphi + \cos\theta_1 \cos\theta_2\right)}{\left(\cos\theta_1 + \cos\theta_2\right)^2}, \tag{6.11}$$
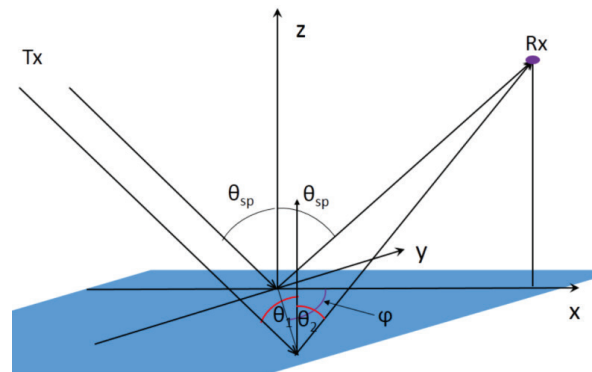
Figure 6.2. Geometry of quasi-specular scattering.

$$\frac{q_\perp^2}{q_z^2} = \frac{\left(\sin\theta_2\cos\varphi - \sin\theta_1\right)^2 + \sin^2\theta_2\sin^2\varphi}{\left(\cos\theta_1 + \cos\theta_2\right)^2}. \quad \textbf{(6.12)}$$

In principle, MSS can be retrieved from Equation 8.10 for any combination of incident and scattering angles θ_1 and θ_2 (and azimuthal scattering angle φ) by solving a transcendental equation:

$$\log mss - \frac{q_\perp^2}{q_z^2 mss} - \log\left[\left|\mathfrak{R}\right|^2\left(\frac{q}{q_z}\right)^4\right] + \log\sigma_0\left(\vec{q}\right) = 0. \quad \textbf{(6.13)}$$

However, it would be more beneficial to use $\sigma_0\left(\theta\right)$ in the specular direction, where $\theta_1 = \theta_2 = \theta$ and $\varphi = 0$. Then Equation 6.10 simplifies to

$$\sigma_0\left(\theta\right) = \frac{\left|\mathfrak{R}\left(\theta\right)\right|^2}{mss}. \quad \textbf{(6.14)}$$

The Fresnel reflection coefficient of the ocean surface, $\mathfrak{R}$, is evaluated in the nominal specular direction described by the incidence angle θ.

6.3.2. Baseline Algorithm

In Chapter 5, Equation 5.20 was obtained, which expresses NBRCS σ_0 through available calibrated measured power values from the L1A calibration described elsewhere and parameters of the system. This equation can be rewritten here as

$$\sigma_0 = \alpha\overline{P}_{\hat{\tau},\hat{f}}^{Sig}, \quad \textbf{(6.15)}$$

where α is a coefficient that depends on various geometric, transmitter, and receiver parameters:

$$\alpha = \frac{\left(4\pi\right)^3 R_T^2 R_R^2 L_{atm}^1 L_{atm}^2}{P_T T_i^2 \lambda^2 G_T G_R \chi_{\hat{\tau},\hat{f}}}, \quad \textbf{(6.16)}$$

where

1. $\overline{P}_{\hat{\tau},\hat{f}}^{Sig}$ is the calibrated L1A DDM, as a function of delay and frequency;
2. R_T is the GPS transmitter to SP path length, calculated using the International GNSS Service (IGS) positions of the GPS satellites and estimated SP location;
3. R_R is the specular point (SP) to CYGNSS satellite path length, calculated using the positions of the CYGNSS spacecraft and estimated SP location;
4. L_{atm}^1 and L_{atm}^2 are the atmospheric losses as the signal travels from the GPS satellite to the surface and from the

surface to the receiver, respectively (These terms will be estimated on the ground using a propagation model at the GPS signal transmit frequency.);

5. P_T is the GPS transmit signal power and is estimated using the absolute power of the direct signal;
6. T_i is the coherent time integration;
7. λ is the signal wavelength;
8. G_T is the GPS antenna gain for the reflection geometry (This will be calculated using a model of the GPS antenna gain pattern generated using power measurements from the direct signal. The above two terms will be estimated together as a single combined quantity.);
9. G_R is the CYGNSS nadir antenna gain, which is a function of reflection geometry and spacecraft orientation (This term will be estimated using a prelaunch calibration of the antenna pattern and the reflection viewing geometry.); and
10. $\chi_{\hat{\tau},\hat{f}}$ is the effective scattering area for the delay-Doppler (DD) bin at $\hat{\tau},\hat{f}$. This area will be estimated based on the delay-Doppler surface geometry calculated using modules within the CYGNSS E2ES.

Details for the calculation of each of the above terms are described in Chapter 5.

For the CYGNSS geometry and system parameters, the coefficient $\alpha \approx 10$ at $\theta = 35°$ for the DDM bin with $\hat{\tau} = 0$, $\hat{f} = 0$, which corresponds to a nominal SP on the surface. The MSS estimation algorithm is found by solving for MSS in Equation 6.14, or

$$mss = \frac{\left|\mathfrak{R}\left(\theta\right)\right|^2}{\sigma_0\left(\theta\right)}, \quad \textbf{(6.17)}$$

where $\mathfrak{R}$ is the Fresnel reflection coefficient evaluated at the incidence angle of the SP for a given complex dielectric constant of the ocean surface ε. Thus, the MSS estimation error is determined by uncertainties of several parameters entering Equation 6.17. Two leading parameters are NBRCS, σ_0, provided by the Level 1 DDM calibration algorithm (Chapter 5), and the absolute value squared of the Fresnel reflection coefficient $\left|\mathfrak{R}\left(\theta\right)\right|^2$. In turn, the Fresnel reflection coefficient is determined by the complex dielectric constant, ε, of the ocean surface and the incidence angle at the SP. Estimation of ε requires knowledge of the sea surface temperature and salinity. Related uncertainties will be analyzed in Section 6.4.

6.4. Performance Characterization

6.4.1. Accuracy

If we put aside the issue of geophysical variability of the MSS of ocean waves, the accuracy of the MSS retrieval based on Equation 6.17 is determined by the uncertainty in two factors entering Equation 6.17: NBRCS σ_0 taken in the specular direction and the absolute value squared of the Fresnel reflection coefficient of the flat ocean surface, $\left|\mathfrak{R}(\theta)\right|^2$, also taken in the specular direction. The analysis of the σ_0 uncertainty is done in Chapter 5.

Let us first start with an estimation of the accuracy of the reflection coefficient. In the case of LHCP, the expression for the complex Fresnel reflection coefficient $\mathfrak{R}$ at the interface between air and a medium (in our case, sea water) with a complex dielectric permittivity ε is

$$\mathfrak{R}(\theta) = \frac{1}{2}\left[\frac{\varepsilon\cos\theta - \sqrt{\varepsilon - \sin^2\theta}}{\varepsilon\cos\theta + \sqrt{\varepsilon - \sin^2\theta}} - \frac{\cos\theta - \sqrt{\varepsilon - \sin^2\theta}}{\cos\theta + \sqrt{\varepsilon - \sin^2\theta}}\right], \quad \textbf{(6.18)}$$

where θ is the local incidence (or reflection) angle. We performed calculations of $\left|\mathfrak{R}(\theta)\right|^2$ for a range of incidence angles θ and various values of water temperature and salinity, which are the two most important driving parameters of the complex dielectric permittivity ε of sea water. The latter can be calculated using either the Klein and Swift model (Klein & Swift, 1977; Ulaby et al., 1986) or the Meissner and Wentz model (Meissner & Wentz, 2004). Those models for sea water permittivity rely on L-band measurements. They are close enough to each other at those frequencies, and no other models have been shown to be more reliable (Ellison et al., 1998). The analytical expressions for ε as a function of

radio frequency, water temperature T, and salinity S for the Klein and Swift model are given in Appendix 6A. The radio frequency of the received signals for CYGNSS is known with high accuracy. It is the L1 band frequency, which is equal to 1.57542 GHz. Figures 6.3a and 6.3b demonstrate the dependence of both the real and imaginary parts of the dielectric permittivity of ocean water (ε' and ε'', respectively) on water temperature and salinity.

Therefore, the retrieval of MSS depends on sea surface temperature (SST) and sea surface salinity (SSS). Analyses reveal that the changes in SSS and SST over time and space are small enough that using a single value of $\left|\mathfrak{R}(\theta)\right|^2$ maintains an acceptable error tolerance (Figure 6.4). Therefore, LUTs for monthly and zonal averaged Fresnel coefficients, at a 1° × 1° resolution, are used for the derivation of MSS (see Figure 6.5).

6.4.2. Error Analysis of the Level 2 MSS Retrieval Algorithm

The creation of the L2 MSS product is contingent on the availability of input observational data (from CYGNSS and ancillary data sources) and accurate estimates of their errors. The accuracy of the L2 MSS product is dependent on the accuracy of the NBRCS σ_0 retrieval, the accuracy of the scattering geometry determination (incidence angle), and the accuracy of the Fresnel reflection coefficient estimates. It should be remembered that this algorithm is built on two basic assumptions: validity of the GO limit of the KA and validity of the Gaussian PDF of slopes. At very rough surface conditions, such as in the hurricane wind maximum areas, both of these assumptions may be violated. These scenarios would require an independent calibration and
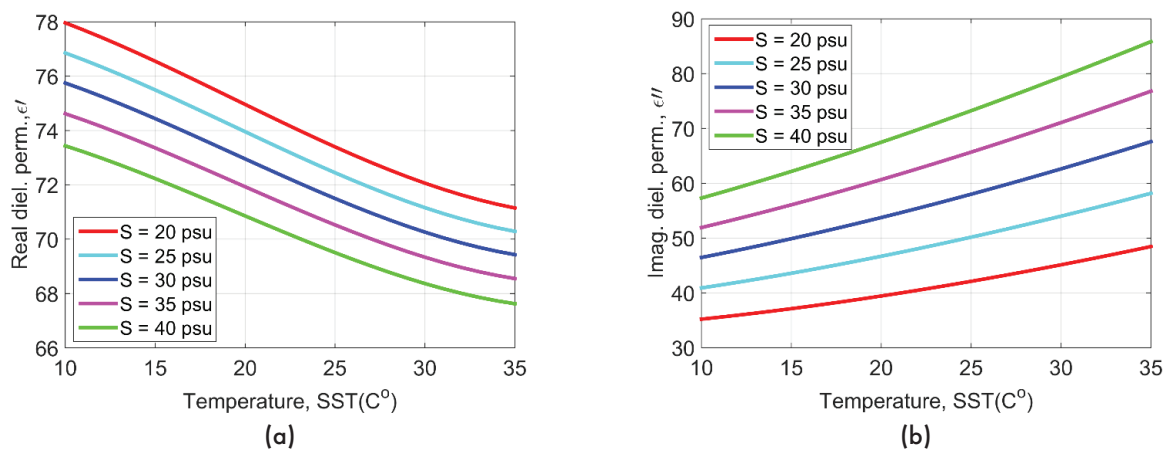
Figure 6.3. Dependence of both real and imaginary parts of dielectric permittivity of ocean water (ε' and ε'', respectively) on water temperature and salinity.
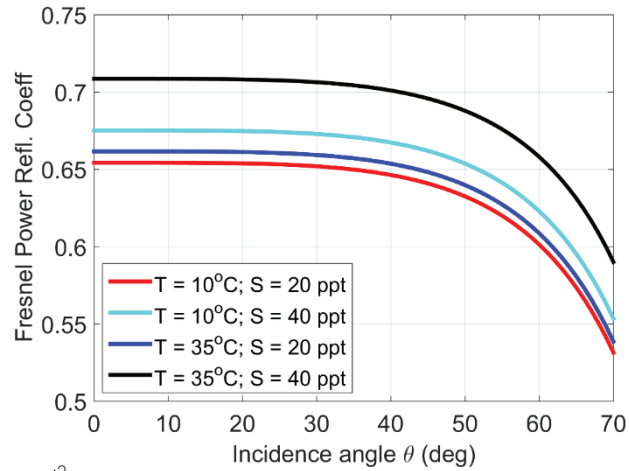
Figure 6.4. Dependence of $\left|\Re(\theta)\right|^2$ on incidence angle for a wide range of temperatures and salinities calculated using the Klein and Swift model (Klein & Swift, 1977; Ulaby et al., 1986).

(a)

(b)
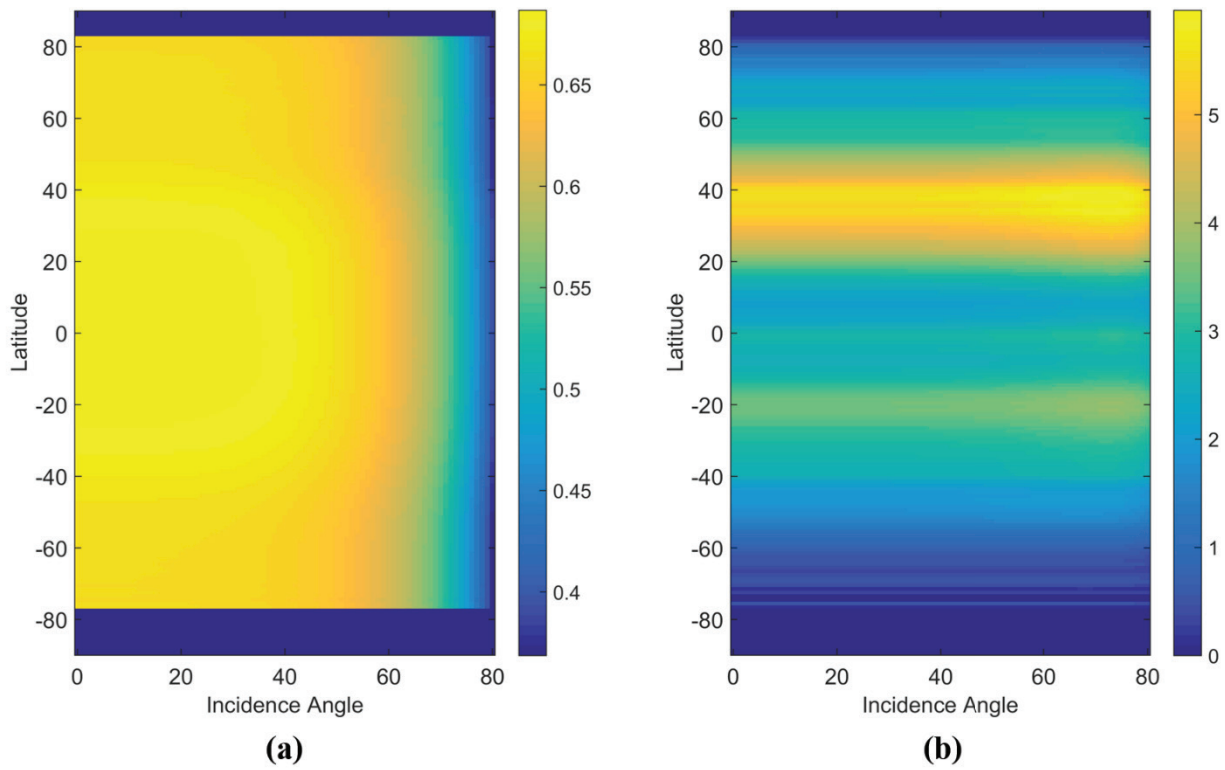
Figure 6.5. (a) Average (zonal and seasonal) Fresnel reflection coefficient $\left|\Re(\theta)\right|^2$; (b) standard deviation (zonal and seasonal) of $\left|\Re(\theta)\right|^2$.

validation of the MSS by using colocated and simultaneous in situ measurements of the MSS. In some circumstances, this may be impractical.

The expression for generating the L2 MSS data product is given by Equation 6.17. The equation is repeated below with the reflection coefficient from Equation 6.18:

$$mss = \frac{\left|\Re(\theta)\right|^2}{\sigma_0(\theta)}. \tag{6.19}$$

Each uncertainty in the L2 MSS retrieval algorithm will be considered as an independent uncorrelated error source. The total error in the L2 MSS retrieval is the root sum square (RSS) of individual errors contributed by the independent variable of Equation 6.19. For relative MSS error, we have

$$\frac{\Delta mss}{mss} = \left[\sum_{i=1}^{4} E^2(p_i)\right]^{1/2}, \tag{6.20}$$

where the error variables are $p_1 = \sigma_0(\theta)$, $p_2 = \theta$, $p_3 = T$, $p_4 = S$. The individual errors $E(p_i)$ can be expressed via partial derivatives as

$$E(p_i) = \frac{1}{mss}\left|\frac{\partial mss}{\partial p_i}\right|\Delta p_i. \tag{6.21}$$

One can specify the error for each of these variables:

$$E(\sigma_0) = \frac{\left|\Re\right|^2}{\sigma_0}\left|\frac{\partial mss}{\partial \sigma_0}\right|\Delta\sigma_0 = \frac{\Delta\sigma_0}{\sigma_0}, \tag{6.22}$$

$$E(\theta) = \frac{\left|\Re\right|^2}{\sigma_0}\left|\frac{\partial mss}{\partial \theta}\right|\Delta\theta = \frac{1}{\left|\Re\right|^2}\left|\frac{\partial\left|\Re\right|^2}{\partial\theta}\right|\Delta\theta, \tag{6.23}$$

$$E(T) = \frac{\left|\Re\right|^2}{\sigma_0}\left|\frac{\partial mss}{\partial T}\right|\Delta T = \frac{1}{\left|\Re\right|^2}\left|\frac{\partial\left|\Re\right|^2}{\partial T}\right|\Delta T, \tag{6.24}$$

$$E(S) = \frac{\left|\Re\right|^2}{\sigma_0}\left|\frac{\partial mss}{\partial S}\right|\Delta S = \frac{1}{\left|\Re\right|^2}\left|\frac{\partial\left|\Re\right|^2}{\partial S}\right|\Delta S. \tag{6.25}$$

To estimate $E(\sigma_0)$, empirically derived values for σ_0 and $\Delta\sigma_0$, based on tests under different wind speeds, are employed. The error estimates for σ_0 also include uncertainties related to the antenna gain model, the low noise amplifier (LNA) model, the GPS transmitter model, and so on. For details, see Chapter 5 and Gleason et al. (2018). Therefore, we use σ_0 and $\Delta\sigma_0$ estimates for 10 m/s reference wind:

σ_0 = 15 dB (31.6) and $\Delta\sigma_0$ = 0.39 dB (1.09) for U_{10} = 10 m/s^{-1}.

Partial derivatives of $\left|\Re\right|^2$ in Equations 6.23–6.25 are computed numerically because the analytical derivation is not practical due to a complicated dependence of $\left|\Re\right|^2$ over the arguments θ, T, and S. Examples of such computations are shown in Figures 6.6–6.8.

Figure 6.6a represents $\frac{1}{\left|\Re\right|^2}\left|\frac{\partial\left|\Re\right|^2}{\partial T}\right|$ as a function incidence angle θ for a range of sea surface temperatures T between 10°C and 35°C and for a fixed sea surface salinity S = 40 psu. Figure 6.6b shows $\frac{1}{\left|\Re\right|^2}\left|\frac{\partial\left|\Re\right|^2}{\partial S}\right|$ as a function
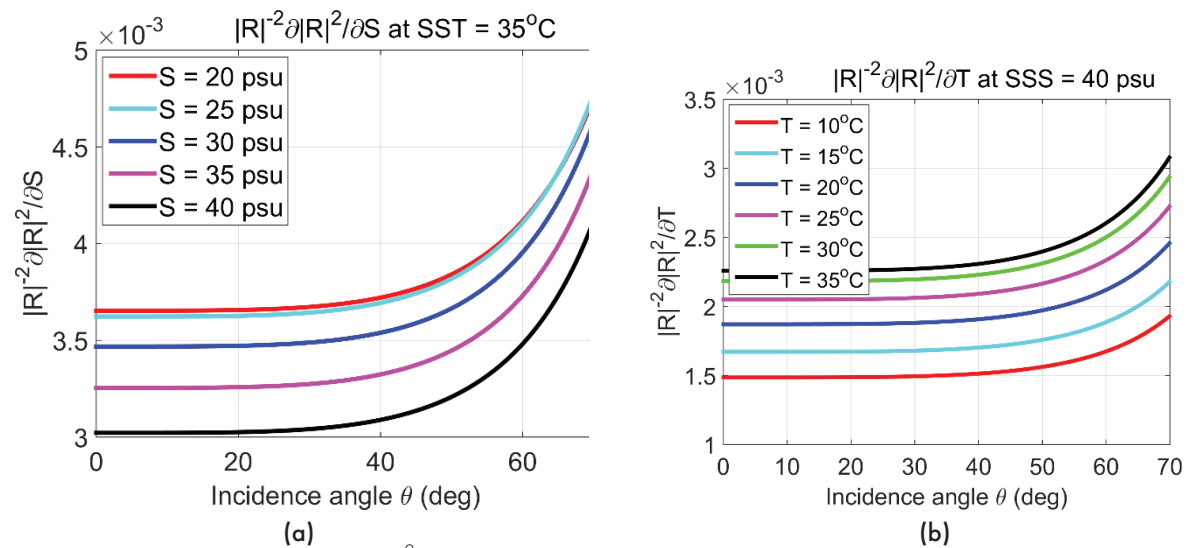
Figure 6.6. Relative partial derivatives of $\left|\Re\right|^2$ over temperature and salinity as a function of incidence angle.
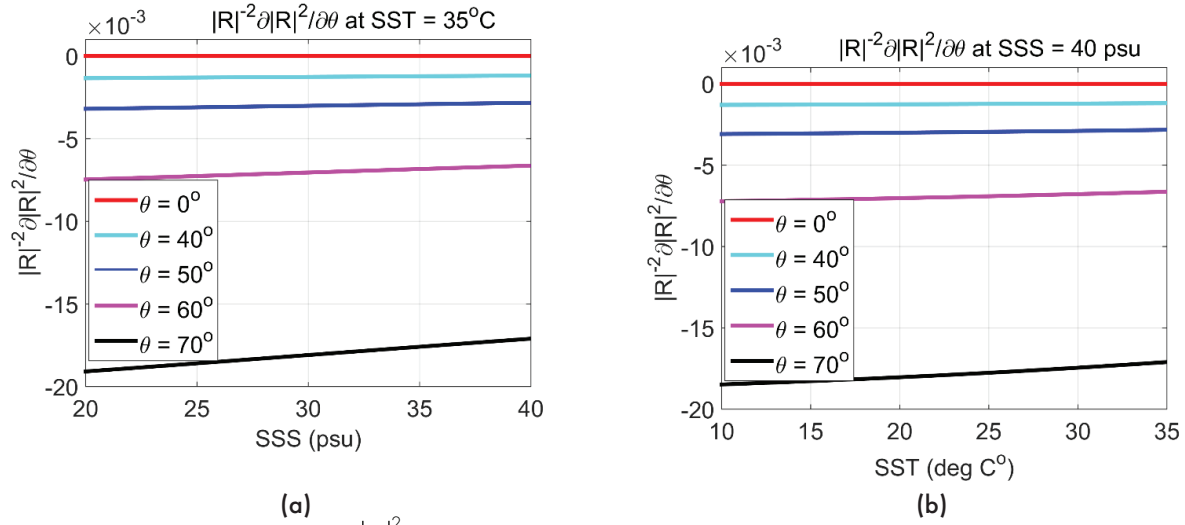
Figure 6.7. Relative partial derivative of $\left|\mathfrak{R}\right|^2$ over incidence angle as a function of temperature and salinity.
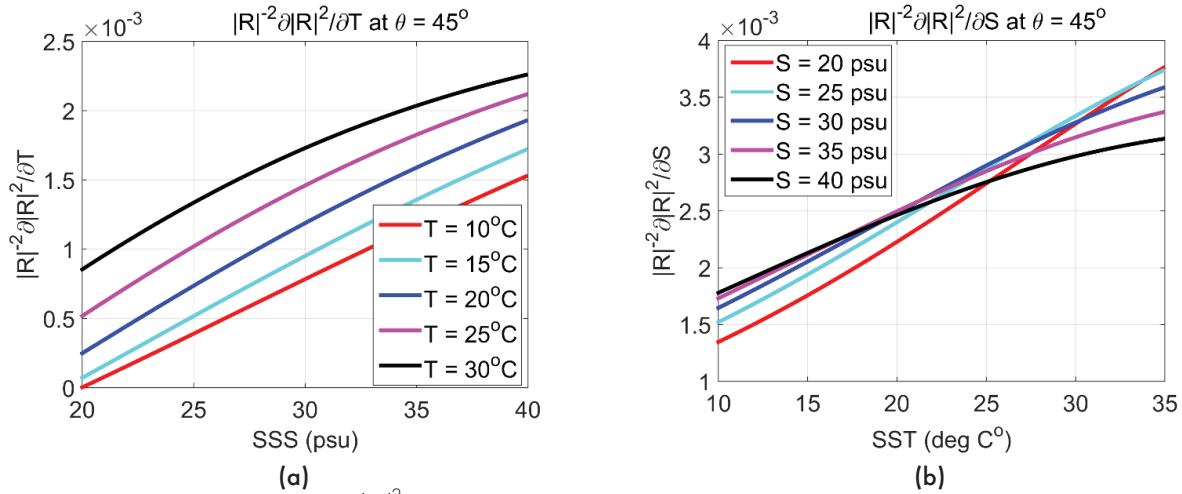
Figure 6.8. Relative partial derivative of $\left|\mathfrak{R}\right|^2$ over temperature and salinity.

incidence angle θ for a range of sea surface salinities S between 10 and 40 psu and for a fixed sea surface temperature $T = 35°C$. Analogously, Figures 6.7a and 6.7b represent, respectively, the dependence of $\dfrac{1}{\left|\mathfrak{R}\right|^2}\left|\dfrac{\partial\left|\mathfrak{R}\right|^2}{\partial\theta}\right|$ on temperature and salinity at fixed salinity and temperature for a range of incidence angles θ. And finally, Figures 6.8a and 6.8b show cuts of functions $\dfrac{1}{\left|\mathfrak{R}\right|^2}\left|\dfrac{\partial\left|\mathfrak{R}\right|^2}{\partial S}\right|$ and $\dfrac{1}{\left|\mathfrak{R}\right|^2}\left|\dfrac{\partial\left|\mathfrak{R}\right|^2}{\partial T}\right|$ along parameters such as temperature and salinity, keeping other parameters constant. All these plots give an idea of the relative magnitudes of values of quantities entering

Equations 6.22–6.25. To obtain values of respective errors, $E(\sigma_0)$, $E(\theta)$, $E(T)$, and $E(S)$, one needs to input errors for $\Delta\sigma_0$, $\Delta\theta$, ΔT, and ΔS. In the following tables, we present results of calculations of the relative MSS error, $\dfrac{\Delta mss}{mss}$, based on Equations 6.20–6.25 for some limiting values of the parameters involved.

For Table 6.1, we used some reasonable values for input errors shown in the header of the table. One can see that the relative MSS error for $U_{10} = 10$ m/s^{-1} and for the range of incidence angles between 0 and 70° lies within 3.7%. The maximum relative MSS errors increase to 4.3% if a more conservative estimate is taken for the input errors shown in the header of Table 6.2. The following conclusions can be

Table 6.1. Relative MSS Error (U_{10} = 10 m/s^{-1}, $\Delta\sigma_0$ = 1.09, $\Delta\theta$ = 0.5°, ΔT = 0.5°C, ΔS = 2 psu)

Parameters	θ = 0°	θ = 35°	θ = 70°
SSS = 20 psu, SST = 10°C	$3.47 \cdot 10^{-2}$	$3.47 \cdot 10^{-2}$	$3.61 \cdot 10^{-2}$
SSS = 40 psu, SST = 10°C	$3.48 \cdot 10^{-2}$	$3.48 \cdot 10^{-2}$	$3.61 \cdot 10^{-2}$
SSS = 20 psu, SST = 35°C	$3.54 \cdot 10^{-2}$	$3.54 \cdot 10^{-2}$	$3.71 \cdot 10^{-2}$
SSS = 40 psu, SST = 35°C	$3.51 \cdot 10^{-2}$	$3.52 \cdot 10^{-2}$	$3.66 \cdot 10^{-2}$

Table 6.2. Relative MSS Error (U_{10} = 10 m/s^{-1}, $\Delta\sigma_0$ = 1.09, $\Delta\theta$ = 1°, ΔT = 1°C, ΔS = 5 psu)

Parameters	θ = 0°	θ = 35°	θ = 70°
SSS = 20 psu, SST = 10°C	$3.52 \cdot 10^{-2}$	$3.52 \cdot 10^{-2}$	$3.68 \cdot 10^{-2}$
SSS = 40 psu, SST = 10°C	$3.57 \cdot 10^{-2}$	$3.57 \cdot 10^{-2}$	$3.76 \cdot 10^{-2}$
SSS = 20 psu, SST = 35°C	$3.91 \cdot 10^{-2}$	$3.92 \cdot 10^{-2}$	$4.31 \cdot 10^{-2}$
SSS = 40 psu, SST = 35°C	$3.78 \cdot 10^{-2}$	$3.79 \cdot 10^{-2}$	$4.13 \cdot 10^{-2}$

drawn from these numbers. For winds near 10 m/s^{-1}, the MSS error is mostly determined by the input SST and SSS errors.

6.4.3. Overall Uncertainty

Above we considered errors in determining the MSS due to thermal and speckle noise assuming that the MSS remains constant within the scene. This is only part of the uncertainty in the MSS retrieval. There are other factors that can add to the overall uncertainty.

There are factors related to the variability of the transmit signal and of the parameters of the receiving system. All of them can be boiled down to an uncertainty in the coefficient α introduced above in Equations 6.15–6.16. The coefficient is needed to calculate MSS from σ_0 measured in the specular direction. The uncertainty in the physical and technical parameters composing it can be eliminated, or significantly reduced, by calibration procedures or by ancillary measurements. These procedures are described in Chapter 5.

First, the most important uncertainty is in the spatial variability of the MSS field, whereas for our estimations, we assume a stable, average wave spectrum. Even given a homogenous wind field, which is an input for the MSS, the variations in the wave elevation spectrum within the spatially limited footprint sampled over a limited time interval can be significant simply due to the statistical nature of the surface wave phenomenon. Additionally, wave statistics can be affected by limited fetch, swell, currents, surfactants, and bathymetry. If the scales of this spatial variability are smaller than or close to the spatial resolution of the system, this factor can affect the accuracy of the MSS retrieval.

Our retrieval algorithm is based on Equation 6.17, which, in turn, is based on the radar bistatic equation and a strong diffuse scattering regime characterized by very large values of the Rayleigh parameter, R_a >> 1. This regime holds for wind speeds greater than 4–5 m/s, and it is described by the GO limit of the KA and Gaussian PDF of surface slopes (Zavorotny & Voronovich, 2000). When this scattering model becomes inaccurate, it can be augmented by the small slope approximation (SSA; Voronovich & Zavorotny, 2014). For the case of a small Rayleigh parameter, R_a < 1 (and respectively small MSS), which corresponds to low winds U_{10} < 4–5 m/s^{-1}, the scattering mechanism transitions to a weak diffuse scattering (Voronovich & Zavorotny, 2017). For extremely low winds with U_{10} < 2 m/s^{-1}, the weak diffuse scattering decreases further, and the coherent scattering emerges. In this case, a traditional bistatic radar equation needs to be augmented by an additional coherent term. An improved bistatic radar equation that accounts for the coherent scattering and other previously omitted effects is developed by Voronovich and Zavorotny (2018). Since the NBRCS σ_0 at the weak diffuse and coherent scattering regime no longer depends on the MSS, the relationship in Equation 6.13 does not hold for winds U_{10} < 4–5 m/s^{-1}, and therefore the MSS retrieval cannot be achieved for this range of winds using the algorithm described above.

The case of very steep and breaking waves can also be challenging for the MSS retrieval based on either GO or the SSA, but in this case, the notion of the MSS itself becomes questionable.

6.5. Use of Measured and Modeled MSS for Improvement of L2 Wind Speed Retrievals

Recently, a modification to the L2 wind retrieval algorithm was proposed (Wang et al., 2018) that aims to exclude the effect of any nonlocally generated swell and/or limited fetch effects from the retrieved MSS and its associated normalized radar cross section. The approach is based on a subtraction from the CYGNSS-observed MSS through the use of an MSS correction that is intended to compensate for non–fully developed sea conditions. The MSS correction is obtained from an ancillary numerical wave model forced by model winds. Note that this process must be performed carefully in order to reduce the possibility of the correction introducing a direct dependence on the model winds used in forcing the wave model. Two methods of computing the MSS correction (one called the "excess MSS" and a second called the "MSS anomaly") have been developed. Below both approaches are briefly described.

6.5.1. Background of Sea State Modeling

In the current L2 retrieval algorithm, the wind speed is retrieved using empirical geophysical model functions (GMFs) based on matchups with the ground truth wind speed. The baseline retrieval algorithm divides the sea state into two different types: a "fully developed" type and a "limited fetch" type. The fully developed sea has a sea state independent of the wind forcing extent (fetch) and/or duration, while the limited fetch sea is typical for situations when the wind is not constant in speed and direction, such as in hurricanes. However, this division oversimplifies the large variety of sea state behaviors

that may occur. It also does not account for the possible presence of swell generated by distant wind systems (Ruf & Balasubramaniam, 2019). Sea state conditions, including the presence of external swell and the degree of wave development, complicate the ocean surface wave spectrum and increase uncertainty in wind speed retrieval.

An attempt to tie the measured NBRCS (or MSS) to the wind speed alone shows significant residual errors (scatter), which have also been observed in TechDemoSat-1 (TDS-1) retrievals (Foti et al., 2015). The error in wind speeds retrieved from the observations is strongly correlated with the significant wave height (SWH) of the ocean (Clarizia and Ruf, 2017). A similar scatter is observed in the first wind speed and MSS retrievals based on the CYGNSS data. These results show that there is a necessity to consider the sea state's influence on the MSS, especially the nonlocal swell contribution to the surface roughness. Also, understanding the L-band signal response to both waves and wind will be helpful to provide higher-accuracy L2 data products for both wind speed and MSS.

6.5.2. Excess MSS Approach

The "excess MSS" is defined as the difference between the MSS calculated using the IFREMER (Institut Francais de Recherche pour l'Exploitation de la Mer) implementation of the WAVE-WATCH III (WW3) numerical model (WAVEWATCH III Development Group, 2016) and the MSS calculated using the Elfouhaily et al. (1997) spectral model for fully developed seas at the local forcing wind speed used in the wave model. The excess MSS then should represent the difference between the WW3-obtained MSS (which includes nonlocal swell, fetch effects, etc.) and that which would occur if the MSS were the result of only the local wind. By subtracting
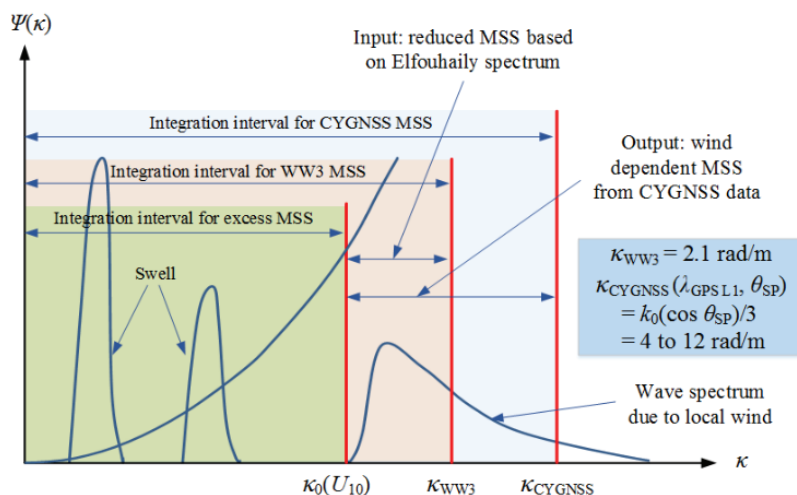
Figure 6.9. Physics of extracting wind-dependent MSS.

the excess MSS from the CYGNSS measured MSS, the resulting MSS should have nonlocal wave and limited fetch effects removed and when converted back into an NBRCS should yield an improved wind speed estimate.

Figure 6.9 illustrates the concept of the method for a situation in which nonlocal swell contributions occur at length scales greater than those associated with local wind-generated waves (although the method is not limited to this case). The IFREMER WW3 numerical model generates an MSS from its computed wave spectrum by integrating over the spectrum up to the WW3 cutoff wavenumber of 2.1 rad/m; the resulting MSS includes both local wind and swell contributions. Use of the local wind speed in the Elfouhaily et al. model and computing the resulting MSS up to the same 2.1 rad/m cutoff wavenumber should estimate the local wind contribution to the MSS. The difference between the WW3 and Elfouhaily et al. MSS values is then the "excess MSS" associated with nonlocal waves. Note that the 2.1 rad/m WW3 cutoff wavenumber is below the 4 to 12 rad/m range (depending on incidence angle) below which ocean spectrum contributions are expected to contribute to the CYGNSS-observed MSS. However, this does not impact the contribution of the excess MSS, since the WW3 and Elfouhaily et al. results are obtained for the same cutoff wavenumber.

Mathematically, the WW3 model takes input wind fields U_{10} and produces a wave spectrum $\Psi_{WW}(\vec{\kappa})$ and associated MSS $\tilde{s}^2_{WW}(\vec{\kappa})$ (up to the cutoff wavenumber κ_{cut} of the WW3 model runs). Using the Elfouhaily et al. model for a fully

developed sea, we have a one-to-one mapping between the wind speed U_{10} and MSS $\tilde{s}^2_{FD}(\vec{\kappa})$ under the assumed Elfouhaily et al. spectrum $\Psi_{FD}(\vec{\kappa})$. The excess MSS is then

$$\Delta\tilde{s}^2 = \tilde{s}^2_{WW}(\vec{\kappa}) - \tilde{s}^2_{FD}(\vec{\kappa}), \qquad (\textbf{6.26})$$

which is the WW3 model prediction of the influence of all sea states—for example, wave age, limited fetch, nonlocal swell, and so on. Note that the excess MSS should have a reduced dependence on local wind forcing, since the estimated fully developed MSS (which is directly dependent on the local wind) is removed.

The next step is to compute the wind-dependent MSS by subtracting the excess MSS from the CYGNSS MSS:

$$\tilde{s}^2_{CY} = s^2_{CY} - \Delta\tilde{s}^2. \qquad (\textbf{6.27})$$

The wind speed retrieval is then performed by converting $\tilde{s}^2_{CY}$ back into a corrected NBRCS and applying the GMF. At present, the GMF used is that for the original CYGNSS dataset; future work will consider rederivation of the GMF using the corrected NBRCS values.

To assess the effectiveness of the correction, the retrieved wind speeds of CYGNSS were checked against the corresponding European Centre for Medium-Range Weather Forecasts (ECMWF) wind speeds as the truth for a period of 200 days starting from March 18, 2017. The upper plot of Figure 6.10 shows, for wind speeds higher than 10 m/s, that the wind speed bias (red curve) after correcting for the
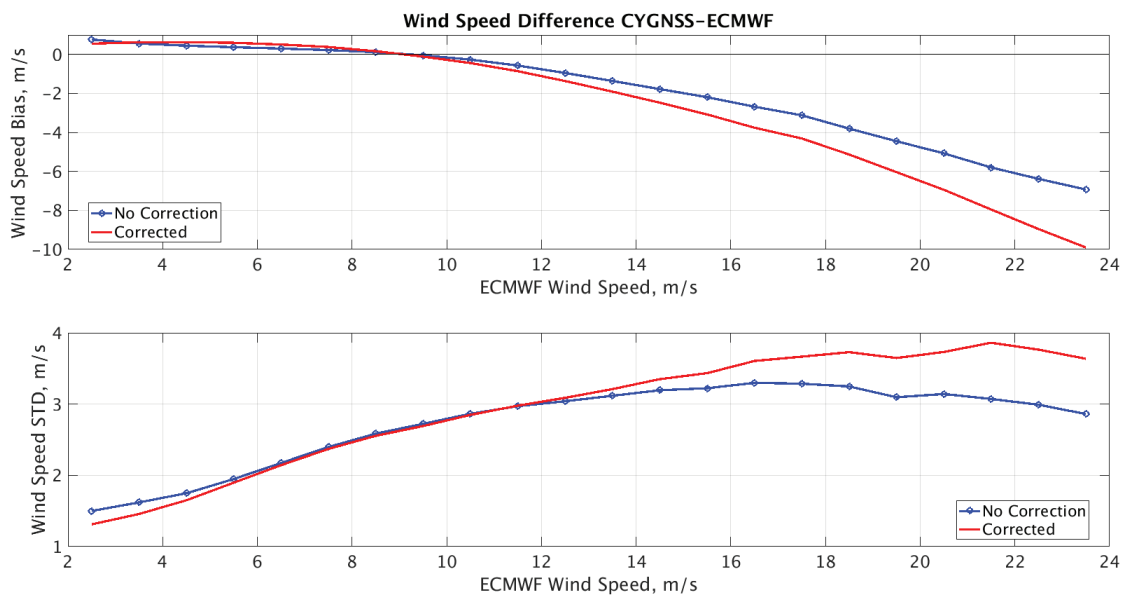
Figure 6.10. Errors of CYGNSS retrieved wind speeds before (blue) and after (red) correcting for the excess MSS.

excess MSS is increased compared to that before the correction (blue curve). The lower plot also shows an increase in the standard deviation of retrieval error (red curve) after the MSS correction is applied for wind speeds higher than 12 m/s. However, a modest improvement in standard deviation with no increased bias is observed for wind speeds less than ~ 7 m/s. These results suggest that the wave model information is most useful at lower wind speeds rather than higher wind speeds.

A more advanced approach would model both the local wind and nonlocal swell spectra for the purpose of a consistency check among the measured MSS, the MSS and SWH modeled with the WW3, and ancillary SWH data; this approach has yet to be implemented.

6.5.3. MSS Anomaly Approach

Analysis of the results in Figure 6.10 suggested that the excess MSS may suffer from the inapplicability of the assumed Elfouhaily et al. model for describing fully developed sea conditions. An alternative approach for estimating the "standard condition" MSS was therefore developed. In this alternative approach, an empirical "standard" MSS was determined by fitting a low-degree polynomial to the WW3 MSS as a function of local wind speed U_{10}. Nonlocal swell or limited fetch effects contributions to the MSS (now called the MSS anomaly) were represented again through a subtraction of the two quantities:

$$\Delta MSSY = MSS_{WW3} - Polynomial\left(U_{10,ECMWF}\right). \qquad \textbf{(6.28)}$$

Figure 6.11 is a scatterplot of WW3 MSS versus the corresponding ECMWF forcing wind speed for CYGNSS measurement samples for 200 days in 2007.

Linear and quadratic fits to the MSS versus U_{10} were examined, and it was found that the linear fit provided improved wind retrieval performance. The upper plot of Figure 6.12 illustrates a reduced bias (red curve) of retrieved wind speeds after correcting for the MSS anomaly for wind speeds higher than 12 m/s. The standard deviation of the retrieval error also does not increase at higher wind speeds (red curve, bottom panel of Figure 6.12) while retaining a similar improved performance at lower wind speeds.

6.6. References

Barrick, D. E. (1968). Relationship between slope probability density function and the physical optics integral in rough surface scattering. *Proceedings of the IEEE, 56*(10), 1728–1729. https://doi.org/10.1109/PROC.1968.6718.

Bass, F. G., & Fuks, I. M. (1979). *Wave scattering from statistically rough surfaces* (Vol. 93). Elmsford, NY: Pergamon.

Cardellach, E., & Rius, A. (2008). A new technique to sense non-Gaussian features of the sea surface from L-band
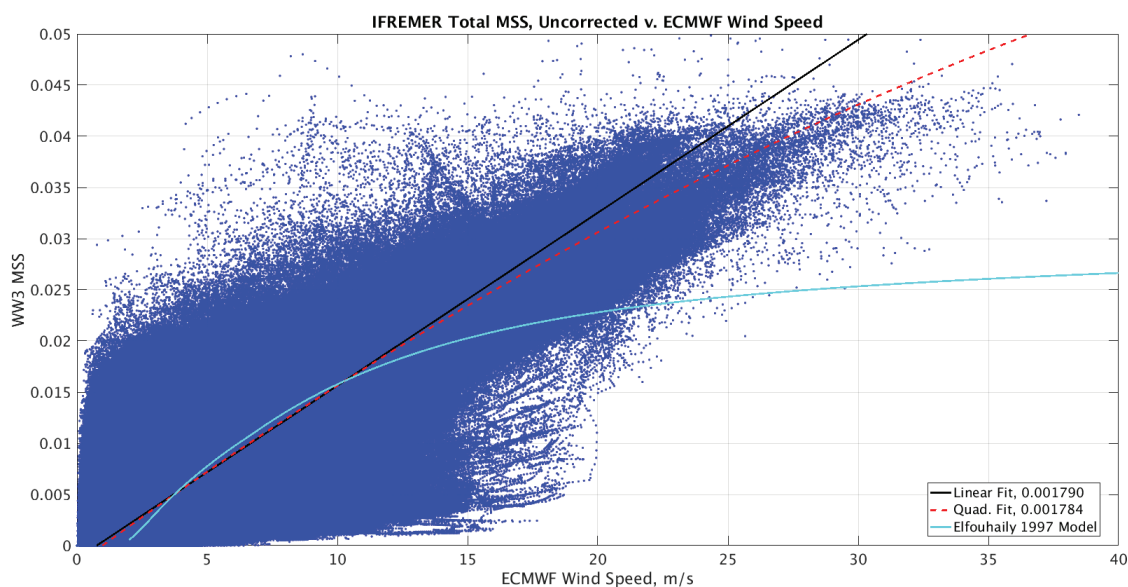
Figure 6.11. A scatterplot (blue dots) of WW3 MSS versus ECMWF wind speeds at the CYGNSS measurement samples. Linear and quadratic fits (black line and red curve) to the data samples and the theoretical model (Elfouhaily et al., 1997) are added.
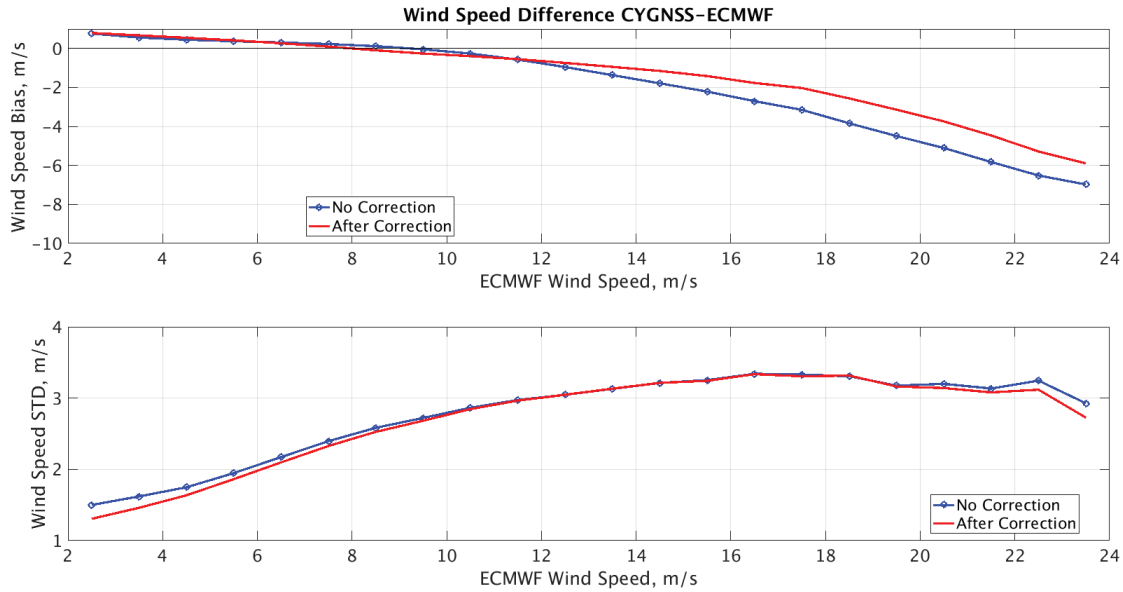
Figure 6.12. Errors of CYGNSS retrieved wind speeds before (blue) and after (red) correcting for the MSS anomaly.

bi-static GNSS reflections. *Remote Sensing of Environment, 112*(6), 2927–2937. https://doi.org/10.1016/j.rse.2008.02.003.

Chapron, B., Kerbaol, V., Vandemark, D., & Elfouhaily, T. (2000). Importance of peakedness in sea surface slope measurements and applications. *Geophysical Research: Oceans (1978–2012), 105*(C7), 17195–17202. https://doi.org/10.1029/2000JC900079.

Clarizia M. P., & Ruf, C. S. (2017). Bayesian wind speed estimation conditioned on significant wave height for GNSS-R ocean observations. *Journal of Atmospheric and Oceanic Technology, 34*(6), 1193–1202. https://doi.org/10.1175/JTECH-D-16-0196.1.

Cox, C., & Munk, W. (1954). Measurement of the roughness of the sea surface from photographs of the sun's glitter. *Journal of the Optical Society of America, 44*(11), 838–850. https://doi.org/10.1364/JOSA.44.000838.

Elfouhaily, T., Chapron, B., Katsaros, K., & Vandemark, D. (1997). A unified directional spectrum for long and short wind-driven waves. *Geophysical Research: Oceans (1978–2012), 102*(C7), 15781–15796. https://doi.org/10.1029/97JC00467.

Elfouhaily, T., Thompson, D. R., & Linstrom, L. (2002). Delay-Doppler analysis of bistatically reflected signals from the ocean surface: Theory and application. *IEEE Transactions on Geoscience and Remote Sensing, 40*(3), 560–573. https://doi.org/10.1109/TGRS.2002.1000316.

Ellison, W., Balana, A., Delbos, G., Lamkaouchi, K., Eymard, L., Guillou, C., & Prigent, C. (1998). New permittivity measurements of seawater. *Radio Science, 33*, 639–648. https://doi.org/10.1029/97RS02223.

Font, J., Lagerloef, G. S., Le Vine, D. M., Camps, A., & Zanifé, O. Z. (2004). The determination of surface salinity with the European SMOS space mission. *IEEE Transactions on Geoscience and Remote Sensing, 42*(10), 2196–2205. https://doi.org/10.1109/TGRS.2004.834649.

Foti, G., Gommenginger, C., Jales P., Unwin, M., Shaw, A., Robertson, C., & Roselló, J. (2015). Spaceborne GNSS reflectometry for ocean winds: First results from the UK TechDemoSat-1 mission. *Geophysical Research Letters, 42*(13), 5435–5441. https://doi.org/10.1002/2015GL064204.

Gleason, S., Ruf, C. S., O'Brien, A. J., & McKague, D. S. (2018). The CYGNSS Level 1 calibration algorithm and error analysis based on on-orbit measurements. *IEEE Journal of Selected Topics in Applied Earth Observations and Remote Sensing, 12*(1), 37–49. https://doi.org/10.1109/JSTARS.2018.2832981.

Guimbard, S., Gourrion, J., Portabella, M., Turiel, A., Gabarró, C., & Font, J. (2012). SMOS semi-empirical ocean forward model adjustment. *IEEE Transactions on Geoscience and Remote Sensing, 50*(5), 1676–1687. https://doi.org/10.1109/TGRS.2012.2188410.

Jähne, B., Münnich, K. O., Bösinger, R., Dutzi, A., Huber, W., & Libner, P. (1987). On the parameters influencing air-water gas exchange. *Journal of Geophysical Research: Oceans (1978–2012), 92*(C2), 1937–1949. https://doi.org/10.1029/JC092iC02p01937.

Klein, L., & Swift, C. T. (1977). An improved model for the dielectric constant of sea water at microwave frequencies. *IEEE Transactions on Antennas and Propagation, 25*(1), 104–111. https://doi.org/10.1109/TAP.1977.1141539.

Liu, Y., Su, M. Y., Yan, X. H., & Liu, W. T. (2000). The mean-square slope of ocean surface waves and its effects on radar backscatter. *Journal of Atmospheric and Oceanic Technology, 17*(8), 1092–1105. https://doi.org/10.1175/1520-0426(2000)017<1092: TMSSOO>2.0.CO;2.

Liu, Y., Yan, X. H., Liu, W. T., & Hwang, P. A. (1997). The probability density function of ocean surface slopes and its effects on radar backscatter. *Journal of Physical Oceanography, 27*(5), 782–797. https://doi.org/10.1175/1520-0485(1997)027<0782:TPDFOO>2.0.CO;2.

Meissner, T., & Wentz, F. J. (2004). The complex dielectric constant of pure and sea water from microwave satellite observations. *IEEE Transactions on Geoscience and Remote Sensing, 42*(9), 1836–1849. https://doi.org/10.1109/TGRS.2004.831888.

Ruf, C. S., & Balasubramaniam, R. (2019). Development of the CYGNSS geophysical model function for wind speed. *IEEE Journal of Selected Topics in Applied Earth Observations and Remote Sensing, 12*(1), 66–77. https://doi.org/10.1109/JSTARS.2018.2833075.

Soulat, F. (2004). *Sea surface remote sensing with GNSS and sunlight reflections* (Unpublished doctoral dissertation). Universitat Politecnica de Catalunya.

Ulaby, F. T, Moore, R. K., & Fung, A. K. (1986). *Microwave remote sensing: Active and passive* (Vol. III). Norwood, MA: Artech House.

Voronovich, A. G., & Zavorotny, V. U. (2014). Full-polarization modeling of monostatic and bistatic radar scattering from a rough sea surface. *IEEE Transactions on Antennas and Propagation, 62*(3), 1362–1371. https://doi.org/10.1109/TAP.2013.2295235.

Voronovich, A. G., & Zavorotny, V. U. (2017). The transition from weak to strong diffuse radar bistatic scattering from rough ocean surface. *IEEE Transactions on Antennas and Propagation, 65*(11), 6029–6034. https://doi.org/10.1109/TAP.2017.2752219.

Voronovich, A. G., & Zavorotny, V. U. (2018). Bistatic radar equation for signals of opportunity revisited. *IEEE Transactions on Geoscience and Remote Sensing, 56*(3), 1959–1968. https://doi.org/10.1109/TGRS.2017.2771253.

Walsh, E. J., Vandemark, D. C., Friehe, C. A., Burns, S. P., Khelif, D., Swift, R. N., & Scott, J. F. (1998). Measuring sea surface mean square slope with a 36-GHz scanning radar altimeter. *Journal of Geophysical Research: Oceans (1978–2012), 103*(C6), 12587–12601. https://doi.org/10.1029/97JC02443.

Wang, T., Zavorotny, V. U., Johnson, J. T., Ruf, C. S., & Yi, Y. (2018). Modeling of sea state conditions for improvement of CYGNSS L2 wind speed retrievals. In *IGARSS 2018—2018 IEEE International Geoscience and Remote Sensing Symposium* (pp. 8297–8300). https://ieeexplore.ieee.org/xpl/conhome/8496405/proceeding.

WAVEWATCH III Development Group. (2016). *User manual and system documentation of WAVEWATCH III version 5.16 MMAB* (Technical Note, 326 pp.+App). https://polar.ncep.noaa.gov/mmab/papers/tn276/MMAB_276.pdf.

Wu, J. (1990). Mean square slopes of the wind-disturbed water surface, their magnitude, directionality, and composition. *Radio Science, 25*(1), 37–48. https://doi.org/10.1029/RS025i001p00037.

Zavorotny, V. U., & Voronovich, A. G. (2000). Scattering of GPS signals from the ocean with wind remote sensing application. *IEEE Transactions on Geoscience and Remote Sensing, 38*(2), 951–964. https://doi.org/10.1109/36.841977.

Appendix 6: Klein-Swift Ocean Dielectric Model

According to the empirical model of Klein and Swift (1977), the real and imaginary parts of the dielectric constant of sea water at microwave frequencies are, respectively,

$$\mathrm{Re}\,\varepsilon = \varepsilon_\infty + \left(\varepsilon_s - \varepsilon_\infty\right)/\left(1+\omega^2\tau^2\right) \qquad \text{(6A1)}$$

and

$$\mathrm{Im}\,\varepsilon = \omega\tau\left(\varepsilon_s - \varepsilon_\infty\right)/\left(1+\omega^2\tau^2\right) + \sigma/\varepsilon_0\omega\,. \qquad \text{(6A2)}$$

Here, $\omega = 2\pi f \cdot 10^9$ is the radian frequency (rad/s), and f is frequency in GHz; $\varepsilon_0 = 8.854 \cdot 10^{-12}$ is the dielectric permittivity of free space in farads per meter. $\varepsilon_\infty = 4.9$ is the dielectric permittivity of water at infinite frequency; $\varepsilon_s = a\varepsilon_{sT}$ is the static dielectric constant, where

$$a = 1+1.613\cdot10^{-5}TS - 3.656\cdot10^{-3}S + 3.210\cdot10^{-5}S^2 - 4.232\cdot10^{-7}S^3, \qquad \text{(6A3)}$$

$$\varepsilon_{sT} = 87.134 - 1.949\cdot10^{-1}T - 1.276\cdot10^{-2}T^2 + 2.491\cdot10^{-4}T^3. \qquad \text{(6A4)}$$

$\sigma = \sigma_0 \exp\left(-\Delta\beta\right)$ is the ionic conductivity in mhos per meter, where

$$\sigma_0 = S\left(0.182521 - 1.46192\cdot10^{-3}S + 2.09324\cdot10^{-5}S^2 - 1.28205\cdot10^{-7}S^3\right), \qquad \text{(6A5)}$$

and $\Delta = 25 - T$,

$$\beta = 2.033\cdot10^{-2} + 1.266\cdot10^{-4}\Delta + 2.464\cdot10^{-6}\Delta^2 - S\left(1.849\cdot10^{-5} - 2.551\cdot10^{-7}\Delta + 2.551\cdot10^{-8}\Delta^2\right). \qquad \text{(6A6)}$$

Here, S is sea water salinity in parts per thousand, and T is sea water temperature in °C.

$\tau = b\tau_0$ is the relaxation time in seconds, where

$$b = 1 + 2.282\cdot10^{-5}ST - 7.638\cdot10^{-4}S - 7.760\cdot10^{-6}S^2 + 1.105\cdot10^{-8}S^3 \qquad \text{(6A7)}$$

and

$$\tau_0 = 1.768\cdot10^{-11} - 6.086\cdot10^{-13}T + 1.104\cdot10^{-14}T^2 - 8.111\cdot10^{-17}T^3. \qquad \text{(6A7)}$$

7. Level 2 Wind Speed Retrieval Algorithm

The Level 2 (L2) wind speed retrieval algorithm described here is the algorithm implemented in the CYGNSS Science Operations Center (SOC). It is similar to the algorithm described in Clarizia and Ruf (2016), although the observable computation and the time-averaging approach are here slightly different, and some of the filters, which were implemented in Clarizia and Ruf (2016) to demonstrate that the resolution requirements are met, are not implemented by the SOC. The geophysical model functions (GMFs) used to map the observables into wind speed are based on empirical parameterized fits to on-orbit measurements, as described in Ruf and Balasubramaniam (2018). Two sets of GMFs are used. One is derived in fully developed seas (FDS) conditions using coincident matchups with European Centre for Medium-Range Weather Forecasts (ECMWF) numerical weather prediction model wind speeds. The other is derived using ECMWF matchups at low wind speeds and matchups at high wind speeds with coincident NOAA P-3 hurricane hunter observations of hurricane force winds made by their stepped frequency microwave radiometers. The latter GMF is referred to as young seas limited fetch (YSLF). A description of the empirical GMF development is included in Appendix 7A.

The basic steps for the L2 retrieval algorithm can be summarized as follows:

1. Two delay-Doppler map (DDM) "observables," the DDM average (DDMA) and the leading edge slope (LES), are derived from L1B DDMs of the radar cross section (RCS) and DDMs of the effective scattering area, both output by the L1 calibration procedure described in Gleason et al. (2016, 2018).
2. Wind speed is estimated from the L1 observable by inversion of the appropriate GMF (either FDS or YSLF) depending on the sea state conditions. This produces both a DDMA- and LES-based wind speed.
3. In FDS conditions, the DDMA and LES winds are optimally combined using a minimum variance (MV) estimator. In YSLF conditions, the DDMA-based wind alone is used, as it has greater sensitivity at high wind speeds.
4. In FDS conditions, time averaging is applied to consecutive samples to produce a consistent 25 km spatial resolution data product whenever it is appropriate to

do so (the appropriate level of averaging depends on the incidence angle of the sample). In YSLF conditions, no time averaging is applied in order to retain the highest possible horizontal spatial resolution in and near the inner core of tropical cyclones.

These steps are described further in the subsequent sections. An assessment of on-orbit performance relative to model-based wind speed estimates is given in Appendix 7A.

7.1. Sample Population of GMF Training Data

The L1 observables used to develop the FDS GMFs were obtained from on-orbit measurements made by the CYGNSS constellation during the period January 1–December 31, 2019. Included are measurements over the entire globe matched up with coincident 10 m referenced ocean surface wind speeds provided by the ECMWF Reanalysis 5th generation (ERA5) model forecast. ERA5 is produced using 4D-Var data assimilation and model forecasts of the ECMWF Integrated Forecast System on a 31 km grid at 1-hour intervals. More details and information about ERA5 products can be found at https://www.ecmwf.int/en/forecasts/datasets/reanalysis-datasets/era5. Bilinear interpolation in space and linear interpolation in time of the reported ERA5 wind product are used to estimate u_{10} at the times and locations of the CYGNSS specular point observations.

The L1 observables used to develop the YSLF GMF were obtained from CYGNSS observations in summer/fall 2018 during overpasses of storms in the Atlantic and Pacific Oceans at and above tropical storm intensity. The measurements were matched up with coincident 10 m referenced ocean surface wind speeds produced by the NOAA / National Centers for Environmental Prediction (NCEP) Hurricane Weather Research and Forecasting (HWRF) model. For each storm overpass, all CYGNSS data within 400 km of the storm center are examined. The location of the storm center at the time of a CYGNSS observation is determined using the NOAA National Hurricane Center's Best Track center fixes. The storm center at that time is estimated by linear interpolation in time of the closest Best Track fixes before and after the observation. A matchup is defined if the location of a CYGNSS sample and an HWRF grid point are within 3 km of each other. The HWRF wind speed for that matchup is the

interpolation in time of the closest HWRF wind speed before and after the observation. However, if the two wind speeds differ by more than 5 m/s, that matchup is discarded from the population.

The storms included in the matchup population are as follows:

- *Atlantic:* Florence, Gordon, Helene, Isaac, Michael, Oscar
- *East Pacific:* Hector, John, Miriam, Norman, Olivia, Rosa, Sergio, Willa
- *West Pacific:* Cimaron, Jebi, Jelawat, Jongdari, Mangkhut, Maria, Shanshan, Soulik, Trami, Yutu

A histogram of all the HWRF wind speeds included in the matchup dataset is shown in Figure 7.1. The high percentage of samples at lower wind speeds generally occur near the outer perimeter of the storms, and the highest wind speeds are ~ 70 m/s.

7.2. DDM Observables: DDMA and LES

Here we present a definition of the observables we use for our retrieval algorithm, derived from the outputs of the L1B calibration described in Gleason et al. (2016, 2018).

7.2.1. Definition of Delay-Doppler Map Average (DDMA)

The DDMA is the average of the L1B DDM of the normalized radar cross section (NRCS) over a given delay-Doppler range window around the specular point (Clarizia et al., 2014; Clarizia & Ruf, 2016). The DDMA exploits the DDM region, which is most sensitive to varying wind speed—namely, the scattered power at and around the specular point. Notably,
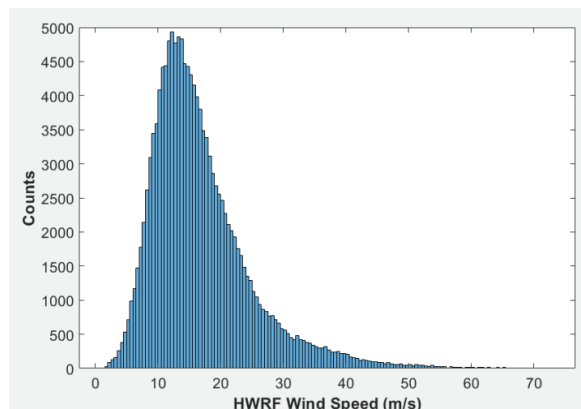
Figure 7.1. Histogram of wind speeds in the matchup population used to train the YSLF GMF.

the DDMA has the advantage of mitigating the effect of noise by averaging the power over the area around the specular point (SP) rather than the power value at the single SP pixel. An illustration of a DDM of scattered power simulated with the CYGNSS E2ES and a qualitative example of the area where the DDMA is calculated (shown as the black box) is shown in Figure 7.2.

7.2.2. Definition of Leading Edge Slope (LES)

The LES is the slope of the leading edge of the integrated delay waveform (IDW), calculated over a specific delay range (Clarizia et al., 2014; Clarizia & Ruf, 2016). IDWs are obtained as an incoherent integration of DDMs of NRCS along the Doppler dimension and over a range of Doppler frequencies. Figure 7.2 illustrates simulated IDWs of integrated power for a fixed geometry and for different wind speeds. The corresponding IDWs of NRCS would only differ from these for a constant scaling factor. Figure 7.3 highlights how the slope of the IDW's rising edge decreases for increasing wind speeds.

7.2.3. Calculation of DDMA and LES Observables

The DDMA is computed as the sum of the L1B DDM of a radar cross section (RCS) over a delay-Doppler window of, respectively, −0.25 chips to 0.25 chips and −1 kHz to 1 kHz divided by the effective scattering area over the same window. The selected delay-Doppler window is a 3 × 5 matrix due to the 0.25 chip delay resolution and the 500 Hz Doppler resolution of the CYGNSS DDMs.

The sum of L1B RCS DDMs can be expressed as follows:

$$\sigma_{DDMA} = \sum_{i=1}^{3}\sum_{j=1}^{5} d(i,j), \tag{7.1}$$

where $d(i,j)$ represents the $(i,j)^{th}$ delay-Doppler bin of the L1B DDM of RCS. The motivation for the choice of such a delay-Doppler window is documented in Clarizia and Ruf (2016).

The LES is calculated as the slope of IDWs obtained from L1A DDMs of received power using the same delay-Doppler (DD) window as the DDMA. The IDWs are obtained by summing the 5 L1A DDM columns (along the Doppler axis) that span the Doppler interval from −1 kHz to 1 kHz. The LES of the IDW leading edge is given by

$$a_{LES} = \frac{N\sum_{i=1}^{3} x_i y_i - \sum_{i=1}^{3} x_i \sum_{i=1}^{3} y_i}{N\sum_{i=1}^{3} x_i^2 - \left(\sum_{i=1}^{3} x_i\right)^2}, \tag{7.2}$$
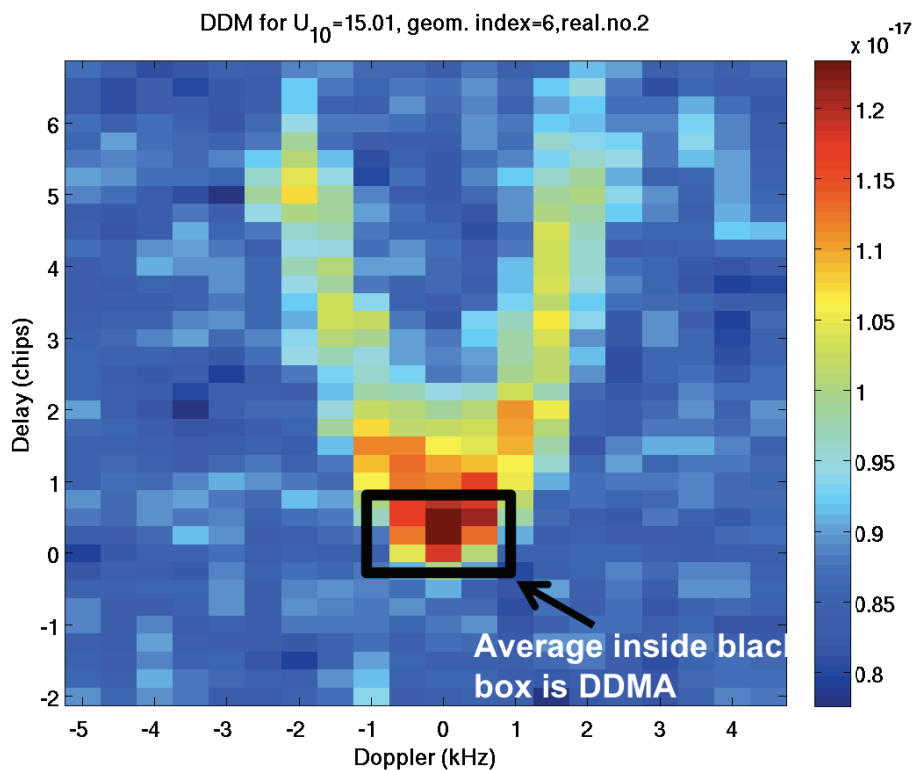
Figure 7.2. A simulated DDM and the DDM area where the DDMA is calculated.
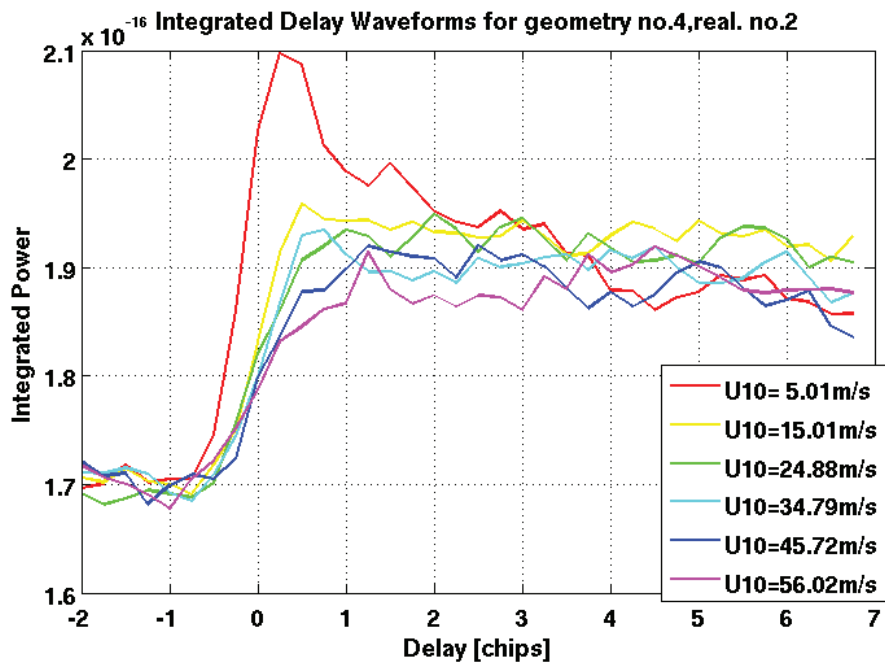
Figure 7.3. Integrated delay waveforms computed from DDMs simulated using different wind speeds.

where x_i is the *i-th* value of the delay within the [−0.25 0.25] chip interval, y_i is the corresponding IDW value, and $N = 3$ is the number of points of the IDW used for the LES computation.

The effective scattering area of the 3 × 5 region that is used for the L1B DDMA and LES calculation is computed from the DDMs of ideal area and effective area for individual DDM bins, both outputs of the L1B calibration process. The DDM effective area of individual bins within the selected DD window is not simply summed, as this would have the effect of accounting for the spreading of the effective area into neighboring bins multiple times, which would result in too big of an effective area. Therefore, the approximation we use for the effective area A_{eff} is

$$A_{eff} = \sum_{i=1}^{3}\sum_{j=1}^{5} A_{id}(i,j) + \frac{1}{2}\sum_{i=1,3}\sum_{j=1,5}\Delta A(i,j) + \frac{1}{4}\sum_{i=1,3}\sum_{j=2,3,4}\Delta A(i,j)$$
$$\Delta A(i,j) = A_{eff}(i,j) - A_{id}(i,j)$$

(**7.3**)

where $A_{id}(i,j)$ and $A_{eff}(i,j)$ are the $(i,j)^{th}$ bin of the ideal and effective scattering area DDMs, respectively.

The final equations for the DDMA and LES are given by

$$DDMA = \frac{\sigma_{DDMA}}{A_{eff}}$$

$$LES = \frac{\alpha_{LES}}{A_{eff}}.$$

(**7.4**)

Computation of the DDMA and LES is also explained in detail in Clarizia and Ruf (2016), although in that case, the DDMA and LES of RCS are normalized by the ideal area, calculated simply as the sum of the DDM ideal area bins within the DD window considered for the observables.

7.3. Time Averaging

An extra processing step that contributes to improving the performance of the algorithm is to apply time averaging to the collected data.

The DD window chosen for the observable computation corresponds to a given instantaneous field of view (IFOV), whose square root is shown as a function of incidence angle in Figure 7.4.

The IFOV is defined here as the physical area at the intersection between the iso-range ellipse at 0.25 chips and the iso-Doppler lines at −1 kHz and 1 kHz. Full details about the relationship among physical area, IFOV, and incidence angle are contained in Clarizia and Ruf (2016) and repeated in Appendix 7A.

It is clear from Figure 7.4 that for a range of incidence angles lower than approximately 54.5°, the IFOV of the collected samples is below the spatial resolution requirement of 25 km. For all these cases, it is possible to average a number of consecutive samples in time to achieve the spatial resolution limit of 25 km. The maximum number of samples n that can be averaged can be easily calculated using some
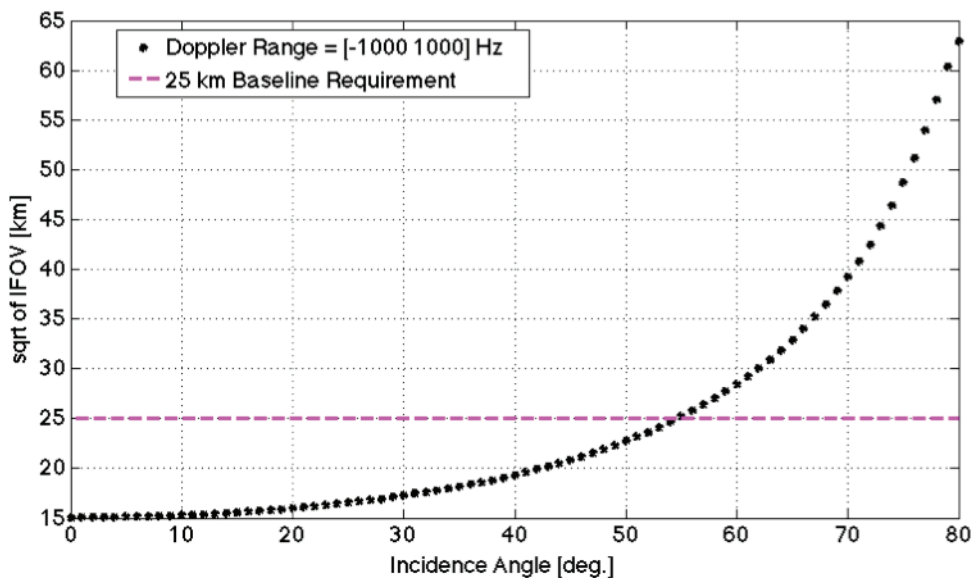
Figure 7.4. Square root of instantaneous field of view (IFOV) versus incidence angle for the DD window spanning −0.25 chip to 0.25 chip and −1 kHz to 1 kHz (black dots) along with the requirements for the CYGNSS mission (dashed magenta line).

simplifications, and after a few simple calculations it turns out to be (Clarizia & Ruf, 2016)

$$n = \frac{EFOV^2}{6\sqrt{IFOV}} - \frac{\sqrt{IFOV}}{6} + 1. \qquad (\textbf{7.5})$$

For each incidence angle, it is therefore possible to know the exact number of samples that can be averaged if a 25 km requirement on the spatial resolution must be met. A precomputed lookup table of n as a function of the incidence angle is used in the time-averaging process of the algorithm, and this table is reported in Appendix 7B. Of course, the calculation of n uses simplified assumptions and does not take into account several aspects, like the real trajectory of the specular point on the surface or the real shape of the IFOV, which is ideally assumed to be a square in Equation 7.5 but depends instead on the configuration of the iso-delay and iso-Doppler lines at the ranges selected for the computation of the observables. However, these simplifications are valid enough to allow a reliable estimation of the number of samples to be averaged together.

Some graphical examples of time averaging are illustrated in Figure 7.5, where the different SP tracks for a single CYGNSS observatory are shown as blue crosses, the sample considered for time averaging is shown in red, and the consecutive samples to be averaged together with the red one are highlighted with black circles.

The time-averaging implementation used in the SOC algorithm follows a few simple rules that mostly aim at avoiding geolocation ambiguities in the resulting time-averaged samples and can be summarized as follows:

1. The nonvalid samples are excluded from the time averaging. These are either the samples with the overall quality flag set to 0 (see Section 7.9) or those whose DDMA or LES value is not valid (−9999).
2. The number of samples to time average before the central sample (i.e., preceding the central samples in time along the track) is always equal or higher than the number of samples to time average after the central sample.
3. The difference between the number of samples before and the number of samples after cannot be greater than 1.

These rules were not applied in the algorithm presented in Clarizia and Ruf (2016), and as a result of them, there are cases when the number of time-averaged samples (n) is less than that prescribed by the incidence angle. As a consequence, the amount of time-averaging applied to the SOC algorithm is in some cases less than that applied in Clarizia and Ruf (2016).
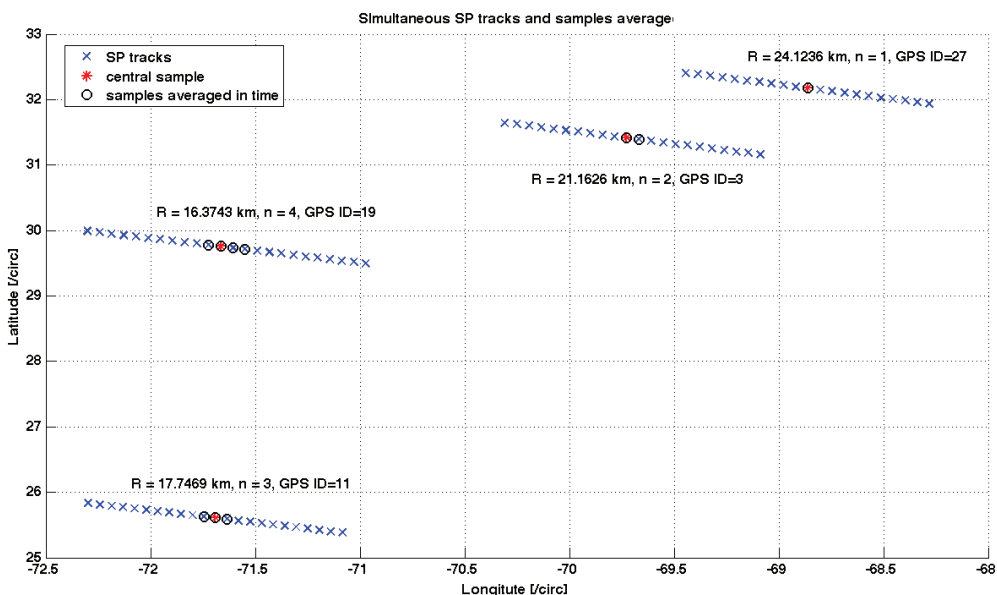
Figure 7.5. An illustration of how the time-averaging (TA) algorithm works for four simultaneous SP tracks acquired by a single CYGNSS observatory.

7.4. Generation of Geophysical Model Functions

7.4.1. Generating the FDS GMF

The dataset used to generate the GMF is formed as the L1B observable, computed over a delay range of [−0.25 0.25] chips and a Doppler range of [−1000 1000] Hz and acquired with high enough range corrected gain (RCG). This is defined as the receiver antenna gain at the specular point multiplied by the range losses there, as given by

$$RCG = \frac{G_{RX}^{SP}}{\left(R_0^{SP} R^{SP}\right)^2} 10^{27}, \quad \textbf{(7.6)}$$

where the range terms are in units of meters and the numeric (not dB) value of the receive antenna gain is used. The scale factor of 10^{27} is applied in order to produce values of order 1–100. The RCG represents those factors affecting the received signal strength that are related to the measurement geometry and are independent of the surface scattering cross section. It is used to filter data according to their expected signal-to-noise quality. Typical ranges of low, medium, and high RCG for the FDS wind product are, respectively, <10, 10–30, and >30. For the YSLF wind product, which is more sensitive to measurement noise, the ranges are <30, 30–150, and >150.

For FDS GMF generation, we use all CYGNSS measurements made in 2019 data with v3.0 Level 1 (L1) calibration and the following filters.

The L1 observables are filtered prior to use as part of the training used to derive the empirical GMF. The filters are for reasons of quality control. Specifically:

- The Doppler coordinate of the specular point in the DDM is required to be greater than the lowest possible value in the map and less than the highest possible value. This discards cases where it is at the edge of the map and the computed Doppler coordinate may be incorrect. In practice, this happens less than 0.1% of the time.
- The delay coordinate of the specular point in the DDM is required to be greater than the lowest possible value in the map and less than the highest possible value. This discards cases where it is at the edge of the map and the computed delay coordinate may be incorrect. In practice, this happens less than 0.1% of the time.

- All NaN values of the observables are discarded. This eliminates samples for which noise in the calibration data can produce nonphysical calibrated L1 data. In practice, this happens less than 0.1% of the time.
- The observables are required to be nonnegative. This eliminates samples for which noise in the calibration data can produce nonphysical calibrated L1 data as well as measurements that are very close to the measurement noise floor. In practice, this happens less than 0.1% of the time.
- All measurements are discarded for which the spacecraft star tracker is not tracking due to solar contamination. Some reported spacecraft attitude data during sun outages are known to be erroneous (with inaccuracies greater than the error allocation in the L1 calibration algorithm for attitude knowledge). This only occurs when the outage is especially long, but all sun outage data are flagged and removed as a precaution. In practice, this happens less than 1% of the time.
- Measurements are discarded when the reported spacecraft roll angle and the commanded roll angle differ by more than 1° in absolute value. In practice, this happens less than 1% of the time.
- All data with a CYGNSS RCG of less than 3 are discarded. RCG is a composite measure of receive signal strength that combines the receive antenna gain in the direction of the specular point with the R^{-2} propagation range loss from the GPS transmitter to the specular point and from the specular point to the CYGNSS receiver. In practice, data with an RCG > ~1 can typically produce useful wind speed retrievals, but only data with a higher signal-to-noise ratio (SNR) are used to train the empirical GMF.

The GMF is two-dimensional—a function of both wind speed and incidence angle—and is derived separately for the DDMA and LES observables. The GMF maps the selected observable to the ERA5 "ground truth" wind speed. The GMFs are computed in the form of lookup tables (LUTs) of DDMA and LES values. The methodology used to derive the GMF is described in detail in Clarizia and Ruf (2020). It was originally developed by Freilich and Challenor (1994) to derive an empirical altimeter wind speed model function. It is based on the assumption that a model function M relating the wind speed w to the observable exists, as given by

$$w = M(O),$$ **(7.7)**

where O denotes the observable. It is assumed that w varies monotonically with O such that the inverse model function $O = M^{-1}(w)$ also exists.

The cumulative distribution function (CDF) of the observable $F_O(O')$ can be written as follows:

$$F_O(O') = P(O \leq O') = P\left(M^{-1}(w) \leq O'\right) =$$ **(7.8)**

$$= P\left(w \geq M(O')\right) = 1 - F_w\left(M(O')\right).$$ **(7.9)**

If $F_O(O') = \beta$, then the corresponding wind speed $w' = M(O')$ is the wind speed for which $1 - F_w(w') = \beta$. The detailed application of this method to the case of CYGNSS is described in Clarizia and Ruf (2020) and summarized here for the case of the DDM observable. A similar approach is followed for the LES observable.

1. Specific axes are set for the wind speed, the incidence angle, and the DDMA. The wind speed axis is chosen to span the range from 0.05 m/s to 69.95 m/s with a 0.1 m/s step. The incidence angle axis ranges from 1° to 70° with a step of 1°. The axis for the DDMA observable ranges from the minimum to the maximum value of the observable measured for the dataset and has 700 elements. We denote wy as the generic wind speed value of the wind speed axes and $DDMA'$ as the generic observable value of the observable axis.
2. The wind speed CDF values $F_{wy}(wy')$ are computed for each value of the wind speed axes.
3. For each 1° incidence angle bin, the DDMA values $DDMAx$ corresponding to wy and forming the LUT are found as follows:
   a. The observables CDF values $F_{DDMA}(DDMA')$ are computed for each value of the DDMA observable axis.
   b. The CDF values of the observables corresponding to the wind speed axes are denoted as β and set as $\beta = 1 - F_{wy}(wy')$.
   c. The observables $DDMAx$ corresponding to the wind speed axes are derived via linear interpolation of the $F_{DDMA}(DDMA')$ versus the DDMA axis at the CDF values β.

After the CDF-matching GMF is generated, it is passed through a running average filter, first with respect to incidence angle (averaging window ± 10°) and then with respect to

wind speed (averaging window ± 3 m/s), to smooth out variations in the dependence on both incidence angle and wind speed.

The final GMF given by ($DDMAx$ and wy) for every incidence angle bin maps wind speed as a function of both the observable and the incidence angle. The advantage of this method, compared to the one previously used in the baseline algorithm to derive the FDS GMF, is its simplicity, its effectiveness, and the fact that it does not require empirical tuning of the GMF (Clarizia and Ruf, 2020). The current method is entirely based on the empirical CDFs of the observables used and geophysical parameters to retrieve, and it can be applied to any global navigation satellite system reflectometry (GNSS-R) observable, provided that the wind speed varies monotonically with the observable.

Examples of the resulting GMFs for both DDMA and LES observables are shown in Figure 7.6.

7.4.2. Generating the YSLF GMF

The population of wind speed matchups used to generate the YSLF GMF is considerably smaller than that used for the FDS case because it is restricted to storm overpasses. In addition, the CDF-matching technique used in the FDS case would be less appropriate to use here because the statistical distribution of wind speeds in storms is much less repeatable. For this reason, the YSLF GMF is created by binning the L1 observables into discrete steps in HWRF wind speed and in the incidence angle of the measurement geometry and averaging the L1 samples in each bin. In addition, only the DDMA L1 observable is used for retrieval of YSLF wind speeds in storm conditions because the LES observable has insufficient sensitivity to changes in wind speed under high wind conditions.

The L1 observables are filtered prior to use as part of the training used to derive the empirical GMF for reasons of quality control. The filters used are the same as those in the FDS case except that the minimum threshold for acceptable RCG values is raised from 3 to 30. This is done to raise the minimum acceptable signal-to-noise quality of the observations, since, in general, scattering from the ocean in high wind conditions tends to be weaker.

The behavior of the empirical GMF as a function of u_{10} and θ_{inc} is smoothed by allowing sequential bins in either dimension to overlap. In the incidence angle dimension, the bin center is incremented every 1° from 1 to 70°, and all samples are included within ± 20° of the center. In the wind speed dimension, the bin center is incremented every 0.1 m/s from 0.05 to 34.95 m/s, and all samples are included within a variable bin width that varies according to the population
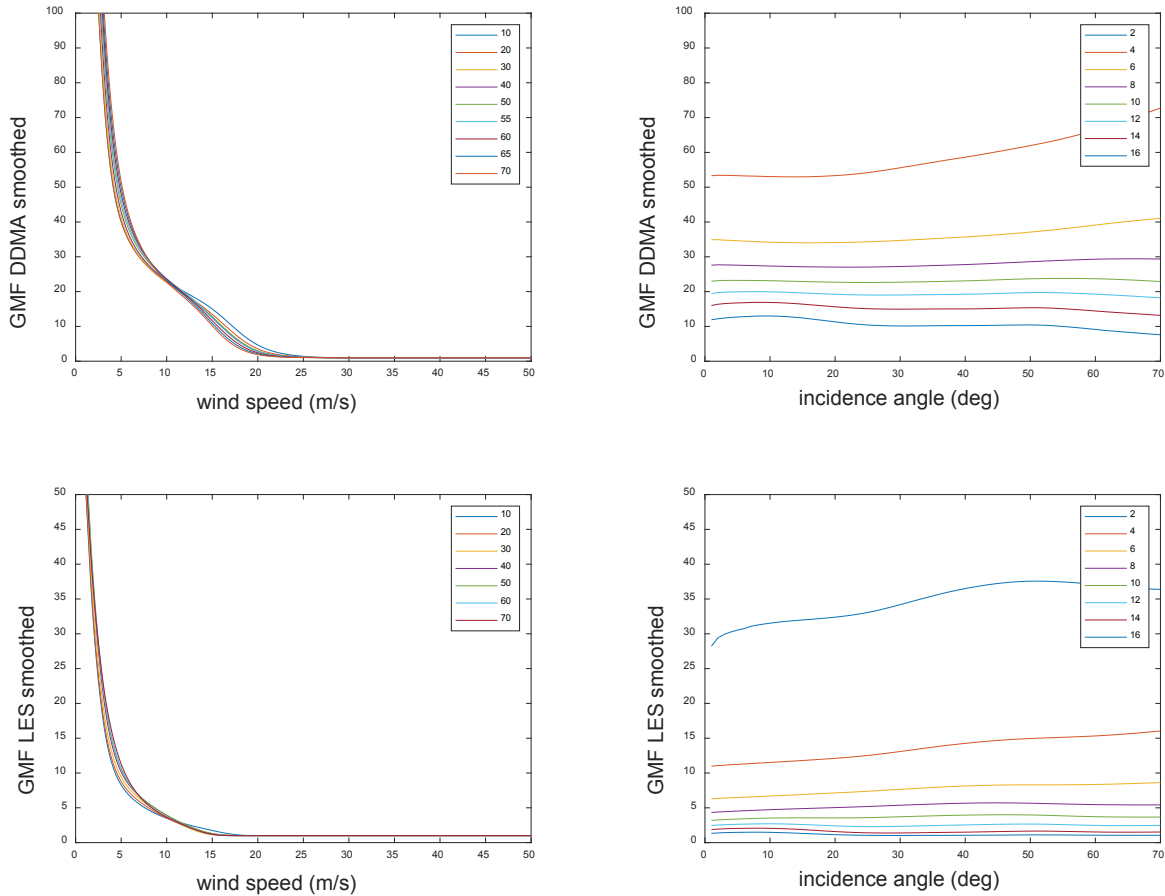
Figure 7.6. FDS GMFs for the two L1 observables, σ_o or DDMA (top) and LES (bottom). The GMFs are plotted as a function of wind speed for different incidence angles (left) and as a function of incidence angle for different wind speeds (right).

density of samples as a function of wind speed. Specifically, the bin widths used are as follows:

- ± 0.4 m/s ($u_{10} \leq 1$ m/s)
- ± 0.5 m/s ($1 < u_{10} \leq 2$ m/s)
- ± 0.6 m/s ($2 < u_{10} \leq 3$ m/s)
- ± 0.7 m/s ($3 < u_{10} \leq 5$ m/s)
- ± 0.8 m/s ($5 < u_{10} \leq 9$ m/s)
- ± 1.0 m/s ($9 < u_{10} \leq 11$ m/s)
- ± 1.5 m/s ($11 < u_{10} \leq 14$ m/s)
- ± 2.0 m/s ($14 < u_{10} \leq 17$ m/s)
- ± 2.5 m/s ($17 < u_{10} \leq 25$ m/s)
- ± 3.0 m/s ($25 < u_{10} \leq 35$ m/s)
- ± 4.0 m/s ($35 < u_{10} \leq 45$ m/s)
- ± 5.0 m/s ($45 < u_{10}$)

A weighted average of all samples within twice these bin width ranges is performed. Samples within ± one bin width of the bin center are given twice as much weight as those between 1 × bin width and 2 × bin width from the bin center. This tapered weighting approach reduces the introduction of artificial higher frequency components into the GMF that are present in the original discrete empirical samples.

The GMF is also forced to be monotonic as a function of wind speed. The GMF value at 7.05 m/s is computed first (since this is generally the most probable wind speed and so has the largest population of samples in its near vicinity). GMF values are then sequentially computed in steps of 0.1 m/s above and below this value using the averaging scheme described above. However, values are allowed to either decrease or stay the same with increasing wind speed and increase or stay the same with decreasing wind speed. This limits the introduction of nonphysical variations into the GMF due to undersampling of certain parts of the (wind speed, incidence angle) state space. In practice, this monotonicity algorithm is only enforced at the highest and lowest wind speeds in the population, where the sampling density tends to be lowest.

After the bin-averaged GMF is generated, it is passed through a final running average smoothing filter, first with respect to incidence angle (averaging window ± 10°) and then with respect to wind speed (averaging window ± 3 m/s).

Examples of the resulting YSLF GMF as a function of wind speed and incidence angle are shown in Figure 7.7.

7.5. Wind Estimation Using the GMF

For each point of the performance evaluation dataset (either DDMA or LES), a wind speed is estimated using the GMF. The estimation is done through interpolation when the observable value falls within the range of values spanned by the GMF and through extrapolation outside of such a range. The mathematical equation to estimate the wind through interpolation is given by (referring to DDMA)

$$\hat{U}_{10}^{DATA} = U_{10}^{LUT} + \alpha \left(DDMA^{DATA} - DDMA\left(U_{10}^{LUT}\right) \right)$$

$$\alpha = \left(V_{10}^{LUT} - U_{10}^{LUT}\right) \Big/ \left(DDMA\left(V_{10}^{LUT}\right) - DDMA\left(U_{10}^{LUT}\right)\right) \quad , \textbf{(7.10)}$$

where $DDMA^{DATA}$ is the DDMA value within the DDMA range of the GMF, $\hat{U}_{10}^{DATA}$ is the wind estimation for DDMA value, the pair of values $\left(U_{10}^{LUT}, DDMA\left(U_{10}^{LUT}\right)\right)$ are the y and x coordinates of the GMF entry whose DDMA value (x coordinate) is immediately below $DDMA^{DATA}$, and the pair of values $\left(V_{10}^{LUT}, DDMA\left(V_{10}^{LUT}\right)\right)$ are the y and x coordinates of the GMF whose DDMA value is immediately above $DDMA^{DATA}$.

The mathematical expression for estimating the wind through extrapolation is given by
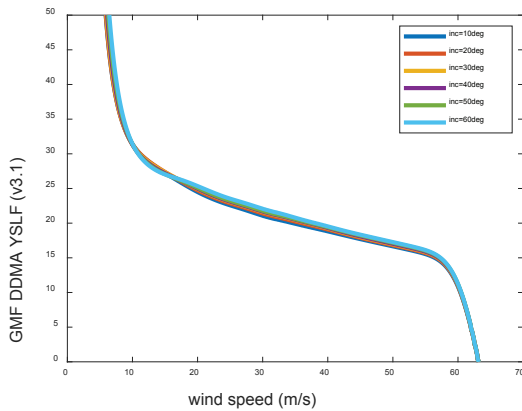
$$\hat{U}_{10}^{EXT} = U_{10}^{i \ LUT} + \alpha^{EXT} \left(DDMA^{DATA} - DDMA\left(U_{10}^{iLUT}\right) \right) \quad i = 1, n,$$

$$\textbf{(7.11)}$$

where the values 1 and n for the index i refer, respectively, to the smallest and largest value of the wind range, $\hat{U}_{10}^{EXT}$ is the wind value to estimate through extrapolation, and α^{EXT} is the slope estimated from the 2 points of the LUT with the lowest wind (if i = 1) or from the 3 points of the GMF with the highest wind (if i = n).

7.6. FDS Wind Speed Additional Processing

7.6.1. Wind Speed MV Estimator

The wind speed estimates from DDMA and LES can be combined to produce a minimum variance (MV) estimator. An MV estimator exploits the degree of decorrelation between the errors in the individual estimates to minimize the root mean square (RMS) error in its wind speed estimate. The advantage of such an estimator lies in the fact that its RMS error will always be better than or equal to the lowest RMS error in the retrieved wind speeds among the individual observables. The lower the correlation between errors in pairs of individual estimators, the better the RMS error performance of the MV estimator. The MV estimator is built as a linear combination of the original estimators, as shown in Clarizia and Gommenginger (2013):

$$u_{MV} = m \cdot u, \quad \textbf{(7.12)}$$

where u is the vector of individual estimates (from DDMA and LES) and m is the vector of coefficients. The coefficients
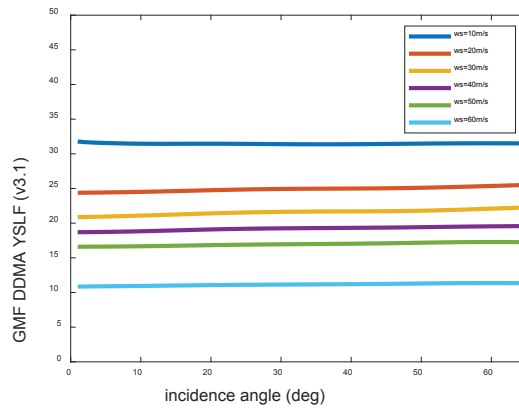
Figure 7.7. YSLF GMF of σ$_o$ (DDMA) versus wind speed at different incidence angles (left) and versus incidence angle at different wind speeds (right).

are obtained by requiring that the MV estimator be unbiased (i.e., the expected value of its retrieval is equal to the true quantity to be estimated) and by minimizing its variance. The mathematical derivation of the coefficients for the estimator is illustrated in Clarizia et al. (2013) and Clarizia and Ruf (2016) and repeated for convenience in Appendix 7B.

The covariance matrix could be estimated from all the retrieval errors; however, a further improvement in the final performances is obtained when a different covariance matrix of retrieval errors is estimated for different ranges of wind speeds. This happens because the correlation between the errors in the retrievals from the two observables decreases for noisier data characterized by higher winds with lower SNR. This allows the MV estimator to contribute more to the performance improvement of those data where the performances are worse due to a lower SNR, so in a sense, the MV approach will help where it is needed most.

A wind speed uncertainty is also associated with each final retrieved wind. The uncertainty values are stored in the form of an LUT indexed by wind speed interval (mean of DDMA and LES wind). The numerical values of this LUT are reported in Table 7B4 in Appendix 7B.

7.6.2. CDF-Matching Debias

A last adjustment is made to the MV wind speed to produce the final "wind_speed" data product reported in the L2 data files. The MV winds are debiased so their probability distribution, assembled using a global set of measurements over several seasons, matches that of near-coincident wind speeds produced by the ERA5 reanalysis numerical weather prediction model. The debiasing algorithm consists of a remapping of the original MV wind speeds to their debiased value. Below 12–15 m/s, the remapping forces agreement between CYGNSS MV and ECMWF reanalysis wind speed probability distributions. At higher winds, where sample populations are low and there is less confidence in the representativeness of the empirical probability distributions, the remapping tapers from full adjustment to the ERA5 distribution (at low winds) to no adjustment of the MV winds (at highest retrieved winds). The exact transition wind speed from full to tapered adjustment is determined by the sample size of the wind speed population. Remapping parameters are derived independently for each wind speed bin used by the MV estimator. Example remapping parameter LUTs are shown in Appendix 7B. Histograms of the model and retrieved Climate Data Record winds for 2019 as a function of CYGNSS Flight Model (FM), antenna, and GPS transmitter are shown in Figure 7.8. In all cases, the histograms of
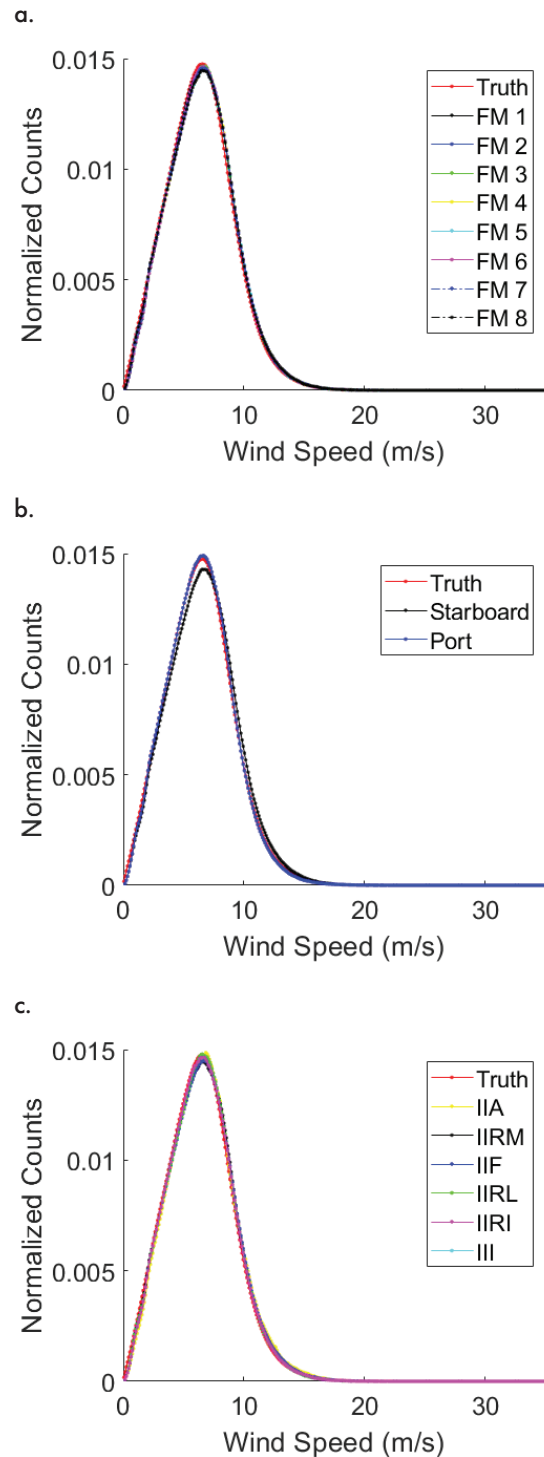
Figure 7.8. Histograms of CDR FDS winds and model ("Truth") winds separated by (a) CYGNSS FM, (b) CYGNSS antenna, and (c) GPS block type.

CYGNSS winds match the model winds quite closely, save for the antenna splits. For this last case, the starboard and port antennas see different distributions of winds as a function of latitude as they look off to each side of the spacecraft, particularly at the extreme high and low latitude ranges of the observations (± 40°), where the truth/model estimates differ significantly for each antenna and the wind speed distributions shift correspondingly. This can be seen in the way that the truth histogram lies directly between the starboard and port histograms in the 7 to 15 m/s range.

7.6.3. Sea State Dependency Correction

GNSS-R signals are sensitive not only to the part of the surface roughness spectrum that responds quickly to variations in the local wind but also to longer wavelength portions of the spectrum that are not necessarily correlated with the local wind (e.g., Chen-Zhang et al., 2016). The lower part of the spectrum will only be correlated with the local wind if it blows uninterrupted with almost the same intensity and direction for a sufficient duration of time. This high correlation condition corresponds to an FDS state. Additionally, swells (long wavelength waves that have dispersed from a distant weather system) can also be present in this part of the spectrum and can even be the dominant waves.

This dual dependency is not represented in the GMF given in Section 7.4 because it is derived empirically from a large population of samples that is optimized by the more common FDS state condition. As a result, wind speed estimates based solely on the GMF can be biased if the sea state is not in the nominal state expected for a particular local wind speed (either because it is not yet fully developed or because of the presence of swells).

The dependency to the sea state is reduced using a correcting 2D LUT with inputs (1) the debiased FDS MV winds and (2) the colocated reference significant wave height (SWH) given by the WW3 model, which is forced by ERA5 reanalysis winds from the ECMWF organization. The SWH is a parameter that characterizes the sea state. It is obtained from the energy (or zeroth-order moment) of the wave spectrum. This allows for the correction of the winds derived with the GMF in scenarios in which the sea is not in its nominal state. The LUT is built as follows:

1. Colocate the reference ERA5 winds and SWHs to the CYGNSS coordinates.
2. Bin the colocated data in rectangular cells of 0.1 m/s × 0.1 m. Clear cells with low number of observations.

3. Compute the mean of the difference between the reference winds and those from CYGNSS ($WS_{ERA5} - WS_{FDS}$) within each cell.
4. Apply a 2D triangular averaging window of size 2.5 m/s × 2.5 m across the observations within each cell.
5. Apply iteratively (two times) two 1D low-pass Gaussian filters of size 2.5 m/s or 2.5 m across the cells.

The configuration parameters have been obtained after a trial-and-error process.

As an example, the LUT for v3.0 FDS winds is presented in Figures 7.9 and 7.10. The table is not defined outside the black line, as the number of samples in these cells was not statistically significant to compute the mean difference. Three regimes can be observed: one dominated by a negative bias, one dominated by a positive bias, and a zero-bias line. In the first case, the GMF overestimates the wind speed. This happens because the SWH is larger than the average one for that particular reference wind speed. This translates into a smaller normalized bistatic radar cross section (NBRCS), which in turn translates into a larger wind speed estimated by the GMF. In the second case, the opposite happens. The GMF underestimates the wind speed because the SWH is smaller than the average one, resulting in a larger NBRCS and therefore a smaller estimated wind speed. In the zero-bias line, the retrieved winds by the GMF are not corrected, as this combination of reference winds and reference SWHs is the typical one.

The corrected FDS winds are obtained by interpolating the uncorrected winds and the colocated SWH over the LUT followed by the CDF-matching debiasing technique described in Section 7.6.2.

7.7. YSLF Wind Speed Additional Processing Significant Wave Height Correction

In a similar manner to the FDS case described above, wind speeds estimated using the YSLF GMF are found to have a retrieval bias, relative to matchups with HWRF wind speeds in tropical cyclones, that is correlated with significant wave height (SWH) as determined from matchups with WW3. A lookup table (LUT) of retrieval bias (HWRF reference – CYGNSS retrieval) as a function of retrieved wind speed and WW3 SWH is generated and applied as a bias correction, similar to the FDS retrieval algorithm. Cuts through the YSLF LUT at selected values of SWH are shown in Figure 7.11.
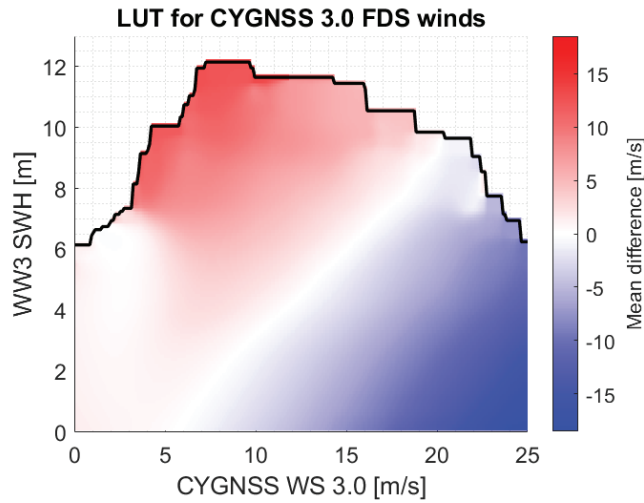
Figure 7.9. Correcting LUT for v3.0 FDS winds.
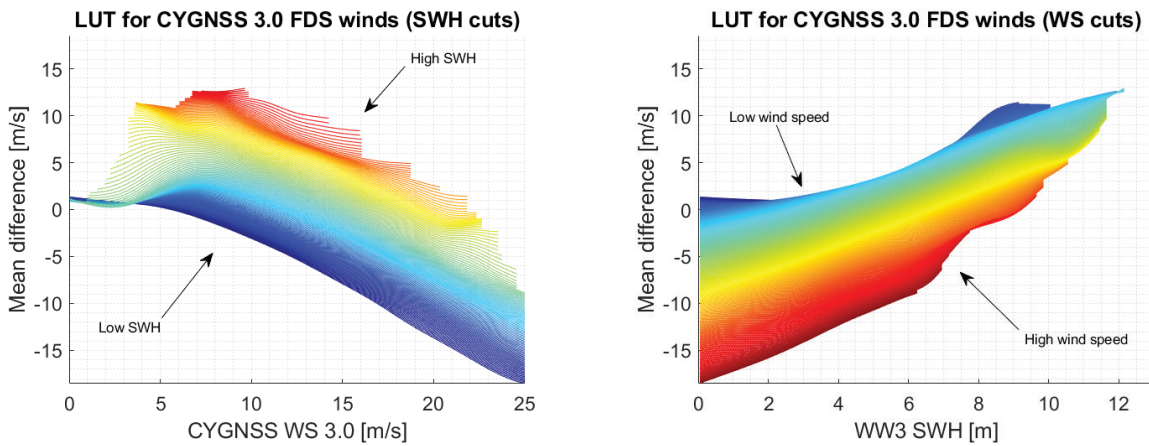
Figure 7.10. Correcting LUT cuts: *left*, SWH cuts; *right*, wind speed cuts.
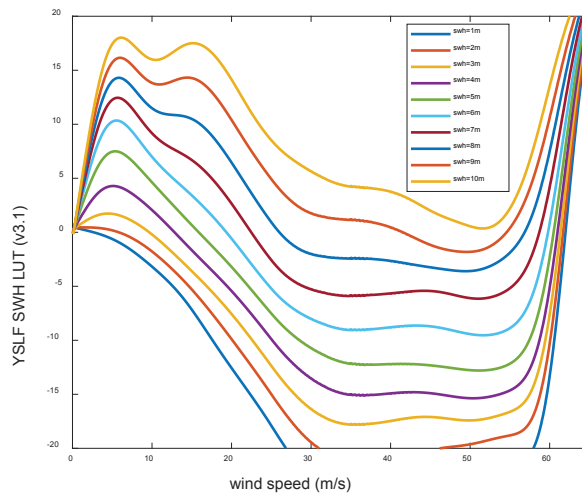
Figure 7.11. Bias correction LUT for YSLF wind speed retrieval as a function of wind speed for different values of significant wave height.

7.8. Effect of Trackwise Correction on L2 Wind Speed

Comparisons between the trackwise corrected L2 CDR and reanalysis matchup wind speeds are made to illustrate the performance of the correction algorithm. Figure 7.12 shows the RMS difference between the two as a function of the reanalysis wind speed using all measurements from January 1, 2018, through December 31, 2018. Also shown is the RMS difference between reanalysis and Sensor Data Record (SDR) L2 wind speeds, which were derived from the original, uncorrected L1 observables. The trackwise correction algorithm reduces the difference at all wind speeds. Note, in particular, that the increase in RMS difference with wind speed above ~12 m/s has been significantly reduced from SDR v2.1 to the CDR winds. Calibration errors such as those caused by the use of erroneous GPS equivalent isotropically radiated power (EIRP) values tend to have a larger effect at higher wind speeds due to the decrease in sensitivity of the L1 observables to wind speed (Ruf et al., 2018).

A more important diagnostic for the behavior of the CDR data product than RMS difference, for purposes of climate-related studies, is the stability of its mean difference, or bias, both temporally and geographically. A time series of the mean difference between the CDR and reanalysis winds from March 18, 2017, through September 30, 2019, is shown in Figure 7.13. Both daily and monthly running averages of the mean are included. Also included is the same mean difference time series for the SDR L2 wind speed. Large shifts in the SDR bias are caused by known changes in GPS transmit power, which are associated with its "flex power" transitions. This is true of both the very sharp increase in bias that occurred on a single day in May 2018 and the more gradual change in bias that occurred over a period of months in fall 2018. Smaller changes in the bias at intermediate time scales may also be due to GPS flex power transitions, but this is

less clear. Whatever their cause or causes, the changes in retrieval bias that are evident in the SDR wind speed data product have been largely removed by the trackwise correction algorithm.

GPS flex power transitions are understood to occur episodically in time and also at some locations more so than others. If left uncorrected, this will introduce location-specific structure to the L2 retrieval bias. The mean bias as a function of location, averaged over the full calendar year 2018, for both the SDR v2.1 and trackwise corrected CDR wind speeds is shown in Figure 7.14. Localized conditions of high or low bias are evident in the SDR v2.1 winds, and they are largely removed in the trackwise corrected CDR case. Notably, some geolocated structure to the bias is still present with CDR winds—for example, a small positive bias in the equatorial Pacific near the intertropical convergence zone (ITCZ). This structure does not coincide with known behavior of the GPS flex power transitions and may be an indication of geophysical oceanographic features. For example, persistent deviations of boundary layer atmospheric stability in the ITCZ from its global average state would alter the sensitivity of ocean surface roughness there to near surface winds, thereby shifting the bias relative to the reanalysis winds.

7.9. Quality Control Flags in the Retrieval Algorithm

The retrieval algorithm reports a number of quality control flags associated with each L2 wind speed estimate. Some are designated as "fatal" and indicate that the reported wind speed either is highly nonphysical (e.g., a large negative value) or has an estimated uncertainty that is much higher than normal. Some are designated as "nonfatal" and are triggered by anomalous conditions that may affect the accuracy of the estimate. A complete list of the flags is provided in tabular form in Appendix 7B.
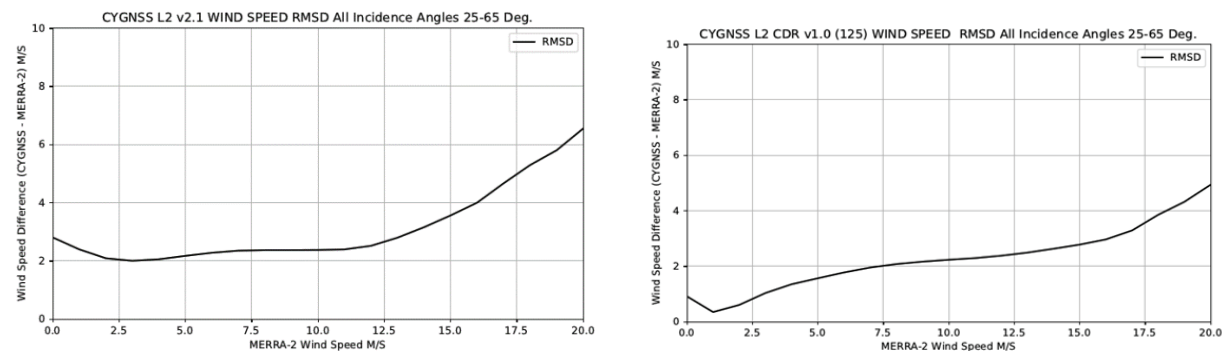
Figure 7.12. RMS difference between reanalysis and v2.1 (left) or trackwise corrected CDR (right) CYGNSS wind speed as a function of the reanalysis winds using all measurements in calendar year 2018.
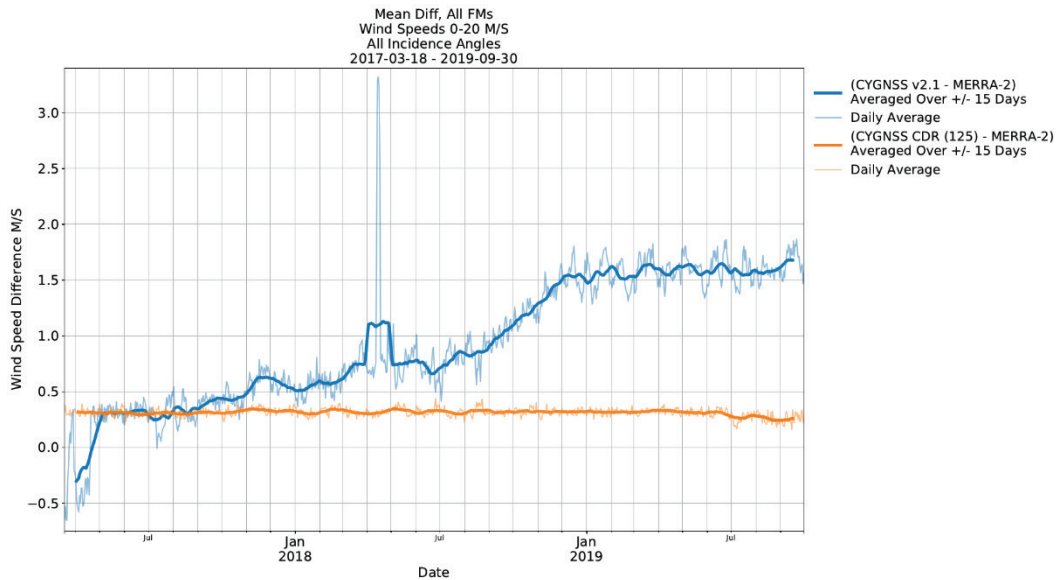
Figure 7.13. Mean differences between reanalysis and SDR v2.1 (blue) or trackwise corrected CDR (green) beginning on the first day of science operations (March 18, 2017) through September 30, 2019. Both daily and monthly running average mean values are shown.
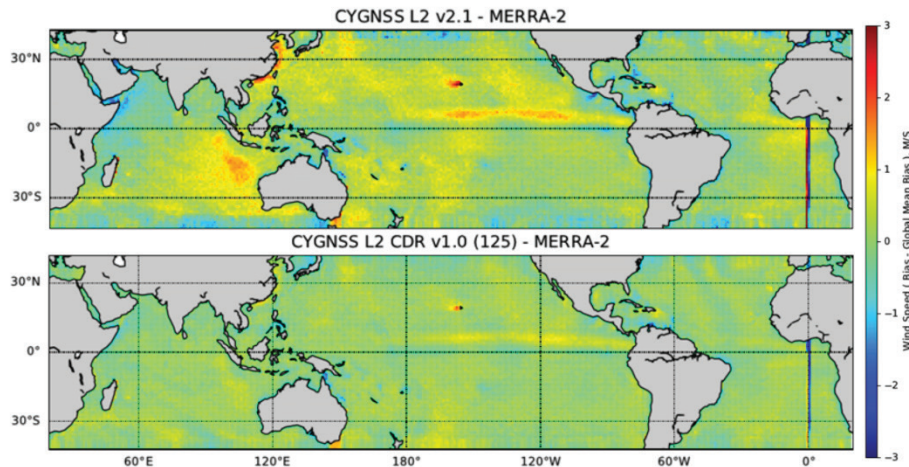
Figure 7.14. Mean difference between reanalysis and SDR v2.1 (top) or trackwise corrected CDR (bottom) CYGNSS wind speed using all measurements in calendar year 2018.

7.10. Summary and Conclusions

Here we summarize the main characteristics of the L2 wind speed retrieval algorithm described here and implemented in the SOC:

- generation of observables from L1B DDMs, computed over a fixed DD range of −0.25 chips to 0.25 chips and −1 kHz to 1 kHz
- derivation of GMFs under FDS and YSLF sea state conditions to map each observable value into an

appropriate wind speed value given the predominant sea state

- time averaging of observables (FDS only)
- wind speed MV estimator using RCG-dependent coefficients derived from the covariance matrix of retrieval errors (FDS only)

It is important to also highlight some differences with respect to the algorithm illustrated in Clarizia and Ruf (2016). These main differences are as follows:

- The time-averaging process follows here some additional rules listed in Section 7.3, and as a result of that, the number of time-averaged observables is in some cases less than that in Clarizia and Ruf (2016).
- No effective field of view (EFOV) filter is applied here; in other words, the present algorithm does not exclude samples acquired with an incidence angle greater than 54.5°.

7.11. References

Chen-Zhang, D. D., Ruf, C. S., Ardhuin, F., & Park, J. (2016). GNSS-R nonlocal sea state dependencies: Model and empirical verification. *Geophysical Research: Oceans (1978–2012), 121*, 8379–8394.

Clarizia, M. P. (2012). *Investigating the effect of ocean waves on GNSS-R microwave remote sensing measurements* (Unpublished doctoral dissertation). University of Southampton.

Clarizia, M. P., & Gommenginger, C. (2013). *Spaceborne GNSS-reflectometry instrument and algorithms: Investigating mean square slope retrieval with UK-DMC GNSS-R data* (Technical Note, ESTEC contract no. 4000106450/12/NL/FF/LF).

Clarizia, M. P., & Ruf, C. S. (2016). Wind speed retrieval algorithm for the Cyclone Global Navigation Satellite System (CYGNSS) mission. *IEEE Transactions on Geoscience and Remote Sensing, 54*(8), 4419–4432. https://doi.org/10.1109/TGRS.2016.2541343.

Clarizia, M. P., & Ruf, C. S. (2020). Statistical derivation of wind speeds from CYGNSS data. *IEEE Transactions on Geoscience and Remote Sensing, 58*(6), 3955–3964. https://doi.org/10.1109/TGRS.2019.2959715.

Clarizia, M. P., Ruf, C., Gommenginger, C., & Jales, P. (2014). Spaceborne GNSS-R minimum variance wind speed estimator. *IEEE Transactions on Geoscience and Remote Sensing, 52*(11), 6829–6843.

Freilich, M., & Challenor, P. (December 1994). A new approach for determining fully empirical altimeter wind speed model functions. *Geophysical Research: Oceans (1978–2012), 99*(C12), 25051–25062. https://doi.org/10.1029/94JC01996.

Gleason, S., Ruf, C. S., Clarizia, M. P., & O'Brien, A. J. (2016). Calibration and unwrapping of the normalized scattering cross section for the Cyclone Global Navigation Satellite System (CYGNSS). *IEEE Transactions on Geoscience and Remote Sensing, 54*(5), 2495–2509. https://doi.org/10.1109/TGRS.2015.2502245.

Gleason, S., Ruf, C. S., O'Brien, A., & McKague, D. S. (2018). The CYGNSS Level 1 calibration algorithm and error analysis based on on-orbit measurements. *IEEE Journal of Selected Topics in Applied Earth Observations and Remote Sensing, 12*(1), 37–49. https://doi.org/10.1109/JSTARS.2018.2832981.

Pascual, D., Clarizia, M. P., & Ruf, C. S. (2021). Improved CYGNSS wind speed retrieval using significant wave height correction. *Remote Sensing, 13*(21), 4313.

Ruf, C., & Balasubramaniam, R. (2018). Development of the CYGNSS geophysical model function for wind speed. *IEEE Journal of Selected Topics in Applied Earth Observations and Remote Sensing, 12*(1), 66–77. https://doi.org/10.1109/JSTARS.2018.2833075.

Ruf, C., Gleason, S., & McKague, D. S. (2018). Assessment of CYGNSS wind speed retrieval uncertainty. *IEEE Journal of Selected Topics in Applied Earth Observations and Remote Sensing, 12*(1), 87–97. https://doi.org/10.1109/JSTARS.2018.2825948.

Appendix 7A: Retrieval Performance Assessment Using On-Orbit Observations

7A.1. FDS Wind Speed Validation and Performance Characterization

FDS wind speed retrieval performance is assessed by comparing the retrieved wind speed to near-coincident matchup wind speeds by ERA5. The matchup population consists of all samples during the period January 1, 2019–December 31, 2019, after the removal of samples for which the fatal quality control flag has been set. Figure 7A1 shows log density scatterplots of the retrieved FDS versus reference ERA5 wind speeds both before (left) and after (right) the SWH-dependent bias correction is applied. The correction both tightens the alignment of samples near the 1:1 (black) line of perfect agreement and improves performance at higher wind speeds.

Figure 7A2 shows the bias and root mean square difference (RMSD) of the FDS MV retrieval versus ERA5 wind speed, again both before (left) and after (right) the SWH-dependent bias correction is applied.

The bias and RMSD are both significantly reduced—in particular, at higher wind speeds—by the SWH-dependent bias correction. Further information about the performance of the v3.1 algorithm can be found in Pascual et al. (2021). Complete tables of wind speed retrieval uncertainty and residual biases (after the SWH-dependent bias correction is applied) are provided in Table B3.

7A.2. YSLF Wind Speed Validation and Performance Characterization

The YSLF wind speed product is assessed in a similar manner, by comparisons with near-coincident matchups with wind speeds produced by the NOAA HWRF model, using all storm overpasses during August–October 2018. A density scatterplot comparing YSLF winds to near-coincident winds modeled by HWRF and a plot of YSLF retrieval RMSD versus HWRF wind speed are shown in Figure 7A3. Details concerning assembly of the matchup population are provided in Section 7.4.2. In Figure 7A3, there is considerable scatter about the 1:1 line of perfect agreement between the retrieved and reference wind speeds. This results largely from the additive noise present in the Level 1 (L1) observations from which the Level 2 (L2) wind speeds are retrieved. The L1 noise is amplified by the inverse slope of the GMF, which becomes very shallow at higher wind speeds (see Figure 7.7).

The effects of noise present in individual L2 wind speed samples can be reduced by restricting the samples considered to be those with higher values of range corrected gain (RCG). In general, RCG partitions the data by received signal strength as determined by the receive antenna gain and signal propagation distance. All available samples are included in Figure 7A3 (i.e., RCG > 1). If only the subset of high signal strength samples for which RCG > 100 are considered, the resulting scatterplot and RMSD are shown in Figure 7A4.
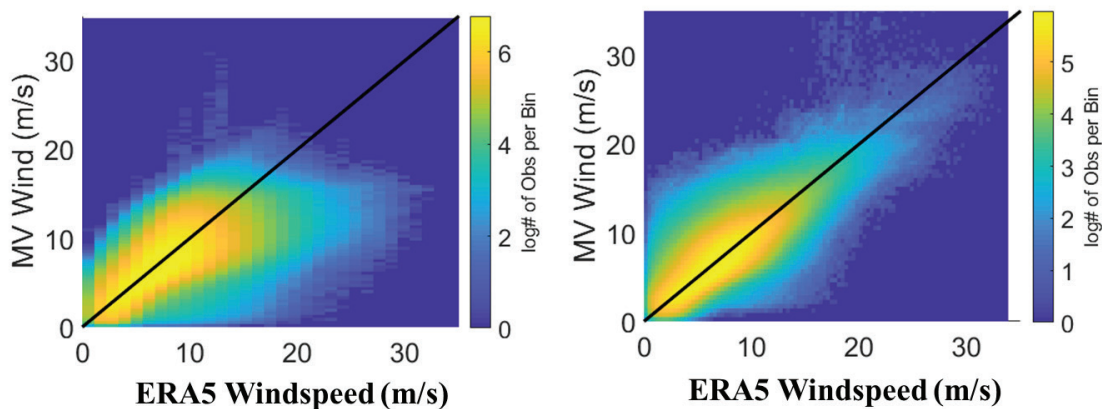
Figure 7A1. FDS minimum variance (MV) wind speed retrieval scatterplots before (left) and after (right) SWH-dependent bias correction versus ERA5 wind speed.
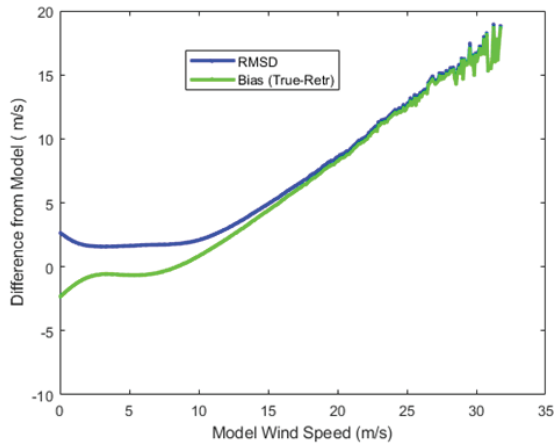
Before SWH Correction

RMSD < 20 m/s: 2.1 m/s
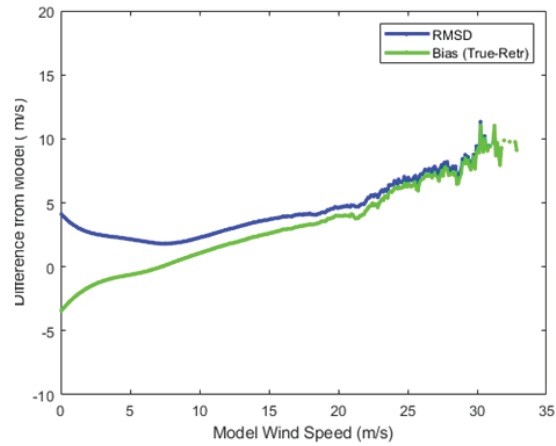
After SWH Correction

RMSD < 20 m/s: 1.7 m/s

Figure 7A2. FDS MV wind speed retrieval bias and RMSD before (left) and after (right) SWH-dependent bias correction versus ERA5 wind speed.
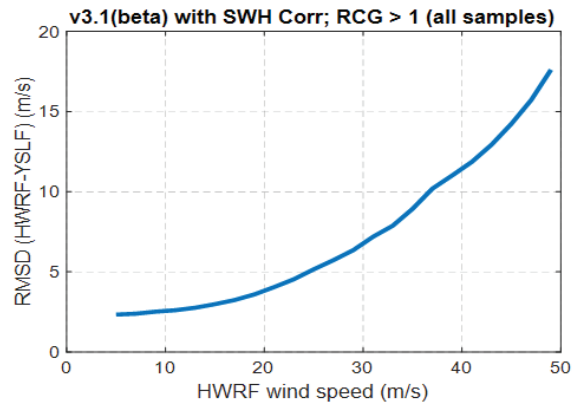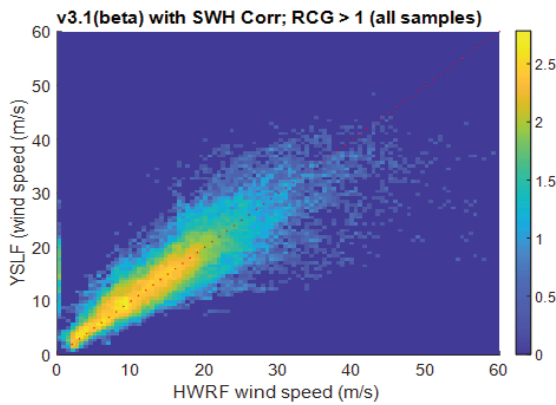
Figure 7A3. L2 YSLF wind speed versus HWRF for complete 2018 matchup population.
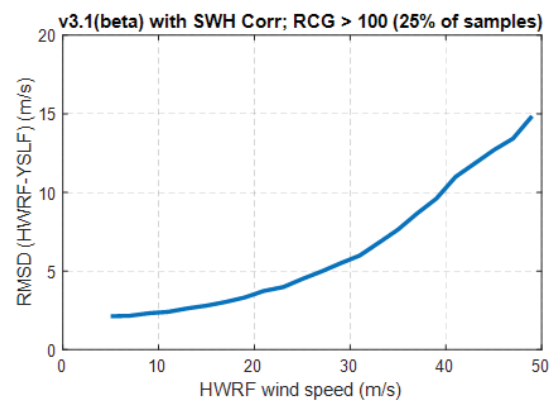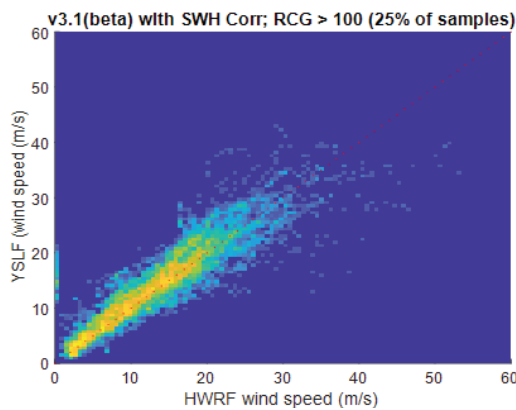
Figure 7A4. L2 YSLF wind speed versus HWRF for subset of 2018 matchup population with RCG > 100.

Appendix 7B: Implementation of On-Orbit Wind Speed Retrieval Algorithm

7B.1. Choice of Delay-Doppler Range for Observable Calculation

A very important aspect of the computation of DDMA and LES is the delay and Doppler range, over which the observables are computed. The choice of the delay and Doppler ranges is a trade-off between the improvement in SNR that results from averaging across more of the diffuse scattered signal in the glistening zone versus the improvement in spatial resolution that results from only averaging over a limited region. The delay and Doppler range depends on the requirement on spatial resolution that one wishes to comply with. For CYGNSS, the baseline requirement on the spatial resolution of the retrieved winds is 25 km × 25 km, and therefore this is the spatial resolution we focus on. Figure 7B1 illustrates two examples of how, for a spatial resolution requirement of 25 × 25 km, the corresponding delay and Doppler range varies. Note that the iso-range ellipses become closer to each other as the delay increases; furthermore, they widen and stretch out with increasing incidence angles without changing their orientation, so the geometrical parameter that mostly influences the configuration of the iso-delay lines is the incidence angle. In the case of iso-Doppler lines, the spacing between them also increases with increasing incidence angle, but they are also strongly affected by the velocity vectors of the transmitter and, above all, of the receiver, which change their orientation.

Figure 7B2 shows curves of the square root of the instantaneous field of view (IFOV) versus the incidence angle for different delay ranges. All the delay ranges considered begin one delay sample before the 0 chip sample to improve the SNR, since the samples adjacent to the specular point one still contain a good amount of

the scattered power from the specular point pixel due to the power spreading caused by the Woodward ambiguity function (WAF). The IFOV is defined here as the physical area included in the iso-range ellipse corresponding to a given delay. It is clear from Figure 7B2 that for a 25 km × 25 km requirement on the spatial resolution (shown as black continuous line), the only suitable choice is a delay range from −0.25 to 0.25.

After selecting the delay range, the Doppler range has to be chosen such that the iso-Doppler lines will not truncate some of the scattered signal within the iso-delay ellipse at 0.25 chips but also will not lie too far from the iso-delay ellipse at 0.25 chips and introduce additional noise without adding more signal. Hence the Doppler range is then chosen to try to satisfy the following two conditions:

- iso-Doppler lines are the closest possible to the iso-delay line selected
- iso-Doppler lines are always outside the iso-delay line selected

Since the iso-delay ellipses change depending on geometry and iso-Doppler lines change their distance to one another and their orientation for different geometries (as shown in Figure 7B1), the Doppler range that satisfies the above conditions for a given iso-delay line is not unique and depends on the particular geometry. Furthermore, the Doppler range has an overall much lower influence on the final IFOV, as is illustrated in Figure 7B3, where curves of square root of IFOV versus incidence angle are shown for a single delay range and a number of different Doppler ranges. It is interesting to observe that the first case of the Doppler range of [−250 250] Hz is different from the others and noisier, since the very small Doppler range chops off part of the area within the iso-delay ellipse at 0.25 chips. Instead, small differences can be observed for the other cases, and mostly at lower incidence angles. This happens because at higher incidence angles, the iso-Doppler lines
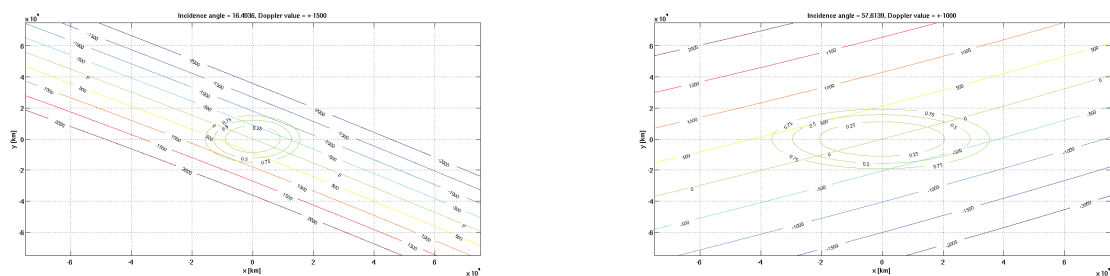
Figure 7B1. Iso-delay and iso-Doppler lines for an incidence angle of 16.5° (left) and of 57.6° (right).
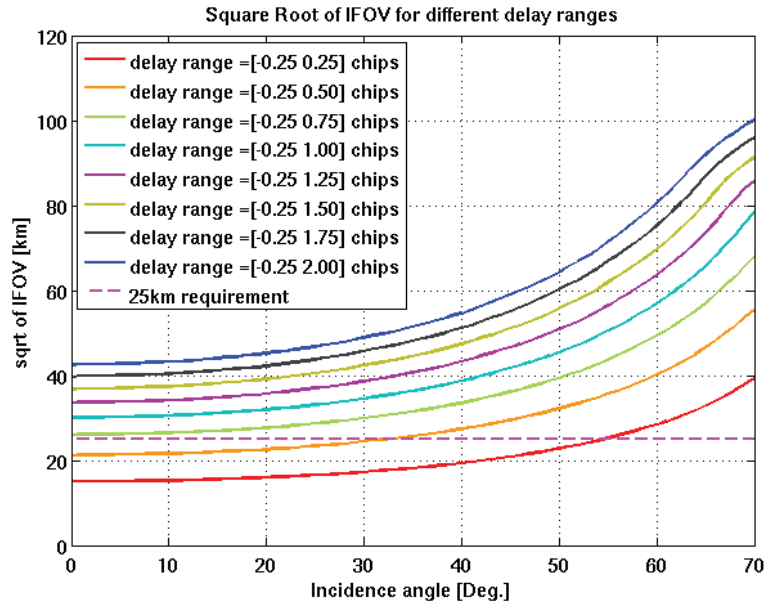
Figure 7B2. Illustration of curves of square root of IFOV versus incidence angle for a variety of delay ranges. The dashed magenta line shows the 25 km requirement.
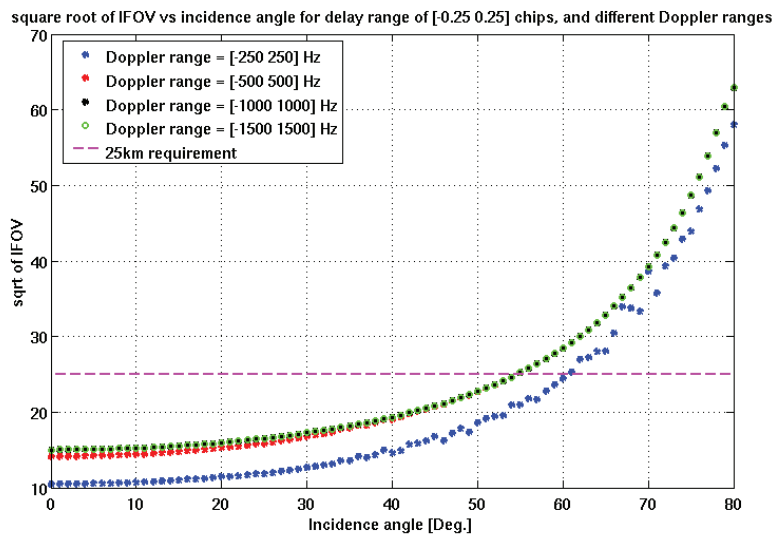
Figure 7B3. Illustration of curves of square root of IFOV versus incidence angle for a fixed delay range of [−0.25 0.25] chips and different Doppler ranges. The dashed magenta line shows the 25 km requirement.

stretch out more rapidly than the iso-delay lines and tend to fall quickly outside the 0.25 iso-delay ellipse; thus, the IFOV for higher incidence angles is entirely determined by the delay range. Furthermore, there is no difference in the IFOV between the [−1000 1000] Hz Doppler range and the [−1500 1500] Doppler range, suggesting that these iso-Doppler lines fall outside the 0.25 chip iso-delay lines for all geometries.

Thus, the final choice has been for a Doppler range of [−1000 1000] Hz. This choice has then been confirmed by applying the full L2 retrieval algorithm to DDMA observables computed using the three different Doppler ranges and by verifying that the Doppler range of [−1000 1000] is the one providing the lowest RMS error among the three.

Note that in this case, only the physical area included in the iso-delay and iso-Doppler lines is considered.

Several additional factors need to be taken into account in order to properly relate the delay and Doppler ranges to the spatial region. These include the following: (1) The spatial boundaries defined by lines of constant iso-delay and iso-Doppler do not conform to a line of constant iso-distance from the specular point. An effective spatial resolution—based, for example, on equal area coverage—needs to be defined. (2) The Woodward ambiguity function and Doppler filter impulse response define weighted response functions for the contribution of different regions of the delay-Doppler domain to the measurements. These weightings should also be accounted for by a suitable definition of the effective spatial resolution. (3) Multiple samples of the DDM can be averaged together in ground processing to reduce measurement noise. This will produce spatial smearing in the direction of motion of the specular point. Each of these factors will be included in a more complete definition of the spatial resolution, which is currently under development.

7B.2. Derivation of Coefficients for Minimum Variance Estimator

The coefficients to combine wind estimates from different observables to form a minimum variance estimator are given by Clarizia et al. (2014):

$$m = \left(\sum_{i=1}^{N} \sum_{j=1}^{N} c_{i,j}^{-1} \right)^{-1} C^{-1} 1 \, , \tag{7B1}$$

where 1 is a vector of ones, C^{-1} is the inverse of the covariance matrix between the individual retrieval errors, and $c_{i,j}^{-1}$ are its elements. The variance of the MV estimator is given by

$$\sigma_{MV}^{2} = \left(\sum_{i=1}^{N} \sum_{j=1}^{N} c_{i,j}^{-1} \right)^{-1} . \tag{7B2}$$

The MV estimator requires knowledge of the covariance matrix of the individual retrieval errors. The covariance is estimated empirically from the retrieval errors and can be factored into two component matrices as

$$C = SRS \, , \tag{7B3}$$

where S is a diagonal matrix of standard deviations of the retrieval errors for each observable (i.e., the square root of the diagonal elements of the covariance matrix) and R is the matrix of correlation coefficients, whose elements are always between −1 and 1.

In practice, the correlation between DDMA and LES retrieval errors is found to vary as a function of the SNR and wind speed of the measurements. For this reason, the covariance matrix assumed by the estimator is varied accordingly in a manner referred to as adaptive covariance (AC). This approach consists of estimating a different covariance matrix, and therefore a different pair of coefficients for the linear combination, for different ranges of the wind speed. The wind speed, taken as the mean of the mean of the LES and DDMA winds in 0.1 m/s bins from 0 to 70 m/s and the estimator with the AC approach included becomes

$$u_{MV}^{i} = m^{i} \cdot u^{i} \; WS_{low} < WS < WS_{high}, \tag{7B4}$$

where i refers to each of the wind speed intervals used to compute the coefficients in the linear combination, m is the vector of coefficients defined in (1), and u is the vector of wind speed estimates from DDMA and LES.

The covariance matrices used to compute the best weighted estimate coefficients are derived empirically from the population of retrievals, since neither the individual probability density functions (PDFs) of DDMA and LES wind retrieval errors nor the joint PDF between the two retrieval errors is available in analytical form. The bias between true and retrieved winds is first computed for each observable and for each wind speed interval and then removed so as to compute the coefficients from unbiased DDMA and LES wind estimates. The coefficients m as well as the bias are calculated from the training dataset (50% of data), where the true wind speeds are known, and then used in the test dataset, where the wind speeds are not known, to assess algorithm performance. This means that the coefficients may be suboptimal when applied to the test dataset, but we expect the performance to be asymptotically optimal for an increasing number of observations, assuming that the statistical properties of the training dataset are the same as those of the test dataset.

7B.3. Minimum Variance Coefficients LUT

The coefficients used to combine the DDMA and LES wind estimates to obtain the final estimated wind are reported in Figure 7B4 as a function of the mean DDMA, LES-retrieved wind speed for the Sensor Data Record (SDR) (a) and CDR (b) L2 products. These coefficients are currently being used by the algorithm implemented in the SOC and

a. SDR

b. CDR
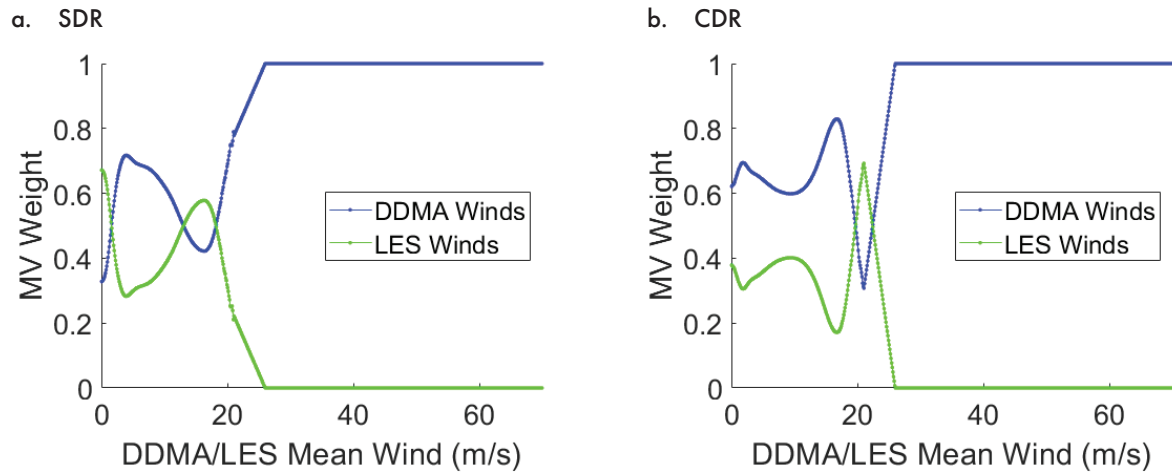
Figure 7B4. Minimum variance coefficients for v3.1 SDR (a) and CDR (b) wind speed retrievals as a function of the mean DDMA/LES-retrieved wind. These were derived from matchups with ERA5 data for 2019.

a. SDR

b. CDR
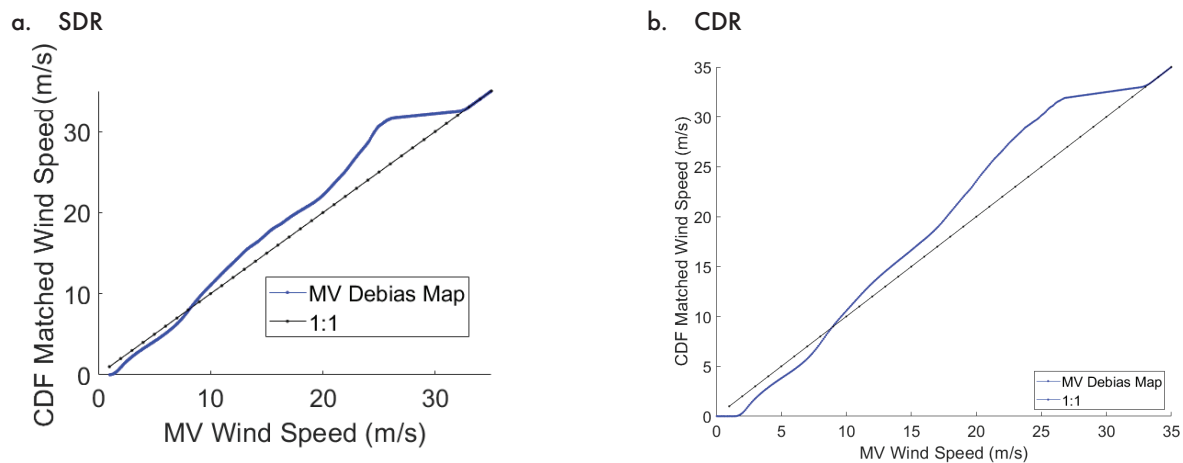
Figure 7B5. Debiasing coefficients used in the SDR (a) and CDR (b) retrievals to match the global probability distribution of CYGNSS L2 fully developed seas minimum variance wind speeds to those of the ERA5 reanalysis numerical weather prediction product. For SDR estimates, separate maps are used for each CYGNSS/GPS transmitter pair, with Flight Model (FM) 1 starboard antenna, SVN 63 shown here (others similar). The same LUT is used for all pairs for the CDR retrievals.

to produce version 3.1 of the wind product. They have been derived from retrieval matchups with ERA5 data for 2019.

7B.4. Debiasing LUT

CDF-matching lookup tables (LUTs) are derived to debias the retrieved FDS winds relative to model-based estimates from ERA5 matched to the data for the 2019 retrievals. Separate tables are developed for the SDR and CDR minimum variance wind speed estimates in 0.1 m/s intervals from 0 to 70 m/s. For the SDR winds, separate LUTs are used for each GPS/CYGNSS transmitter/receiver

pair, while a single LUT is used for all pairs with CDR winds (since the trackwise debiasing removes dependence on the pair). The LUT of debiasing coefficients used by the FDS MV wind speed retrieval algorithm is shown in Figure 7B5. Coefficients that lie along the 45° "one-to-one" line represent wind speed ranges where the probability distributions already match well and no adjustment is needed. Coefficients above and below the 1:1 line represent remappings where a range of retrieved wind speeds is compressed or expanded to more closely match the likelihood of occurrence of the model wind speed for the same wind speed interval.

7B.5. Time-Averaging LUT

The time-averaging LUT contains the number of samples to time average as a function of incidence angle. The incidence angle axis is defined as going from 0° to 89° with a step of 1°. Values are reported in Table 7B1 for specific incidence angle intervals.

7B.6. Standard Deviation of the Retrieval Error LUT

The standard deviation (uncertainty) and mean (bias) error in the retrieved wind associated with each GPS block type, RCG, incidence angle, and wind speed interval are reported in Table 7B2 for FDS winds and Table 7B3 for YSLF winds. The values are empirically derived from statistical comparisons between retrieved winds and matchup ground truth winds provided by ERA5 (for the FDS MV retrievals) and by HWRF (for the YSLF retrievals at the higher wind speed intervals).

Table 7B1. Number of Samples to Time Average as a Function of Incidence Angle

Number of samples to time average	Incidence angle interval (°)
5	$0° < \theta \leq 17°$
4	$17° < \theta \leq 31°$
3	$31° < \theta \leq 41°$
2	$41° < \theta \leq 48°$
1	$\theta > 48°$

Table 7B2. Uncertainty and Bias of FDS MV Wind Speed Retrieval Error

Uncertainty table—block IIA (SVN = 34)

Minimum variance wind speed range	Incidence angle ≤ 10°		
	$RCG \leq 10$	$10 < RCG \leq 60$	$60 < RCG$
$0 < u_{MV} \leq 5$ m/s	1.5	1.5	1.5
$5 < u_{MV} \leq 10$ m/s	1.5	1.5	1.5
$10 < u_{MV} \leq 15$ m/s	2.0	2.0	2.0
$15 < u_{MV} \leq 20$ m/s	2.5	2.5	2.5
$20 < u_{MV} \leq 25$ m/s	3.5	3.5	3.5
25 m/s $< u_{MV}$	5.0	5.0	5.0
Minimum variance wind speed range	**Incidence 10° < incidence angle ≤ 60°**		
	$RCG \leq 10$	$10 < RCG \leq 60$	$60 < RCG$
$0 < u_{MV} \leq 5$ m/s	1.5	1.5	1.5
$5 < u_{MV} \leq 10$ m/s	1.5	1.5	1.5
$10 < u_{MV} \leq 15$ m/s	1.5	1.5	1.5
$15 < u_{MV} \leq 20$ m/s	2.0	2.0	2.0
$20 < u_{MV} \leq 25$ m/s	3.0	3.0	3.0
25 m/s $< u_{MV}$	5.0	5.0	5.0
Minimum variance wind speed range	**60°< incidence angle**		
	$RCG \leq 10$	$10 < RCG \leq 60$	$60 < RCG$
$0 < u_{MV} \leq 5$ m/s	1.5	1.5	1.5
$5 < u_{MV} \leq 10$ m/s	1.5	1.5	1.5
$10 < u_{MV} \leq 15$ m/s	1.5	1.5	1.5
$15 < u_{MV} \leq 20$ m/s	2.0	2.0	2.0
$20 < u_{MV} \leq 25$ m/s	3.0	3.0	3.0
25 m/s $< u_{MV}$	5.0	5.0	5.0

Table 7B2. Uncertainty and Bias of FDS MV Wind Speed Retrieval Error (*continued*)
Uncertainty table—block IIR-legacy (SVN = 41, 43, 44, 45, 46, 51, 54, 56)

Minimum variance wind speed range	Incidence angle ≤ 10°		
	RCG ≤ 10	*10 < RCG ≤ 60*	*60 < RCG*
0 < u_{MV} ≤ 5 m/s	1.5	1.5	1.5
5 < u_{MV} ≤ 10 m/s	1.5	1.5	1.5
10 < u_{MV} ≤ 15 m/s	2.0	2.0	2.0
15 < u_{MV} ≤ 20 m/s	2.5	2.5	2.5
20 < u_{MV} ≤ 25 m/s	2.5	2.5	2.5
25 m/s < u_{MV}	4.0	4.0	4.0
Minimum variance wind speed range	Incidence 10° < incidence angle ≤ 60°		
	RCG ≤ 10	*10 < RCG ≤ 60*	*60 < RCG*
0 < u_{MV} ≤ 5 m/s	1.5	1.5	1.5
5 < u_{MV} ≤ 10 m/s	1.5	1.5	1.5
10 < u_{MV} ≤ 15 m/s	2.0	2.0	2.0
15 < u_{MV} ≤ 20 m/s	2.5	2.5	2.5
20 < u_{MV} ≤ 25 m/s	2.5	2.5	2.5
25 m/s < u_{MV}	4.0	4.0	4.0
Minimum variance wind speed range	60° < incidence angle		
	RCG ≤ 10	*10 < RCG ≤ 60*	*60 < RCG*
0 < u_{MV} ≤ 5 m/s	1.5	1.5	1.5
5 < u_{MV} ≤ 10 m/s	1.5	1.5	1.5
10 < u_{MV} ≤ 15 m/s	2.0	2.0	2.0
15 < u_{MV} ≤ 20 m/s	3.0	3.0	3.0
20 < u_{MV} ≤ 25 m/s	3.5	3.5	3.5
25 m/s < u_{MV}	3.5	3.5	3.5

Table 7B2. Uncertainty and Bias of FDS MV Wind Speed Retrieval Error (*continued*)
Uncertainty table—block IIR improved (SVN = 47, 59, 60, 61)

Minimum variance wind speed range	Incidence angle ≤ 10°		
	$RCG \leq 10$	$10 < RCG \leq 60$	$60 < RCG$
$0 < u_{MV} \leq 5$ m/s	1.5	1.5	1.5
$5 < u_{MV} \leq 10$ m/s	1.5	1.5	1.5
$10 < u_{MV} \leq 15$ m/s	1.5	1.5	1.5
$15 < u_{MV} \leq 20$ m/s	2.0	2.0	2.0
$20 < u_{MV} \leq 25$ m/s	3.0	3.0	3.0
25 m/s $< u_{MV}$	3.5	3.5	3.5
Minimum variance wind speed range	Incidence 10° < incidence angle ≤ 60°		
	$RCG \leq 10$	$10 < RCG \leq 60$	$60 < RCG$
$0 < u_{MV} \leq 5$ m/s	1.5	1.5	1.5
$5 < u_{MV} \leq 10$ m/s	1.5	1.5	1.5
$10 < u_{MV} \leq 15$ m/s	1.5	1.5	1.5
$15 < u_{MV} \leq 20$ m/s	2.0	2.0	2.0
$20 < u_{MV} \leq 25$ m/s	3.0	3.0	3.0
25 m/s $< u_{MV}$	3.0	3.0	3.0
Minimum variance wind speed range	60° < incidence angle		
	$RCG \leq 10$	$10 < RCG \leq 60$	$60 < RCG$
$0 < u_{MV} \leq 5$ m/s	1.5	1.5	1.5
$5 < u_{MV} \leq 10$ m/s	1.5	1.5	1.5
$10 < u_{MV} \leq 15$ m/s	1.5	1.5	1.5
$15 < u_{MV} \leq 20$ m/s	2.0	2.0	2.0
$20 < u_{MV} \leq 25$ m/s	3.5	3.5	3.5
25 m/s $< u_{MV}$	6.0	4.5	4.5

Table 7B2. Uncertainty and Bias of FDS MV Wind Speed Retrieval Error (*continued*)
Uncertainty table—block IIR-M (SVN = 48, 50, 52, 53, 55, 57, 58)

Minimum variance wind speed range	Incidence angle ≤ 10°		
	RCG ≤ 10	*10 < RCG ≤ 60*	*60 < RCG*
0 < u_{MV} ≤ 5 m/s	1.5	1.5	1.5
5 < u_{MV} ≤ 10 m/s	1.5	1.5	1.5
10 < u_{MV} ≤ 15 m/s	1.5	1.5	1.5
15 < u_{MV} ≤ 20 m/s	2.0	2.0	2.0
20 < u_{MV} ≤ 25 m/s	2.5	2.5	2.5
25 m/s < u_{MV}	4.5	4.5	4.5

Minimum variance wind speed range	Incidence 10° < incidence angle ≤ 60°		
	RCG ≤ 10	*10 < RCG ≤ 60*	*60 < RCG*
0 < u_{MV} ≤ 5 m/s	1.5	1.5	1.5
5 < u_{MV} ≤ 10 m/s	1.5	1.5	1.5
10 < u_{MV} ≤ 15 m/s	1.5	1.5	1.5
15 < u_{MV} ≤ 20 m/s	2.0	2.0	2.0
20 < u_{MV} ≤ 25 m/s	2.5	2.5	2.5
25 m/s < u_{MV}	3.5	3.5	3.5

Minimum variance wind speed range	60° < incidence angle		
	RCG ≤ 10	*10 < RCG ≤ 60*	*60 < RCG*
0 < u_{MV} ≤ 5 m/s	1.5	1.5	1.5
5 < u_{MV} ≤ 10 m/s	1.5	1.5	1.5
10 < u_{MV} ≤ 15 m/s	1.5	1.5	1.5
15 < u_{MV} ≤ 20 m/s	2.0	2.0	2.0
20 < u_{MV} ≤ 25 m/s	2.5	2.5	2.5
25 m/s < u_{MV}	4.0	4.0	4.0

Table 7B2. Uncertainty and Bias of FDS MV Wind Speed Retrieval Error (*continued*)
Uncertainty table—block IIF (SVN = 62, 63, 64, 65, 66, 67, 68, 69, 70, 71, 72, 73)

Minimum variance wind speed range	Incidence angle ≤ 10°		
	RCG ≤ 10	*10 < RCG ≤ 60*	*60 < RCG*
$0 < u_{MV} \leq 5$ m/s	1.5	1.5	1.5
$5 < u_{MV} \leq 10$ m/s	1.5	1.5	1.5
$10 < u_{MV} \leq 15$ m/s	1.5	1.5	1.5
$15 < u_{MV} \leq 20$ m/s	2.0	2.0	2.0
$20 < u_{MV} \leq 25$ m/s	2.5	2.5	2.5
25 m/s $< u_{MV}$	3.0	3.0	3.0
Minimum variance wind speed range	**Incidence 10° < incidence angle ≤ 60°**		
	RCG ≤ 10	*10 < RCG ≤ 60*	*60 < RCG*
$0 < u_{MV} \leq 5$ m/s	1.5	1.5	1.5
$5 < u_{MV} \leq 10$ m/s	1.5	1.5	1.5
$10 < u_{MV} \leq 15$ m/s	1.5	1.5	1.5
$15 < u_{MV} \leq 20$ m/s	2.0	2.0	2.0
$20 < u_{MV} \leq 25$ m/s	2.5	2.5	2.5
25 m/s $< u_{MV}$	4.0	4.0	4.0
Minimum variance wind speed range	**60° < incidence angle**		
	RCG ≤ 10	*10 < RCG ≤ 60*	*60 < RCG*
$0 < u_{MV} \leq 5$ m/s	1.5	1.5	1.5
$5 < u_{MV} \leq 10$ m/s	1.5	1.5	1.5
$10 < u_{MV} \leq 15$ m/s	1.5	1.5	1.5
$15 < u_{MV} \leq 20$ m/s	2.5	2.5	2.5
$20 < u_{MV} \leq 25$ m/s	3.0	3.0	3.0
25 m/s $< u_{MV}$	4.5	4.5	4.5

Table 7B2.   Uncertainty and Bias of FDS MV Wind Speed Retrieval Error (*continued*)
Bias table—block IIA (SVN = 34)

Minimum variance wind speed range	Incidence angle ≤ 10°		
	Roll = – 10 °	*Roll = 0 °*	*Roll = +10 °*
0 < u$_{MV}$ ≤ 5 m/s	0.3	0.3	–0.6
5 < u$_{MV}$ ≤ 10 m/s	0.0	0.1	–0.8
10 < u$_{MV}$ ≤ 15 m/s	–1.1	–0.8	–1.7
15 < u$_{MV}$ ≤ 20 m/s	–3.3	–1.5	–2.4
20 < u$_{MV}$ ≤ 25 m/s	–4.2	–2.4	–3.3
25 m/s < u$_{MV}$	–5.0	–4.8	–5.0
Minimum variance wind speed range	Incidence 10° < incidence angle ≤ 60°		
	Roll = – 10°	*Roll = 0°*	*Roll = +10°*
0 < u$_{MV}$ ≤ 5 m/s	0.7	0.5	1.0
5 < u$_{MV}$ ≤ 10 m/s	0.3	0.1	–0.3
10 < u$_{MV}$ ≤ 15 m/s	–0.9	–0.9	–1.2
15 < u$_{MV}$ ≤ 20 m/s	–1.6	–1.7	–2.0
20 < u$_{MV}$ ≤ 25 m/s	–2.3	–2.4	–3.7
25 m/s < u$_{MV}$	–3.7	–3.8	–4.2
Minimum variance wind speed range	60° < incidence angle		
	Roll = – 10 °	*Roll = 0 °*	*Roll = +10 °*
0 < u$_{MV}$ ≤ 5 m/s	0.5	0.3	0.9
5 < u$_{MV}$ ≤ 10 m/s	–0.1	–0.3	–0.8
10 < u$_{MV}$ ≤ 15 m/s	–1.0	–1.2	–2.2
15 < u$_{MV}$ ≤ 20 m/s	–2.3	–2.5	–3.5
20 < u$_{MV}$ ≤ 25 m/s	–4.7	–4.9	–5.0
25 m/s < u$_{MV}$	–5.0	5.0	–5.0

Table 7B2. Uncertainty and Bias of FDS MV Wind Speed Retrieval Error (*continued*)
Bias table—block IIR-legacy (SVN = 41, 43, 44, 45, 46, 51, 54, 56)

Minimum variance wind speed range	Incidence angle ≤ 10°		
	Roll = – 10 °	*Roll = 0 °*	*Roll = +10 °*
$0 < u_{MV} \leq 5$ m/s	0.3	0.7	0.3
$5 < u_{MV} \leq 10$ m/s	0.2	0.6	0.0
$10 < u_{MV} \leq 15$ m/s	−1.0	−0.9	−0.8
$15 < u_{MV} \leq 20$ m/s	−1.4	−1.6	−1.5
$20 < u_{MV} \leq 25$ m/s	−2.0	−2.2	−2.1
25 m/s $< u_{MV}$	−2.6	−2.8	−2.7
Minimum variance wind speed range	Incidence 10° < incidence angle ≤ 60°		
	Roll = – 10°	*Roll = 0°*	*Roll = +10°*
$0 < u_{MV} \leq 5$ m/s	0.8	0.5	0.5
$5 < u_{MV} \leq 10$ m/s	0.2	0.1	−0.2
$10 < u_{MV} \leq 15$ m/s	−1.2	−1.0	−1.1
$15 < u_{MV} \leq 20$ m/s	−1.6	−1.8	−2.9
$20 < u_{MV} \leq 25$ m/s	−1.8	−1.8	−2.9
25 m/s $< u_{MV}$	−3.4	−3.4	−4.5
Minimum variance wind speed range	60° < incidence angle		
	Roll = – 10°	*Roll = 0°*	*Roll = +10°*
$0 < u_{MV} \leq 5$ m/s	0.6	0.4	0.8
$5 < u_{MV} \leq 10$ m/s	0.2	−0.2	−0.3
$10 < u_{MV} \leq 15$ m/s	−1.6	−1.2	−1.5
$15 < u_{MV} \leq 20$ m/s	−1.7	−1.9	−2.2
$20 < u_{MV} \leq 25$ m/s	−0.3	−0.5	−0.8
25 m/s $< u_{MV}$	0.1	−0.1	−0.4

Table 7B2. Uncertainty and Bias of FDS MV Wind Speed Retrieval Error (*continued*)
Bias table—block IIR improved (SVN = 47, 59, 60, 61)

Minimum variance wind speed range	Incidence angle ≤ 10°		
	Roll = – 10 °	*Roll = 0 °*	*Roll = +10 °*
$0 < u_{MV} \leq 5$ m/s	0.2	0.3	0.3
$5 < u_{MV} \leq 10$ m/s	−0.3	−0.1	−0.4
$10 < u_{MV} \leq 15$ m/s	−0.6	−1.1	−0.7
$15 < u_{MV} \leq 20$ m/s	−1.8	−2.3	−1.9
$20 < u_{MV} \leq 25$ m/s	−2.7	−3.2	−2.8
25 m/s $< u_{MV}$	−3.6	−4.1	−3.7
Minimum variance wind speed range	Incidence 10° < incidence angle ≤ 60°		
	Roll = – 10°	*Roll = 0°*	*Roll = +10°*
$0 < u_{MV} \leq 5$ m/s	0.8	0.5	0.4
$5 < u_{MV} \leq 10$ m/s	0.1	0.1	−0.4
$10 < u_{MV} \leq 15$ m/s	−1.1	−1.0	−1.0
$15 < u_{MV} \leq 20$ m/s	−1.6	−1.8	−1.9
$20 < u_{MV} \leq 25$ m/s	−2.3	−2.5	−2.8
25 m/s $< u_{MV}$	−3.0	−3.2	−3.5
Minimum variance wind speed range	60 ° < incidence angle		
	Roll = – 10°	*Roll = 0°*	*Roll = +10°*
$0 < u_{MV} \leq 5$ m/s	0.8	0.4	0.6
$5 < u_{MV} \leq 10$ m/s	0.1	−0.1	−0.4
$10 < u_{MV} \leq 15$ m/s	−1.1	−1.2	−1.2
$15 < u_{MV} \leq 20$ m/s	−2.0	−2.6	−2.6
$20 < u_{MV} \leq 25$ m/s	−2.4	−3.0	−3.0
25 m/s $< u_{MV}$	−2.8	−3.4	−3.4

Table 7B2. Uncertainty and Bias of FDS MV Wind Speed Retrieval Error (*continued*)
Bias table—block IIR-M (SVN = 48, 50, 52, 53, 55, 57, 58)

	Incidence angle ≤ 10°		
Minimum variance wind speed range	*Roll = – 10°*	*Roll = 0°*	*Roll = +10°*
$0 < u_{MV} \leq 5$ m/s	0.5	0.3	0.4
$5 < u_{MV} \leq 10$ m/s	0.4	−0.1	0.0
$10 < u_{MV} \leq 15$ m/s	−0.7	−0.8	−0.9
$15 < u_{MV} \leq 20$ m/s	−2.1	−2.2	−2.3
$20 < u_{MV} \leq 25$ m/s	−2.2	−2.3	−2.4
25 m/s $< u_{MV}$	−2.3	−2.4	−2.5
	Incidence 10° < incidence angle ≤ 60°		
Minimum variance wind speed range	*Roll = – 10°*	*Roll = 0°*	*Roll = +10°*
$0 < u_{MV} \leq 5$ m/s	0.8	0.5	0.4
$5 < u_{MV} \leq 10$ m/s	0.1	−0.1	−0.3
$10 < u_{MV} \leq 15$ m/s	−1.1	−1.2	−1.2
$15 < u_{MV} \leq 20$ m/s	−1.3	−1.5	−1.5
$20 < u_{MV} \leq 25$ m/s	−1.7	−1.9	−1.9
25 m/s $< u_{MV}$	−1.8	−2.0	−2.0
	60° < incidence angle		
Minimum variance wind speed range	*Roll = – 10°*	*Roll = 0°*	*Roll = +10°*
$0 < u_{MV} \leq 5$ m/s	0.7	0.5	0.7
$5 < u_{MV} \leq 10$ m/s	0.2	−0.1	−0.1
$10 < u_{MV} \leq 15$ m/s	−1.0	−1.1	−1.3
$15 < u_{MV} \leq 20$ m/s	−1.4	−2.0	−1.3
$20 < u_{MV} \leq 25$ m/s	−1.5	−2.1	−1.4
25 m/s $< u_{MV}$	−1.6	−2.2	−1.5

Table 7B2. Uncertainty and Bias of FDS MV Wind Speed Retrieval Error (*continued*)
Bias table—block IIF (SVN = 62, 63, 64, 65, 66, 67, 68, 69, 70, 71, 72, 73)

Minimum variance wind speed range	Incidence angle ≤ 10°		
	Roll = −10°	*Roll = 0°*	*Roll = +10°*
0 < u_{MV} ≤ 5 m/s	0.5	0.4	0.4
5 < u_{MV} ≤ 10 m/s	0.1	0.0	0.0
10 < u_{MV} ≤ 15 m/s	−1.2	−1.2	−0.9
15 < u_{MV} ≤ 20 m/s	−2.2	−2.2	−1.9
20 < u_{MV} ≤ 25 m/s	−3.2	−3.2	−2.9
25 m/s < u_{MV}	−4.2	−4.2	−3.9

Minimum variance wind speed range	Incidence 10° < incidence angle ≤ 60°		
	Roll = −10°	*Roll = 0°*	*Roll = +10°*
0 < u_{MV} ≤ 5 m/s	0.8	0.5	0.4
5 < u_{MV} ≤ 10 m/s	0.1	0.0	−0.3
10 < u_{MV} ≤ 15 m/s	−1.2	−1.1	−1.2
15 < u_{MV} ≤ 20 m/s	−1.7	−2.0	−2.7
20 < u_{MV} ≤ 25 m/s	−1.8	−2.1	−2.8
25 m/s < u_{MV}	−4.1	−4.2	−4.9

Minimum variance wind speed range	60° < incidence angle		
	Roll = −10°	*Roll = 0°*	*Roll = +10°*
0 < u_{MV} ≤ 5 m/s	0.8	0.5	0.9
5 < u_{MV} ≤ 10 m/s	0.0	−0.1	−0.2
10 < u_{MV} ≤ 15 m/s	−1.3	−1.2	−1.4
15 < u_{MV} ≤ 20 m/s	−2.4	−2.3	−3.3
20 < u_{MV} ≤ 25 m/s	−2.5	−2.4	−4.7
25 m/s < u_{MV}	−4.5	−4.4	−5.0

Table 7B3. Uncertainty of YSLF Wind Speed Retrieval Error

YSLF wind speed range	RCG ≤ 10	10 < RCG ≤ 50	50 < RCG ≤ 100	100 < RCG ≤ 150	150 < RCG
0 < u ≤ 20 m/s	3.0	3.0	3.0	2.0	2.0
20 < u ≤ 30 m/s	7.0	6.0	5.0	4.0	3.0
30 < u ≤ 40 m/s	10.0	8.0	7.0	5.0	4.0
40 < u ≤ 50 m/s	15.0	12.0	9.0	7.0	5.0
50 m/s < u	20.0	15.0	11.0	8.0	6.0

7B.7. L2 Data Dictionary

Table 7B4 lists all the variables in the L2 wind speed netCDF files.

Table 7B4. List of Data Fields Contained in the L2 Wind Retrieval Data Files

Name	Long name	netCDF type	CF conventions units	netCDF dimensions	Comment
Global values					
time_coverage_start	<none>	file attribute, string	<none>	<none>	sample_time of the first sample in the file in ISO-8601 form
time_coverage_end	<none>	file attribute, string	<none>	<none>	sample_time of the last sample in the file in ISO-8601 form
time_coverage_duration	<none>	file attribute, string	<none>	<none>	The time interval between test_coverage_start and test_coverage_end in ISO-1806 form
time_coverage_resolution	<none>	file attribute, string	<none>	<none>	The nominal time interval between samples in ISO-1806 form
ddm_source	Level 0 data source	byte	<none>	<none>	The source of the Level 0 DDM raw counts and metadata utilized to derive wind_speed. 0 = E2ES (CYGNSS end-to-end simulator) 1 = GPS signal simulator 2 = CYGNSS spacecraft 3 = Source unknown
nbrcs_les_sel_lookup_tables_version	<none>	file attribute, string	<none>	<none>	The GMF NBRCS and LES selection lookup table version number
time_averaging_lookup_tables_version	<none>	file attribute, string	<none>	<none>	The GMF time-averaging lookup table version number
nbrcs_wind_lookup_tables_version	<none>	file attribute, string	<none>	<none>	The GMF NBRCS to wind speed lookup table version number
les_wind_lookup_tables_version	<none>	file attribute, string	<none>	<none>	The GMF LES to wind speed lookup table version number
covariance_lookup_tables_version	<none>	file attribute, string	<none>	<none>	The GMF minimum covariance lookup table version number
standard_deviation_lookup_table_version	<none>	file attribute, string	<none>	<none>	The GMF standard deviation lookup table version number
l2_algorithm_version	<none>	file attribute, string	<none>	<none>	L2 processing algorithm version number
source	<none>	file attribute, string	<none>	<none>	L1 netCDF source file names

(continued)

Table 7B4. List of Data Fields Contained in the L2 Wind Retrieval Data Files (*continued*)

Name	Long name	netCDF type	CF conventions units	netCDF dimensions	Comment
Per-sample values					
spacecraft_id	CCSDS spacecraft identifier	short	1	sample	The CCSDS spacecraft identifier: 0xF7 (247): CYGNSS 1 0xF9 (249): CYGNSS 2 0x2B (43): CYGNSS 3 0x2C (44): CYGNSS 4 0x2F (47): CYGNSS 5 0x36 (54): CYGNSS 6 0x37 (55): CYGNSS 7 0x49 (73): CYGNSS 8 0x00 (0): E2ES 0x0E (14): engineering model 0x0D (15): default 0xFF (255): unknown
spacecraft_num	CYGNSS spacecraft number	byte	1	sample	The CYGNSS spacecraft number: Ranges from 1 through 8 and 99; 1 through 8 are on-orbit spacecraft; 99 is the CYGNSS end-to-end simulator
prn_code	GPS PRN code	byte	1	sample	The PRN code of the GPS signal associated with the DDMs utilized to derive wind_speed. Ranges from 0 to 32; 0 = reflectometry channel idle; 1 to 32 represents PRN code
sv_num	GPS space vehicle number	short	1	sample	The GPS unique space vehicle number that transmitted prn_code
antenna	Receive antenna	byte	\<none\>	sample	The CYGNSS nadir antenna that received the reflected GPS signal associated with the DDMs utilized to derive wind_speed 0 = none 1 = zenith (never used) 2 = nadir_starboard 3 = nadir_port
sample_time	Sample time	double	seconds since time_ coverage_ start	sample	The mean of ddm_timestamp_utc of the DDMs that were utilized to derive wind_speed. Note that the DDM sampling period is not synchronized with the UTC change of second, so sample_time can occur at any time relative to the UTC change of second.
lat	Latitude	float	degrees_ north	sample	The mean of the specular point latitudes of the DDMs that were utilized to derive wind_speed, ºN.
lon	Longitude	float	degrees_ east	sample	The mean of the specular point longitudes of the DDMs that were utilized to derive wind_speed, ºE.
sc_lat	Subsatellite point latitude	float	degrees_ north	sample	The mean of the subsatellite point latitudes of the DDMs that were utilized to derive wind_speed, ºN.

(continued)

Table 7B4. List of Data Fields Contained in the L2 Wind Retrieval Data Files (*continued*)

Name	Long name	netCDF type	CF conventions units	netCDF dimensions	Comment
sc_lon	Subsatellite point longitude	float	degrees_east	sample	The mean of the subsatellite point longitudes of the DDMs that were utilized to derive wind_speed, ºE.
sc_alt	Spacecraft altitude	int	meter	sample	The mean of the satellite altitudes above the WGS-84 ellipsoid of the DDMs that were utilized to derive wind_speed, meters.
wind_speed	Retrieved wind speed using minimum variance estimator applied to fully developed seas retrievals from NBRCS and LES	float	m s−1	sample	The average surface wind speed of the 25 × 25 km cell centered on latitude and longitude derived from both the NBRCS and the LES observables using the fully developed seas geophysical model function, m/s. Multiple DDMs are utilized to derive wind_speed. The number of utilized DDMs ranges from 1 to 5.
fds_nbrcs_wind_speed	Fully developed sea retrieval of wind speed from NBRCS	float	m s−1	sample	The average surface wind speed of the 25 × 25 km cell centered on latitude and longitude derived only from the NBRCS observable using the fully developed seas geophysical model function, m/s. Multiple DDMs are utilized to derive fds_nbrcs_wind_speed. The number of DDMs ranges from 1 to 5.
fds_les_wind_speed	Fully developed seas retrieval of wind speed from LES	float	m s−1	sample	The average surface wind speed of the 25 × 25 km cell centered on latitude and longitude derived only from the LES observable using the fully developed seas geophysical model function, m/s. Multiple DDMs are utilized to derive fds_les_wind_speed. The number of DDMs ranges from 1 to 5.
wind_speed_uncertainty	Uncertainty in MV FDS wind speed	float	m s−1	sample	Standard deviation of the additive wind speed error in the minimum variance fully developed seas wind speed retrieval (dependent on the RCG of the specular point location, the block type of the GPS satellite, and the wind speed), in m/s.
yslf_nbrcs_wind_speed	Young seas / limited fetch retrieval of wind speed from NBRCS	float	m s−1	sample	The surface wind speed centered on latitude and longitude derived only from the NBRCS observable using the young seas / limited fetch geophysical model function, m/s. Multiple DDMs are utilized to derive wind_speed. The number of utilized DDMs ranges from 1 to 5.

Table 7B4. List of Data Fields Contained in the L2 Wind Retrieval Data Files (*continued*)

Name	Long name	netCDF type	CF conventions units	netCDF dimensions	Comment
yslf_les_wind_speed	Young seas / limited fetch retrieval of wind speed from LES	float	m s−1	sample	The surface wind speed centered on latitude and longitude derived only from the LES observable using the young seas / limited fetch geophysical model function, m/s. Multiple DDMs are utilized to derive wind_speed. The number of utilized DDMs ranges from 1 to 5.
yslf_nbrcs_wind_speed_uncertainty	Uncertainty in NBRCS YSLF wind speed	float	m s−1	sample	Standard deviation of the additive wind speed error in yslf_nbrcs_wind_speed (dependent on the RCG of the specular point location, the block type of the GPS satellite, and the wind speed), in m/s.
yslf_les_wind_speed_uncertainty	Uncertainty in LES YSLF wind speed	float	m s−1	sample	Standard deviation of the additive wind speed error in yslf_les_wind_speed (dependent on the RCG of the specular point location, the block type of the GPS satellite, and the wind speed), in m/s.
mean_square_slope	Mean square slope (MSS)	float	1	sample	The average MSS of the 25 × 25 km cell centered on latitude and longitude, unitless.
mean_square_slope_uncertainty	Mean square slope uncertainty	float	1	sample	The uncertainty of mean_square_slope, unitless.
incidence_angle	Incidence angle	float	degree	sample	The mean of the incidence angles of the specular points of the DDMs that were utilized to derive wind_speed, degrees.
azimuth_angle	Azimuth angle	float	degree	sample	The mean of the orbit frame azimuth angles of the specular points of the DDMs that were utilized to derive wind_speed, degrees.
nbrcs_mean	NBRCS mean	float	1	sample	The mean of the DDM NBRCS values that were utilized to derive wind_speed, unitless.
les_mean	LES mean	float	1	sample	The mean of the DDM LES values that were utilized to derive wind_speed, unitless.
range_corr_gain	Range corrected gain	float	1e-27 dBi meter-4	sample	The mean of the RCGs of the DDMs that were utilized to produce wind_speed. Individual RCGs are equal to the receive antenna gain in the direction of the specular point multiplied by 1e27 divided by the square of the receiver to the specular point range and the square of the transmitter to specular point range. Units: 1e27 *dBi * m^-4.
fresnel_coeff	Fresnel power reflection coefficient	float	1	sample	The square of the left-hand circularly polarized Fresnel electromagnetic voltage reflection coefficient at 1575 MHz for a smooth ocean surface at latitude, longitude. See University of Michigan (UM) document 148-0361 for a description of the calculation of the Fresnel coefficient, unitless.

Table 7B4. List of Data Fields Contained in the L2 Wind Retrieval Data Files (*continued*)

Name	Long name	netCDF type	CF conventions units	netCDF dimensions	Comment
num_ddms_utilized	Number of DDM utilized	byte	1	sample	The number of DDMs averaged together to produce wind_speed. The number of DDMs utilized depends on the incidence angle. Ranges from 1 to 5.
sample_flags	General status flags for the sample	short	\<none\>	sample	Set of flags indicating general conditions for the sample, set to 1 if condition is true. Flag bit masks: 1 = low_quality_gps_ant_knowledge. The directional gain pattern of the GPS transmit antenna, and hence the value of its gain in the direction of the specular point, is less well known for block type IIF GPS satellites. This flag indicates that L1 calibration was based on a GPS antenna gain value with a higher-than-normal uncertainty. The impact on retrieved wind speed values is typically less than 1 m/s at low to moderate wind speeds, so this is considered a nonfatal flag. The increase in uncertainty at higher wind speeds is reflected in the uncertainty data fields.
fds_sample_flags	Sample status flags for fully developed seas wind speed retrieval	short	\<none\>	sample	Set of FDS status flags, set to 1 if condition is true. Flag bit masks: 1 = fatal_composite_wind_speed_flag, logical OR of fatal FDS flags (fatal_neg_wind_speed OR fatal_high_wind_speed OR fatal_retrieval_ambiguity OR fatal_low_range_corr_gain) 2 = non_fatal_neg_wind_speed_flag, $-5 <$ wind_speed < 0 m/s 4 = non_fatal_neg_fds_nbrcs_wind_speed, $-5 <$ fds_nbrcs_wind_speed < 0 m/s 8 = non_fatal_neg_fds_les_wind_speed, $-5 <$ fds_les_wind_speed < 0 m/s 16 = fatal_neg_wind_speed, wind_speed $<= -5$ m/s 32 = fatal_neg_fds_nbrcs_wind_speed, fds_nbrcs_wind_speed $<=-5$ m/s 64 = fatal_neg_fds_les_wind_speed, fds_les_wind_speed $<= -5$ m/s 128 = fatal_high_wind_speed, fatal_high_fds_nbrcs_wind_speed and fatal_high_fds_les_wind_speed are both 1 256 = fatal_high_fds_nbrcs_wind_speed, nbrcs_mean corresponds to a wind speed > maximum FDS NBRCS lookup table wind speed at incidence_angle 512 = fatal_high_fds_les_wind_speed, les_mean corresponds to a wind speed > maximum FDS LES lookup table wind speed at incidence_angle

(continued)

Table 7B4.   List of Data Fields Contained in the L2 Wind Retrieval Data Files (*continued*)

Name	Long name	netCDF type	CF conventions units	netCDF dimensions	Comment
					1024 = non_fatal_ascending, satellite is on the ascending node of the orbit (subsatellite point latitude is increasing) 2048 = fatal_retrieval_ambiguity, wind_speed was derived from both fds_nbrcs_wind_speed and fds_les_wind_speed and the absolute value of the difference between fds_nbrcs_wind_speed and fds_les_wind_speed is > 10.0 m/s 4096 = non_fatal_single_observable, wind_speed was derived from a single observable, either fds_nbrcs_wind_speed or fds_les_wind_speed but not both 8192 = fatal_low_range_corr_gain, range_corr_gain < 1 16384 = non_fatal_low_quality_gps_ant_ knowledge. The directional gain pattern of the GPS transmit antenna, and hence the value of its gain in the direction of the specular point, is less well known for block type IIF GPS satellites. This flag indicates that L1 calibration was based on a GPS antenna gain value with a higher-than-normal uncertainty. The impact on retrieved wind speed values is typically less than 1 m/s at low to moderate wind speeds, so this is considered a nonfatal flag. The increase in uncertainty at higher wind speeds is reflected in the wind_speed_uncertainty data field.
yslf_sample_flags	Sample status flags for young seas / limited fetch wind speed retrieval	short	<none>	sample	Set of YSLF status flags, set to 1 if condition is true. Flag bit masks: 1 = fatal_composite_yslf_wind_speed, logical OR of fatal YSLF flags (fatal_neg_yslf_wind_speed OR fatal_high_yslf_ wind_speed OR fatal_yslf_retrieval_ambiguity OR fatal_low_range_corr_gain) 2 = spare_3, always zero 4 = spare_4, always zero 8 = fatal_neg_yslf_wind_speed, non_fatal_neg_yslf_nbrcs_wind_speed and non_fatal_neg_yslf_les_wind_speed are both 1 16 = non_fatal_neg_yslf_nbrcs_wind_speed, yslf_nbrcs_wind_speed <= –5 m/s 32 = non_fatal_neg_yslf_les_wind_speed, yslf_les_wind_speed <=-5 m/s

(continued)

Table 7B4. List of Data Fields Contained in the L2 Wind Retrieval Data Files (*continued*)

Name	Long name	netCDF type	CF conventions units	netCDF dimensions	Comment
					64 = fatal_yslf_retrieval_ambiguity, the absolute value of the difference between yslf_nbrcs_wind_speed and 1.43*yslf_les_wind_speed is > 12.0 m/s 128 = fatal_high_yslf_wind_speed, either fatal_high_yslf_nbrcs_wind_speed or fatal_high_yslf_les_wind_speed is one (or both are one) 256 = fatal_high_yslf_nbrcs_wind_speed, nbrcs_mean corresponds to a YSLF wind speed ≥ 99.9 m/s 512 = fatal_high_yslf_les_wind_speed, les_mean corresponds to a YSLF wind speed ≥ 99.9 m/s
					1024 = non_fatal_ascending, satellite is on the ascending node of the orbit (subsatellite point latitude is increasing) 2048 = spare_6, always zero 4096 = spare_7, always zero 8192 = fatal_low_yslf_range_corr_gain, range corrected gain of the DDM used for YSLF winds is < 1 16384 = non_fatal_low_quality_gps_ant_knowledge. The directional gain pattern of the GPS transmit antenna, and hence the value of its gain in the direction of the specular point, is less well known for block IIF GPS satellites. This flag indicates that L1 calibration was based on a GPS antenna gain value with a higher-than-normal uncertainty. The impact on retrieved wind speed values is typically less than 1 m/s at low to moderate wind speeds, so this is considered a nonfatal flag. The increase in uncertainty at higher wind speeds is reflected in the yslf_nbrcs_wind_speed_uncertainty and yslf_les_wind_speed_uncertainty data fields.

(continued)

Table 7B4. List of Data Fields Contained in the L2 Wind Retrieval Data Files (*continued*)

Name	Long name	netCDF type	CF conventions units	netCDF dimensions	Comment
sum_neg_brcs_ values_used_for_ nbrcs_flags	Sum of negative bistatic radar cross section (BRCS) values used for NBRCS flags	byte	1	sample	The number of DDMs utilized to produce wind_speed that used at least one negative BRCS value to calculate NBRCS. Ranges from 1 to 5.
Per-DDM values					
Wind retrievals are produced utilizing from one to five DDMs. The values below are five element arrays, which contain per-DDM values. The DDMs that were utilized for wind retrieval are indicated by the ddm_obs_ utilized_flag array. Unutilized DDMs are assigned fill values.					
ddm_obs_ utilized_flag	DDM-utilized flags	byte	1	sample, ddm	A five-element array, one element per DDM. Each element is a flag set to 1 if the corresponding DDM was utilized to produce wind_speed.
ddm_sample_ index	Level 1 netCDF sample indices	int	1	sample, ddm	A five-element array, one per DDM. Contains the L1 netCDF sample index of the corresponding DDM. Can be utilized together with ddm_channel, spacecraft_num and "source" to look up the corresponding L1 DDM data and metadata.
ddm_channel	Level 1 DDM reflectometry channels	byte	1	sample, ddm	A five-element array, one per DDM. Contains the L1 netCDF reflectometry channel of the corresponding DDM. Can be utilized together with the ddm_sample_index, spacecraft_num and "source" to look up the corresponding L1 DDM data and metadata.
ddm_les	DDM leading edge slope observables	float	1	sample, ddm	A five-element array, one element per DDM. Contains the corresponding DDM leading edge slope value, unitless.
ddm_nbrcs	DDM normalized bistatic radar cross section observables	float	1	sample, ddm	A five-element array, one element per DDM. Contains the corresponding DDM normalized bistatic radar cross section value, unitless.

Key: CCSDS, Consultative Committee for Space Data Systems; CF, netCDF Climate and Forecast Metadata Convention; PRN, pseudorandom noise; UTC, Coordinated Universal Time.

8. Level 2 Ocean Surface Heat Flux Product

8.1. Summary

The ocean surface heat flux dataset is provided as a service to the oceanographic and meteorological research communities on behalf of a NASA Research Opportunities in Space and Earth Sciences (ROSES)–funded project within the CYGNSS Science Team in direct collaboration with the CYGNSS mission. This document details the CYGNSS Level 2 Science Data Record Version 2.0 dataset, which provides data on CYGNSS specular points on a nominal 25 km diameter footprint in daily netCDF-4 files. Development and distribution of this dataset are made possible through funding provided by NASA.

8.2. Processing Methodology

The Coupled Ocean-Atmosphere Response Experiment (COARE) algorithm (Edson et al., 2013) is a widely used parameterization to estimate latent and sensible fluxes and their respective transfer coefficients. The COARE bulk flux algorithm is based on the Monin-Obukhov similarity theory (MOST; Fairall et al., 1996, 1997) and has been widely used to estimate surface heat fluxes over the open oceans. While COARE's initial intentions were for low to moderate wind speeds, the version used for this product, COARE 3.5, has been verified with direct in situ flux measurements for wind speeds up to 25 m/s.

COARE 3.5 utilizes bulk aerodynamic formulas in order to estimate latent (LHF) and sensible heat fluxes (SHF), which are as follows:

$$LHF = \rho_a L_v C_{DE} U \left(q_s - q_a \right) \tag{8.1}$$

$$SHF = \rho_a c_p C_{DH} U \left(T_s - T_a \right) \tag{8.2}$$

Here, ρ_a is the air density at the surface [kg m^{-3}]; L_v is the latent heat of condensation (2.5×10^6 J kg^{-1}); and c_p is specific heat at constant pressure (1004 J K^{-1} kg^{-1}). C_{DE} and C_{DH} are, respectively, the exchange coefficients of moisture and sensible heat [unitless]; U is the surface winds [m s^{-1}], T_s and q_s are temperature [K] and specific humidity [kg kg^{-1}], respectively, at the surface, while T_a and q_a are the same but at 10 m above the surface.

Since CYGNSS does not provide temperature, humidity, surface pressure, or density, we obtain these values from the European Centre for Medium-Range Weather Forecasts (ECMWF) Reanalysis, Version 5 (ERA5; Hersbach et al., 2020). ERA5 uses data assimilation to combine all available in situ and satellite observation data with an initial estimate of the atmospheric state provided by a global atmospheric model. Variables required for the surface heat flux estimates are available with a temporal resolution of one hour and a spatial resolution of 0.25° × 0.25°, with the exception of air density, which is at a 0.5° × 0.5° spatial resolution.

COARE 3.5 parameterizes the drag coefficients (C_{DE} and C_{DH}) in the bulk formulas (Equations 8.1 and 8.2) as a function of gustiness, surface roughness, and atmospheric stability; it is mathematically expressed as

$$C_D \left(z / z_o, z / L, G \right) = \frac{-\overline{uw}}{U_r S_r} = \frac{-\overline{uw}}{U_r^2 G}$$

$$= \left[\frac{\kappa}{\ln \left(z / z_o \right) - \psi_m \left(z / L \right)} \right]^2. \tag{8.3}$$

Here, z is the height above the surface [m]; K is the von Kármán constant (set to a value of 0.4; unitless); z_o is the aerodynamic roughness length [m], and ψ_m is a dimensionless function that accounts for the effects of atmospheric stratification. G is the gustiness parameter, defined as the ratio of the wind speed, S_r [m s^{-1}], to the vector-averaged wind, U_r [m s^{-1}] (Beljaars and Holtslag, 1991; Edson et al., 2013). This parameterization attempts to account for mass, momentum, and heat transfer at lower wind speeds but is nonzero because of the gustiness. This results in shear-driven turbulence produced by gusts that significantly drive exchanges in convective conditions (Fairall et al., 1996; Edson et al., 2013).

In order to use ERA5 data at each CYGNSS specular point, the nearest ERA5 grid point needs to be matched in time and space. Since ERA5 features an hourly temporal resolution and 0.25° × 0.25° spatial resolution, we use a trilinear interpolation method to match the CYGNSS and Modern-Era Retrospective Analysis for Research and Applications (MERRA)-2 data. The inputs from ERA5 include temperature and humidity (at the surface and 10 m) and air density.

For surface winds, two wind speed products are used from CYGNSS's L2 V3.1 science data record (SDR)

wind speed product: the fully developed seas (FDS) wind speed and young seas limited fetch (YSLF) wind speeds. In order to maintain consistency for the data users analyzing surface fluxes and wind speeds from CYGNSS, LHF and SHF are calculated throughout the whole mission using both wind speed products. While it is ultimately up to the users to decide when it is best to use FDS and YSLF products, it is generally recommended that the FDS products are used for most applications and analysis, while the YSLF product should be utilized for higher wind situations, rapidly developing systems, and strong curvature in the flow (i.e., tropical and extratropical cyclones).

Given that COARE 3.5 is validated for wind speeds up to 25 m/s, LHF and SHF estimates are flagged when wind speeds surpass this limit. When wind speeds exceed 25 m/s, sea spray ejected from the ocean surface has a nonnegligible effect on the air-sea heat fluxes (Richter & Stern, 2014). Additionally, estimates of the drag coefficient break down above this threshold; these result in the LHF and SHF estimates becoming increasingly erroneous.

Additional quality flags are produced for range corrected gain (RCG) less than 3 due to unreliability in wind speeds.

Inputs from every CYGNSS specular point and matched ERA5 data are inserted into the COARE 3.5 algorithm to estimate latent and sensible heat fluxes. Since ERA5 atmospheric temperature and dew point data are at 2 m, COARE uses Monin-Obukhov similarity theory (MOST) to estimate temperature and humidity at 10 m in order to estimate the fluxes. COARE produces a first guess of the surface heat fluxes and uses this guess to initialize a stability iteration loop. Within this loop, COARE computes the Monin-Obukhov length, roughness length, and transfer coefficients along with a stability dependence. For the initial version of the surface heat flux product, the loop is repeated 10 times, as various trials have shown that this is the minimum needed for the values to reach an asymptote at each specular point. Future versions of this product may alter the loop so that it automatically terminates when the values converge.

The transfer coefficients calculated within the loop are used to estimate LHF and SHF using the bulk aerodynamic formulas (Equations 8.1 and 8.2), combined with both wind speed products from CYGNSS and the thermodynamic variables from MERRA-2. This results in two products each for LHF and SHF (Crespo et al., 2019), which are listed in Section 8.4.3.

8.3. Calibration and Validation

Direct in situ measurements of latent and sensible heat fluxes are limited within CYGNSS's orbit and are often only available during field campaigns or on a limited number of research buoys. Though these comparisons may be available for future versions of this product, for now, we have been able to use estimates from buoy data that match up with CYGNSS observations. While these buoys may not measure the fluxes directly, they do measure wind speeds, temperature, and humidity, which can be inputted into the same COARE algorithm used to estimate the fluxes for the L2 CYGNSS estimates (Crespo et al., 2019).

Buoy data was obtained from the following buoy networks: Prediction and Research Moored Array in the Tropical Atlantic (PIRATA), Triangle Trans-Ocean Buoy Network (TRITON), and the Tropical Atmosphere Ocean Array (TAO). These comparisons were done with data from August 1, 2018, through December 31, 2021.

For these comparisons, any values from the CYGNSS surface heat flux product that had a quality flag associated with them were removed. The remaining specular points were then used to compare the fluxes estimated from the buoys, with the resulting comparison in Figure 8.1. As shown in Figure 8.1, at lower flux values, the CYGNSS surface heat fluxes compare well with the buoy data and are along the one-to-one line. While the density plot shows a decent width (at least for LHF) around this line, overall, most of the fluxes from CYGNSS are in agreement and validate well with the buoy data.

However, as the fluxes increase, there is greater scatter and disagreement between CYGNSS and the buoy data. For the LHF results, while CYGNSS overestimated some of the fluxes, it more often underestimated the fluxes, whereas it consistently underestimated higher SHF values. As a result, the overall root mean square difference (RMSD) for LHF was 37.92 W/m^2, while SHF RMSD was 9.61 W/m^2.

The differences observed at higher flux values likely came from uncertainties in the L2 CYGNSS wind speed, as there have been known errors at higher wind speeds. Additionally, there may be other errors from MERRA-2 that were not factored in, such as errors related to precipitation. Granted, the number of comparisons at the higher flux values were limited, which may have resulted in the observed scatter. Future releases of the CYGNSS L2 wind speeds are expected to reduce these residual errors, while further investigation is also needed to assess and address the introduction of uncertainties from ERA5 in future product releases.
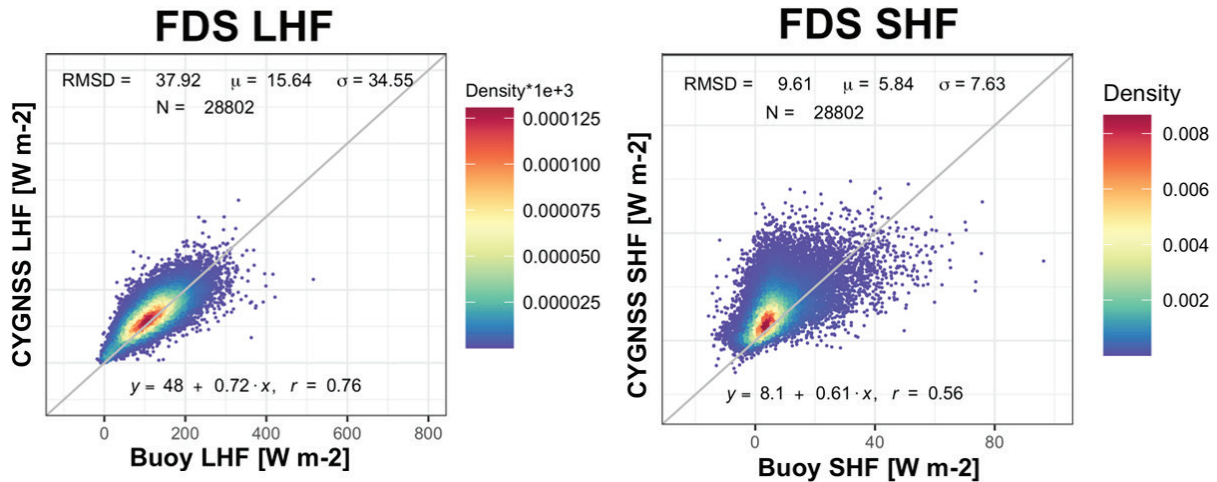
Figure 8.1. CYGNSS surface heat flux comparisons (y-axis) compared to flux estimates from buoys (x-axis). *Left:* Latent heat flux. *Right:* Sensible heat flux.

Despite these likely errors and uncertainties, the fluxes from the CYGNSS Surface Heat Flux product compare well with the ground truth from the buoy data. Future releases hope to include comparisons and validation with various field campaigns (e.g., PISTON, CAMP2Ex) as well as more buoy data, especially at higher flux estimates.

8.4. Dataset Description

This dataset is being distributed in netCDF-4 format using internal compression (more computationally efficient compared to external compression such as gzip) and adhering to netCDF Climate and Forecast (CF) Metadata Convention v1.6 and ISO-8601 conventions. Each file is unique to a particular calendar day of a year and consists of one complete orbital revolution (assuming no data gaps).

The file naming convention is cyg.ddmi.sYYYYMMDD-HHMMSS-eYYYYMMDD-HHMMSS.l2.surface-flux-cdr.aAA.dVV.nc, where

- cyg = CYGNSS, which is the mission and platform source of the dataset.
- ddmi = Delay-Doppler mapping instrument.
- sYYYYMMDD = The year, month, and day of the starting point of the first data in the file.

HHMMSS = Hours, minutes, and seconds (respectively) of date/time stamp.

eYYYYMMDD = The year, month, and day of the ending point of the last data in the file.

l2 = Level 2 processing.

surface-flux-cdr = Surface flux dataset (Climate Data Record version).

aAA = Algorithm version, where AA is the numerical algorithm version identifier (e.g., "a11" = Algorithm Version 1.1). *Note:* The algorithm version is numerically decoupled from the dataset version (see below).

dVV = Dataset version, where VV is the numerical dataset version identifier (e.g., "d11" = Dataset Version 1.1). *Note:* The dataset version is numerically decoupled from the algorithm version (see above).

.nc = The file extension indicating the usage of netCDF data formatting.

The date and time represented by the file name is with respect to GMT (Coordinated Universal Time [UTC]). Greater precision of the start and stop times is available in the netCDF global attributes.

8.4.1. Variable Types

Table 8.1. Dataset Variable Description

Name	Data type	Missing value	Description
sample	long	N/A	The netCDF coordinate variable associated with the sample dimension, which enumerates the zero-justified index range of the delay-Doppler map (DDM) time instants contained in the file.
sample_time	double	–9999.f	The mean UTC timestamp of the DDMs that were utilized to derive wind_speed from the original CYGNSS L2 data files. Note that the DDM sampling period is not synchronized with the UTC change of second, so sample_time can occur at any time relative to the UTC change of second.
spacecraft_id	short	–9999s	The CCSDS spacecraft identifier:\n\t0xF7 (247): CYGNSS 1\n\t0xF9 (249): CYGNSS 2\n\t0x2B (43): CYGNSS 3\n\t0x2C (44): CYGNSS 4\n\t0x2F (47): CYGNSS 5\n\t0x36 (54): CYGNSS 6\n\t0x37 (55): CYGNSS 7\n\t0x49 (73): CYGNSS 8\n\t0x00 (0): end-to-end simulator\n\t0x0E (14): engineering model\n\t0x0D (15): default\n\t0xFF (255): unknown\n
spacecraft_num	byte	–99b	The CYGNSS spacecraft number: Ranges from 1 through 8 and 99; 1 through 8 are on-orbit spacecraft; 99 is the CYGNSS end-to-end simulator.
antenna	byte	–99b	The CYGNSS nadir antenna that received the reflected GPS signal associated with the DDMs utilized to derive wind_speed.\n\t0 = none\n\t1 = zenith (never used)\n\t2 = nadir_starboard\n\t3 = nadir_port
prn_code	byte	–99b	The PRN code of the GPS signal associated with the DDMs utilized to derive heat fluxes. Ranges from 0 to 32; 0 = reflectometry channel idle; 1 to 32 represent a PRN code.
lat	float	N/A	The mean of the specular point latitudes of the DDMs that were utilized to derive wind_speed, ºN.
lon	float	N/A	The mean of the specular point longitudes of the DDMs that were utilized to derive wind_speed, ºE.
air_density	float	–9999.f	Air density at surface received from the MERRA-2 variable \"RHOA\."
effective_surface_humidity	float	–9999.f	Effective surface specific humidity received from the MERRA-2 variable \"QSH\."
specific_humidity	float	–9999.f	10 m specific humidity received from the MERRA-2 variable \"QV10M\."
surface_pressure	float	–9999.f	Surface pressure received from the MERRA-2 variable \"PS\."
air_temperature	float	–9999.f	10 m air temperature received from the MERRA-2 variable \"T10M\."
lhf	float	–9999.f	The latent heat flux estimates at each specular point using the CYGNSS L2 wind_speed FDS minimum variance product.
shf	float	–9999.f	The sensible heat flux estimates at each specular point using the CYGNSS L2 wind_speed FDS minimum variance product.
lhf_yslf	float	–9999.f	The latent heat flux estimates at each specular point using the CYGNSS L2 YSLF product.
shf_yslf	float	–9999.f	The sensible heat flux estimates at each specular point using the CYGNSS L2 YSLF product.

(continued)

Name	Data type	Missing value	Description
lhf_uncertainty	float	–9999.f	Standard deviation of the additive latent heat flux error, based on known and reported uncertainties from CYGNSS L2 FDS winds, and MERRA-2 temperature and humidity. Dependent on lhf, in W m-2.
shf_uncertainty	float	–9999.f	Standard deviation of the additive sensible heat flux error, based on known and reported uncertainties from CYGNSS L2 FDS winds, and MERRA-2 temperature and humidity. Dependent on shf, in W m-2.
lhf_uncertainty_yslf	float	–9999.f	Standard deviation of the additive latent heat flux error, based on known and reported uncertainties from CYGNSS L2 YSLF winds, and MERRA-2 temperature and humidity. Dependent on lhf_yslf, in W m-2.
shf_uncertainty_yslf	float	–9999.f	Standard deviation of the additive sensible heat flux error, based on known and reported uncertainties from CYGNSS L2 YSLF winds, and MERRA-2 temperature and humidity. Dependent on shf_yslf, in W m-2.
cygnss_l2_sample_index	long	N/A	A sample index for the corresponding CYGNSS L2 sample index used for deriving the heat fluxes. This can be used with \"source\" to look up the CYGNSS L2 data and metadata.
quality_flags	short	–9999s	See Section 8.4.2 below.

Key: CCSDS, Consultative Committee for Space Data Systems; PRN, pseudorandom noise.

8.4.2. Bit-by-Bit Description of Quality Flag Variable

The following table describes all the bits in the quality flag variable.

Bit number (0 = LSB)	Flag value (2^bit#)	Bit name	Meaning when bit is 1 (1 means bit has been set; 0 means unset)
0	1	poor_overall_quality	If any one of the following flags are set, then poor_overall_quality will be set: low_quality_gps_ant_knowledge OR low_range_corrected_gain OR cygnss_l2_fatal_flag OR low_FDS_wind_speed OR low_yslf_nbrcs_wind_speed OR high_FDS_wind_speed OR high_yslf_nbrcs_wind_speed
1	2	spare_1	Always zero.
2	4	low_range_corrected_gain	Range corrected gain is less than 3.
3	8	ascending_satellite	Satellite is on the ascending node of the orbit (subsatellite point latitude is increasing).
4	16	cygnss_l2_fatal_flag	CYGNSS L2 fully developed seas (FDS) sample flag is set to fatal; data are discarded for FDS wind speed.
5	32	low_general_wind_speed	CYGNSS L2 FDS wind speed < 0 m/s.
6	64	low_yslf_wind_speed	CYGNSS L2 YSLF wind speed < 0 m/s.
7	128	high_general_wind_speed	CYGNSS L2 FDS wind speed > 25 m/s.
8	256	high_yslf_wind_speed	CYGNSS L2 YSLF wind speed > 25 m/s.
9	512	cygnss_l2_yslf_fatal_flag	CYGNSS L2 YSLF sample flag is set to fatal.

Key: LSB, least significant bit.

8.4.3. Grid Description

Given that LHF and SHF are calculated at every specular point observed by CYGNSS, the spatial distribution of the CYGNSS Heat Flux Product is the same as the Level 2 CYGNSS Climate Data Record (CDR) Wind Speed Product (see Chapter 7 for details). Each specular point is 25 km wide; at the beginning of the mission, each spacecraft was observing up to four specular points per second (32 per second for the entire constellation). Beginning in July 2019, the sampling was reduced from once per second to once every half second, reducing along-track beam smearing and now resulting in up to 64 wind speed observations per second for the entire constellation. The reflected signal from the GPS satellite will remain within CYGNSS's antenna view pattern, allowing for long swaths of continuous specular point observations; the length of these swaths is not consistent.

Though CYGNSS's orbit reaches the 35th parallel in both hemispheres, it can consistently make observations up to the 38th parallel, allowing it to observe nontropical systems (Crespo et al., 2017, 2019). On average, CYGNSS has a median revisit time of just under 3 hours and a mean of around 7 hours. However, this is not consistent across its orbit. Near the edge of its orbit, CYGNSS's revisit time is much longer, though it can feature many observations within the span of a few hours; revisit times are much shorter near the equator (Park et al., 2019).

8.4.4. Related Products

All related data products are referenced here: https://podaac.jpl.nasa.gov/cygnss.

8.5. Data Access

8.5.1. Obtaining Data and Documentation

Note: The documentation (/doc) is located one directory level above the data directories.

MD5 checksum files are also available for all datasets in the data directories to assist you in verifying the integrity of each data file/granule. To learn more about MD5 checksums, you may visit https://en.wikipedia.org/wiki/MD5.

The POCLOUD (PO.DAAC Cloud data service) HTTPS service is now available to browse and download all data: https://cmr.earthdata.nasa.gov/virtual-directory/collections/C2247621105-POCLOUD.

For information on how to cite this data in presentations or publications, please read https://podaac.jpl.nasa.gov/CitingPODAAC.

For general news, announcements, and information on this and all other ocean and sea ice datasets available at the Physical Oceanography Distributed Active Archive Center (PO.DAAC), please visit the PO.DAAC web portal: https://podaac.jpl.nasa.gov/.

8.5.2. Contact Information

Questions and comments should be directed to PO.DAAC at the NASA Jet Propulsion Laboratory (JPL). Please note that email is always the preferred method of communication, but the PO.DAAC users forum is highly recommended as a first point of entry to address frequently asked questions.

```
Email:   podaac@podaac.jpl.nasa.gov
WWW:     https://podaac.jpl.nasa.gov/forum
Mail:    PO.DAAC User Services Office
         Jet Propulsion Laboratory
         M/S T1721-202
         4800 Oak Grove Drive
         Pasadena, CA 91109
```

8.6. Read Software

Sample netCDF software readers are currently available in IDL, MATLAB, R, and Python at the following location: https://github.com/podaac/data-readers.

8.7. References

Beljaars, A. C. M., & Holtslag, A. A. M. (1991). Flux parameterization over land surfaces for atmospheric models. *Journal of Applied Meteorology and Climatology, 30*, 327–341.

Crespo, J. A., Posselt, D. J., & Asharaf, S. (2019). CYGNSS surface heat flux product development. *Remote Sensing, 11*, 2294. https://doi.org/10.3390/rs11192294.

Crespo, J. A., Posselt, D. J., Naud, C. M., & Bussy-Virat, C. D. (2017). Assessing CYGNSS's potential to observe extratropical fronts and cyclones. *Journal of Applied Meteorology and Climatology, 56*(7), 2027–2034. https://doi.org/10.1175/JAMC-D-17-0050.1.

Edson, J., Jampana, V., Weller, R., Bigorre, S., Plueddemann, A., Fairall, C., Miller, S., Mahrt, L., Vickers, D., & Hersbach, H. (2013). On the exchange of momentum over the open ocean. *Journal of Physical Oceanography, 43*(8), 1589–1610. https://doi.org/10.1175/JPO-D-12-0173.1.

Fairall, C. W., Bradley, E. F., Rogers, D. P., Edson, J. B., & Young, G. S. (1996). Bulk parameterization of air–sea fluxes for tropical ocean–global atmosphere coupled ocean–atmosphere response experiment. *Geophysical Research: Oceans (1978–2012), 101*(C2), 3747–3764. https://doi.org/10.1029/95JC03205.

Fairall, C. W., White, A. B., Edson, J. B., & Hare, J. E. (1997). Integrated shipboard measurements of the marine boundary layer. *Journal of Atmospheric and Oceanic Technology, 14*, 338–359.

Hersbach, H., Bell, B., Berrisford, P., Hirahara, S., Horányi, A., Muñoz-Sabater, J., Nicolas, J., Peubey, C., Radu, R., Schepers, D., Simmons, A., Soci, C., Abdalla, S., Abellan, X., Balsamo, G., Bechtold, P., Biavati, G., Bidlot, J., Bonavita, M., . . . Thépaut, J.-N. (2020). The ERA5 global reanalysis. *Quarterly Journal of the Royal Meteorological Society, 146*(730), 1999–2049. https://doi.org/10.1002/qj.3803.

Park, J., Johnson, J. T., Yi, Y., & O'Brien, A. J. (2019). Using "rapid revisit" CYGNSS wind speed measurements to detect convective activity. *IEEE Journal of Selected Topics in Applied Earth Observations and Remote Sensing, 12*(1), 98–106. https://doi.org/10.1109/JSTARS.2018.2848267.

Richter, D. H., & Stern, D. P. (2014). Evidence of spray-mediated air-sea enthalpy flux within tropical cyclones. *Geophysical Research Letters, 41*(8), 2997–3003. https://doi.org/10.1002/2014GL059746.

9. Level 3 Wind Speed Science Data Products

9.1. Level 3 Gridded Wind Speed

9.1.1. Summary

This section describes the algorithm and data processing implementation used to produce a CYGNSS Level 3 gridded wind speed Science Data Product. The algorithm uses as its input the mission baseline Level 2 wind speed Science Data Product, which provides its wind speed values at the time and location at which the measurements were made (i.e., in sensor-specific latitude, longitude, and time coordinates) for each of the eight observatories in the CYGNSS constellation and for each of the four bistatic radar channels on each observatory. This Level 3 gridded product combines all 8 × 4 = 32 wind speed measurements made by the CYGNSS constellation each second, sorts them into a uniform (latitude, longitude, time) grid, and reports certain statistics of the samples in each bin (e.g., number, mean value, . . .), together with a compilation of the quality flags set for each of the samples in the bin.

9.1.2. Algorithm Objectives

The objective of this algorithm is to produce a gridded wind speed Science Data Product that is uniformly sampled in latitude, longitude, and time. This Level 3 product is generated from the full set of Level 2 wind speed samples produced by the constellation of observatories. In addition to a best estimate of the mean ocean surface wind speed within any particular bin, the algorithm also produces statistics of the wind speed that are derived from the population of samples of the Level 2 wind speed made by the constellation within that bin. A compilation of the quality flags associated with the population of individual Level 2 wind speed samples is also produced.

9.1.3. Input Data Description

The input data required by this algorithm are listed here.

All relevant quality flags associated with the Level 1B bistatic radar cross section (BRCS) data that are used to produce the Level 2 wind speed data products are included as inputs. These quality flags (Gleason, 2014) are shown in Table 9.1.

The relevant input products required from the Level 2 wind speed algorithm (Clarizia et al., 2021) are shown in Table 9.2.

9.1.4. Algorithm Production Overview

The binning algorithm produces a minimum variance estimate of the mean wind speed in the bin over the spatial and temporal intervals specified by the bin's boundaries. This is done using an inverse-variance weighted average of all Level 2 samples of the wind speed that were made within the bin. Specifically, for bin boundaries Lat_{min}, Lat_{max}, Lon_{min}, Lon_{max}, T_{min} and T_{max}, let S be the set of all Level 2 samples of the wind speed satisfying the following conditions:

$$S = \{Sample_i \mid Lat_{min} \leq Lat_i < Lat_{max};$$
$$Lon_{min} \leq Lon_i < Lon_{max}; T_{min} \leq T_i < T_{max}\}, \tag{9.1}$$

where the ith sample has bin coordinates (Lat_i, Lon_i, T_i). Sort all Level 2 wind speed samples, together with their uncertainties, that are in S. The uncertainties are the estimated standard deviations of the wind speed estimates. The Level 3 wind speed estimate for that bin is given by

$$u_{L3}(S) = \frac{\sum_{i \in S} u_i \sigma_i^{-2}}{\sum_{i \in S} \sigma_i^{-2}}, \tag{9.2}$$

where u_i is the ith Level 2 minimum variance wind speed in S, and σ_i is its uncertainty.

The uncertainty (i.e., standard deviation) in u_{L3} is given by

$$\sigma_{L3} = \sqrt{\frac{1}{\sum_{i \in S} \sigma_i^{-2}}}. \tag{9.3}$$

Relevant quality flags from the Level 2 wind speed algorithm are compiled into an aggregate set of quality flags for the Level 3 wind speed produced here. The wind-speed-dependent quality flags are shown in Table 9.3. For each flag, a value N will be prescribed, which is the number of samples in S for which the threshold in column two is met.

Table 9.4 shows the rolled-up versions of the quality flags produced by the Level 1B DDM algorithm. For each flag, a value M will be prescribed, which is the number of samples in S for which the threshold in column two is met.

Table 9.1. Quality Flags From Level 1B BRCS Data Used for Level 1 Wind Speed Data Products

Flag	Flag values	Comment
Large spacecraft attitude error	0 = false, 1 = true	
Overall delay-Doppler map (DDM) quality	0 = poor, 1 = good	This is the logical OR of other quality flags; TBD: detailed description
Negative signal power in Level 2 delay-Doppler map area (DDMA)		At least one bin in Level 2 DDMA has a negative power value
Negative σ_0 in Level 2 DDMA		At least one bin in Level 2 DDMA has a negative power value
Low confidence in DDM noise floor estimate	0 = false, 1 = true	
Low confidence in open ocean noise floor estimate	0 = false, 1 = true	
Low confidence in open ocean noise temperature estimate	0 = false, 1 = true	
Land present in DDM	0 = false, 1 = true	
Specular point over open ocean	0 = false, 1 = true	
Large step change in DDM noise floor	0 = false, 1 = true	
Large step change in low noise amplifier (LNA) temperature	0 = false, 1 = true	
Direct signal in DDM	0 = false, 1 = true	
Low Rx antenna range corrected gain	0 = false, 1 = true	
High specular point incidence angle	0 = false, 1 = true	
High cross-correlation power present	0 = false, 1 = true	
Low confidence in GPS equivalent isotropically radiated power (EIRP) estimate	0 = false, 1 = true	

Table 9.2. Input Products From Level 2 Wind Speed Algorithm

Flag	Flag values
Minimum variance (MV) wind speed estimate	
Uncertainty in MV wind speed estimate	
Negative wind speed quality flag	0 = nonnegative, 1 = negative
The >70 m/s^{-1} wind speed quality flag	0 = <70 m/s^{-1}, 1 = >70 m/s^{-1}

Table 9.3. Wind-Speed-Dependent Quality Flags

Flag	Flag values
Fatal negative wind speed quality flag	1 = wind speed less than −5 m/s^{-1}
Fatal high wind speed quality flag	1 = wind speed greater than 100 m/s^{-1}
Nonfatal negative wind speed quality flag	1 = wind speed between −5 m/s^{-1} and 0
Nonfatal high wind speed quality flag	1 = wind speed between 70 m/s^{-1} and 100 m/s^{-1}

Table 9.4. Rolled-Up Versions of Quality Flags From Level 1B DDM Algorithm

Flag	Flag values
Large spacecraft attitude error	1 = true
Negative signal power in Level 2 DDMA area	At least one bin in the Level 2 DDMA has a negative power value
Negative σ_0 in Level 2 DDMA area	At least one bin in the Level 2 DDMA has a negative power value
Low confidence in DDM noise floor estimate	1 = true
Low confidence in open ocean noise floor estimate	1 = true
Low confidence in open ocean noise temperature estimate	1 = true
Land present in DDM	1 = true
Specular point over open ocean	1 = true
Large step change in DDM noise floor	1 = true
Large step change in LNA temperature	1 = true
Direct signal in DDM	1 = true
Low Rx antenna range corrected gain	1 = true
High specular point incidence angle	1 = true
High cross-correlation power present	1 = true
Low confidence in GPS EIRP estimate	1 = true

9.1.5. Output Data Product Description

The following output data values will be available:

- u_{L3} = The minimum variance estimate of the mean wind speed averaged over the time and space intervals defined by Equation 9.1 for a particular bin, as given by Equation 9.2 (units of meters/second)
- σ_{L3} = The standard deviation of u_{L3} for a particular bin, as given by Equation 9.3 (units of meters/second)
- S = The number of samples used to calculate u_{L3}.

The output data quality flags are presented in Table 9.5.

Table 9.5. Quality Flags for the Output Data

Flag or condition	Flag values
Overall Level 3 wind speed quality	0 = poor, 1 = good
Fatal negative wind speed quality flag	N = # of wind speed samples in the latitude, longitude boundary of S but not included in S because wind speed is less than -5 m/s^{-1}
Fatal high wind speed quality flag	N = # of wind speed samples in the latitude, longitude boundary of S but not included in S because the wind speed is greater than 100 m/s^{-1}
Nonfatal negative wind speed quality flag	N = # of wind speed samples in S for which the = wind speed is between -5 m/s^{-1} and 0
Nonfatal high wind speed quality flag	N = # of wind speed samples in S for which the wind speed is between 70 m/s^{-1} and 100 m/s^{-1}
Negative signal power In Level 2 DDMA	M = # of DDM samples in S where at least one bin in the Level 2 DDMA has a negative power value
Negative σ_0 in Level 2 DDMA	M = # of DDM samples in S where at least one bin in the Level 2 DDMA has a negative power value
Large spacecraft attitude error	# of true DDM samples
Low confidence in DDM noise floor estimate	# of true DDM samples
Low confidence in open ocean noise floor estimate	# of true DDM samples
Low confidence in open ocean noise temperature estimate	# of true DDM samples
Land present in DDM	# of true DDM samples
Specular point over open ocean	# of true DDM samples
Large step change in DDM noise floor	# of true DDM samples
Large step change in LNA temperature	# of true DDM samples
Direct signal in DDM	# of true DDM samples
Low Rx antenna range corrected gain	# of true DDM samples
High specular point incidence angle	# of true DDM samples
High cross-correlation power present	# of true DDM samples
Low confidence in GPS EIRP estimate	# of true DDM samples

Note: N and M are the number of samples that meet the condition described in column 2.

9.1.6. Algorithm Configuration Parameter Values

The principle configuration parameters for this algorithm are the latitude, longitude, and time boundaries of the bins. The bins are uniformly spaced every 0.2° in latitude from −40° N to +40° N, every 0.2° in longitude from 0 to 360° E and every 1 hour in time. Specifically,

- Lat_{min} = −40°, −39.8°, . . . , +39.8° N latitude
- Lat_{max} = −39.8°, −39.6°, . . . , +40° N latitude
- Lon_{min} = 0°, 0.2°, . . . , 359.8° E longitude
- Lon_{max} = 0.2°, 0.4°, . . . , 360.0° E longitude
- T_{min} = (year, day of year, 0 hr UT), (yr, DOY, 1 hr UT), . . . , (yr, DOY, 23 hr UT)
- T_{max} = (year, day of year, 1 hr UT), (yr, DOY, 2 hr UT), . . . , (yr, DOY, 24 hr UT)

9.2. Level 3 Storm-centric Gridded Wind Speed

9.2.1. Summary

This section describes the algorithm and data processing implementation used to produce CYGNSS Level 3 storm-centric gridded wind speed Science Data Products. The algorithm uses as its input the Level 2 wind speed Science Data Products, which provide wind speed values at the time and location of the surface reflection. This product reports averaged wind speeds in a regular 7.2° × 7.2° grid centered on the tropical cyclone. Gridded wind speeds are reported every 6 hours for each tropical cyclone, although some 6-hourly increments may be missing if there were no available overpasses during that time interval. Each wind speed measurement is made by a particular combination of CYGNSS spacecraft and GPS spacecraft. Because there are 8 CYGNSS spacecraft and 32 GPS spacecraft, there are 256 different combinations of spacecraft that combine to make measurements. Much work has been done to minimize differences between the spacecraft, but there are small remaining differences and possible anomalies. This product only reports wind speeds that have passed an intertrack comparison test to increase reliability.

9.2.2. Algorithm Overview

9.2.2.1. Algorithm Objectives

The objective of this algorithm is to produce regular 6-hourly gridded wind speeds for tropical cyclones (TCs) with increased reliability by incorporating averaging and comparisons between colocated measurements. This product, which is only available around TCs, is a more sophisticated version of the globally available standard CYGNSS L3 product. All reported wind speeds in this storm-centric product are an average of wind speeds from at least two different "tracks" (combinations of CYGNSS receiver and GPS transmitter) that agree reasonably well. This removes most problematic data and wind speeds that are biased from track to track. Averaging also works to reduce noise in the measurement. Storm-centric coordinates are utilized to allow for a larger temporal averaging window without smearing between grid cells. A large temporal averaging window increases the typical number of tracks in each grid cell, allowing for more frequent intertrack comparisons to be made.

9.2.2.2. Input Data Description

The input data required by this algorithm are listed here.

1. Wind speed inputs are CYGNSS Level 2 Sensor Data Record (SDR) Version 3.1 (Clarizia, 2015; Ruf et al., 2019). These wind speeds incorporate improvements made to the Level 1 SDR calibration to compensate for variations in GPS transmit power level (Wang et al., 2021).
2. Storm center locations are from NOAA National Hurricane Center (NHC) Best Track analysis and/or the Joint Typhoon Warning Center (JTWC; Landsea & Franklin, 2013).

9.2.2.3. Data Organization

The original CYGNSS Level 3 wind speed product is a standard gridded wind speed. The surface of the Earth is divided into a 0.2° × 0.2° grid. All wind speed samples that fall into a grid cell in an hour are combined via an inverse-variance weighted average of the wind speeds. This product is available globally and is only restricted to where CYGNSS can make wind speed measurements.

In contrast, this new CYGNSS Level 3 wind speed product with storm-centric averaging is only available within 400 km of the center of a tropical cyclone (TC). The primary function of this new product is to use intertrack comparisons to identify and remove outlier tracks. Note that a track is defined as a particular combination of GPS and CYGNSS satellite whose specular point on the ocean's surface traces a continuous curved path or "track." Intertrack comparisons are valuable if a GPS/CYGNSS satellite combination has an unforeseen bias or calibration issue. To perform intertrack comparisons with most CYGNSS measurements, samples from multiple tracks must be colocated a significant fraction of the time. The fraction of colocated samples is a function of the temporal and spatial windows used in the colocation. To

retain high-resolution storm information, the width of the spatial window should not be made much larger than the spatial resolution of CYGNSS (25 km). The maximum temporal window depends on the speed of the storm (movement of the storm center, not the wind speed). Typical TCs can move up to about 25 km per hour, so a temporal window of just 1–2 hours can cause smearing of the TC wind field.

Storm-centric coordinates (relative latitude/longitude pairs rather than absolute) are used in this algorithm to widen the temporal window of colocation without smearing the TC wind field. A time-continuous storm center location is required to compute relative latitude and longitude coordinates for each sample. To approximate this, National Hurricane Center (NHC) or JTWC Best Track locations (available at primary synoptic hours) are linearly interpolated.

Figure 9.1 shows the general algorithm used to create the storm-centric gridded L3 data product. Best Track data show when TCs are active and provide storm center locations every 6 hours for storms in the northern Atlantic and eastern Pacific (NHC) and in the Indian Ocean, western Pacific, Southern Hemisphere, and central Pacific (JTWC). First, CYGNSS Level 2 wind speeds within a 4.0° × 4.0° box centered on

Figure 9.1. Data flow in the storm-centric Level 3 algorithm.

a TC are selected. Every 6 hours (0, 6, 12, 18 Coordinated Universal Time [UTC]), a 3.6° × 3.6° grid centered on the Best Track storm center is populated with CYGNSS wind speeds according to the temporal window and the grid spacing. Each 6-hourly grid contains wind speeds from ± 6 hours, which means there is some overlap between the two adjacent synoptic times. To prevent redundancy, data from ± 3 hours is required for a grid cell to report a wind speed. At least one track in a cell must be from ± 3 hours, but other data from a larger window of ± 6 hours are used for intertrack comparison. A ± 6-hour window was chosen to balance data availability and error due to real change in the TC's wind field. For example, a ± 24-hour window is too large in most cases because the storm's size and intensity are likely to change significantly over 48 hours. Even a ± 6-hour window is too large in some cases. The Best Track storm intensity and wind radii are reported along with the storm-centric Level 3 winds to inform the user of how quickly the storm is changing. There is also a "quality_status" parameter, which rates the consistency of tracks relative to storm intensity.

Once relevant data have been selected within the temporal window of ± 6 hours, the data are divided into grid cells. The grid cell spacing or reporting interval is 0.15° (16.7 km). When populating each grid cell, data are taken from a square of ± 0.30°, which is twice the grid spacing. This creates an overlap with adjacent cells, and the grid spacing is an oversampling of the wind field. Figure 9.2 demonstrates how the cells overlap and where the data are selected. The red dot in the grid center is the grid cell that is the focus of this example. The black lines represent a portion of the grid. The shaded red region, which overlaps with all surrounding cells, is the area from where data can be taken to populate the center cell.

The maximum distance between samples in a cell is 0.85°, but a typical distance is smaller than this. Note that samples are averaged together within a cell so that the effective spatial resolution will become coarser. The impact on spatial resolution depends on the distribution of the samples within the cell.

Using the gridding system explained above, a typical cell has 1.2 tracks per cell. Note that a minimum of 2 tracks is required to report a wind speed.

9.2.2.4. Intertrack Comparison and Averaging
The reported wind speed of a cell and the handling of multiple tracks are determined by the number of tracks T in the cell. Each cell must contain wind speed measurements ("samples") from at least two tracks for a cell-averaged wind speed to be reported. If there is only one track in a cell,
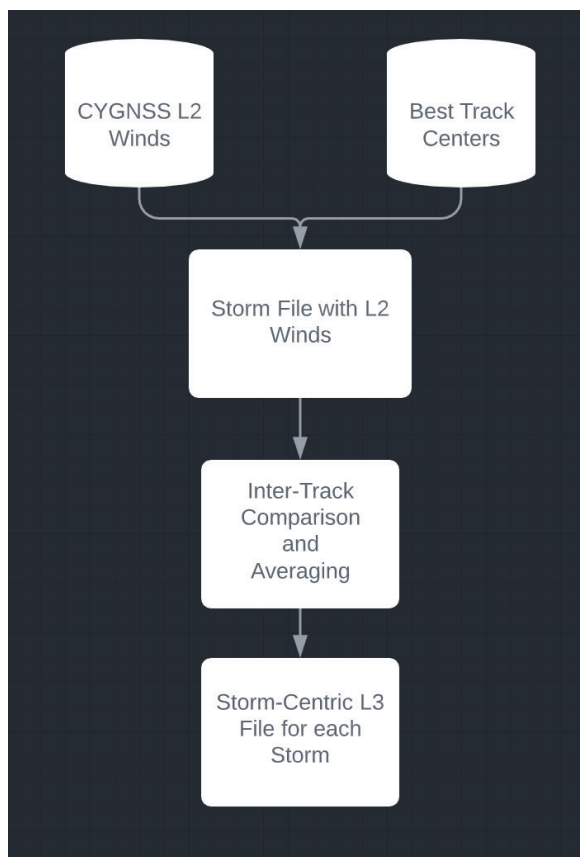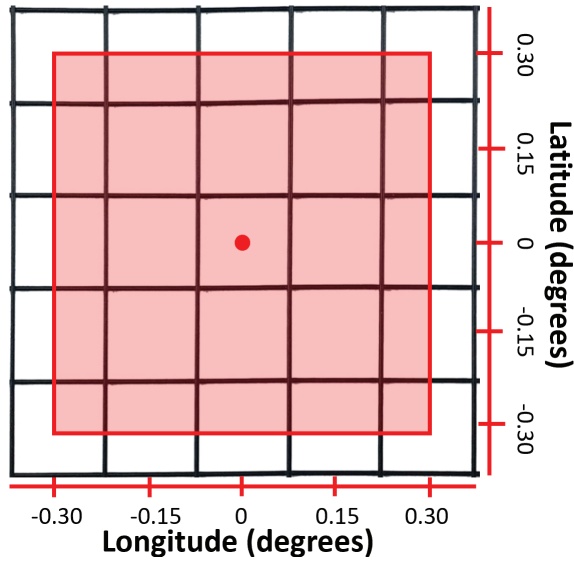
Figure 9.2. The red dot is the center of an arbitrary grid cell. The reporting interval is 0.15 ° and is represented by the black squares. Each black square is a different grid cell that contains its own set of CYGNSS samples and its own averaged wind speed. The red square represents the area from which the center grid cell derives its CYGNSS samples.

there is no way to verify that the wind speeds of that track are not problematic. When there are two tracks or more in the cell, the mean track wind speed $\overline{u}_t$ is computed for each track. There are N samples in the cell and T tracks with N_t samples in the tth track. The mean track wind speed for the tth track is given by

$$\overline{u}_t = \frac{1}{N_t}\sum_{j=1}^{N_t} u_{j'} \tag{9.1}$$

where u_j is the wind speed of the jth sample in the tth track. For the case $T = 2$, $\overline{u}_t$ must agree to within the threshold given by

$$\left|\overline{u}_{t1} - \overline{u}_{t2}\right| < 0.4\overline{u}_C + 3, \tag{9.2}$$

where $\overline{u}_C$ is the average of all wind speeds in the cell expressed as

$$\overline{u}_C = \frac{1}{N}\sum_{t=1}^{t=T} N_t \overline{u}_t. \tag{9.3}$$

The threshold as a function of the mean cell wind speed is derived empirically from the behavior of a large population of samples. If the difference between the two mean track wind speeds is below the threshold, the mean cell wind speed $\overline{u}_C$ is reported as Equation 9.3. If the difference is above the threshold, no wind speed is reported for the cell.

When there is a large difference between two tracks, there is no way to determine which mean track wind speed should be used.

When there are more than two tracks in a cell ($T > 2$), an outlier test is done to check if any mean track wind speeds $\overline{u}_t$ are anomalous. Track x is not an outlier if its mean track wind speed is within 3 standard deviations of the mean cell wind speed computed without track x. This is represented by the following condition:

$$\overline{u}_C^{-x} - 3\sigma_C^{-x} < \overline{u}_x < \overline{u}_C^{-x} + 3\sigma_C^{-x}, \tag{9.4}$$

where the superscript $-x$ indicates that track x is excluded when computing the term and where

$$\sigma_C^{-x} = \sqrt{\frac{1}{(T-1)-1}\sum_{t \neq x}\left|\overline{u}_t - \mu\right|^2} \tag{9.5}$$

and

$$\mu = \frac{1}{T-1}\sum_{t \neq x}\overline{u}_t. \tag{9.6}$$

Any outlier tracks that are flagged by this method are removed from further consideration. Before moving on, the algorithm checks to see if the removal of outlier track(s) removed all the samples within ± 3 hours. If there are no remaining samples within ± 3 hours, no wind speed is reported for the cell. This is because there are no measurements in the ± 3-hour window of the cell that support the wind speed that would be reported.

Next, the variation of the mean track wind speeds $\overline{\mu}_t$ is examined to see if the spread is typical. This is done whether outliers were found or not. First, the expected standard deviation is computed from the following relation:

$$\sigma_{Expected} = 0.26 \times \left(\overline{u}_{top2} - 3.5\right), \tag{9.7}$$

where $\overline{u}_{top2}$ is the average of the two highest mean track wind speeds $\overline{\mu}_t$ after removal of the outlier track(s). If the standard deviation of the mean track wind speeds is more than 3 greater than the expected standard deviation, no wind speed is reported for the cell.

$$\sigma_C^{-Outliers} > \sigma_{Expected} + 3 \tag{9.8}$$

If the condition in Equation 9.8 is not met, then the wind speed for the cell is reported as Equation 9.3 but with outlier track(s) excluded.

This intertrack comparison algorithm is done for all grid cells. Typical SCG wind speed products are shown in

Figure 9.3, together with standard gridded L3 YSLF winds during the same time period for comparison.

9.2.2.5. Intertrack Comparison

One of the primary benefits of using storm-centric coordinates and intertrack comparisons is the additional consistency it imposes on the reported wind speeds. The standard deviation of the wind speeds within each cell can be used to quantify the consistency of the winds that are used to generate the reported cell wind speed. Figure 9.4 shows the probability distribution function (PDF) for the standard deviation of individual wind speed samples that are averaged together to produce a grid cell's wind speed before and after applying intertrack quality control. The average standard deviation is 4.53 without the intertrack quality control and this is reduced to 3.53 with intertrack quality control applied. As outlier tracks are removed in the intertrack comparison process, the variance within each grid cell decreases. Because of this, there is a much smaller tail of high standard deviations in the distribution when inter-track quality control is applied. The skewness of the distribution decreases from 1.85 to 1.40, which means that more samples are closer to the mean and fewer are in the high standard deviation tail with intertrack quality control.

9.2.2.6. Output Data Product Description

The key output data fields produced include the following:

u_{L3} The minimum variance estimate of the mean wind speed averaged over the time and space intervals defined by Equation 9.1 for a particular bin, as given by Equation 9.2 (units of meters/second)

σ_{L3} The standard deviation of u_{L3} for a particular bin, as given by Equation 9.3 (units of meters/second)

S Number of samples used to calculate u_{L3}.

A full list of the data fields is provided in Section 9.2.2.8.
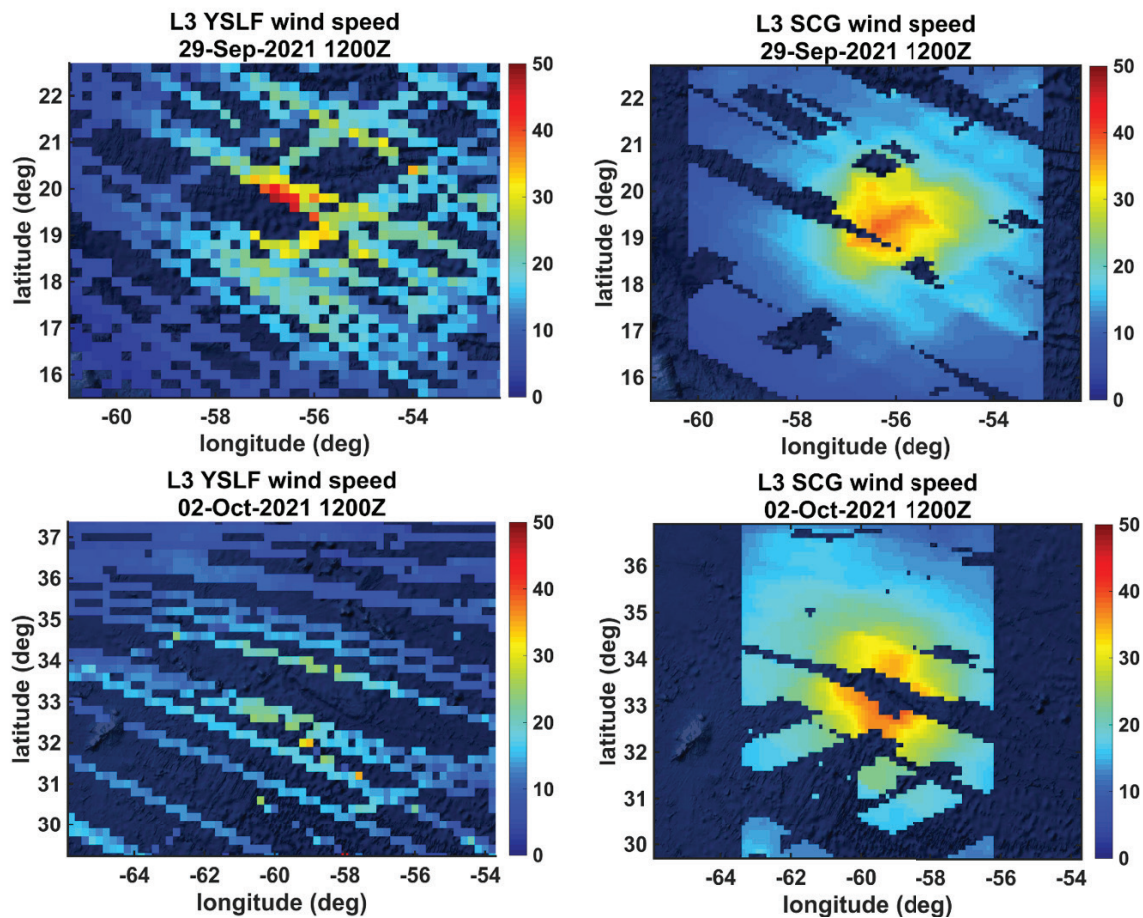
Figure 9.3. Examples of standard L3 young seas limited fetch (YSLF) winds without storm-centric regridding (left column) and L3 storm-centric gridded (SCG) wind fields covering the same time period (right) for two Hurricane Sam overpasses. The gaps in the L3 SCG fields are cells that either do not contain CYGNSS samples from multiple tracks or have disagreement between tracks.
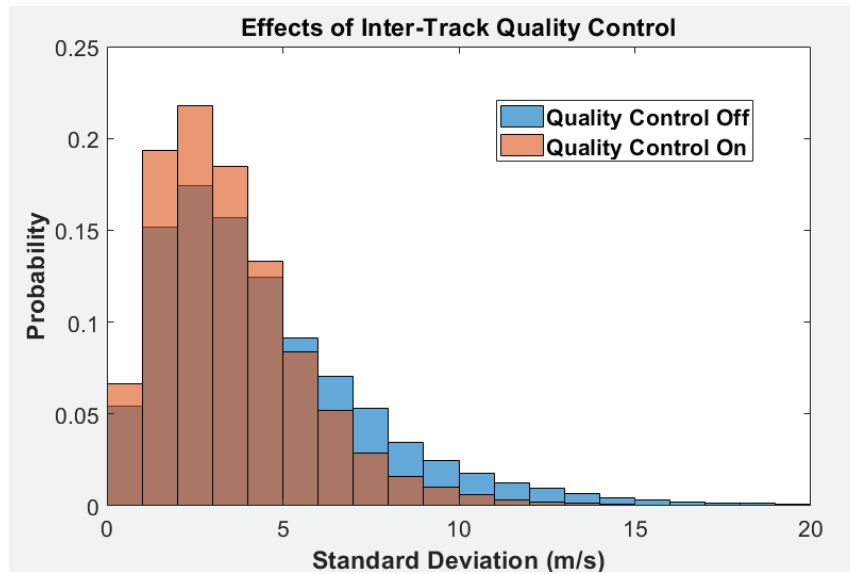
Figure 9.4. The probability distribution of wind speed standard deviation within a grid cell with two or more tracks. Each grid cell contains many wind speed measurements. The standard deviation of those wind speeds tends to be lower after the intertrack quality control is applied. The average standard deviation is 4.53 and 3.53 without and with quality control, respectively. The skewness is 1.85 without intertrack quality control and 1.40 with.

9.2.2.7. Algorithm Configuration Parameter Values

The principle configuration parameters for this algorithm are the latitude, longitude, and time boundaries of the bins. The bins are uniformly spaced every 0.2° in latitude from −40° N to +40° N, every 0.2° in longitude from 0 to 360° E, and every 1 hour in time. Specifically,

Lat_{min} =-40°,-39.8°, . . . , +39.8° N latitude

Lat_{max} =-39.8°,-39.6°, . . . , +40° N latitude

Lon_{min} = 0°, 0.2°, . . . , 359.8° E longitude

Lon_{max} = 0.2°, 0.4°, . . . , 360.0° E longitude

T_{min} = (year, day of year, 0 hr UT), (yr, DOY, 1 hr UT), . . . , (yr, DOY, 23 hr UT)

T_{max} = (year, day of year, 1 hr UT), (yr, DOY, 2 hr UT), . . . , (yr, DOY, 24 hr UT)

9.2.2.8. L3 SCG Data Dictionary

Name	Long name	netCDF dimensions	Comment
Global attributes			
bin_resolution_hr	<none>	<none>	Bin resolution in hours.
l3_storm_centric_algorithm_version	<none>	<none>	L3 storm-centric processing algorithm version number.
source	<none>	<none>	Level 2 netCDF source file names.
storm_name	<none>	<none>	Name of storm.
geospatial_min_lat	<none>	<none>	Minimum latitude of the grid that bounds the whole storm's path.
geospatial_max_lat	<none>	<none>	Maximum latitude of the grid that bounds the whole storm's path.
geospatial_min_lon	<none>	<none>	Minimum longitude of the grid that bounds the whole storm's path.
geospatial_max_lon	<none>	<none>	Maximum longitude of the grid that bounds the whole storm's path.
time_coverage_start	<none>	<none>	sample_time of the first sample in the file in ISO-8601 form.
time_coverage_end	<none>	<none>	sample_time of the last sample in the file in ISO-8601 form.
time_coverage_duration	<none>	<none>	The time interval between test_coverage_start and test_coverage_end in ISO-1806 form.
time_coverage_resolution	<none>	<none>	The nominal time interval between samples in ISO-1806 form.
Dimensions			
time	Time	<none>	Timestamp coordinate at the center of the 12 hr bin at 6 hr resolution. The range length is unique to each storm.
epoch_time	Time centering of data based on epoch reference	<none>	Timestamp coordinate is at the center of the 12 hr bin at 6 hr resolution referenced by the historical epoch reference date/time. The epoch reference date/time corresponds to the first observation time window in the CYGNSS historical data record. Total number of timestamps in a file corresponds to one UTC day. This value is rounded to the nearest hour, since leap seconds may have occurred, making the number of hours since the start of the mission not exact.
storm_centric_lat	Latitude relative to best_track_storm_center_lat	<none>	Relative latitude coordinate at the center of the bin, °_north, at 0.1° resolution. Range is –3.6 to 3.6.
storm_centric_lon	Longitude relative to best_track_storm_center_lon	<none>	Relative longitude coordinate at the center of the bin, °_east, at 0.1 ° resolution. Range is –3.6 to 3.6.

9.2.2.8. L3 SCG Data Dictionary (continued)

Name	Long name	netCDF dimensions	Comment
lat	Latitude	\<none>	Absolute latitude coordinate at the center of the bin, °_north, at 0.1° resolution. Range is geospatial_min_lat to geospatial_max_lat.
lon	Longitude	\<none>	Absolute longitude coordinate at the center of the bin, °_east, at 0.1° resolution. Range is geospatial_min_lon to geospatial_max_lon.
Per-time step values			
best_track_storm_center_lat	Storm center latitude	time	Latitude coordinate of the storm center at the given time as reported by the NHC/JTWC's Tropical Cyclone Best Track data product. Range is –90 to 90.
best_track_storm_center_lon	Storm center longitude	time	Longitude coordinate of the storm center at the given time as reported by the NHC/JTWC's Tropical Cyclone Best Track data product. Range is –180 to 180.
storm_status	Storm status	time	The level of storm development as reported by the NHC/JTWC's Tropical Cyclone Best Track data product: 0 = tropical depression 1 = tropical storm 2 = typhoon 3 = super typhoon 4 = tropical cyclone 5 = hurricane 6 = subtropical depression 7 = subtropical storm 8 = extratropical systems 9 = monsoon depression 10 = inland 11 = dissipating 12 = low 13 = tropical wave 14 = extrapolated 15 = unknown 16 = disturbance 17 = error
best_track_max_sustained_wind_speed	Maximum sustained wind speed	time	Maximum sustained wind speed in meters per second as reported by the NHC/JTWC's Tropical Cyclone Best Track data product.
best_track_r34_ne	Radial extent of 34 knot winds in northeast	time	In the northeast quadrant, how far from the storm center 34 knot winds exist as reported by the NHC/JTWC's Tropical Cyclone Best Track data product.
best_track_r34_nw	Radial extent of 34 knot winds in northwest	time	In the northwest quadrant, how far from the storm center 34 knot winds exist as reported by the NHC/JTWC's Tropical Cyclone Best Track data product.
best_track_r34_sw	Radial extent of 34 knot winds in southwest	time	In the southwest quadrant, how far from the storm center 34 knot winds exist as reported by the NHC/JTWC's Tropical Cyclone Best Track data product.

(continued)

9.2.2.8. *L3 SCG Data Dictionary (continued)*

Name	Long name	netCDF dimensions	Comment
best_track_r34_se	Radial extent of 34 knot winds in southeast	time	In the southeast quadrant, how far from the storm center 34 knot winds exist as reported by the NHC/JTWC's Tropical Cyclone Best Track data product.
quality_status	Quality status	time	The quality status measures how well all samples in the "time" dimension perform in intertrack comparison tests relative to the storm intensity: –1 = Wind speeds were not computed 0 = Not enough data to determine status 1 = Poor quality 2 = Average quality 3 = High quality
Storm-centric per-grid values			
storm_centric_wind_speed	Storm-centric wind speed	time, storm_centric_lat, storm_centric_lon	Averaged CYGNSS L2 YSLF wind speed of samples in the bin over the spatial and temporal intervals specified by the bin's boundaries. Some wind speed tracks may be removed from averaging if they do not meet intertrack quality control standards. Wind speeds gridded relative to the storm_centeric_lat and storm_centeric_lon.
wind_averaging_status	Wind speed averaging status	time, storm_centric_lat, storm_centric_lon	Wind speed averaging status based on the number of tracks used in the calculation. Everything with a value of 1 and lower is considered poor quality. Values: –7 = Grid cell is located outside of the CYGNSS range –6 = Grid cell is located near land –5 = Three or more tracks with outliers, no close tracks, and high standard deviation –4 = Three or more tracks with outliers and no close tracks –3 = Three or more tracks with no outliers and high standard deviation –2 = Two tracks with disagreement 0 = No data 1 = Only one track 2 = Two tracks with agreement 3 = Three or more tracks with no outliers and low standard deviation 4 = Three or more tracks with outliers and close tracks
num_wind_speed_tracks	Number of wind speed tracks	time, storm_centric_lat, storm_centric_lon	The number of L2 wind speed tracks in grid cell.
num_winds	Number of wind speeds	time, storm_centric_lat, storm_centric_lon	The number of L2 wind speeds in grid cell.

9.2.2.8. *L3 SCG Data Dictionary (continued)*

Name	Long name	netCDF dimensions	Comment
Whole storm per-grid values			
wind_speed	Wind speed	time, lat, lon	Averaged CYGNSS L2 YSLF wind speed of samples in the bin over the spatial and temporal intervals specified by the bin's boundaries. Some wind speed tracks may be removed from averaging if they do not meet intertrack quality control standards. Wind speeds are output on a grid bound by geospatial_min_lat, geospatial_max_lat, geospatial_min_lon, and geospatial_max_lon.

9.3. References

Clarizia, M. P. (19 Nov. 2015). *Algorithm Theoretical Basis Document Level 2 wind speed retrieval.* CYGNSS Project Document, SPRL 148-0138, Rev 2, Chg 2.

Clarizia, M. P., Pascual D., Zavortony V., McKague D., Ruf, C. (2021). CYGNSS Algorithm Theoretical Basis Document Level 2 wind speed retrieval. Revision 2, Change 2, University of Michigan Doc. 148-0138, 95 pp. https://gnss-x.ac.cn/docs/gnssr/148-0138_ATBD_L2_Wind_Speed_Retrieval_R7.pdf.

Gleason, S. (19 Nov. 2014). *Algorithm Theoretical Basis Document Level 1B DDM calibration.* CYGNSS Project Document, SPRL 148-0137, Rev 1, Chg 0.

Landsea, C. W., & Franklin, J. L. (2013). Atlantic hurricane database uncertainty and presentation of a new database format. *Monthly Weather Review, 141,* 3576–3592. https://doi.org/10.1175/MWR-D-12-00254.1.

Ruf, C. S., Asharaf, S., Balasubramaniam, R., Gleason, S., Lang, T., McKague, D., Twigg, D., & Waliser, D. (2019). In-orbit performance of the constellation of CYGNSS hurricane satellites. *Bulletin of the American Meteorological Society, 100*(10), 2009–2023. https://doi.org/10.1175/BAMS-D-18-0337.1.

Wang, T., Ruf, C. S., Gleason, S., O'Brien, A. J., McKague, D. S., Block, B. P., & Russel, A. (2021). Dynamic calibration of GPS effective isotropic radiated power for GNSS-reflectometry Earth remote sensing. *IEEE Transactions on Geoscience and Remote Sensing, 60.* https://doi.org/10.1109/TGRS.2021.3070238.

10. Level 3 Soil Moisture Product

10.1. Introduction

The University Corporation for Atmospheric Research, University of Colorado (UCAR/CU) Cyclone Global Navigation Satellite System (CYGNSS) Soil Moisture Product is an L-band bistatic radar dataset that provides estimates of 0–5 cm soil moisture at a 6-hour discretization for the majority of the extratropics. CYGNSS is a constellation of eight small satellites that was designed to observe ocean surface wind speed during hurricanes (PI Chris Ruf, University of Michigan); it is a NASA Earth Ventures Mission that was launched in December 2016. These satellites employ a relatively new remote sensing technique called global navigation satellite system reflectometry (GNSS-R), which records L-band signals transmitted by navigation satellites that have reflected off the Earth's surface and back into space.

Traditional radar remote sensing requires a transmitter; by using existing signals from navigation satellites, GNSS-R satellites avoid this requirement. All that is needed is a receiver, which significantly reduces the cost of a satellite mission. Because of this, several receivers can be launched for a fraction of the cost of one traditional remote sensing satellite. The outcome is more data that are collected more frequently, albeit with trade-offs that will be described in his handbook.

CYGNSS, in effect, is repurposing the existing GNSS signals—using them for ocean surface remote sensing instead of navigation. Here, we repurpose the CYGNSS data to estimate soil moisture over land. This product should be used with caution—there are many known issues with the current version of the data, and the data are not final. Users should keep the following in mind when exploring the data: The CYGNSS mission was not designed for soil moisture remote sensing. Data are calibrated and recorded assuming that the rough ocean surface is the target. Only two people have been wholly responsible for the data provided here: recalibration over land, algorithm development, validation, and code generation, with a small amount of money generously provided by UCAR. In addition, using GNSS-R for remote sensing of the land surface is such a new field that much of the theory behind the signal scattering over the land surface is still being understood. Our algorithm makes assumptions about the scattered signal that at best are simplifications and at worst are incorrect. Keeping this in mind, we hope that users will not see these soil moisture retrievals as the best

that GNSS-R, or even CYGNSS, can provide, but we do hope they will serve as a launching point for learning about the true capabilities of this new field.

We would like to acknowledge Dr. Chris Ruf and the rest of the CYGNSS team for working hard to provide such high-quality GNSS-R to the community. Without their efforts, of course, there would be no soil moisture product. We would also like to acknowledge Jan Weiss, Maggie Sleziak, and Michael Rousseau at UCAR for helping put the retrievals online.

10.2. Soil Moisture Sensing Using GNSS-R

10.2.1. Previous Work

Historically, the majority of spaceborne GNSS-R studies focused on signals reflecting from the ocean surface either for the purpose of relating ocean surface roughness to wind speed or for altimetric applications. Ground- and aircraft-based experiments had shown success in measuring GNSS-R signals over land and relating them to changes in near surface (0–5 cm) soil moisture or vegetation water content, but it had generally been assumed that spaceborne GNSS-R signals recorded over the land surface would be too weak to be useful for these kinds of applications.

After the launch of TechDemoSat-1 (TDS-1) in 2014, observational evidence began to mount in favor of developing GNSS-R for land applications. Both Camps et al. (2016) and Chew et al. (2016) analyzed data from TDS-1 for sensitivity to soil moisture and found spatial and temporal variations in the GNSS reflected signal that appeared to be driven by soil moisture. Since then, both TDS-1 and the SMAP radar receiver (adapted to record GNSS-R signals) have shown sensitivity to a variety of land surface variables, including wetland extent (Nghiem et al., 2017) and surface freeze/thaw (Chew et al., 2017). Both TDS-1 and SMAP, though garnering the largest spaceborne GNSS-R datasets of their time, do not collect enough data to provide operational products and are mostly limited to proof-of-concept investigations.

NASA's Cyclone GNSS (CYGNSS) constellation, launched in December of 2016, however, does provide enough data. Instead of being a single instrument, CYGNSS comprises eight GNSS-R satellites in low Earth orbit around

the tropics. This vastly decreases the temporal repeat time. For instance, for the latitudinal band ~±38°, CYGNSS samples approximately 80% of SMAP's 36 km EASE-2 grid cells every day, and most of the time, CYGNSS will have multiple observations for these grid cells.

10.2.2. Remote Sensing at L-Band

Data collected by CYGNSS are sensitive to near surface soil moisture for the same reason that all instruments that collect signals at L-band are sensitive to soil moisture. How strongly any signal reflects off a surface is dependent on the dielectric constant of the surface. At L-band, the dielectric constant of the Earth is mostly controlled by its moisture content, with wetter surfaces producing stronger reflections. There is a secondary dependence on soil texture (i.e., the relative amounts of sand, silt, and clay that compose a soil), though it is small compared to the effect from soil moisture.

L-band is often quoted as the wavelength of choice when it comes to soil moisture remote sensing. Higher frequencies like X- or C-band cannot penetrate even minimal vegetation canopies, whereas L-band can. L-band can penetrate the soil surface to some extent, and the amount of penetration also depends on soil moisture (Njoku & Entekhabi, 1996). In general, the effective penetration depth of an L-band signal, and thus of GNSS-R signals, is 0–5 cm. Longer wavelength signals, like P-band, have been studied for their ability to sense rootzone soil moisture, though its penetration depth will also depend on moisture content, which leads to greater

uncertainty in knowing what depth the retrieved soil moisture is actually representing. Restrictions on the transmission of this wavelength have also limited its development.

10.2.3. GNSS-R Sensitivity to Soil Moisture

Since 2015, there have been several studies investigating the sensitivity of GNSS-R to soil moisture (Camps et al., 2016; Chew et al., 2016; Chew, Colliander, et al., 2017; Chew & Small, 2018; Chew et al., 2018). Most of these studies have been conducted using empirical observations from CYGNSS or TechDemoSat-1. Observational evidence clearly shows that GNSS-R is very sensitive to surface water from lakes and rivers (Figure 10.1), even in the presence of an overlying vegetation canopy.

Measuring the sensitivity of GNSS-R/CYGNSS observations to soil moisture, however, is more challenging. Spatial variations in both land cover and topography, which affect the roughness of the surface, will also affect $P_{r,eff}$. This is exemplified in Figure 10.2, which shows a satellite image of northern India along with CYGNSS observations of $P_{r,eff}$. Although higher $P_{r,eff}$ is observed in vegetated areas, which should have higher soil moisture than the surrounding arid regions, one can also see the influence of mountain ranges and other surface features on $P_{r,eff}$.

In order to untangle the response of $P_{r,eff}$ to both soil moisture and land cover/surface roughness, we assume that over time only soil moisture changes, whereas land cover and surface roughness remain largely static. Of course, this
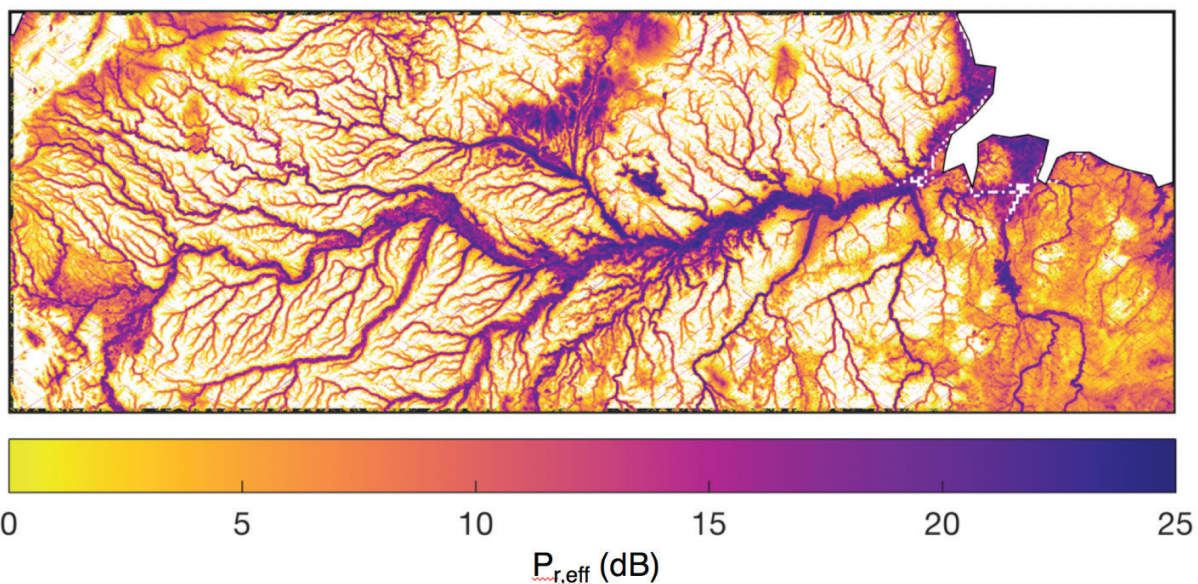
Figure 10.1. Observations of $P_{r,eff}$ over the Amazon basin.

approach ignores changes in vegetation water content. By looking at temporal fluctuations in both soil moisture and $P_{r,eff}$, we can quantify the sensitivity of $P_{r,eff}$ to soil moisture. Figure 10.3 shows an example of this kind of analysis in India, where changes in SMAP soil moisture are compared to gridded changes in $P_{r,eff}$. The correlation between the two is strong (r = 0.84).

10.3. The UCAR/CU Retrieval Algorithm

10.3.1. Introduction to the Algorithm

Our algorithm uses colocated soil moisture retrievals from the soil moisture active passive (SMAP) mission as "ground truth" to calibrate concurrent (same day) CYGNSS observations. For a given location, a linear relationship between SMAP soil moisture and CYGNSS reflectivity is determined, and the relationship is used to transform all CYGNSS observations into soil moisture, even at times when there are no SMAP matchups.

Using SMAP data as "ground truth" of course comes with many drawbacks, the major one being that SMAP soil moisture retrievals are not actual ground truth observations and have their own errors and uncertainties. One must be careful when using CYGNSS data in areas where it is known that SMAP performs poorly. In addition, SMAP's 40 km spatial resolution is *likely* coarser than that of CYGNSS, though this is still up for debate. Intelligent upscaling of CYGNSS data to the 36 km EASE grid that SMAP uses is necessary. If the resolution of CYGNSS is smaller than 36 km, then we are in effect degrading the CYGNSS data by doing this and not using it to its full potential. However, in the absence of mature or validated GNSS-R scattering models, empirical algorithms must suffice, and SMAP data are considered to be the most accurate of the existing soil moisture products.

10.3.2. Algorithm Description

This section is a step-by-step guide to the soil moisture retrieval algorithm. It assumes a working knowledge of the CYGNSS
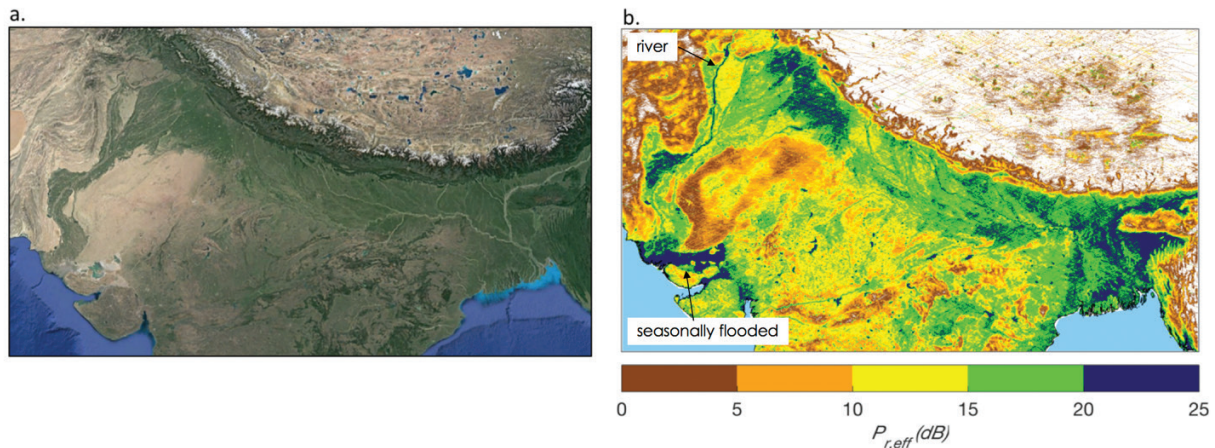
Figure 10.2. (a) Google Earth image of northern India. (b) CYGNSS observations of $P_{r,eff}$ over the same region. The color bar is continuous and is only chunked by 5 dB to highlight the response of $P_{r,eff}$ to different land cover types.
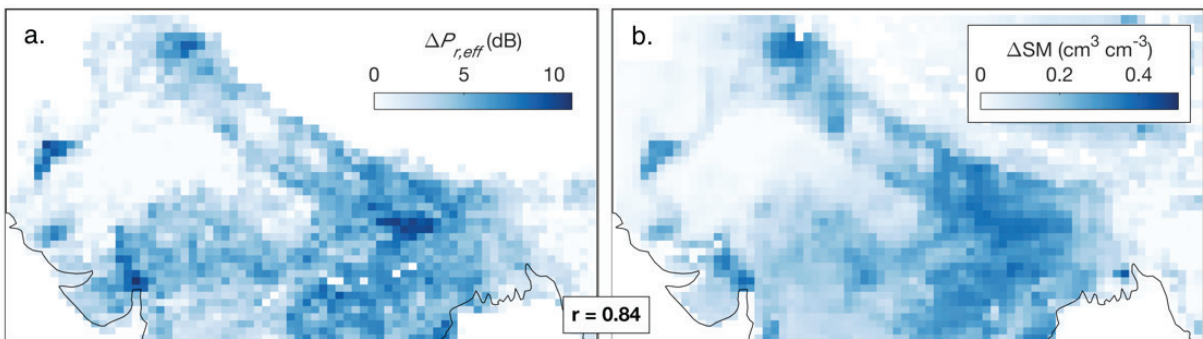
Figure 10.3. (a) Changes in $P_{r,eff}$, gridded to 36 km, between May and August 2017. (b) Changes in soil moisture from SMAP between May and August 2017. Adapted from Chew and Small (2018).

Level 1, version 2.1 netCDF files, all of which are available here: https://podaac.jpl.nasa.gov/CYGNSS. In general, for every day of the year, there will be eight Level 1 files, one for each CYGNSS satellite. Each of the eight files contains information pertaining to the thousands of reflections recorded on that day. The following steps are applied to each reflection in each file.

10.3.2.1. Processing of Delay-Doppler Maps (DDMs)

In previous works, we used the signal-to-noise ratio (SNR) as the signal of interest, which in the CYGNSS files is contained in the metadata as a variable called "ddm_snr." However, as time went on, we realized we were getting better results if we instead just pulled the peak value of the analog DDMs (variable name: power_analog) themselves and did not worry about the noise floor. We do not know why this is the case—possibly the noise floor itself is too noisy—and we do still utilize the SNR value itself for quality control. The peak value of the analog DDM is found and converted to dB, which we thereafter call *Pr*. The delay bin at which *Pr* occurs is also found during this step.

10.3.2.2. Correction of Pr for Other Effects to Derive P$_{r,eff}$

Pr is not just affected by soil moisture or surface roughness; it is also affected by the gain of the receiving antenna, bistatic range, and the transmitted power of the GPS satellite. *Pr* is then corrected for antenna gain, range, and the GPS transmit power assuming a coherent reflection:

$$P_{rl}^{r} = \frac{P_r^t G^t}{4\pi \left(R_{ts} + R_{sr}\right)^2} \frac{G^r \lambda^2}{4\pi} \Gamma_{rl},$$ **(10.1)**

where P_r^t is the transmitted right-hand circularly polarized (RHCP) power, G^t is the gain of the transmitting antenna, R_{ts} is the distance between the transmitter and the specular reflection point, R_{sr} is the distance between the specular reflection point and the receiver, G^r is the gain of the receiving antenna, λ is the GPS wavelength (0.19 m), and Γ_{rl} is the surface reflectivity. P_{rl}^r is the *Pr* as explained above. If you want to do this yourself, you will need the following variables: "sp_rx_gain" (G^r), "rx_to_sp_range" (R_{sr}), "tx_to_sp_range" (R_{ts}), and "gps_eirp" ($P_r^t G^t$).

What we actually want to do is solve for Γ_{rl}, and we do this by converting all terms to dB (some of them are already in dB in the CYGNSS files). We tend to call Γ_{rl} (in dB) that has been corrected for all these effects P$_{r,eff}$, which stands for effective reflectivity.

10.3.2.3. Land Calibration

We make additional empirical calibrations for the GPS transmit power, which we have not described in previous papers. While these corrections are suboptimal, it is much better than doing nothing. It is no secret that v2.1 GPS transmit powers are rough estimates, and we have found some biases in *Pr* depending on GPS pseudorandom noise (PRN) #. However, unlike other researchers, we have not found that removing the block IIF satellites is necessary, so we keep them in to preserve more than a third of the total observations.

We currently calibrate the CYGNSS data in part of the Sahara Desert where *Pr* is relatively stable throughout the year and soil moisture and vegetation changes have a negligible effect. In future versions, we will recalibrate over a longer time period and use data from dedicated CYGNSS cal/val sites, which at this time are still being determined. Figure 10.4 shows the part of the Sahara where the current calibration was completed (limits are indicated by the pins):

Figure 10.5 shows what P$_{r,eff}$ (labeled as SNR in the plot) looks like for the outlined region. Black dots are limits of what we will call subcells, which here we chose to be approximately 7 km × 7 km. In order to calculate PRN biases, we take the mean of *Pr* observations within each subcell and then calculate deviations from the mean (Figure 10.6). Because soil moisture, vegetation, and roughness should be expected to minimally affect *Pr* for each subcell, we assume that deviations from the mean are the result of suboptimal PRN corrections (and incidence angle variations, described in the next section).

The goal of this exercise was to decrease the standard deviation of the distribution as much as possible (Figure 10.6). It turns out that if you bin this distribution by PRN, you see some consistent biases (Figure 10.7).

These biases are removed from P$_{r,eff}$ as the empirical calibration. It is likely that these biases actually change over time, and in future versions we will update these calibrations. Table 10.1 shows the biases themselves.

10.3.2.4. Incidence Angle Correction

Incidence angle is also expected to affect a coherent reflection, though angle only significantly affects the P$_{r,eff}$ when the angle is above 40 or 50°. We modeled how P$_{r,eff}$ should be affected by incidence angle for several different soil moisture values (Figure 10.8). If you normalize everything to 0° incidence, then you find that soil moisture only slightly changes the relationship between P$_{r,eff}$ and incidence angle. (This normalization is also done in Al-Khaldi et al., 2019.) We compared the mean, modeled relationship to observations of P$_{r,eff}$ and confirmed the overall drop in P$_{r,eff}$ as the incidence
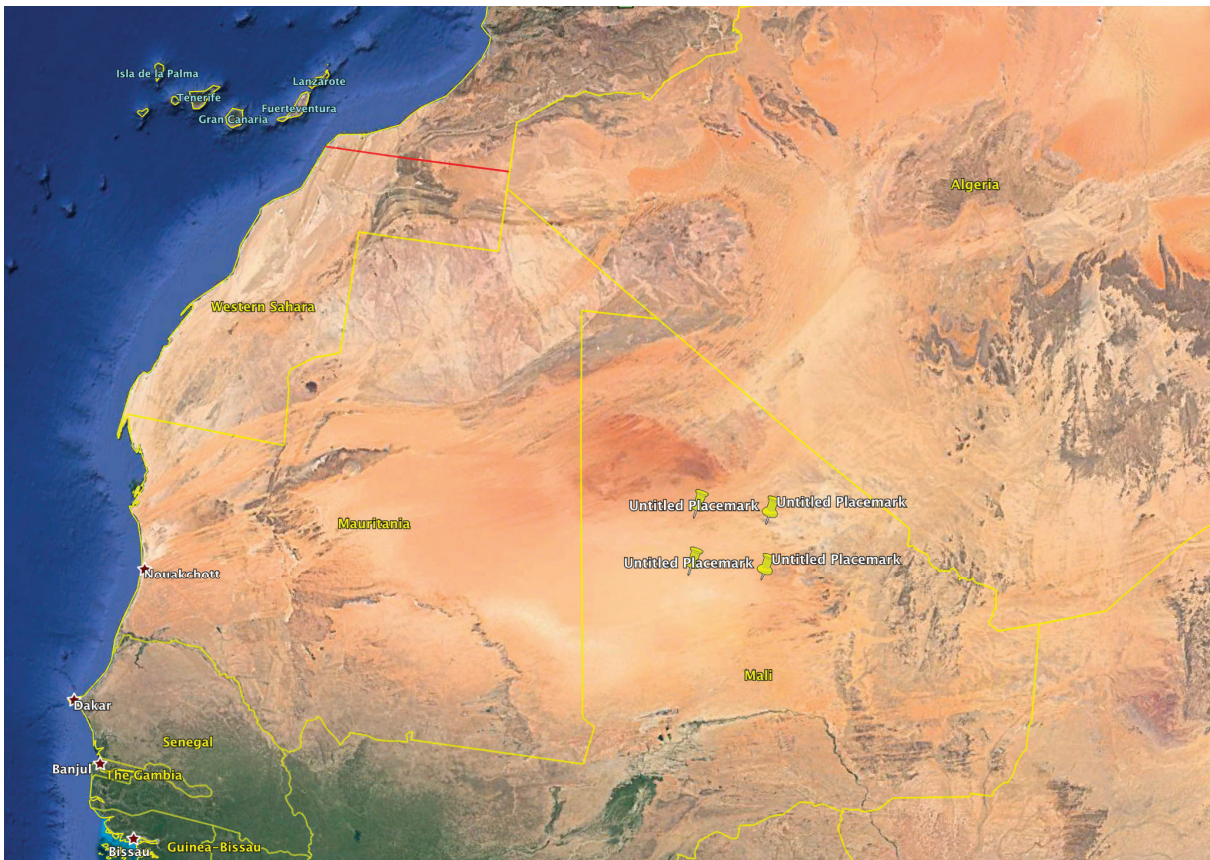
Figure 10.4. The region used for calibration is outlined by the yellow pins.
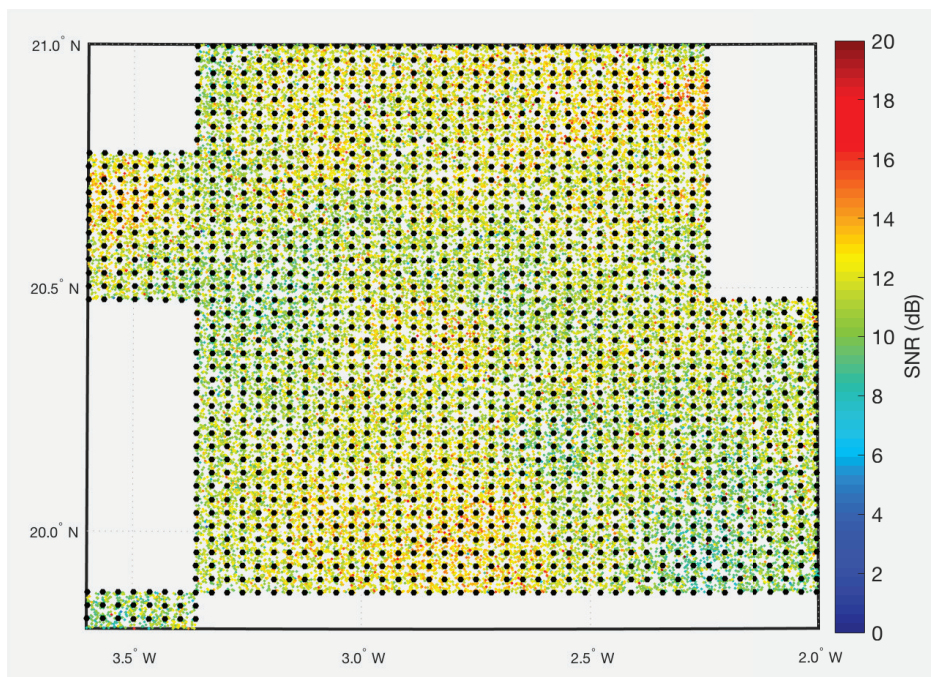
Figure 10.5. Observations of $P_{r,eff}$ (colored dots). Black dots outline 7 km × 7 km subcells.
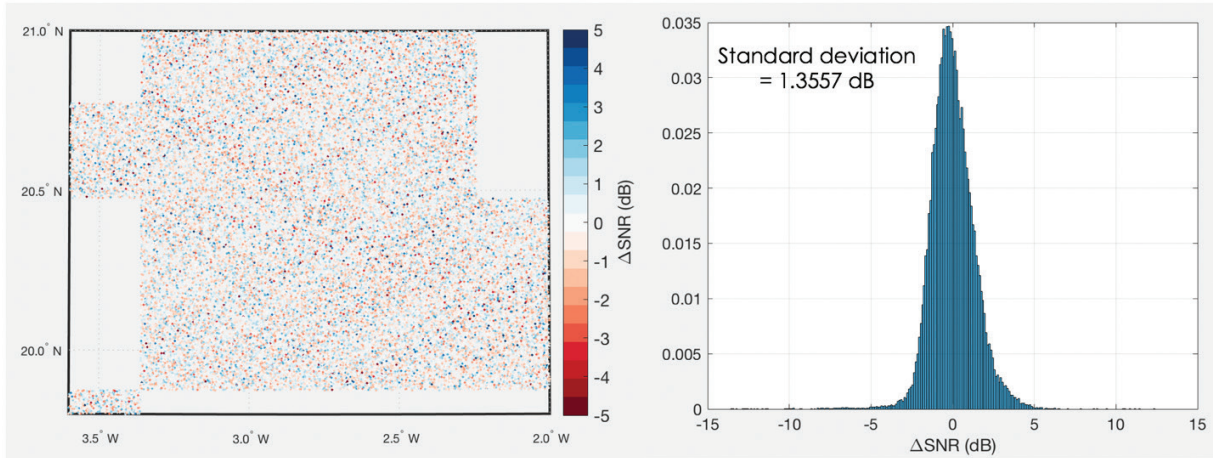
Figure 10.6. *Left:* Deviations of $P_{r,eff}$ from the mean for each subcell. *Right:* Histogram of deviations of $P_{r,eff}$. The standard deviation of the distribution is 1.3557 dB.
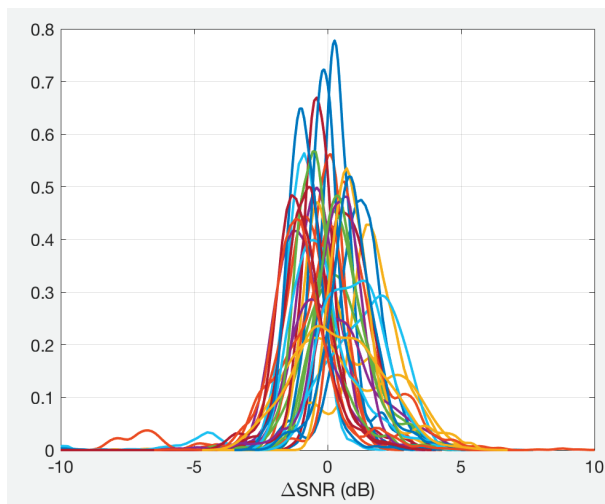
Figure 10.7. Distributions of $P_{r,eff}$ (labeled as SNR) as a function of PRN (unlabeled colored lines).

Table 10.1. Empirical Biases in $P_{r,eff}$ Found According to PRN

PRN	Bias (dB)	PRN	Bias (dB)	PRN	Bias (dB)
1	1.017	11	-0.230	21	-0.909
2	0.004	12	-1.021	22	-0.838
3	1.636	13	0.007	23	-0.858
4	NaN	14	-0.730	24	1.140
5	-0.610	15	-0.376	25	0.880
6	0.241	16	-0.481	26	0.163
7	-0.709	17	0.256	27	0.409
8	0.605	18	-0.474	28	-0.712
9	1.498	19	-0.206	29	-1.032
10	-0.783	20	0.345	30	0.877
				31	-0.562
				32	-0.819
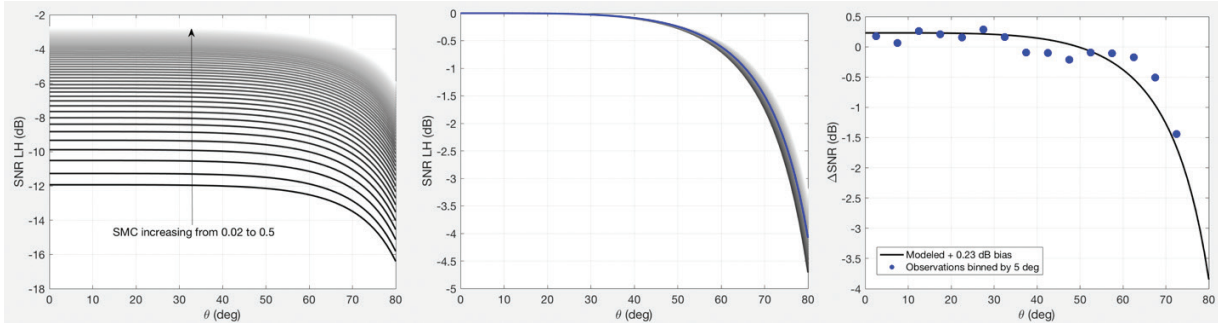
Figure 10.8. *Left:* Modeled relationship for how $P_{r,eff}$ should vary depending on incidence angle and soil moisture. *Middle:* Same as the left-hand panel, though here modeled $P_{r,eff}$ has been normalized to show that soil moisture does not significantly change the relationship between $P_{r,eff}$ and incidence angle. The blue line is the mean of the normalized relationships. *Right:* We binned observations of $P_{r,eff}$ over the Sahara in 5° increments to confirm that the modeled relationship at least loosely resembles what is seen in the observations.
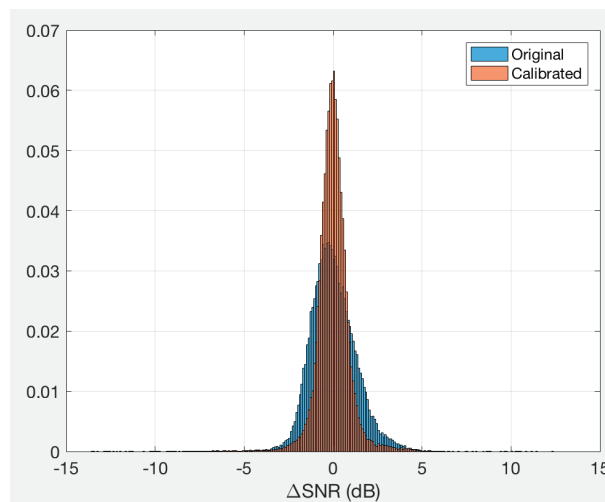
Figure 10.9. Distribution of changes of $P_{r,eff}$ over the Sahara before (blue) and after (orange) calibration and adjustment for incidence angle.

angle increases beyond 40°. We use the mean, modeled relationship to correct variations in $P_{r,eff}$ due to incidence angle.

After calibrating $P_{r,eff}$ for PRN biases and incidence angle, we see a significant decrease in the standard deviation of changes in $P_{r,eff}$ over the Sahara (Figure 10.9). The standard deviation decreased from 1.3 to 1 dB, which significantly improved soil moisture retrievals.

10.3.2.5. Outlier Identification

Standard quality flags are used in the CYGNSS metadata to remove some outliers—the specific flags we use are 2, 4, 5, 8, 16, and 17, which in order are S-band transmitter powered up, spacecraft attitude error, black body DDM, DDM is a test pattern, direct signal in DDM, and low confidence in the GPS equivalent isotropically radiated power (EIRP) estimate.

We perform additional quality control and remove the following: any observations with a (precorrected) SNR

value less than 2 dB, observations with a receiver antenna gain less than 0, observations with an incidence angle greater than 65°, and any data with a *Pr* coming in at a delay bin outside of 7–10 pixels (exclusive). In addition, we have found that results are improved if we impose a requirement that (precorrected) SNR must be less than or equal to the receiver antenna gain + 14. Lastly, we remove observations if the receiver gain is greater than 13 but still has a corrected $P_{r,eff}$ value less than 0. These are empirical corrections that are not standardized among other researchers using CYGNSS data.

Lastly, any data before ~December 2017 reflecting from a surface elevation above 600 m are removed. Because CYGNSS was optimized for ocean surface sensing, the satellites did not record DDMs that contained the full surface reflection coming from above about 600 m altitude because they were not looking for data from these heights.

The CYGNSS team changed the software after December 2017 to include these data.

10.3.2.6. Removal of Data Affected by Open Water

The removal of specular reflection points that are affected by open water is a critical step before retrieving soil moisture. Even small water bodies ~25 m wide can significantly affect $P_{r,eff}$, which then means that these $P_{r,eff}$ observations will not be affected by soil moisture as strongly (Figure 10.10). We have probably tried a dozen different ways to mask open water, and none of them is perfect because no currently available water mask is perfect. Thus far, we have found the best success using the Pekel et al. (2016) dataset (https://global-surface-water.appspot.com), which is a 30 m optically derived water mask. Because it is derived from optical data, it underestimates the amount of water beneath vegetation.

The current algorithm removes open water using the "seasonality" data product provided by Pekel et al. This product represents how many months out of a year a pixel is inundated (0–12). For our purposes, we make this product binary by considering any value greater than 1 to be flagged as water and anything below this to be nonwater. We do this because sometimes the permanent water bodies are seasonally covered by vegetation, which makes the Pekel et al. dataset represent them as less than 12 (permanent).

For each specular reflection point, we find the amount of water within a 7 × 7 km region surrounding the point. This is a simplification of the actual footprint, but it is computationally more efficient than rotating axes to form actual ellipses, which themselves are simplifications and not well quantified. If the amount of water in the 7 × 7 km region exceeds 1%, we remove that CYGNSS observation from consideration. Changing these thresholds or region sizes changes the results, though never uniformly increasing or decreasing error across regions.

10.3.2.7. Transforming $P_{r,eff}$ Into Soil Moisture

Here, we will describe how $P_{r,eff}$ is transformed into soil moisture, using SMAP soil moisture retrievals to calibrate CYGNSS observations. Our calibration period was chosen to be March 17, 2017–October 1, 2018.

Our algorithm is very simple: It assumes that $P_{r,eff}$ is linearly related to SMAP soil moisture. This relationship is expected to vary spatially, though in its current form, we assume that it does not change over time (future versions will allow for these changes). For a given location, we calculated the slope of the best fit linear regression between SMAP soil moisture and CYGNSS $P_{r,eff}$ after having removed the mean of each for the entire time series. Before we can describe this in more detail, however, we have to understand what "a given location" means in this context.

We already described that we assume that $P_{r,eff}$ has a finer spatial resolution than SMAP's 40 km resolution. We have found that we get the best results when we grid our $P_{r,eff}$ observations to ~3 × 3 km "subcells" and then aggregate the gridded observations to the 36 km SMAP EASE-2 grid resolution (Figure 10.11). Why subcells? If we were to aggregate
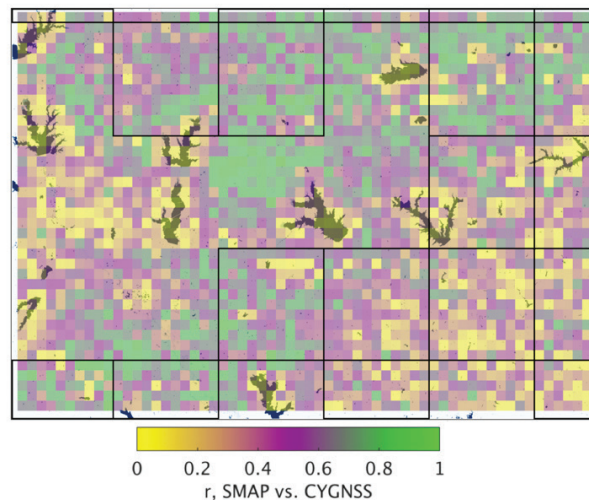
Figure 10.10. The correlation between CYGNSS observations and SMAP soil moisture for part of the United States (colored pixels). The Pekel et al. (2016) dataset for this region is also shown—the area is dominated by large reservoirs and smaller lakes. The correlation between SMAP and CYGNSS is low when observations fall on or near water bodies, which is expected. For reference, large black outlined boxes are the 36 km EASE-2 grid used by SMAP, which normally contains high-quality SMAP soil moisture observations.
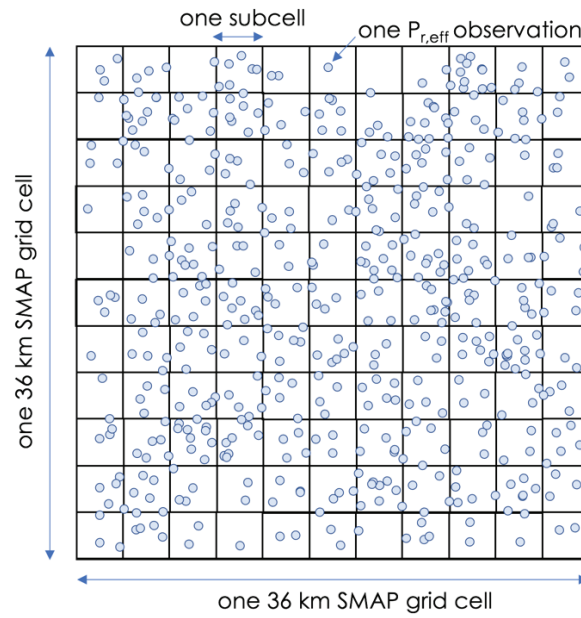
Figure 10.11. Depiction of how observations of $P_{r,eff}$ are gridded into subcells within a 36 km SMAP cell.
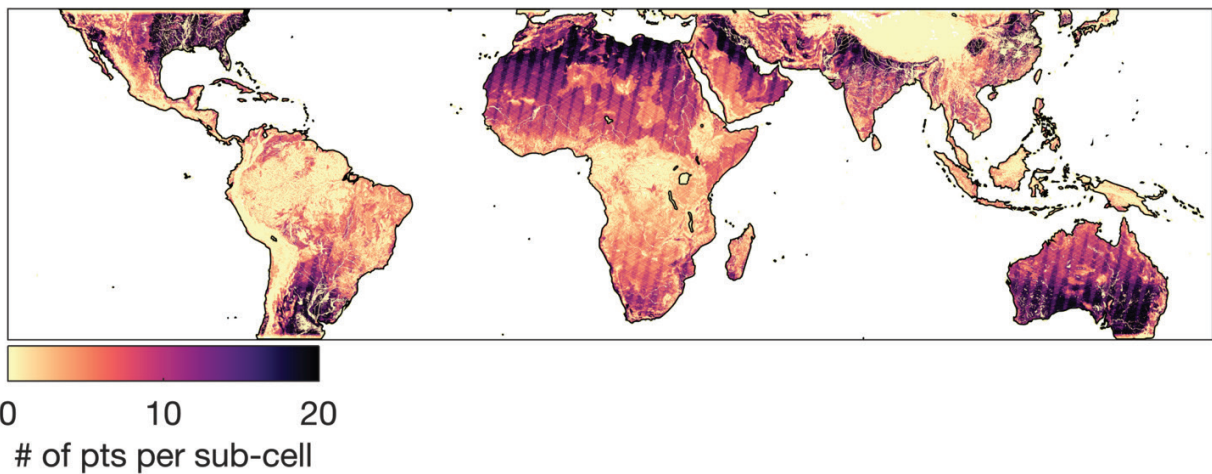
Figure 10.12. The number of CYGNSS observations for each subcell that were used for calibration. Fewer observations are found in higher elevation areas, which only have "good" data for about half the time series, relative to the lower elevation areas. Observations over open water have already been removed.

all observations of $P_{r,eff}$ in one 36 km grid cell and look at how $P_{r,eff}$ varied within that grid cell, we would see variations in $P_{r,eff}$ due to factors like land cover type and topography. By dividing the grid cell into smaller subcells, we see more consistent relationships between $P_{r,eff}$ and soil moisture. The subcells effectively help remove the confounding effects of land cover and topography on $P_{r,eff}$. The number of points per subcell in the calibration period is shown in Figure 10.12; subcells with less than 3 observations were not used for calibration.

Within each subcell, we calculated the linear regression between SMAP soil moisture and $P_{r,eff}$ matchups (occurring on the same day) after having removed the mean from both SMAP and $P_{r,eff}$ in that cell (correlation coefficients for this relationship are shown in Figure 10.13). The mean values of both SMAP and CYGNSS during the calibration period serve as our reference values in order to return an absolute value of soil moisture from CYGNSS. In our algorithm, the reference value is the mean soil moisture for the entire calibration period. We call the slope of the best fit line β, which is conceptualized in Figure 10.14.

β is used to estimate soil moisture from CYGNSS for data falling outside the calibration period as well as data within
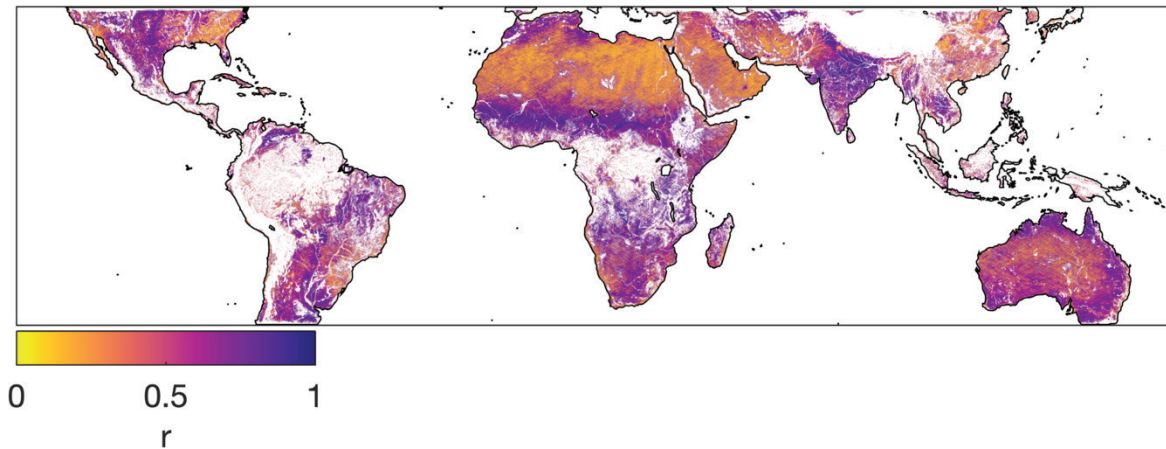
Figure 10.13. The correlation coefficient between SMAP soil moisture and CYGNSS reflectivity observations. Open water points have been removed. It is "easier" to get a higher correlation coefficient when there is significant soil moisture variability throughout the year.
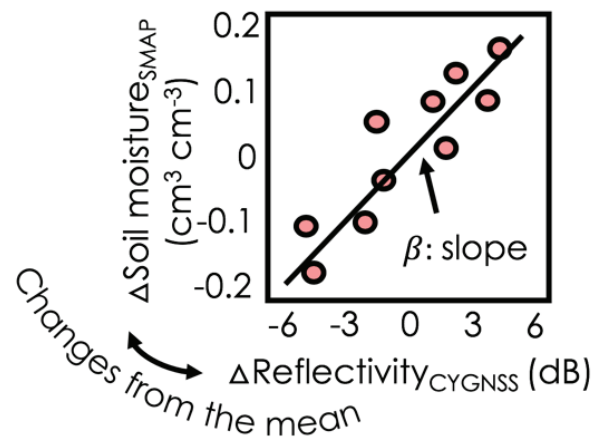
Figure 10.14. The slope of the best fit line between SMAP soil moisture and $P_{r,eff}$ (labeled as "Reflectivity") matchups is called β and is used to calculate soil moisture from CYGNSS.

the calibration period when there are no SMAP matchups (since SMAP has a 2–3 day overpass period):

$$Soil\,moisture_{CYGNSS} = \beta \times \ P_{r,eff} + \overline{Soil\,moisture_{SMAP}}.$$

β varies spatially (Figure 10.15). Unfortunately, sometimes it looks like β is influenced by noise in regions where soil moisture shows little or no variability throughout the year. We are looking into parameter regionalization to minimize these effects.

We then combine the subcell soil moisture retrievals by taking the average for a selected time period (either every 6 hours or every day) to upscale them to the EASE-2 36 km resolution. We are currently investigating whether or not the ~3 km retrievals are valid on their own—if so, we will release them in a future version.

10.3.2.8. Daily and Subdaily Retrievals

We currently provide soil moisture retrievals on daily and subdaily (6 hourly) time steps. For the daily retrievals, we average all observations within a particular grid cell that fall within the 24-hour time period. For the subdaily retrievals, we average all observations for a particular grid cell in 6-hour intervals, which are currently midnight–6 a.m., 6 a.m.–noon, noon–6 p.m., and 6 p.m.–midnight (Coordinated Universal Time [UTC]).

10.3.2.9. Quality Control

Currently, quality control is minimal—we remove soil moisture retrievals that indicate soil moisture being less than 0.01 or greater than 0.65 $cm^3\,cm^{-3}$.
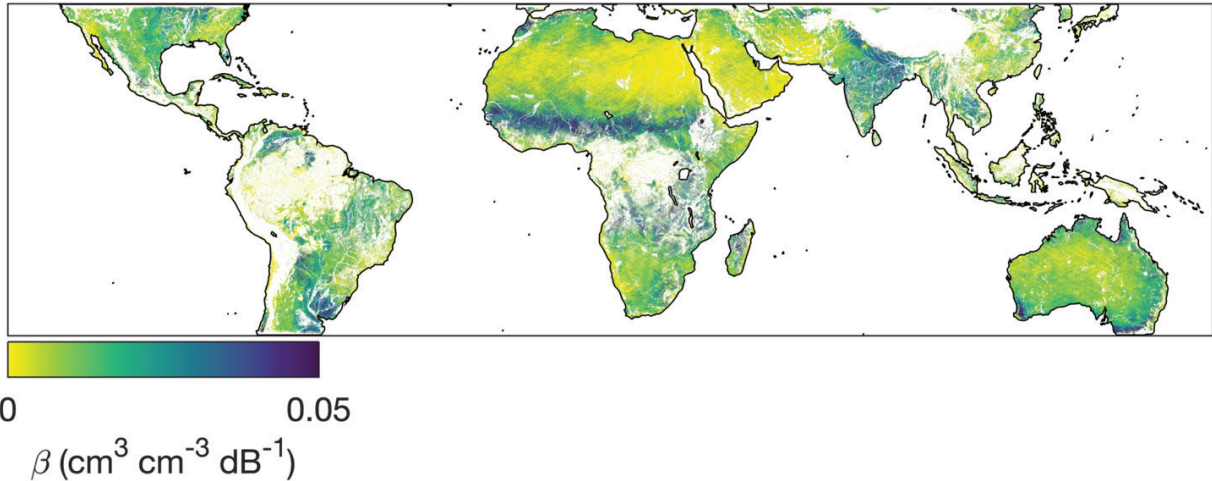
Figure 10.15. The slope of the linear regression between CYGNSS reflectivity observations and SMAP soil moisture (β). This represents the sensitivity of CYGNSS to soil moisture, with lower values indicating a higher sensitivity—though low values are also found in regions where soil moisture does not tend to vary. Higher values of β mean that CYGNSS is not as affected by increases or decreases in soil moisture. Be careful in interpreting this, as imperfect open water masking will cause an apparent insensitivity to soil moisture.
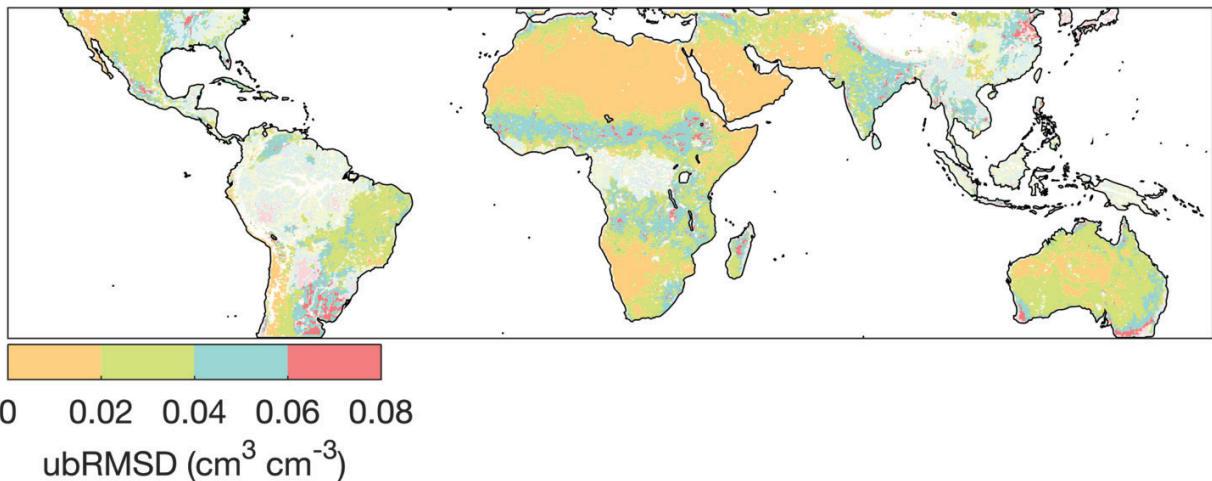
Figure 10.16. Unbiased root mean square difference between SMAP and CYGNSS soil moisture retrievals. Regions where SMAP always flags the data as being "poor quality" are semitransparent, such as the Amazon, central Africa, Indonesia, Japan, Southeast Asia, and the majority of the eastern United States. In these regions, you should be careful when using either SMAP or CYGNSS soil moisture data. Higher ubRMSD in regions with "good quality" SMAP data tend to be found in regions that are seasonally flooded or near coastlines. It is possible that in these areas, the seasonal water influence on CYGNSS reflectivity may overwhelm the soil moisture signal. Or it is also possible that the soil moisture signal in SMAP data is a red herring, and the brightness temperatures are actually responding to the increase in the flooded area instead of soil moisture. Answering this question will be the subject of future research.

10.3.2.10. *Soil Moisture Retrieval Uncertainty*

Figure 10.16 shows the unbiased root mean square difference (ubRMSD) between CYGNSS and SMAP soil moisture retrievals for the calibration period (March 18, 2017–October 1, 2018). Semitransparent regions are those frequently flagged by SMAP as being poor quality. Note that we tend to get higher ubRMSD in areas that flood seasonally.

10.4. Thoughts on Gridding

The gridding scheme described in Section 10.3.2.7 that utilizes ~3.3 km subcells in which to aggregate the CYGNSS data will come as a surprise to some—the majority of researchers analyzing CYGNSS data aggregate the observations to a much larger grid size (say, 25 km). However, we have found that we get the best results when we grid

to a much smaller grid size and then upscale the retrievals afterward.

The following represents a small, and possibly inappropriate, attempt to show why we believe the CYGNSS data respond to land surface characteristics on these scales. We wanted to find an area where we could quantify how much "blurring" of the CYGNSS signal there is as the soil transitions from dry to wet. These examples are actually not that easy to find (we were trying to avoid looking at transitions between water / dry land), and we settled on looking at the transition between desert and agricultural land in the Punjab region of Pakistan (Figure 10.17).

As a reminder, we currently think of the spatial footprint of CYGNSS to be an elongated ellipse, as shown in Figure 10.18. One might think that if the patch of land surface contained within this ellipse were completely dry, then $P_{r,eff}$ would be low, and if the patch of land were wet, then $P_{r,eff}$ would be high. If the ellipse were centered on the transition between wet and dry such that half the ellipse was wet and half was dry, then the resulting value of $P_{r,eff}$ would be in between the low and high values (Figure 10.18). The transition distance between high and low values of $P_{r,eff}$ as it moves across the landscape could be thought of as the blurring of an image.

Figure 10.18 also shows larger example footprints with diameters of 36 km. In the case of the yellow footprints, the westernmost one does not overlap with the cropland, and the resulting signal will not be contaminated by the cropland. In the case of the blue footprints, the westernmost one still overlaps with the cropland, so in this case, we would expect to see a higher signal than if we also had data from the
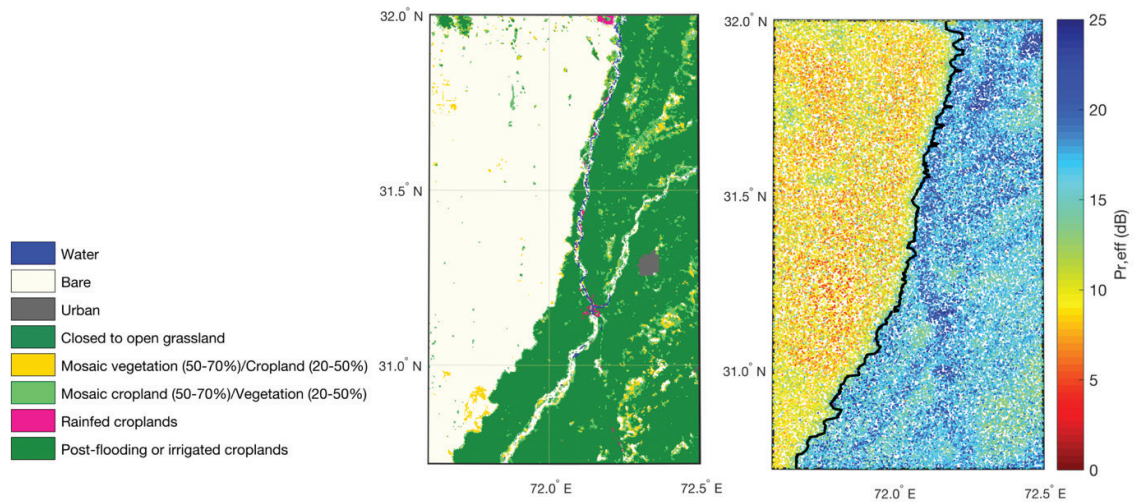
Figure 10.17. *Left:* GlobCover 2009 land cover map of the transitional region between desert and cropland in Punjab, Pakistan. *Right:* CYGNSS observations for the same region. The black line is our delineation between bare/croplands, which we gleaned from the land cover map.
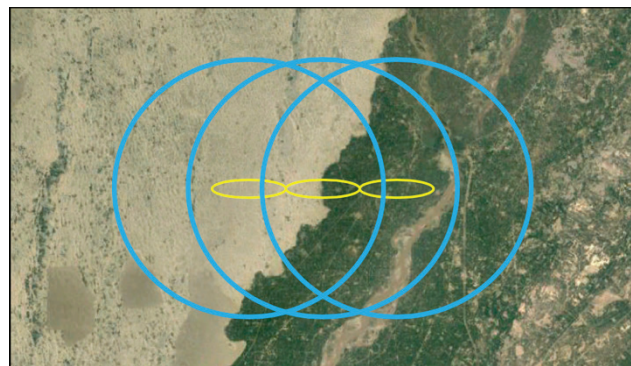
Figure 10.18. Simplified footprints to illustrate how a remote sensing image will appear more or less blurred depending on footprint size. Yellow footprints are approximately 7 × 0.5 km in size, which is the smallest theoretical footprint for CYGNSS, given its current integration time of 1 second. Blue footprints have a diameter of approximately 36 km.

westernmost yellow footprint. In this case, we would expect the blue footprints to show more blurring than the yellow ones.

We attempted to quantify the "blurriness" of both CYGNSS $P_{r,eff}$ observations and ungridded, Level 1, SMAP brightness temperature observations across this transition zone (Figure 10.20) by identifying the delineation between desert and croplands using the GlobCover 2009 land cover map (300 m resolution). Our fundamental goal in this exercise was to quantify how "long" (distance-wise) it took for $P_{r,eff}$ and brightness temperature observations to transition from their mean values over the desert to their mean values over the croplands. The easiest way to do this was to grid the CYGNSS and SMAP observations to the 300 m GlobCover 2009 resolution and then quantify how many grid cells it took for CYGNSS and SMAP to transition across the entire

region shown in Figure 10.17. Of course, the transition line is not directly oriented N–S, so we had to reference all pixels with respect to the line in order to collapse the dependence on latitude (Figure 10.19).

We then quantified the transition distance as being the distance that it took for $P_{r,eff}$ to increase from its mean value over the desert to its mean value over croplands (Figure 10.20). We found this distance to be 8.65 km, which is only slightly larger than the theoretical smallest along-track resolution of 7 km.

We repeated this exercise for the Level 1 SMAP V-pol brightness temperatures and found the transition distance to be approximately 38 km, which is pretty close to its actual resolution of 40 km; however, these could all be coincidences and need to be analyzed further before any blanket statements can be made.
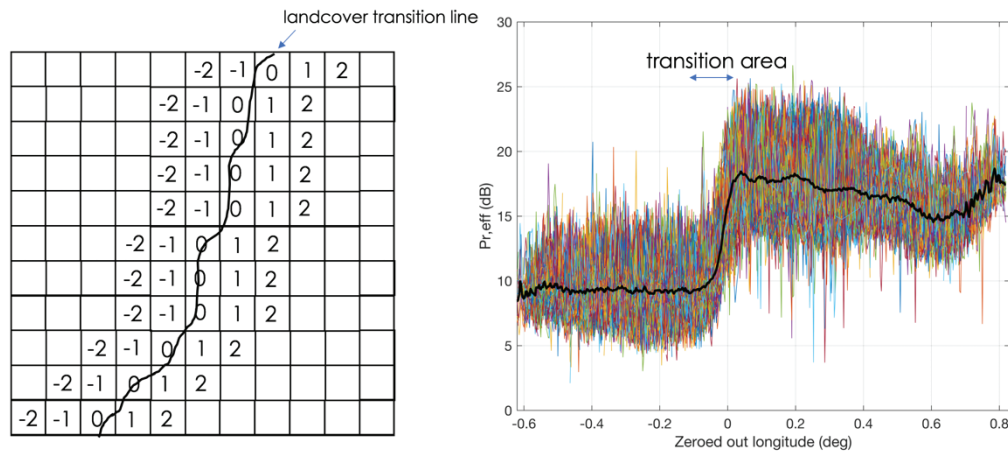
Figure 10.19. *Left:* A depiction of how the Punjab was gridded and referenced to the transition line between desert and cropland. *Right:* Colored lines are gridded $P_{r,eff}$, with each line representing one 300 m strip of grid cells, going N–S. The black line is the mean. The transition area is the distance it takes for $P_{r,eff}$ to change from its mean value over the desert to its mean value over croplands.
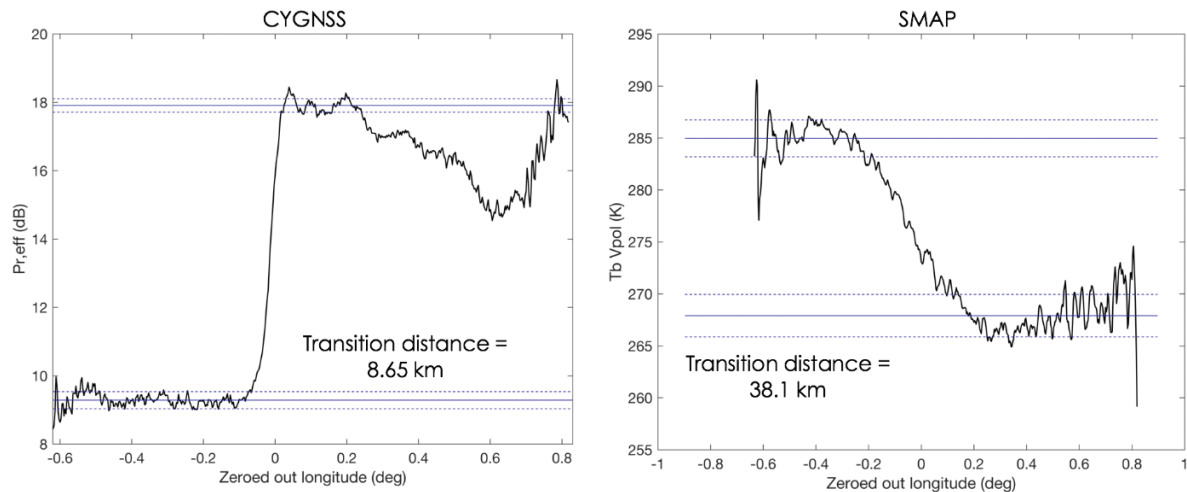
Figure 10.20. The transition distances across the Punjab for CYGNSS (left) and SMAP (right).

Finally, we have tested various gridding schemes on the CYGNSS data, and we find that both ubRMSD and the correlation between SMAP soil moisture and CYGNSS decrease and increase, respectively, when smaller grid sizes are used (Figure 10.21).

10.5. In Situ Validation

We are currently validating the CYGNSS soil moisture retrievals against in situ observations for the time period March 17, 2017–March 1, 2019. The networks we have chosen for validation are the following: Cosmic-Ray Soil Moisture Observing System (COSMOS), Plate Boundary Observatory Water (PBOH2O), Soil Climate Analysis Network (SCAN), Utah Snow Telemetry (SNOTEL), and US Climate Reference Network (USCRN), though not all networks have data for the entire validation time period. Although other networks exist (like iRON and SOILSCAPE), we found there to be little to no data that were useful for validation. We also removed some stations from our chosen validation networks that had long periods of nonsensical soil moisture data. In total, we used 203 different sites for validation.

In the figures and tables that follow, we show example CYGNSS soil moisture time series and the unbiased root mean square error (ubRMSE) between CYGNSS and in situ soil moisture, as well as the ubRMSE between SMAP and in situ soil moisture for context. In general, SMAP and CYGNSS showed similar ubRMSEs, which one would expect, given that CYGNSS was calibrated from SMAP. CYGNSS sneaked away with a slightly lower ubRMSE overall (Table 10.2). Of course, ubRMSE is not a perfect

Table 10.2. Unbiased Root Mean Square Error (ubRMSE) Between CYGNSS Soil Moisture/In Situ and SMAP Soil Moisture/In Situ for All 203 Stations and Divided by Network

Network	ubRMSE CYGNSS cm3 cm-3	ubRMSE SMAP cm3 cm-3
All	0.0471	0.0502
COSMOS	0.0426	0.0407
PBOH2O	0.0488	0.0471
SCAN	0.0461	0.0477
SNOTEL	0.0692	0.0754
USCRN	0.0438	0.0496
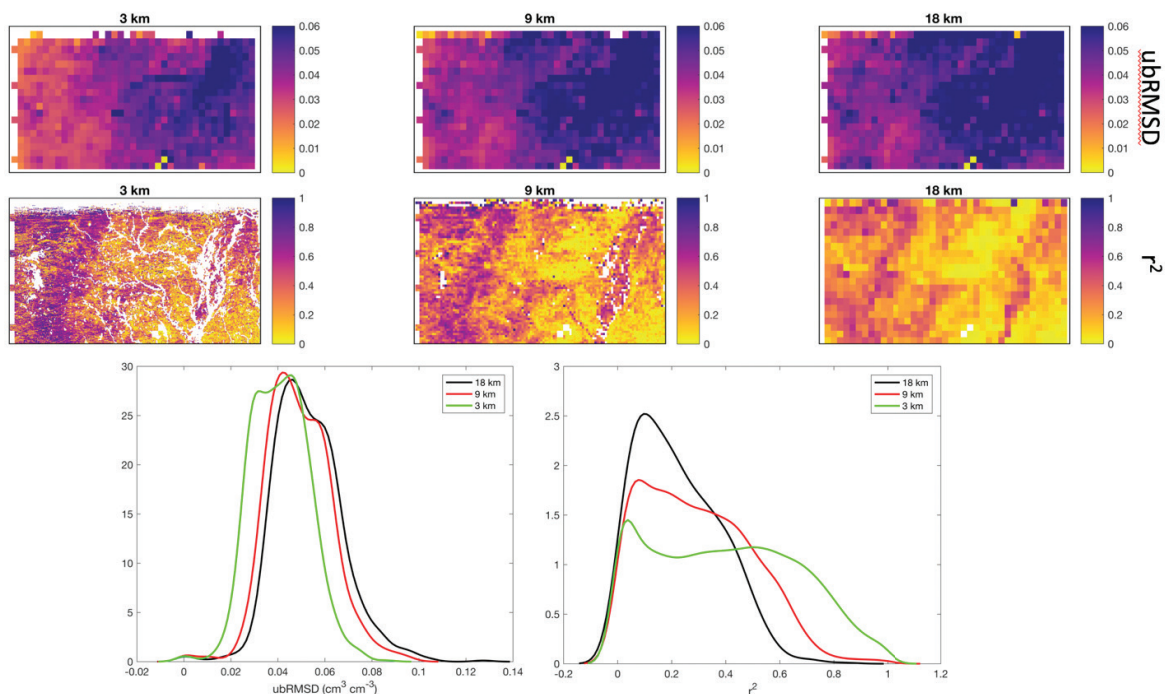
Figure 10.21. This figure uses a region in Oklahoma to exemplify the effect of the different subcell grid sizes on resulting CYGNSS soil moisture retrievals. Longitude and latitude were erroneously not labeled in these figures. (top row) The unbiased root mean square difference (cm^3 cm^{-3}) between SMAP and CYGNSS soil moisture retrievals when different subcell sizes are used—ubRMSD decreases when the subcell size decreases. (middle row) The r^2 value between SMAP soil moisture and P$_{r,eff}$ when different subcell sizes are used—r^2 increases when subcell size decreases. (bottom row) Distributions of ubRMSD (cm^3 cm^{-3}) and r^2 for the region shown in the top two rows.
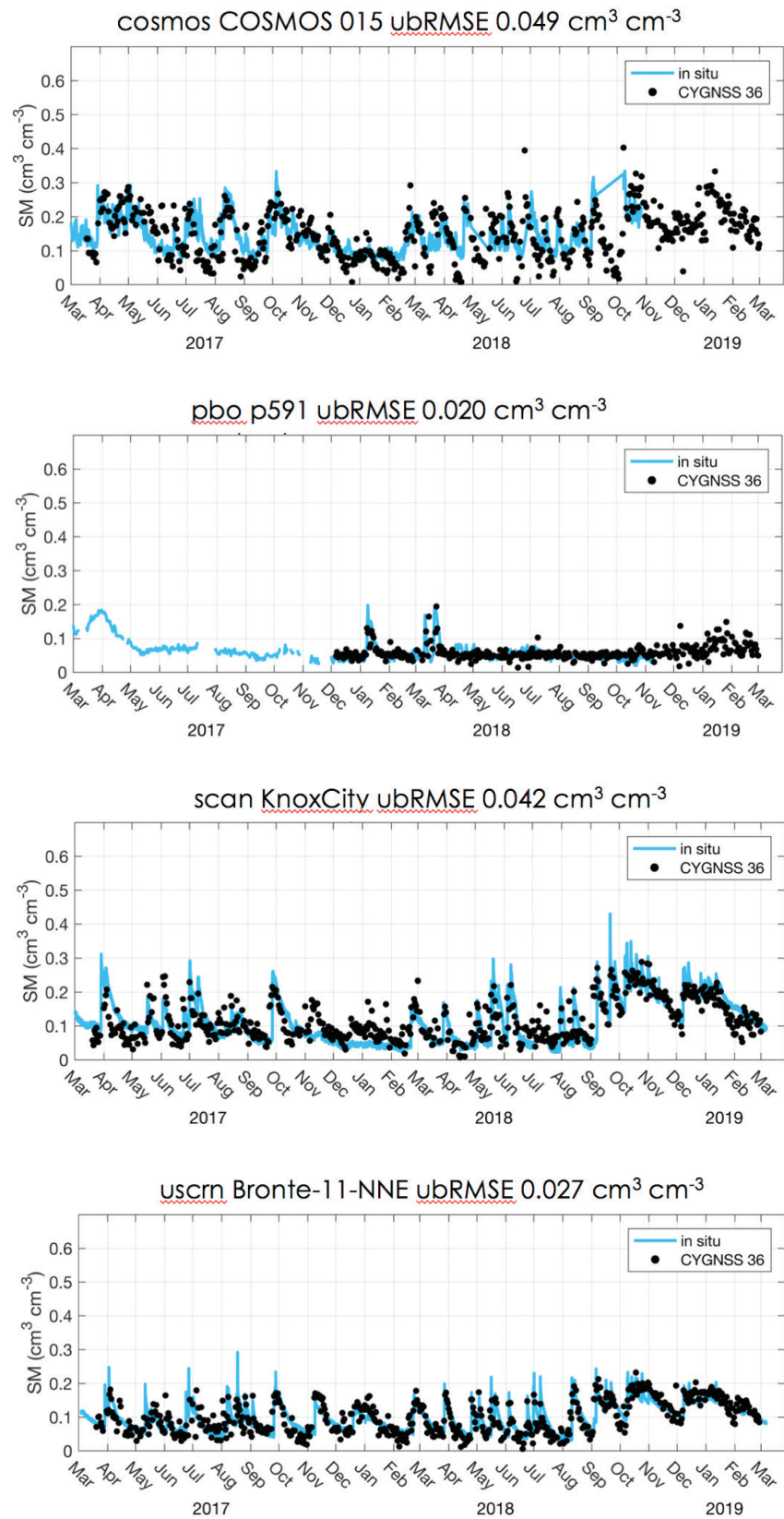
Figure 10.22. Example time series from various in situ validation networks (blue line) with CYGNSS soil moisture retrievals (black dots).

descriptor of how well SMAP or CYGNSS reproduces in situ time series, but it is the most commonly used one.

Keep in mind that stations within these networks often contain only in situ data for a particular point, and that point may not be representative of the 36 km regional soil moisture. For example, many stations are located near water bodies or in agricultural fields. Stations near the ocean are particularly bad, since the SMAP data near coastlines are generally not at all representative of the coastal soil moisture. Given that the in situ observations used for validation by SMAP are not available to the public, we had to make do with these.
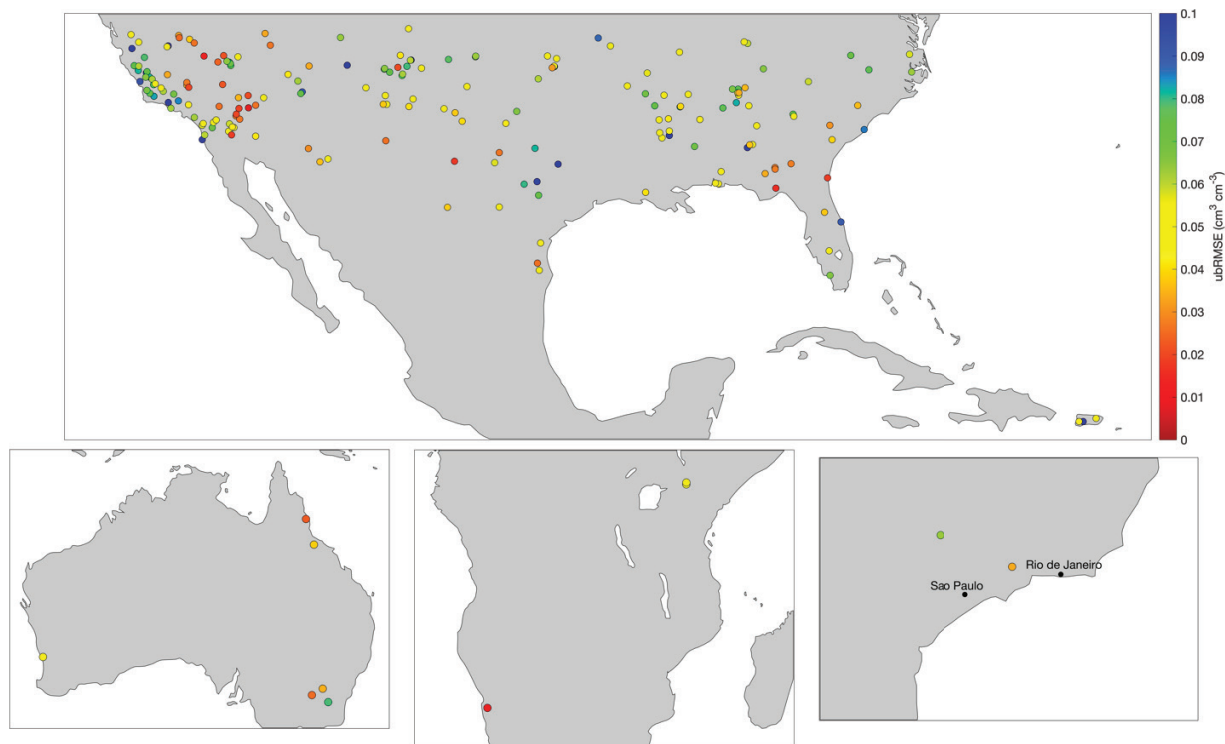
Figure 10.23. Maps showing the unbiased root mean square error between CYGNSS soil moisture and in situ observations around the world.

Table 10.3. In Situ Soil Moisture Sites Used for Validation and the ubRMSE of These In Situ Data With Respect to CYGNSS and SMAP

Network	Station	Lat	Lon	ubRMSE CYGNSS cm3 cm-3	ubRMSE SMAP cm3 cm-3	# Obs CYGNSS	# Obs SMAP
'cosmos'	'COSMOS_015'	36.61	-97.49	0.049	0.062	441	266
'cosmos'	'COSMOS_064'	35.19	-102.10	0.049	0.044	127	80
'cosmos'	'COSMOS_024'	33.73	-117.70	0.062	0.159	338	209
'cosmos'	'COSMOS_101'	-22.68	-45.00	0.034	0.020	350	247
'cosmos'	'COSMOS_023'	33.61	-116.45	0.045	0.031	542	328
'cosmos'	'COSMOS_061'	35.45	-111.77	0.062	0.027	105	176
'cosmos'	'COSMOS_057'	29.95	-98.00	0.073	0.056	319	140
'cosmos'	'COSMOS_081'	-31.38	115.71	0.043	0.125	132	64
'cosmos'	'COSMOS_089'	-23.55	15.05	0.013	0.013	23	14
'cosmos'	'COSMOS_067'	34.26	-89.87	0.040	0.050	491	293
'cosmos'	'COSMOS_052'	31.24	-84.46	0.028	0.042	45	30
'cosmos'	'COSMOS_055'	0.28	36.87	0.050	0.042	231	239
'cosmos'	'COSMOS_050'	0.49	36.87	0.049	0.048	152	121
'cosmos'	'COSMOS_034'	37.07	-119.19	0.111	0.056	141	311
'cosmos'	'COSMOS_044'	-21.62	-47.63	0.063	0.030	187	188
'cosmos'	'COSMOS_073'	-17.12	145.63	0.023	0.031	31	33
'cosmos'	'COSMOS_014'	36.06	-97.22	0.032	0.034	539	314
'cosmos'	'COSMOS_033'	37.03	-119.26	0.047	0.047	28	31
'cosmos'	'COSMOS_085'	-34.40	147.53	0.034	0.049	153	86
'cosmos'	'COSMOS_077'	-35.66	148.15	0.079	0.082	83	70
'cosmos'	'COSMOS_074'	-19.88	146.54	0.038	0.026	110	76
'cosmos'	'COSMOS_079'	-35.01	146.30	0.025	0.039	145	86
'pbo'	'bkap'	35.29	-116.08	0.023	0.024	437	277
'pbo'	'crrs'	33.07	-115.74	0.046	0.047	476	206
'pbo'	'csci'	34.17	-119.04	0.062	0.046	397	238
'pbo'	'ctdm'	34.52	-118.61	0.085	0.063	230	179
'pbo'	'fgst'	34.73	-120.01	0.083	0.061	335	274
'pbo'	'glrs'	33.27	-115.52	0.043	0.122	437	203
'pbo'	'gnps'	34.31	-114.19	0.026	0.030	371	253
'pbo'	'hunt'	35.88	-120.40	0.074	0.055	297	248
'pbo'	'hvys'	34.44	-119.19	0.101	0.135	404	275
'pbo'	'imps'	34.16	-115.15	0.020	0.022	465	236
'pbo'	'masw'	35.83	-120.44	0.106	0.091	330	257
'pbo'	'ndap'	34.77	-114.62	0.021	0.017	420	274
'pbo'	'ok02'	36.49	-96.96	0.050	0.048	65	43
'pbo'	'p008'	36.14	-111.13	0.034	0.037	127	167
'pbo'	'p010'	34.67	-113.73	0.049	0.047	62	112
'pbo'	'p035'	34.60	-105.18	0.055	0.055	276	273
'pbo'	'p036'	36.42	-105.29	0.100	0.103	99	120
'pbo'	'p038'	34.15	-103.41	0.047	0.034	291	203
'pbo'	'p039'	36.45	-103.15	0.078	0.060	273	267
'pbo'	'p070'	36.04	-104.70	0.049	0.045	282	260
'pbo'	'p094'	37.20	-117.70	0.027	0.025	120	196
'pbo'	'p107'	35.13	-107.88	0.049	0.055	224	247
'pbo'	'p123'	36.64	-105.91	0.041	0.043	236	248
'pbo'	'p250'	36.95	-121.27	0.121	0.090	225	246
'pbo'	'p255'	37.58	-121.32	0.048	0.024	139	265
'pbo'	'p284'	35.93	-120.91	0.081	0.049	320	204
'pbo'	'p288'	36.14	-120.88	0.060	0.043	382	251
'pbo'	'p472'	32.89	-117.10	0.060	0.047	417	252
'pbo'	'p474'	33.36	-117.25	0.057	0.041	442	273
'pbo'	'p475'	32.67	-117.24	0.101	0.158	437	264
'pbo'	'p482'	33.24	-116.67	0.069	0.057	128	274
'pbo'	'p498'	32.90	-115.57	0.018	0.021	472	205
'pbo'	'p505'	33.42	-115.69	0.059	0.124	434	201
'pbo'	'p508'	33.25	-115.43	0.047	0.121	431	199
'pbo'	'p511'	33.89	-115.30	0.020	0.023	457	253
'pbo'	'p514'	35.01	-120.41	0.067	0.045	390	244
'pbo'	'p515'	34.87	-120.24	0.073	0.061	98	194
'pbo'	'p525'	35.43	-120.81	0.093	0.121	382	266
'pbo'	'p530'	35.62	-120.48	0.065	0.050	333	258
'pbo'	'p532'	35.63	-120.27	0.081	0.068	310	244
'pbo'	'p536'	35.28	-120.03	0.075	0.061	287	248
'pbo'	'p537'	35.32	-119.94	0.047	0.032	301	261

Table 10.4. In Situ Sites Used for Validation

Note: Also shown are the number of observations used for validation—many in situ sites did not have data for the full time period used for validation (March 17, 2017–March 1, 2019).

'pbo'	'p538'	35.53	-120.11	0.061	0.054	339	236
'pbo'	'p553'	34.84	-118.88	0.067	0.070	378	271
'pbo'	'p565'	35.74	-119.24	0.034	0.032	442	268
'pbo'	'p568'	35.25	-118.13	0.034	0.029	191	206
'pbo'	'p569'	35.38	-118.12	0.027	0.036	134	161
'pbo'	'p587'	34.33	-118.03	0.042	0.039	257	203
'pbo'	'p591'	35.15	-118.02	0.020	0.034	275	214
'pbo'	'p623'	34.19	-114.60	0.008	0.010	26	19
'pbo'	'p645'	37.54	-118.59	0.033	0.062	11	242
'pbo'	'p724'	37.44	-118.56	0.025	0.023	12	232
'pbo'	'p742'	33.50	-116.60	0.049	0.048	262	272
'pbo'	'p807'	30.49	-98.82	0.080	0.058	393	240
'pbo'	'p811'	35.15	-118.02	0.020	0.030	275	214
'pbo'	'qcy2'	36.16	-121.14	0.075	0.054	397	197
'pbo'	'sdhl'	34.26	-116.28	0.026	0.018	268	272
'scan'	'AAMU-jtg'	34.78	-86.55	0.055	0.059	608	349
'scan'	'AdamsRanch#1'	34.25	-105.42	0.040	0.038	335	343
'scan'	'Alcalde'	36.08	-106.05	0.021	0.032	123	160
'scan'	'AllenFarms'	35.07	-86.90	0.066	0.059	559	328
'scan'	'BraggFarm'	34.90	-86.60	0.050	0.047	607	354
'scan'	'BroadAcres'	32.28	-86.05	0.103	0.082	217	140
'scan'	'Charkiln'	36.37	-115.83	0.064	0.052	348	352
'scan'	'CochoraRanch'	35.12	-119.60	0.046	0.033	312	351
'scan'	'Corozal'	18.32	-66.03	0.047	0.054	30	29
'scan'	'DeathValleyJCT'	36.33	-116.35	0.024	0.026	156	175
'scan'	'DeepSprings'	37.37	-117.97	0.038	0.031	15	308
'scan'	'DesertCenter'	33.80	-115.31	0.027	0.026	474	268
'scan'	'Dexter'	36.78	-89.93	0.044	0.075	590	337
'scan'	'EastviewFarm'	35.13	-86.18	0.036	0.040	437	267
'scan'	'Enterprise'	37.63	-113.65	0.034	0.048	5	319
'scan'	'Essex'	34.67	-115.17	0.035	0.022	528	265
'scan'	'FordDryLake'	33.65	-115.10	0.027	0.020	584	341
'scan'	'FortReno#1'	35.55	-98.02	0.061	0.063	625	351
'scan'	'GoodwinCreekTimber'	34.23	-89.90	0.077	0.055	582	354
'scan'	'GuilarteForest'	18.15	-66.77	0.117	0.115	369	263
'scan'	'Kingsville'	27.55	-97.88	0.044	0.040	201	118
'scan'	'KnoxCity'	33.45	-99.87	0.042	0.047	596	335
'scan'	'KoptisFarms'	30.52	-87.70	0.048	0.046	537	315
'scan'	'Levelland'	33.55	-102.37	0.040	0.052	402	351
'scan'	'LittleRiver'	31.50	-83.55	0.028	0.031	381	265
'scan'	'LosLunasPmc'	34.77	-106.77	0.047	0.043	378	335
'scan'	'LovellSummit'	36.17	-115.62	0.072	0.063	273	350
'scan'	'MammothCave'	37.18	-86.03	0.059	0.055	444	347
'scan'	'MaricaoForest'	18.15	-67.00	0.043	0.042	445	263
'scan'	'Mayday'	32.87	-90.52	0.117	0.102	472	353
'scan'	'McalisterFarm'	35.07	-86.58	0.076	0.062	607	354
'scan'	'MccrackenMesa'	37.45	-109.33	0.063	0.052	23	333
'scan'	'MonoclineRidge'	36.54	-120.55	0.079	0.056	535	351
'scan'	'MorrisFarms'	32.42	-85.92	0.037	0.042	579	354
'scan'	'MtVernon'	37.07	-93.88	0.056	0.051	475	343
'scan'	'NorthIssaquena'	33.00	-91.07	0.051	0.078	585	274
'scan'	'Onward'	32.75	-90.93	0.052	0.053	218	305
'scan'	'PeeDee'	34.30	-79.73	0.036	0.042	382	221
'scan'	'PerdidoRivFarms'	31.12	-87.55	0.054	0.040	617	354
'scan'	'PineNut'	36.57	-115.20	0.046	0.039	304	344
'scan'	'ReynoldsHomestead'	36.63	-80.13	0.071	0.050	324	223
'scan'	'Riesel'	31.48	-96.88	0.104	0.089	489	284
'scan'	'RiverRoadFarms'	31.02	-85.03	0.034	0.043	596	349
'scan'	'SanAngelo'	31.55	-100.51	0.057	0.058	482	266
'scan'	'SandHollow'	37.10	-113.35	0.027	0.026	225	345
'scan'	'SandyRidge'	33.67	-90.57	0.042	0.070	542	330
'scan'	'Scott'	33.62	-91.10	0.049	0.074	589	264
'scan'	'SellersLake#1'	29.10	-81.63	0.037	0.056	523	356
'scan'	'Sevilleta'	34.35	-106.68	0.045	0.035	234	128
'scan'	'SilverCity'	33.08	-90.52	0.043	0.063	472	353
'scan'	'StanleyFarm'	34.43	-86.68	0.082	0.059	619	355

Table 10.5. Table of In Situ Sites Used Together With CYGNSS and SMAP RMSE, Number of CYGNSS, and Number of SMAP Samples Used

Note: Table spans 3 pages. Bias, slope, r values, and so on can be provided upon request. Tan cells are those where CYGNSS had a smaller ubRMSE than SMAP, though in general they were very similar.

'scan'	'Starkville'	33.63	-88.77	0.043	0.049	595	354
'scan'	'Stephenville'	32.25	-98.20	0.082	0.058	626	286
'scan'	'Stubblefield'	34.97	-119.48	0.061	0.042	390	351
'scan'	'SudduthFarms'	34.18	-87.45	0.076	0.058	603	274
'scan'	'Tidewater#1'	35.87	-76.65	0.063	0.064	337	210
'scan'	'TidewaterArec'	36.68	-76.77	0.058	0.046	566	349
'scan'	'Tuskegee'	32.43	-85.75	0.054	0.046	612	282
'scan'	'UAPBDewitt'	34.28	-91.35	0.074	0.066	339	328
'scan'	'UAPBLonokeFarm'	34.85	-91.88	0.069	0.051	565	354
'scan'	'UAPBMarianna'	34.78	-90.82	0.052	0.065	603	266
'scan'	'UAPBPointRemove'	35.22	-92.92	0.047	0.037	595	354
'scan'	'Uvalde'	29.36	-100.25	0.054	0.046	615	353
'scan'	'Vernon'	34.02	-99.25	0.065	NaN	609	NaN
'scan'	'WTARS'	34.90	-86.53	0.035	0.044	396	232
'scan'	'Wakulla#1'	30.30	-84.42	0.016	0.026	424	247
'scan'	'WalnutGulch#1'	31.73	-110.05	0.045	0.032	389	260
'scan'	'Watkinsville#1'	33.88	-83.43	0.068	0.036	259	143
'scan'	'Wedowee'	33.33	-85.52	0.045	0.035	460	214
'scan'	'Weslaco'	26.16	-97.96	0.053	0.050	524	355
'scan'	'YoumansFarm'	32.67	-81.20	0.039	0.045	628	354
'snotel'	'BRISTLECONETRAIL'	36.32	-115.70	0.095	0.099	331	345
'snotel'	'BarM'	34.86	-111.61	0.074	0.068	276	309
'snotel'	'ElkCabin'	35.70	-105.81	0.069	0.052	213	243
'snotel'	'LEECANYON'	36.31	-115.68	0.080	0.082	331	345
'snotel'	'MEDANOPASS'	37.85	-105.44	0.044	0.065	4	261
'snotel'	'MormonMountain'	34.94	-111.52	0.090	0.090	276	309
'snotel'	'NAVAJOWHISKEYCK'	36.18	-108.95	0.100	0.082	230	229
'snotel'	'PALO'	36.41	-105.33	0.060	0.080	318	205
'snotel'	'RAINBOWCANYON'	36.25	-115.63	0.070	0.074	331	345
'snotel'	'SantaFe'	35.77	-105.78	0.062	0.074	156	201
'snotel'	'SenoritaDivide#2'	36.00	-106.83	0.066	0.071	269	303
'snotel'	'TresRitos'	36.13	-105.53	0.079	0.084	98	222
'snotel'	'VacasLocas'	36.03	-106.81	0.064	0.067	269	303
'uscrn'	'Asheville-13-S'	35.42	-82.56	0.059	0.058	370	330
'uscrn'	'Austin-33-NW'	30.62	-98.08	0.098	0.080	619	263
'uscrn'	'Batesville-8-WNW'	35.82	-91.78	0.057	0.054	601	348
'uscrn'	'Blackville-3-W'	33.36	-81.33	0.031	0.032	173	106
'uscrn'	'Bowling-Green-21-NNE'	37.25	-86.23	0.047	0.059	434	343
'uscrn'	'Bronte-11-NNE'	32.04	-100.25	0.027	0.038	596	312
'uscrn'	'Brunswick-23-S'	30.81	-81.46	0.019	0.048	521	353
'uscrn'	'Crossville-7-NW'	36.01	-85.13	0.065	0.055	372	224
'uscrn'	'Durham-11-W'	35.97	-79.09	0.076	0.050	566	347
'uscrn'	'Edinburg-17-NNE'	26.53	-98.06	0.026	0.033	496	304
'uscrn'	'Elgin-5-S'	31.59	-110.51	0.036	0.028	369	254
'uscrn'	'Everglades-City-5-NE'	25.90	-81.32	0.065	0.077	396	264
'uscrn'	'Fairhope-3-NE'	30.55	-87.88	0.047	0.063	284	170
'uscrn'	'Fallbrook-5-NE'	33.44	-117.19	0.053	0.026	554	350
'uscrn'	'Gadsden-19-N'	34.29	-85.96	0.052	0.037	590	352
'uscrn'	'Goodwell-2-E'	36.60	-101.60	0.063	0.059	372	345
'uscrn'	'Goodwell-2-SE'	36.57	-101.61	0.063	0.060	372	345
'uscrn'	'Holly-Springs-4-N'	34.82	-89.43	0.052	0.048	610	348
'uscrn'	'Joplin-24-N'	37.43	-94.58	0.087	0.077	193	340
'uscrn'	'Lafayette-13-SE'	30.09	-91.87	0.041	0.056	556	263
'uscrn'	'Las-Cruces-20-N'	32.61	-106.74	0.026	0.029	386	259
'uscrn'	'Los-Alamos-13-W'	35.86	-106.52	0.075	0.065	18	248
'uscrn'	'McClellanville-7-NE'	33.15	-79.36	0.086	0.085	549	333
'uscrn'	'Merced-23-WSW'	37.24	-120.88	0.046	0.054	430	270
'uscrn'	'Mercury-3-SSW'	36.62	-116.02	0.022	0.020	325	349
'uscrn'	'Monahans-6-ENE'	31.62	-102.81	0.018	0.025	380	348
'uscrn'	'Muleshoe-19-S'	33.96	-102.77	0.038	0.041	380	325
'uscrn'	'Newton-5-ENE'	32.34	-89.07	0.069	0.055	605	349
'uscrn'	'Newton-8-W'	31.31	-84.47	0.029	0.051	608	348
'uscrn'	'Panther-Junction-2-N'	29.35	-103.21	0.038	0.027	358	348
'uscrn'	'Sebring-23-SSE'	27.15	-81.37	0.047	0.047	52	29
'uscrn'	'Socorro-20-N'	34.36	-106.89	0.038	0.034	370	342

(continued)

Table 10.5. Table of In Situ Sites Used Together With CYGNSS and SMAP RMSE, Number of CYGNSS, and Number of SMAP Samples Used (*continued*)

'uscrn'	'Stillwater-2-W'	36.12	-97.09	0.077	0.059	610	344
'uscrn'	'Stillwater-5-WNW'	36.13	-97.11	0.055	0.045	596	347
'uscrn'	'Stovepipe-Wells-1-SW'	36.60	-117.14	0.013	0.013	495	350
'uscrn'	'Titusville-7-E'	28.62	-80.69	0.090	0.087	382	294
'uscrn'	'Tucson-11-W'	32.24	-111.17	0.030	0.021	447	349
'uscrn'	'Watkinsville-5-SSE'	33.78	-83.39	0.047	0.034	553	331
'uscrn'	'Williams-35-NNW'	35.76	-112.34	0.041	0.042	351	268
'uscrn'	'Yuma-27-ENE'	32.83	-114.19	0.042	0.034	572	329

10.6. Plans for Future Versions

We hope to keep improving our product: A more robust calibration of the signal over land is a priority. We are considering releasing the 3 km soil moisture retrievals themselves if there is sufficient interest. We would also like to explore "smart gridding" of the data that allows for a more flexible mesh based on land cover type or topography to remove imposing arbitrary grid lines on the landscape. In the future, we will also explore parameter regionalization to increase the accuracy of CYGNSS soil moisture retrievals near coastlines, where SMAP has trouble retrieving soil moisture due to its larger footprint.

10.7. File Overview and Loading the Data

Spatial coverage	N: 38, S: –38 E: 164, W: –135	Data format	netCDF4
Spatial resolution	36 km × 36 km	Platform	CYGNSS
Temporal coverage	18 March 2017 to present	Sensor	CYGNSS GNSS-R receivers
Temporal resolution	6 hours	Version	V1.0
Data contributors	Chew, C. C., Small, E. E.		

File naming convention: ucar_cu_cygnss_sm_v1_ YYYY_DDD.nc
YYYY: 4-digit year
DDD: 3-digit day of year

Each netCDF file contains the following variables:

latitude: Refers to the latitude of the center of the grid cell. Dimensions: 252 × 802.

longitude: Refers to the longitude of the center of the grid cell. Dimensions: 252 × 802.

timeintervals: The start and stop time for the subdaily soil moisture retrievals. For example, the first row is (0,6), which means that the first of the reported subdaily soil moisture retrievals were recorded between midnight and 6 a.m. Dimensions: 4 × 2.

SM_daily: The average soil moisture for each grid cell recorded during the full 24-hour period. Dimensions: 252 × 802.

SM_subdaily: The average soil moisture for each grid cell recorded during each specified time interval. Dimensions: 252 × 802 × 4.

SIGMA_daily: The standard deviation of soil moisture observations for each grid cell for the full 24-hour period. Dimensions: 252 × 802.

SIGMA_subdaily: The standard deviation of soil moisture observations for each grid cell during each time interval. Dimensions: 252 × 802 × 4.

10.8. Quality Flags—Important

In order to keep file size to a minimum, we provide quality flags in a separate file (BoulderCYGSM_static_flags.nc). Just because they are in a separate file does not mean you can ignore them, though. As we have tried to emphasize throughout this handbook, the retrievals we have provided are only version 1 and have known problems.

To encourage the use of the quality flags, we have provided them in simple grids. We do not mean to say that you should not use data that are flagged, but you should use them with caution and not be surprised if retrievals are not what you would expect.

The following are quality flag meanings and how we derived them. For all flags, a value of 1 = true, and a value of 0 = false:

latitude: Refers to the latitude of the center of the grid cell. Dimensions: 252 × 802.

longitude: Refers to the longitude of the center of the grid cell. Dimensions: 252 × 802.

flag_poor_SMAP: Indicates that CYGNSS was calibrated to SMAP data where a large portion

(>90%) of the SMAP soil moisture retrievals were flagged as "not recommended for retrieval." Dimensions: 252 × 802.

flag_small_SM_range: Indicates that CYGNSS was calibrated to SMAP data with a small range of soil moisture values (< 0.1 cm^3 cm^{-3}), which means the uncertainty in β is large. Dimensions: 252 × 802.

flag_high_ubrmsd: Indicates a high unbiased root mean square difference between CYGNSS and SMAP retrievals (> 0.08 cm^3 cm^{-3}). Dimensions: 252 × 802.

flag_few_obs: Indicates a small number of observations in the grid cell for calibration, leading to a less certain β (n < 100). Dimensions: 252 × 802.

flag_low_signal: Indicates low mean $P_{r,eff}$ after water point removal in the cell, which likely means that roughness or vegetation effects are dominant (mean $P_{r,eff}$ < 5 dB). Dimensions: 252 × 802.

10.9. References

Al-Khaldi, M. M., Johnson, J. T., O'Brien, A. T., Balenzano, A., & Mattia, F. (2019). Time-series retrieval of soil moisture using CYGNSS. *IEEE Transactions on Geoscience and Remote Sensing, 57*(7), 4322–4331. https://doi.org/10.1109/TGRS.2018.2890646.

Camps, A., Park, H., Pablos, M., Foti, G., & Gommenginger, C. P. (2016). Sensitivity of GNSS-R spaceborne observations to soil moisture and vegetation. *IEEE Journal of Selected Topics in Applied Earth Observations and Remote Sensing, 9*(10), 4730–4742.

Chew, C., Colliander, A., Shah, R., Zuffada, C., & Burgin, M. (2017). The sensitivity of ground-reflected GNSS signals to near-surface soil moisture, as recorded by spaceborne receivers. *International Geoscience and Remote Sensing Symposium (IGARSS)* (Vol. 2017–July). https://doi.org/10.1109/IGARSS.2017.8127544.

Chew, C. C., & Small, E. E. (2018). Soil moisture sensing using spaceborne GNSS reflections: Comparison of CYGNSS reflectivity to SMAP soil moisture. *Geophysical Research Letters, 45*(9), 4049–4057. https://doi.org/10.1029/2018GL077905.

Chew, C. C., Small, E. E., & Podest, E. (2018). Monitoring land surface hydrology using CYGNSS. *IGARSS 2018—2018 IEEE International Geoscience and Remote Sensing Symposium*, pp. 8309–8311, https://doi.org/10.1109/IGARSS.2018.8517971.

Chew, C., Reager, J. T., & Small, E. (2018). CYGNSS data map flood inundation during the 2017 Atlantic hurricane season. *Scientific Reports, 8*(1). https://doi.org/10.1038/s41598-018-27673-x.

Chew, C., Shah, R., Zuffada, C., Hajj, G., Masters, D., & Mannucci, A. J. (2016). Demonstrating soil moisture remote sensing with observations from the UK TechDemoSat-1 satellite mission. *Geophysical Research Letters, 43*(7). https://doi.org/10.1002/2016GL068189.

Nghiem, S. V., Zuffada, C., Shah, R., Chew, C., Lowe, S. T., Mannucci, A. J., . . . Rosenqvist, A. (2017). Wetland monitoring with global navigation satellite system reflectometry. *Earth and Space Science, 4*(1). https://doi.org/10.1002/2016EA000194.

11. Level 1 and 2 Uncertainty Analyses

The CYGNSS mission consists of eight spacecraft dispersed around a common low Earth orbit at 35° inclination and 520 km altitude. Each spacecraft carries a four-channel global navigation satellite system reflectometry (GNSS-R) radar receiver capable of measuring GPS Level 1 (L1) signals scattered from the ocean surface (Ruf et al., 2013). Those received signals are first calibrated into L1 measurements of bistatic radar cross section (Gleason et al., 2016, 2018) from which the L1 observables of normalized bistatic radar cross section (NBRCS) and leading edge slope (LES) are derived. The L1 observables are then used to retrieve Level 2 (L2) estimates of the 10 m referenced wind speed above the ocean surface (u_{10}; Clarizia & Ruf, 2016). A detailed description of the mission and of the algorithms associated with production of its L1 and L2 Science Data Products is provided in Chapters 5–9. This chapter examines bottom-up and top-down assessments of the uncertainty in both the L1 NBRCS and LES and the L2 wind speed products. Particular attention is paid to the performance at the low NBRCS and LES values and high wind speeds encountered in tropical cyclones. One primary objective of this work is an assessment of performance relative to mission-level requirements on wind speed measurement uncertainty of ± 2 m/s at wind speeds below 20 m/s and ±10% at wind speeds above 20 m/s.

11.1. L1 Calibration of Ocean Surface Scattering Cross Section

CYGNSS L1 calibration is performed in two steps. First, L0 measurements by the onboard instrument are converted from units of raw digital counts to a L1A delay-Doppler map (DDM) of signal power in units of watts. This is performed using an estimate of the individual DDM noise floor, a near-time coincident black body calibration load noise power estimate, and prelaunch instrument noise calibration tables, which characterize the instrument noise power variations with temperature. Second, the L1A DDM is converted to a L1B DDM of bistatic radar cross section (BRCS) values by an unwrapping of the other terms appearing in the bistatic radar equation. The primary correction terms in the L1B calibration include the transmitter effective isotropic radiated power (EIRP), the receive antenna gain pattern, and the transmit path loss.

After calibration, a 3 delay bin by 5 Doppler bin subregion of the L1B DDM centered on the specular point is used to derive the two L1 observables. The NBRCS observable is computed as the summation of the L1B DDM over the 3 × 5 region divided by the effective surface scattering area of the region. The LES observable is computed as the slope of the integrated delay waveform, found by summing across all 5 Doppler bins at each delay value and considering the result as a function of delay only. More details on the L1 calibration and error analysis can be found in Gleason et al. (2016, 2018).

11.1.1. Bottom-Up Estimate of L1A and L1B Errors

Bottom-up error analysis of the L1 calibration was performed using best estimates of the individual terms in the L1A and L1B calibration equations. This consisted, when possible, of performing error analyses on prelaunch measurements of satellite hardware (e.g., in the case of the low noise amplifier [LNA] noise power versus temperature characterization) and in other cases by using component specifications together with models to predict errors (e.g., in the case of the impact of spacecraft attitude knowledge uncertainty on receive antenna gain error). Individual term-by-term estimates for all L1 error parameters are described in greater detail in Gleason et al. (2016, 2018).

One significant error term in the L1 calibration is uncertainty in the GPS EIRP, which is caused by errors in knowledge of the GPS transmit power and transmit antenna gain. The EIRP is monitored by a ground-based GPS power monitor and those measurements are used to reduce the uncertainty in the GPS antenna patterns and in the transmit power of individual GPS satellites [13]. This results in a GPS EIRP uncertainty of 0.24 dB. The combined uncertainty due to all other sources of error in L1 calibration is 0.30 dB. The total L1 uncertainty is the root-sum-square of these two terms, or 0.38 dB (Gleason et al., 2018).

11.1.2. Top-Down Estimate of L1B Error

Top-down performance assessments are most often performed of the geophysical parameters estimated by a sensor rather than of its L1 measurements, largely because it can be difficult to obtain accurate independent estimates of the L1 measurements with which to compare. In the case of CYGNSS, closely spaced satellites often make

measurements that should be nearly identical to one another. Differences between the actual measurements can be used to assess many of the errors associated with L1 calibration. This "trailing pair" technique is used here to provide a top-down assessment of the uncertainty in the L1 Science Data Products.

A trailing pair dataset was assembled from measurements made by the CYGNSS constellation during the period July 31 to August 23, 2017. All possible pairs of measurements made by two different spacecraft were considered and only those that met the following criteria were selected: difference in measurement time < 10 minutes; difference in specular point location < 5 km; and difference in incidence angle of observation < 1°. In every case, the two measurements shared the same GPS transmitting satellite. This selection results in a total of ~200,000 pairs of measurements, which represents ~3% of the total number of samples made during this 24-day interval. Suitable trailing pair measurements are found using a variety of possible pairs of the eight satellites

in the constellation—typically sequential pairs separated by less than 10 minutes around the orbit plane. The tight restrictions on the similarity between the measurements are imposed to ensure that observations are made of a nearly identical ocean surface at the same measurement geometry. Scatterplots of the measurements by one satellite versus the other for both NBRCS and LES L1 observables are shown in Figure 11.1.

The highest density of samples lies along the 1:1 center line in both plots, as expected. The statistical spread of the difference between the pair of measurements quantifies the measurement error due to all sources other than those related to knowledge of the GPS transmission characteristics (i.e., the GPS EIRP), which are common to both measurements. Histograms of the difference are shown in Figure 11.2. Note that Figure 11.1 shows the numeric data values themselves, whereas Figure 11.2 shows the relative differences in units of dB.

The root mean square (RMS) values of the relative differences, estimated from the populations shown in Figure 11.2,
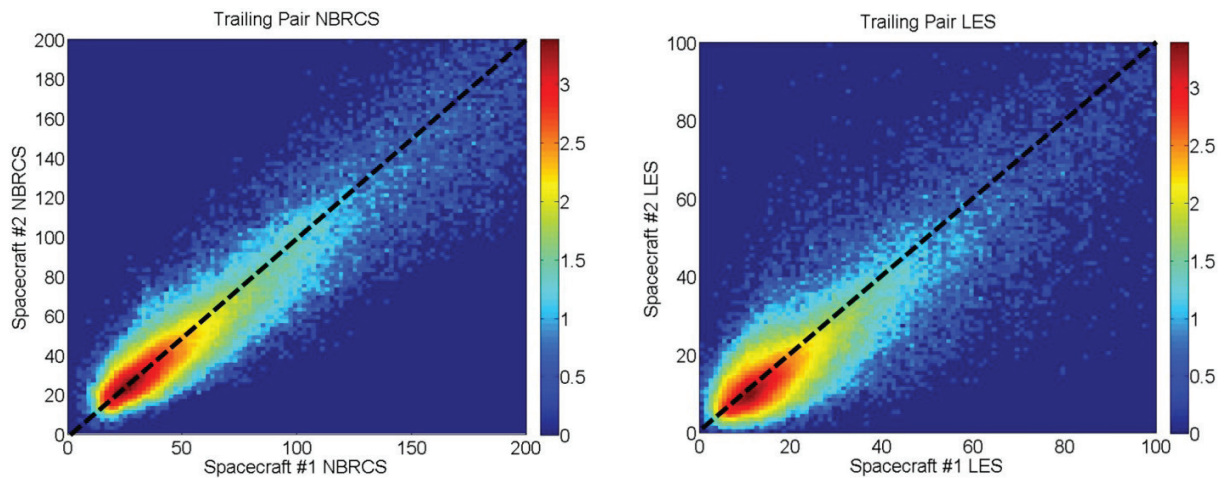
Figure 11.1. Trailing pair log(density) scatterplots of (a) normalized bistatic radar cross section (NBRCS) and (b) leading edge slope (LES) measurements by CYGNSS. The diagonal black dashed line is the line of 1:1 agreement. The color scale is the $\log_{10}$ of the number density of points.
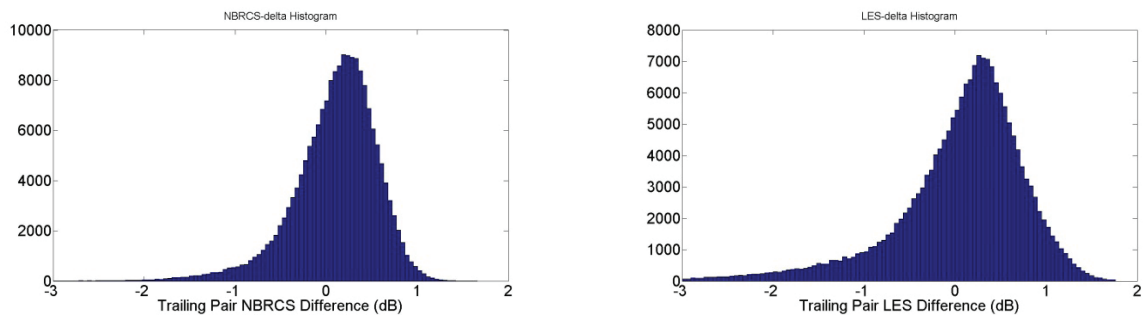
Figure 11.2. Trailing pair difference histograms of normalized bistatic radar cross section (left) and leading edge slope (right) measurements by CYGNSS.

are 0.48 dB and 0.71 dB for the NBRCS and LES observables, respectively. Since these are differences between two spacecraft measurements with independent measurement noise and calibration errors, the uncertainty in one of the measurements is lower by a factor of $\sqrt{2}$. Therefore, the top-down estimate of uncertainty in L1 measurements due to all factors other than error in knowledge of the GPS EIRP is given by 0.34 dB (NBRCS) and 0.50 dB (LES).

11.1.3. Comparison of Bottom-Up and Top-Down Results

The bottom-up error budget discussed in Section 11.1.2 specifies 0.30 dB as the bottom-up estimate of measurement uncertainty in NBRCS due to all noise and calibration error effects other than GPS EIRP. This compares favorably to the top-down estimate of 0.34 dB found using the trailing pair method. The larger error in the case of the top-down estimate may be a result of larger actual errors than were assumed in the bottom-up analysis, or they may result from small differences in the ocean surface scattering cross section given the separations between pairs of observations of up to 10 minutes and 5 km. A conservative approach is to assume the top-down value of 0.34 dB as an upper bound on the uncertainty. Combining it via root-sum-square addition with the GPS EIRP uncertainty of 0.24 dB noted in Section 11.1.2 gives the total uncertainty in NBRCS. Likewise, the trailing pair estimate of LES uncertainty of 0.50 dB should also be combined via root-sum-square addition with the GPS EIRP uncertainty. The resulting total uncertainties in the L1 observables are given by

NBRCS RMS uncertainty = 0.42 dB   (**11.1**)

LES RMS uncertainty = 0.55 dB.

11.2. L2 Retrieval of Wind Speed

The CYGNSS mission's baseline wind speed retrieval algorithm, used to produce its L2 wind speed Science Data Product, is described in detail in Clarizia and Ruf (2016). In summary, the algorithm uses geophysical model functions (GMFs), which relate u_{10} to the L1 observables, NBRCS and LES. The GMFs are derived empirically from a large population of coincident CYGNSS L1 measurements and independent estimates of u_{10} made by either numerical weather prediction models at low to moderate wind speeds or instruments on NOAA P-3 hurricane hunter aircraft at high

wind speeds (Ruf & Balasubramaniam, 2018). The low to moderate wind versions are referred to as the fully developed seas (FDS) GMFs, and the high-wind versions are referred to as the young seas limited fetch (YSLF) GMFs. They differ as a result of the sensitivity of the measurements to long wave swell, which tends to be significantly more underdeveloped in the high wind conditions experienced in tropical cyclones.

Each GMF provides a unique mapping from u_{10} to an L1 observable, and the retrieval algorithm inverts it given a measurement of the observable. This produces two estimates of u_{10}, one for each observable, and they are combined together by a minimum variance estimator to produce the final wind speed estimate (Clarizia et al., 2014). Examples of the FDS GMFs for low to moderate wind speeds for both L1 observables are shown in Figure 11.3a, and the YSLF GMFs at high wind speeds are shown in Figure 11.3b.

Several features of the GMFs are noteworthy. At wind speeds below 5–10 m/s, the slope of the GMF ($dObs/du_{10}$) becomes very steep, and small changes in wind speed correspond to large changes in the L1 observable. The component of wind speed retrieval error that is dependent on measurement error can be expected to be lowest in this regime. At higher wind speeds, the slope decreases markedly. The value of u_{10} at which this transition occurs differs for the two observables and also depends weakly on incidence angle. The component of wind speed error due to measurement error will be higher here.

11.2.1. Bottom-Up Estimate of L2 Uncertainty

Bottom-up construction of an error model for the retrieved L2 wind speed consists of two parts. The uncertainty in measurement of the L1 observables, due to both measurement noise and calibration error, is scaled to a corresponding error in the wind speed using a propagation-of-errors analysis. Intrinsic error in the wind speed retrieval algorithm is also considered. Intrinsic error represents a retrieval error that would have been present even if the measurements had been perfect. It accounts for such things as the dependence of the observable on other geophysical variables than wind speed that are not properly accounted for in the retrieval algorithm or a nonunique mapping from wind speed to the observable. These two error sources are considered to be statistically independent, and their RMS errors are combined by root-sum-square addition to produce the overall bottom-up uncertainty.

For small errors in the L1 observable, the corresponding wind speed retrieval error can be estimated by linearizing the GMF. The resulting wind speed retrieval error is given by
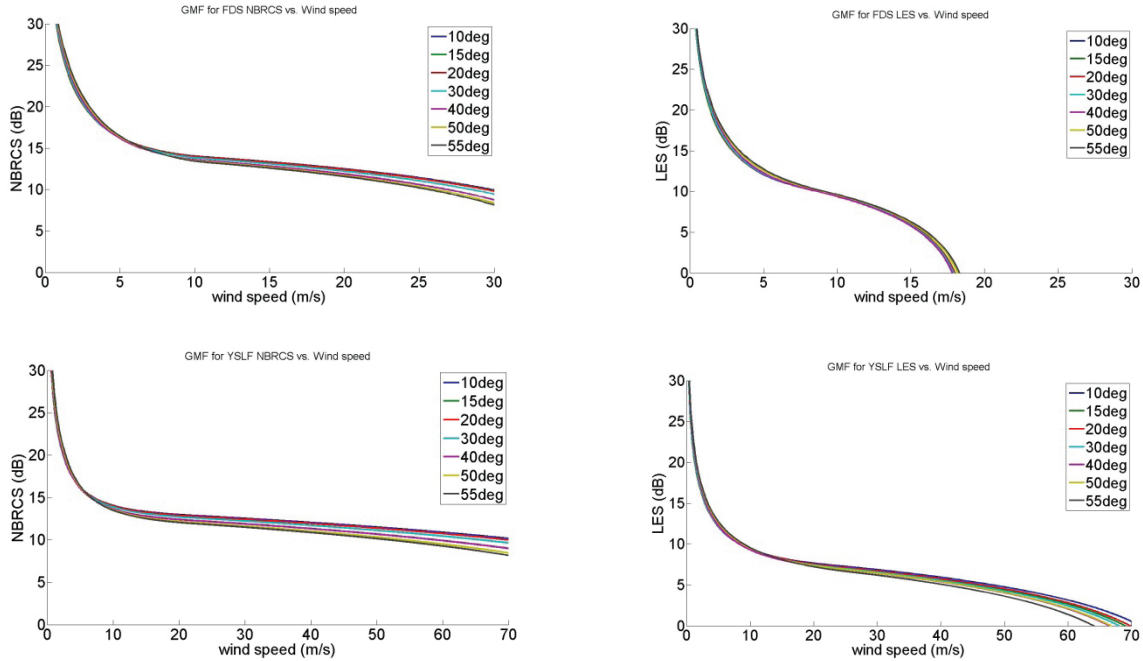
Figure 11.3. Geophysical model functions at low to moderate wind speeds in fully developed seas (FDS) (a, top row) and high wind speeds in young seas limited fetch (YSLF) conditions (b, bottom row) for the L1 observables NBRCS (left) and LES (right) at incidence angles of 10, 15, . . . , 55°.
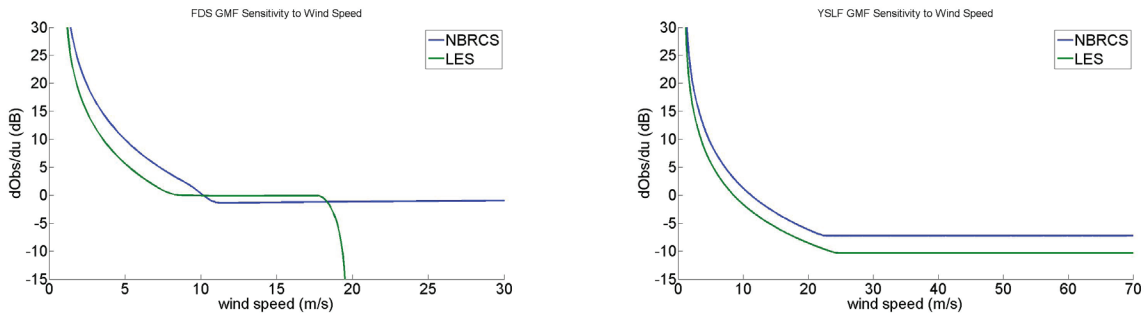
Figure 11.4. Sensitivity (defined as $dObs/du_{10}$) of the (a) FDS GMF and (b) YSLF GMF to wind speed for L1 observables NBRCS (blue) and LES (green) at an incidence angle of 30°.

$$\varepsilon_{Obs}\left(u_{10}\right) = \left|\frac{dObs}{du_{10}}\right|^{-1} \varepsilon\left(Obs\right), \qquad (\textbf{11.2})$$

where $\varepsilon(Obs)$ is the RMS error in either the NBRCS or LES observable and the functional dependence of the observable on u_{10} as shown in Figure 11.3. The values of the error are stated in Equation 11.1. The slopes of the GMFs ($dObs/du_{10}$) for both L1 observables are shown in Figure 11.4a for the low to moderate wind speed case and the slopes at high wind speeds are shown in Figure 11.4b. Results are only shown for an incidence angle of 30°, but the sensitivity is very similar at other angles.

In both FDS and YSLF conditions, the NBRCS observable typically has a higher sensitivity to wind speed than does the

LES observable. The exception is at wind speeds between ~10 and 18 m/s in the FDS case, where LES sensitivity is slightly higher. Above ~18 m/s in FDS conditions, the LES observable becomes very small and effectively loses sensitivity to changes in wind speed. In YSLF conditions, the sensitivity for both observables is low but constant at high (> 25 m/s) wind speeds.

The component of uncertainty in L2 retrieved wind speed due to errors in the L1 observables follows directly from Equations 11.1 and 11.2, using the values of $dObs/du_{10}$ shown in Figure 11.4. Plots of the resulting values of $\varepsilon(u_{10})$ with the NBRCS and LES observables are shown in Figures 11.5a and 11.5b, respectively. Note that $\varepsilon(u_{10})$ is in both cases close

to zero at very low wind speeds due to the high sensitivity (large $dObs/du_{10}$) there. Note also that $\varepsilon(u_{10})$ becomes very large with the LES observable at wind speeds above ~18 m/s. This is consistent with its loss of sensitivity to wind speed, as seen in Figures 11.3a and 11.4a.

The CYGNSS baseline L2 minimum variance (MV) retrieved wind speed is an inverse variance weighted average of the L2 winds derived from the two L1 observables. The component of its uncertainty due to errors in the L1 observables is a similarly inverse variance weighted average of the two $\varepsilon_{Obs}(u_{10})$ values (Wang et al., 2019). In addition, a third component of uncertainty is the intrinsic error in the retrieval algorithm itself, caused by the nonuniqueness of the relationship between u_{10} and the L1 observables. Intrinsic error is estimated using simulated observations produced by an end-to-end simulator (E2ES; Ruf & Balasubramaniam, 2018). The E2ES allows for noise-free L1 measurements without calibration errors to be simulated given a known wind speed. The RMS error in MV retrieval performance using these simulated data is found to be 1.3 m/s for wind speeds below 25 m/s. The overall uncertainty in the MV wind speed can be expressed as

$$\varepsilon_{MV}\left(u_{10}\right) = \left(\left(\varepsilon_{intrinsic}\right)^2 + \left(\frac{1}{\left(\varepsilon_{NBRCS}\right)^2} + \frac{1}{\left(\varepsilon_{LES}\right)^2}\right)^{-1}\right)^{0.5}, \quad \textbf{(11.3)}$$

where $\varepsilon_{intrinsic}$ = 1.3 m/s and ε_{NBRCS} and ε_{LES} are given by Equation 9.2 and shown in Figures 11.5a–11.5b. The resulting bottom-up uncertainty in the minimum variance retrieved wind speed, ε_{MV}, is shown in Figure 11.5c. At low wind speeds, contributions from L1 measurement error are small, and the MV retrieval uncertainty is dominated by the intrinsic error. Above ~10 m/s, MV uncertainty begins to increase as the contributions from L1 measurement error become significant. Above ~18 m/s, the LES observable loses sensitivity to wind speed, and the MV uncertainty is dominated by errors in the measurement of NBRCS.

A bottom-up estimate of L2 wind speed uncertainty for high wind retrievals using the YSLF GMF follows the same approach, with the appropriate YSLF sensitivity values shown in Figure 11.4b used instead. In and near tropical cyclones, the mission baseline Science Data Product uses YSLF retrievals based only on the NBRCS L1 observable. This is done because of their significantly higher sensitivity at all wind speeds than retrievals based on the LES observable. The bottom-up YSLF uncertainty is shown in Figure 11.6. In the figure, results are shown for different time averaging scenarios. The baseline CYGNSS L2 wind speed retrieval algorithm implements a variable amount of along-track averaging to account for changes in spatial resolution with incidence angles that result from the range of time delays and Doppler shifts, centered on the specular point values, which are used to compute the L1 observables (Gleason et al., 2018).
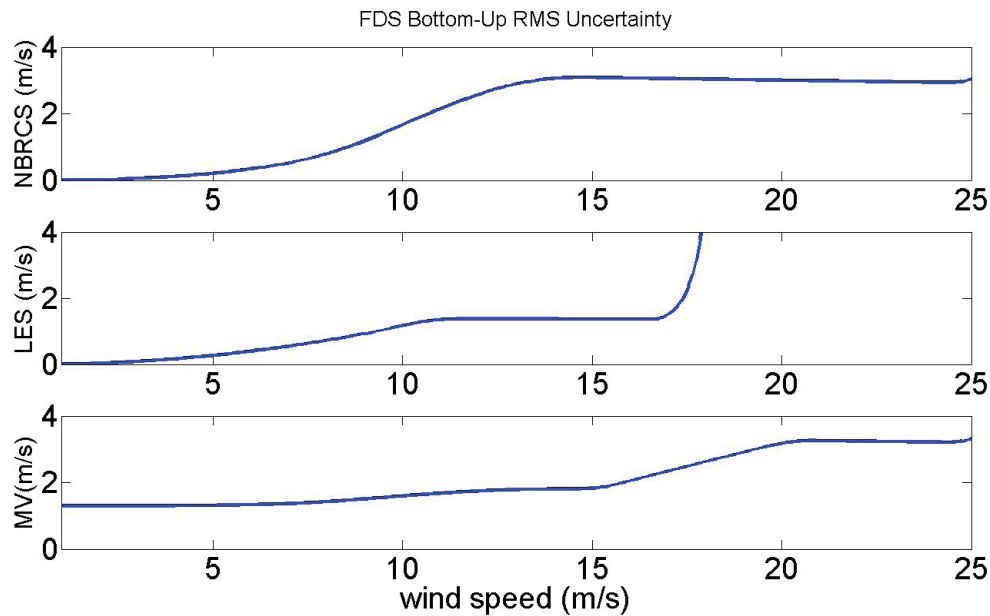
Figure 11.5. Bottom-up L2 wind speed retrieval uncertainty for low to moderate wind speeds in fully developed seas. (a) Component due to errors in L1 NBRCS observable; (b) component due to errors in L1 LES observable; (c) overall uncertainty in minimum variance estimate, including contributions from both errors in L1 observables and intrinsic error in the retrieval algorithm.
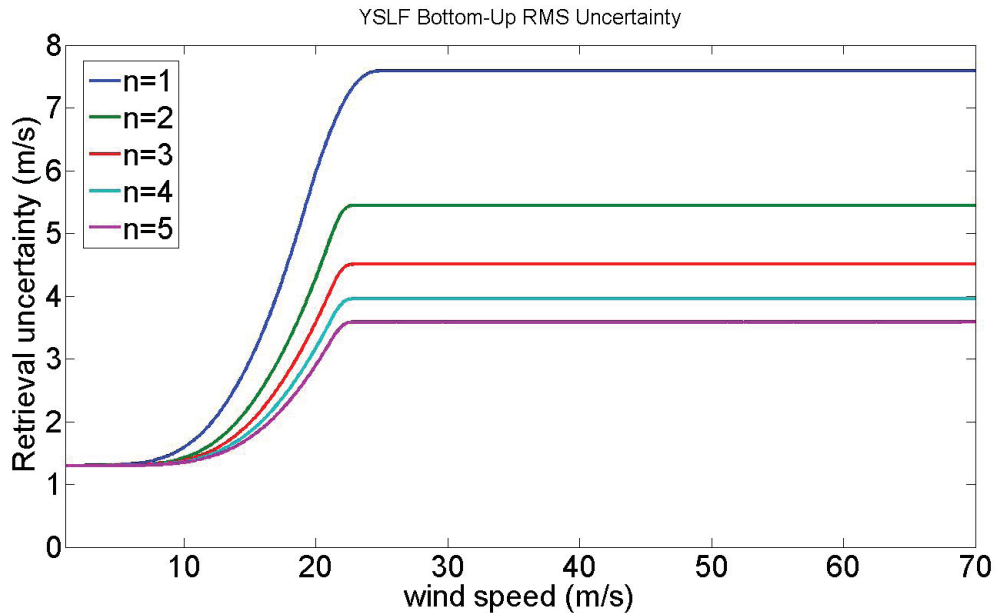
Figure 11.6. Bottom-up L2 wind speed retrieval uncertainty for high wind speeds in young seas limited fetch. The family of curves represents different numbers, n, of sequential samples averaged together. The number varies to account for the dependence of spatial resolution on incidence angle, with n = 1 above 50°, n = 5 below 15°, and n = 3 near the center of the field of view at 30°.

Individual measurements at the highest incidence angles (> 50°) have spatial resolutions of ~25 km, so no additional averaging is performed. Measurements at the lowest incidence angles (< 15°) have spatial resolution of ~15 km, and n = 5 sequential samples are averaged to produce an effective 25 km resolution. Measurements at the center of the field of view (~ 30°) have n = 3 sequential samples averaged to produce the same effective resolution of 25 km. Averaging reduces the component of L2 retrieval uncertainty due to L1 measurement error but not the intrinsic retrieval error. This is reflected in Figure 11.6. At lower wind speeds, the total uncertainty is dominated by the intrinsic component, and there is little dependence on the number of samples averaged. At higher wind speeds, L1 measurement errors are dominant, and the total uncertainty decreases from 7.6 m/s for a single sample to 4.0 m/s with four samples averaged together.

11.2.2. Top-Down Estimate of L2 Uncertainty

Top-down assessment of the uncertainty in the L2 data product at low to moderate wind speeds uses near-coincident matchups between CYGNSS measurements and 10 m referenced ocean surface wind speeds provided by the European Centre for Medium-Range Weather Forecasts (ECMWF) numerical weather prediction model (Andersson et al., 2015). All CYGNSS measurements made during September and October 2017 are used in the analysis. ECMWF winds, reported on

a 0.25° grid, are bilinearly interpolated in space and linearly interpolated in time to the location and time of the CYGNSS measurements. Several quality control filters are applied to the matchup data. The ECMWF values are compared to similarly interpolated gridded outputs from the Global Data Assimilation System (GDAS) numerical weather prediction model (NOAA, 2018), and a matchup is discarded if ECMWF and GDAS differ by more than 3 m/s. CYGNSS quality control filters include the use of samples that lie in the main beam of the nadir antenna footprint at antenna gain values within ~10 dB of the peak gain. In addition, samples are excluded if the GPS satellite is of block type IIF. These satellites have been found to suffer from considerably more transmit power variability than the earlier block types (IIR and IIR-M). After all quality control filters are applied, the total number of remaining pairs of samples in the matchup population is 30,883,518.

A density scatterplot of the matchup samples is shown in Figure 11.7. The scatterplot is logarithmic in number density of samples to more clearly illustrate the distribution of samples both in the region of highest density and in the outlier regions with larger retrieval errors. The highest density of samples occurs along the 1:1 line where ECMWF and CYGNSS winds agree. Asymmetry in the distribution of samples away from the 1:1 line can introduce biases into the retrieval (non–zero mean differences between CYGNSS and ECMWF). Asymmetries can be seen in the figure to increase at higher wind speeds.
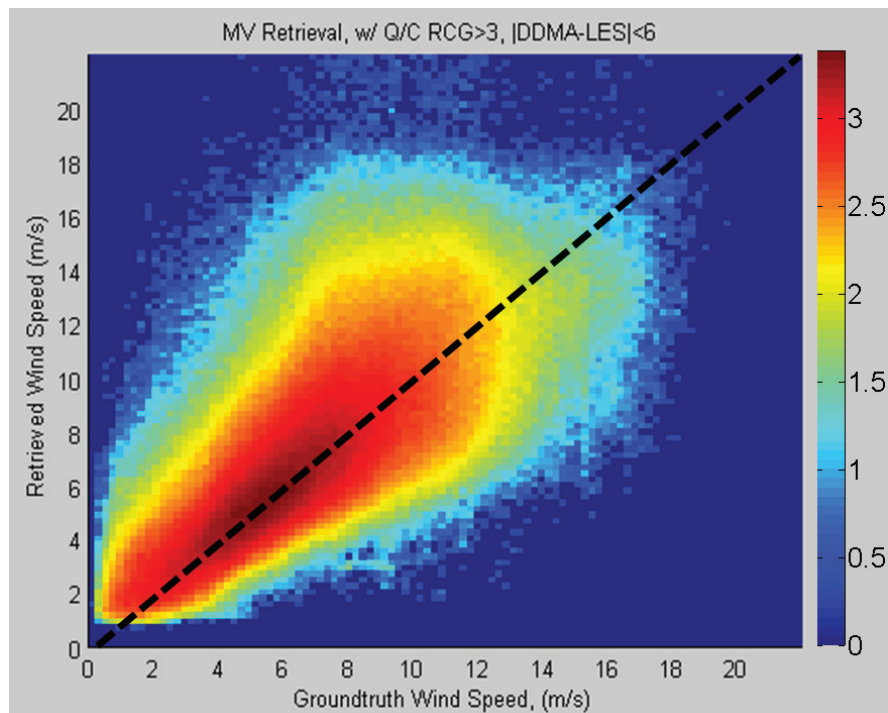
Figure 11.7. Log(density) scatterplot of CYGNSS and matchup ECMWF "ground truth" wind speed samples used for top-down determination of wind speed retrieval uncertainty below 20 m/s. The diagonal black dashed line is the line of 1:1 agreement. The color scale is the log 10 of the number density of points.

The mean and RMS differences between ECMWF and CYGNSS wind speeds are shown in Figures 11.8a–c as a function of (a) ECMWF, (b) CYGNSS, and (c) the average of ECMWF and CYGNSS wind speeds. The dependence of the mean difference (or bias) on wind speed is markedly different in each of these three cases. The dependence of bias on ECMWF wind speed (Figure 11.8a) is slightly negative at lower wind speeds, has a zero-crossing to positive bias near 9 m/s, and grows increasingly positive at higher wind speeds. Since the bias is reported as (ECMWF – CYGNSS), this indicates that CYGNSS overestimates lower wind speeds and underestimates higher wind speeds. The dependence of bias on CYGNSS wind speed (Figure 11.8b) is slightly positive at lower wind speeds, has a zero-crossing to negative bias near 7 m/s, and then grows increasingly negative at higher wind speeds. The difference in sign of the small bias at low wind speeds in Figures 11.8a and 11.8b results because, while CYGNSS tends to overestimate low wind conditions (as reported by ECMWF) by several 10ths of a meter per second, its underestimation at high winds is significantly larger in magnitude, resulting in an overall shift in the low wind bias to several 10ths of a meter per second positive when sorted by the CYGNSS reported wind. The larger difference in sign and magnitude between Figures 11.8a and 11.8b at

higher wind speeds results from the larger magnitude of the bias there, which produces a larger swing between sorting options. The dependence of bias on the average of ECMWF and CYGNSS winds (Figure 11.8c) lies roughly halfway between the other two cases, with negligible bias at low winds and a small negative bias above ~15 m/s.

The behavior of the RMS difference versus wind speed is similar in all three cases. It includes a primary contribution from the CYGNSS retrieval errors plus smaller secondary contributions from errors in the original ECMWF wind fields and possible errors introduced by the spatial and temporal interpolation process used to align the two datasets. When comparing the bottom-up uncertainty estimate shown in Figure 11.5c with the top-down one in Figure 11.8, several common traits are evident. The RMS uncertainty rises only gradually with wind speed below ~10 m/s, with values slightly below 2 m/s (the fraction of this value due to CYGNSS will depend on the allocation for errors in ECMWF and in the interpolation). The bottom-up error model attributes this fairly flat dependence to the fact that the intrinsic component of retrieval error is the dominant contributor. The uncertainty rises more steeply above 10 m/s in both cases. The bottom-up error model attributes the steeper rise to the decreasing sensitivity of the L1 observables to wind speed
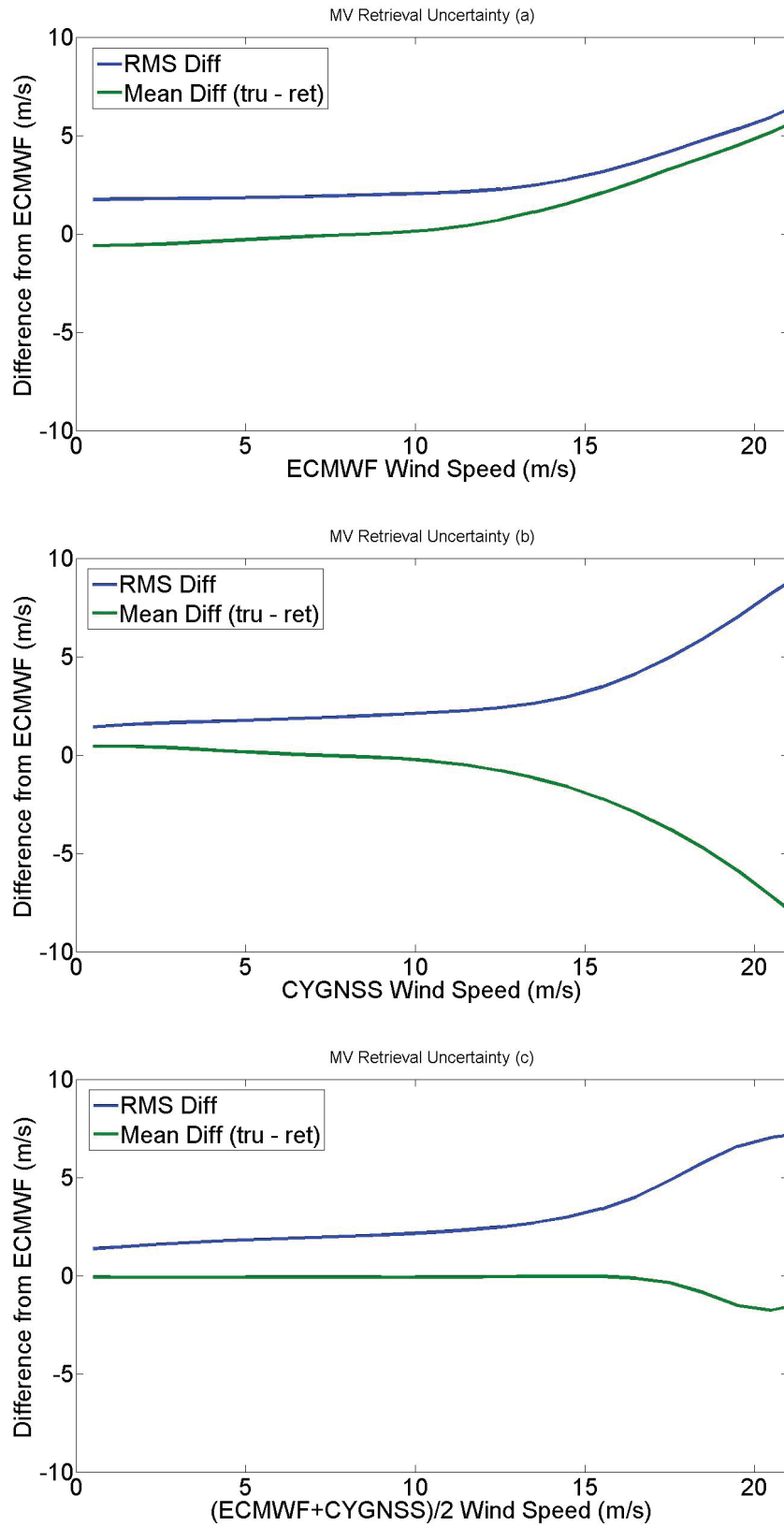
Figure 11.8. RMS and mean difference between matchup CYGNSS and ECMWF wind speeds plotted versus three difference measurements of wind speed: (a) ECMWF, (b) CYGNSS, and (c) the average of ECMWF and CYGNSS.

and hence the increased sensitivity of the retrieved wind speed to errors in measurement of those observables. RMS uncertainty rises to ~4 m/s at 20 m/s for the bottom-up estimate and ~6 m/s for the top-down estimate. The difference is likely attributable to the bias evident in the top-down comparison, which is small below ~ 12 m/s but increases at higher wind speeds. Bias removal, either algorithmically or through improved calibration of the L1 observables, is a continuing topic of research by the CYGNSS science team. The overall RMS difference, including all samples with ECMWF winds below 20 m/s, is 1.96 m/s. This value is weighted by the distribution of wind speeds in the matchup population, which is approximately Rayleigh distributed with a mean near 7 m/s.

For a top-down estimate of uncertainty at high wind speeds in tropical cyclones, matchups are compiled from 20 coincident overpasses of hurricanes by CYGNSS and NOAA P-3 "hurricane hunter" aircraft that occurred during the 2017 Atlantic hurricane season. Coincidence is defined by locating the aircraft ground track during one of its eyewall penetrations that was closest to a CYGNSS specular point track for that overpass and requiring that they occurred within 30 minutes and 12.5 km of one another. The 20 cases considered include overpasses of Hurricanes Harvey on day of year (DOY) 236 (4 overpasses) and DOY 237; Irma on DOY 248; Jose on DOY 258 (2 overpasses), DOY

259, and DOY 264 (4 overpasses); and Maria on DOY 266 (2 overpasses), DOY 267 (4 overpasses), and DOY 270. Comparison wind speeds were measured by stepped frequency microwave radiometers (SFMRs) installed on the P-3 aircraft (Uhlhorn et al., 2007). The maximum wind speed measured by the SFMR in the intercomparison dataset is 54 m/s (120 mph, Cat 3).

Estimation of the uncertainty in CYGNSS wind speed retrievals in and near hurricanes is done in two ways: first by qualitatively examining individual hurricane overpasses and examining the impact of time averaging on the retrievals and second by quantitatively comparing the population of matchup samples. Six examples of hurricane overpasses are shown in Figure 11.9. Both the winds retrieved by CYGNSS and measured by the SFMR on the P-3 are shown. Considering only samples for which SFMR wind speed is greater than 20 m/s, the RMS difference between CYGNSS and SFMR is 5.2 m/s, and the mean difference (bias) is 1.0 m/s.

11.2.3. Rolled-Up Performance Assessment

The overall top-down RMS difference between CYGNSS and ECMWF wind speeds, including all coincident matchup samples for which ECMWF winds are less than or equal to 20 m/s, was found to be 1.96 m/s. Note that this value includes components of error due to both CYGNSS and
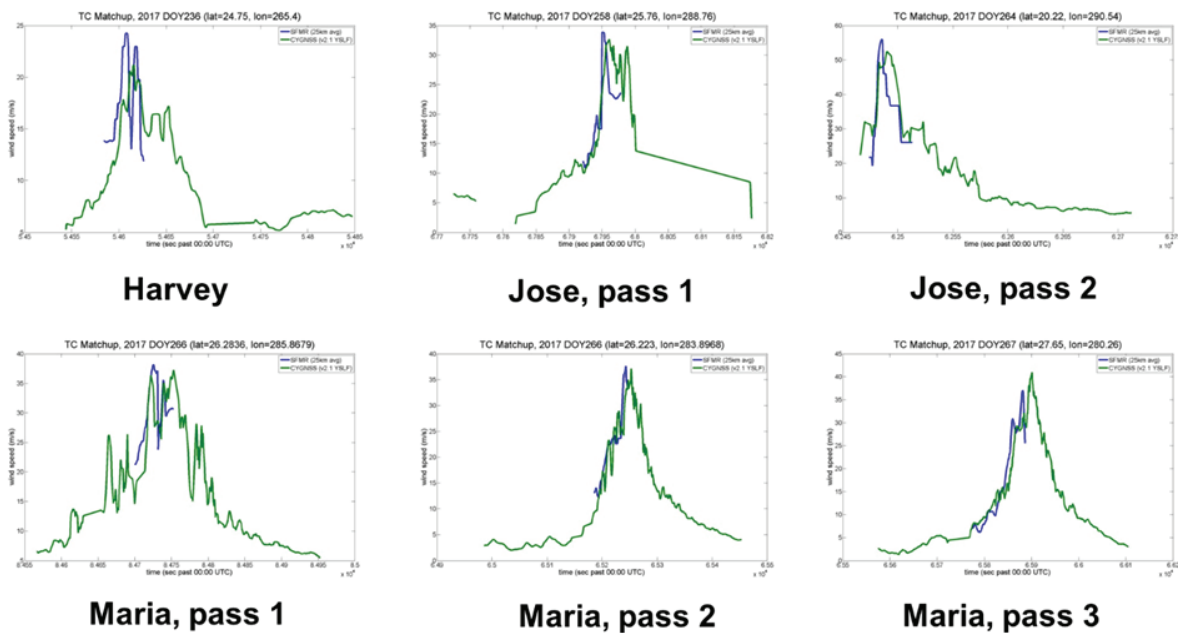
Figure 11.9. Examples of CYGNSS overpasses of Hurricanes Harvey, Jose, and Maria during 2017, which were coincident with NOAA P-3 hurricane hunter aircraft flights on (a) DOY 236, (b) DOY 258, (c) DOY 264, (d) DOY 266, (e) DOY 266, and (f) DOY 267. SFMR measurements of u10 are shown in blue, and CYGNSS measurements are shown in green.

ECMWF uncertainty as well as interpolation errors associated with estimating ECMWF winds at the time and place of the CYGNSS samples. As such, it should be considered an upper bound on the uncertainty in the CYGNSS values. The uncertainty in ECMWF reported wind speeds has been assessed by intercomparisons with a large number of deep water National Data Buoy Center (NDBC) buoy measurements during 1979–2009 (Stopa & Cheng, 2014). The RMS error in ECMWF reanalysis winds over the tropics was found to be 1.33 m/s. If this error is removed from the overall 1.96 RMS difference (using root-difference-square subtraction), the remaining uncertainty in the CYGNSS wind speed is 1.44 m/s.

The top-down RMS difference between CYGNSS and SFMR wind speeds, including matchups taken during mutual hurricane overpasses and using samples for which SFMR winds are greater than or equal to 20 m/s, was found to be 5.2 m/s. For this sample population, the average SFMR wind speed was 28.8 m/s. As in the lower wind speed case, this value should be considered an upper bound on CYGNSS uncertainty because the RMS difference statistic also includes errors in the SFMR measurement of wind speed and the effects of temporal and spatial decorrelation because the two measurements are not made at exactly the same time and place. The uncertainty in SFMR reported wind speeds up to 70 m/s has been assessed by intercomparisons with 186 coincident dropwindsonde measurements made on 70 hurricane hunter aircraft flights during the 2005 Atlantic hurricane season (Uhlhorn et al., 2007). The RMS difference between SFMR and dropwindsonde 10 m referenced wind speeds was found to be 4 m/s. If this error is removed from the overall 5.2 RMS difference (using root-difference-square subtraction), the remaining uncertainty in the CYGNSS wind speed is 3.2 m/s. As a fraction of the average SFMR wind speed of 28.8 m/s, the high wind CYGNSS retrieval uncertainty is 11.3%.

11.3. Discussion

Bottom-up and top-down approaches to assessing the uncertainty in CYGNSS wind speed measurements show some similarities and some differences, both of which provide some insight into the characterization of performance. At low to moderate wind speeds using the retrieval algorithm based on a fully developed seas geophysical model function (GMF), the agreement between bottom-up model predictions and top-down empirical comparisons with "ground truth" winds is generally good, in terms of both the absolute value of the RMS uncertainty and the relative dependence of

the uncertainty on wind speed. Below ~15 m/s, the retrieval error grows slowly with wind speed as the sensitivity of the measurements to wind speed (the slope of the GMF) decreases. Above 15 m/s, retrieval error increases more rapidly because of both a further decrease in sensitivity and an increase in the retrieval bias (the mean difference between retrieved and ground truth wind speeds). The two effects are likely coupled in that a fixed bias in an L1 observable (e.g., due to calibration errors) will cause a larger retrieval bias at higher wind speeds due to the lower sensitivity there. It is hoped that future refinements in instrument calibration will lower the L1 bias, decrease the resulting L2 wind speed bias, and ultimately improve the overall uncertainty.

The GMF used by the CYGNSS wind speed retrieval algorithm is constructed from ECMWF and SFMR u_{10} winds at low and high wind speeds, respectively. Both of these report actual 10 m referenced values, whereas the CYGNSS scattering measurements, which are sensitive to surface roughness forced by wind stress, should be more directly related to the equivalent neutral wind speed (Verspeek et al., 2010; Ebuchi, 2017). The difference between the actual and equivalent neutral wind speeds is estimated to be 0.2 m/s globally (Hersbach, 2008; Verhoef et al., 2008), and this difference will contribute to the error in CYGNSS retrievals of actual wind speed. A possible future refinement for CYGNSS is the retrieval of 10 m equivalent neutral wind speed, similar to the practice in ocean wind scatterometry, to eliminate this source of error.

The discrepancy between bottom-up and top-down performance estimates is larger at high wind speeds using the retrieval algorithm based on the young seas limited fetch GMF. The bottom-up model predicts that retrieval noise can be significantly reduced by time averaging of the data, and this is borne out by the behavior of the observations. Individual measurements are made with a 1-second average. Additional time averaging is performed in ground processing, with 3–5 seconds of averaging typically used to produce a wind speed product with 25 km spatial resolution. The discrepancy between bottom-up and top-down performance is likely attributable at least in part to the use of a simplified two-regime approach by the wind speed retrieval algorithm to account for variations in sea age and fetch length in and near tropical cyclones. It uses a single limited fetch GMF when near a storm without regard for the continuously varying transition that actually occurs from a fully developed state far from the storm center. A more proper, physically based approach should account for this transition zone and should also consider the variability of sea age, fetch length, and the resulting long wave swell within the storm, for example, as a

function of the storm quadrant. This is also an area of active research by the CYGNSS science team, with the expectation that future versions of the L2 wind speed retrieval algorithm will incorporate ancillary information about the sea state by adjusting either the GMF or the L1 observables appropriately.

The mission level requirements on wind speed measurement uncertainty are ± 2 m/s at wind speeds below 20 m/s and +10% above 20 m/s. The top-down performance assessment of 1.4 m/s uncertainty at low to moderate wind speeds using the FDS GMF demonstrates that the requirement has been met below 20 m/s. At higher wind speeds, the top-down assessment using the YSLF GMF during hurricane overpasses demonstrates an 11% uncertainty, and the requirement has not been met. Future improvements to the retrieval algorithm will focus on two primary sources of error. Calibration of the L1 observables can be improved, most notably by lowering the uncertainty in knowledge of the GPS EIRP through better characterization of the transmitter properties of the GPS constellation of satellites (Wang et al., 2019). Improved L1 calibration should ameliorate the increase in retrieval uncertainty that occurs at higher wind speeds because the sensitivity of the L1 observables to changes in wind speed is reduced. At high wind speeds in tropical cyclones, the dependence of the L1 observables on long wave swell, in addition to wind-driven capillary waves, is another significant source of retrieval error. Future improvements will attempt to incorporate ancillary sea state information to better account for this sensitivity. The improvement to L1 calibration should improve performance and reduce uncertainty at all wind speeds. An improved sea state–dependent retrieval algorithm should further reduce the uncertainty at high wind speeds. Between those two improvements, the high wind measurement uncertainty of 11% should be lowered closer to the 10% mission requirement.

11.4. References

Andersson, E., Persson, A., & Tsonevsky, I. (2015). User Guide to ECMWF Forecast Products, ECMWF, v2.1, 121 pp.

Clarizia, M. P., & Ruf, C. S. (2016). Wind speed retrieval algorithm for the Cyclone Global Navigation Satellite System (CYGNSS) mission. *IEEE Transactions on Geoscience and Remote Sensing, 54*(8). https://doi.org/10.1109/TGRS.2016.2541343.

Clarizia, M. P., Ruf, C., Jales, P., & Gommenginger, C. (2014). Spaceborne GNSS-R minimum variance wind speed estimator. *IEEE Transactions on Geoscience and Remote Sensing, 52*(11), 6829–6843. https://doi.org/10.1109/TGRS.2014.2303831.

Ebuchi, N. (2017). Evaluation of marine surface wind speed observed by AMSR2 on GCOM-W. *IEEE Journal of Selected Topics in Applied Earth Observations and Remote Sensing, 10*(9), 3955–3962. https://doi.org/10.1109/JSTARS.2017.2685432.

Gleason, S., Ruf, C., Clarizia, M. P., & O'Brien, A. (2016). Calibration and unwrapping of the normalized scattering cross section for the Cyclone Global Navigation Satellite System (CYGNSS). *IEEE Transactions on Geoscience and Remote Sensing, 54*(5), 2495–2509. https://doi.org/10.1109/TGRS.2015.2502245.

Gleason, S., Ruf, C. S., O'Brien, A., & McKague, D. S. (2018). The CYGNSS Level 1 calibration algorithm and error analysis based on on-orbit measurements. *IEEE Journal of Selected Topics in Applied Earth Observations and Remote Sensing, 12*(1), 37–49. https://doi.org/10.1109/JSTARS.2018.2832981.

Hersbach, H. (2008). CMOD5.N: A C-band geophysical model function for equivalent neutral wind. *Technical Memorandum, ECMWF*(554), 20 pp. http://www.ecmwf.int/sites/default/files/elibrary/2008/9873-cmod5n-c-band-geophysical-model-function-equivalent-neutral-wind.pdf.

NOAA. (2018). National Centers for Environmental Information, Global Data Assimilation System. https://www.ncei.noaa.gov/access/metadata/landing-page/bin/iso?id=gov.noaa.ncdc:C00379.

Ruf, C., & Balasubramaniam, R. (2018). Development of the CYGNSS geophysical model function for wind speed. *IEEE Journal of Selected Topics in Applied Earth Observations and Remote Sensing, 12*(1), 66–77. https://doi.org/10.1109/JSTARS.2018.2833075.

Ruf, C., Unwin, M., Dickinson, J., Rose, R., Rose, D., Vincent, M., & Lyons, A. (2013). CYGNSS: Enabling the future of hurricane prediction. *IEEE Geoscience and Remote Sensing Magazine, 1*(2), 52–67. https://doi.org/10.1109/MGRS.2013.2260911.

Stopa, J. E., & Cheung, K. F. (2014). Intercomparison of wind and wave data from the ECMWF reanalysis interim and the NCEP climate forecast system reanalysis. *Ocean Modeling, 75*, 65–83.

Uhlhorn, E. W., Black, P. G., Franklin, J. L., Goodberlet, M. A., Carswell, J. R., & Goldstein, A. S. (2007).

Hurricane surface wind measurements from an operational stepped frequency microwave radiometer. *Monthly Weather Review, 135,* 3070–3085. https://doi.org/10.1175/MWR3454.1.

Verhoef, A., Portabella, M., Stoffelen, A., and & Hersbach, H. (2008). *CMOD5.n—the CMOD5 GMF for neutral winds* (EUMETSAT Tech. Note, SAF/OSI/CDOP/KNMI/TEC/TN/165), 13 pp.

Verspeek, J., Stoffelen, A., Portabella, M., Bonekamp, H., Anderson, C., & Figa Saldaña, J. (2010). Validation and calibration of ASCAT using CMOD5.n. *IEEE Transactions on Geoscience and Remote Sensing, 48*(1), 386–395.

Wang, T., Ruf, C. S., Block, B., McKague, D. S., & Gleason, S. (2019). Design and performance of a GPS constellation power monitor system for improved CYGNSS L1B calibration. *IEEE Journal of Selected Topics in Applied Earth Observations and Remote Sensing, 12*(1), 26–36. https://doi.org/10.1109/JSTARS.2018.2867773.

12. Project Publications

This section provides a table of CYGNSS-related publications and conference presentations at the time this handbook was originally compiled.

Author(s)	Title	Conference/journal	Date
Chen, D.; Gleason, S.; Ruf, C.; Adjrad, M.	Spectral dependence of the response time of sea state to local wind forcing	IGARSS 2012	2012 Jul 12
Ruf, C.; Gleason, S.; Jelenak, Z.; Katzberg, S.; Ridley, A.; Rose, R.; Scherrer, J.; Zavorotny, V.	The NASA EV-2 Cyclone Global Navigation Satellite System (CYGNSS) mission	IEEE Aerospace Conference	2013 Mar 13
Clarizia, M. P.; Ruf, C.; Jales, P.; Gommenginger, C.	Spaceborne GNSS-R minimum variance wind speed estimator	*IEEE Transactions on Geoscience and Remote Sensing*	2014 Nov 14
Lang, T.; Mecikalski, J.; Li, X.; Chronis, T.; Brewer, A.; Chrunside, J.; McCarty, B.	Exploring the utility of the planned CYGNSS mission for investigating the initiation and development of the Madden-Julian oscillation	31st Conference on Hurricanes and Tropical Meteorology, San Diego, CA	2014 Apr
Miller, S.A.; Killough, R. L.; Cook, S. W.; Ruf, C.	Onboard science processing on a microsatellite with limited resources	*Proceedings of the 2014 IEEE Aerospace Conference*, Big Sky, MT	2014 Mar 14
Park, J.; Johnson, J. T.; Lowe, S. T.	Studies of GNSS-R ocean altimetry using full DDM-based retrieval	URSI National Radio Science Meeting	2014 Jan
Park, J.; Johnson, J. T.; Lowe, S. T.	A study of the electromagnetic bias in GNSS-R altimetry	IGARSS 2014/35th CSRS (Quebec City, Canada)	2014 Jul 14
Powell, S.; Akos, D.; Zavorotny, V.	GPS SBAS L1/L5 bistatic radar altimeter	IGARSS 2014 / 35th CSRS (Quebec City, Canada)	2014 Jul 14
Riley, E. M.; Maloney, E. D.	Analysis of the MJO–wind speed relationship in the indian ocean using observations and models	31st Conference on Hurricanes and Tropical Meteorology, San Diego, CA	2014 Apr
Rose, C.; Wells, W.; Rose, D.; Nave, K.; Pruitt, J.; Dickinson, J.	The CYGNSS Microsatellite Constellation Earth Venture Mission	IGARSS 2014/35th CSRS (Quebec City, Canada)	2014 Jul 14
Rose, D.; R.; Wells, W.; Rose, D.; Ridley, A.; Nave, K.	Nanosat technology and managed risk; an update of the CYGNSS microsatellite constellation mission development	28th Annual AIAA/USU Conference on Small Satellites (SmallSat), Logan, UT	2014 Aug 14
Rose, R.; Gleason, S.; Ruf, C.	The NASA CYGNSS mission: A pathfinder for GNSS scatterometry remote sensing applications	SPIE Remote Sensing Conference, Amsterdam, Netherlands	2014 Sep
Ruf, C.; Clarizia, M. P.; Gleason, S.; Rose, R.; Ridley, A.	The NASA EV-2 Cyclone Global Navigation Satellite System (CYGNSS) Mission	2014 International Geoscience and Remote Sensing Symposium	2014 Jul 14
Ruf, C.; Clarizia, M. P.; Gleason, S.; Rose, R.; Ridley, A.	The NASA Cyclone Global Navigation Satellite System (CYGNSS) mission	*Advanced RF Sensors and Remote Sensing Instruments*	2014 Nov 14
Ruf, C.; Clarizia, M. P.; O'Brien, A.; Johnson, J.; Ridley, A.; Yi, Y.	Enhanced spatial & temporal sampling of air/sea interaction in tropical cyclones by the NASA CYGNSS mission	31st Conference on Hurricanes and Tropical Meteorology, San Diego, CA	2014 Apr

(continued)

Author(s)	Title	Conference/journal	Date
Ruf, C.; Clarizia, M. P.; O'Brien, A.; Ridley, A.; Johnson, J.; Yi, Y.	The NASA Cyclone Global Navigation Satellite System (CYGNSS) mission	18th Conference Integrated Observing and Assimilation Systems for Atmosphere, Oceans, and Land Surface, AMS Annual Conference	2014 Feb 14
Ruf, C.; Ridley, A.; Clarizia, M. P.; Gleason, S.; Rose, R.; Scherrer, J.	The NASA CYGNSS mission: Design and predicted performance	2014 International Geoscience and Remote Sensing Symposium	2014 Jul 14
Voronovich, A.; Zavorotny, V.	Full-polarization modeling of monostatic and bistatic radar scattering from a rough sea surface	*IEEE Transactions on Antennas and Propagation*	2014 Mar 14
Zavorotny, V.; Gleason, S.; Cardellach, E.; Camps, A.	Tutorial on remote sensing using GNSS bistatic radar of opportunity	*IEEE Geoscience and Remote Sensing Magazine*	2014 Dec 14
Zavorotny, V.; Voronovich, A.	Recent progress on forward scattering modeling for GNSS reflectometry	IGARSS 2014/35th CSRS (Quebec City, Canada)	2014 Jul 14
Buchanan, M.; O'Brien, A.; Block, B.	Design of a ground-based beacon signal for calibration of spaceborne GNSS remote sensing instruments	ION GNSS+ 2015	2015 Sep 15
Clarizia, M. P.; Ruf, C. S.; Braca, P.; Willet, P.	Target detection using GPS signals of Opportunity	*18th International Conference on Information Fusion (Fusion)*, pp. 1429–1436	2015 Jul
Fritz, M.; Shoer, J.; Singh, L.; Henderson, T.; McGee, J.; Rose, C.	Attitude determination and control system design for the CYGNSS microsatellite	IEEE Aerospace Conference	2015 Mar 15
Gleason, S.; Ruf, C.	Overview of the delay Doppler mapping instrument (DDMI) for the Cyclone Global Navigation Satellite Systems Mission (CYGNSS)	*Proceedings of the 2015 International Microwave Symposium*, Phoenix, AZ, https://ieeexplore.ieee.org/document/7166775	2015 May
Hannah, W. M.; Mapes, B. E.; Elsaesser, G. S.	A Lagrangian view of moisture dynamics during DYNAMO	*Journal of the Atmospheric Sciences*, http://journals.ametsoc.org/doi/abs/10.1175/JAS-D-15-0243.1	2015
Riley Dellaripa, E. M.; Maloney, E. D.	Analysis of MJO wind-flux feedbacks in the Indian Ocean using RAMA buoy observations	*Journal of the Meteorological Society of Japan*, http://dx.doi.org/10.2151/jmsj.2015-021	2015
Rodriguez-Alvarez, N.; Garrison, J. L.	Generalized linear observables for ocean wind retrieval from calibrated GNSS-R delay-Doppler maps	*Geoscience and Remote Sensing, IEEE Transactions*	2015 Sep 22
Rose, C.; Scherrer, J.; Wells, J.	The CYGNSS flight segment: Mainstream science on a micro-budget	IEEE Aerospace Conference	2015 Mar 15
Ruf, C. S.; Atlas, R.; Chang, P. S.; Clarizia, M. P.; Garrison, J. L.; Gleason, S.; Katzberg, S. J.; Jelenak, Z.; Johnson, J. T.; Majumdar, S. J.; O'Brien, A.; Posselt, D. J.; Ridley, A. J.; Rose, R. J.; Zavorotny, V. U.	New ocean winds satellite mission to probe hurricanes and tropical convection	*Bulletin of the American Meteorological Society*	2015 Jun 15
Said, F.; Soisuvarn, S.; Katzberg, S.; Jelenak, Z.; Chang, P. S.	Estimation of maximum hurricane wind speed using simulated CYGNSS measurements	Geoscience and Remote Sensing Symposium (IGARSS)	2015 Jul

Author(s)	Title	Conference/journal	Date
Shoer, J.; Singh, L.; Henderson, T.	Conical scanning approach for sun pointing on the CYGNSS microsatellite	IEEE Aerospace Conference	2015 Mar 15
Wells, J.; Scherrer, J.; Van Noord, J.; Law, R.	Early development of the first earth venture mission: How CYGNSS is using engineering models to validate the design	IEEE Aerospace Conference	2015 Mar 15
Allen, T.; Mapes, B. E.; Cavanaugh, N.	Informativeness of wind data in linear Madden-Julian oscillation prediction	*Atmospheric Science Letters*, https://doi.org/10.1002/asl.666/full	2016
Castillo, T.; Mecikalski, J.; Lang, T.; Chronis, T.; Li, X.	Understanding how CYGNSS will depict convective variability by ingesting a high temporal resolution WRF simulation in NASA's end-to-end simulator	4th Symposium on Prediction of the Madden-Julian Oscillation: Processes, Prediction and Impact, 96th American Meteorological Society Annual Meeting, New Orleans, LA	2016 Jan 9–14
Chen, D. D.; Ruf, C. S.; Gleason, S. T.	Response time of mean square slope to wind forcing: An empirical investigation	*Journal of Geophysical Research: Oceans, 121*(4), https://doi.org/10.1002/2016JC011661	2016
Chen-Zhang, D. D.; Ruf, C. S.; Ardhuin, F.; Park, J.	GNSS-R nonlocal sea state dependencies: Model and empirical verification	*Journal of Geophysical Research: Oceans, 121*(11), https://doi.org/10.1002/2016JC012308	2016
Clarizia, M. P.; Ruf, C. S.	On the spatial resolution of GNSS-reflectometry	*IEEE Geoscience and Remote Sensing Letters, 13*(8), https://doi.org/10.1109/LGRS.2016.2565380	2016
Clarizia, M. P.; Ruf, C. S.	Wind speed retrieval algorithm for the Cyclone Global Navigation Satellite System (CYGNSS) mission	*IEEE Transactions on Geoscience and Remote Sensing, 54*(8), https://doi.org/10.1109/TGRS.2016.2541343	2016 Aug
Clarizia, M. P.; Ruf, C.; Cipollini, P.; Zuffada, C.	first spaceborne observation of sea surface height using GPS reflectometry	*Geophysical Research Letters, 43*, https://doi.org/10.1002/2015GL066624	2016
Giangregorio, G.; di Bisceglie, M.; Addabbo, P.; Beltramonte, T.; D'Addio, S.; Galdi, C.	Stochastic modeling and simulation of delay–Doppler maps in GNSS-R over the ocean	*IEEE Transactions on Geoscience and Remote Sensing, 54*(4), 2056–2069	2016 Apr
Gleason, S.; Ruf, C.; Clarizia, M. P.; O'Brien, A.	Calibration and unwrapping of the normalized scattering cross section for the Cyclone Global Navigation Satellite System (CYGNSS)	*IEEE Transactions on Geoscience and Remote Sensing, 54*(5), 2495–2509, https://doi.org/10.1109/TGRS.2015.2502245	2016
Hoover, K.	Evaluation of CYGNSS in understanding the convective winds in the weak December 2011 MJO event captured by the DYNAMO field experiment	Master's thesis, University of Alabama in Huntsville, 116pp.	2016
Hoover, K.; Mecikalski, J.; Li, X.; Lang, T.; Chronis, T.	Use of CYGNSS in understanding the onset and convective properties in a weak MJO from the DYNAMO December 2011 Event	4th Symposium on Prediction of the Madden-Julian Oscillation: Processes, Prediction and Impact, 96th American Meteorological Society Annual Meeting, New Orleans, LA	2016 Jan 9–14

(continued)

Author(s)	Title	Conference/journal	Date
Morris, M.; Chen, D. D.; Ruf, C. S.	Earth antenna temperature variability for CYGNSS	*Proceedings of the 2016 International Geoscience and Remote Sensing Symposium*, Beijing, China, pp. 846–849, https://doi.org/10.1109/IGARSS.2016.7729214	2016 Jul
Pu, Z.; Zhang, S.	Impact of CYGNSS data on hurricane analyses and forecast in regional OSSEs with HWRF model	21st AMS Conference on Satellite Meteorology, Oceanography, and Climatology, Madison, WI	2016 Aug 15–19
Ruf, C. S.; Atlas, R.; Chang, P. S.; Clarizia, M. P.; Garrison, J. L.; Gleason, S.; Katzberg, S. J.; Jelenak, Z.; Johnson, J. T.; Majumdar, S. J.; O'Brien, A.; Posselt, D. J.; Ridley, A. J.; Rose, R. J.; Zavorotny, V. U.	New ocean winds satellite mission to probe hurricanes and tropical convection	*Bulletin of the American Meteorological Society*, pp. 385–395, https://doi.org/10.1175/BAMS-D-14-00218.1	2016 Mar
Addabbo, P.; di Bisceglie, M.; Galdi, C.; Giangregorio, G.	Performance of the delay-Doppler scattered power volume observable for wind speed estimation with CYGNSS	GNSS+R 2017, Specialist Meeting on Reflectometry Using GNSS and Other Signals of Opportunity, Ann Arbor, MI	2017 May 23–25
Anguelova, M. D.; Bettenhausen, M. H.	Effect of a sea spray layer on L-band signal from ocean surface	GNSS+R Workshop, Ann Arbor, MI	2017 May 23–25
Anguelova, M. D.; Huq, P.	Effects of salinity on surface lifetime of large individual bubbles	*Journal of Marine Science and Engineering, 5*(3), 41, https://doi.org/10.3390/jmse5030041	2017 Sep 1
Balasubramaniam, R.; Ruf, C. S.; McKague, D.; Clarizia, M. P.; Gleason, S.	Calibration and validation processing for the CYGNSS wind speed retrieval algorithm	*Proceedings of the 2017 International Geoscience and Remote Sensing Symposium*, Houston, TX, pp. 4117–4120, https://doi.org/10.1109/IGARSS.2017.8127906	2017 Jul
Clarizia, M. P.; Ruf, C. S.; Gleason, S.; Balasubramaniam, R.; McKague, D.	Generation of CYGNSS Level 2 wind speed data products	*Proceedings of the 2017 International Geoscience and Remote Sensing Symposium*, Houston, TX, pp. 2647–2649, https://doi.org/10.1109/IGARSS.2017.8127539	2017 Jul
Clarizia, M.; Ruf, C.	Bayesian wind speed estimation conditioned on significant wave height for GNSS-R ocean observations	*Journal of Atmospheric and Oceanic Technology, 34*(6), 1193–1202, https://doi.org/10.1175/JTECH-D-16-0196.1	2017
Crespo, J. A.; Posselt, D. J.; Naud, C. M.; Bussy-Virat, C.	Assessing CYGNSS's potential to observe extratropical fronts and cyclones	*Journal of Applied Meteorology and Climatology, 56*(7), 2027–2034.	2017
Fan, Y.; Hwang, P.	Kinetic energy flux budget across air-sea interface	*Ocean Modeling, 120, 27–40*	2017
Gleason, S.; Ruf, C.; Clarizia, M. P.; Johnson, J.; O'Brien, A.; Chang, P.; Jelenek, Z.; Said, F.; Soisuvarn, S.	Calibration and validation of the CYGNSS Level 1 data products	*Proceedings of the 2017 International Geoscience and Remote Sensing Symposium*, Houston, TX, pp. 2644–2646, https://doi.org/10.1109/IGARSS.2017.8127538	2017 Jul

(continued)

Author(s)	Title	Conference/journal	Date
Hwang, P. A.; Fan, Y.	Effective fetch and duration of tropical cyclone wind fields estimated from simultaneous wind and wave measurements: Surface wave and air-sea exchange computation	*Journal of Physical Oceanography, 47,* 447–470	2017
Hwang, P. A.; Fan, Y.; Ocampo-Torres, F. J.; García-Nava, H.	Ocean surface wave spectra inside tropical cyclones	*Journal of Physical Oceanography, 47,* 2293–2417	2017
Hwang, P. A.; Li, X.; Zhang, B.	Retrieving hurricane wind speed from dominant wave parameters	*IEEE J-STARS, 10*(6), 2589–2598	2017
Lang, T. J.	Analysis and modeling of tropical convection observed by CYGNSS	Fall Meeting, American Geophysical Union, New Orleans, LA	2017 Dec
Lang, T. J.	Using CYGNSS to investigate relationships between wind-driven surface fluxes and tropical oceanic convection	GNSS+R Workshop, Ann Arbor, MI	2017 May 23–25
Ling, J.; Li, C.; Li, T.; Jia, X.; Khouider, B.; Maloney, E.; Vitart, F.; Zhang, C.	Meeting summary: Challenges and opportunities of MJO study	*Bulletin of the American Meteorological Society, 98,* ES53–56	2017
McKague, D. S.; Ruf, C. S.	CYGNSS constellation intercalibration	*Proceedings of the 2017 International Geoscience and Remote Sensing Symposium,* Houston, TX, pp. 2654–2656, https://doi.org/10.1109/IGARSS.2017.8127541	2017 Jul
Morris, M.; Ruf, C. S.	Determining tropical cyclone surface wind speed structure and intensity with the CYGNSS satellite constellation	*Journal of Applied Meteorology and Climatology, 56*(7), 1847–1865, https://doi.org/10.1175/JAMC-D-16-0375.1	2017
Morris, M.; Ruf, C. S.	Estimating tropical cyclone integrated kinetic energy with the CYGNSS satellite constellation	*Journal of Applied Meteorology and Climatology, 56,* 235–245, https://doi.org/10.1175/JAMC-D16-0176.1	2017
Principe, S.; Beltramonte, T.; di Bisceglie, M.; Galdi, C.	Statistical modeling and simulation of delay-Doppler maps in the time-varying regime	*Proceedings of the 2017 International Geoscience and Remote Sensing Symposium,* Houston, TX, pp. 4121–4124, https://doi.org/10.1109/IGARSS.2017.8127907.	2017 Jul
Riley Dellaripa, E.; Maloney, E.; van den Heever, S.	Wind-flux feedbacks and convective organization during the November 2011 MJO event in a high resolution model	*Journal of the Atmospheric Sciences, 75,* 57–84	2017
Ruf, C. S.; Gleason, S.; Ridley, A.; Rose, R.; Scherrer, J.	The NASA CYGNSS mission: Overview and status update	*Proceedings of the 2017 International Geoscience and Remote Sensing Symposium,* Houston, TX, pp. 2641–2643, https://doi.org/10.1109/IGARSS.2017.8127537	2017 Jul
Wang, T.; Ruf, C.; Gleason, S.; Block, B.; McKague, D.; Provost, D.	Development of GPS constellation power monitor system for high accuracy calibration/validation of the CYGNSS L1B data	*Proceedings of the 2017 International Geoscience and Remote Sensing Symposium,* Houston, TX, pp. 1008–1011, https://doi.org/10.1109/IGARSS.2017.8127125	2017 Jul

(continued)

Author(s)	Title	Conference/journal	Date
Warnock, A. M.; Ruf, C. S.; Morris, M.	Storm surge predictions with CYGNSS winds	*Proceedings of the 2017 International Geoscience and Remote Sensing Symposium*, Houston, TX, pp. 2975–2978, https://doi.org/10.1109/IGARSS.2017.8127624	2017 Jul
Zhang, S.; Pu, Z.; Posselt, D. J.; Atlas, R.	Impact of CYGNSS ocean surface wind speeds on numerical simulations of a hurricane in observing system simulation experiments	*Journal of Atmospheric and Oceanic Technology, 34*, 375–383, http://dx.doi.org/10.1175/JTECH-D-16-0144.1	2017
Addabbo, P; di Bisceglie, M.; Galdi, C.; Giangregorio, G.	An algorithm for wind speed retrieval from CYGNSS space observatories	*Proceedings of the IGARSS 2018—2018 IEEE International Geoscience and Remote Sensing Symposium*, Valencia, Spain, pp. 4281–4284	2018 Jul
Anguelova, M. D., Bettenhausen, M. H.	Effect of a sea spray layer on ocean surface signal at GPS frequencies	AMS 21st ASI Conference, Oklahoma City, OK	2018 Jun 11–15
Anguelova, M. D.; Huq, P.	Effects of salinity on bubble cloud characteristics	*Journal of Marine Science and Engineering, 6*(1), 1, https://doi.org/10.3390/jmse6010001	2018
Balasubramaniam, R.; Ruf, C. S.	Improved calibration of CYGNSS measurements for downbursts in the intertropical convergence zone	*Proceedings of the 2018 International Geoscience and Remote Sensing Symposium*, Valencia, Spain, pp. 3987–3990, https://doi.org/10.1109/IGARSS.2018.8517571	2018 Jul
Burrage, D. M., Anguelova, M. D.; Wang, D. W.; Wesson, J. C.	Modeling L-Band Reflection and emission from seawater, foam, and whitecaps using the finite-difference time-domain method	*IEEE Geoscience and Remote Sensing Letters, 16*(5), 682–686	2018
Burrage, D. M., Anguelova, M. D.; Wang, D. W.; Wesson, J. C.	Predicting L-band emissivity of a wind-roughened sea with foam layers or whitecaps and overlying spray, using a finite-difference time-domain model	MicroRad 2018, Cambridge, MA	2018 Mar 27–30
Bussy-Virat, C. D.; Ruf, C. S.; Ridley, A. J.	Relationship between temporal and spatial resolution for a constellation of GNSS-R satellites	*IEEE Journal of Selected Topics in Applied Earth Observations and Remote Sensing*, https://doi.org/10.1109/JSTARS.2018.2833426	2018
Crespo, J. A.; Posselt, D. J.	CYGNSS observations of low-latitude extratropical cyclones and estimates of surface heat fluxes	22nd Conference on Satellite Meteorology and Oceanography at the 98th American Meteorological Society Annual Meeting, Austin, TX	2018 Jan 7–11
Cui, Z.; Pu, Z.; Tallapragada, V.; Ruf, C.; Atlas, R.	Assimilation of CYGNSS ocean surface winds with NCEP HWRF model GSI-based ensemble-variational data assimilation systems for improved numerical simulations of tropical cyclones and tropical convection	33rd Conference on Hurricanes and Tropical Meteorology, Ponte Vedra, FL	2018 Apr 16–20

(continued)

Author(s)	Title	Conference/journal	Date
Giangregorio, G.; Addabbo, P.; Galdi, C.; di Bisceglie, M.	Ocean wind speed estimation from the GNSS scattered power function volume	*IEEE Journal of Selected Topics in Applied Earth Observations and Remote Sensing, 12*(1), 78–86	2018
Gleason, S.; Ruf, C. S.; O'Brien, A.; McKague, D. S.	The CYGNSS Level 1 calibration algorithm and error analysis based on on-orbit measurements	*IEEE Journal of Selected Topics in Applied Earth Observations and Remote Sensing*, https://doi.org/10.1109/JSTARS.2018.2832981	2018
Hoover, K. E.; Mecikalski, J. R.; Lang, T. J.; Li, X.; Castillo, T. J.; Chronis, T.	Use of an end-to-end-simulator to analyze CYGNSS	*Journal of Atmospheric and Oceanic Technology*, https://doi.org/10.1175/JTECH-D-17-0036.1	2018
Hwang, P. A.	High wind drag coefficient and whitecap coverage derived from microwave radiometer observations in tropical cyclones	*Journal of Physical Oceanography, 48*, 2221–2232, https://doi.org/10.1175/JPO-D-18-0107.1	2018
Hwang, P. A.; Fan, Y.	Low-frequency mean square slopes and dominant wave spectral properties: Toward tropical cyclone remote sensing	*IEEE Transactions on Geoscience and Remote Sensing, 56*, 7359–7368, https://doi.org/10.1109/TGRS.2018.2850969	2018
Hwang, P. A.; Walsh, E. J.	Estimating maximum significant wave height and dominant wave period inside tropical cyclones	*Weather and Forecasting, 33.* https://doi.org/10.1175/WAF-D-17-0186.1	2018
Hwang, P. A.; Walsh, E. J.	Propagation directions of ocean surface waves inside tropical cyclones	*Journal of Physical Oceanography, 48*(7), 1495–1511	2018
Killough, R.; Scherrer, J.; Rose, R.; Brody, A.; Redfern, J.; Smith, K.; Ruf, C. S.; Yee, T.	CYGNSS launch and early ops: Parenting octuplets	*Proceedings of the 31st Annual AIAA/USU Conference on Small Satellites, Year in Review*, SSC17-X-01, http://digitalcommons.usu.edu/smallsat/2017/all2017/136/	2018 Aug
Kim, D.; Maloney, E. D.; Zhang, C.	Review: MJO propagation over the maritime continent	*The Global Monsoon System*, 4th ed., C.-P. Chang et al., eds.	2018
Krien, Y.; Arnaud, G.; Cécé, C.; Belmadani, A.; Khan, J.; Bernard, D.; Islam, A. K. M. S.; Durand, F.; Testut, L.; Palany, P.; Zahibo, N.	Can we improve parametric cyclonic wind fields using recent satellite remote sensing data?	*Remote Sensing, 10*, 1963, https://doi.org/10.3390/rs10121963	2018
Li, W.; Cardellach, E.; Fabra, F.; Ribó, S.; Rius, A	Altimetry over sea ice using coherent GNSS reflections	International Geoscience and Remote Sensing Symposium (IGARSS), Valencia, Spain	2018 Jul
Li, W.; Cardellach, E.; Fabra, F.; Ribó, S.; Rius, A.	Lake level and surface topography measured with spaceborne GNSS-reflectometry from CYGNSS mission: Example for the Lake Qinghai	*IEEE Geophysical Research Letters, 45*(24), 13,332–13,341	2018
Li, X.; Janiga, M.; Wang, S.; Tao, W.-K.; Rowe, A.; Xu, W.; Liu, C.; Matsui, T.	Evolution of precipitation structure during the November DYNAMO MJO event: Cloud-resolving model inter-comparison and cross-validation using radar observations	*Journal of Geophysical Research, 123*, https://doi.org/10.1002/2017JD027775	2018

(continued)

Author(s)	Title	Conference/journal	Date
Mantripragada, S.; Aiyyer, A.; Schreck, C. J.	Interaction of Kelvin and easterly waves over the Atlantic and implications for tropical cyclogenesis	33rd Conference on Hurricanes and Tropical Meteorology, Ponte Vedra, FL; American Meteorological Society, 3B.5, https://ams.confex.com/ams/33HURRICANE/webprogram/Paper340571.html	2018 Apr 16–20
Mayers, D.; Ruf, C. S.	Measuring ice thickness with CYGNSS altimetry	*Proceedings of the 2018 International Geoscience and Remote Sensing Symposium*, Valencia, Spain, pp. 8535–8538, https://doi.org/10.1109/IGARSS.2018.8519310	2018 Jul
Norris, R.; Ruf, C.; Loria, E.; O'Brien, A.	Comparison of wide bandwidth conventional and interferometric GNSS-R techniques for possible CYGNSS follow-on mission	*Proceedings of the 2018 International Geoscience and Remote Sensing Symposium*, Valencia, Spain, pp. 4277–4280, https://doi.org/10.1109/IGARSS.2018.8517480	2018 Jul
Ruf, C. S.; Balasubramaniam, R.	Development of the CYGNSS geophysical model function for wind speed	*IEEE Journal of Selected Topics in Applied Earth Observations and Remote Sensing*, https://doi.org/10.1109/JSTARS.2018.2833075	2018
Ruf, C. S.; Bussy-Virat, C.; McKague, D.; Ridley, A.; Morris, M.	Enabling sampling properties of the CYGNSS satellite constellation	*Proceedings of the 2018 International Geoscience and Remote Sensing Symposium*, Valencia, Spain, pp. 277–280, https://doi.org/10.1109/IGARSS.2018.8518454	2018 Jul
Ruf, C. S.; Chew, C.; Lang, T.; Morris, M. G., Nave, K.; Ridley, A.; Balasubramaniam, R.	A new paradigm in Earth environmental monitoring with the CYGNSS small satellite constellation	*Scientific Reports, 8*(1), 8782	2018
Ruf, C. S.; Gleason, S.; McKague, D. S.	Assessment of CYGNSS wind speed retrieval uncertainty	*IEEE Journal of Selected Topics in Applied Earth Observations and Remote Sensing*, https://doi.org/10.1109/JSTARS.2018.2825948	2018
Wang, T.; Ruf, C. S.; Block, B.; McKague, D. S.; Gleason, S.	Design and performance of a GPS constellation power monitor system for improved CYGNSS L1B calibration	*IEEE Journal of Selected Topics in Applied Earth Observations and Remote Sensing*, https://doi.org/10.1109/JSTARS.2018.2867773	2018
Wang, T.; Ruf, C.; Block, B.; McKague, D.	Characterization of the transmit power and antenna pattern of the GPS constellation for the CYGNSS mission	*Proceedings of the 2018 International Geoscience and Remote Sensing Symposium*, Valencia, Spain, pp. 4011–4014, https://doi.org/10.1109/IGARSS.2018.8518531	2018 Jul
Wang, T.; Zavorotny, V. U.; Johnson, J.; Ruf, C.; Yi, Y.	Modeling of sea state conditions for improvement of CYGNSS L2 wind speed retrievals	*Proceedings of the 2018 International Geoscience and Remote Sensing Symposium*, Valencia, Spain, pp. 8288–8291, https://doi.org/10.1109/IGARSS.2018.8518686	2018 Jul
Zhang, L.; Han, W.; Li, Y.; Maloney, E. D.	2018: Role of north Indian Ocean air-sea interaction in summer monsoon intraseasonal oscillation	*Journal of Climate, 31*, 7885–7908	2018

(continued)

Author(s)	Title	Conference/journal	Date
Al-Khaldi, M. M.; Johnson, J. T.; O'Brien, A.; Balenzano, A.; Mattia, F.	Time-series retrieval of soil moisture using CYGNSS	*IEEE Transactions on Geoscience and Remote Sensing, 57*(7), 4322–4331, https://doi.org/10.1109/tgrs.2018.2890646	2019
Balakhder, A.; Al-Khaldi, M. M.; Johnson, J. T.	On the coherency of ocean and land surface specular scattering for GNSS-R and signals of opportunity systems	*IEEE Transactions on Geoscience and Remote Sensing, 57*(12), 10426–10436, https://doi.org/10.1109/tgrs.2019.2935257	2019
Balasubramaniam, R.; Ruf, C.	The impact of rain on L1 GNSS-R radar scattering cross-section	*Proceedings of the 2019 International Geoscience and Remote Sensing Symposium*, Yokohama, Japan, https://doi.org/10.1109/IGARSS.2019.8900302	2019 Jul
Bui, H. X.; Maloney, E. D.	Mechanisms for global warming impacts on Madden-Julian oscillation precipitation amplitude	*Journal of Climate, 32*, 6961–6975	2019
Cardellach, E.; Li, W.; Rius, A.; Semmling, M.; Wickert, J.; Ruf, C.; Buontempo, C.	First precise spaceborne sea surface altimetry with GNSS reflected signals	*IEEE Journal of Selected Topics in Applied Earth Observations and Remote Sensing*, https://doi.org/10.1109/JSTARS.2019.2952694	2019
Cardellach, E.; Li, W.; Rius, A.; Semmling, M.; Wickert, J.; Zus, F.; Ruf, C.	First evidences of spaceborne carrier phase altimetry using GNSS reflected signals at grazing angles of observation over open sea water	2019 International Geoscience and Remote Sensing Symposium, Yokohama, Japan	2019 Jul
Crespo, J. A.; Posselt, D. J.; Asharaf, S.	CYGNSS surface heat flux product development	*Remote Sensing, 11*(19), 2294; https://doi.org/10.3390/rs11192294	2019
Cui, Z.; Pu, Z.; Tallapragada, V.; Atlas, C. S.	A preliminary impact study of CYGNSS ocean surface wind speeds on numerical simulations of hurricanes	*Geophysical Research Letters*, https://doi.org/10.1029/2019GL082236	2019
di Bisceglie, M.; Galdi, C.; Giangregorio, G.	Sensitivity of delay-Doppler maps to wind direction with a deconvolution approach	*Proceedings of the 2019 International Geoscience and Remote Sensing Symposium*, Yokohama, Japan, July 2019	2019 Jul
Gerlein-Safdi, C.; Ruf, C. S.	A CYGNSS-based algorithm for the detection of inland waterbodies	*Geophysical Research Letters, 46*(21), 12065–12072, https://doi.org/10.1029/2019GL085134	2019
Gleason, S.; Johnson, J.; Ruf, C.; Bussy-Virat, C.	Characterizing background signals and noise in spaceborne GNSS reflection ocean observations	*IEEE Geoscience and Remote Sensing Letters*, https://doi.org/10.1109/LGRS.2019.2926695	2019
Gu, W.; Xu H.; Tsang, L.	A numerical Kirchhoff simulator for GNSS-R land applications	*Progress in Electromagnetics Research, 164*, 119–133, https://doi.org/10.2528/PIER18121803	2019
Hwang, P. A.	Surface foam and L-band microwave radiometer measurements in high winds	*IEEE Transactions on Geoscience and Remote Sensing*, https://doi.org/10.1109/TGRS.2018.2876972	2019

Author(s)	Title	Conference/journal	Date
Kang, Y.; Kubatko, E.	Effects of CYGNSS-derived parametric wind fields on storm surge modeling	Finite Elements in Fluids, Chicago, IL	2019 Mar 31–Apr 3
Li, X.	Assimilation of CYGNSS wind data for improving tropical convection forecasts	99th Annual Meeting, American Meteorological Society, Phoenix, AZ	2019
Liu, Y.; Collett, I.; Morton, Y. J.	Application of neural network to GNSS-R wind speed retrieval	*IEEE Transactions on Geoscience and Remote Sensing, 57*(12), 9756–9766, https://doi.org/10.1109/TGRS.2019.2929002	2019
Mayers, D.; Ruf, C. S.	Determining tropical cyclone center location with CYGNSS wind speed measurements	*Proceedings of the 2019 International Geoscience and Remote Sensing Symposium*, Yokohama, Japan, https://doi.org/10.1109/IGARSS.2019.8900346	2019 Jul
Mayers, D.; Ruf, C. S.	Tropical cyclone center fix using CYGNSS winds	*Journal of Applied Meteorology and Climatology*, https://doi.org/10.1175/JAMC-D-19-0054.1	2019
McKague, D.; Ruf, C. S.	On-Orbit Trending of CYGNSS Data	*Proceedings of the 2019 International Geoscience and Remote Sensing Symposium*, Yokohama, Japan, https://doi.org/10.1109/IGARSS.2019.8898395	2019 Jul
Natoli, M. B.; Maloney, E. D.	Intraseasonal variability of the diurnal cycle of precipitation in the Philippines	*Journal of the Atmospheric Sciences, 76*, 3633–3654	2019
Riley Dellaripa, E. M.; Maloney, E. D.; Toms, B. A.; Saleeby, S. M.; van den Heever, S. C.	Topographic effects on the Luzon diurnal cycle during the BSISO	100th Annual Fall Meeting, American Geophysical Union, San Francisco, CA	2019
Roberts, J. B.; Lang, T. J.	Use of Kalman filtering to improve CYNSS air-sea interaction applications	99th Annual Meeting, American Meteorological Society, Phoenix, AZ	2019
Ruf, C. S.	Assimilation of TC inner core surface winds by CYGNSS into forecast models	Asia Oceania Geosciences Society 16th Annual Meeting, Singapore	2019 Jul
Ruf, C. S.; Asharaf, S.; Balasubramaniam, R.; Gleason, S.; Lang, T.; McKague, D.; Twigg, D.; Waliser, D.	In-orbit performance of the constellation of CYGNSS hurricane satellites	*Bulletin of the American Meteorological Society*, 2009–2023, https://doi.org/10.1175/BAMS-D-18-0337.1	2019 Oct
Ruf, C. S.; McKague, D.; Gleason, S.	CYGNSS SmallSat mission design, engineering performance and science results	*Proceedings of the 2019 International Geoscience and Remote Sensing Symposium*, Yokohama, Japan, https://doi.org/10.1109/IGARSS.2019.8900271	2019 Jul

(continued)

Author(s)	Title	Conference/journal	Date
Ruf, C. S.; McKague, D.; Morris, M.; Posselt, D.; Moghaddam, M.	The GNSS-R CYGNSS mission: An update	*Proceedings of the 2019 International Geoscience and Remote Sensing Symposium, Yokohama, Japan,* https://doi.org/10.1109/IGARSS.2019.8900604	2019 Jul
Wang, T.; Ruf, C.; Gleason, S.; Block, B.; McKague, D.; O'Brien, A.	A real-time EIRP Level 1 calibration algorithm for the CYGNSS mission using the zenith measurements	*Proceedings of the 2019 International Geoscience and Remote Sensing Symposium, Yokohama, Japan,* https://doi.org/10.1109/IGARSS.2019.8900456	2019 Jul
Warnock, A.; Ruf, C.	Response to variations in river flowrate by a spaceborne GNSS-R river width estimator	*Remote Sensing, 11*(20), 2450, https://doi.org/10.3390/rs11202450	2019
Zhu, J.; Tsang, L.; Xu, H.	A physical patch model for GNSS-R land applications	*Progress in Electromagnetics Research, 165,* 93–105, https://doi.org/10.2528/PIER19031003	2019
Adames, A. F.; Kim, D.; Maloney, E. D.; Sobel, A. H.	The moisture mode framework of the Madden-Julian oscillation	*The Global Monsoon System,* C.-P. Chang et al., eds.	2020
Annane, B.; McNoldy, B.; Leidner, S.; Hoffman, R.; Atlas, R.; Majumdar, S.	A study of the HWRF analysis and forecast impact of realistically simulated CYGNSS Observations assimilated as scalar wind speeds and as VAM wind vectors	*Monthly Weather Review, 146,* 2221–2236	2020
Balasubramaniam, R.; Ruf, C.	Characterization of rain impact on L-band GNSS-R ocean surface measurements	*Remote Sensing of Environment, 239*(15), https://doi.org/10.1016/j.rse.2019.111607	2020
Bui, H. X.; Maloney, E. D.; Riley Dellaripa, E. M.; Singh, B.	Wind speed, surface flux, and intraseasonal convection coupling from CYGNSS data	*Geophysical Research Letters, 47,* e2020GL090376, https://doi.org/10.1029/2020GL090376	2020
Campbell, J.; Melebari, A.; Moghaddam, M.	Modeling the effects of topography on delay-Doppler maps	*IEEE Journal of Selected Topics in Applied Earth Observations and Remote Sensing, 13*(12), 1740–1751, https://doi.org/10.1109/jstars.2020.2981570	2020
Carreno-Luengo, H.; Ruf, C.; Warnock, A.; Brunner, K.	Investigating the impact of coherent and incoherent scattering terms in GNSS-R delay Doppler maps	*Proceedings of the 2020 International Geoscience and Remote Sensing Symposium, virtual,* https://doi.org/10.1109/IGARSS39084.2020.9324404	2020 Oct
Clarizia, M. P.; Ruf, C. S.	Statistical derivation of wind speeds from CYGNSS data	*IEEE Transactions on Geoscience and Remote Sensing,* https://doi.org/10.1109/TGRS.2019.2959715	2020
Gleason, S.; O'Brien, A.; Russel, A.; Al-Khaldi, M. M.; Johnson, J. T.	Geolocation, calibration and surface resolution of CYGNSS GNSS-R land observations	*Remote Sensing, 12*(8), 1317, https://doi.org/10.3390/rs12081317	2020
Hoseini, M, Asgarimehr, M.; Zavorotny, V.; Nahavandchi, H.; Ruf, C.; Wickert, J.	First evidence of mesoscale ocean eddies signature in GNSS reflectometry measurements	*Remote Sensing, 12*(3), 542. https://doi.org/10.3390/rs12030542	2020

Author(s)	Title	Conference/journal	Date
Huang, F.; Garrison, J. L.; Leidner, S. M.; Annane, B.; Hoffman, R. N.; Grieco, G.; Stoffelen, A.	A forward model for data assimilation of GNSS ocean reflectometry delay-Doppler maps	*IEEE Transactions on Geoscience and Remote Sensing*, https://doi.org/10.1109/TGRS.2020.3002801	2020
Jiang, X.; Adames-Corraliza, A.; Kim, D.; Maloney, E.; Lin, H.; Kim, H.; Zhang, C.; DeMott, C.; Klingaman, N.	Fifty years of research on the Madden-Julian oscillation: Recent progress, challenges, and perspectives	*Journal of Geophysical Research, 125*, e2019JD030911	2020
Kim, D.; Maloney, E. D.; Zhang, C.	MJO propagation over the maritime continent	*The Global Monsoon System*, 4th ed., C.-P. Chang et al., eds.	2020
Lang, T. J.	Comparing winds near tropical oceanic precipitation systems with and without lightning	*Remote Sensing, 12*, 3968. https://doi.org/10.3390/rs12233968	2020
Li, X.; Mecikalski, J.; Lang, T.	A study on assimilation of CYGNSS wind speed data for tropical convection during 2018 January MJO	*Remote Sensing, 12*, 1243. https://doi.org/10.3390/rs12081243	2020
Mayers, D.; Ruf, C. S.	Estimating the true maximum sustained wind speed of a tropical cyclone from spatially averaged observations	*Journal of Applied Meteorology and Climatology*, https://doi.org/10.1175/JAMC-D-19-0177.1	2020
Reynolds, J.; Clarizia, M. P.; Santi, E.	Wind speed estimation from CYGNSS using artificial neural networks	*IEEE Journal of Selected Topics in Applied Earth Observations and Remote Sensing, 13*, art. no. 8984235, pp. 708–716, https://doi.org/10.1109/JSTARS.2020.2968156	2020
Riley Dellaripa, E. M.; Maloney, E. D.; Toms, B.; Saleeby, S.; van den Heever, S. C.	Topographic effects on the Luzon diurnal cycle during the BSISO	*Journal of the Atmospheric Sciences, 77*, 3–30, https://doi.org/10.1175/JAS-D-19-0046.1	2020
Ruf, C.; Carreno-Luengo, H.; Chew, C.; Moghaddam, M.; Warnock, A.	Remote sensing of the terrestrial water cycle with the Cyclone Global Navigation Satellite System (CYGNSS)	*AGU* 2020, https://doi.org/10.1002/essoar.10504786.1	2020
Santi, E.; Paloscia, S.; Pettinato, S.; Fontanelli, G.; Clarizia, M. P.; Comite, D.; Dente, L.; Guerriero, L.; Pierdicca, N.; Floury, N.	Remote sensing of forest biomass using GNSS reflectometry	*IEEE Journal of Selected Topics in Applied Earth Observations and Remote Sensing, 13*, art. no. 9085901, pp. 2351–2368, https://doi.org/10.1109/JSTARS.2020.2982993	2020
Toms, B. A.; van den Heever, S. C; Riley Dellaripa, E. M.; Saleeby, S. M.; Maloney, E. D.	The relationship between the boreal summertime Madden-Julian oscillation and tropical moist convective morphology	*Journal of the Atmospheric Sciences, 33*, 647–667	2020
Wang, Y.; Morton, Y. J.	Coherent GNSS reflection signal processing for high-precision and high-resolution spaceborne applications	*IEEE Transactions on Geoscience and Remote Sensing, 59*(1), 831–842, https://doi.org/10.1109/TGRS.2020.2993804	2020

(continued)

Author(s)	Title	Conference/journal	Date
Xu, H.; Zhu, J.; Tsang, L.; Kim, S. B.	A fine scale partially coherent patch model including topographical effects for GNSS-R DDM simulations	*Progress in Electromagnetics Research, 170, 97–128*, https://doi.org/10.2528/PIER20121201	2020
Al-Khaldi, M. M.; Johnson, J. T.; Gleason, S.; Chew, C.; Gerlein-Safdi, C.; Shah, R.; Zuffada, C.	Inland water body mapping using CYGNSS coherence detection	*IEEE Transactions on Geoscience and Remote Sensing, 59*(9), 7385–7394, https://doi.org/10.1109/tgrs.2020.3047075,2021	2021
Al-Khaldi, M. M.; Johnson, J. T.; Gleason, S.; Loria, E.; O'Brien, A.; Yi, Y.	An algorithm for detecting coherence in Cyclone Global Navigation Satellite System mission Level-1 delay-Doppler maps	*IEEE Transactions on Geoscience and Remote Sensing, 59*(5), 4454–4463, https://doi.org/10.1109/tgrs.2020.3009784	2021
Al-Khaldi, M. M.; Shah, R.; Chew, C.; Johnson, J. T.; Gleason, S.	Mapping the dynamics of the south asian monsoon using CYGNSS's Level-1 signal coherency	*IEEE Journal of Selected Topics in Applied Earth Observations and Remote Sensing, 14, 1111–1119*, https://doi.org/10.1109/jstars.2020.3042170	2021
Asharaf, S.; Waliser, D. E.; Posselt, D. J.; Ruf, C. S.; Zhang, C.; Putra, A. W.	CYGNSS ocean surface wind validation in the tropics	*Journal of Atmospheric and Oceanic Technology, 38, 711–724*, https://doi.org/10.1175/JTECH-D-20-0079.1	2021
Carreno-Luengo, H.	The IEEE-SA Working Group on Spaceborne GNSS-R: Scene study	*IEEE Access*, https://doi.org/10.1109/ACCESS.2021.3089762	2021
Carreno-Luengo, H.; Crespo, J.; Akbar, R.; Bringer, A.; Warnock, A.; Morris, M.; Ruf, C.	The CYGNSS mission: On-going science team investigations	*Remote Sensing, 13*(9), 1814, https://doi.org/10.3390/rs13091814	2021
Carreno-Luengo, H.; Ruf, C. S.	Retrieving freeze/thaw surface state from CYGNSS measurements	*IEEE Transactions on Geoscience and Remote Sensing*, https://doi.org/10.1109/TGRS.2021.3120932	2021
Collett, I.; Wang, Y.; Shah, R.; Morton, Y. J.	Phase coherence of GPS signal land reflections and its dependence on surface characteristics	*Geoscience and Remote Sensing Letters, 19, 1–6*, https://doi.org/10.1109/LGRS.2021.3094407	2021
Crespo, J. A.; Naud, C. M.; Posselt, D. J.	CYGNSS observations and analysis of low-latitude extratropical cyclones	*Journal of Applied Meteorology and Climatology, 60*(4), 527–541, https://doi.org/10.1175/JAMC-D-20-0190.1.	2021
Evans, M. C.; Ruf, C. S.	Towards the detection and imaging of ocean microplastics with a spaceborne radar	*IEEE Transactions on Geoscience and Remote Sensing*, https://doi.org/10.1109/TGRS.2021.3081691	2021
Gerlein-Safdi, C.; Bloom, A. A.; Plant, G.; Kort, E.; Ruf, C. S.	Improving representation of tropical wetland methane emissions with CYGNSS inundation maps	*Global Biogeochemical Cycles, 35*(12), 1–14, https://doi.org/10.1029/2020GB006890	2021
Gleason, S.; Al-Khaldi, M. M.; Ruf, C.; McKague, D. S.; Wang, T.; Russel, A.	Characterizing and mitigating digital sampling effects on the CYGNSS Level 1 calibration	*IEEE Transactions on Geoscience and Remote Sensing*, https://doi.org/10.1109/TGRS.2021.3120026	2021
Huaman, L.; Maloney, E. D.; Schumacher, C.; Kiladis, G. N.	Easterly waves in the East Pacific during the OTREC 2019 field campaign	*Journal of the Atmospheric Sciences, 78, 4071–4088.2021*	2021

Author(s)	Title	Conference/journal	Date
Kim, H.; Lakshmi, V.; Kwon, Y.; Kumar, S.	First attempt of global-scale assimilation of sub-daily scale soil moisture estimates from CYGNSS and SMAP into a land surface model	*Environmental Research Letters, 16,* 074041, https://iopscience.iop .org/article/10.1088/1748-9326/ ac0ddf	2021
Mueller, M.J., Annane, B.; Leidner, S. M.; Cucurull, L.	Impact of CYGNSS-derived winds on tropical cyclone forecasts in a global and regional model	*Monthly Weather Review,* *149*(10):3433–3447	2021
Natoli, M. B.; Maloney, E. D.	Quasi-biweekly extensions of the monsoon winds and the Philippines diurnal cycle	*Monthly Weather Review, 149,* 3939–3960	2021
Naud, C. M., Crespo, J. A.; Posselt, D. J.	On the relationship between CYGNSS surface heat fluxes and the lifecycle of low-latitude ocean extratropical cyclones	*Journal of Applied Meteorology and Climatology, 60*(11), 1575–1590, https://doi.org/10.1175/JAMC-D -21-0074.1	2021
Pascual, D.; Clarizia, M. P.; Ruf, C. S.	Improved CYGNSS wind speed retrieval using significant wave height correction	*Remote Sensing,* https://doi.org/10 .3390/rs13214313	2021
Pascual, D.; Clarizia, M. P.; Ruf, C. S.	Spaceborne demonstration of GNSS-R scattering cross-section sensitivity to wind direction	*Geoscience and Remote Sensing Letters,* https://doi.org/10.1109/ LGRS.2021.3049526	2021
Ren, B.; Zhu J.; Tsang, L.; Xu, H.	Analytical Kirchhoff solutions (AKS) and numerical Kirchhoff approach (NKA) for first-principle calculations of coherent waves and incoherent waves at P band and L band in signals of opportunity (SoOp)	*Progress in Electromagnetics Research, 171,* 35–73, https://doi .org/10.2528/PIER21050607	2021
Riley Dellaripa, E. M.; Funk, A.; Scumacher, C.; Bai, H.; Spangehl, T.	Adapting the COSP radar simulator to compare GCM output and GPM precipitation radar observations	*Journal of Atmospheric and Oceanic Technology, 38,* 1457–1475, https://doi.org/10.1175/JTECH-D -20-0089.1	2021
Riley Dellaripa, E. M.; Maloney, E. D.; Bui, H.; Singh, B.	Intraseasonal variability in precipitation and fluxes across the tropics observed by buoys and CYGNSS	Tropical Pacific Observing Needs to Advance Process Understanding and Representation in Models Workshop, US CLIVAR	2021
Riley Dellaripa, E. M.; Maloney, E. D.; Saleeby, S. M.; Toms, B. A.; DeMott, C.; van den Heever, S. C.	The effects of topography and air-sea feedbacks on the diurnal cycle of convection over Luzon during the BSISO	101st Annual Meeting, American Meteorological Society	2021
Riley Dellaripa, E. M.; Maloney, E. D.; Toms, B. A.; Saleeby, S. M.; van den Heever, S. C.	The effects of topography and air-sea feedbacks on the diurnal cycle of convection over Luzon during the BSISO	34th Conference on Hurricanes and Tropical Meteorology, American Meteorological Society	2021
Roberts, T. M.; Colwell, I.; Shah, R.; Lowe, S.; Chew, C.	GNSS-R soil moisture retrieval with a deep learning approach	*Proceedings of the International Geoscience and Remote Sensing Symposium (IGARSS),* pp. 147–150, https://ieeexplore.ieee.org/ document/9555022	2021 Jul

(continued)

Author(s)	Title	Conference/journal	Date
Ruf. C.; Chew, C.; Gerlein-Safdi, C.; Warnock, A.	Resolving inland waterways with CYGNSS	Proceedings of the 2021 International Geoscience and Remote Sensing Symposium, https://doi.org/10 .1109/IGARSS47720.2021.9554192	2021
Santi, E.; Pettinato, S.; Paloscia, S.; Clarizia, M. P.; Dente, L.; Guerriero, L.; Comite, D.; Pierdicca, N.	Soil moisture and forest biomass retrieval on a global scale by using CYGNSS data and artificial neural networks	*Proceedings of the International Geoscience and Remote Sensing Symposium (IGARSS)*, art. no. 9323896, pp. 5905–5908, 2020, https://doi.org/10.1109/ IGARSS39084.2020.9323896	2021 Jul
Wang, T.; Ruf, C. S.; Gleason, S.; O'Brien, A. J.; McKague, D. S.; Block, B. P.; Russel, A.	Dynamic calibration of GPS effective isotropic radiated power for GNSS-reflectometry Earth remote sensing	*IEEE Transactions on Geoscience and Remote Sensing*, https://doi.org/10 .1109/TGRS.2021.3070238	2021
Wang, Y.; Morton, Y. J.	River slope observation from spaceborne GNSS-R carrier phase measurements: A case study	*Geoscience and Remote Sensing Letters, 19*, 1–5, https://doi.org/10 .1109/LGRS.2021.3127750	2021
Al-Khaldi, M. M.; Johnson, J. T.	Soil moisture retrievals using CYGNSS data in a time-series ratio method: Progress update and error analysis	*IEEE Geoscience and Remote Sensing Letters, 19*, 1–5, https://doi .org/10.1109/lgrs.2021.3086092	2022
Asgarimehr, M.; Arnold, C.; Weigel, T.; Ruf, C.; Wickert, J.	GNSS reflectometry global ocean wind speed using deep learning: Development and assessment of CyGNSSnet	*Remote Sensing of Environment*, https://doi.org/10.1016/j.rse.2021 .112801	2022
Natoli, M. B.; Maloney, E. D.	The tropical diurnal cycle under varying states of the monsoonal background wind	*Journal of the Atmospheric Sciences* (submitted)	2022
Powell, C. E.; Ruf, C. S.; Russel, A.	An improved blackbody calibration cadence for CYGNSS	*IEEE Transactions on Geoscience and Remote Sensing*, https://doi.org/10 .1109/TGRS.2022.3165001	2022
Pu, Z.; Wang, Y.; Li, X.; Ruf, C.; Bi, L.; Mehra, A.	Impacts of assimilating CYGNSS satellite ocean surface wind on prediction of landfalling hurricanes with the HWRF model	*Remote Sensing, 14*, 2118, https://doi .org/10.3390/rs14092118	2022
Santi, E.; Clarizia, M. P.; Comite, D.; Dente, L.; Guerriero, L.; Pierdicca, N.	Detecting fire disturbances in forests by using GNSS reflectometry and machine learning: A case study in Angola	*Remote Sensing of Environment, 270*, art. no. 112878, https://doi.org/10 .1016/j.rse.2021.112878	2022

13. Acronyms

AC	adaptive covariance
ADC	analog to digital convertor
AER	automated event recognition
AGC	automatic gain control
ASCAT	advanced scatterometer
ATBD	Algorithm Theoretical Basis Document
ATS	Absolute Time Sequence
BB	black body
BR	bin ratio
BRCS	bistatic radar cross section
C/A	clear acquisition signal
CCSDS	Consultative Committee for Space Data Systems
CDR	Climate Data Record
CDR	Critical Design Review
CF	netCDF Climate and Forecast (CF) Metadata Convention
CFDP	CCSDS File Delivery Protocol
COAMPS-TC	Coupled Ocean Atmosphere Mesoscale Prediction System model
COARE	Coupled Ocean-Atmosphere Response Experiment
CU	University of Colorado
CYGNSS	Cyclone Global Navigation Satellite System
DAAC	NASA Distributed Active Archive Center
DD	delay-Doppler
DDM	delay-Doppler map
DDMA	delay-Doppler map area
DDMA	delay-Doppler map average
DDMI	delay-Doppler mapping instrument
DEM	Digital Elevation Map
DM	deployment module
DOY	day of year
E2ES	end-to-end simulator
EASE	Equal-Area Scalable Earth
ECEF	Earth-centered, Earth-fixed (coordinate system)
ECI	Earth-centered inertial (coordinate system)
ECMWF	European Centre for Medium-Range Weather Forecasts
EFOV	effective field of view
EIRP	equivalent isotropically radiated power
EM	electromagnetic
EM	engineering model

ENSO	El Niño Southern Oscillation
EOPACE	Electro-Optical Propagation Assessment in Coastal Environments
ERS	European Remote Sensing Satellite
ESSP	Earth System Science Pathfinder program
EUMETSAT	European Organisation for the Exploitation of Meteorological Satellites
FDS	fully developed seas
FFT	Fast Fourier Transform
FM	Flight Model
FOM	figure of merit
FPGA	field-programmable gate array
FSW	Flight Software
GCF	gain correction factor
GCPM	GPS constellation power monitor
GDAS	Global Data Assimilation System
GFDL	Geophysical Fluid Dynamics Laboratory
GFS	Global Forecast System (from NOAA)
GMF	geophysical model function
GNSS	global navigation satellite system
GNSS-R	global navigation satellite system reflectometry
GO	geometric optics
GOES	Geostationary Operational Environmental Satellites
GOTS	government off-the-shelf
GPM	Global Precipitation Measurement satellite
GPS	global positioning system
GPS-R	GPS-reflectometry
WRF	Hurricane Weather Research and Forecasting model
IDL	Interactive Data Language
IDW	integrated delay waveform
IF	intermediate frequency
IFOV	instantaneous field of view
IFREMER	Institut Francais de Recherche pour l'Exploitation de la Mer
IGS	International GNSS Service
IOC	initial operational capability
ISRO	Indian Space Research Organization
ITCZ	intertropical convergence zone
ITOS	Integrated Test and Operations System
ITU	International Telecommunication Union
JPL	Jet Propulsion Laboratory
KA	Kirchhoff approximation

KDP	Key Decision Point		RMSD	root mean squared difference
KEO	Kuroshio Extension Observatory		RMSE	root mean squared error
LES	leading edge slope		RSS	root sum square
LGEM	logistic growth equation model		Rx	receiving
L CP	left-hand circularly polarized		SAR	synthetic aperture radar
L F	latent heat flux		S/C	spacecraft
LNA	low noise amplifier		SCG	storm-centric gridded
LUT	lookup table **LVPS** low-voltage power supply		SDR	Sensor Data Record
			SFMR	stepped frequency microwave radiometer
MD5	Message-Digest Algorithm		S F	sensible heat flux
MERRA	Modern-Era Retrospective Analysis for Research and Applications		S IPS	statistical hurricane intensity prediction scheme
MJO	Madden-Julian Oscillation		SIR	System Integration Review
MOC	Mission Operations Center		SMAP	soil moisture active passive
MOST	Monin-Obukhov similarity theory		SMMR	Scanning Multichannel Microwave Radiometer
MSS	mean square slope		SNC	Sierra Nevada Corporation
MV	minimum variance		SNR	signal-to-noise ratio
NASA	National Aeronautics and Space Administration		SOC	Science Operations Center
NAVGEM	Navy Global Environmental Model		SP	specular point
NBRCS	normalized bistatic radar cross section		SRR	System Requirements Review
NCEP	National Centers for Environmental Prediction		SSA	small slope approximation
			SSA1	small slope approximation of the 1st order
NDBC	National Data Buoy Center		SSC	Swedish Space Corporation
netCDF	Network Common Data Form		SSS	sea surface salinity
NF	noise figure **NHC** National Hurricane Center		SST	sea surface temperature
			STOL	spacecraft test and operations language
NMC	Network Management Center		SV	space vehicle
NOAA	National Oceanic and Atmospheric Administration		SVN	space vehicle number
			SW	significant wave height
NRCS	normalized radar cross section		SwRI	Southwest Research Institute
NSCAT	NASA Scatterometer		TA	time averaging
NWP	numerical weather prediction		TAO	Tropical Atmosphere Ocean Array
OSCAT	Ocean Scatterometer		TBD	to be determined
PDF	probability density function		TC	tropical cyclone
PDR	Preliminary Design Review		TDS	TechDemoSat
PI	principal investigator		TOPEX	Ocean TOPography Experiment
PIRATA: Prediction and Research Moored Array in the Tropical Atlantic			TRITON	Triangle Trans-Ocean Buoy Network
			TRMM	Tropical Rainfall Measuring Mission (and satellite)
PO.DAAC	NASA Physical Oceanography Distributed Active Archive Center		Tx	transmitting
			UK	United Kingdom
POES	Polar-Orbiting Environmental Satellites		UKMET	UK Meteorological Office
PPT	peak power tracker		UM	University of Michigan
PRN	pseudorandom number		USN	Universal Space Network
RCG	range corrected gain		UTC	Coordinated Universal Time
RCS	radar cross section		WAF	Woodward ambiguity function
RFI	radio frequency interference		WGS	World Geodetic System
R CP	right-hand circularly polarized		YSLF	young seas limited fetch
RMS	root mean square			

Appendix: Ocean Surface Bistatic Scattering Forward Model

A.1. Propagation

CYGNSS uses the GPS L1 frequency (1575 MHz), which suffers negligible rain attenuation, even under heavy precipitating conditions. For completeness, the expression for rain path attenuation, G_{rain}, is given by

$$G_{rain} = \exp(-\alpha h (\csc \theta_t + \csc \theta_r)), \qquad (\textbf{A.1})$$

where h is the freezing level in km, α is the specific attenuation (dB km^{-1}), and θ_t and θ_r are elevation angles to the transmitter and receiver, respectively. Note that each of these parameters will vary over the ocean surface, and this spatial variation is included in the complete forward model. For simplicity, the model assumes a constant rain rate from the surface up to the freezing level.

The specific attenuation α is obtained from the International Telecommunication Union (ITU) R838-3 model,

$$\alpha = aR^b, \qquad (\textbf{A.2})$$

where R is the rain rate (mm hr^{-1}) and the coefficients a and b for circular polarization at the GPS L1 frequency are $a = 24.312 \times 10^{-5}$ and $b = 0.9567$. The values of the coefficients have been developed by curve-fitting to power-law coefficients derived from scattering calculations.

Figure A.1 shows a plot of rain attenuation versus rain rate for a freezing level of 6 km. In the figure, each curve corresponds to a different elevation angle (the elevation angle to the receiver and transmitter are assumed to be equal, as would be the case at the specular point [SP]).

It should be noted that in simulated hurricane wind fields, extremely large rain rates have been observed; however, these convective cells are highly localized, move very rapidly, and evolve very quickly. While they can have a high rain rate, it typically lasts for only a few minutes, so the peak rain rates are very high but only occur for brief periods in fast-moving cells. Furthermore, the nature of the GPS ambiguity function causes the rain field to be effectively smoothed over approximately a 20 km area (in the same way as the wind fields are smoothed) so that the effects of small regions of high rain attenuation are effectively reduced.

A.2. Rough Surface Scattering

A.2.1. Introduction

In GPS bistatic radar, the complex amplitude of the received signal (the voltage) is cross correlated with a replica of the
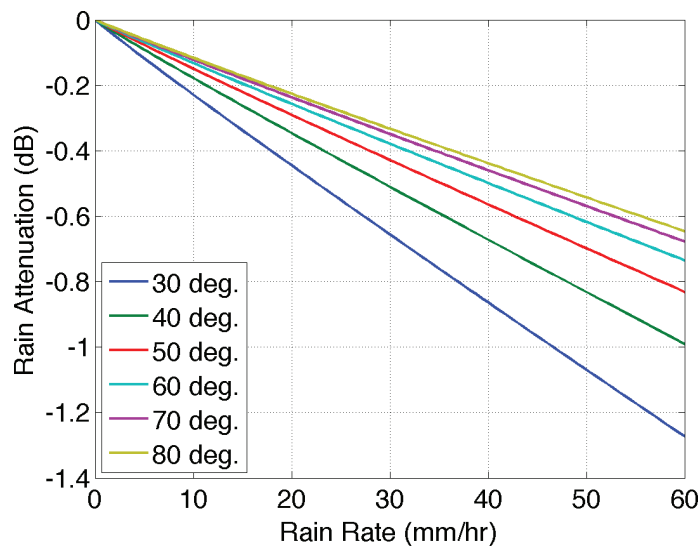
Figure A.1. Rain attenuation versus rain rate for various elevation angles.

emitted signal over a coherent integration time, T_i. This procedure is often referred to as match-filter signal processing. The end result of this type of coherent signal processing is an ability to form a synthetic footprint, which would ultimately determine the shape of the recorded 1D integrated delay waveform (IDW), or 2D delay-Doppler map (DDM), and the spatial resolution of the GPS bistatic radar. For every epoch, t_0, the code cross correlation relative to the received signal, u, taken at a variety of delays, τ, can be expressed as the integral (Parkinson et al., 1996; Zavorotny & Voronovich, 2000):

$$Y(t_0, \tau, f_c) = \frac{1}{T_i} \int_0^{T_i} a(t_0 + t') u(t_0 + t' + \tau) \exp(2\pi i f_c t') dt' \quad \text{(A.3)}$$

Here T_i is the coherent integration time, and $a(t)$ is the replica of the pseudorandom noise (PRN) code sequence taking values of $\{-1, +1\}$ over a time duration, τ_c. The coherent integration time T_i should be comparable to or smaller than the coherence time, τ_{cor}, of the scattered field at the receiver point in order to perform the convolution procedure (Equation A.3) with linear phase shift between replica $a(t)$ and signal $u(t)$. The oscillating factor containing f_c is meant to compensate for a possible Doppler shift of the signal $u(t)$ associated with this phenomenon. For signals received from spacecraft, the signal coherence time τ_{cor}, has been observed to be on the order of 1 ms (Gleason et al., 2005, 2006), while signals received from aircraft can remain coherent for considerably longer durations, on the order of 5–10 ms, depending on aircraft speed and altitude.

Only scattered waves with equal time delays and equal Doppler shifts could be successfully aligned with the code replica in order to produce a maximum correlation according to Equation A.3, and this always happens within the so-called glistening zone caused by a random distribution of the surface slopes. The size of the glistening zone is driven by the variance of surface slopes, where the larger the variance of surface slopes, the larger the glistening zone extends across the surface.

The scattering toward the receiver is produced mostly by specular reflections from a statistical ensemble of large-scale (larger than several radio wavelengths) slopes of the surface. Therefore, the strongest scattered signal comes only from the center of the glistening zone near the nominal SP on the mean sea surface. Away from the glistening zone, the contribution from the quasi-specular reflections diminishes, eventually to be replaced with significantly weaker diffraction scattering from a small-scale surface component. This type of scattering can be neglected, as it is too weak to make a significant contribution to the total received signal power. As a result, a geometric optics–Kirchhoff theoretical model can be applied here (Bass & Fuks, 1979). This model represents the signal scattering from a rough ocean surface as a sum of contributions from specularly reflecting surface facets. This approach was used in Zavorotny and Voronovich (2000) to derive a bistatic radar equation for the GPS scattered signal.

The scattered GPS signal, $u(t)$, arriving at the receiver position, $\vec{R}_r$, can then be modeled by the integral taken over the mean sea surface (Zavorotny & Voronovich, 2000),

$$u(\vec{R}_r, t) = \int D(\vec{\rho}) a\left[t - (R_0(t) + R(t))/c\right] g(\vec{\rho}, t) d^2\rho, \quad \text{(A.4)}$$

where $D(\vec{\rho})$ is the amplitude footprint of the receiver antenna; $a(t)$ is the GPS signal PRN code; and $R0(t)$ and $R(t)$ are distances from the transmitter and the receiver, respectively, to some point $(\vec{\rho}, z = \zeta(\vec{\rho}, t))$ on the "smoothed" rough sea surface with an elevation of $\zeta(\vec{\rho}, t)$, fluctuating about the mean surface level. Over the individual local tangent planes, the Earth's curvature is neglected; $\vec{\rho} = (x, y)$; the transmitter and receiver positions are in the $x = 0$ plane, and z is a vertical axis or the plane normal to the surface.

In the Kirchhoff approximation. the function g describes the propagation and scattering processes

$$g(\vec{\rho}, t) = -\Re(\vec{\rho}) q^2 \exp\left[ik(R_0(t) + R(t))\right]/4\pi i R_0 R q_z, \quad \text{(A.5)}$$

where $\Re$ is the Fresnel reflection coefficient; q is an absolute value of the so-called scattering vector $\vec{q} = k(\vec{n} - \vec{m})$, where $k = 2\pi/\lambda$ is the wave number; $\vec{m}$ is the unit vector of the incident wave; and $\vec{n}$ is the unit vector of the scattered wave. Substituting Equation A.5 into A.4 and then into A.3 gives one a correlation complex amplitude $Y(t_0, \tau, f_c)$ of the received signal expressed through the surface realization within a footprint. This amplitude is highly fluctuating due to the Rayleigh fading process. To obtain an average correlation power as a function of a time delay and Doppler frequency offset (also called a delay-Doppler map [DDM]), one needs to take an absolute value square of $Y(t_0, \tau, f_c)$ and integrate it over the accumulation time T_a, which should be much longer than the coherent integration time T_i. It is reasonable to assume that such a temporal averaging is equivalent to averaging over a statistical ensemble of surface elevations. As a result, we arrive at an expression for the delay-Doppler map:

$$DDM(\tau, f) = \left\langle |Y(\tau, f)|^2 \right\rangle = \frac{1}{T_a} \int_0^{T_a} |Y(t_0, \tau, f)|^2 dt_0. \quad \text{(A.6)}$$

Recently, the above approach for deriving a bistatic radar equation for the GPS reflected signal was revisited in order to eliminate a set of limiting assumptions made in it (Voronovich

& Zavorotny, 2018). One of them is the use of the Kirchhoff approximation in geometric optics, which assumes strong diffuse (noncoherent) scattering typical for very rough surfaces. This equation would produce an incorrect result for the case of weak diffuse scattering or in the presence of coherent reflection. It was shown that the assumption of strong diffuse scattering is not necessary in deriving such an equation. To derive a bistatic radar equation, it is necessary to assume that roughness statistics are spatially homogeneous. Thus the new bistatic equation is applicable for a much wider range of surface conditions and scattering geometries. This approach allows one to correctly describe the transition from partially coherent scattering to completely noncoherent, strong diffuse scattering. As shown in Voronovich and Zavorotny (2018), the DDM can be split into two terms, the coherent and incoherent one:

$$DDM_{tot}(\tau, f) = DDM_{coh}(\tau, f) + DDM_{n-c}(\tau, f),$$ **(A.7)**

where

$$DDM_{coh}(\tau, f) =$$

$$\frac{P_T G_T \lambda^2 G_R}{(4\pi)^2 (R_T + R_R)^2} \Lambda^2(\tau) |S(f)|^2 |V_{Fr}|^2 \exp\left(-4R_a^2\right),$$ **(A.8)**

$$DDM_{n-c}(\tau, f) =$$

$$\frac{P_T G_T \lambda^2 G_R}{(4\pi)^3} \iint F(\vec{\rho}) \Lambda^2(\tau, \vec{\rho}) |S(f, \vec{\rho})|^2 R_0^{-2} R^{-2} \sigma_0(\vec{\rho}) d^2\rho.$$ **(A.9)**

Here, P_T is the transmitter power; G_T is the transmit antenna gain; G_R is the receive antenna gain; $\Lambda^2(\tau)$ is the annulus function due to the cross correlation with the replica; and $|S(f)|^2$ is the Doppler zone function due to the relative motions of both the transmitter and receiver with respect to the scattering surface. In the coherent DDM, V_{Fr} is an average Fresnel reflection coefficient, and R_T and R_R are distances from a nominal specular point on the surface to the transmitter and receiver, respectively, whereas in the noncoherent DDM, R_0 and R are distances from a point $\vec{\rho}$ on the surface to the transmitter and receiver, respectively. Also, $\Lambda^2(\tau)$ and $|S(f)|^2$ in the noncoherent DDM are functions of surface coordinates. The $\sigma_0(\vec{\rho})$ is the normalized bistatic radar cross section (NBRCS) of the rough surface, which generally is a function of two angles: the incidence and the scattering angle. Here, in Equation A.9, it is written as a function of surface coordinates.

The reflected signal described by the coherent term is created by the mirrorlike image of the source in the mean reflecting plane, the coherence of which is slightly corrupted by the surface roughness. This reduction of the coherence is described by the term $\exp\left(-4R_a^2\right)$, where $R_a = k\langle \eta^2 \rangle^{\frac{1}{2}} \cos\theta$ is a Rayleigh parameter of the ocean rough surface having η^2 as a variance of surface elevations.

If the surface roughness is small so that $R_a \ll 1$, the coherent term in Equation A.7 will dominate; if the opposite is true, the noncoherent term in Equation A.7 will dominate. For the intermediate case, both terms should be kept. For the L-band signal scattered from the wind-roughened ocean surface, $R_a \sim 1$, depending on the incidence angle, corresponds to the wind speed of 1–3 m/s (and with an absence of swell), which does not often take place in practice. Therefore, the noncoherent scattering prevails in the real scenarios, which will be the main focus of this section.

The noncoherent scattered signal described by Equation A.10 comes from the area formed by the intersection of the iso-range zones (from the annulus function, $\Lambda^2(\tau, \vec{\rho})$) and iso-Doppler zones (from the Doppler zone function, $|S(f, \vec{\rho})|^2$). The width of the iso-range zone depends on the code length (different for course acquisition [C/A] and P codes) and on all relevant geometric parameters of the problem. The width of the Doppler zone depends on the receiver velocity and is inversely proportional to the coherent integration time, as given by $f_{Dop} = 2 / T_i$.

The product of the correlation function $\Lambda(\tau)$ and the Doppler zone function constitutes the Woodward ambiguity function (WAF) originally introdusced in radar techniques. The WAF that enters Equation A.9 is similar to the WAF used in the unfocused synthetic aperture radar (SAR) technique (Elachi, 1988). For fixed positions of the transmitter and the receiver, both WAF and NBRCS are functions of the reference surface S coordinates. The WAF is close to unity within an area formed by the annulus zone and the Doppler zone and tends to zero outside of this area. The geometry of these zones for two different elevation angles for a typical spacecraft receiver is shown in Figures A.2a and A.2b.

A.2.2. Delay and Doppler Coordinate System

Consider the properties of the delay and Doppler zones in more detail. The scattered signal can be thought of as a superposition of components scattered from various points on the sea surface. Each component will have a shift in both the time at which the signal arrives at the receiver (delay shift) and the frequency of the signal (Doppler shift). The
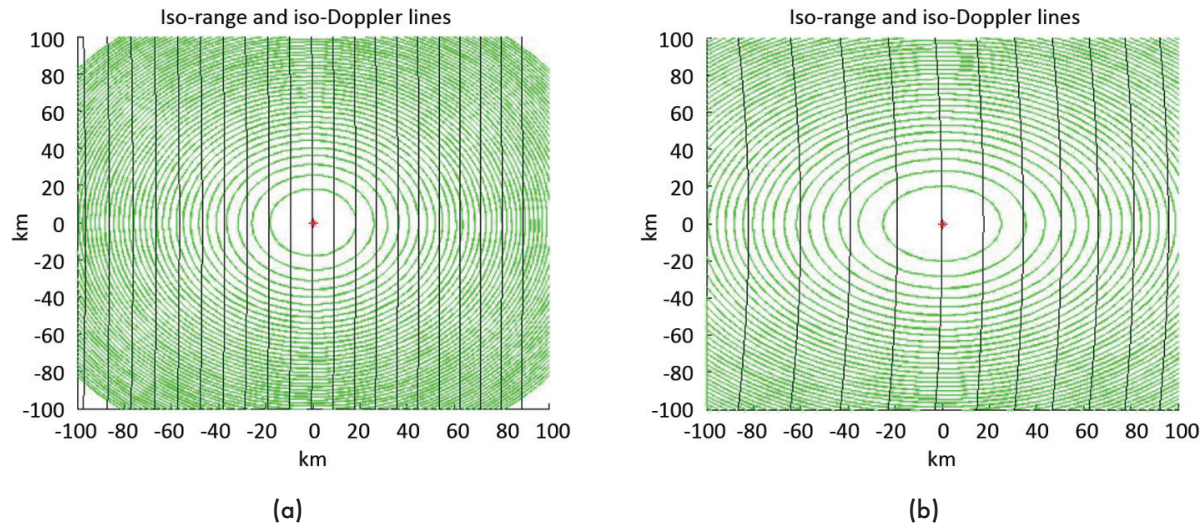
Figure A.2. Surface iso-range and iso-Doppler lines for cases of 10° (a) and 40° (b) incidence. *Figure taken from "GNSS Applications and Methods," Gleason and Gebre-Egziabher (© 2009), reused with authors' permission.*

diversity in delay is due to different paths followed by each scattered signal, while different frequency shifts are caused by the relative motion between the transmitter, the scattering point on the surface, and the receiver. Each point in the glistening zone is therefore characterized by its own delay and Doppler shift.

The pair of delay-Doppler (DD) values with which each point in space can be associated represents a new domain in which the glistening zone can be mapped, and this is referred to as the delay-Doppler domain. Such a domain is fundamental for bistatic radar processing, since it is the domain in which bistatic radar data are commonly presented and mapped in the form of DDMs. However, different points on the sea surface will correspond to the same pair of delay-Doppler values. Lines corresponding to constant delays (iso-range) and constant Doppler shifts (iso-Doppler) can be identified on the sea surface, and they have, respectively, an elliptical and parabolic shape. Lines of constant delays, also called iso-range lines, are given by concentric ellipses around the SP, and they correspond to increasing delays for increasing distance from the SP, which is the point of minimum delay. Rigorously speaking, the iso-range lines are the intersections of spheroids (equi-range surfaces) having the receiver and transmitter as foci with the sea surface, which causes the ellipses to be not exactly concentric as their centers move toward the transmitter (Zuffada et al., 2004). The iso-Doppler lines are parabolic-shaped lines cutting through the glistening zone. They are also asymmetric and characterized by complicated equations, and lines of lower and higher Doppler frequency shifts cannot be predicted, since they strictly depend on the relative velocities among

the transmitter, the scattering point, and the receiver. From Figure A.3, we note that a generic point, P, on the glistening zone can be described by a delay and Doppler coordinate. Such a correspondence is, however, not unique, as there is an ambiguity, since the intersection between an iso-range and iso-Doppler line consists of two points in space, which will have the same delay and Doppler frequency, such as the points P and Q in Figure A.3. Despite that, it is interesting to note that there exists a line free of ambiguity, which can be thought of as the transverse axis of the hyperbolic iso-Doppler lines, shown in red in Figure A.3.

The space-to-DD transformation of coordinates is also what gives the DDM a characteristic horseshoe shape. Such a transformation operates on the spatial domain by "folding" the glistening zone along the free ambiguity line and by "bending" it at the SP, or at the peak power point in the DDM. The scattered power at the SP corresponds, therefore, to the central point of the horseshoe shape, and the horseshoe branches correspond to the scattered power from the glistening zone, with areas farther from the SP spanning larger delays and Doppler shifts.

One other important aspect of the DD coordinate system is its dependence on the geometry and, in particular, on the incidence angle, which strongly influences the configuration of the iso-delay and iso-Doppler lines. Figure A.4 shows the change in the iso-delay contours over a footprint of 100×100 km^2 for different incidence angles, where the incidence angle is the angle between the transmitter or receiver range and the normal to the surface. The iso-delay ellipses tend to stretch out and become wider for higher incidence angles. Here the transmitter and receiver altitudes
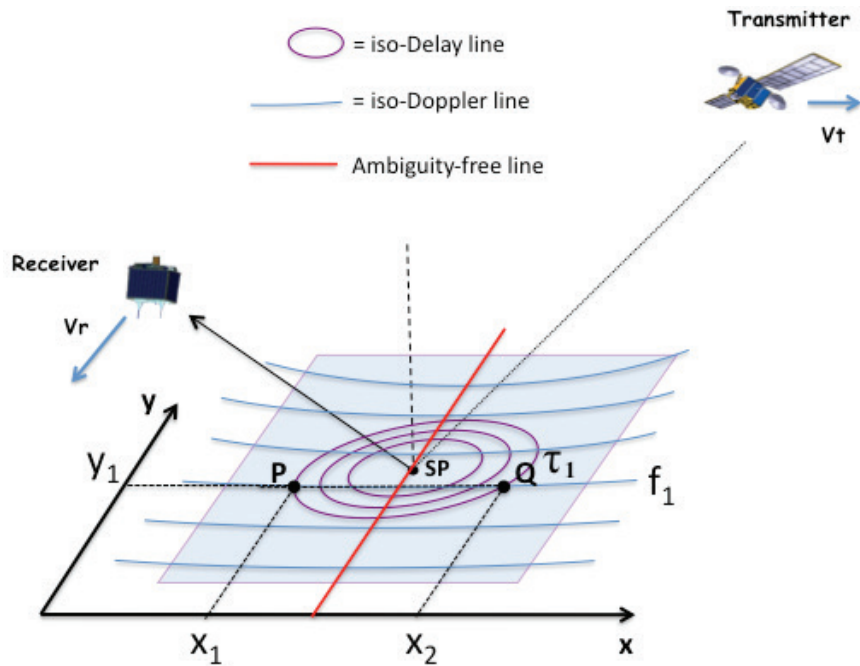
Figure A.3. Delay-Doppler (DD) coordinates in bistatic radar and their relation to the space coordinate system. *Reused from Clarizia and Ruf (2016), © 2016 IEEE.*
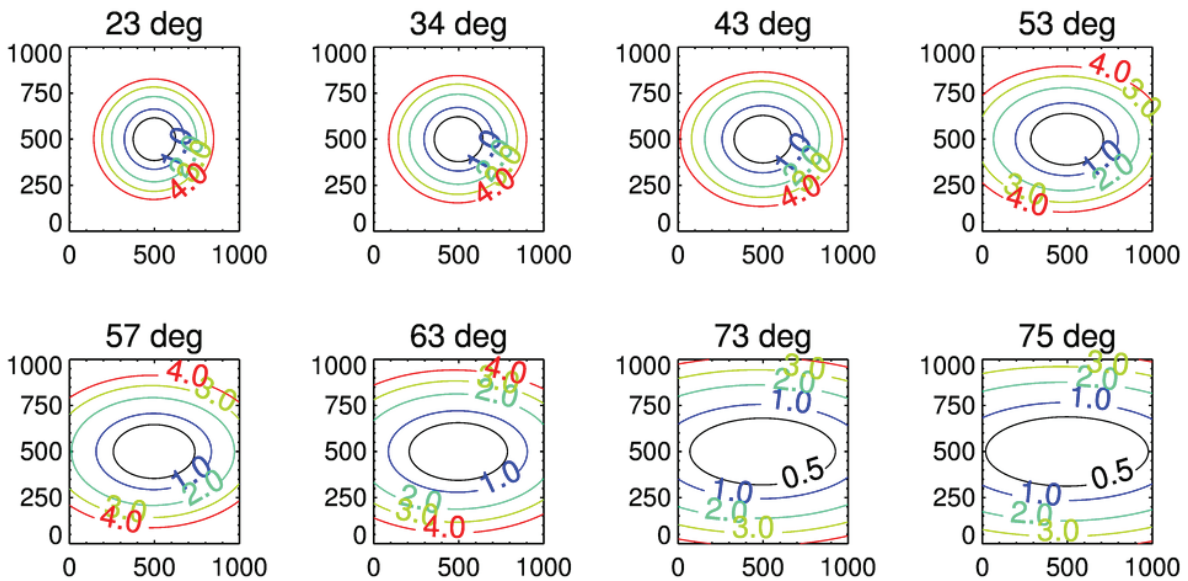
Figure A.4. Iso-delay contours over a footprint of 100 × 100 km for the following incidence angles. Top, left to right: 23°, 34°, 43°, 53°; bottom, left to right: 57°, 63°, 73°, 75°.

have been assumed to be, respectively, equal to that of the GPS satellites (~20,200 km) and 475 km.

Figure A.5 shows the range of maximum delays (a) and maximum Doppler frequencies (b) within a 50 × 50 km footprint as a function of incidence angle. In Figure A.5b, a specific velocity vector has been assumed for the GPS and the receiver satellite. In principle, once the geometry is known (i.e., transmitter and receiver altitudes, incidence angles, and velocity vectors), the range of delays and Doppler frequencies spanned by a footprint of a given size can be calculated numerically.

A.2.3. The Bistatic Radar Cross Section: Geometric Optics (GO) Approximation

The effect of surface roughness is described by σ_0, the NBRCS of the rough surface. In the geometric-optics limit of the Kirchhoff approximation, this term is represented by the following expression (Barrick, 1968; Bass & Fuks, 1979):

$$\sigma_0 = \pi |\mathfrak{R}|^2 \left(q / q_z\right)^4 P\left(-q_\perp / q_z\right) \tag{A.10}$$

Although this value is a function of the scattering vector, $\vec{q}$, for fixed positions of the transmitter and the receiver above a surface, this vector can be regarded as a function of the coordinate $\vec{\rho}$ in the mean surface plane. The value of σ_0 depends on the complex Fresnel coefficient $\mathfrak{R}$, which in turn depends on a signal polarization state; the complex dielectric constant of the reflecting medium, ε; and the local incidence angle. In the case of GPS, the polarization state of the reflected signal is left-hand circularly polarized (LHCP). In this case, the Fresnel reflection coefficient $\mathfrak{R}$ for sea water is (Zavorotny & Voronovich, 2000):

$$\mathfrak{R} = \frac{1}{2} \left[\frac{\varepsilon \cos\theta - \sqrt{\varepsilon - \sin^2\theta}}{\varepsilon \cos\theta + \sqrt{\varepsilon - \sin^2\theta}} - \frac{\cos\theta - \sqrt{\varepsilon - \sin^2\theta}}{\cos\theta + \sqrt{\varepsilon - \sin^2\theta}} \right], \tag{A.11}$$

where ε is the complex dielectric permittivity of sea water, and θ is the local incidence angle.

According to the Klein-Swift model (Klein & Swift, 1977), at S = 35 ppt and T = 10°C ε = 74.62+i51.92 for L1 = 1.57542 GHz; ε = 75.02+i62.39 for L2 = 1.22760 GHz; at S = 30; T = 10 ° C ε = 76.16+i55.30 for L1; and ε = 75.02+i62.39 for L2.

Factor $P(\vec{s})$ in Equation A.10 is the probability density function (PDF) of large-scale "smoothed" surface slopes, $\vec{s} = \nabla_\perp \zeta(\vec{\rho})$. Usually, the most probable orientation of surface slopes is parallel to the mean plane, $z = 0$. Then the PDF has a maximum at $s = 0$, and the bistatic cross section σ_0 has a maximum at $\vec{q}_\perp = 0$—that is, in the nominal specular direction with respect to the mean surface. Note that the width of σ_0 in terms of ρ describes a glistening zone produced by quasi-specular points on the surface.

Some GPS reflection receivers have the capability to sample the waveform only with respect to time delay, τ, while the frequency offset f is fixed and intended to compensate for the Doppler shift associated with the nominal SP on the Earth's surface. In this case, we deal with 1D delay waveforms, as shown in Figures A.6 (a)–(d). The leading edge of such waveforms up to the peak value is produced by the central elliptic annulus zone (filtered by the S function) when it expands from zero to its maximal value. The 1D waveform forms a decreasing trailing edge after the peak because of the WAF's behavior as a function of time lag and/or because of the bistatic radar cross
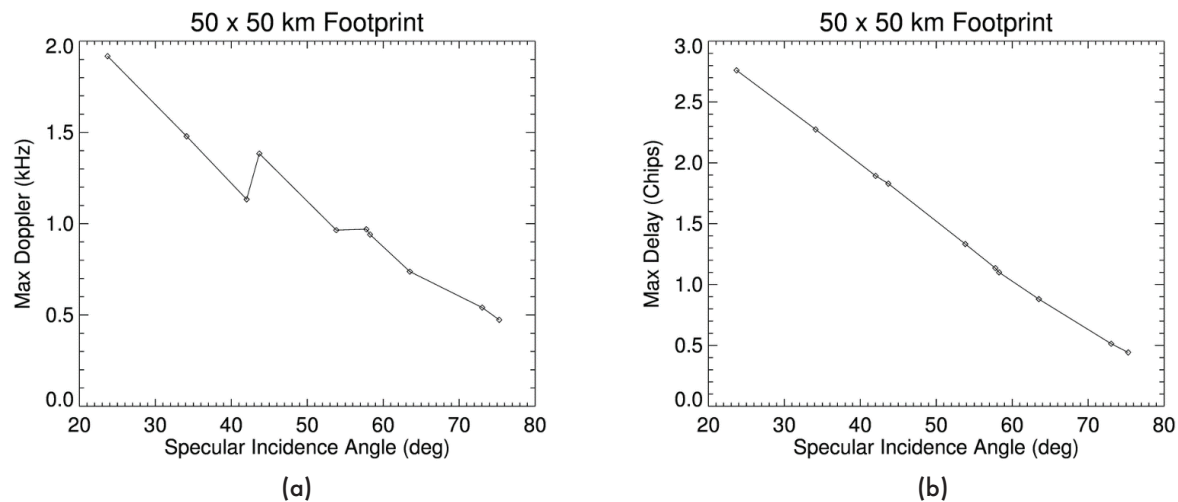
Figure A.5. (a) Maximum delay as a function of incidence angle, within a 50 × 50 km² footprint; (b) maximum Doppler frequency as a function of incidence angle within the same footprint.
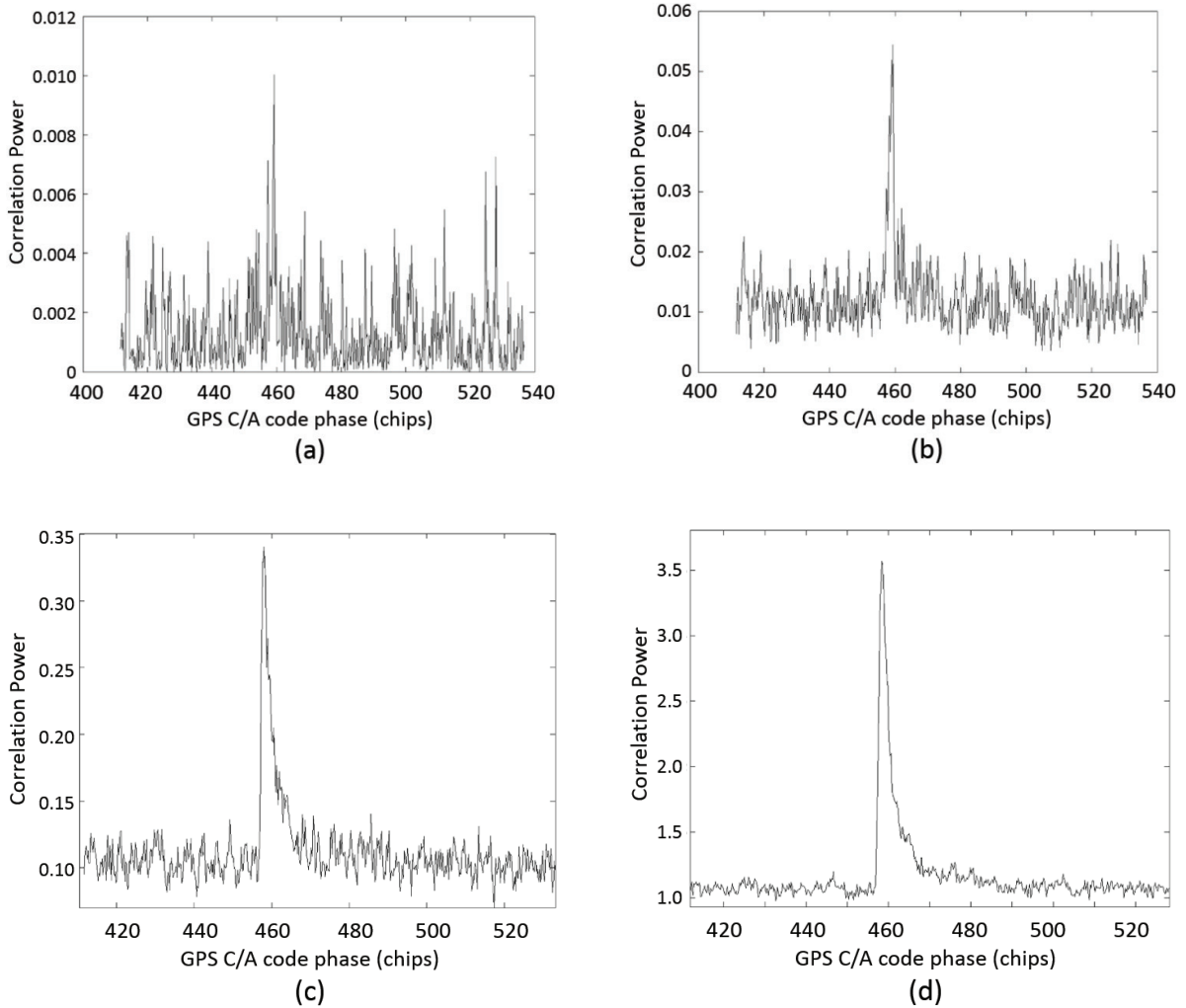
Figure A.6. Examples of global navigation satellite system (GNSS) reflected waveforms observed in the UK Disaster Monitoring Constellation (DMC) satellite experiment on March 23, 2004, for GPS satellite PRN28 using incoherent integration times of (a) 1 ms, (b) 10 ms, (c) 100 ms, and (d) 1 s. *Figure taken from "GNSS Applications and Methods," Gleason and Gebre-Egziabher (© 2009), reused with authors' permission.*

section (BRCS) recession in radial directions according to the distribution of surface slopes. As a result of the latter reason, the specific shape of the leading edge and the exact position of the correlation power peak are functions of surface roughness. For rougher surfaces, the leading edge is more stretched, and the peak is more shifted toward later time lags.

Equation A.9 deals with values obtained by averaging over a limited number of independent samples. Such values themselves contain residual noise, which might affect our ability to accurately measure the average waveform (the issue of noise in waveforms and their impact on the accuracy of remote sensing of ocean wind is addressed

in Section A.3 of this appendix). Equation A.9 relies on the condition that $T_i < \tau_{cor}$. The coherence time can be estimated as $\tau_{cor} = \rho_{coh} / v_r$, where ρ_{coh} is the coherence length of the scattered field at the reception point, and v_r is the velocity of the receiver. According to the Van-Cittert-Zernike theorem, ρ_{coh} in the far zone increases linearly with the distance from the instantaneous footprint patch on a scattering surface. The size of the footprint patch—or in our case, an annulus zone—depends on the current time delay between the replica and the reflected signal. Therefore, a computation of the coherence time becomes a nontrivial problem, which was addressed in Zuffada and Zavorotny (2001) and You et al. (2004, 2006).

The strength of the bistatically scattered signal from the ocean surface is mostly affected by the surface roughness, since variations in salinity of the ocean are rather small. It is believed that for linear surface gravity waves, the slope PDF $P(\vec{s})$ can be approximated by the anisotropic bivariate Gaussian distribution (Zavorotny & Voronovich, 2000; Elfouhaily et al., 2002; Soulat, 2004):

$$P(\vec{s}) = \frac{1}{2\pi\sqrt{\det(M)}} \exp\left[-\frac{1}{2} \begin{pmatrix} s_x \\ s_y \end{pmatrix}^\dagger M^{-1} \begin{pmatrix} s_x \\ s_y \end{pmatrix} \right], \quad \text{(A.12)}$$

where matrix M is

$$M = \begin{pmatrix} \cos\varphi_0 & -\sin\varphi_0 \\ \sin\varphi_0 & \cos\varphi_0 \end{pmatrix} \cdot \begin{pmatrix} \sigma_u^2 & 0 \\ 0 & \sigma_c^2 \end{pmatrix} \cdot \begin{pmatrix} \cos\varphi_0 & \sin\varphi_0 \\ -\sin\varphi_0 & \cos\varphi_0 \end{pmatrix}, \quad \text{(A.13)}$$

where φ_0 is the angle between the up-down wind direction and x-axis, which is chosen here to lie within the incidence plane; σ_u^2 is an upwind mean square slope (MSS; upwind MSS); and σ_c^2 is a cross-wind MSS (cross-wind MSS). $\sigma_{u,c}^2$ are wind dependent and can be derived from a surface elevation spectrum $\Psi(\vec{\kappa})$ by integration over wave numbers K smaller than a scale-dividing wave number κ_*. Sometimes, it is convenient to characterize the statistics of slopes by a single parameter, called a total MSS. There are two definitions of the total MSS. One is the arithmetic mean of the two orthogonal components (Elfouhaily et al., 1997):

$$\sigma_{tot,1}^2 = \sigma_u^2 + \sigma_c^2. \quad \text{(A.14)}$$

Another definition of the total MSS is the geometric mean of the two orthogonal components (Soulat, 2004):

$$\sigma_{tot,2}^2 = 2\sigma_u\sigma_c. \quad \text{(A.15)}$$

Regardless of the wind direction, Equation A.12 can be rewritten in general Cartesian terms as

$$P(\vec{s}) = \frac{1}{2\pi\sigma_x\sigma_y\sqrt{(1-b_{x,y}^2)}}$$
$$\exp\left[-\frac{1}{2(1-b_{x,y}^2)}\left(\frac{s_x^2}{\sigma_x^2} - 2b_{x,y}\frac{s_x s_y}{\sigma_x\sigma_y} + \frac{s_y^2}{\sigma_y^2} \right) \right], \quad \text{(A.16)}$$

where σ_x^2 and σ_y^2 are MSSs of the sea surface for two orthogonal components and $b_{x,y}$ is the correlation coefficient between two slope components:

$$\sigma_{x,y}^2 = \left\langle s_{x,y}^2 \right\rangle = \iint_{\kappa<\kappa_*} \kappa_{x,y}^2 \Psi(\vec{\kappa})d^2\kappa, \quad \text{(A.17)}$$

$$b_{x,y} = \left\langle s_x s_y \right\rangle / \sigma_x\sigma_y, \quad \text{(A.18)}$$

$$\left\langle s_x s_y \right\rangle = \iint_{\kappa<\kappa_*} \kappa_x\kappa_y \Psi(\vec{\kappa})d^2\kappa. \quad \text{(A.19)}$$

The PDF of slopes also can be expressed in terms of the up-/down-wind and across the wind direction components, $\sigma_{u,c}^2$, and angle φ_0, introduced above in Equation A.13. Generally, regardless of the origin of the surface roughness, φ_0 is the angle between the x-axis and the slope distribution principle axis. In the case of locally generated wind waves, angle φ_0 is a wind direction angle. For this representation, it is more convenient to use a polar representation for slopes: $s_x = s\cos\psi, s_y = s\sin\psi$. Then Equation A.16 takes this shape:

$$P_s(s,\psi) = \frac{1}{2\pi\sigma_u\sigma_c}$$
$$\exp\left(-\frac{s^2}{2\sigma_c^2\sigma_u^2}\left[\sigma_u^2 + \sigma_c^2 - 2\left(\sigma_u^2 - \sigma_c^2\right)\cos\varphi_0 \sin\varphi_0 \cos\psi \sin\psi \right] \right). \quad \text{(A.20)}$$

One advantage of a Gaussian distribution is that the variance of slope components in Equations A.16 and A.20 can be derived solely from a wave spectrum, $\Psi(\vec{\kappa})$, of full surface elevations by integrating it over wave numbers, K, which are smaller than a dividing parameter, κ_*.

There are some indications that the actual PDF of slopes does not exactly follow a Gaussian shape at its tails (Cardellach & Ruis, 2008). In terms of the glistening zone, it implies that this departure affects a periphery of the zone. This would translate into some discrepancy for the value of the waveform at relatively large time delays, τ, and large frequency offsets, f. An ability to discern the difference caused by the departure from the Gaussian PDF of slopes depends on the residual noise in the measurements for the peripheral area of the DDM.

One of the most popular models for the spectrum $\Psi(\vec{\kappa})$ is the model proposed by Elfouhaily et al. (1997). The integrand in Equation A.17 is called a slope spectral density. An example of the Elfouhaily et al. (1997) slope spectrum taken along the wind direction is shown in Figure A.7.

This model describes wind-driven waves in deep water under diverse wave age (often called "fetch") conditions and agrees with the in situ observations of the first sun-glint derived wave slope measurements of Cox and Munk (1954),
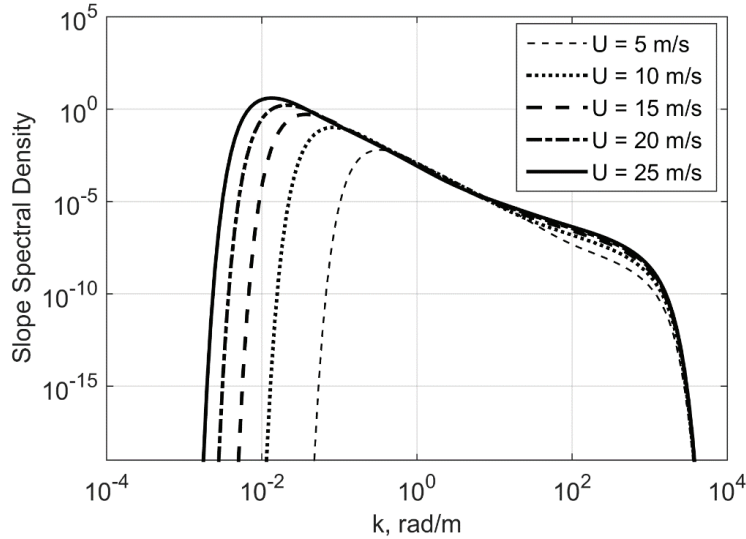
Figure A.7. An example of the Elfouhaily et al. (1997) slope spectrum taken along the wind direction for various wind speed values.

performed several decades ago. According to the Elfouhaily et al. (1997) model, an elevation spectrum of well-developed, wind-driven sea surface can be represented as a product of the radial, or omnidirectional, part of the spectrum and the azimuthal part of the spectrum. The azimuthal part of the spectrum reproduces two main features of the directional spectrum: its anisotropy, or directionality, and the wavenumber dependence of the angular spectral width. The azimuthal part of the spectrum is a two-sided function; it does not distinguish between up- and down-wind directions. There are other situations when wind direction does not coincide with the maximum of the spectrum—for example, when gravity waves undergo refraction on currents or on bathymetry or waves generated by a local wind are superimposed with a swell or waves generated under hurricane conditions. Such complicated scenarios are not described by the Elfouhaily et al. (1997) spectrum. Also, it should be mentioned that the Elfouhaily et al. spectral model describes an average spectrum, which has a nice smooth analytical shape. In reality, the spectrum obtained by sampling wave slope data over a limited ocean area during a short period of time will have a substantial amount of variations.

As was pointed out above, the MSSs that determine the BRCS through the PDF of slopes are not full wave slopes, because the sea surface contains wave harmonic components both larger and shorter than the L-band electromagnetic (EM) waves. The short waves can be disregarded in a process of forward quasi-specular reflection under the GO approximation. Therefore, the full surface spectrum should be cut off at the high end of wave numbers. There are various choices of

cutoff wave numbers, κ_*. For example, there exists a "three-lambda" heuristic criterion for κ_* proposed by Brown (1978) based on fitting modeled curves for microwave backscattering cross sections with cross sections obtained in experiments with satellite radar altimeters. The same criterion was initially applied for use of the Kirchhoff approximation for the two-scale calculations of the bistatic cross sections (Zavorotny & Voronovich, 2000). Later on, a reasonable $\kappa_* = \kappa \cos\theta / 3$ on the incidence angle θ was assumed in Garrison et al. (2002). In Thompson et al. (2005), an expression for κ_* is obtained, which also contains a dependence on wind speed, $\kappa_* = k \cos\theta \left(1 + U_{10} / 20\right) / 7.5$. It was obtained by fitting modeled curves for GPS BRCSs with cross sections obtained in that particular aircraft experiment.

An alternative approach is to obtain an empirical model for the MSS ($\sigma_{u,c}^2$) of slopes versus wind speed by performing multiple measurements of GPS waveforms under controlled wind conditions. The best fit between measured waveforms and modeled ones for various MSS values will give the sought dependence MSS versus wind speed. This approach was adopted in Katzberg et al. (2006). The empirical model from Katzberg et al. (2006) gives the following expression:

$$mss_{\parallel} \equiv \sigma_u^2 = 0.45 \cdot (0.00 + 0.00316 f(U))$$

$$mss_{\perp} \equiv \sigma_c^2 = 0.45 \cdot (0.03 + 0.00192 f(U)), \qquad \textbf{(A.21)}$$

where

$$f(U) = \begin{cases} U & 0.00 < U < 3.49 \\ 6 \cdot \ln(U) - 4.0 & 3.49 < U < 46 \\ 0.411 \cdot U & U > 46.0 \end{cases} . \qquad \textbf{(A.22)}$$

Wind speed U here is m s^{-1} and measured at 10 m height. The extension of $f(U)$ beyond $U = 46$ m s^{-1} proposed in Katzberg et al. (2006) was rather arbitrary because GPS reflection data were not available for such high winds.

In Figure A.8, we present comparisons between MSS calculated using all three approaches: two based on the Elfouhaily et al. (1997) spectrum with two different cutoff numbers κ_* from Garrison et al. (2002) and Thompson et al. (2005) and the empirical one from Katzberg et al. (2006). Normal incidence is assumed here.

Figure A.8 demonstrates a comparison among three GO models for MSS in the up-down wind direction (solid curves) and in the cross-wind direction (dashed curves) for the range of winds between 0 and 25 m/s^{-1}. Some disagreement among them is seen, but overall it is not significant. Figure A.9 shows a comparison among three modeled MSS and MSS retrieved from DDM measurements during aircraft experiments (Rodriguez-Alvarez et al., 2013; Valencia et al., 2014).

In order to make a choice among these three models, we performed calculations of σ_0 using a more accurate (than the GO) approximation—that is, the small slope approximation, SSA1, which does not require the use of spectral dividing parameter κ_*. This material is presented below.
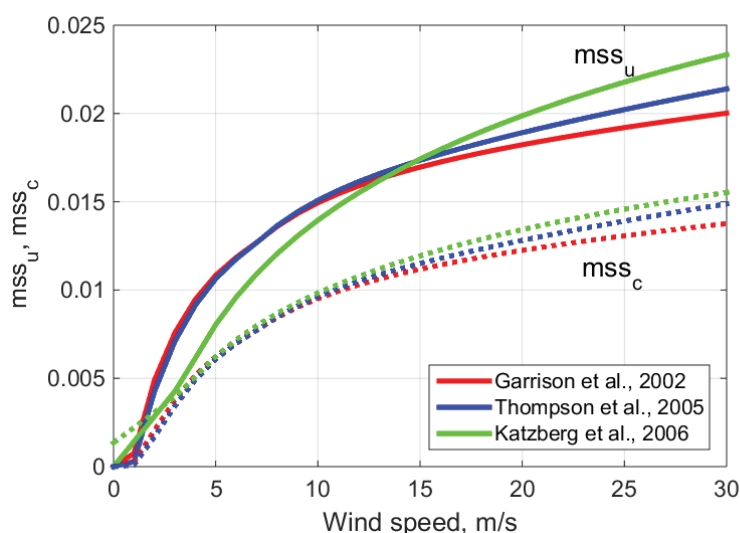
Figure A.8. Comparisons between MSS calculated using three different approaches for normal incidence.
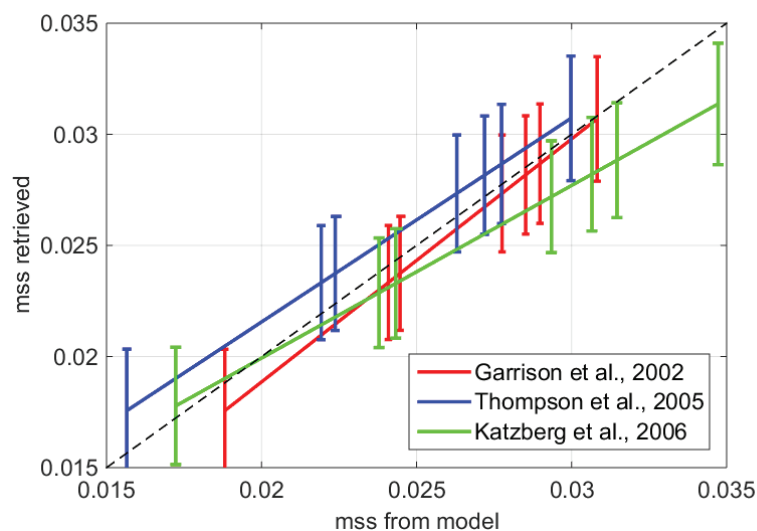
Figure A.9. Comparison between modeled and experimentally measured MSS.

A.2.4. Integrated Scattering Model: The Bistatic Radar Cross Section in SSA

The SSA was developed earlier (Voronovich, 1994, 1999) and was used successfully for solving various scattering and radiometric problems (see, e.g., Voronovich & Zavorotny, 2001; Elfouhaily & Guérin, 2004; Bourlier et al., 2005; Johnson, 2005; Arnold-Bos et al., 2007a; Arnold-Bos et al., 2007b; Johnson & Elfouhaily, 2007; Soriano & Guérin, 2008; Guérin et al., 2010; Johnson & Ouellette, 2014; Voronovich & Zavorotny, 2014). The geometry of the scattering problem is shown in Figure A.10. Three typical scenarios are depicted, although the model considered below allows any possible combination of incident, scattering, and azimuthal angles and arbitrary polarization states. There are two known approximations of the SSA: the SSA of the first order and the SSA of the second order. The latter is more accurate than the former and is required for solving backscattering problems with shorter EM wavelengths such as the X- and K-bands. Practice shows that for the L-band and for the forward scattering regime, it suffices to use the SSA of the first order, or SSA1.

Note that the expression for the scattering amplitude in the SSA1 coincides with the expression for scattering amplitude in the Kirchhoff approximation (KA) to the accuracy of the preintegral factor. The major difference, however, is that KA gives a correct answer only for the roughness $h(\vec{r})$, which is smooth on the wavelength scale; in this case, the corresponding integral can be evaluated by the stationary phase method, thus leading to the GO approximation. The difference between the GO and KA approximations most likely exceeds the accuracy of the KA itself. In contrast to

the KA, SSA1 allows $h(\vec{r})$ to contain a component with a horizontal scale comparable to (or even less than) the wavelength, provided that the slope remains small. In this case, the corresponding integral also describes the Bragg scattering process and cannot be calculated by the stationary phase method.

For the case of a large Rayleigh parameter, when the contribution from the average-field-related terms can be neglected, the SSA1 gives the following expression for the BRCS (Voronovich, 1994; Johnson, 2005; Voronovich & Zavorotny, 2017):

$$\sigma^0_{\alpha\beta,\alpha'\beta'}(\vec{k},\vec{k}_0) =$$

$$\frac{4q_k^2 q_{k_0}^2}{\pi(q_k+q_{k_0})^2} B_{\alpha\beta}(\vec{k},\vec{k}_0) B^*_{\alpha'\beta'}(\vec{k},\vec{k}_0) \exp\left[-(q_k+q_{k_0})^2 W(0)\right]$$

$$-\int_{\rho<\rho_{max}} \exp\left[i(\vec{k}-\vec{k}_0)\vec{\rho}\right]\left[\exp\left[(q_k+q_{k_0})^2 W(\vec{\rho})\right]-1\right]d\vec{\rho}, \quad \textbf{(A.23)}$$

where ρ_{max} determines the area significant for integration. $\alpha,\beta,=1,2$ and $\alpha',\beta'=1,2$ are linear polarization indices for incident and scattering waves, respectively. Function $B_{\alpha,\beta}(\vec{k},\vec{k}_0)$ in Equation A.23 is a 2 × 2 matrix representing polarizations (1 stands for vertical and 2 stands for horizontal linear polarization), respectively; they depend on the scattering geometry and dielectric constant of the medium. Expressions for them can be found in Voronovich and Zavorotny (2001).

Equation A.23 contains the same integral as the expression for σ_0 obtained with the Kirchhoff approximation; the factor in front of the integral is, however, different (see, e.g.,
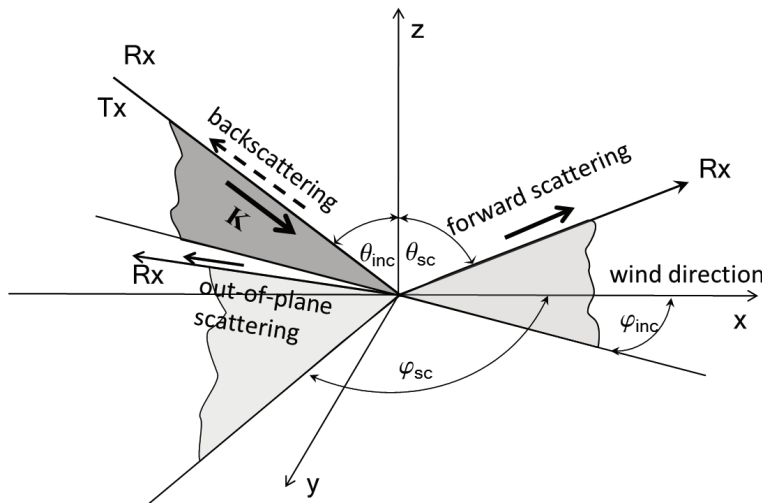
Figure A.10. Bistatic scattering geometry. *Reused from Voronovich and Zavorotny (2014), © 2014 IEEE.*

Voronovich, 1999; Elfouhaily & Guérin, 2004). The most important difference between the Kirchhoff approximation and the SSA1 is that the correlation function in Equation A.23

$$W\left(\vec{\rho}\right)=\left\langle h(\vec{r})h(\vec{r}+\vec{\rho})\right\rangle=\int\exp\left(i\vec{\kappa}\cdot\vec{\rho}\right)\Psi(\vec{\kappa})d\vec{\kappa} \qquad \textbf{(A.24)}$$

is not generally assumed to be slowly varying (on the scale of wavelength) and may contain small-scale components responsible for Bragg scattering. The discussion of the superior accuracy of the SSA compared to the Kirchhoff approximation and discrepancies between them can be found in Voronovich (1999), Elfouhaily and Guérin (2004), Voronovich and Zavorotny (2001), and Voronovich and Zavorotny (2014).

For moderate values of the Rayleigh parameter R_a, the exponential in Equation A.21 can be approximated by a polynomial with a finite number of terms:

$$\exp\left[i(q_k+q_{k_0})^2 W(\vec{\rho})\right]-1\approx\sum_{l=1}^{L}\frac{(q_k+q_{k_0})^{2l}}{l!}W^l(\vec{\rho}). \quad \textbf{(A.25)}$$

Substituting this expansion into Equation A.23 yields

$$\sigma_{\alpha\beta,\alpha'\beta'}^0(\vec{k},\vec{k}_0)=16\pi q_k^2 q_{k_0}^2 B_{\alpha\beta}\left(\vec{k},\vec{k}_0\right)B_{\alpha'\beta'}^*\left(\vec{k},\vec{k}_0\right)$$
$$\times\exp\left[-(q_k+q_{k_0})^2 W(0)\right]\sum_{l=1}^{L}\frac{(q_k+q_{k_0})^{2l-2}}{l!}\Psi^{(l)}(\vec{k}-\vec{k}_0), \qquad \textbf{(A.26)}$$

where

$$\Psi^{(l)}\left(\vec{\kappa}\right)=\frac{1}{(2\pi)^2}\int\exp\left(-i\vec{\kappa}\cdot\vec{\rho}\right)W^l(\vec{\rho})d\vec{\rho}. \qquad \textbf{(A.27)}$$

The calculation of $\sigma_0(\vec{k},\vec{k}_0)$ according to Equation A.26 for a not-too-large L is feasible on desktop computers. The number of series terms L is different for each case of incidence angle and wind speed, and it is determined by the value of the Rayleigh parameter R_a: the larger R_a is, the larger the number L that should be used. Because of this, the numerical implementation based on a summation of series terms in Equation A.26 is more suitable for a regime of weak diffuse scattering characterized by moderate and small values of R_a (low winds). Examples of $\sigma_0(\vec{k},\vec{k}_0)$ calculations for this regime can be found in Voronovich and Zavorotny (2017).

For the case of strong diffuse scattering ($R_a \gg 1$), there exists an approximate but faster method to calculate the SSA1 integral in Equation A.23 developed in Voronovich and Zavorotny (2014). Calculations using the SSA1 integral still require more time than the GO approximation. We use it

here mostly to verify the accuracy of the GO results. In what follows, we will limit our consideration to the case of strong diffuse scattering, which allows linking $\sigma_0(\vec{k},\vec{k}_0)$ to the mean square slope of ocean waves via the GO approximation.

Expressions for the LHCP and right-hand circularly polarized (RHCP) NBRCS can be expressed through corresponding cross sections for linear polarization as follows (Zuffada et al., 2004):

$$\sigma_{RL}^0=\frac{1}{4}\left\{\sigma_{11,11}^0+\sigma_{22,22}^0+\sigma_{12,12}^0+\sigma_{21,21}^0\right.$$
$$\left.+2\left[\mp\text{Re}\sigma_{11,22}^0\pm\text{Re}\sigma_{12,21}^0\mp\text{Im}\left(\sigma_{11,12}^0+\sigma_{11,21}^0+\sigma_{12,22}^0+\sigma_{21,22}^0\right)\right]\right\}. \qquad \textbf{(A.28)}$$

Terms $\sigma_{11,11}^0$, $\sigma_{22,22}^0$ and $\text{Re}\sigma_{11,22}^0$ are dominant, and the rest can be omitted with high accuracy for near specular scattering geometry. Term $\text{Re}\sigma_{11,22}^0$ changes sign when incidence angle θ crosses the pseudo-Brewster angle, which is $\theta_{Br}\approx 84°$ for sea water.

We performed calculations of LHCP BRCS using Equations A.26 and A.28 and compared them with corresponding BRCS based on the above described GO model for a typical CYGNSS setting and for a range of incidence angles and winds. These results are discussed below.

A.2.5. BRCS as Function of the Incidence Angle and Wind: Comparisons of Three Models

Here, we present comparisons between the SSA1 results and results obtained with the GO model, one using an MSS based on the Elfouhaily et al. (1997) spectrum and the cutoff frequency from Garrison et al. (2002) and another one using the empirical MSS model from Katzberg et al. (2006). We will call these two GO models the "VZ model" and the "SK model," respectively. First, we present plots showing the corresponding LHCP NBRCS σ_0 in a forward, specular direction as a function of the zenith scattering angle (which in this case equals the incidence angle) for a range of wind speeds from 4 to 30 m/s[-1]. The results for the VZ, KS, and SSA models are shown in Figures A.11a, A.11b, and A.12, respectively. Each plot has 12 curves. The top curve on each plot corresponds to wind speed $U = 4$ m/s[-1]. The rest of the curves correspond to 5, 6, 7, 8, 9, 10, 12, 15, 20, 25, and 30 m/s[-1] consecutively.

This dependence on wind speed reflects the fact that increased wind produces a stronger surface roughness, which, in turn, decreases scattering in the specular direction. One can see that σ_0 behaves differently for each of these models at scattering angles larger than 60°–70°.

Remember that any of those models are valid at large scattering angles, so we can disregard this discrepancy. For the case of a CYGNSS antenna pointing angle of about 30°, this discrepancy is not relevant. Note that the SK model from Katzberg et al. (2006) was built on GPS reflection data obtained for low incidence/scattering angles, < 45°; therefore, it might not reflect the actual behavior of the scattering at larger angles. At the same time, all three models demonstrate quite similar behavior over wind speeds for angles below 45°.

To investigate this behavior in more detail, we plot the wind dependence of σ_0 for a set of small scattering angles and for a fixed moderate incidence angle below 45°. Of interest is how predictions for σ_0 from all three models correspond to each other for scattering originated from various points on the surface area limited to some number of delay zones that contribute to the DDM. The corresponding scattering geometry is shown in Figure A.13.

Notation in Figure A.13 is as follows. a_n and b_n are major semiaxes of the elliptic delay zones, where index n corresponds to a. They can be expressed through the chip length l, receiver altitude H, and incidence angle θ_{in}:

$$a_n = b_n / \cos\theta_{in}, \quad b_n = \left(2nlH / \cos\theta_{in}\right)^{1/2}. \tag{A.29}$$

Figure A.14 shows how angles $\theta_{sc,min}$, $\theta_{sc,max}$ and ϕ_{sc} from Figure A.13 can be related to the corresponding points on the delay-zone ellipse for a range of delay-zone indices (from 0 to 10). The curves are plotted for $\theta_{in} = 30°$, $H = 600$ km, and $l = 300$ m (or C/A code).

The data callout highlighted in this figure shows that for the first delay zone, the maximum azimuth scattering angle is equal to 2.56°.

In Figure A.15(a–d), we present plots of σ_0 obtained with the three models for $\theta_{in} = 30°$, $H = 600$ km, and four directions of the scattering vector described by the

(a) VZ model   **(b) SK model**
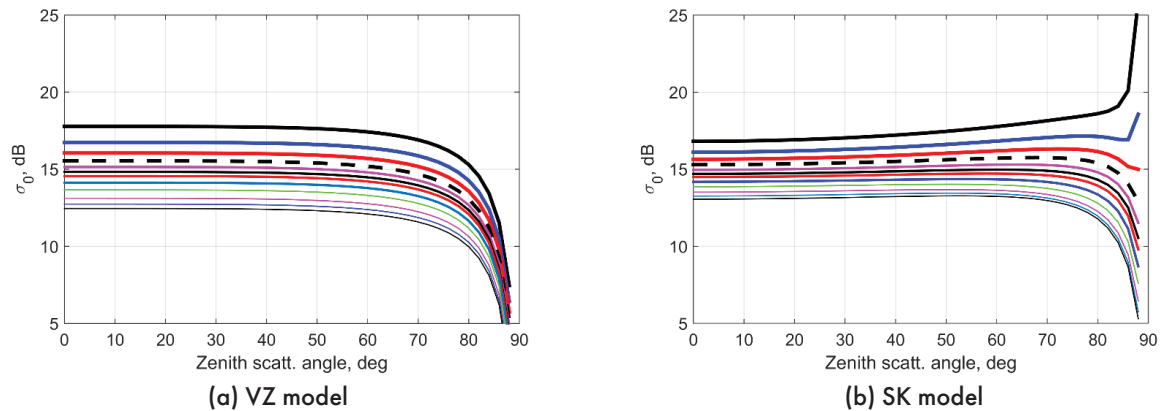
Figure A.11. The LHCP NBRCS σ_0 in a forward, specular direction as a function of the zenith scattering angle for VZ (a) and SK (b) models, respectively. *Reused from Zavorotny and Voronovich (2014), © 2014 IEEE.*
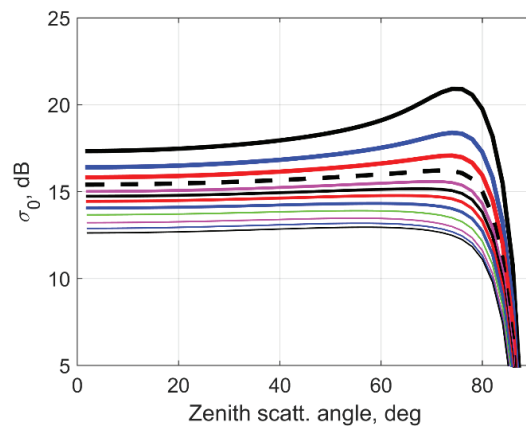
Figure A.12. The LHCP BRCS σ_0 in a forward, specular direction as a function of the zenith scattering angle for the SSA model. *Reused from Zavorotny and Voronovich (2014), © 2014 IEEE.*
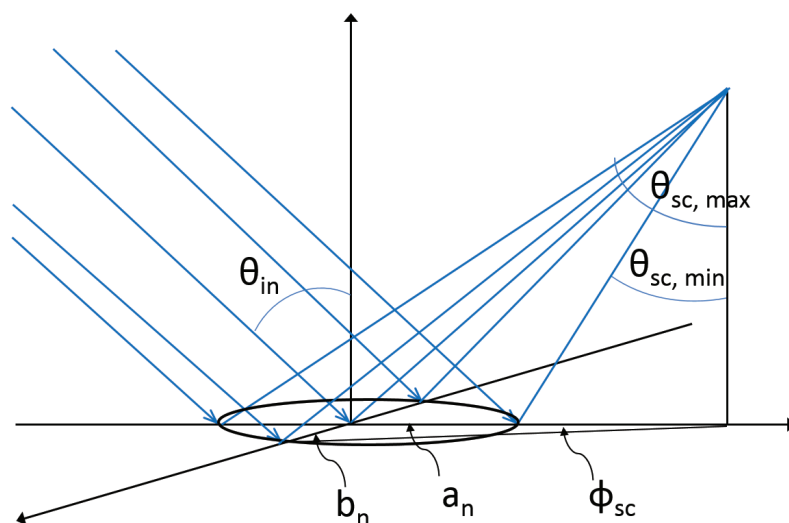
Figure A.13. Scattering geometry, where a_n and b_n are major semiaxes of the elliptic delay zones, where index n corresponds to a.
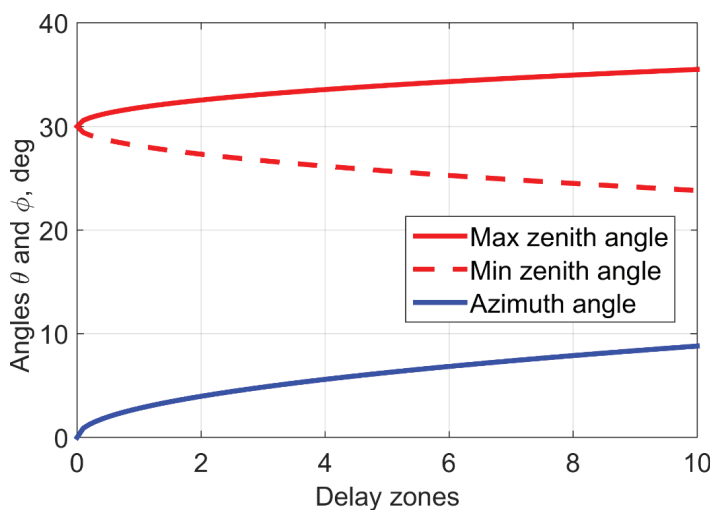
Figure A.14. Relationship between values of scattering and zenith angles and the corresponding points on the delay-zone ellipse for a range of delay-zone indices (from 0 to 10).

following combinations of zenith and azimuth scattering angles: (a) $\theta_{sc} = 30°$, $\phi_{sc} = 0°$; (b) $\theta_{sc} = 30°$, $\phi_{sc} = 2.56°$; (c) $\theta_{sc} = 28°$, $\phi_{sc} = 0°$; and (d) $\theta_{sc} = 32°$, $\phi_{sc} = 0°$. This set of angles gives an angular extent for the first delay zone ($n = 1$). Case (a) describes a nominal specular direction originating from the center of the delay zone. Case (b) describes a scattering direction originating from both the left- and right-most distant (in a cross direction) points of the first delay-zone ellipse. This is an example of out-of-plane scattering. Here, by "plane" we mean a specular plane, which by definition passes through the SP on the surface and both transmitter and receiver points. Case (c) describes a scattering direction

originating from the closest point on the first delay-zone ellipse. Correspondingly, case (d) is for the farthest point on the first delay-zone ellipse.

One can see that the curves in Figure A.15 practically repeat themselves at each panel. This means that while LHCP BRCS σ_0 is changing with the wind speed, it does not appreciably change over the angles within the first delay zone. The discrepancy between curves for all three models are within 0.5 dB for wind speed below 15–17 m/s^{-1}, which is rather negligible given such adverse factors as speckle noise and natural wind speed variability that accompany real measurements. The discrepancy between the SSA curve and the SK
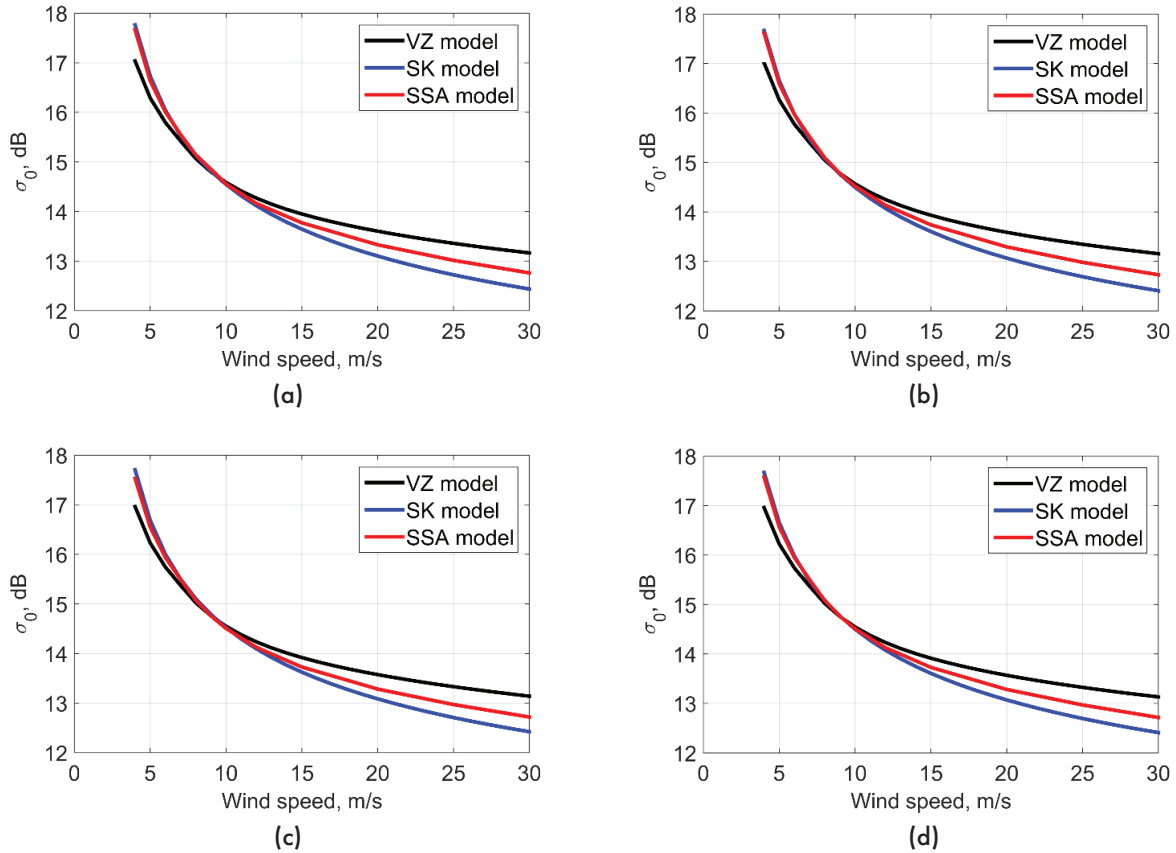
Figure A.15. The LHCP BRCS σ_0 at $\theta_{sc} = 30°$ as a function of wind speed for three models for (a) a nominal specular direction originating from the center of the delay zone; (b) a scattering direction originating from both the left- and right-most distant (in a cross direction) points of the first delay-zone ellipse; (c) a scattering direction originating from the closest point on the first delay-zone ellipse; (d) the farthest point on the first delay-zone ellipse.

curve (which we use in the E2ES) is less than 0.5 dB for the entire range of wind speeds used for this simulation—that is, below 30 m/s^{-1}. More important is that the slopes of these two curves are close to each other, which would result in a similar accuracy of the wind retrievals from the real bistatic radar data.

In Figures A.16(a–d), we present similar plots of σ_0 obtained with the three models for the same basic geometry with an angular extent for the 10th delay zone ($n = 10$). The 10th delay zone covers the surface area, which contributes to the DDM that will be routinely used during the CYGNSS mission. Here, therefore, (a) $\theta_{sc} = 30°$, $\phi_{sc} = 0°$ (this plot repeats plot [a] from the previous figure; it is given for comparison purposes); (b) $\theta_{sc} = 30°$, $\phi_{sc} = 8°$; (c) $\theta_{sc} = 25°$, $\phi_{sc} = 0°$; and (d) $\theta_{sc} = 35°$, $\phi_{sc} = 0°$.

As one can see, there is no significant difference between this set of plots and the one from the previous figure. Therefore, the same statement about σ_0 behavior can be made here for the case of the 10th delay zone.

A.2.6. Chapter Summary

In this chapter, we described how the NBRCS σ_0 of the ocean, wind-driven rough surface emerges within the framework of the bistatic radar equation, which governs the average bistatic radar signal in the delay-Doppler domain. We presented two alternative approaches to simulate σ_0. One of them is based on the GO limit of the KA (Barrick, 1968; Bass & Fuks, 1979), and another one is the Voronovich SSA1 (Voronovich, 1994, 1999; Voronovich & Zavorotny, 2014). The latter approach is superior to the former one because it combines two scattering mechanisms—quasi-specular reflections at steep incidence and the Bragg resonant scattering at the shallower incidence—whereas the GO approximation relies only on the first mechanism for the whole range of incidence angles. Both of these approaches require knowledge of the ocean wave spectrum, or as in the case of the GO approach, the model of the MSS will suffice. To this end, the theoretical model based on Elfouhaily's ocean wave
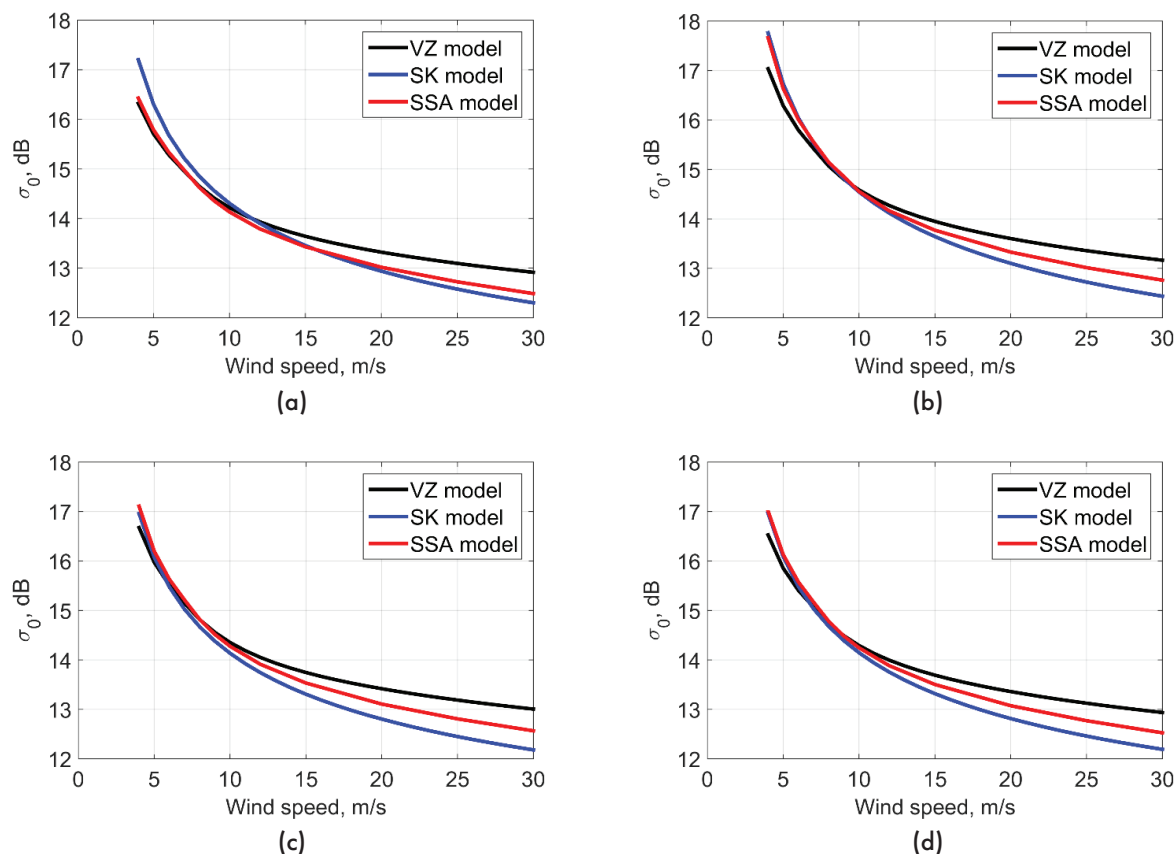
Figure A.16. Same as in Figure A.15 but for an angular extent that corresponds to the 10th delay zone ($n = 10$).

spectrum (Elfouhaily et al., 1997) with two different frequency cutoffs was tested as well as the Katzberg empirical MSS model (Katzberg et al., 2006). All these models demonstrate good agreement for weak and intermediate winds. They depart from each other only for strong winds, and this departure is rather tolerable given such adverse factors as speckle noise and natural wind speed variability that accompany real measurements.

Originally, the Katzberg empirical MSS model was used in the E2ES for simulating DDMs. This choice was made because this model is based on a collection of aircraft GPS reflection measurements obtained for a large variety of wind speeds, including for hurricane conditions. Comparisons between σ_0 modeled with both the GO and the SSA approaches show that for the geometry of CYGNSS orbital observatories and for the range of winds up to 30 m/s^{-1}, the GO approximation with Katzberg's empirical MSS model works very well. The advantage of the GO approximation is its simplicity and high speed of calculations, whereas the SSA approximation is more time consuming. All this makes our choice for the σ_0 computational algorithm even more substantiated.

Previously, some concerns have been expressed (see, e.g., Thompson et al., 2000) that the GO approximation might not work well for the GNSS reflectometry because it cannot properly account for out-of-plane scattering. Generally, the GO approximation has its own limitations, especially for calculations of the RHCP σ_0 and particularly for the out-of-plane configuration. However, as was demonstrated here, for small deviations from the specular plane, the LHCP σ_0 is quite close to the one predicted by the more accurate SSA approximation.

The more fundamental limitation of all of the above models lies in the fact that either they have been proven only for global winds below 25–30 m/s^{-1} (such as for those based on the Elfouhaily et al. [1997] spectrum) or their accuracy is not high for strong hurricane winds (such as in the case of Katzberg's MSS model). For hurricane conditions, a feasible wave-spectral model should include, apart from a local wind speed, also several other parameters, such as a distance from the hurricane center, azimuthal angle (a quadrant), the hurricane velocity, and other hurricane parameters.

Recently, the analysis of MSS retrievals obtained from the airborne GPS reflection data collected during 2008's

Hurricane Ike was performed (Gleason et al., 2018). The detailed study of several GPS-reflectometry (GPS-R) MSS measurement techniques across two eye transects of Hurricane Ike in 2008 was completed. It demonstrated areas of strong and weak wind/wave correlation near and outside the hurricane eye. The finer processing possible with the raw intermediate frequency (IF) sampled data allowed for a detailed comparison of MSS and wind speed fluctuations across the dramatically changing conditions in the hurricane environment. It was found that for these two tracks, the area ahead of the hurricane eye showed stronger correlation between the GPS-R MSS and the flight level and stepped frequency microwave radiometer (SFMR) wind speeds than the area behind it. An empirical relationship between GPSR estimated MSS and SFMR wind speed was derived over the full range of wind speeds present in the hurricane. A conclusion relevant to the CYGNSS mission is made that forward scattered L-band GPS signals can be used to monitor hurricane winds with a speed up to 40 m/s, but the GPS-R measured MSS values may not always correlate well with wind speeds in some areas of a hurricane.

These results underscore the importance of characterization of various sources of MSS retrieval uncertainty, which can be divided into two groups. First, there are factors related to the variability of the transmit signal, uncertainties in parameters of the receiving system, and imperfections in L1 retrieval algorithms. Those factors can be eliminated, or significantly reduced, by improving calibration procedures, performing ancillary measurements, and perfecting the retrieval algorithms. The second group of factors is related to the geophysical uncertainty in the spatial distribution of the MSS field. Among the most important factors are the presence of nonlocal swell and variations in wave development (limited fetch). Other factors may include currents, surfactants, and bathymetry.

Recently, a closed-loop L2 wind retrieval algorithm was proposed (Wang et al., 2018). It aims to exclude the effect of the nonlocal swell and limited fetch from the retrieved MSS. The approach is based on the calculation of an excess MSS responsible for the sea-state development effects using the IFREMER implementation of the WAVEWATCH III (WW3) numerical model (WAVEWATCH III Development Group, 2016) and subtracting it from the CYGNSS measured MSS. The resulting MSS then should be dependent only on the local wind speed. This may lead to the development of more accurate geophysical model functions (GMFs) for the GNSS wind retrievals.

A.3. Statistics of the GPS Reflected Signal

A.3.1. Mean Power and Signal-to-Noise Ratio

Let us represent the instantaneous complex signal (the voltage) u, which is acquired directly by the receiver from the antenna output, or as a result of some coherent processing, in the form

$$u(t) = s(t) + n(t), \tag{A.30}$$

where $s(t)$ is the complex amplitude of the scattered signal and $n(t)$ is the complex amplitude of the additive noise. We assume that $s(t)$ and $n(t)$ are two uncorrelated, stationary random processes; both obey circular Gaussian statistics; and both have different time scales and different variances $\sigma_1^2 \equiv \sigma_{\mathrm{Re}\,s}^2 \equiv \sigma_{\mathrm{Im}\,s}^2$ and $\sigma_2^2 \equiv \sigma_{\mathrm{Re}\,n}^2 \equiv \sigma_{\mathrm{Im}\,n}^2$, with zero means. The Gaussian statistics for $s(t)$ can be justified if the signal at the antenna is formed by contributions from a large number of independent surface scatterers. Here, we exclude from consideration fluctuations of the signal caused by propagation through ionospheric and tropospheric irregularities. Fluctuations of $s(t)$ generate multiplicative, self-noise (also called interference noise, Rayleigh fading, and speckle noise), which are proportional to the signal, whereas fluctuations of $n(t)$ produce additive, background noise (i.e., thermal noise or shot noise). In a more complex situation, the additive noise could include extraneous emitted signals. So in what follows, we limit that background noise to thermal noise.

A coherent processing of the scattered GPS signal by the correlator channel of the CYGNSS receiver consists of the convolution (correlation) of voltage $u(t)$ with the replica a of the GPS broadcast signal over a relatively short (milliseconds) coherent integration time T_i:

$$Y(t_0, \tau) = \frac{1}{T_i} \int_0^{T_i} a(t_0 + t') u(t_0 + t' + \tau) dt'. \tag{A.31}$$

Taking into account Equation A.30, we obtain from Equation A.31 that

$$Y(t_0, \tau) = Y_s(t_0, \tau) + Y_n(t_0, \tau), \tag{A.32}$$

where

$$Y_s(t_0, \tau) = \frac{1}{T_i} \int_0^{T_i} a(t_0 + t') s(t_0 + t' + \tau) dt', \tag{A.33}$$

$$Y_n(t_0, \tau) = \frac{1}{T_i} \int_0^{T_i} a(t_0 + t') n(t_0 + t' + \tau) dt'. \tag{A.34}$$

Therefore, the quantities in Equations A.33 and A.34 are short-integrated (practically instantaneous) correlation voltages, respectively, for the signal and noise. The next step of the signal processing is obtaining the mean power of the correlator output. It is obtained by an additional averaging of $\left|Y(t_0,\tau)\right|^2$ over a long enough observation time, so both thermal and surface-induced fluctuations are substantially averaged out. The result is

$$\left\langle\left|Y(t_0,\tau)\right|^2\right\rangle=\left\langle\left|Y_s(t_0,\tau)\right|^2\right\rangle+\left\langle\left|Y_n(t_0,\tau)\right|^2\right\rangle. \tag{A.35}$$

The first term in Equation A.35 is an average signal introduced above in Equation A.7. The second term in Equation A.35 is the background noise term. It can be written as a double integral over the coherent integration time:

$$\left\langle\left|Y_n(t_0,\tau,f)\right|^2\right\rangle=\frac{1}{T_i^2}\int_0^{T_i}dt'\int_0^{T_i}dt''a(t_0+t',f)a(t_0+t'',f)$$

$$\times\left\langle n(t_0+\tau+t')n^*(t_0+\tau+t'')\right\rangle. \tag{A.36}$$

Assume that the thermal noise is the "white" (δ-correlated) noise—that is,

$$\left\langle n(t')n^*(t'')\right\rangle=kT°B_nb_n(t'-t''), \tag{A.37}$$

where k is Boltzmann's constant, $T°$ is the receiver noise equivalent temperature in Kelvin, $B_n=1/T_{cor}$ is the receiver-front-end bandwidth, and T_{cor}, is a temporal correlation scale of the noise filtered by the front end:

$$; \int_0^{T_i}b_n(t)dt=T_{cor}. \tag{A.38}$$

Here $W_n(f)$ is the normalized temporal spectrum of the noise. Usually, background noise has a much smaller temporal correlation scale, T_{cor}, than the C/A chip length, $\tau_{chip}=1\,\mu$s. Or in other words, the noise bandwidth is much greater than the bandwidth of the C/A pseudorandom phase modulation of the GPS signals. Then we can regard function $b_n(t'-t'')$ as a δ function, so two integrations over time can be performed trivially. The result is

$$\left\langle\left|Y_n(t_0,\tau,f)\right|^2\right\rangle=kT°B_D, \tag{A.39}$$

where $B_D=1/T_i$ is the Doppler bandwidth of the signal.

The thermal noise is correlated between delay-Doppler bins. The cross-correlation function between the noise in different bins is given by

$$\left\langle Y_n(t_0,\tau,f)Y^*{}_n(t_0,\tau',f')\right\rangle=\frac{1}{T_i^2}\int_0^{T_i}dt'\int_0^{T_i}dt''a(t_0+t',f)a^*(t_0+t'',f')$$

$$\times\left\langle n(t_0+\tau+t')n^*(t_0+\tau'+t'')\right\rangle \tag{A.40}$$

Since the noise is uncorrelated with the reference signal, the reference signal acts as a filter for the noise, causing it to be correlated with respect to delay and Doppler according to the GPS C/A code ambiguity function. Equation A.40 can be reduced to

$$\left\langle Y_n(t_0,\tau,f)Y^*{}_n(t_0,\tau',f')\right\rangle=kT°B_D\Lambda^2(d\tau)\left|S(df)\right|^2. \tag{A.41}$$

In the forward model, zero mean white Gaussian noise is generated with respect to delay and Doppler using the power level in Equation A.9 and then convolved with the ambiguity function to produce the correct bin-to-bin correlations.

Now we can construct the signal-to-noise ratio (SNR). There are various definitions of SNR. We use here the simplest one, which shows how much the mean power of the signal exceeds the mean noise level:

$$SNR=\left\langle\left|Y_s(t_0,\tau)\right|^2\right\rangle\bigg/\left\langle\left|Y_n(t_0,\tau)\right|^2\right\rangle. \tag{A.42}$$

Recall that the SNR is the function of parameters τ and f_{dop}—that is, the SNR is different for different portions of waveforms taken at different time delays and Doppler frequency offsets.

A.3.2. Statistics of the Partially Averaged Reflections From Thermal and Speckle Noise

Previously, we considered the effect of additive thermal noise on the average SNR. It exists due to the physical temperature of both the receiver and the scene even in the absence of the GPS reflected signal. Another type of noise, the multiplicative one, is a result of distractive and constructive interference of coherent signals arriving at the antenna upon scattering from a rough ocean surface. It is called Rayleigh fading, or speckle noise, and it is proportional to the signal itself. Below we consider statistics of the partially averaged signal affected by both thermal and speckle noise.

In a real situation, we deal with values averaged over a finite time interval. It happens for at least two reasons. First, any measuring device has a finite time response. Second, signals often need to be accumulated over some time in order to improve the SNR. Since the integration or averaging time is finite, the procedure does not lead to constant time-independent values. These partially averaged values are still random quantities and need to be described

in statistical terms. Note that an instantaneous power U of the signal + noise is not only composed of the sum of the instantaneous powers S and N for the signal and the noise, respectively. It also contains cross terms of s and n. Indeed, according to Equation A.30,

$$U(t) \equiv |u(t)|^2 = \left[s(t) + n(t) \right] \left[s^*(t) + n^*(t) \right] =$$

$$S(t) + N(t) + C(t) + C^*(t), \qquad \text{(A.43)}$$

where

$$C(t) = s(t)n^*(t). \qquad \text{(A.44)}$$

During the measurement, we obtain an estimate of the signal + noise from the power of the received signal + noise averaged over an arbitrary time interval T (a bar above refers to that type of averaging):

$$\overline{U}(t) \equiv \overline{S}(t) + \overline{N}(t) + \overline{C}(t) + \overline{C}^*(t) =$$

$$\frac{1}{T} \int_{-T/2}^{T/2} \left[S(t+t') + N(t+t') + C(t+t') + C^*(t+t') \right] dt'. \qquad \text{(A.45)}$$

An estimate of the signal can be done by obtaining an estimate of the signal + noise, then obtaining an estimate of noise from an independent measurement, and then subtracting one from another:

$$\tilde{S}(t) = \overline{U}(t) - \overline{N}(t_0). \qquad \text{(A.46)}$$

Since these estimates are obtained from an averaging over a finite period of time, the estimate of the signal, $\tilde{S}(t)$, is a fluctuating quantity. The accuracy of the estimate is governed by the variance of estimate $\tilde{S}(t)$. Since $\overline{U}(t)$ and $\overline{N}(t_0)$ are statistically independent, the following equality holds:

$$\sigma_{\tilde{S}}^2 = \sigma_{\overline{U}}^2 + \sigma_{\overline{N}}^2. \qquad \text{(A.47)}$$

Observe that the mean value of the estimated power of the signal + noise is simply

$$\left\langle \overline{U} \right\rangle = \left\langle S \right\rangle + \left\langle N \right\rangle. \qquad \text{(A.48)}$$

The variance of the total power of signal + noise is

$$\sigma_{\overline{U}}^2 = \frac{1}{T^2} \left\langle \left| \int_{-T/2}^{T/2} \left[S(t') + N(t') + C(t') + C^*(t') \right] dt' \right|^2 \right\rangle - \left\langle \overline{U} \right\rangle^2. \qquad \text{(A.49)}$$

The variance of the noise power is

$$\sigma_{\overline{N}}^2 = \frac{1}{T^2} \left\langle \left| \int_{-T/2}^{T/2} N(t') dt' \right|^2 \right\rangle - \left\langle N \right\rangle^2. \qquad \text{(A.50)}$$

Assuming statistical stationarity of both the signal and the noise and making several additional simplifying assumptions, without loss of generality, the standard deviation of the estimated signal power can be obtained in the following form:

$$\frac{\sigma_{\tilde{S}}}{\left\langle S \right\rangle} = \left[\left(1 + 2\left\langle S \right\rangle + 2T_{\text{int}} / \tau_{\text{cor}} \left\langle S \right\rangle^2 \right) / N \right]^{1/2}. \qquad \text{(A.51)}$$

For $T \gg \tau_{\text{cor}}$ the parameter $N = T / \tau_{\text{cor}}$ is the number of correlation intervals contained within the measurement time, T. Or it could be interpreted as a number N of independent samples.

In order to proceed further, we need to choose the value of the correlation time of the signal, τ_{cor}. The approach for calculation of the correlation time is based on the power spectrum of the scattered signal or, equivalently, through the coherence function of the signal that was developed in Zuffada and Zavorotny (2001) and You et al. (2004, 2006).

Actually, the time correlation can be estimated using the Van Cittert-Zernike theorem. From it, it follows that the size of the field correlation zone at the wavelength λ is

$$r_{\text{cor}} = \lambda R / D, \qquad \text{(A.52)}$$

where R is a distance from the surface to the receiver and D is the size of the illuminated area. At the peak correlation power, the illuminated area is the first annulus zone modified by the smaller Doppler zone. The smallest size matters because it created the biggest r_{cor}, which translates into the largest correlation time $\tau_{\text{cor}} = r_{\text{cor}} / v_{\text{sat}}$ (see, e.g., Figure 1 in Zuffada & Zavorotny, 2001). The size of the Doppler zone is dictated by the coherent integration time. The analysis shows that $\tau_{\text{cor}} \approx 2T_i$, therefore, if T_i is 1 ms, $\tau_{\text{cor}} = 2$ ms. Taking this into account, Equation A.51 simplifies to

$$\frac{\sigma_{\tilde{S}}}{\left\langle S \right\rangle} = \left(1 + 2\left\langle S \right\rangle^{-1} + 2T_{\text{int}}\tau_{\text{cor}}^{-1} \left\langle S \right\rangle^{-2} \right)^{1/2} N^{-1/2} \approx \frac{1 + 1/\left\langle S \right\rangle}{\sqrt{N}}. \qquad \text{(A.53)}$$

From here we can produce an expression for the standard deviation of S after incoherent averaging over N statistically independent samples:

$$\sigma_{\tilde{S}} = \frac{\left\langle S \right\rangle + 1}{\sqrt{N}}. \qquad \text{(A.54)}$$

Similarly, the standard deviation of partially averaged SNR is proportional to the average SNR plus one divided by $\sqrt{N}$. In a general case of arbitrary T_{int} and τ_{cor},

$$\sigma_{SNR} = \frac{\sqrt{\langle SNR \rangle^2 + 2SNR + 2T_{int}\tau_{cor}^{-1}}}{\sqrt{N}}. \qquad \textbf{(A.55)}$$

A.4. Simulation of Speckle Noise

The reflected signal received by each CYGNSS observatory is formed by contributions from a large number of independent surface scatterers. This random scattering generates multiplicative self-noise (i.e., Rayleigh fading or speckle noise), which is proportional to the signal. This is in contrast to thermal noise, which is additive. This section describes how this speckle noise is accounted for in the forward model.

Recall the bistatic radar Equation A.9 for the noncoherent component. The expected value of the power of the reflected signal versus delay and Doppler can be rewritten as

$$\left\langle \left| Y_s(t_0, \tau, f) \right|^2 \right\rangle = \iint H(\vec{\rho}) \Lambda^2(\tau, \vec{\rho}) \left| S(f, \vec{\rho}) \right|^2 d^2\rho , \qquad \textbf{(A.56)}$$

where

$$H(\vec{\rho}) = \frac{P_T G_T \lambda^2 G_R}{(4\pi)^3} R_0^{-2} R^{-2} \sigma_0(\vec{\rho}) \qquad \textbf{(A.57)}$$

represents the contribution of each location on the surface to the total expected power of the reflected signal at a particular delay and Doppler.

In the forward model, DDMs are formed from integrations performed over finite time intervals rather than expected values (such as in Equation A.56). We must model the effect of speckle noise, but for the surface areas involved in space-borne GPS reflectometry, it would be unrealistic to instantiate the actual random rough surface and use a computational electromagnetics approach. Rather, we have chosen a suitable one to accurately capture the effects of speckle noise.

First, we take the square root of the power contribution in Equation A.57 and include a time-varying phase term $\phi(t, \rho)$ to make the contribution complex:

$$h(t, \rho) = \sqrt{H(\rho)} e^{j\phi(t,\rho)}. \qquad \textbf{(A.58)}$$

This is an approximate representation of the contribution of each location on the surface to the voltage DDM and can be thought of as the transfer function over the surface. The approximate voltage DDM is given by

$$Y_s(t, \tau, f) = \iint h(t, \vec{\rho}) \Lambda(\tau, \vec{\rho}) S(f, \vec{\rho}) d^2\rho . \qquad \textbf{(A.59)}$$

The DDM is formed by integrating for 1 second, t will be between t_0 and $(t_0 + 1)$, where t_0 is the start of the integration. This produces

$$\left| Y_s(t_0, \tau, f) \right|^2 = \int_{t_0}^{t_0+T} Y_s(t, \tau, f) Y_s^*(t, \tau, f) dt, \qquad \textbf{(A.60)}$$

where $T = 1$. The phase term $\phi(t, \rho)$ must be chosen such that the expectation of Equation A.60 is equal to one from Equation A.56. Also, it must result in the temporal correlation of speckle noise.

First, a random phase, $\phi_0(\rho)$, is associated with each location on the surface. This random phase is assumed to be uniformly distributed between 0 and 2π and represents the phase shift caused by the random rough surface at that location. This phase will evolve in time according to the changing geometry of the satellites. Thus, the total phase associated with the reflection of a particular point on the surface is a combination of the random phase and the phase associated with the total path length,

$$\phi(\rho) = \phi_0(\rho) + \frac{2\pi}{\lambda} R(t, \rho). \qquad \textbf{(A.61)}$$

where λ is the wavelength at the GPS L1 center frequency and $R(t, \rho)$ is the total path length from the transmitter to the surface location at ρ and up to the receiver at time t. Since it is such a short duration, the time variation in the path length can be accurately approximated using the Doppler at the start of the integration $f_D(t_0, \rho)$,

$$R(t, \rho) = R(t_0, \rho) - (t - t_0) \lambda f_D(t_0, \rho). \qquad \textbf{(A.62)}$$

Each point on the surface will exhibit a different time-varying phase depending on the relative motion of the satellites. Over short time delays (e.g., less than one millisecond), the change in geometry will be small, and the speckle noise will remain correlated in time. For longer delays, the speckle noise will be completely decorrelated, as is expected from reflections from a real ocean surface.

A.5. References

Arnold-Bos, A., Khenchaf, A., & Martin, A. (2007a). Bistatic radar imaging of the marine environment—part I: Theoretical background. *IEEE Transactions on Geoscience and Remote Sensing, 45*(11), 3372–3383. https://doi.org/10.1109/TGRS.2007.897436.

Arnold-Bos, A., Khenchaf, A., & Martin, A. (2007b). Bistatic radar imaging of the marine environment—part

II: Simulation and results analysis. *IEEE Transactions on Geoscience and Remote Sensing, 45*(11), 3384–3396. https://doi.org/10.1109/TGRS.2007.899812.

Barrick, D. E. (1968). Relationship between slope probability density function and the physical optics integral in rough surface scattering. *Proceedings of the IEEE, 56*(10), 1728–1729. https://doi.org/10.1109/PROC.1968.6718.

Bass, F. G., & Fuks, I. M. (1979). *Wave scattering from statistically rough surfaces* (Vol. 93). Elmsford, NY: Pergamon.

Bourlier, C., Déchamps, N., & Berginc, G. (2005). Comparison of asymptotic backscattering models (SSA, WCA, and LCA) from one-dimensional Gaussian ocean-like surfaces. *IEEE Transactions on Antennas and Propagation, 53*(5), 1640–1652. https://doi.org/10.1109/TAP.2005.846800.

Brown, G. S. (1978). Backscattering from a Gaussian-distributed perfectly conducting rough surface. *IEEE Transactions on Antennas and Propagation, 26*(3), 472–482. https://doi.org/10.1109/TAP.1978.1141854.

Cardellach, E., & Rius, A. (2008). A new technique to sense non-Gaussian features of the sea surface from L-band bi-static GNSS reflections. *Remote Sensing of Environment, 112*(6), 2927–2937. https://doi.org/10.1016/j.rse.2008.02.003.

Clarizia, M. P., & Ruf, C. (2016). Wind speed retrieval algorithm for the Cyclone Global Navigation Satellite System (CYGNSS) mission. *IEEE Transactions on Geoscience and Remote Sensing, 54*(8), 4419–4432. https://doi.org/10.1109/TGRS.2016.2541343.

Cox, C., & Munk, W. (1954). Measurement of the roughness of the sea surface from photographs of the Sun's glitter. *Journal of the Optical Society of America, 44*(11), 838–850. https://doi.org/10.1364/JOSA.44.000838.

Elachi, C. (1988). *Spaceborne radar remote sensing: applications and techniques.* New York: IEEE Press.

Elfouhaily, T., Chapron, B., Katsaros, K., & Vandemark, D. (1997). A unified directional spectrum for long and short wind-driven waves. *Geophysical Research: Oceans (1978–2012), 102*(C7), 15781–15796. https://doi.org/10.1029/97JC00467.

Elfouhaily, T. M., & Guérin, C. A. (2004). A critical survey of approximate scattering wave theories from random rough surfaces. *Waves in Random Media, 14*(4),

R1–R40. https://doi.org/10.1088/0959-7174/14/4/R01.

Elfouhaily, T., Thompson, D. R., & Linstrom, L. (2002). Delay-Doppler analysis of bistatically reflected signals from the ocean surface: Theory and application. *IEEE Transactions on Geoscience and Remote Sensing, 40*(3), 560–573. https://doi.org/10.1109/TGRS.2002.1000316.

Garrison, J. L., Komjathy, A., Zavorotny, V. U., & Katzberg, S. J. (2002). Wind speed measurement using forward scattered GPS signals. *IEEE Transactions on Geoscience and Remote Sensing, 40*(1), 50–65. https://doi.org/10.1109/36.981349.

Gleason, S. (2006). *Remote sensing of ocean, ice and land surfaces using bistatically scattered GNSS signals from low Earth orbit* (Unpublished doctoral dissertation). University of Surrey.

Gleason, S., Hodgart, S., Sun, Y., Gommenginger, C., Mackin, S., Adjrad, M., & Unwin, M. (2005). Detection and processing of bistatically reflected GPS signals from low Earth orbit for the purpose of ocean remote sensing. *IEEE Transactions on Geoscience and Remote Sensing, 43*(6), 1229–1241. https://doi.org/10.1109/TGRS.2005.845643.

Gleason, S., Zavorotny, V., Akos, D., Hrbek, S., Popstefanija, I., Walsh, E., Masters, D., & Grant, M. (2018). Study of surface wind and mean square slope correlation in Hurricane Ike with multiple sensors. *IEEE Journal of Selected Topics in Applied Earth Observations and Remote Sensing, 11*(6), 1975–1988. https://doi.org/10.1109/JSTARS.2018.2827045.

Guérin, C.-A., Soriano, G., & Chapron, B. (2010). The weighted curvature approximation in scattering from sea surfaces. *Waves in Random and Complex Media, 20*(3), 364–384. http://dx.doi.org/10.1080/17455030903563824.

Johnson, J. T. (2005). A study of ocean-like surface thermal emission and reflection using Voronovich's small slope approximation. *IEEE Transactions on Geoscience and Remote Sensing, 43*(2), 306–314. https://doi.org/10.1109/TGRS.2004.841480.

Johnson, J. T., & Elfouhaily, T. M. (2007). Computation of oceanlike surface thermal emission and bistatic scattering with the reduced local curvature approximation. *IEEE Transactions on Geoscience and Remote Sensing, 45*(7), 2108–2115. https://doi.org/10.1109/TGRS.2006.890420.

Johnson, J. T., & Ouellette, J. D. (2014). Polarization features in bistatic scattering from rough surfaces. *IEEE Transactions on Geoscience and Remote Sensing, 52*(3), 1616–1626. https://doi.org/10.1109/TGRS.2013.2252909.

Katzberg, S. J., Torres, O., & Ganoe, G. (2006). Calibration of reflected GPS for tropical storm wind speed retrievals. *Geophysical Research Letters, 33*(18). https://doi.org/10.1029/2006GL026825.

Klein, L., & Swift, C. T. (1977). An improved model for the dielectric constant of sea water at microwave frequencies. *IEEE Transactions on Antennas and Propagation, 25*(1), 104–111. https://doi.org/10.1109/TAP.1977.1141539.

Parkinson, B. W., Spilker, J. J., Axelrad, P., & Enge, P. (eds.). (1996). *Global positioning system: Theory and applications* (Vol. II). Washington, DC: AIAA.

Rodriguez-Alvarez, N., Akos, D. M., Zavorotny, V. U., Smith, J. A., Camps, A., & Fairall, C. W. (2013). Airborne GNSS-R wind retrievals using delay-Doppler maps. *IEEE Transactions on Geoscience and Remote Sensing, 51*(1), 626–641. https://doi.org/10.1109/TGRS.2012.2196437.

Soriano, G., & Guérin, C.-A. (2008). A cutoff invariant two-scale model in electromagnetic scattering from sea surfaces. *IEEE Geoscience and Remote Sensing Letters, 5*(2), 199–203. https://doi.org/10.1109/LGRS.2008.915746.

Soulat, F. (2004). *Sea surface remote sensing with GNSS and sunlight reflections* (Unpublished doctoral dissertation). Universitat Politecnica de Catalunya.

Thompson, D. R., Elfouhaily, T. M., & Garrison, J. L. (2005). An improved geometrical optics model for bistatic GPS scattering from the ocean surface. *IEEE Transactions on Geoscience and Remote Sensing, 43*(12), 2810–2821. https://doi.org/10.1109/TGRS.2005.857895.

Thompson, D. R., Elfouhaily, T. M., & Gasparovic, R. F. (2000). Polarization dependence of GPS signals reflected from the ocean. In *IGARSS 2000—2000 IEEE International Geoscience and Remote Sensing Symposium* (Vol. 7, pp. 3099–3101). https://doi.org/10.1109/IGARSS.2000.860349.

Valencia, E., Zavorotny, V. U., Akos, D. M., & Camps, A. (2014). Using DDM asymmetry metrics for wind direction retrieval from GPS ocean-scattered signals in airborne experiments. *IEEE Transactions on Geoscience and Remote Sensing, 52*(7), 3924–3936. https://doi.org/10.1109/TGRS.2013.2278151.

Voronovich, A. G. (1994). Small-slope approximation for electromagnetic wave scattering at a rough interface of two dielectric half-spaces. *Waves in Random Media, 4*(3), 337–368. https://doi.org/10.1088/0959-7174/4/3/008.

Voronovich, A. G. (1999). *Wave scattering from rough surfaces* (2nd ed.). Berlin: Springer.

Voronovich, A. G., & Zavorotny, V. U. (2001). Theoretical model for scattering of radar signals in K_u- and C-bands from a rough sea-surface with breaking waves. *Waves in Random Media, 11*(3), 247–269. https://doi.org/10.1080/13616670109409784.

Voronovich, A. G., & Zavorotny, V. U. (2014). Full-polarization modeling of monostatic and bistatic radar scattering from a rough sea surface. *IEEE Transactions on Antennas and Propagation, 62*(3), 1362–1371. https://doi.org/10.1109/TAP.2013.2295235.

Voronovich, A. G., & Zavorotny, V. U. (2017). The transition from weak to strong diffuse radar bistatic scattering from rough ocean surface. *IEEE Transactions on Antennas and Propagation, 65*(11), 6029–6034. https://doi.org/10.1109/TAP.2017.2752219.

Voronovich, A. G., & Zavorotny, V. U. (2018). Bistatic radar equation for signals of opportunity revisited. *IEEE Transactions on Geoscience and Remote Sensing, 56*(3), 1959–1968. https://doi.org/10.1109/TGRS.2017.2771253.

WAVEWATCH III Development Group. (2016). *User manual and system documentation of WAVEWATCH III version 5.16 MMAB* (Technical Note, 326 pp.+App). https://polar.ncep.noaa.gov/mmab/papers/tn276/MMAB_276.pdf.

You, H., Garrison, J. L., Heckler, G., & Smajlovic, D. (2006). The autocorrelation of waveforms generated from ocean-scattered GPS signals. *IEEE Geoscience and Remote Sensing Letters, 3*(1), 78–82. https://doi.org/10.1109/LGRS.2005.856704.

You, H., Garrison, J. L., Heckler, G., & Zavorotny, V. U. (2004). Stochastic voltage model and experimental measurement of ocean-scattered GPS signal statistics. *IEEE Transactions on Geoscience and Remote Sensing, 42*(10), 2160–2169. https://doi.org/10.1109/TGRS.2004.834628.

Zavorotny, V. U., & Voronovich, A. G. (2000). Scattering of GPS signals from the ocean with wind remote sensing

application. *IEEE Transactions on Geoscience and Remote Sensing, 38*(2), 951–964. https://doi.org/10.1109/36.841977.

Zavorotny, V. U., & Voronovich, A. G. (2014, July). Recent progress on forward scattering modeling for GNSS reflectometry. In *Geoscience and Remote Sensing Symposium (IGARSS), 2014 IEEE International* (pp. 3814–3817). https://doi.org/10.1109/IGARSS .2014.6947315.

Zuffada, C., Fung, A., Parker, J., Okolicanyi, M., & Huang, E. (2004). Polarization properties of the GPS signal scattered off a wind-driven ocean. *IEEE Transactions on Antennas and Propagation, 52*(1), 172–188. https://doi.org/10.1109/TAP.2003.822438.

Zuffada, C., & Zavorotny, V. (2001). Coherence time and statistical properties of the GPS signal scattered off the ocean surface and their impact on the accuracy of remote sensing of sea surface topography and winds. In *Geoscience and Remote Sensing Symposium, 2001. IGARSS'01. IEEE 2001 International* (Vol. *7*, pp. 3332–3334). https://doi.org/10.1109/IGARSS .2001.978344.